

TESE EM COTUTELA APRESENTADA  
PARA OBTER O TÍTULO DE  
DOUTOR PELA  
UNIVERSIDADE FEDERAL DE SANTA CATARINA  
E PELA UNIVERSIDADE DE BORDEAUX

PROGRAMA DE PÓS-GRADUAÇÃO EM QUÍMICA DA UFSC  
ESCOLA DE DOUTORADO EM CIÊNCIAS QUÍMICAS DA UB  
ESPECIALIDADE EM QUÍMICA ORGÂNICA

Hugo MARCHI LUCIANO

**NOVOS MATERIAIS LUMINESCENTES E LÍQUIDO CRISTALINOS DE  
SIMETRIA TERNÁRIA**

Sob a direção de Hugo GALLARDO  
e Harald BOCK

Defendido em 2 de março de 2023 em Florianópolis

Membros da banca:

Sr. Vieira, André	Universidade Federal da Bahia	Presidente e Relator
Sra. Orth, Elisa	Universidade Federal do Paraná	Relatora
Sr. Gallardo, Hugo	Universidade Federal de Santa Catarina	Supervisor
Sr. Bock, Harald	Centre de Recherche Paul Pascal	Surpevisor

Hugo Marchi Luciano

**Novel luminescent and liquid crystalline materials of threefold symmetry**

Tese submetida ao Programa de Pós-Graduação em Química da Universidade Federal de Santa Catarina para a obtenção do título de Doutor em Química.  
Orientadores: Prof. Dr. Hugo Alejandro Gallardo Olmedo, Dr. Harald Bock.

Florianópolis

2023

Ficha de identificação da obra elaborada pelo autor,  
através do Programa de Geração Automática da Biblioteca Universitária da UFSC.

Marchi Luciano, Hugo

Novel luminescent and liquid crystalline materials of  
threefold symmetry / Hugo Marchi Luciano ; orientador,  
Hugo Gallardo, orientador, Harald Bock, 2023.

268 p.

Tese (doutorado) - Universidade Federal de Santa  
Catarina, Centro de Ciências Físicas e Matemáticas,  
Programa de Pós-Graduação em Química, Florianópolis, 2023.

Inclui referências.

Trabalho elaborado em regime de co-tutela.

1. Química. 2. Síntese orgânica. 3. Luminescência. 4.  
Cristais líquidos. 5. OLEDs. I. Gallardo, Hugo. II. Bock,  
Harald III. Universidade Federal de Santa Catarina.  
Programa de Pós-Graduação em Química. IV. Título.

Hugo Marchi Luciano

**Novel luminescent and liquid crystalline materials of threefold symmetry**

O presente trabalho em nível de doutorado foi avaliado e aprovado por banca examinadora composta pelos seguintes membros:

Prof. Dr. André Alexandre Vieira  
Universidade Federal da Bahia – UFBA

Profa. Dra. Elisa Souza Orth  
Universidade Federal do Paraná - UFPR

Certificamos que esta é a **versão original e final** do trabalho de conclusão que foi julgado adequado para obtenção do título de doutor em química orgânica.

---

Coordenação do Programa de Pós-Graduação

---

Prof. Dr. Hugo Alejandro Gallardo Olmedo  
Orientador



---

Dr. Harald Bock  
Orientador

Florianópolis, 2023.

This work is dedicated to my family, especially to my grandfather  
Waldemar Luciano.

## ACKNOWLEDGMENTS

Despite the challenges, there are always those who make the journey more enjoyable and enriching, both professionally and personally. Throughout my undergraduate, master's, and doctoral studies, I have encountered many people who have played a role in my journey. Some for short periods, others for longer stretches, and sometimes for a lifetime. While all the people around me during these past years contributed to my success, directly through daily scientific discussions or indirectly through specific days or unique moments, only a few will receive special recognition. I want to express a special thank you to my advisors, Professor Dr. Hugo Gallardo, and Dr. Harald Bock. Professor Gallardo has always believed in me and helped me join his research group, and I owe much of my success to him. He has always been like a scientific and life father, maintaining a professional relationship but, above all, a friendship with those around him. He is a professor of enormous knowledge and an even bigger heart, teaching chemistry, and life lessons. He is a builder of people and professionals. Dr. Bock is a top-notch researcher and, above all, a humble person with a giant heart. He provided me with one of the best life experiences, both professionally by allowing me to be part of his research group in Bordeaux, France, for half of my doctoral studies and personally by showing me different cultures and teaching me a lot about life. I am deeply grateful to both for all the scientific discussions and beers we shared together. A special thank you to my lab mates. To the Molecular and Mesomorphic Materials Research Group (GPM<sub>3</sub>), Professor Eduard, Priscila, Gustavo, Monike, Wilson, Samuel, Carolina, Sabrina, Antonio, Manuela, Joice, and Henrique. In particular, to the old members who contributed significantly to my learning and professional growth, Dra. Marli, Dr. Edivandro, Dr. Saul, Dra. Patricia, and Dr. Carlos. To the Molecular Materials and Magnetism Research Group (M<sub>3</sub>) at the Paul Pascal Research Center, the permanent members who made my experience in Europe enriching, Xavier, Dr. Rodolphe, Professor Pierre, Dr. Fabien, Dr. Andrej, Professora Corinne, and Mathieu. To the non-permanent members, Abhijit, Katia, Vincent, Dandan, Meng-Ting, Dr. Long-fei, and Dr. Nathan. A special thank you to those who shared the laboratory with me and participated in my daily life, making my adaptation easier, Dra. Ludmilla, Dr. Frédéric, Luc. My companion on this journey and cachaça throughout Europe, Dra. Marília Gabriela, taught me much about life and true friendship. To Fabrícia Nunes, for sharing new experiences during my Ph.D. year. To the true friends I made during the two years I lived in France, who made my days happier and full of cultural learning, Dra. Arantza, Dra. Alejandra, Dr. In-seong, Dra. Andrea, Amandine,

David, Henri, Rehina, Tatjana, Dr. Wael, Zi Lin, Rafael, I am very grateful for your friendship. To my friends from UFSC, who have always been with me in difficult and joyful moments, Vinícius, Eduardo, José Mario, Guilherme Schutz, Marco Antônio, Marcos, Marco Rodriguez, and Luciano, among others. To the Liquid Engineers group members, Nicolas, Well, and Dra. Marília Gabriela, who provided me with the best trips to different countries. Finally, to my family members who have always supported me in pursuing my dreams. In particular, to my parents, Roque and Maria Rosa, who always encouraged me to study and fight to achieve what I desired. To my second mother, Vera Lúcia, who was always there when I needed her. To my brother Bruno, who is my brother and my friend. You have been a part of my accomplishment, and I am very grateful for everything.

*If you had one shot, or one opportunity. To seize everything, you ever wanted in one moment. Would you capture it or just let it slip?*

Eminem

*If you want something you've never had, you must be willing to do something you've never done.*

Thomas Jefferson

*Nobody believes in you. You have lost again and again. The lights are cut off, but you are still looking at your dream. Reviewing it every day and saying to yourself, 'It is not over until I win.'*

Les Brown



## ABSTRACT

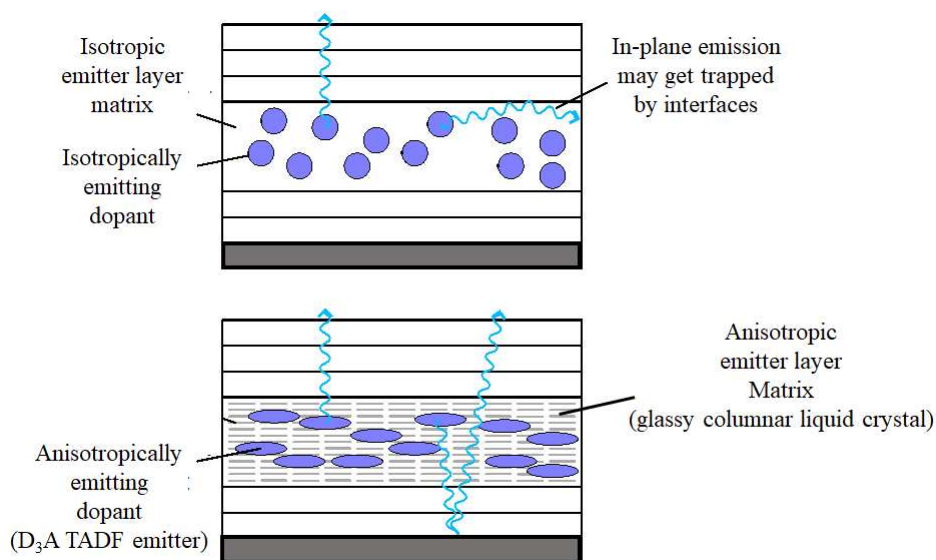
Incorporating thiophene bridges containing sulfur into D<sub>3</sub>A-type structures with a 2,4- pattern has been shown to produce new phosphorescent and delayed fluorescence emitters. Emitters with a 1,3,5-triazine core demonstrated different emission mechanisms depending on the donor unit used. While molecules with a carbazole unit showed phosphorescence at room temperature (with lifetimes of 0.7 ms), derivation with acridine led to thermally delayed fluorescence (TADF) emission with lifetimes ranging from 0.02 to 0.5 ms. Molecules based on the *tris*[1,2,4]triazolo[1,3,5]triazine (TTT) core exhibited phosphorescence regardless of the donor used, with lifetimes ranging from 0.1 to 3.5 ms, and also showed delayed fluorescence through a triplet-triplet annihilation (TTA) mechanism (with lifetimes ranging from 0.5 to 0.8 ms). The photoluminescence quantum yield (PLQY) for all compounds was in the range of 0.01 to 0.25. Although the presence of the sulfur atom increases spin-orbit coupling (SOC) and therefore increases the intersystem crossing rate, these materials also had a high non-radiative decay rate, which was reduced in the solid state due to the restriction of mobility and thus increased the lifetime of these processes. The observed room temperature phosphorescence in solution is attributed to the protection of the <sup>3</sup>LE excited state centered in the acceptor-thiophene portion (in both series) by the bulky donors, which prevent non-radiative decay through collisions and interactions with the environment. To increase the efficiency of light outcoupling in organic light emitting diode (OLED) devices, it is essential to have anisotropic emission. This can be achieved by incorporating the emitter into a liquid crystal (LC) matrix, specifically a glassy discotic LC. Ester-substituted *tris*(phenanthryl)triazines have been found to form upon cooling hexagonal columnar mesophases without crystallization. Their glass transition temperature depends on the length of the alkyl chain substituent, and short alkyl chains with a glassy state above room temperature can only be obtained with extremely high clearing temperatures. Ester-substituted *tris*([4]helicenyl)triazines with short alkyl chains were synthesized to overcome this limitation, resulting in hexagonal columnar mesophases with easily attainable melting and clearing temperatures. The propyl ester derivative exhibits a unique transition between two hexagonal columnar mesophases with a sudden increase of column lattice order. A molecular design based on configurational flexibility, a well-dosed intrinsic deviation from planarity, and short alkyl ester substituents has been shown to enable the stabilization of a solid-like hexagonal columnar mesophase at room temperature and an accessible transition to the isotropic liquid, allowing for the formation of surface-aligned glassy samples by cooling from the liquid.

**Keywords:** Room temperature phosphorescence, Delayed fluorescence, glassy discotic liquid crystal, light outcoupling.

## EXTENDED ABSTRACT

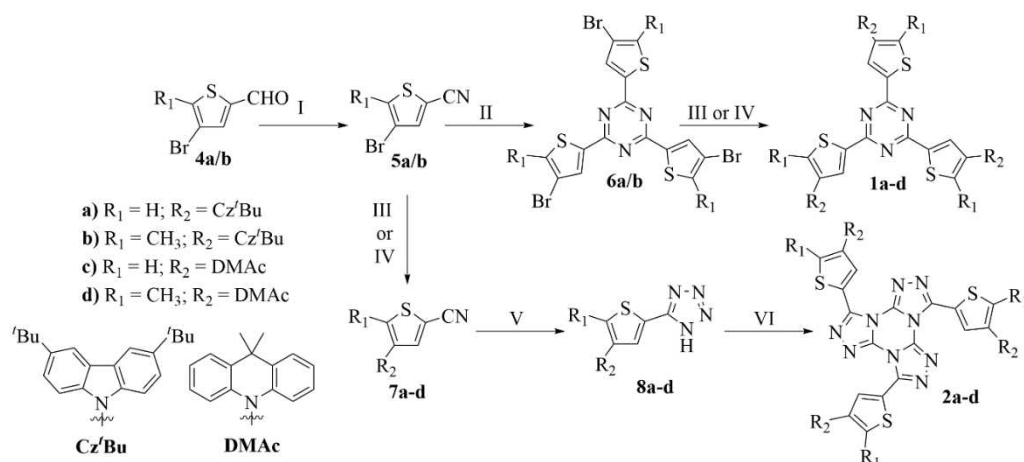
Organic light-emitting diodes (OLEDs) have increasingly been consolidated in the display market. In recent years, these materials have achieved greater efficiency thanks to major modifications and optimizations of the molecular emission mechanism and of the device structure. Today, OLED devices can already achieve an internal efficiency of 100% without heavy metals through the mechanism of thermally activated delayed fluorescence (TADF). A TADF material is able to convert all non-emissive triplet states formed after electrical excitation into emissive singlets through reverse intersystem crossing (rISC). rISC can occur when there is a sufficiently small energy difference between the excited triplet and singlet states ( $\Delta E_{ST}$ ) so that the thermal energy present at room temperature enables rISC. Another mechanism of delayed fluorescence is triplet-triplet annihilation (TTA). This bi-molecular mechanism has a lower efficiency due to the energy of an excited triplet state of one molecule being transferred and promoting rISC of another triplet-excited molecule. TADF emitters are generally obtained through donor-acceptor structures. This structure reduces the overlap of the highest occupied molecular orbital (HOMO) and lowest unoccupied molecular orbital (LUMO) orbitals, and low values of  $\Delta E_{ST}$  are obtained. Various molecular strategies have recently been studied to obtain increasingly efficient TADF emitters. The insertion of linker bridges separating the donor and acceptor units, with bulky groups that change the dihedral angles between the donor and acceptor units, or with different substitution patterns that tune the conjugation between donor and acceptor units, is an efficient approach for spatially separating frontier orbitals and allowing the TADF mechanism to occur. The external, i.e. overall efficiency of an OLED device is composed of an internal factor, which includes spin statistics, quantum efficiency, and electron-hole ratio, and an external light output factor which depends on light trapping within the device. Suppose the emitter is in an isotropic matrix. In that case, most of the light emitted in the emitter layer will be trapped in the device cavity, and only about 20% of the light will be emitted and seen by an observer. Recently, advances in light out-coupling in OLEDs have shown that the shape and orientation of emitters are crucial in increasing the light output value. The parallel orientation of dipoles with the device layers favors a greater light output. This type of orientation can be obtained in materials that form an anisotropic molecular glass. It is known that discotic liquid crystals can self-assemble into columns capable of unidirectionally transporting charge due to their specific anisotropic structure (a planar aromatic core surrounded by aliphatic chains). When homeotropically aligned (i.e. with the aromatic centers parallel to the substrate), these materials can be helpful in light extraction and, consequently, in

obtaining more efficient devices. Combining mesomorphism with luminescence can thus have an important impact on the performance of electro-optical devices, such as OLEDs. The uniform alignment that can be obtained in these materials and their ability of self-healing of defect such as grain boundaries, combined with the luminescence phenomenon, may allow for the elaboration of a simpler and more efficient OLED structure, where the emitter and transport layer can be the same. Although fluorescent and phosphorescent liquid crystals are reported in the literature, there are still only few liquid crystals with delayed fluorescence. Combining these two properties – liquid-crystallinity and triplet-based emission – in a single molecule may be an excellent alternative in searching for efficient materials, but it is a non-trivial task. The non-planarity, due to large twist angles between donor and acceptor moieties, of TADF materials is hardly compatible with the planarity required in discotic mesogens. This structural antagonism is the main barrier to obtaining a TADF-LC material. Recently, some research groups have obtained such materials, but not efficiently, showing that there is still a gap to be filled. An alternative more accessible alternative to combine these properties in the same device is to embed an efficient TADF emitter in a discotic liquid crystal matrix, specifically, a glassy columnar liquid crystal. Donor-acceptor structures with an internal electron-accepting aromatic unit and three twisted external electron-donating units show an increase in oscillator strength compared to simple donor-acceptor systems. Strong spin-orbit coupling (SOC) allows intersystem crossing between singlet and triplet states, resulting in efficient electroluminescent dyes with emission both by the singlet and triplet states. The *N*-heterocycles 1,3,5-triazine and *tris*[1,2,4]triazolo[1,3,5]triazine (TTT) are well known mesogenic centers, with a wide range of liquid crystals reported in the literature. In recent years, with the increasing search for TADF emitters, these two aromatic centers have shown to be effective as electron-accepting units in new efficient luminescent materials, in particular, to obtain blue emitters. It is necessary to work in an RGB (red, green, and blue) system of colors to obtain an OLED that emits throughout the visible range. Red and green emitters are already well established in the market, with good lifetimes and satisfactory color purity. However, there is still a gap for blue emitters, as these materials have high energy in the excited state and, consequently, lower stability. An excellent blue emitter can be used alone to manufacture an OLED device where the red and green colors can be obtained through external photoluminescent layers, drastically reducing complexity, and increasing the production efficiency of these devices.



**Light output in OLED devices.** Isotropic emission (top) and anisotropic emission (bottom)

In this perspective, we designed and synthesized two new series of D<sub>3</sub>A emitters based on the TTT and 1,3,5-triazine centers in the first part of this doctoral thesis. As a linking bridge, we chose to replace the commonly used phenylene group with the 2,4-disubstituted thiophene unit. The 2,4-disubstitution pattern is similar to the 1,3-disubstitution in benzene, which has been shown to be more efficient for obtaining low  $\Delta E_{ST}$  values than the 1,4-pattern. The inclusion of the sulfur atom in the structure of our emitters aimed to explore the heavy atom effect, increasing the spin-orbit coupling in these materials and favoring the intersystem crossing. To probe the effect of sterical hindrance on torsion angles and thus torsion-dependent emission properties, we used thiophene bridges with and without a sterically demanding methyl substituent.



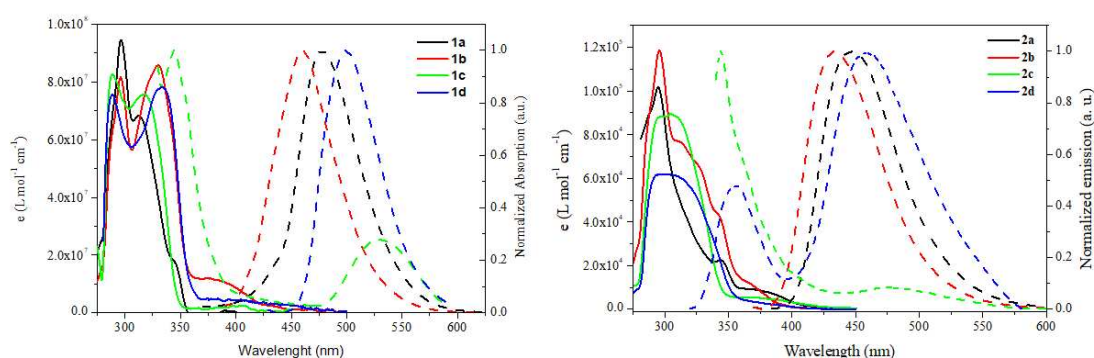
**Synthesis of D<sub>3</sub>A structures.** I) NH<sub>4</sub>OH(aq), I<sub>2</sub>, THF, **5a**: 82%, **5b**: 72%; II) CF<sub>3</sub>SO<sub>3</sub>H, **6a**: 67%, **6b**: 55%; III) 3,6-di-tert-butyl-9H-carbazole, K<sub>2</sub>CO<sub>3</sub>, CuSO<sub>4</sub>·5H<sub>2</sub>O, 1-methylnaphthalene, **1a**: 52%, **1b**: 39%, **7a**: 48%, **7b**: 34%;

IV) 9,9-dimethyl-9,10-dihydroacridine, [Pd(OAc)<sub>2</sub>], Xphos, NaO<sup>t</sup>-Bu, toluene, **1c**: 57%, **1d**: 52%, **7c**: 42%, **7d**: 46%; V) NaN<sub>3</sub>, NH<sub>4</sub>Cl, DMF, **8a**: 88%, **8b**: 83%, **8c**: 81%, **8d**: 79%; VI) C<sub>3</sub>N<sub>3</sub>Cl<sub>3</sub>, 2,6-lutidine, toluene, **2a**: 38%, **2b**: 32%, **2c**: 39%, **2d**: 35%.

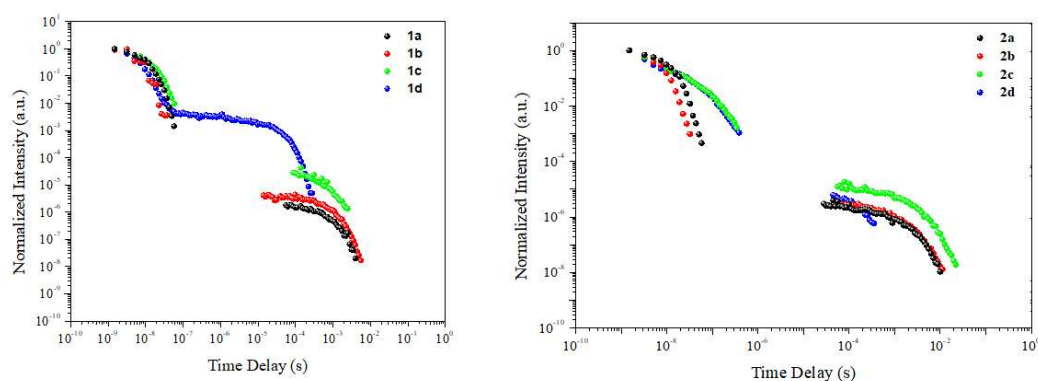
The emitters based on 1,3,5-triazine presented different emission mechanisms according to the donor unit used. After time-resolved photoluminescence analyses, 3,6-tertbutylcarbazol derivatives are phosphorescent emitters, while 9,10-dimethylacridine derivatives are TADF materials. The high  $\Delta E_{ST}$  value found for the molecules containing the 3,6-tertbutylcarbazol donor ( $> 0.5$  eV) makes it impossible for the thermally activated reverse intersystem crossing to occur and therefore does not allow TADF emission by these carbazole-triazine couples. The phosphorescence in these emitters is attributed to the effect of the sulfur atom on the spin-orbit coupling, increasing the intersystem crossing rate by relaxing the spin selection rule and enabling the  $T_1 \rightarrow S_0$  radiative decay. These materials presented a phosphorescence lifetime ( $\tau_{\text{Phosph}}$ ) of 0.7 ms for both compounds in toluene solution. Changing the donor unit to 9,10-dimethylacridine, it was possible to obtain lower  $\Delta E_{ST}$  values ( $< 0.3$  eV), sufficient for thermally activated reverse intersystem crossing to occur and for the TADF emission mechanism to be observed, with lifetimes in the range of 0.02 and 0.5 ms. Although these materials show TADF at room temperature, time-resolved photoluminescence analyses at low temperatures in solid state showed that these materials are also phosphorescent, with lifetimes between 6.8 and 17.8 ms. The derivative without the methyl group on the thiophene bridge in addition showed phosphorescence at room temperature with a short lifetime of 10.5 ms. Steady-state photoluminescence analyses showed that this derivative exhibits a dual emission in toluene solution attributed to a localized excitation (LE) emission from the 9,10-dimethylacridine unit and a charge transfer (CT) type emission between the donor-acceptor units. This demonstrates that the donor-acceptor system is decoupled, with an almost orthogonal dihedral angle ( $\sim 90^\circ$ ). The insertion of the methyl group in the linking bridge decreases this angle and increases the coupling of the moieties, leading to only one CT-type emission in the steady-state photoluminescence spectrum. Changing the accepting unit from triazine to TTT, we obtain a same emission mechanism regardless of the employed donor unit. All derivatives showed room temperature phosphorescence in solution with lifetimes in the range of 0.1 - 3.5 ms. In addition, for the two carbazole derivatives and the acridine derivative without methyl in the 2,4-thiophene bridge, the triplet-triplet annihilation delayed fluorescence (TTA) mechanism was also observed, with lifetimes in the range of 0.5 - 0.8 ms. The high value of  $\Delta E_{ST}$  found for these materials prevents the TADF mechanism from occurring, leading instead to delayed

fluorescence by the TTA mechanism. This mechanism is confirmed by its absence in the solid state. The restriction of molecular mobility prevents collision between two triplet-excited molecules, thus disabling the TTA mechanism. The steady-state photoluminescence spectrum showed that the acridine derivatives present a dual emission corresponding to the isolated unit's LE emission and the CT emission between the acridine and TTT units. As previously observed for one of the triazine-based emitters, this indicates that the units are close to orthogonal. In fact, theoretical calculations using density functional theory (DFT) have shown that in these derivatives, the dihedral angle is in the range of  $80^\circ$ , with lower values in the bridge-methylated emitter. Time-dependent DFT (TD-DFT) and spin-orbit coupling TD-DFT (SOC-TD-DFT) calculations showed that the first three excited states  $S_n$  have a CT configuration in the carbazole derivatives. However, these transitions have high oscillator strength ( $f$ ) values characteristic of a LE state. Therefore, the emission of these materials is from a mixed  $^1\text{LE}/^1\text{CT}$  state. For the acridine derivatives, the lowest energy emission showed CT configurations for the excited states and low  $f$  values. The observed emission at the highest energy (shortest wavelengths) is related to the LE state centered on the TTT-thiophene unit. We observed that the optimized geometries of the  $S_1$  states show little change in dihedral angles, resulting in little change in oscillator strength in these states compared to the ground state. On the other hand, the geometry in the excited state  $T_1$  changes significantly, resulting in a planarization of the molecule and an increasing  $\pi$ -system conjugation, resulting in  $^3\text{LE}$  configurations for the  $T_1$ ,  $T_2$ , and  $T_3$  states centered on the TTT-thiophene unit. The  $T_4$  state has an energy similar to the  $S_1$  state and therefore presents a CT configuration. To evaluate the effect of spin-orbit coupling on intersystem crossing and phosphorescence of these materials, we used a spin-orbit coupling matrix element (SOCME) obtained from spin-orbit coupling-time-dependent density functional theory calculations. Larger values were found for carbazole derivatives than for the acridine derivatives, in agreement with the observed quantum yields of photoluminescence. These values are similar to those found in the literature for simple donor-acceptor systems and for molecules containing sulfur atoms. The SOC between the excited states allows the otherwise forbidden transition  $T_1 \rightarrow S_0$ . The acridine derivative with the methyl group on the thiophene bridge showed low values of  $\tau_{\text{phosph}}$  compared to the other three compounds and only weak RTP. The observed RTP for these compounds in solution is attributed to the protection of the bulky donor groups from nonradiative deactivation by the  $^3\text{LE}$  excited state centered on the acceptor-thiophene portion. In both series, low photoluminescence quantum yield values were obtained. Although these materials have high spin-orbit coupling due to the heavy atom effect

that the thiophene sulfur-containing bridge adds to the system, all compounds have a high nonradiative decay rate, suggesting structural modifications to increase the rigidity of these systems. Time-resolved photoluminescence analyses in the solid state showed lower nonradiative decay rates. At low temperatures, the lifetime of these processes is longer, as expected, due to the restriction of mobility in the rigid matrix, which is more pronounced at low temperatures. The thermal stability of all eight emitters was determined by thermogravimetric analysis (TGA), and all compounds showed good stability ( $T_{\text{dec}} > 400^{\circ}\text{C}$ ), with carbazole derivatives being more stable than acridine derivatives in both series. When comparing different acceptor centers with the same donor unit, we observe that the triazine-based emitters are more thermally stable than the TTT derivatives, possibly due to the thermal isomerization that can occur in the latter.

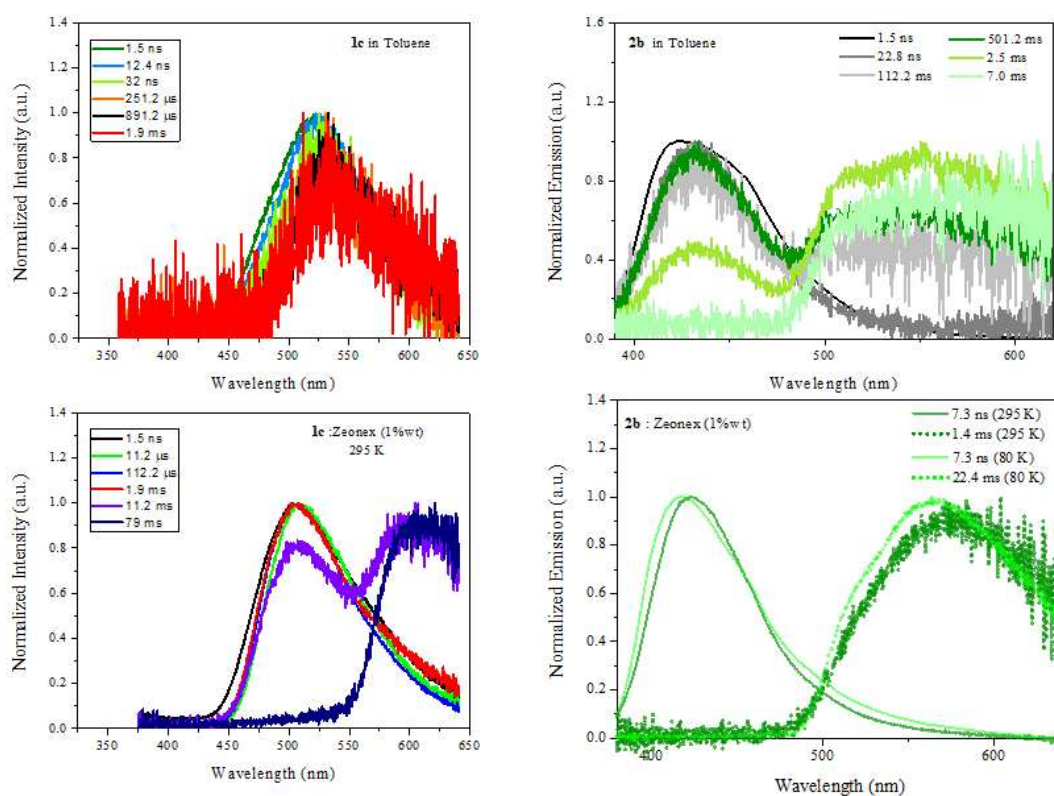


**Absorption and emission spectra.** 1a-d (left) and 2a-d (right) in dilute toluene solution ( $10^{-5} \text{ mol L}^{-1}$ ).



**Time-resolved decay curves in toluene.** The excitation wavelength was 355 nm. All measurements were performed in the absence of oxygen.

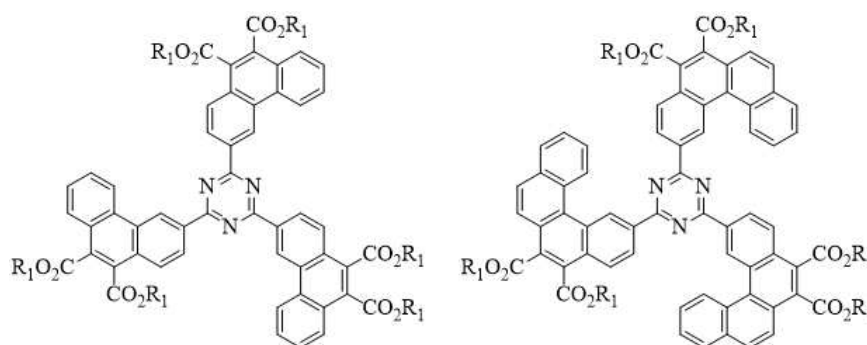




**Normalized spectra taken after different delay times. 1c and 2b** in solution (up) and solid state (bottom). The excitation wavelength was 355 nm. All measurements were performed in the absence of oxygen.

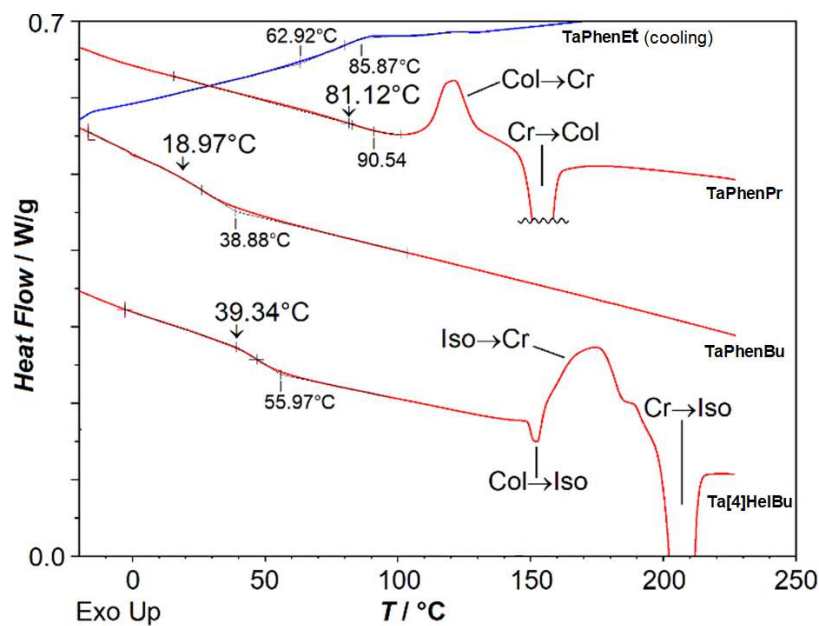
In the second part of this thesis, we planned and synthesized a series of glassy discotic liquid crystals based on the 1,3,5-triazine center decorated with short esters for use as matrices for TADF emitters in the fabrication of new OLED devices. First, we synthesized *tris*(phenanthryl)triazine derivatives with different ester chains (TaPhenEst; ethyl, propyl, butyl). Differential scanning calorimetry (DSC) analyses showed that the ethyl derivative transitions between two different crystalline phases without exhibiting mesomorphism. On the other hand, the TaPhenPr and TaPhenBu derivatives exhibit enantiotropic hexagonal columnar mesophases confirmed by X-ray diffraction. The lack of an attainable transition to the isotropic liquid below 375°C prevented the growth of defined textures in a polarizing optical microscope (POM). Both derivatives exhibited a mesomorphic glassy state during cooling, where the derivative with the longer ester alkyl chains, TaPhenBu, had at much lower glass transition temperature, showing that the transition temperature is strongly dependent on the size of the alkyl chain. This showed us that a glassy state above room temperature could only be obtained with short alkyl chains, at the expense of unattainably high clearing points (>375°C). To solve this problem, we decided to expand the aromatic region by synthesizing

*tris*([4]helicenyl)triazine ester derivatives, Ta[4]HelEst, with the same chain lengths as in the analog phenanthrene series. All derivatives presented a transition to the isotropic liquid in the range of 205-332 °C. The shortest chain derivative, Ta[4]HelEt, did not exhibit mesomorphism according to DSC and X-ray diffraction but presented a singular transition between two hexagonal crystalline phases. In contrast, the longer ester derivatives Ta[4]HelPr and Ta[4]HelBu exhibited monotropic hexagonal columnar mesomorphism with the growth of mesophase textures and X-ray diffraction peaks characteristic of this mesophase symmetry. No glass transition was observed for the Ta[4]HelPr derivative due to the already highly ordered nature of the lower-temperature one of its two hexagonal mesophases. In contrast, the Ta[4]HelBu derivative exhibited a glass transition 39°C, forming a mesomorphic glass at room temperature, thus yielding the targeted hexagonal columnar mesomorphic glass in combination with an accessible clearing point, showing it to be an excellent candidate for use as a matrix in electro-organic devices.

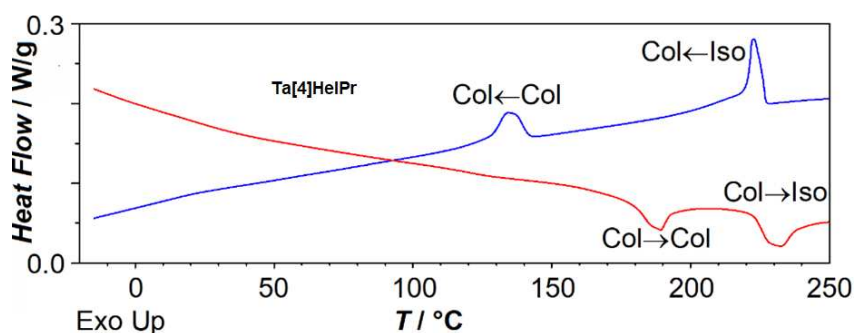


R<sub>1</sub> = Propyl, Butyl

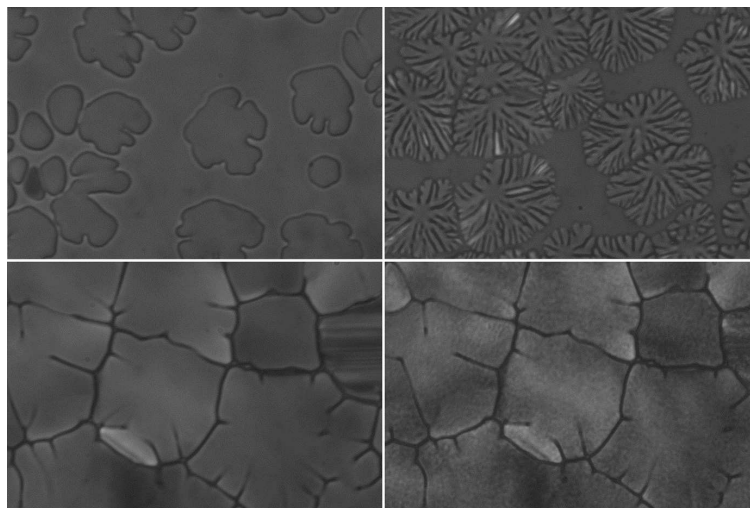
**Hexagonal columnar liquid crystalline triazine derivatives** with glass transition in the mesophase above room temperature.



**Differential calorimetry.** Heating scans (red) of **TaPhenPr**, **TaPhenBu** and **Ta[4]HelBu**, at  $+10^\circ\text{C}/\text{min}$  (after initial heating above the melting point and subsequent cooling at  $-10^\circ\text{C}/\text{min}$ ), and cooling scan (blue) of **TaPhenEt** at  $-10^\circ\text{C}/\text{min}$ ; glass transition onset temperatures on heating are indicated above vertical arrows; phase transitions are marked between Col = hexagonal columnar mesophase, Cr = crystalline state, and Iso = isotropic liquid.

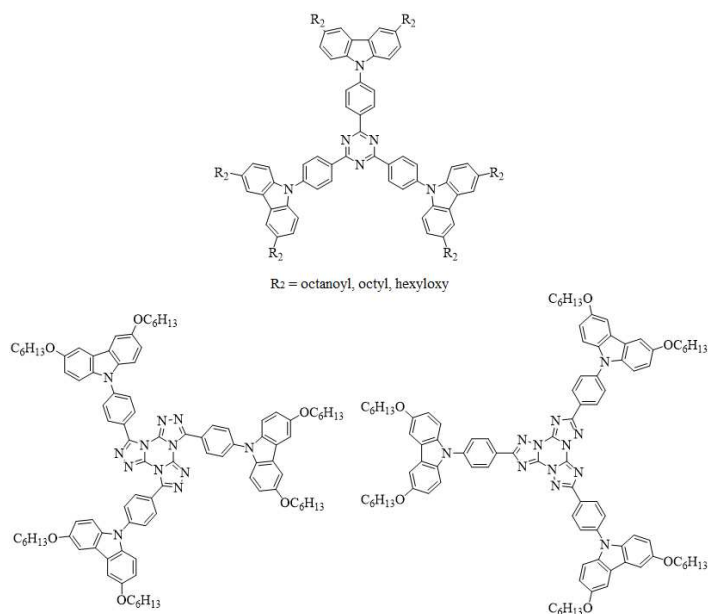


**Differential calorimetry.** Cooling (blue) and subsequent heating (red) scans of **Ta[4]HelPr** at  $\pm 10^\circ\text{C}/\text{min}$  (after initial heating above the melting point); with phase transitions between two hexagonal columnar (Col) mesophases and between the higher temperature mesophase and the isotropic liquid (Iso).



**Growth between glass plates of the hexagonal columnar mesophase of Ta[4]HelPr (top left) and Ta[4]HelBu (top right) in homeotropic alignment upon cooling through the isotropic-columnar phase transition, and homeotropic texture of the high temperature mesophase of Ta[4]HelPr at 200°C (bottom left) and of the low temperature mesophase at 100°C (bottom right) after cooling from the isotropic liquid followed by reheating; polarizing light optical microscopy with slightly uncrossed polarizers.**

We also attempted to induce mesomorphism in the  $D_{3A}$  structures described in the first part of this doctoral thesis and in those reported in the literature based on 1,3,5-triazine and TTT, by introducing alkyl chains in the 3,6-disubstituted carbazole donor unit. We introduced acyl, alkyl, and alkoxy chains in the triazine-based molecules. However, unfortunately, no material in this session displayed mesomorphism. We believe that the non-planarity in these materials, characteristic of TADF systems, makes it difficult for the molecules to stack and consequently prevents the formation of the columnar mesophase. We introduced alkoxy chains as well in the TTT-based  $D_{3A}$  molecules, again without success. Not even isomerizing the central unit to the radial, more extended, isomer of the triaryl-TTT center was enough to induce mesomorphism.



**Structure of D<sub>3</sub>A molecules.** Donors decorated with acyl, alkyl, and alkoxy chains.

In conclusion, the inclusion of thiophene bridges in a 2,4- substitution pattern in D<sub>3</sub>A type molecules significantly increases the spin-orbit coupling in these materials and thus enables the T<sub>1</sub>→S<sub>0</sub> forbidden transition, allowing these materials to emit phosphorescence at room temperature. Additionally, the solution RTP observed is unexpected due to the high triplet state lifetime and competition with non-radiative decay. Theoretical calculations have shown that phosphorescence is derived from a <sup>3</sup>LE state centered on the acceptor-thiophene portion. We believe that the bulky donor groups protect this state from non-radiative decay, allowing for sufficient time for phosphorescence emission. Changing the donor unit in the TTT center is not enough to decrease ΔE<sub>ST</sub> and enable TADF emission, although these materials have a TTA mechanism. In contrast, changing from carbazole to acridine dramatically changes the ΔE<sub>ST</sub> values in triazine-based materials. Acridine derivatives showed low values, possibly due to the almost orthogonality of the units, allowing for thermally activated reverse intersystem crossing and TADF emission, while carbazole derivatives only showed phosphorescence. In addition to these longer-lived emissions, all compounds showed prompt fluorescence, with carbazole derivatives in both series showing emission in the blue region. Inserting a methyl group in the thiophene unit has different effects on the dihedral angles of the carbazole and acridine derivatives. While there is an increase in the dihedral angle in the former, there is a decrease when the donor unit is acridine. The design of D<sub>3</sub>A-type molecules containing the thiophene unit in the 2,4- substitution pattern has proven to be a helpful strategy in the search for new

RTP and TADF emitters. Triphenanthryl-triazine-hexaesters where the alkyl ester chain is larger than the ethyl group, such as propyl and butyl esters, showed enantiotropic mesomorphism with the formation of a mesomorphic glass upon cooling. However, these materials' clearing points were not easily accessible, in view of aligning them on a substrate. The expansion of the aromatic region to *tris*[4]helicenyl-triazine-hexaesters resulted in a slight deplanarization, sufficient to destabilize the mesophases, being only observed during cooling, but also leading to accessible transition temperatures to the isotropic liquid state whilst yielding glass transitions above room temperature. Molecular planning based on configurational flexibility and including a slight deviation from planarity with short-chain alkyl ester substituents, has been shown to allow the stabilization of a solid hexagonal columnar mesophase at room temperature with an accessible transition to isotropic liquid. Cooling from the liquid allows for forming aligned samples on the surface. In contrast, the strategy of only inserting alkyl chains into donor units of D<sub>3</sub>A systems was not sufficient to induce mesomorphism. Asymmetric molecular designs where only one twisted portion of the molecule is responsible for TADF behavior, and the larger remaining planar part of the molecule is responsible for mesomorphism can be more promising approach to obtain discotic liquid-crystalline TADF materials.

**Keywords:** Room temperature phosphorescence, Delayed fluorescence, glassy discotic liquid crystal, light outcoupling.

## RÉSUMÉ

L'incorporation de ponts thiophène contenant du soufre dans des structures de type D<sub>3</sub>A avec un motif de substitution 2,4 a permis de produire de nouveaux émetteurs phosphorescents et à fluorescence retardée. Les émetteurs à noyau accepteur 1,3,5-triazine ont montré des mécanismes d'émission différents en fonction de l'unité donneuse utilisée. Alors que les molécules à unités carbazole comme donneur ont montré une phosphorescence à température ambiante (avec des durées de vie de 0.7 ms), la dérivation avec de l'acridine comme donneur a entraîné une émission de fluorescence retardée thermiquement (*TADF*) avec des durées de vie allant de 0,02 à 0,5 ms. Les molécules basées sur le noyau *tris*[1,2,4]triazolo[1,3,5]triazine (TTT) ont présenté une phosphorescence indépendamment du la donneur utilisé, avec des durées de vie allant de 0,1 à 3,5 ms, et ont également montré une fluorescence retardée par un mécanisme d'annihilation triplet-triplet (*TTA*) (avec des durées de vie allant de 0,5 à 0,8 ms). Le rendement quantique de luminescence (*PLQY*) pour tous les composés était compris entre 0,01 et 0,25. Bien que la présence de l'atome de soufre augmente le couplage spin-orbite (*SOC*) et accélère ainsi la vitesse de passage intersystème, ces matériaux ont également un fort taux de désexcitation non-radiative, qui a été limitée dans l'état solide en raison de la restriction de la mobilité et a ainsi augmenté la durée de ces processus. La phosphorescence observée à température ambiante en solution est attribuée à la protection de l'état excité <sup>3</sup>LE centré dans la partie accepteur-thiophène (dans les deux séries) par les donneurs volumineux, qui empêchent la désexcitation non-radiative par collisions et interactions avec l'environnement. Pour augmenter l'efficacité de l'échappement de la lumière depuis les dispositifs électroluminescents organiques (*OLED*), il est essentiel d'avoir une émission anisotrope. Cela peut être obtenu en incorporant l'émetteur dans une matrice de cristaux liquides (*CL*), en particulier un *CL* discotique vitreux. Des *tris*(phénanthryles)triazines substitués par des esters ont été observés de former, lors du refroidissement, des mésophases hexagonales colonnaires sans cristallisation. Leur température de transition vitreuse dépend de la longueur de la chaîne alkyl substituante, avec des chaînes alkyl courtes induisant un état vitreux supérieur à la température ambiante, mais aussi des températures de clarification extrêmement élevées. Des *tris*([4]hélicényl)triazines substitués par des esters courts ont été synthétisés pour surmonter cette limitation, ce qui a abouti à des mésophases hexagonales colonnaires avec des températures de fusion et de clarification facilement atteignables. Le dérivé ester propylique présente une transition singulière entre deux mésophases hexagonales colonnaires avec une augmentation soudaine de l'ordre du réseau colonnaire. Une conception moléculaire basé sur la

flexibilité configurationnelle, une déviation intrinsèque bien dosée de la planéité et des substituants esters alkyl courts a ainsi permis de stabiliser une mésophase hexagonale colonnaire en état solide à température ambiante et une transition accessible vers le liquide isotrope, permettant la formation d'échantillons vitreux orientés par les surfaces en refroidissant à partir du liquide.

**Mots Clés:** Phosphorescence à température ambiante, Fluorescence retardée, cristaux liquides discotiques vitreux, efficacité d'échappement de la lumière.

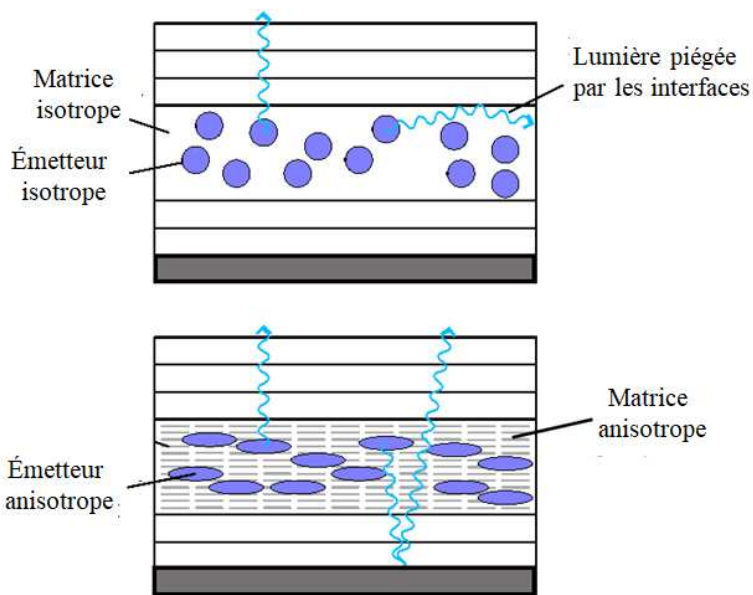


## RÉSUMÉ DÉTAILLÉ

Les diodes électroluminescentes organiques (OLED) se sont progressivement imposées sur le marché des écrans. Ces dernières années, ces matériaux ont atteint une plus grande efficacité grâce à d'importantes modifications et optimisations du mécanisme d'émission moléculaire et de la structure du dispositif. Aujourd'hui, les dispositifs OLED peuvent déjà atteindre un rendement interne de 100 % sans métaux lourds grâce au mécanisme de fluorescence retardée activée thermiquement (TADF). Un matériau TADF est capable de convertir tous les états triplets non émissifs formés après excitation électrique en états singlets émissifs par le biais d'un croisement intersystème inverse (rISC). Le rISC peut se produire lorsqu'il existe une différence d'énergie suffisamment faible entre les états triplets et singlets excités ( $\Delta E_{ST}$ ) pour que l'énergie thermique présente à température ambiante permette le rISC. Un autre mécanisme de fluorescence retardée est l'annihilation triplet-triplet (TTA). Ce mécanisme bi-moléculaire a une efficacité plus faible en raison de l'énergie d'un état triplet excité d'une molécule qui est transférée et favorise le rISC d'une autre molécule excitée en triplet. Les émetteurs de TADF sont généralement obtenus par des structures donneur-accepteur. Cette structure réduit le chevauchement des orbitales moléculaires occupées les plus élevées (HOMO) et des orbitales moléculaires inoccupées les plus basses (LUMO), et de faibles valeurs de  $\Delta E_{ST}$  sont obtenues. De diverses stratégies moléculaires ont récemment été étudiées pour obtenir des émetteurs TADF de plus en plus efficaces. L'insertion de ponts étendus séparant les unités donneur et accepteur, avec des groupes volumineux qui modifient les angles dièdres entre les unités donneur et accepteur, ou avec différents modèles de substitution qui modifient la conjugaison entre les unités donneur et accepteur, est une approche efficace pour séparer spatialement les orbitales frontières et permettre au mécanisme TADF de se produire. L'efficacité externe, c'est-à-dire globale, d'un dispositif OLED est composée d'un facteur interne, qui comprend les statistiques de spin, l'efficacité quantique et le rapport électron-trou, et d'un facteur externe d'échappement de lumière qui dépend du piégeage de la lumière dans le dispositif. Supposons que l'émetteur se trouve dans une matrice isotrope. Dans ce cas, la plupart de la lumière émise dans la couche de l'émetteur sera piégée dans la cavité du dispositif, et seulement environ 20 % de la lumière s'échappe du dispositif et peut être vue par un observateur. Récemment, les progrès réalisés en matière d'échappement de la lumière depuis les OLED ont montré que la forme et l'orientation des émetteurs sont cruciales pour augmenter la quantité de lumière émise vers l'extérieur. L'orientation parallèle des dipôles avec les couches du dispositif favorise ceci. Ce type d'orientation peut être obtenu dans des matériaux qui forment un verre moléculaire anisotrope. Il est connu que les cristaux liquides discotiques peuvent s'auto-assembler en colonnes, capables de

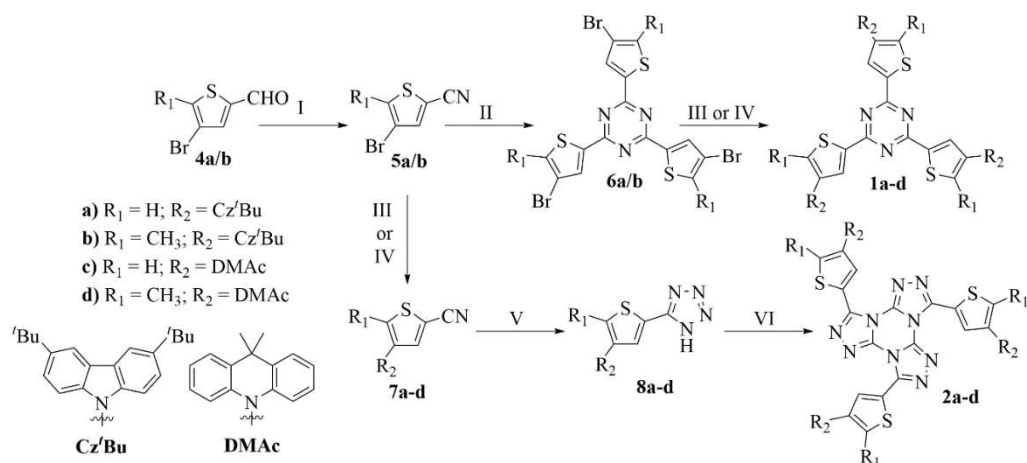
transporter des charges de manière unidirectionnelle grâce à leur structure anisotrope spécifique (un centre aromatique plan entouré de chaînes aliphatiques). Lorsqu'ils sont alignés de manière homéotrope (c'est-à-dire avec les centres aromatiques parallèles au substrat), ces matériaux peuvent être utiles pour l'extraction de la lumière et, par conséquent, pour obtenir des dispositifs plus efficaces. La combinaison du mésomorphisme avec la luminescence peut donc avoir un impact important sur les performances des dispositifs électro-optiques, tels que les OLED. L'alignement uniforme qui peut être obtenu dans ces matériaux et leur capacité d'auto-réparation des défauts tels que les joints de grains, combinés au phénomène de luminescence, peuvent permettre l'élaboration d'une structure OLED plus simple et plus efficace, où la couche émettrice et la couche de transport peuvent être les mêmes. Bien que des cristaux liquides fluorescents et phosphorescents soient rapportés dans la littérature, il n'existe encore que peu de cristaux liquides à fluorescence retardée. La combinaison de ces deux propriétés - cristallinité liquide et émission à base de triplets - dans une seule molécule peut être une excellente alternative dans la recherche de matériaux efficaces, mais il s'agit d'une tâche non triviale. La non-planéité, due aux grands angles de torsion entre les parties donneuses et acceptrices, des matériaux TADF est difficilement compatible avec la planéité requise dans les mésogènes discotiques. Cet antagonisme structurel est le principal obstacle à l'obtention d'un matériau TADF mésomorphe. Récemment, certains groupes de recherche ont obtenu de tels matériaux, mais pas de manière efficace, ce qui montre qu'il y a encore une lacune à combler. Une alternative, plus accessible, pour combiner ces propriétés dans un même dispositif est d'intégrer un émetteur TADF efficace dans une matrice de cristaux liquides discotiques, plus précisément : dans un cristal liquide vitreux colonnaire. Les structures donneur-accepteur avec une unité aromatique interne acceptrices d'électrons et trois unités externes torsadées donneuses d'électrons montrent une augmentation de la force de l'oscillateur par rapport aux systèmes donneur-accepteur simples. Un fort couplage spin-orbite (SOC) permet le croisement intersystème entre les états singlet et triplet, ce qui donne des colorants électroluminescents efficaces avec une émission à la fois par les états singlet et triplet. Les N-hétérocycles 1,3,5-triazine et tris[1,2,4]triazolo[1,3,5]triazine (TTT) sont des centres mésogènes bien connus, avec une large gamme de cristaux liquides rapportés dans la littérature. Ces dernières années, avec la recherche croissante d'émetteurs TADF, ces deux centres aromatiques se sont révélés efficaces comme unités acceptrices d'électrons dans de nouveaux matériaux luminescents efficaces, en particulier pour obtenir des émetteurs bleus. Il est nécessaire de travailler dans un système de couleurs RGB (rouge, vert et bleu) pour obtenir une OLED qui émet dans tout le domaine visible. Les émetteurs rouges et verts sont déjà bien

implantés sur le marché, avec de bonnes durées de vie et une pureté de couleur satisfaisante. Cependant, il existe encore une lacune pour les émetteurs bleus, car ces matériaux ont une énergie élevée dans l'état excité et, par conséquent, une stabilité moindre. Un excellent émetteur bleu peut être utilisé seul pour fabriquer un dispositif OLED où les couleurs rouge et verte peuvent être obtenues par des couches photoluminescentes externes, ce qui réduit considérablement la complexité et augmente l'efficacité de production de ces dispositifs.



**Emission depuis un OLED.** Émission isotrope (haut) et anisotrope (bas).

Dans cette perspective, nous avons conçu et synthétisé deux nouvelles séries d'émetteurs D<sub>3</sub>A basés sur les centres TTT et 1,3,5-triazine dans la première partie de cette thèse de doctorat. Comme pont, nous avons choisi de remplacer le groupe phénylène couramment utilisé par l'unité thiophène 2,4-disubstituée. Le motif de disubstitution 2,4 est similaire à la disubstitution 1,3 dans le benzène, qui s'est avérée plus efficace pour obtenir de faibles valeurs  $\Delta E_{ST}$  que le motif 1,4. L'inclusion de l'atome de soufre dans la structure de nos émetteurs visait à explorer l'effet d'atome lourd, augmentant le couplage spin-orbite dans ces matériaux et favorisant le croisement intersystème. Pour sonder l'effet de l'encombrement stérique sur les angles de torsion et donc sur les propriétés d'émission dépendant de la torsion, nous avons utilisé des ponts thiophène avec et sans substituant méthyle stériquement exigeant.

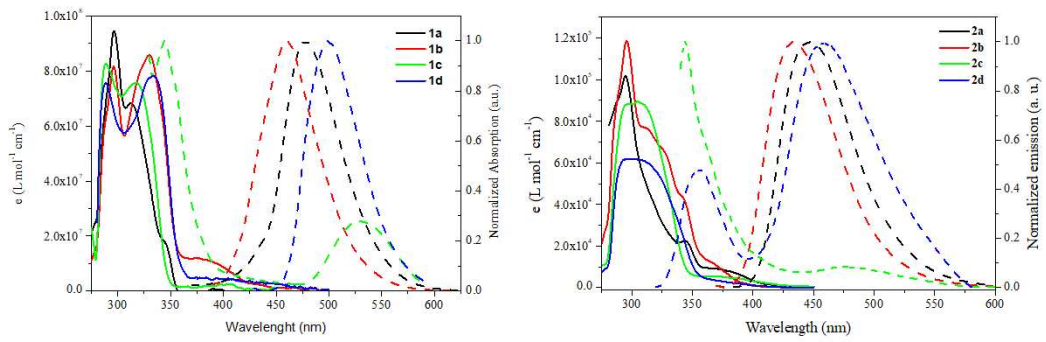


**Synthèse de structures D3A.** I)  $NH_4OH(aq)$ ,  $I_2$ , THF, **5a**: 82%, **5b**: 72%; II)  $CF_3SO_3H$ , **6a**: 67%, **6b**: 55%; III) 3,6-di-tert-butyl-9H-carbazole,  $K_2CO_3$ ,  $CuSO_4 \cdot 5H_2O$ , 1-methylnaphthalene, **1a**: 52%, **1b**: 39%, **7a**: 48%, **7b**: 34%; IV) 9,9-diméthyl-9,10-dihydroacridine,  $[Pd(OAc)_2]$ , Xphos,  $NaO^t-Bu$ , toluene, **1c**: 57%, **1d**: 52%, **7c**: 42%, **7d**: 46%; V)  $NaN_3$ ,  $NH_4Cl$ , DMF, **8a**: 88%, **8b**: 83%, **8c**: 81%, **8d**: 79%; VI)  $C_3N_3Cl_3$ , 2,6-lutidine, toluene, **2a**: 38%, **2b**: 32%, **2c**: 39%, **2d**: 35%.

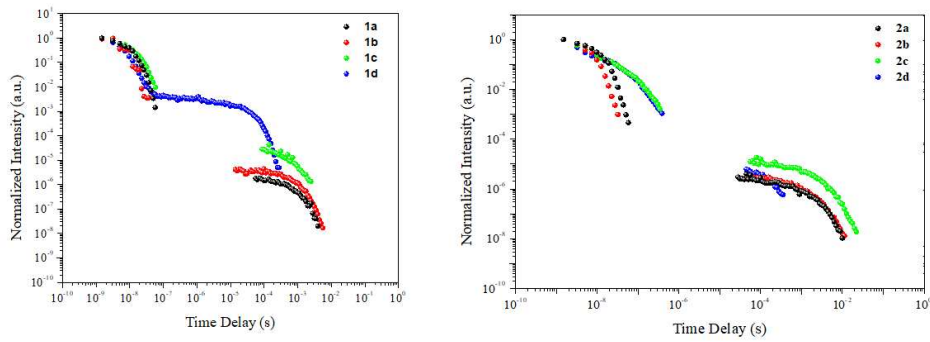
Les émetteurs basés sur la 1,3,5-triazine ont présenté des mécanismes d'émission différents selon l'unité donneuse utilisée. Après des analyses de photoluminescence résolue en temps, les dérivés de 3,6-tertbutylcarbazole sont des émetteurs phosphorescents, tandis que les dérivés de 9,10-diméthylacridine sont des matériaux TADF. La valeur élevée de  $\Delta E_{ST}$  trouvée pour les molécules contenant le donneur 3,6-tertbutylcarbazole ( $>0,5$  eV) rend impossible le croisement intersystème inverse activé thermiquement et ne permet donc pas l'émission de TADF par ces couples carbazole-triazine. La phosphorescence dans ces émetteurs est attribuée à l'effet de l'atome de soufre sur le couplage spin-orbite, augmentant le taux de croisement intersystème en relaxant la règle de sélection de spin et permettant la désexcitation radiative  $T_1 \rightarrow S_0$ . Ces matériaux ont présenté une durée de vie de phosphorescence ( $\tau_{Phosph}$ ) de 0,7 ms dans le toluène. En changeant l'unité donneuse pour la 9,10-diméthylacridine, il a été possible d'obtenir des valeurs  $\Delta E_{ST}$  plus faibles ( $<0,3$  eV), suffisantes pour que le croisement intersystème inverse activé thermiquement se produise et que le mécanisme d'émission TADF soit observé, avec des durées de vie comprises entre 0.02 et 0.5 ms. Bien que ces matériaux présentent une TADF à température ambiante, les analyses de photoluminescence résolue en temps à basse température ont montré que ces matériaux sont également phosphorescents, avec des durées de vie comprises entre 6.8 et 17.8 ms. Le dérivé sans le groupe méthyle sur le pont thiophène a en outre montré une phosphorescence à température ambiante avec une courte durée de vie de 10.5 ms. Les analyses de photoluminescence en régime continu ont montré que ce dérivé présente une double émission dans le toluène, attribuée à une émission par excitation localisée (LE)

provenant de l'unité 9,10-diméthylacridine et à une émission de type transfert de charge (CT) entre les unités donneur-accepteur. Ceci démontre que le système donneur-accepteur est dissocié, avec un angle dièdre presque orthogonal ( $\sim 90^\circ$ ). L'insertion du groupe méthyle dans le pont de liaison diminue cet angle et augmente le couplage des parties, ce qui conduit à une seule émission de type CT dans le spectre de photoluminescence en régime continu. En changeant l'unité acceptrice de triazine à TTT, nous obtenons un même mécanisme d'émission quelle que soit l'unité donneuse employée. Tous les dérivés ont montré une phosphorescence à température ambiante en solution avec des durées de vie comprises entre 0,1 et 3,5 ms. De plus, pour les deux dérivés carbazole et le dérivé acridine sans méthyle dans le pont 2,4-thiophène, le mécanisme de fluorescence retardée par annihilation triplet-triplet (TTA) a également été observé, avec des durées de vie dans la gamme de 0,5 - 0,8 ms. La valeur élevée de  $\Delta E_{ST}$  trouvée pour ces matériaux empêche le mécanisme TADF, conduisant plutôt à une fluorescence retardée par le mécanisme TTA. Ce mécanisme est confirmé par son absence à l'état solide : Dans le solide, la restriction de la mobilité moléculaire empêche la collision entre deux molécules excitées en triplet, désactivant ainsi le mécanisme TTA. Le spectre de photoluminescence en régime permanent a montré que les dérivés de l'acridine présentent une double émission correspondant à l'émission LE de l'unité isolée et à l'émission CT entre les unités acridine et TTT. Comme observé précédemment pour l'un des émetteurs à base de triazine, cela indique que les unités sont proches de l'orthogonalité. En fait, les calculs théoriques utilisant la théorie de la fonctionnelle de la densité (DFT) ont montré que dans ces dérivés, l'angle dièdre est de l'ordre de  $80^\circ$ , avec des valeurs plus faibles dans l'émetteur méthylé en pont. Les calculs DFT dépendant du temps (TD-DFT) et TD-DFT à couplage spin-orbite (SOC-TD-DFT) ont montré que les trois premiers états excités  $S_n$  ont une configuration CT dans les dérivés du carbazole. Cependant, ces transitions ont des valeurs de force d'oscillateur ( $f$ ) élevées, caractéristiques d'un état LE. Par conséquent, l'émission de ces matériaux provient d'un état mixte  $^1LE/{}^1CT$ . Pour les dérivés de l'acridine, l'émission la plus faible en énergie présente des configurations CT pour les états excités et des valeurs de  $f$  faibles. L'émission observée à la plus haute énergie (longueurs d'onde les plus courtes) est liée à l'état LE centré sur l'unité TTT-thiophène. Nous avons observé que les géométries optimisées des états  $S_1$  présentent peu de changement dans les angles dièdres, ce qui entraîne un faible changement de la force d'oscillation dans ces états par rapport à l'état fondamental. En revanche, la géométrie de l'état excité  $T_1$  change de manière significative, entraînant une planarisation de la molécule et une conjugaison croissante du système  $\pi$ , ce qui donne lieu à des configurations  ${}^3LE$  pour les

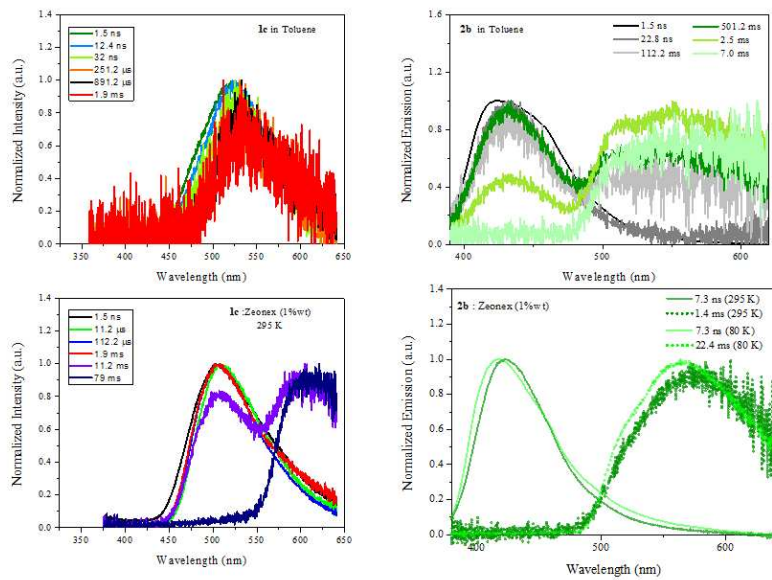
états T<sub>1</sub>, T<sub>2</sub> et T<sub>3</sub> centrés sur l'unité TTT-thiophène. L'état T<sub>4</sub> a une énergie similaire à l'état S<sub>1</sub> et présente donc une configuration CT. Pour évaluer l'effet du couplage spin-orbite sur le croisement intersystème et la phosphorescence de ces matériaux, nous avons utilisé un élément de matrice de couplage spin-orbite (SOCME) obtenu à partir de calculs de SOC-TD-DFT. Des valeurs plus importantes ont été trouvées pour les dérivés du carbazole que pour les dérivés de l'acridine, en accord avec les rendements quantiques de photoluminescence observés. Ces valeurs sont similaires à celles trouvées dans la littérature pour des systèmes simples donneur-accepteur et pour des molécules contenant des atomes de soufre. Le SOC entre les états excités permet la transition T<sub>1</sub>→S<sub>0</sub>, autrement interdite. Le dérivé d'acridine avec le groupe méthyle sur le pont thiophène a montré de faibles valeurs de  $\tau_{\text{Phosph}}$  par rapport aux trois autres composés et seulement une faible RTP. La RTP observé pour ces composés en solution est attribuée à la protection des groupes donneurs volumineux contre la désactivation non radiative par l'état excité <sup>3</sup>LE centré sur la partie accepteur-thiophène. Dans les deux séries, de faibles valeurs de rendement quantique de photoluminescence ont été obtenues. Bien que ces matériaux présentent un couplage spin-orbite élevé en raison de l'effet d'atome lourd que le pont sulfuré du thiophène ajoute au système, tous les composés ont un taux de désexcitation non radiative élevé, ce qui suggère des modifications structurelles pour augmenter la rigidité de ces systèmes. Les analyses de photoluminescence résolue dans le temps à l'état solide ont montré des taux de désintégration non radiative plus faibles. À basse température, la durée de vie de ces processus est plus longue, comme prévu, en raison de la restriction de la mobilité dans la matrice rigide, qui est plus prononcée à basse température. La stabilité thermique des huit émetteurs a été déterminée par analyse thermogravimétrique (TGA), et tous les composés ont montré une bonne stabilité ( $T_{\text{décomposition}} > 400^{\circ}\text{C}$ ), les dérivés de carbazole étant plus stables que les dérivés d'acridine. En comparant différents centres accepteurs avec la même unité donneuse, nous observons que les émetteurs à base de triazine sont plus stables thermiquement que les dérivés TTT, peut-être en raison de l'isomérisation thermique qui peut se produire dans ces derniers.



**Spectres d'absorption et d'émission. 1a-d (à gauche) et 2a-d (à droite) en solution diluée de toluène ( $10^{-6}$  mol L $^{-1}$ ).**



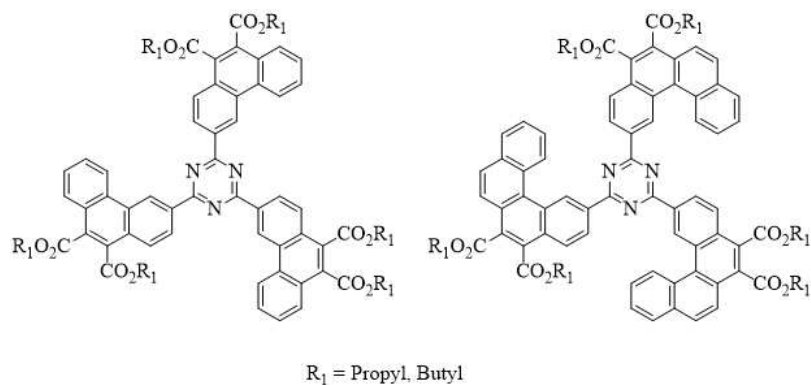
**Emission résolue dans le temps dans le toluène. En absence d'oxygène. Excitation à 355 nm.**



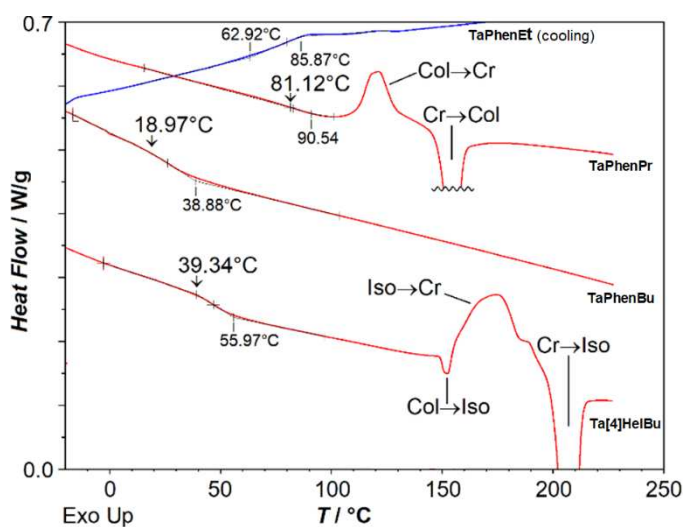
**Spectres normalisés prises après différents intervalles d'attente. 1c et 2b en solution (haut) et état solide (bas). Excitation à 355 nm. En absence d'oxygène.**

Dans une deuxième partie de cette thèse, nous avons planifié et synthétisé une série de cristaux liquides discotiques vitreux basés sur le centre 1,3,5-triazine décoré avec des esters courts pour être utilisés comme matrices pour des émetteurs TADF dans la fabrication de nouveaux dispositifs OLED. Nous avons d'abord synthétisé des dérivés de *tris*(phénanthryl)triazine avec différentes chaînes esters (TaPhenEst ; éthyle, propyle, butyle). Les analyses par calorimétrie différentielle à balayage (DSC) ont montré que le dérivé éthyle transite entre deux phases cristallines différentes sans présenter de mésomorphisme. D'autre part, les dérivés TaPhenPr et TaPhenBu présentent des mésophases colonnaires hexagonales énantiotropes confirmées par diffraction des rayons X. L'absence de transition possible vers le liquide isotrope en dessous de 375°C a empêché la croissance de textures définies dans un microscope optique polarisant (POM). Les deux dérivés ont présenté un état vitreux mésomorphe pendant le refroidissement, où le dérivé avec les chaînes alkyle ester les plus longues, TaPhenBu, avait une température de transition vitreuse beaucoup plus basse, montrant que la température de transition dépend fortement de la taille de la chaîne alkyle. Cela nous a montré qu'un état vitreux présent à des températures supérieures à la température ambiante ne pouvait être obtenu qu'avec des chaînes alkyle courtes, au prix de points de clarification trop élevés (>375°C). Pour résoudre ce problème, nous avons décidé d'étendre la région aromatique en synthétisant des dérivés de *tris*([4]hélécényl)triazine-ester, Ta[4]HelEst, avec les mêmes longueurs de chaîne que dans la série des phénanthrènes analogues. Tous les dérivés ont présenté une transition vers le liquide isotrope dans la gamme de 205-332 °C. Le dérivé à chaîne la plus courte, Ta[4]HelEt, n'a pas présenté de mésomorphisme selon la calorimétrie différentielle à balayage (DSC) et la diffraction des rayons X mais a présenté une transition singulière entre deux phases cristallines hexagonales. En revanche, les dérivés esters plus longs Ta[4]HelPr et Ta[4]HelBu ont présenté un mésomorphisme colonnaire hexagonal monotrope avec la croissance de textures de mésophase et de pics de diffraction des rayons X caractéristiques de cette symétrie de mésophase. Aucune transition vitreuse n'a été observée pour le dérivé Ta[4]HelPr en raison de la nature déjà hautement ordonnée de celle de ses deux mésophases hexagonales qui est présente à basse température. En revanche, le dérivé Ta[4]HelBu a présenté une transition vitreuse à 39°C, formant un verre mésomorphe à température ambiante, donnant ainsi le verre mésomorphe hexagonal colonnaire ciblé en combinaison avec un point de clarification accessible, ce qui en fait un excellent candidat pour une utilisation comme matrice dans des dispositifs électro-organiques.

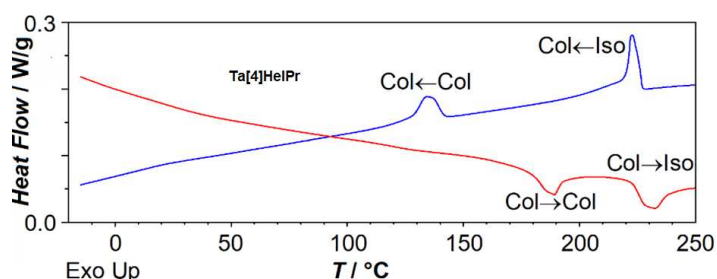




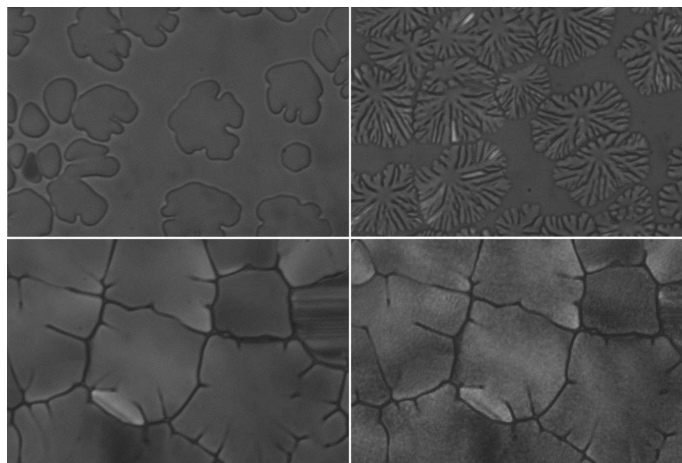
**Dérivés de triazine cristallins-liquides colonnaires hexagonaux à transitions vitreuses dans la mésophase au-dessus de la température ambiante.**



**Balayage de chauffage de calorimétrie différentielle (rouge) de TaPhenPr, TaPhenBu and Ta[4]HelBu à +10°C/min (après un chauffage initial au-dessus du point de fusion et un refroidissement ultérieur à -10 °C/min), et balayage de refroidissement (bleu) de TaPhenEt à -10°C/min ; les températures de début de transition vitreuse lors du chauffage sont indiquées au-dessus des flèches verticales ; les transitions de phase sont marquées entre Col = mésophase hexagonale colonnaire, Cr = état cristallin, et Iso = liquide isotrope.**

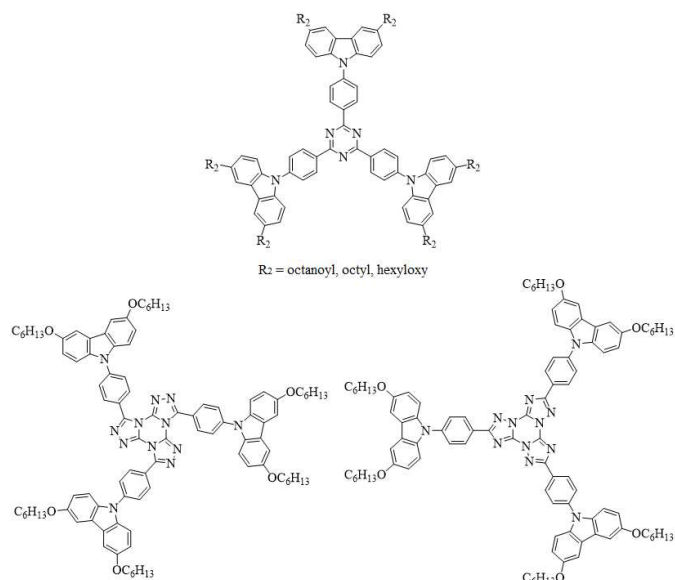


**Balayage de refroidissement (bleu) et de chauffage ultérieur (rouge) du Ta[4]HelPr par calorimétrie différentielle à ±10°C/min (après un chauffage initial au-dessus du point de fusion) ; avec des transitions de phase entre deux mésophases hexagonales colonnaires (Col) et entre la mésophase à plus haute température et le liquide isotrope (Iso).**



**Croissance entre des plaques de verre de la mésophase colonnaire hexagonale de TaPhenPr** (en haut à gauche) et de **Ta[4]HelBu** (en haut à droite) en alignement homéotrope lors du refroidissement à travers la transition de phase isotrope-colonnaire, et texture homéotrope de la mésophase de **TaPhenPr** à haute température à 200°C (en bas à gauche) et de la mésophase à basse température à 100°C (en bas à droite) après refroidissement à partir du liquide isotrope suivi d'un réchauffage ; microscopie optique en lumière polarisée avec des polariseurs légèrement décroisés.

Nous avons également tenté d'induire un mésomorphisme dans les structures  $D_3A$  décrites dans la première partie de cette thèse de doctorat et dans celles rapportées dans la littérature à base de 1,3,5-triazine et de TTT, en introduisant des chaînes alkyles dans l'unité donneuse carbazole 3,6-disubstituée. Nous avons introduit des chaînes acyle, alkyle et alcoxy dans les molécules à base de triazine. Malheureusement, aucun de ces matériaux n'a présenté de mésomorphisme. Nous pensons que la non-planéité de ces matériaux, caractéristique des systèmes TADF, rend difficile l'empilement des molécules et empêche par conséquent la formation de la mésophase colonnaire. Nous avons également introduit des chaînes alcoxy dans les molécules de  $D_3A$  à base de TTT, toujours sans succès. Même l'isomérisation de l'unité centrale vers l'isomère radial, plus étendu, du centre triaryl-TTT n'a pas suffi à induire le mésomorphisme.



**Structure des molécules D<sub>3</sub>A.** Donneurs décorés avec des chaînes acyle, alkyle et alkoxy.

En conclusion, l'inclusion de ponts thiophène selon un schéma de 2,4-substitution dans les molécules de type D<sub>3</sub>A augmente significativement le couplage spin-orbite dans ces matériaux et permet ainsi la transition interdite  $T_1 \rightarrow S_0$ , permettant à ces matériaux d'émettre de la fluorescence à température ambiante. De plus, la RTP observée en solution est inattendue en raison de la durée de vie élevée de l'état triplet et de la compétition avec la désintégration non radiative. Les calculs théoriques ont montré que la phosphorescence est issue d'un état  $^3LE$  centré sur la partie accepteur-thiophène. Nous pensons que les groupes donneurs volumineux protègent cet état de la désintégration non radiative, ce qui permet un temps suffisant pour l'émission de phosphorescence. Changer le groupe donneur dans le centre TTT n'est pas suffisant pour diminuer  $\Delta E_{ST}$  et permettre l'émission TADF, bien que ces matériaux montrent de la fluorescence retardée selon le mécanisme TTA. En revanche, le passage du carbazole à l'acridine modifie considérablement les valeurs de  $\Delta E_{ST}$  dans les matériaux à base de triazine. Les dérivés de l'acridine ont montré de faibles valeurs, probablement en raison de la quasi-orthogonalité des unités, permettant le croisement intersystème inverse activé thermiquement et l'émission TADF, tandis que les dérivés du carbazole ont seulement montré une phosphorescence. En plus de ces émissions à plus longue durée de vie, tous les composés ont montré une fluorescence immédiate, avec des dérivés du carbazole dans les deux séries montrant une émission dans la région bleue. L'insertion d'un groupe méthyle dans l'unité thiophène a des effets différents sur les angles dièdres des dérivés carbazole et acridine. Alors qu'il y a une augmentation de l'angle dièdre dans le premier, il y a une diminution lorsque l'unité

donneuse est l'acridine. La conception de molécules de type D<sub>3</sub>A contenant l'unité thiophène avec un motif de substitution 2,4 s'est avérée être une stratégie utile dans la recherche de nouveaux émetteurs RTP et TADF. Les hexaesters de triphénanthryl-triazine où la chaîne ester alkylique est plus grande que le groupe éthyle, tels que les esters de propyle et de butyle, ont montré un mésomorphisme énantiotrope avec la formation d'un verre mésomorphe lors du refroidissement. Cependant, les les points de clarification de ces matériaux n'étaient pas facilement accessibles, en vue d'alignement sur substrat. L'expansion de la région aromatique aux *tris*[4]helicenyl-triazine-hexaesters a entraîné une légère déplanarisation, suffisante pour déstabiliser les mésophases, observées uniquement lors du refroidissement, mais conduisant aussi à des températures de transition accessibles vers l'état liquide isotrope tout en donnant des transitions vitreuses supérieures à la température ambiante. Il a été démontré que la conception moléculaire basée sur la flexibilité configurationnelle et incluant une légère déviation de la planéité avec des substituants esters alkyles à chaîne courte, permet l'obtention d'une mésophase colonnaire hexagonale solide à température ambiante avec une transition accessible vers le liquide isotrope. Le refroidissement du liquide permet de former des échantillons uniformément alignés sur la surface. En revanche, la stratégie consistant uniquement à insérer des chaînes alkyle dans les unités donneuses des systèmes D<sub>3</sub>A n'était pas suffisante pour induire le mésomorphisme. Les conceptions moléculaires asymétriques où une seule partie torsadée de la molécule est responsable du comportement TADF et la partie plane restante plus grande de la molécule est responsable du mésomorphisme peuvent être une approche plus prometteuse pour obtenir des matériaux TADF discotiques liquides-cristallins.

**Mots Clés:** Phosphorescence à température ambiante, Fluorescence retardée, cristaux liquides discotiques vitreux, efficacité d'échappement de la lumière.

## RESUMO

A incorporação de pontes de tiofeno contendo enxofre em estruturas do tipo D<sub>3</sub>A com um padrão de substituição 2,4- tem demonstrado produzir novos emissores fosforescentes e de fluorescência atrasada. Emissores com um núcleo de 1,3,5-triazina mostraram diferentes mecanismos de emissão dependendo da unidade doadora empregada. Enquanto moléculas com uma unidade carbazol apresentaram fosforescência a temperatura ambiente (com tempos de vida de 0,7 ms), a derivação com acridina levou à emissão de fluorescência atrasada termicamente ativada (*TADF*) com tempos de vida variando de 0,02 a 0,5 ms. Moléculas baseadas no núcleo *tris*[1,2,4]triazolo[1,3,5]triazina (TTT) apresentaram fosforescência independentemente da unidade doadora empregada, com tempos de vida variando de 0,1 a 3,5 ms, e também mostraram fluorescência atrasada através de um mecanismo de aniquilação tripleto-triplete (*TTA*) (com tempos de vida variando de 0,5 a 0,8 ms). O rendimento quântico de fotoluminescência (*PLQY*) para todos os compostos está na faixa de 0,01 a 0,25. Embora a presença do átomo de enxofre aumente o acoplamento spin-órbita (*SOC*) e, portanto, aumenta a taxa de cruzamento intersistemas, esses materiais também apresentaram uma alta taxa de decaimento não radiativo, que foi reduzida no estado sólido devido à restrição de mobilidade e, assim, apresentando um maior tempo de vida nesses processos. A fosforescência a temperatura ambiente observada em solução é atribuída à proteção do estado excitado <sup>3</sup>LE centrado na parte aceitador-tiofeno (em ambas as séries) pelos doadores volumosos, que impedem o decaimento não radiativo através de colisões e interações com o ambiente. Para aumentar a eficiência de saída de luz em diodos orgânicos emissores de luz (*OLED*), é essencial ter uma emissão anisotrópica. Isso pode ser alcançado incorporando o emissor em uma matriz de cristal líquido (CL), especificamente um CL discótico vítreo. *Tris*(fenantril)triazinas substituídas por éster formam, no resfriamento, mesofases colunares hexagonais sem cristalização. A temperatura de transição vítrea nesses materiais depende do comprimento da cadeia alquílica substituinte, e cadeias alquílicas curtas com um estado vítreo acima da temperatura ambiente só podem ser obtidas com temperaturas de clareamento extremamente elevadas. *Tris*([4]helicenil)triazinas substituídas por éster com cadeias alquílicas curtas foram sintetizadas para suprir esta limitação, resultando em mesofases colunares hexagonais com temperaturas de fusão e clareamento facilmente alcançáveis. O derivado éster proprílico apresenta uma transição única entre duas mesofases colunares hexagonais com um aumento súbito na ordem do conjunto de colunas. Um planejamento molecular baseado na flexibilidade configuracional, um desvio intrínseco leve da planaridade e substituintes ésters alquílicos de cadeia curta demonstrou permitir a estabilização

de uma mesofase colunar hexagonal semelhante a um sólido a temperatura ambiente e uma transição acessível para o líquido isotrópico, permitindo a formação de amostras vítreas alinhadas na superfície no resfriamento a partir do líquido.

**Palavras-chave:** Fosforescência a temperatura ambiente, Fluorescência atrasada, Cristais líquidos discóticos vítreos, Saída de luz.

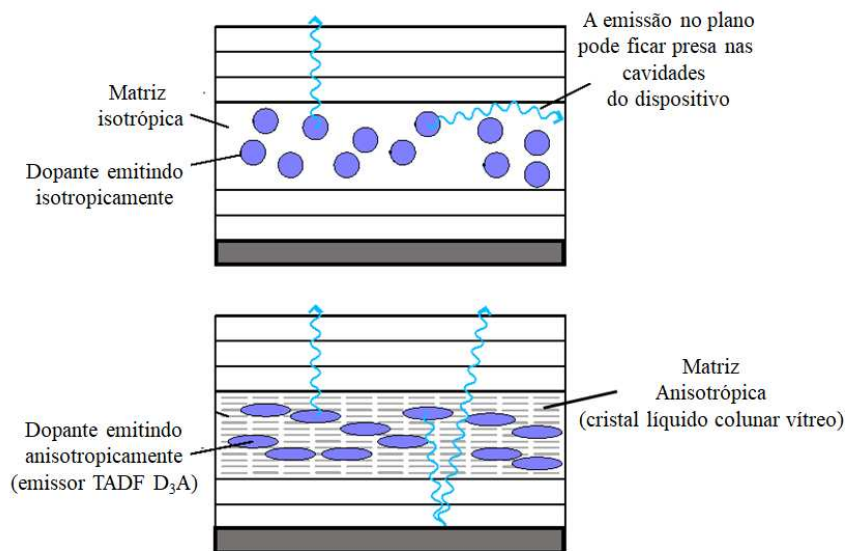
## RESUMO EXPANDIDO

Os diodos orgânicos emissores de luz (*OLEDs*) têm se consolidado cada vez mais no mercado de displays. Nos últimos anos, esses materiais têm alcançado maior eficiência graças às grandes modificações e otimizações do mecanismo de emissão molecular e da estrutura do dispositivo. Hoje, os dispositivos *OLED* já podem alcançar uma eficiência interna de 100% sem o uso de metais pesados através do mecanismo de fluorescência atrasada termicamente ativado (*TADF*). Um material *TADF* é capaz de converter todos os estados triplôs não-emissivos, formados após a excitação elétrica em estados singletos emissivos através do cruzamento intersistemas reverso (*rISC*). O *rISC* pode ocorrer quando há uma diferença de energia suficientemente pequena entre os estados excitados triplêto e singletos ( $\Delta E_{ST}$ ) de modo que a energia térmica presente na temperatura ambiente possibilita o *rISC*. Outro mecanismo de fluorescência atrasada é a aniquilação triplêto-triplêto (*TTA*). Este mecanismo bi-molecular tem uma eficiência menor devido à transferência de energia de um estado triplêto excitado de uma molécula para promover o *rISC* de outra molécula triplêto excitada. Os emissores *TADF* são geralmente obtidos através de estruturas do tipo doador-aceitador. Essa estrutura reduz a sobreposição do orbital molecular ocupado de mais alta energia (*HOMO*) e o orbital molecular desocupado de mais baixa energia (*LUMO*), e valores baixos de  $\Delta E_{ST}$  são obtidos. Várias estratégias moleculares têm sido recentemente estudadas para obter cada vez mais emissores *TADF* eficientes. A inserção de pontes de ligação separando as unidades doador e aceitador, com grupos volumosos que mudam os ângulos diédricos entre as unidades doadora e aceitadora, ou com diferentes padrões de substituição que ajusta a conjugação entre as unidades doador e aceitador, é uma abordagem eficiente para separar espacialmente os orbitais de fronteira e permitir que o mecanismo *TADF* ocorra. A eficiência externa, ou geral, de um dispositivo *OLED* é composta por um fator interno, que inclui estatísticas de spin, eficiência quântica e razão elétron-buraco, e um fator externo de saída de luz que depende do aprisionamento da luz dentro do dispositivo. Suponha que o emissor esteja em uma matriz isotrópica. Nesse caso, a maioria da luz emitida na camada emissora ficará presa na cavidade do dispositivo e apenas cerca de 20% da luz será emitida e vista por um observador. Recentemente, avanços no acoplamento de luz em *OLEDs* mostraram que a forma e orientação dos emissores são cruciais para aumentar o valor da saída de luz. A orientação paralela de dipolos com as camadas do dispositivo favorece uma maior saída de luz. Este tipo de orientação pode ser obtido em materiais que formam um vidro molecular anisotrópico. Sabe-se que os cristais líquidos discóticos podem se auto-organizar em colunas capazes de transportar carga

unidirecionalmente devido à sua estrutura anisotrópica específica (um núcleo aromático plano cercado por cadeias alifáticas). Quando alinhados homeotrópicamente (ou seja, com os centros aromáticos paralelos ao substrato), esses materiais podem ser úteis na extração de luz e, conseqüentemente, na obtenção de dispositivos mais eficientes. A combinação de mesomorfismo com luminescência pode assim ter um impacto importante no desempenho de dispositivos eletro-ópticos, como os *OLEDs*. O alinhamento uniforme que pode ser obtido nesses materiais e sua capacidade de auto-cura de defeitos, como as fronteiras de grão, combinado com o fenômeno de luminescência, pode permitir a elaboração de uma estrutura *OLED* mais simples e eficiente, onde a camada emissora e de transporte podem ser a mesma. Embora os cristais líquidos fluorescentes e fosforescentes sejam relatados na literatura, ainda há poucos cristais líquidos com fluorescência atrasada. A combinação destas duas propriedades - cristalinidade líquida e emissão de estados tripleto - em uma única molécula pode ser uma excelente alternativa na busca de materiais eficientes, mas é uma tarefa não-trivial. A não planaridade, devido aos grandes ângulos de torção entre doador e aceitador, dos materiais *TADF* é dificilmente compatível com a planaridade requerida nos mesógenos discóticos. Este antagonismo estrutural é a principal barreira para a obtenção de um material *TADF-LC*. Recentemente, alguns grupos de pesquisa obtiveram tais materiais, mas não de forma eficiente, mostrando que ainda há uma lacuna a ser preenchida. Uma alternativa mais acessível para combinar estas propriedades no mesmo dispositivo é incorporar um emissor *TADF* eficiente em uma matriz de cristal líquido discótico, especificamente, um cristal líquido colunar vítreo. As estruturas do tipo doador-aceitador com uma unidade aromática interna de aceitadora de elétrons e três unidades externas torcidas de doação de elétrons mostram um aumento na força do oscilador ( $f$ ) em comparação com sistemas doador-aceitador simples. O forte acoplamento spin-orbita (*SOC*) permite o cruzamento entre os estados singleto e tripleto, resultando em corantes eletroluminescentes eficientes com emissão tanto pelo estado singleto quanto pelo tripleto. Os *N*-heterociclos 1,3,5-triazina e *tris*[1,2,4]triazolo[1,3,5]triazina (TTT) são centros mesogênicos bem conhecidos, com uma ampla gama de cristais líquidos relatados na literatura. Nos últimos anos, com a crescente busca por emissores *TADF*, estes dois centros aromáticos têm se mostrado eficazes como unidades aceitadoras de elétrons em novos materiais luminescentes eficientes, em particular, para a obtenção de emissores azuis. É necessário trabalhar em um sistema de cores *RGB* (vermelho, verde e azul) para obter um *OLED* que emita em toda a faixa visível. Os emissores vermelhos e verdes já estão bem estabelecidos no mercado, com boa vida útil e pureza de cor satisfatória. Entretanto, ainda existe uma lacuna

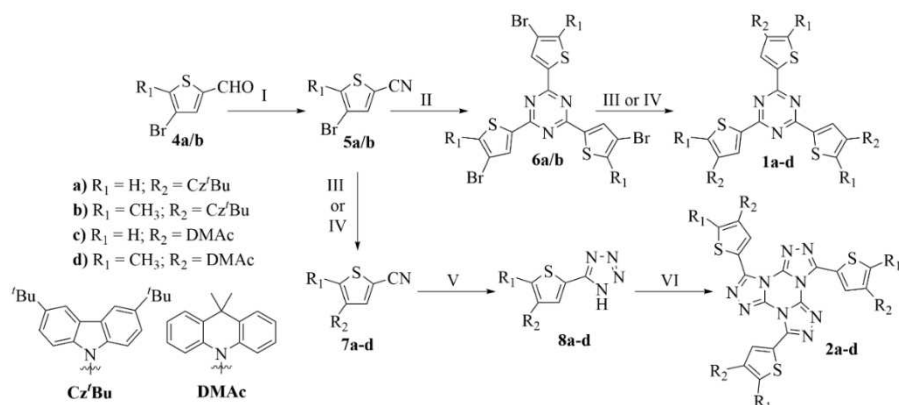


para os emissores azuis, pois estes materiais têm alta energia no estado excitado e, conseqüentemente, menor estabilidade. Um excelente emissor azul pode ser usado sozinho para fabricar um dispositivo *OLED* onde as cores vermelha e verde podem ser obtidas através de camadas externas fotoluminescentes, reduzindo drasticamente a complexidade e aumentando a eficiência de produção destes dispositivos.



**A saída de luz em dispositivos OLED.** Emissão isotrópica (superior) e emissão anisotrópica (inferior).

Sob esta perspectiva, na primeira parte desta tese de doutorado, projetamos e sintetizamos duas novas séries de emissores do tipo D<sub>3</sub>A com base nos centros TTT e 1,3,5-triazina. Como ponte de ligação, escolhemos substituir o grupo de fenileno comumente empregado pela unidade de tiofeno 2,4-disubstituído. O padrão de disubstituição 2,4 é similar ao padrão de disubstituição 1,3 no benzeno, que se mostrou mais eficiente para obter valores baixos em  $\Delta E_{ST}$  do que o padrão 1,4. A inclusão do átomo de enxofre na estrutura de nossos emissores visou explorar o efeito do átomo pesado, aumentando o acoplamento spin-orbita nestes materiais e favorecendo o cruzamento intersistemas. Para sondar o efeito do impedimento estérico nos ângulos de torção e, portanto, nas propriedades de emissão dependentes da torção, usamos pontes de tiofeno com e sem o substituinte metila estereticamente pronunciado.

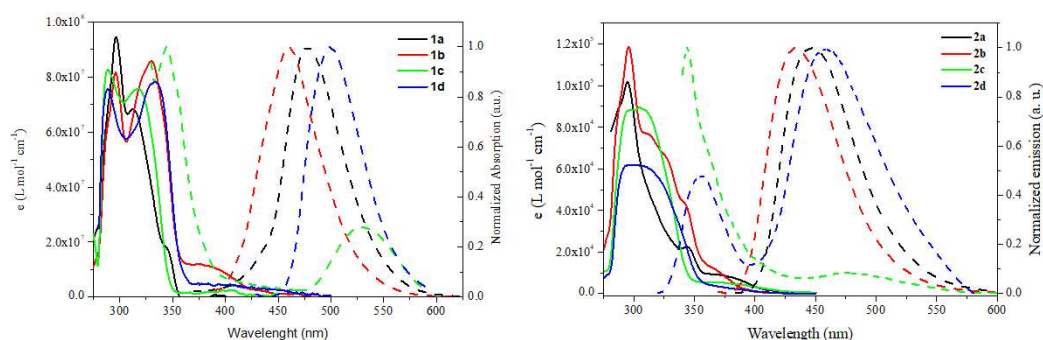


**Síntese de estruturas D<sub>3</sub>A.** I)  $NH_4OH(aq)$ ,  $I_2$ , THF, **5a**: 82%, **5b**: 72%; II)  $CF_3SO_3H$ , **6a**: 67%, **6b**: 55%; III) 3,6-di-*tert*-butil-9H-carbazol,  $K_2CO_3$ ,  $CuSO_4 \cdot 5H_2O$ , 1-metilnftaleno, **1a**: 52%, **1b**: 39%, **7a**: 48%, **7b**: 34%; IV) 9,9-dimetil-9,10-dihidroacridina,  $[Pd(OAc)_2]$ , Xphos,  $NaO^t-Bu$ , tolueno, **1c**: 57%, **1d**: 52%, **7c**: 42%, **7d**: 46%; V)  $NaN_3$ ,  $NH_4Cl$ , DMF, **8a**: 88%, **8b**: 83%, **8c**: 81%, **8d**: 79%; VI)  $C_3N_3Cl_3$ , 2,6-lutidina, tolueno, **2a**: 38%, **2b**: 32%, **2c**: 39%, **2d**: 35%.

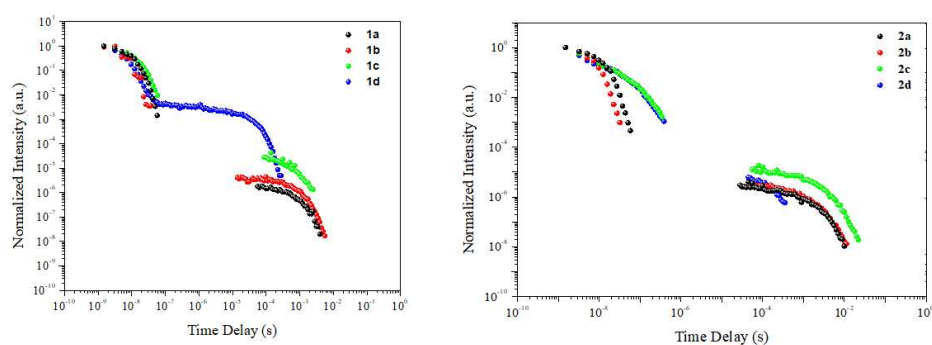
Os emissores baseados no centro 1,3,5-triazina apresentaram diferentes mecanismos de emissão, de acordo com a unidade doadora empregada. Após análises de fotoluminescência resolvidas no tempo, os derivados de 3,6-*tert*butilcarbazol são emissores fosforescentes, enquanto os derivados de 9,10-dimetilacridina são materiais *TADF*. O alto valor de  $\Delta E_{ST}$  encontrado para as moléculas contendo o doador de 3,6-*tert*butilcarbazol ( $> 0,5$  eV) torna impossível o cruzamento intersistemas reversível termicamente ativado e, portanto, não permite a emissão de *TADF* por esses pares de carbazol-triazina. A fosforescência nestes emissores é atribuída ao efeito do átomo de enxofre sobre o acoplamento de spin-orbita, aumentando a taxa de cruzamento intersistemas ao relaxar a regra de seleção de spin e permitindo o decaimento radiativo  $T_1 \rightarrow S_0$ . Estes materiais apresentaram tempo de vida de fosforescência ( $\tau_{Phosph}$ ) de 0,7 ms para ambos os compostos em solução de tolueno. Mudando a unidade doadora para 9,10-dimetilacridina, foi possível obter menores valores de  $\Delta E_{ST}$  ( $< 0,3$  eV), suficientes para que ocorresse o cruzamento intersistemas reverso termicamente ativado e para que o mecanismo de emissão *TADF* fosse observado, com tempos de vida na faixa de 0.02 e 0.5 ms. Embora estes materiais apresentem *TADF* à temperatura ambiente, análises de fotoluminescência resolvida no tempo a baixas temperaturas em estado sólido mostraram que estes materiais também são fosforescentes, com tempos de vida entre 6.8 e 17.8 ms. O derivado sem o grupo metil na ponte de tiofeno, além disso, apresentou fosforescência à temperatura ambiente, com um curto tempo de vida de 10.5 ms. Análises de fotoluminescência no estado estacionário mostraram que este derivado apresenta uma emissão dupla em solução tolueno atribuída a uma emissão de excitação localizada (*LE*) da unidade de 9,10-dimetilacridina e uma emissão do tipo

transferência de carga (*CT*) entre as unidades doadoras-aceitadora. Isto demonstra que o sistema doador-aceitador está desacoplado, com um ângulo diedral quase ortogonal ( $\sim 90^\circ$ ). A inserção do grupo metil na ponte de ligação diminui este ângulo e aumenta o acoplamento das unidades, levando a apenas uma emissão do tipo *CT* no espectro de fotoluminescência no estado estacionário. Mudando a unidade aceitadora da triazina para TTT, obtemos um mesmo mecanismo de emissão, independentemente da unidade doadora empregada. Todos os derivados mostraram fosforescência à temperatura ambiente em solução com tempo de vida na faixa de 0,1 - 3,5 ms. Além disso, para os dois derivados de carbazol e o derivado de acridina sem o grupo metil na ponte de 2,4-tiofeno, também foi observado o mecanismo de fluorescência atrasada por aniquilação tripleto-tripletto (*TTA*), com tempos de vida na faixa de 0,5 - 0,8 ms. O alto valor de  $\Delta E_{ST}$  encontrado para estes materiais impede que o mecanismo *TADF* ocorra, levando em vez disso à fluorescência atrasada pelo mecanismo *TTA*. Este mecanismo foi confirmado por sua ausência no estado sólido. A restrição de mobilidade molecular impede a colisão entre duas moléculas no estado excitado tripleto, desabilitando assim o mecanismo *TTA*. O espectro de fotoluminescência no estado estacionário mostrou que os derivados da acridina apresentam uma emissão dupla correspondente à emissão *LE* da unidade isolada e a emissão *CT* entre as unidades de acridina e TTT. Como observado anteriormente para um dos emissores baseados na triazina, isto indica que as unidades estão próximas à ortogonalidade. De fato, cálculos teóricos utilizando a teoria funcional da densidade (*DFT*) mostraram que nestes derivados, o ângulo diedro está na faixa de  $80^\circ$ , com valores mais baixos no emissor de ponte-metilada. Os cálculos de *DFT* dependente do tempo (*TD-DFT*) e acoplamento de spin-orbita *TD-DFT* (*SOC-TD-DFT*) mostraram que os três primeiros estados excitados  $S_n$  têm uma configuração *CT* nos derivados do carbazol. Entretanto, estas transições têm alta força oscilante (*f*) característica de um estado *LE*. Portanto, a emissão destes materiais é proveniente de um estado misto  $^1LE/CT$ . Para os derivados de acridina, a emissão de menor energia mostrou configurações *CT* para os estados excitados e baixos valores de *f*. A emissão observada em energia mais alta (comprimentos de onda menores) está relacionada ao estado *LE* centrado na unidade TTT-thiophene. Observamos que as geometrias otimizadas dos estados  $S_1$  mostram pouca mudança nos ângulos diedros, resultando em pouca mudança na força do oscilador nestes estados em comparação com o estado fundamental. Por outro lado, a geometria no estado excitado  $T_1$  muda significativamente, resultando em uma planarização da molécula e uma conjugação crescente do sistema  $\pi$ , resultando em configurações  $^3LE$  para os estados  $T_1$ ,  $T_2$ , e  $T_3$  centradas na unidade TTT-tiofeno. O estado  $T_4$  tem uma energia semelhante ao estado  $S_1$  e,

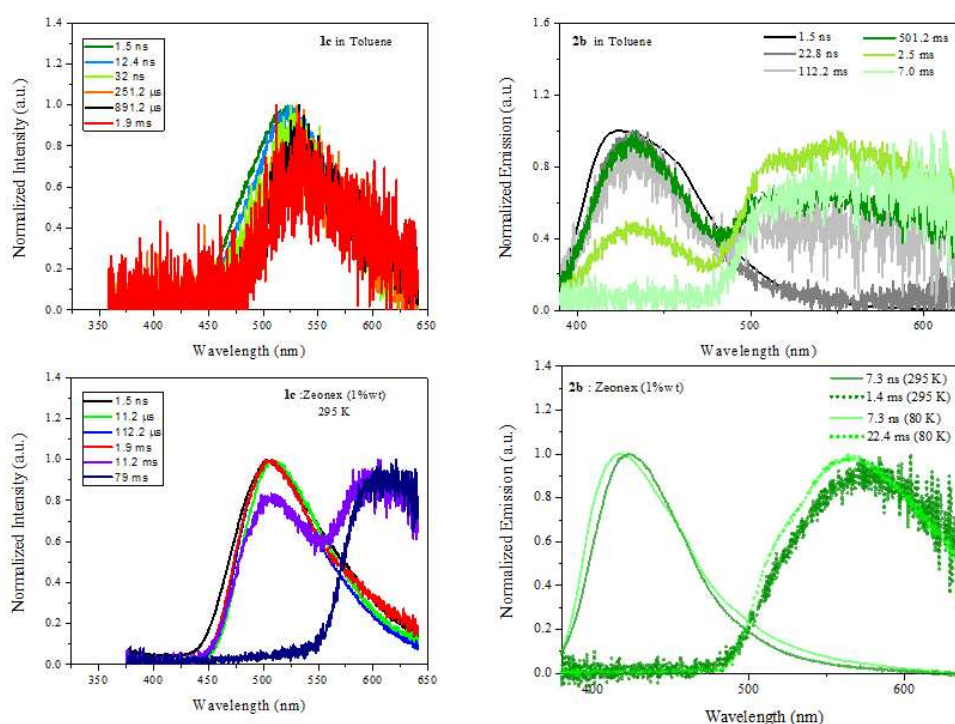
portanto, apresenta uma configuração *CT*. Para avaliar o efeito do acoplamento spin-orbita no cruzamento intersistemas e na fosforescência destes materiais, usamos o elemento de matriz *SOC* (*SOCME*) obtido a partir de cálculos *SOC-TD-DFT*. Foram encontrados maiores valores para os derivados de carbazol do que para os derivados de acridina, em concordância com os rendimentos quânticos de fotoluminescência observados. Estes valores são similares aos encontrados na literatura para sistemas doador-aceitador simples e para moléculas contendo átomos de enxofre. O *SOC* entre os estados excitados permite a transição proibida  $T_1 \rightarrow S_0$ . O derivado de acridina com o grupo metil na ponte de tiofeno apresentou baixos valores de  $\tau_{\text{Phosph}}$  em comparação com os outros três compostos e apenas uma *RTP* fraca. A *RTP* observada para estes compostos em solução é atribuída à proteção dos volumosos grupos doadores contra a desativação não-radiativa do estado excitado  $^3\text{LE}$  centrado na porção aceitador-tiofeno. Em ambas as séries, foram obtidos baixos valores de rendimento quântico de fotoluminescência. Embora estes materiais apresentem alto acoplamento spin-orbita devido ao efeito do átomo pesado que a ponte tiofeno contendo enxofre adiciona ao sistema, todos os compostos têm uma alta taxa de decaimento não radiativo, sugerindo modificações estruturais necessárias para aumentar a rigidez destes sistemas. As análises de fotoluminescência resolvidas no tempo em estado sólido mostraram taxas de decaimento não radiativos menores. Em baixas temperaturas, o tempo de vida destes processos é maior, como esperado, devido à restrição da mobilidade na matriz rígida, que é mais pronunciada em baixas temperaturas. A estabilidade térmica de todos os oito emissores foi determinada pela análise termogravimétrica (*TGA*), e todos os compostos mostraram boa estabilidade ( $T_{\text{dec}} > 400^\circ\text{C}$ ), sendo os derivados de carbazol mais estáveis do que os derivados de acridina em ambas as séries. Ao comparar diferentes centros aceitadores com a mesma unidade doadora, observamos que os emissores à base de triazina são mais estáveis termicamente que os derivados de TTT, possivelmente devido à isomerização térmica que pode ocorrer neste último.



**Espectros de absorção e emissão.** 1a-d (esquerda) e 2a-d (direita) em solução diluída de tolueno ( $10^{-5} \text{ mol L}^{-1}$ ).



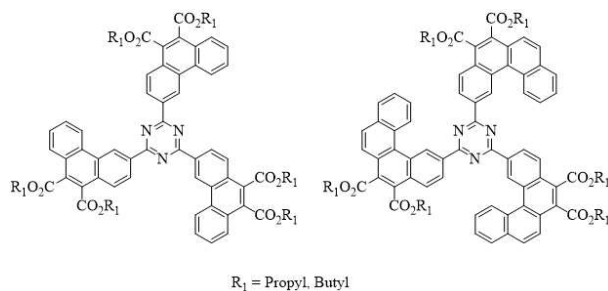
**Curvas de decaimento resolvidas no tempo em tolueno.** O comprimento de onda de excitação foi 355 nm. Todas as medidas foram realizadas na ausência de oxigênio.



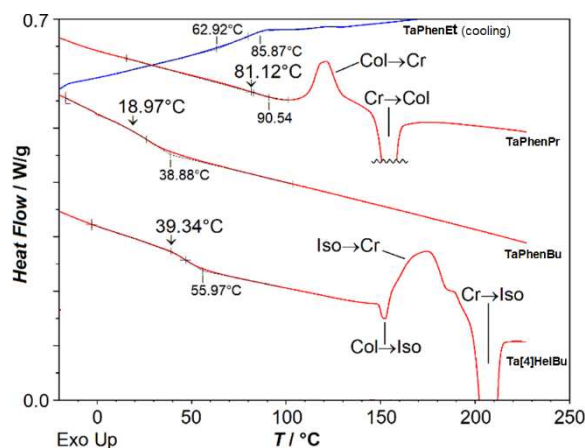
**Espectros normalizados obtidos em diferentes tempos.** 1c e 2b em solução (cima) e estado sólido (baixo). O comprimento de onda de excitação foi 355 nm. Todas as medidas foram realizadas na ausência de oxigênio.

Na segunda parte desta tese, planejamos e sintetizamos uma série de cristais líquidos discóticos vítreos baseados no centro 1,3,5-triazina substituída com ésteres curtos para uso como matrizes para emissores *TADF* na fabricação de novos dispositivos *OLED*. Primeiro, sintetizamos os derivados de *tris*(fenantril)triazina com diferentes cadeias de ésteres (TaPhenEst; etil, propil, butil). As análises de calorimetria diferencial de varredura (*DSC*) mostraram que o derivado de etil apresenta uma transição entre duas fases cristalinas diferentes sem exibir mesomorfismo. Por outro lado, os derivados TaPhenPr e TaPhenBu exibem mesofases hexagonais colunares enantiotrópicas confirmadas por difração de raios X (*XRD*). A

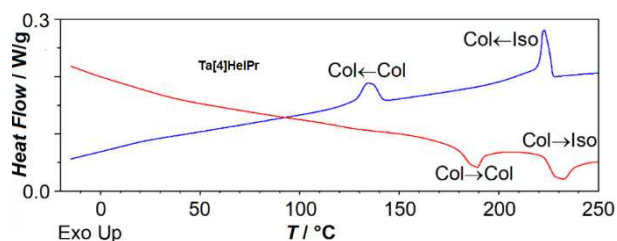
falta de uma transição atingível para o líquido isotrópico abaixo de 375°C impediu o crescimento de texturas definidas em um microscópio óptico de luz polarizada (*POM*). Ambos os derivados exibiram um estado vítreo mesomórfico durante o resfriamento, onde o derivado com as cadeias alquílicas ésteres mais longos, TaPhenBu, teve uma temperatura de transição vítrea muito mais baixa, mostrando que a temperatura de transição é fortemente dependente do tamanho da cadeia alquílica. Isto nos mostrou que um estado vítreo acima da temperatura ambiente só poderia ser obtido com cadeias alquílicas curtas, às custas de pontos de clareamento inatingível (>375°C). Para resolver este problema, decidimos expandir a região aromática sintetizando os derivados de éster *tris*([4]helicenil)triazina, Ta[4]HelEst, com os mesmos comprimentos de cadeia que na série análoga de fenantreno. Todos os derivados apresentaram uma transição para o líquido isotrópico na faixa de 205-332 °C. O derivado de cadeia mais curta, Ta[4]HelEt, não exibiu mesomorfismo de acordo com *DSC* e *XRD*, mas apresentou uma transição singular entre duas fases cristalinas hexagonais. Em contraste, os derivados ésteres de cadeias mais longas Ta[4]HelPr e Ta[4]HelBu exibiram mesomorfismo hexagonal colunar monotrópico com o crescimento de texturas mesofásicas e picos de difração de raios X característicos desta simetria mesofásica. Nenhuma transição vítrea foi observada para o derivado Ta[4]HelPr devido à natureza já altamente ordenada da mesofase de mais baixa temperatura entre suas duas mesofases hexagonais. Em contraste, o derivado Ta[4]HelBu exibiu uma transição vítrea de 39°C, formando um vidro mesomórfico à temperatura ambiente, produzindo assim o vidro mesomórfico colunar hexagonal almejado, em combinação com um ponto de clareamento acessível, mostrando ser um excelente candidato para uso como matriz em dispositivos eletro-orgânicos.



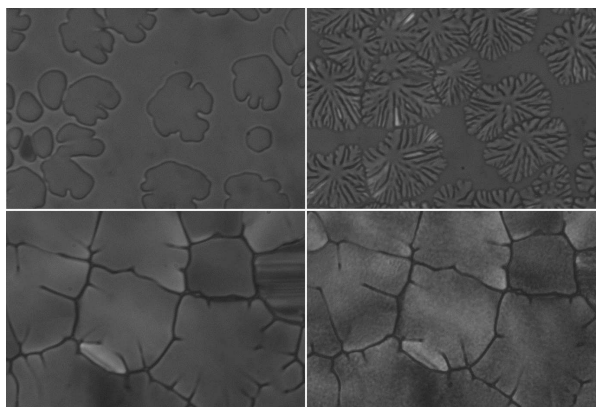
**Cristais líquidos colunares hexagonais derivados da triazina** com transições vítreas na mesofases acima da temperatura ambiente.



**Calorimetria diferencial.** Varreduras de aquecimento (vermelho) de **TaPhenPr**, **TaPhenBu** e **Ta[4]HelBu**, a  $+10^{\circ}\text{C}/\text{min}$  (após aquecimento inicial acima do ponto de fusão e subsequente resfriamento a  $-10^{\circ}\text{C}/\text{min}$ ), e varredura de resfriamento (azul) de **TaPhenEt** a  $-10^{\circ}\text{C}/\text{min}$ ; temperaturas de início de transição vítrea no aquecimento são indicadas acima das setas verticais; transições de fase são marcadas entre Col = mesofásico colunar hexagonal, Cr = estado cristalino, e Iso = líquido isotrópico.



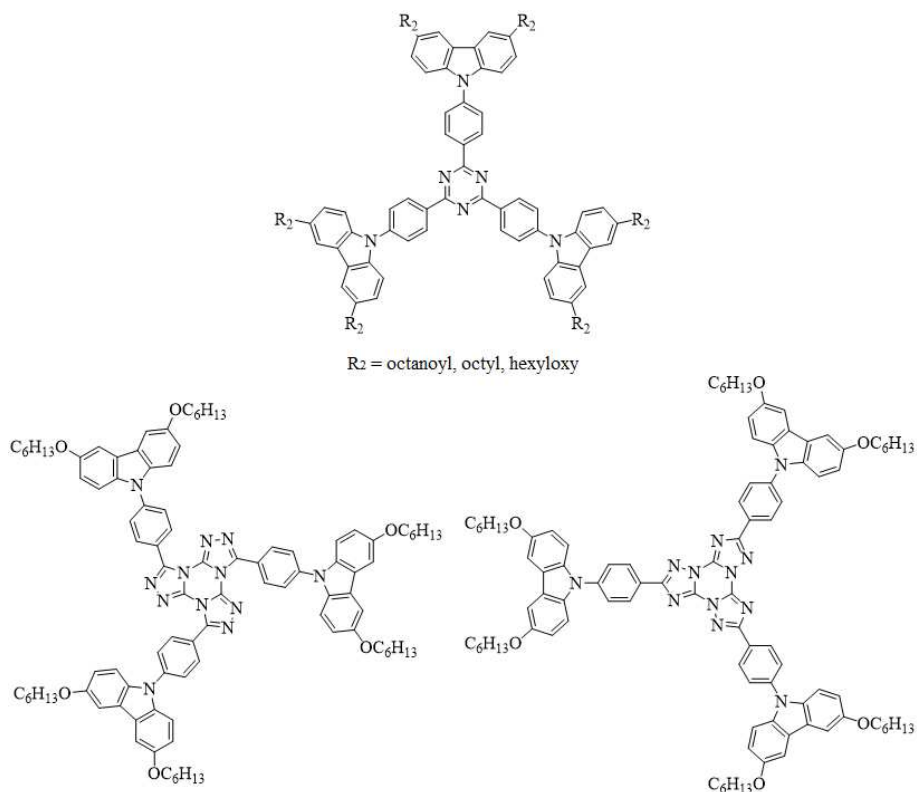
**Calorimetria diferencial.** Varreduras de resfriamento (azul) e posterior aquecimento (vermelho) de **Ta[4]HelPr** a  $\pm 10^{\circ}\text{C}/\text{min}$  (após aquecimento inicial acima do ponto de fusão); com transições de fase entre duas mesofases hexagonais colunares (Col) e entre a mesofase de temperatura mais alta e o líquido isotrópico (Iso).



**Crescimento entre as placas de vidro da mesofase colunar hexagonal.** **Ta[4]HelPr** (superior esquerdo) e **Ta[4]HelBu** (superior direito) em alinhamento homeotrópico após resfriamento através da transição de fase isotrópica-colunar, e textura homeotrópica da mesofase de alta temperatura de **Ta[4]HelPr** a  $200^{\circ}\text{C}$  (inferior esquerdo) e da mesofase de baixa temperatura a  $100^{\circ}\text{C}$  (inferior direito) após resfriamento do líquido isotrópico seguido de reaquecimento; microscopia óptica de luz polarizada com polarizadores ligeiramente descruzados.

Nós tentamos também induzir mesomorfismo nas estruturas  $D_3A$  descritas na primeira parte desta tese de doutorado e naquelas relatadas na literatura derivadas de 1,3,5-triazina e TTT, introduzindo cadeias alquílicas na unidade doadora carbazol 3,6-disubstituído. Introduzimos

cadeias acil, alquil e alcóxi nas moléculas à base de triazina. No entanto, infelizmente, nenhum material nesta sessão apresentou mesomorfismo. Acreditamos que a não planaridade desses materiais, característica dos sistemas *TADF*, dificulta o empilhamento das moléculas e conseqüentemente impede a formação da mesofase colunar. Introduzimos também cadeias alcóxi nas moléculas *D<sub>3</sub>A* baseadas no TTT, novamente sem sucesso. Nem mesmo a isomerização da unidade central ao isômero radial, mais estendido, do centro do triaril-TTT foi suficiente para induzir o mesomorfismo.



**Estrutura das moléculas *D<sub>3</sub>A*.** Doadores substituídos com cadeias acil, alquil e alcóxi.

Em conclusão, a inclusão de pontes de tiofeno em um padrão de substituição 2,4 em moléculas do tipo *D<sub>3</sub>A* aumenta significativamente o acoplamento spin-orbita nestes materiais e assim permite a transição proibida  $T_1 \rightarrow S_0$ , permitindo que estes materiais emitam fosforescência à temperatura ambiente. Além disso, *RTP* em solução observada é inesperada devido há alto tempo de vida do estado tripleto e à competição com a decaimento não-radiativo. Cálculos teóricos mostraram que a fosforescência é derivada de um estado  $^3LE$  centrado na porção aceitador-tiofeno. Acreditamos que os grupos doadores volumosos protegem este estado do decaimento não-radiativo, permitindo tempo suficiente para a emissão de fosforescência. Mudar a unidade doadora no centro TTT não é suficiente para diminuir  $\Delta E_{ST}$  e permitir a



emissão de *TADF*, embora estes materiais tenham um mecanismo de *TTA*. Em contraste, a mudança de carbazol para acridina altera drasticamente os valores  $\Delta E_{ST}$  em materiais baseados na triazina. Os derivados de acridina mostraram baixos valores, possivelmente devido à quase ortogonalidade das unidades, permitindo o cruzamento intersistemas reverso ativado termicamente e a emissão de *TADF*, enquanto os derivados de carbazol mostraram apenas fosforescência. Além destas emissões com tempo de vida mais longo, todos os compostos apresentaram fluorescência direta, com derivados do carbazol em ambas as séries mostrando emissão na região azul. A inserção de um grupo metil na unidade de tiofeno tem efeitos diferentes sobre os ângulos diedros do carbazol e dos derivados de acridina. Enquanto há um aumento no ângulo diédrico no primeiro, há uma diminuição quando a unidade doadora é a acridina. O projeto de moléculas do tipo  $D_3A$  contendo a unidade de tiofeno no padrão 2,4 de substituição provou ser uma estratégia útil na busca de novos emissores *RTP* e *TADF*. Os ésteres trifenantril-triazina-hexaésteres onde a cadeia de ésteres alquílicos é maior que o grupo etílico, como os ésteres propílico e butílico, mostraram um mesomorfismo enantiotrópico com a formação de um vidro mesomórfico no resfriamento. No entanto, os pontos de clareamento destes materiais não foram facilmente acessíveis, tendo em vista alinhá-los sobre um substrato. A expansão da região aromática para *tris*[4]helicenil-triazina-hexaésteres resultou em uma leve desplanarização, suficiente para desestabilizar as mesofases, sendo observada apenas durante o resfriamento, mas também levando a temperaturas de transição acessíveis para o estado líquido isotrópico, ao mesmo tempo em que produzia transições vítreas acima da temperatura ambiente. O planejamento molecular baseado na flexibilidade configuracional e incluindo um leve desvio da planaridade com substituintes ésteres alquílicos de cadeia curta, demonstrou permitir a estabilização de uma mesofase hexagonal colunar sólida à temperatura ambiente com uma transição acessível para líquido isotrópico. O resfriamento a partir do líquido permite a formação de amostras alinhadas na superfície. Em contraste, a estratégia de apenas inserir cadeias alquílicas nas unidades doadoras dos sistemas  $D_3A$  não foi suficiente para induzir o mesomorfismo. Projetos moleculares assimétricos onde apenas uma porção torcida da molécula é responsável pelo comportamento do *TADF*, e a maior parte restante da molécula plana responsável pelo mesomorfismo pode ser uma abordagem mais promissora para a obtenção de materiais *TADF* líquido cristalinos discóticos.

**Palavras-chave:** Fosforescência a temperatura ambiente, Fluorescência atrasada, Cristais líquidos discóticos vítreos, Saída de luz.

## LIST OF FIGURES

<b>Figure 1</b> Device structure made by Tang and Van Slyke - the first heterojunction OLED.....	68
<b>Figure 2</b> Schematic representation of light output in OLED devices. Isotropic emission (top) and anisotropic emission (bottom). .....	74
<b>Figure 3</b> Simplified representation of the luminescence phenomenon. Excitation and emission. ....	74
<b>Figure 4</b> Jablonski diagram, representation of the photophysical processes present in the luminescence phenomenon. IC: internal conversion; VR: vibrational relaxation; ISC: intersystem crossing; rISC: reverse intersystem crossing, $\Delta E_{ST}$ - Energy difference between the excited states $S_1$ and $T_1$ . Adapted from the literature. ....	75
<b>Figure 5</b> Representation of the processes responsible for delayed fluorescence. a) TADF, intramolecular process; b) TTA, intermolecular process. ....	78
<b>Figure 6</b> Representation of electroluminescence in OLED. a) 1st generation OLEDs: prompt fluorescence; b) 2nd generation OLEDs: phosphorescence; c) 3rd generation OLEDs: thermally activated delayed fluorescence. ....	79
<b>Figure 7</b> Strategies to adjust $\Delta E_{ST}$ and $k_r$ . a) Orbital overlap in benzophenone. Large $\pi$ - $\pi^*$ overlap induces large $\Delta E_{ST}$ (top) and weak n- $\pi^*$ overlap induces small $\Delta E_{ST}$ (bottom); b) Design principles of organic TADF materials. ....	80
<b>Figure 8</b> Representation of molecular organization in the different states of matter. a) solid, liquid and gaseous states; b) liquid crystalline state: representation of nematic and smectic mesophases. ....	81
<b>Figure 9</b> The first liquid crystal. a) structure of cholesteryl benzoate; b) demonstration of the experiment by Lehmann: Texture observed under polarized light microscope (174°C, 10x); c) demonstration of the experiment by Reinitzer: from left to right: solid phase, mesophase, isotropic liquid. ....	82
<b>Figure 10</b> Calamitic liquid crystals. a) Rod-like anisometry; b) Schematic structure of calamitic mesogens. ....	84
<b>Figure 11</b> Molecular organization in calamitic liquid crystal mesophases. a) nematic mesophase (N); b) non-tilted smectic mesophase (SmA); c) tilted smectic mesophase (SmC). ....	85
<b>Figure 12</b> First discotic liquid crystal synthesized by Chandrasekhar and coworkers. Cr: cristal phase; Col: columnar mesophase; I: isotropic phase. ....	85

<b>Figure 13</b> Discotic liquid crystals. a) Disk-like anisometry; b) Schematic structure of discotic mesogens. ....	86
<b>Figure 14</b> Nematic mesophases in disk-like mesogens. a) Nematic discotic mesophase (ND); b) Cholesteric nematic discotic mesophase (ND*); c) Nematic columnar mesophase (NC)...	86
<b>Figure 15</b> Intracolumnar order. a) ordered stacking; b) disordered stacking. ....	87
<b>Figure 16</b> Different arrangements in columnar mesophases, cross sections viewed from above. a) Columnar hexagonal; b) Columnar rectangular; c) Columnar oblique; d) Columnar rectangular with P2 <sub>1</sub> /a symmetry; e) Columnar rectangular with P2/a symmetry. ....	88
<b>Figure 17</b> $\pi$ -stacking interaction and one-dimensional charge transport present in columnar mesophases. Adapted from the literature. ....	89
<b>Figure 18</b> The three possible triazine systems: 1,2,3-, 1,2,4-, 1,3,5-triazine.....	91
<b>Figure 19</b> 1,3,5-triazine synthesis. a) First reported synthesis from hydrogen cyanide; b) Synthesis of 1,3,5-triazine derivatives from 2,4,6-trichloro-1,3,5-triazine; Top: synthesis of asymmetric derivatives (temperature control); Bottom: synthesis of symmetric derivatives. .	92
<b>Figure 20</b> Different protocols for the trimerization of the nitrile group in the synthesis of 1,3,5-triazine; a) Protic acid; b) High pressure; c) Lewis acid. ....	92
<b>Figure 21</b> Simplified mechanism of acid-catalyzed nitrile group trimerization in the synthesis of s-triazine. ....	93
<b>Figure 22</b> Target D <sub>3</sub> A molecules based on the 1,3,5-triazine core. Donor units are 3,6-di-tert-butyl-9H-carbazole and 9,9-dimethyl-9,10-dihydroacridine.....	94
<b>Figure 23</b> IR and <sup>1</sup> H NMR spectra of intermediates <b>4a</b> , <b>5a</b> and <b>6a</b> . IR spectra region 2.000 – 2.500 cm <sup>-1</sup> , monitoring of the CN stretching band (left). <sup>1</sup> H NMR spectra (400 MHz, <b>5a</b> : CDCl <sub>3</sub> , <b>6a</b> : C <sub>2</sub> D <sub>2</sub> Cl <sub>4</sub> ). Aromatic region (right).....	96
<b>Figure 24</b> IR and <sup>1</sup> H NMR spectra of intermediates <b>4b</b> , <b>5b</b> and <b>6b</b> . IR spectra region 2.000 – 2.500 cm <sup>-1</sup> , monitoring of the CN stretching band (left). <sup>1</sup> H NMR spectrum (400 MHz, C <sub>2</sub> D <sub>2</sub> Cl <sub>4</sub> ) (right).....	97
<b>Figure 25</b> <sup>1</sup> H NMR spectra of the final molecules <b>1a</b> and <b>1b</b> (400 MHz, CDCl <sub>3</sub> ). Aromatic region.....	98
<b>Figure 26</b> <sup>1</sup> H NMR spectra of the final molecules <b>1c</b> and <b>1d</b> (400 MHz, <b>1c</b> : CDCl <sub>3</sub> , <b>1d</b> : C <sub>2</sub> D <sub>2</sub> Cl <sub>4</sub> ). Aromatic region. ....	99
<b>Figure 27</b> Mass loss patterns determined through TGA measurements in N <sub>2</sub> with heating rate of 10 °C min <sup>-1</sup> . ....	100

<b>Figure 28</b> CV curves of the Triazine-based emitters in DMF solution. 0.1 mol L <sup>-1</sup> of Bu <sub>4</sub> NPF <sub>6</sub> (tetrabutylammonium hexafluorophosphate) as a supporting electrolyte. Scan rate: 100 mV s <sup>-1</sup> . .....	101
<b>Figure 29</b> Absorption and emission spectra of <b>1a-d</b> in dilute toluene solution (10 <sup>-6</sup> mol L <sup>-1</sup> ). .....	102
<b>Figure 30</b> Absorption and normalized photoluminescence spectra in toluene and 2-MeTHF solutions.....	103
<b>Figure 31</b> Normalized absorption and photoluminescence spectra in zeonex excited at the peak of the lowest energy band.....	104
<b>Figure 32</b> Emission spectra in degassed (solid lines) and air-equilibrated (filled areas) in dilute toluene solution at room temperature. ....	105
<b>Figure 33</b> Time-resolved decay curves in toluene. The excitation wavelength was 355 nm. All measurements were performed in the absence of oxygen. ....	106
<b>Figure 34</b> Normalized spectra taken after different delay times at room temperature in toluene solutions. The excitation wavelength was 355 nm. All measurements were performed in the absence of oxygen. ....	107
<b>Figure 35</b> Left: Time-resolved decay in zeonex, 295 K and 80 K. Right: Normalized spectra after different delay times, 295K.....	109
<b>Figure 36</b> Isomeric forms of the TTT core. ....	113
<b>Figure 37</b> Synthetic methodologies of TTT core; a) from 3,5-diamino-1,2,4-tetrazole (first report); b) from cyanuric chloride (Huisgen reaction); c) r-TTT from 3-R-5-chloro-1,2,4-triazole; d) thermoisomerization t-TTT to r-TTT.....	114
<b>Figure 38</b> Synthetic mechanism TTT core; a) Huisgen reaction; b) Thermoisomerization, Dimroth rearrangement.....	115
<b>Figure 39</b> TADF emitters based on TTT core. ....	116
<b>Figure 40</b> Target D <sub>3</sub> A molecules based on the TTT core. Donor units are 3,6-di-tert-butyl-9H-carbazole and 9,9-dimethyl-9,10-dihydroacridine. ....	117
<b>Figure 41</b> IR and <sup>1</sup> H NMR spectra of intermediates <b>5a</b> , <b>7a</b> and <b>8a</b> . IR spectra region 2.000 – 2.500 cm <sup>-1</sup> , monitoring of the CN stretching band (left). <sup>1</sup> H NMR spectra (400 MHz, <b>5a</b> and <b>7a</b> : CDCl <sub>3</sub> , <b>8a</b> : DMSO-d <sub>6</sub> ). Aromatic region (right).....	119
<b>Figure 42</b> <sup>1</sup> H NMR spectrum of final molecule <b>2a</b> (400 MHz, C <sub>2</sub> D <sub>2</sub> Cl <sub>4</sub> ) (top). <sup>13</sup> C NMR spectrum from <b>8a</b> and <b>2a</b> (101 MHz, <b>2a</b> : C <sub>2</sub> D <sub>2</sub> Cl <sub>4</sub> , <b>8a</b> : DMSO-d <sub>6</sub> ) (bottom).....	120

<b>Figure 43</b> IR and <sup>1</sup> H NMR spectra of intermediates <b>5a</b> , <b>7c</b> and <b>8c</b> . IR spectra region 2.000 – 2.500 cm <sup>-1</sup> , monitoring of the CN stretching band (left). <sup>1</sup> H NMR spectra (400 MHz, <b>5a</b> and <b>7a</b> : CDCl <sub>3</sub> , <b>8a</b> : DMSO-d <sub>6</sub> ). Aromatic region (right).....	121
<b>Figure 44</b> <sup>1</sup> H NMR spectrum of final molecule <b>2c</b> (400 MHz, CDCl <sub>3</sub> ) (top). <sup>13</sup> C NMR spectrum from <b>8c</b> and <b>2c</b> (101 MHz, <b>8c</b> : DMSO-d <sub>6</sub> , <b>2c</b> : C <sub>2</sub> D <sub>2</sub> Cl <sub>4</sub> ) (bottom). .....	122
<b>Figure 45</b> Mass loss patterns determined through TGA measurements in N <sub>2</sub> with heating rate of 10 °C min <sup>-1</sup> . .....	123
<b>Figure 46</b> CV curves of the TTT emitters in DMF solution. 0.1 mol L <sup>-1</sup> of Bu <sub>4</sub> NPF <sub>6</sub> (tetrabutylammonium hexafluorophosphate) as a supporting electrolyte. Scan rate: 100 mV s <sup>-1</sup> . .....	124
<b>Figure 47</b> Absorption and emission spectra of <b>2a-d</b> in dilute toluene solution (10 <sup>-5</sup> mol L <sup>-1</sup> ). .....	125
<b>Figure 48</b> Absorption and normalized photoluminescence spectra in toluene and 2-MeTHF solutions.....	127
<b>Figure 49</b> Normalized absorption and photoluminescence spectra in zeonex excited at the peak of the lowest energy band. ....	128
<b>Figure 50</b> The TTT derivatives time-resolved decay curves in toluene. The excitation wavelength was 355 nm. All measurements were performed in the absence of oxygen. ....	129
<b>Figure 51</b> Normalized spectra taken after different delay times at room temperature in toluene solutions. The excitation wavelength was 355 nm. All measurements were performed in the absence of oxygen. ....	130
<b>Figure 52</b> Emission spectra in degassed (solid lines) and air-equilibrated (filled areas) in dilute toluene solution at room temperature. ....	132
<b>Figure 53</b> a: Time-resolved decay in zeonex. b: Normalized spectra after different delay times. ....	133
<b>Figure 54</b> Optimized ground state geometries within B3LYP/def2-SVP level of theory. ....	136
<b>Figure 55</b> Optimized S <sub>1</sub> state geometries within CAM-B3LYP/def2-SVP level of theory. .	137
<b>Figure 56</b> Optimized T <sub>1</sub> state geometries within B3LYP/def2-SVP level of theory.....	138
<b>Figure 57</b> Triazine-based mesogenic compounds.....	142
<b>Figure 58</b> Examples of discotic liquid crystals based on the TTT core.....	143
<b>Figure 59</b> Target molecules based on the triazine center synthesized by Fabrícia Nunes da Silva.....	145
<b>Figure 60</b> Target compounds in the search for discotic liquid crystals with TADF.....	149

<b>Figure 61</b> IR (top) and <sup>1</sup> H NMR (bottom) spectrum of intermediates <b>10</b> , <b>11</b> and <b>13</b> (400 MHz, <b>10</b> and <b>13</b> : CD <sub>2</sub> Cl <sub>2</sub> , <b>11</b> : CDCl <sub>3</sub> ). .....	151
<b>Figure 62</b> IR spectrum of intermediates <b>14</b> and <b>15</b> . Monitoring CN stretch band. ....	153
<b>Figure 63</b> <sup>1</sup> H NMR spectrum of the final molecules <b>16a-c</b> (400 MHz, <b>16a</b> and <b>16b</b> : CD <sub>2</sub> Cl <sub>2</sub> , <b>16c</b> : CDCl <sub>3</sub> ). .....	153
<b>Figure 64</b> <sup>1</sup> H NMR spectrum of the final molecule <b>17c</b> (400 MHz, CDCl <sub>3</sub> ). ....	154
<b>Figure 65</b> <sup>1</sup> H NMR spectrum of intermediates <b>18</b> and <b>19</b> (400 MHz, DMSO-d <sub>6</sub> ). ....	156
<b>Figure 66</b> IR spectrum of intermediates <b>18</b> and <b>19</b> . Monitoring CN stretch band. ....	156
<b>Figure 67</b> <sup>1</sup> H NMR spectrum of the final molecules <b>20</b> and <b>21</b> (400 MHz, C <sub>2</sub> D <sub>2</sub> Cl <sub>4</sub> ). .....	157

## LIST OF SCHEMES

<b>Scheme 1</b> Classification of liquid crystals. ....	83
<b>Scheme 2</b> Synthesis of compounds 1a-d. i) Br <sub>2</sub> , AcOH; ii) NH <sub>4</sub> OH(aq), I <sub>2</sub> , THF; iii) CF <sub>3</sub> SO <sub>3</sub> H; iv) (a-b) 3,6-di-tert-butyl-9H-carbazole, K <sub>2</sub> CO <sub>3</sub> , CuSO <sub>4</sub> .5H <sub>2</sub> O, 1-methylnaphthalene; v) (c-d) 9,9-dimethyl-9,10-dihydroacridine, [Pd(OAc) <sub>2</sub> ], Xphos, NaOt-Bu, toluene. ....	95
<b>Scheme 3</b> Synthetic approach to 2a-d; i) Br <sub>2</sub> , AcOH; ii) NH <sub>4</sub> OH(aq), I <sub>2</sub> , THF; iii) (a-b) 3,6-di-tert-butyl-9H-carbazole, K <sub>2</sub> CO <sub>3</sub> , CuSO <sub>4</sub> .5H <sub>2</sub> O, 1-methylnaphthalene; iv) (c-d) 9,9-dimethyl-9,10-dihydroacridine, [Pd(OAc) <sub>2</sub> ], Xphos, NaOt-Bu, toluene; v) NaN <sub>3</sub> , NH <sub>4</sub> Cl, DMF; vi) C <sub>3</sub> N <sub>3</sub> Cl <sub>3</sub> , 2,6-lutidine, toluene. ....	118
<b>Scheme 4</b> Synthetic approach for the synthesis of triazine-based mesogens. i) CF <sub>3</sub> SO <sub>3</sub> H; ii) phenylglyoxylic acid, acetic anhydride, triethylamine, THF; iii) alkyl alcohol, bromoalkene, triethylamine, THF; iv) iodine, ethyl acetate, light; v) 2-naphthylglyoxylic acid, acetic anhydride, triethylamine, THF. ....	145
<b>Scheme 5</b> Synthetic approach for 9H-carbazole derivatives; i) octanoyl chloride, AlCl <sub>3</sub> , dichloromethane; ii) LiAlH <sub>4</sub> , AlCl <sub>3</sub> , THF; iii) hexan-1-ol, Na, CuI, DMF.....	150
<b>Scheme 6</b> Synthetic approach to 16a-c and 17c; i) CF <sub>3</sub> SO <sub>3</sub> H; ii) a - 1,1'-(9H-carbazole-3,6-diyl)bis(octan-1-one) and b - 3,6-dioctyl-9H-carbazole, Cs <sub>2</sub> CO <sub>3</sub> , dimethylacetamide; iii) c - 3,6-bis(hexyloxy)-9H-carbazole, K <sub>2</sub> CO <sub>3</sub> , CuSO <sub>4</sub> .5H <sub>2</sub> O, 1-methylnaphthalene. ....	152
<b>Scheme 7</b> Synthetic approach to 20 and 21; i) 3,6-bis(hexyloxy)-9H-carbazole, Cs <sub>2</sub> CO <sub>3</sub> , dimethylacetamide; ii) NaN <sub>3</sub> , NH <sub>4</sub> Cl, DMF; iii) C <sub>3</sub> N <sub>3</sub> Cl <sub>3</sub> , 2,6-lutidine, toluene; iv) K <sub>2</sub> CO <sub>3</sub> , 1,2-dichlorobenzene.....	155

## LIST OF TABLES

<b>Table 1</b> Average timescales for radiative and no-radiative processes.....	76
<b>Table 2</b> Decomposition temperatures of triazine-based emitters obtained through TGA analyses.....	100
<b>Table 3</b> Quantum yields $\Phi$ in toluene solution.....	106
<b>Table 4</b> Lifetimes $\tau$ in toluene solution.....	108
<b>Table 5</b> Lifetimes $\tau$ , quantum yield $\Phi$ , and $S_1$ & $T_1$ energies in zeonex matrix.....	111
<b>Table 6</b> Decomposition temperatures of TTT-based emitters obtained through TGA analyses.....	123
<b>Table 7</b> Lifetimes $\tau$ and quantum yields $\Phi$ in toluene solution.....	131
<b>Table 8</b> Lifetimes $\tau$ , quantum yields $\Phi$ and $S_1$ & $T_2$ energies in zeonex matrix.....	135
<b>Table 9</b> SOCME and adiabatic energy differences.....	139
<b>Table 10</b> Calorimetric phase transition onset temperatures ( $^{\circ}\text{C}$ ) and enthalpies (J/g [in brackets]), and glass transition onset temperatures, on heating with $10^{\circ}\text{C}/\text{min}$ ; Cr= crystalline phase, Col <sub>hex</sub> = hexagonal columnar mesophase, Iso = isotropic liquid, $T_g(\text{Col})$ = glass transition temperature in the hexagonal columnar mesophase; monotropic transitions (observed on second heating only, after cooling from the isotropic liquid) in italics.....	146



## LIST OF ABBREVIATIONS

OLED - Organic Light Emitting Diodes

TADF - Thermally Activated Delayed Fluorescence

rISC - Reverse Inter-System Crossing

ISC – Inter-System Crossing

D-A - Donor-Acceptor

HOMO – Highest Occupied Molecular Orbital

LUMO - Lowest Unoccupied Molecular Orbital

SOC - Spin-Orbit Coupling

TTT - *Tris*[1,2,4]Triazolo[1,3,5]Triazine

*r*-TTT – Radially substitutable TTT = *Tris*[1,2,4]Triazolo[1,5-*a*:1',5'-*c*:1'',5''-*e*][1,3,5]Triazine

*t*-TTT – Tangentially substitutable TTT = *Tris*[1,2,4]Triazolo[4,3-*a*:4',3'-*c*:4'',3''-*e*][1,3,5]Triazine

RTP – Room Temperature Phosphorescence

TTA - Triplet-Triplet Annihilation

EQE - External Quantum Efficiency

IQE - Internal Quantum Efficiency

HAE - Heavy Atom Effect

FWHM - Full Width at Half Maximum

IC - Internal Conversion

VR - Vibrational Relaxation

PF - Prompt Fluorescence

DF - Delayed Fluorescence

LC - Liquid Crystal

N – Nematic mesophase

Sm – Smectic mesophase

N<sub>D</sub>\* - Cholesteric nematic discotic mesophase

N<sub>C</sub> - Nematic columnar mesophase

N<sub>D</sub> - Nematic discotic mesophase

Col<sub>h</sub> - Columnar hexagonal mesophase

Col<sub>r</sub> - Columnar rectangular mesophase

Col<sub>ob</sub> - Columnar oblique mesophase

IR – Infra-red

$^1\text{H}$  NMR – Proton Nuclear Magnetic Resonance

$^{13}\text{C}$  NMR – Carbon 13 Nuclear Magnetic Resonance

TGA – Thermo-Gravimetric Analysis

CV – Cyclic Voltammetry

PLQY – Photo-Luminescence Quantum Yield

TRPL – Time-Resolved Photo-Luminescence

CT – Charge Transfer

LE – Locally Excited

XRD – X-Ray Diffraction

DSC – Differential Scanning Calorimetry

POM – Polarized Optical Microscopy

DFT – Density Functional Theory

TD-DFT – Time-Dependent Density Functional Theory

SOCME – Spin-Orbit Coupling Matrix Element

SOC-TD-DFT – Spin-Orbit Coupling Time-Dependent Density Functional Theory

## LIST OF SIMBOLS

$S_0$  - Singlet ground state

$S_n$  - Singlet excited state

$T_n$  - Triplet excited state

$\Delta E_{ST}$  - Energy difference between the  $T_1$  and  $S_1$  states

$k_r$  - Radiative decay rate

$k_{ISC}$  - Intersystem crossing rate

$k_{IC}$  - Internal conversion rate

$k_{nr}$  - Non-radiative decay rate

$\Phi_{PF}$  - Quantum yield of prompt fluorescence

$\Phi_{Phosph}$  - Quantum yield of phosphorescence

$\Phi_{DF}$  - Quantum yield of delayed Fluorescence

$\tau_{PF}$  - Lifetime of prompt fluorescence

$\tau_{Phosph}$  - Lifetime of phosphorescence

$\tau_{DF}$  - Lifetime of delayed fluorescence

## CONTENTS

<b>1</b>	<b>INTRODUCTION .....</b>	<b>65</b>
1.1	ORGANIC LIGHT-EMITTING DIODE – OLED .....	68
<b>1.1.1</b>	<b>Fluorescent OLEDs: first generation.....</b>	<b>70</b>
<b>1.1.2</b>	<b>Phosphorescent OLEDs: second generation .....</b>	<b>70</b>
<b>1.1.3</b>	<b>Delayed Fluorescence (TADF) OLEDs: third generation.....</b>	<b>71</b>
<b>1.1.4</b>	<b>Light outcoupling from OLED devices.....</b>	<b>72</b>
1.2	LUMINESCENCE .....	74
<b>1.2.1</b>	<b>Delayed fluorescence .....</b>	<b>77</b>
1.3	LIQUID CRYSTALS .....	80
<b>1.3.1</b>	<b>Types of liquid crystals.....</b>	<b>82</b>
<i>1.3.1.1</i>	<i>Calamitic liquid crystals.....</i>	<i>83</i>
<i>1.3.1.2</i>	<i>Discotic liquid crystals .....</i>	<i>85</i>
<b>2</b>	<b>GOALS .....</b>	<b>90</b>
<b>2.1.1</b>	<b>General Goals.....</b>	<b>90</b>
<b>2.1.2</b>	<b>Specific Goals .....</b>	<b>90</b>
<b>3</b>	<b>New D<sub>3</sub>A-type emitters. Thermally Activated Delayed Fluorescence (TADF) and Room Temperature Phosphorescence (RTP) Materials.....</b>	<b>91</b>
3.1	1,3,5-TRIAZINE: TADF & RTP EMITTERS.....	91
<b>3.1.1</b>	<b>Introduction .....</b>	<b>91</b>
<b>3.1.2</b>	<b>Results and Discussions.....</b>	<b>94</b>
<i>3.1.2.1</i>	<i>Design of emitters based on the s-triazine core. ....</i>	<i>94</i>
<i>3.1.2.2</i>	<i>Synthesis and Characterization .....</i>	<i>95</i>
<i>3.1.2.3</i>	<i>Thermogravimetric analysis (TGA).....</i>	<i>100</i>
<i>3.1.2.4</i>	<i>Cyclic voltammetry (CV) .....</i>	<i>101</i>
<i>3.1.2.5</i>	<i>Photophysical Properties.....</i>	<i>101</i>
<i>3.1.2.5.1</i>	<i>Steady-State Photoluminescence – Solution and Solid State .....</i>	<i>102</i>

3.1.2.5.2	Time-resolved photoluminescence – Solution and Solid State .....	106
3.1.2.6	<i>Theoretical investigations</i> .....	112
<b>3.1.3</b>	<b>Conclusions</b> .....	<b>112</b>
3.2	<i>TRIS[1,2,4]TRIAZOLO[1,3,5]TRIAZINE: RTP &amp; TTA EMITTERS</i> .....	113
<b>3.2.1</b>	<b>Introduction</b> .....	<b>113</b>
<b>3.2.2</b>	<b>Results and Discussions</b> .....	<b>116</b>
3.2.2.1	<i>Design of the TTT-based emitters</i> .....	116
3.2.2.2	<i>Synthesis and Characterization</i> .....	117
3.2.2.3	<i>Thermogravimetric analysis (TGA)</i> .....	123
3.2.2.4	<i>Cyclic voltammetry (CV)</i> .....	124
3.2.2.5	<i>Photophysical Properties</i> .....	125
3.2.2.5.1	Steady-State Photoluminescence – Solution and Solid State .....	125
3.2.2.5.2	Time-resolved photoluminescence – Solution and Solid State .....	128
3.2.2.6	<i>Theoretical investigations</i> .....	135
<b>3.2.3</b>	<b>Conclusions</b> .....	<b>139</b>
<b>4</b>	<b>TOWARDS ANISOTROPIC DELAYED LUMINESCENCE FROM LIQUID CRYSTALS</b> .....	<b>141</b>
4.1	INTRODUCTION .....	141
4.1.1	<b>s-triazine</b> .....	<b>141</b>
4.1.2	<b>TTT</b> .....	<b>142</b>
4.1.3	<b>Triazine-based columnar matrices for OLED devices</b> .....	<b>143</b>
4.2	RESULTS AND DISCUSSIONS .....	144
4.2.1	<b>Columnar liquid crystalline glasses based on triazine core</b> .....	<b>144</b>
4.2.1.1	<i>Differential scanning calorimetry (DSC)</i> .....	146
4.2.1.2	<i>Polarized optical microscopy (POM)</i> .....	147
4.2.1.3	<i>X-ray diffraction (XRD)</i> .....	147
4.2.2	<b>Towards mesomorphic properties in delayed luminescence molecules</b> .....	<b>149</b>

<b>4.2.3</b>	<b>Synthesis and Characterization.....</b>	<b>150</b>
4.2.3.1	<i>9H-carbazole derivatives.....</i>	150
4.2.3.2	<i>1,3,5-triazine.....</i>	152
4.2.3.3	<i>r-TTT.....</i>	155
4.3	CONCLUSIONS .....	157
<b>5</b>	<b>experimental details.....</b>	<b>159</b>
5.1	TECHNIQUES AND EQUIPMENT .....	159
5.2	SYNTHESIS.....	160
<b>5.2.1</b>	<b>Emitters .....</b>	<b>160</b>
<b>5.2.2</b>	<b>Aliphatic chains decorated emitters.....</b>	<b>173</b>
<b>6</b>	<b>PUBLICATIONS.....</b>	<b>181</b>
<b>7</b>	<b>bibliography .....</b>	<b>197</b>
<b>8</b>	<b>ANNEXES .....</b>	<b>209</b>
8.1	NMR <sup>1</sup> H AND <sup>13</sup> C .....	209
<b>8.1.1</b>	<b>s-Triazine emitters .....</b>	<b>209</b>
<b>8.1.2</b>	<b>TTT emitters .....</b>	<b>219</b>
<b>8.1.3</b>	<b>Emitters decorated with aliphatic chains .....</b>	<b>231</b>
8.2	IR .....	244
<b>8.2.1</b>	<b>Triazine-based emitters.....</b>	<b>244</b>
<b>8.2.2</b>	<b>TTT-based emitters .....</b>	<b>247</b>
<b>8.2.3</b>	<b>Emitters decorated with aliphatic chains .....</b>	<b>252</b>
8.3	MASS SPECTROMETRY .....	254
<b>8.3.1</b>	<b>Triazine-based emitters.....</b>	<b>254</b>
<b>8.3.2</b>	<b>TTT-based emitters .....</b>	<b>256</b>
<b>8.3.3</b>	<b>Emitters decorated with aliphatic chains .....</b>	<b>258</b>
8.4	THEORETICAL INVESTIGATION .....	261
<b>8.4.1</b>	<b>TTT-based emitters .....</b>	<b>261</b>

8.5	GLASSY DISCOTIC LIQUID CRYSTAL .....	266
8.5.1	DSC .....	266
8.5.2	POM.....	267
8.5.3	DRX.....	268





## 1 INTRODUCTION

Organic light emitting diodes (OLEDs) have been extensively studied academically and industrially due to their application in electronic display technology (e.g., color televisions, smartphones, etc.). These materials have numerous advantages: low weight, fast response, large viewing angle, low power consumption, compatibility with flexible substrates, and easy chemical modification of the emitting molecules. According to the emission mechanisms, different types of OLEDs have been developed. The first-generation OLEDs employ prompt-fluorescent molecules in the emitting layer, which are limited by spin statistics to 25% maximal internal quantum yield. The second generation is based on phosphorescent molecules, which allow a maximal internal quantum yield of unity, but suffer from reduced molecular stability due to the presence of weakly bound heavy atoms. Recently, with the discovery thermally activated delayed fluorescence (TADF) in organic molecules, the third generation of OLEDs has emerged, which maintains the efficiency of the second-generation materials and the stability of the first generation. In recent years, many researchers have been making efforts to improve the efficiency and quality of these materials. Based on this, there is great interest in third-generation OLEDs. Molecules that exhibit the TADF mechanism can convert dark triplet states into emissive singlet states, which entails an increase in internal efficiency to 100% without using heavy metals and is thus economically viable. There are some factors responsible for obtaining a TADF material. Among them, it is essential to highlight that low values of  $\Delta E_{ST}$  are essential to allow reverse intersystem crossing (rISC), and a high rate of radioactive decay ( $k$ ) by the  $S_1$  exciton is required. To this end, novel molecular design strategies have been developed since it is conflicting to obtain a low value of  $\Delta E_{ST}$  and a high value of  $k$ . Donor-acceptor (D-A) type structures have been shown to reduce the overlap of the HOMO and LUMO orbitals, and therefore, it is possible to obtain small  $\Delta E_{ST}$  values, thus enabling rISC. The insertion of bridges between the units and bulky groups that change the dihedral angle, favoring the spatial separation of the HOMO-LUMO pair, have been widely employed in synthesizing these materials. Donor-acceptor scaffolds with an inner electron-accepting aromatic unit and three twisted outer electron-donating units ( $D_3A$ ) exhibit enhanced oscillator strength compared to simple donor-acceptor systems and have been shown to be efficient electroluminescent dyes, as strong spin-orbit coupling (SOC) allows for fast singlet-triplet rISC leading to emission from both singlet and initial triplet states.

In recent years, electron-accepting *N*-heterocycles, such as 1,3,5-triazine and *tris*[1,2,4]triazolo[1,3,5]triazine (TTT), have been employed as the acceptor unit in D<sub>3</sub>-A type molecules that exhibit TADF. In addition to being present in the structure of molecules that exhibit delayed fluorescence, these two *N*-heterocycles have been employed as a central unit in liquid crystal synthesis due to their high ability to perform  $\pi$ -stacking interactions and easy functionalization. Liquid crystalline self-assembly is intrinsically anisotropic and can thus induce polarized emission, which is of interest for 3D displays. The use of liquid crystals as emitter layer and/or electron carrier layer in optoelectronic devices also allows for avoiding the phenomenon of light outcoupling and, consequently, increases the efficiency of these materials. Thus, synthesizing new liquid crystals that act as emitters and carrier layers or only as a matrix in OLED devices is a strategy for obtaining efficient materials. Several research groups have been trying to combine the properties of liquid crystals with the TADF phenomenon. Although this combination is possible on paper, it is not easy in practice. Efficient symmetric C<sub>3</sub> emitters must be non-planar to have a good spin-orbit coupling (SOC) without heavy atoms, while planar discotic structures favor liquid crystalline phases. But exceptions are known, among them tangentially triphenyl-substituted TTTs, which are both mesogenic and pronouncedly non-planar units. Both the delayed fluorescence behavior and the liquid-crystalline self-assembly in these systems may be improved by introducing heteroaromatic donors.

Looking for new TADF materials, we designed two new series of D<sub>3</sub>A star-shaped molecules. As the acceptor unit, we employed the *N*-heterocycles 1,3,5-triazine and *tris*[1,2,4]triazolo[1,3,5]triazine. The donor units were 3,6-di-*tert*-butyl-9H-carbazole and 9,9-dimethyl-9,10-dihydroacridine. Considering that heavy atoms facilitate spin-orbital coupling and, therefore, can enhance delayed fluorescence and phosphorescence through interconversion between singlet and triplet states, we inserted sulfur-including thiophene bridges between the donor and acceptor units

After the synthesis and characterization of all molecules, time-dependent fluorescence spectroscopy studies were performed to verify the type of radiative decay these materials present. All the molecules of the TTT series showed phosphorescence at room temperature (RTP) and most of them delayed fluorescence in a triplet-triplet annihilation (TTA) mechanism. Although they do not show TADF, this result is significant because it was possible to obtain phosphorescent materials without heavy metals in solid and solution, possibly by inserting the S atom of the thiophene bridge. For the series of materials based on 1,3,5-triazine, we obtained

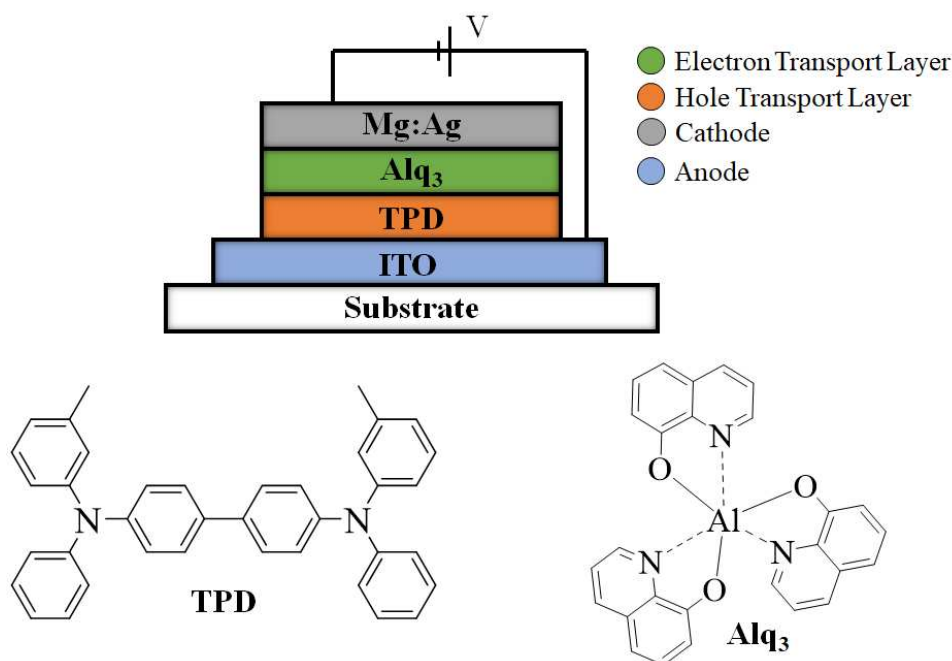
both RTP and TADF. The compounds where the donor unit was the heterocycle 3,6-di-tert-butyl-9H-carbazole showed only phosphorescence. When we changed the donor unit to 9,9-dimethyl-9,10-dihydroacridine, the TADF phenomenon was observed besides RTP. Unfortunately, although the materials showed TADF behavior, the quantum yield is very low.

To induce liquid crystalline behavior in the molecules synthesized in this Ph.D. thesis and those already reported in the literature, we chose to introduce aliphatic chains in the 9H-carbazole donor unit. Two series were synthesized, one based on the TTT core and the other on the 1,3,5-triazine heterocycle. Unfortunately, none of the six molecules synthesized exhibited liquid crystalline behavior. Alternatively, we plan and synthesize a series of discotic liquid crystals based on s-triazine with esters on the disk periphery to use as a matrix for our luminescent molecules in the fabrication of optoelectronic devices. Combining the polarized emission of the liquid crystals with efficient emitters aims at obtaining OLEDs with improve efficiency.

## 1.1 ORGANIC LIGHT-EMITTING DIODE – OLED

An organic light-emitting diode (OLED) is a light-emitting diode where the emitting layer is a film of an organic. The use of these organic materials in the emitting layer allows the use of a wide variety of chemical compounds in the fabrication of new emitters so that structural modifications to these materials allow the optimization of these devices concerning lifetime, brightness, and color.<sup>1</sup>

Although electroluminescence in organic semiconductors was first reported in the 1960s, with work on anthracene and its derivatives, it was only in the 1980s that Tang and Van Slyke presented significant developments in the field.<sup>2-5</sup> The authors developed an OLED by stacking four different layers. Indium-Tin-Oxide (ITO) and Mg/Ag are used as the anode and cathode, respectively. The organic layer was split between a hole carrier layer (N,N'-diphenyl-N,N'-bis(3-methylphenyl)-1,1'-biphenyl-4,4'-diamine - TPD) and an electron carrier layer (tris(8-hydroxyquinoline) aluminum - Alq<sub>3</sub>). This configuration allows for the recombination and emission of light between the organic layers.<sup>2</sup> **Figure 1** shows the structure of the device.



**Figure 1** Device structure made by Tang and Van Slyke - the first heterojunction OLED.

Three significant factors determine an OLED efficiency: charge injection, charge transport, and light emission. Over the years, the pursuit of improving OLED has allowed the development of new heterojunctions structures with more and more layers.<sup>1,6</sup>

In OLEDs, the emission process is activated by applying a driving voltage of 5 to 10 V or lower. This causes electrons to be injected from the metal cathode into the electron-transporting layer, while holes are injected into the hole conducting layer from the anode. Electrons and holes both move towards the recombination layer from opposite directions and can combine there to form excitons. When the conditions are suitable, this leads to a population of excited states in the emitter material, which subsequently emits light through a recombination process in which excitons release energy and emit photons in the visible range.<sup>7</sup> There are three dominant mechanisms for light emission in OLEDs: fluorescence, phosphorescence, and thermally activated delayed fluorescent (TADF). Fluorescence occurs when opposite charges recombine at the organic layer and emit photons through a singlet-to-singlet transition. Phosphorescence involves desexcitation from a triplet to a singlet state and is often achieved using heavy metal complexes such as iridium, platinum. TADF is a particularly efficient mechanism for fluorescence in OLEDs because it converts triplet excitons into singlet excitons through reverse intersystem crossing (rISC).<sup>1,7</sup>

For the past two decades, researchers have been trying to improve the performance of OLEDs for commercial use. One aspect of this effort has been using phosphorescent materials to increase the external quantum efficiency (EQE) of OLEDs by enhancing spin-orbit coupling in the new emitters, which allows for emission from the triplet state.<sup>8,9</sup> While OLEDs have already been used successfully in commercial products such as tablets, smartwatches, and smartphones, there is still a challenge known as the "blue gap," which refers to the difficulty in creating high-quality blue displays using OLED technology.<sup>10</sup> To solve this problem, researchers are exploring various approaches, including fluorescence, phosphorescence, and thermally activated delayed fluorescence (TADF), to improve OLED performance.<sup>1</sup>

The creation of full-color OLED displays requires the development of red, green, and blue pixels. One approach involves depositing individual red, green, and blue subpixels, while another involves using a white OLED with color filters. A third approach involves using a blue OLED layer with a film of green- and red-photoluminescent subpixels on top as color-change layer.<sup>11,12</sup>

In addition to the limited quantum efficiency of the emitter molecules, there are several other reasons for losses in OLED performance, such as poor adjustments of the work functions of the electrodes relative to the HOMO or LUMO of the adjacent organic layers, poor alignment of the HOMOs and LUMOs of the different organic layers relative to each other,

which can cause charge carrier trapping and unfavorable space charges, unbalanced electron and hole transport, low electron or hole mobility, ohmic losses, low cross sections for electron-hole recombination, and low light outcoupling efficiency.<sup>6,13,14</sup>

The efficiency of light emission from OLEDs depends on spin statistics. OLED devices generate singlet and triplet excitons in a 25% to 75% ratio. To achieve high-performance OLED devices with high external quantum efficiencies (EQEs), the development and design of light-emitting materials that can fully harvest singlet and triplet excitons are crucial.<sup>15</sup>

### 1.1.1 Fluorescent OLEDs: first generation

Prompt-fluorescent OLEDs, also known as first-generation OLEDs, utilize organic dyes. The non-radiative intersystem crossing (ISC) transition between states with different electronic spin multiplicity limits fluorescence efficiency, as only the transition from singlet excitons to the singlet ground state ( $S_1 \rightarrow S_0$ ) can theoretically produce fluorescence. Only approximately 25% of singlet excitons can be utilized for luminescence. Without additional optical outcoupling, the maximum external quantum efficiency (EQE) of OLEDs using conventional fluorescent emitters is limited to 5%.<sup>1</sup>

The first generation of OLEDs utilized 8-hydroxyquinoline aluminum (Alq3) as the fluorescent green emitter, which exhibited a brightness of over  $1,000 \text{ cd m}^{-2}$ , green emission peaking at 550 nm, and a driving voltage of less than 10 V.<sup>2</sup> In 1989, orange-red emitters were introduced. However, red fluorescent materials were predominantly utilized as dopants in red OLEDs due to concentration-dependent quenching caused by aggregation.<sup>16</sup> Blue fluorescent emitters, frequently based on anthracene derivatives, have a wide bandgap and good thermal stability. However, their emission color is often shifted from deep blue to light blue (cyan) due to the aggregation of molecules in the thin film.<sup>17,18</sup>

### 1.1.2 Phosphorescent OLEDs: second generation

Phosphorescent heavy-metal complexes have been employed as second-generation emitters in OLEDs to utilize the remaining 75% of excitons in triplet states. These complexes, which include heavy metals such as iridium and platinum, facilitate intersystem crossing from the singlet state to the triplet state  $T_1$  and accelerate the radiative deactivation of  $T_1$  to the ground state  $S_0$  through enhanced spin-orbit coupling. This use of triplet to ground state relaxation

allows phosphorescent heavy-metal-based emitters to reach an internal quantum efficiency (IQE) of up to 100%.<sup>1</sup>

$\text{Ir}(\text{ppy})_3$  as a green emitter in OLEDs has been extensively studied because of its stability and electroluminescent performance.<sup>19</sup> Since its introduction in 1999, various other green emitters have been developed, including Ir(III) complexes with different ligand field strengths, bulky substituents, and coordination geometries, which have contributed to the improvement and development of more efficient and stable green OLEDs.<sup>20-22</sup> Red phosphorescent materials like per-deuterated and per-fluorinated materials and cyclometalated neutral iridium complexes have limitations like high cost and complex synthesis.<sup>1,23</sup>

In recent years, there has been significant interest in using iridium and platinum complexes as blue phosphorescent emitters in OLEDs. Ir(III) complexes as color-switchable emitters in OLEDs have also been extensively studied.<sup>1</sup>

Phosphorescence is often limited in certain materials due to their inability to absorb light by  $S_0$  to  $T_1$  excitation and the sensitivity of the triplet excited states towards nonradiative decay. Typically, phosphorescence can only be observed in low-temperature rigid matrices.<sup>24</sup> To achieve stable phosphorescence at room temperature, it is necessary to facilitate the ISC process and suppress nonradiative dissipation. One method for promoting intersystem crossing is the heavy atom effect (HAE), which occurs when heavy atoms, i.e. those with high atomic numbers, are present in a molecule and increase spin-orbit coupling.<sup>25</sup> The HAE can be either internal, where the heavy atom is covalently bonded to an aromatic system, or external, where the heavy atom is present in a separate molecule that interacts with the system.<sup>26,27</sup> Recently, high phosphorescence quantum yields at ambient conditions have nevertheless been reported in purely organic, metal-free materials. These materials are alternatives to organometallic materials in OLED applications.<sup>24</sup>

### **1.1.3 Delayed Fluorescence (TADF) OLEDs: third generation**

The use of third-generation emitters has garnered significant attention due to their potential to replace heavy-metal-based phosphorescent emitters, which have cost and environmental limitations. One promising option is TADF (Thermally Activated Delayed Fluorescence), which relies on a small energy gap between the excited singlet and triplet states. Under conditions where the lifetime of triplet excitons is sufficient, a reverse intersystem crossing process can occur, allowing for the conversion of triplet excitons into singlet excitons,

which subsequently relax to the ground state. This process results in a theoretical internal quantum efficiency of 100%.<sup>1,7</sup>

The first TADF OLED was reported in 2012, with an external quantum efficiency (EQE) of 11.9% and a peak wavelength of 580 nm.<sup>28</sup> Since then, TADF emitters have made significant progress, with devices achieving EQEs of up to 30%.<sup>29–31</sup> However, the development of purely red TADF-based OLEDs has been slower due to limitations in their photosensitivity and luminescent properties.<sup>1</sup> Research has also been conducted on developing NIR TADF emitters with wavelengths above 700 nm, but progress in this area has been slower.<sup>32</sup> Blue OLEDs have historically faced challenges due to the high energy of blue light, which can lead to issues with device lifetime and material degradation. As a result, developing stable blue emitters and OLEDs has been a significant challenge. In recent years, there have been several notable advancements in blue TADF emitters and OLEDs, including developing TADF emitters with high EQE and deep blue color, as well as addressing the issue of efficiency roll-off in blue OLEDs (decrease of efficiency when increasing device brightness with voltage).<sup>33–35</sup> These advancements have led to the development of highly efficient blue OLEDs with EQEs of up to 25%. Green TADF OLEDs have also made significant progress in recent years, with EQEs of up to 37.8%.<sup>36</sup> Pure green OLEDs with EQEs of up to 22.0% and full width at half maximum (FWHM) of 25 nm have also been developed using TADF emitters.<sup>37</sup> Vacuum-deposited OLEDs with green emission (552 nm) and an EQE of 23.9%, as well as solution-processable OLEDs with an EQE of 21.8% have also been developed using a TADF emitter.<sup>38,39</sup>

#### **1.1.4 Light outcoupling from OLED devices**

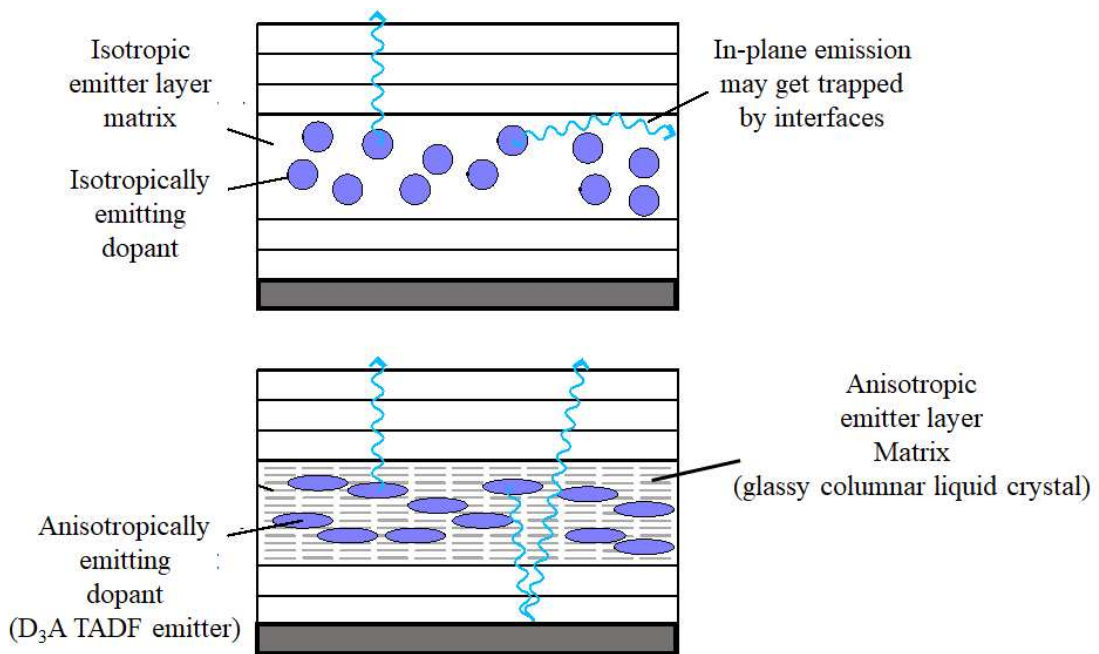
One of the main challenges in organic light-emitting diodes is improving their outcoupling efficiency, which is the fraction of emitted light actually leaving the device cavity and visible to the observer. Currently, most OLEDs only extract around 30% of the photons they produce.<sup>40</sup> The extraction efficiency of planar OLEDs is typically low due to the organic materials' high refractive index and the metal electrode's presence, which can cause strong reflection and absorption. The external quantum efficiency of an OLED is influenced by internal factors such as charge balance, spin statistics, and radiative exciton decay, as well as an outcoupling factor.<sup>41,42</sup> The shape and orientation of the molecules used as emitters in OLEDs play a significant role in the device's efficiency. For example, rod-like or disc-like



molecules tend to form optically anisotropic thin films, which can affect the orientation of the emitters.<sup>43,44</sup>

Recent advances in the understanding of emitter orientation in OLEDs, have led to the discovery that evaporated thin films of organic semiconductors can form anisotropic molecular glasses.<sup>43,45</sup> The orientation of these molecules may or may not have time to diffuse and readjust before being covered by the next deposited layer, depending on factors such as substrate temperature, evaporation rate, and molecular shape. As a result, film growth and morphology are kinetically controlled processes. It was found that the orientation of these films is influenced by the substrate temperature relative to the organic material's glass transition temperature. A completely horizontal orientation of thin organic films, which leads to pronounced birefringence, can be achieved for a specific ratio of substrate temperature to the glass transition temperature.<sup>43,45,46</sup> This has allowed for the creation of TADF emitters with a strongly horizontal orientation by film growth on cooled substrates, significantly improving the efficiency of OLEDs.

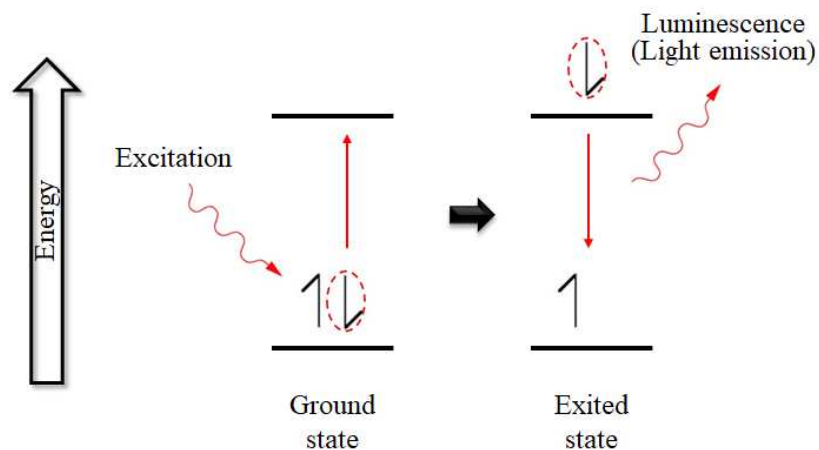
The orientation of TADF emitters can be influenced by various factors, including the intrinsic properties of the emitter molecules, the glass transition temperature of the host matrix in which the emitters are placed, and the alignment of the host material. A higher glass transition temperature in the host matrix may result in a greater tendency for the matrix molecules to lie flat. At the same time, the alignment of the host material may also promote the orientation of the TADF emitters.<sup>43,45-47</sup> Suppose the emitter layer, which contains a high-quantum-yield luminogen embedded in a large-band gap matrix to reduce self-quenching effects, are in a randomly oriented glassy state. In that case, the emission is mainly isotropic, leading to some of the emitted light being trapped within the device cavity (**figure 2**, top). However, if the emitting dipoles are oriented parallel to the device interfaces, emission occurs mainly perpendicular to the device, minimizing light trapping and potentially increasing the light output by approximately 50%.<sup>45</sup> One way to orient the dipoles of the emitters parallel to the device layers is to use a glassy discotic liquid crystal matrix (**figure 2**, bottom). Additionally, a columnar matrix for TADF emitters should have a large energy gap between the molecular singlet ground state ( $S_0$ ) and the first excited triplet state ( $T_1$ ) to prevent quenching of the excited emitter by the matrix.<sup>48,49</sup>



**Figure 2** Schematic representation of light output in OLED devices. Isotropic emission (top) and anisotropic emission (bottom).

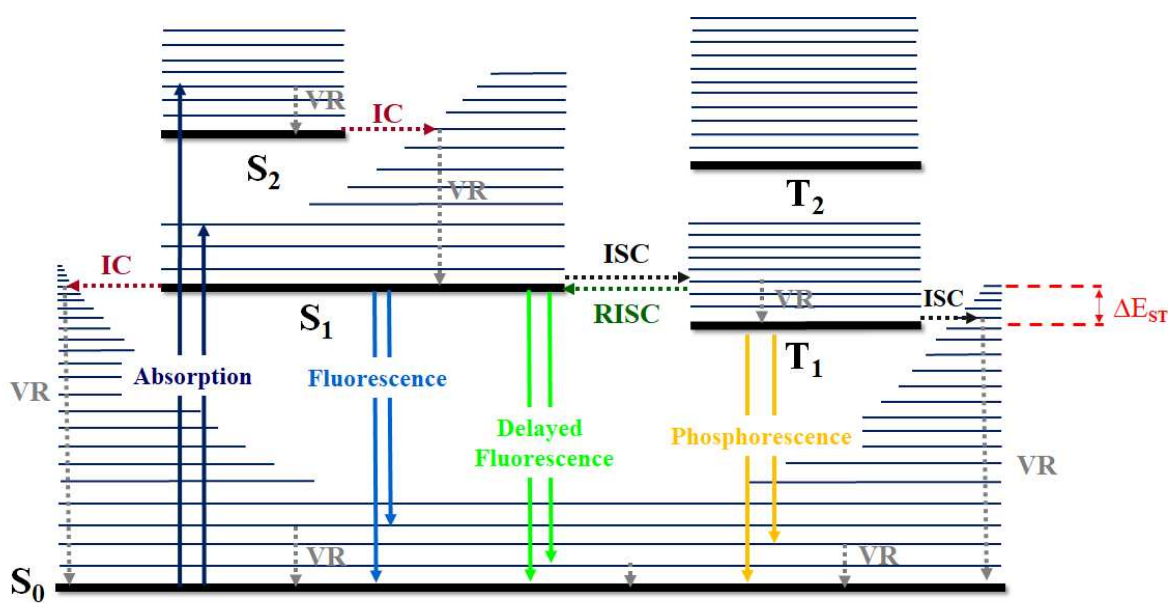
## 1.2 LUMINESCENCE

Light emission in response to absorption of energy is known as luminescence. This energy absorption promotes electronic transitions from the fundamental state to a higher energy electronic state (excited state). In the (at least partial) absence of nonradiative desexcitation pathways, the return from the excited state to the fundamental state is responsible for the emission of energy in the form of light (**figure 3**). There are several ways to perform electronic excitation, such as absorption of light (photoluminescence), injection of electrons (electroluminescence), and a chemical reaction (chemiluminescence).<sup>50</sup>



**Figure 3** Simplified representation of the luminescence phenomenon. Excitation and emission.

If we consider photoluminescence, after absorbing a photon with sufficient energy to promote an electron from the fundamental state to the excited state, several processes can occur until the relaxation to the fundamental state. These photophysical phenomena can be described using the Jablonski diagram (**figure 4**).<sup>31</sup>



**Figure 4** Jablonski diagram, representation of the photophysical processes present in the luminescence phenomenon. IC: internal conversion; VR: vibrational relaxation; ISC: intersystem crossing; rISC: reverse intersystem crossing,  $\Delta E_{ST}$  - Energy difference between the excited states  $S_1$  and  $T_1$ . Adapted from the literature.

When the molecule is excited from the fundamental state ( $S_0$ ) to a higher energy level ( $S_1, S_2, \dots, S_n$ ), the release of energy by the excited species can occur by radiative and non-radiative processes. In the excitation, one of the electrons is transferred from the HOMO to the LUMO. The electrons have an antiparallel configuration in the fundamental state of most molecules. This configuration infers a total spin number of 0 ( $-\frac{1}{2} + \frac{1}{2}$ ) and spin multiplicity ( $2S+1$ ) equal to 1, indicating a singlet state. If the spin of one of the electrons inverts, the total spin number becomes 1 ( $\frac{1}{2} + \frac{1}{2}$ ) and the spin multiplicity 3 (triplet state).

For reasons of practicality, non-radiative mechanisms arising from intermolecular interactions (e.g., charge transfer, proton transfer, etc.) will not be discussed. An excited species may exhibit internal conversion (IC,  $S_1 \rightarrow S_0$ ) and vibrational relaxation (VR) as non-radiative decay, or the relaxation from the  $S_1$  state to the fundamental state may result in the release of energy in the form of a photon (radiative decay), a phenomenon known as fluorescence. The de-excitation of the excited state  $S_1$  may involve an intersystem crossing (ISC), leading to the

triplet state ( $T_1$ ). This crossover, ISC, involves two states of different spin multiplicity and the same vibrational energy. The triplet state can undergo de-excitation by non-radiative processes, a new intersystem crossing to the  $S_0$  state of the same vibrational energy followed by vibrational relaxation, or a radiative decay from the triplet state ( $T_1 \rightarrow S_0$ ), which is termed phosphorescence.<sup>51</sup>

A reverse intersystem crossing (rISC,  $T_1 \rightarrow S_1$ ) can occur when the energy difference between the  $T_1$  and  $S_1$  states ( $\Delta E_{ST}$ ) is small enough and the lifetime of the triplet state is sufficiently long. rISC causes delayed fluorescence. The main difference between prompt and delayed fluorescence is the duration of the process. In the case of delayed fluorescence, the lifetime is longer because the molecules have been in the  $T_1$  state for a while before emission from the  $S_1$  state. All the radiative and non-radiative decays have different lifetimes and compete with each other.<sup>52</sup> **Table 1** shows the lifetime of each photophysical event (excitation and de-excitation).

**Table 1** Average timescales for radiative and no-radiative processes.

TRANSITION	TIME SCALE
<b>Absorption</b>	$10^{-15}$ s
<b>Vibrational Relaxation (VR)</b>	$10^{-12} - 10^{-10}$ s
<b>Intersystem Crossing (ISC)</b>	$10^{-10} - 10^{-8}$ s
<b>Internal Conversion (IC)</b>	$10^{-11} - 10^{-9}$ s
<b>Prompt fluorescence</b>	$10^{-10} - 10^{-7}$ s
<b>Delayed fluorescence</b>	$\sim 10^{-3}$ s
<b>Phosphorescence</b>	$10^{-6} - 10$ s

The fluorescence lifetime ( $\tau_F$ ) and the quantum yield ( $\Phi_F$ ) are the most relevant characteristics of a fluorophore (species responsible for luminescence). The quantum yield is interpreted as the ratio of the number of photons emitted by  $S_1$  over the number of photons absorbed by  $S_0$  (**equation 1a**). Considering that the depopulation of excited states is the sum of radiative and non-radiative processes, we can mathematically express the fluorescence yield as shown in **equation 1b**. The fluorescence emission rate is defined by  $\Gamma$ , while the non-radiative decay rate is  $k_{nr}$ , where  $k_{nr}$  is the sum of the non-radiative decay rates ( $k_{IC} + k_{ISC}$ ).

$$(1a) \Phi_F = \frac{\text{number of photons emitted by } S_1}{\text{number of photons absorbed by } S_0}$$

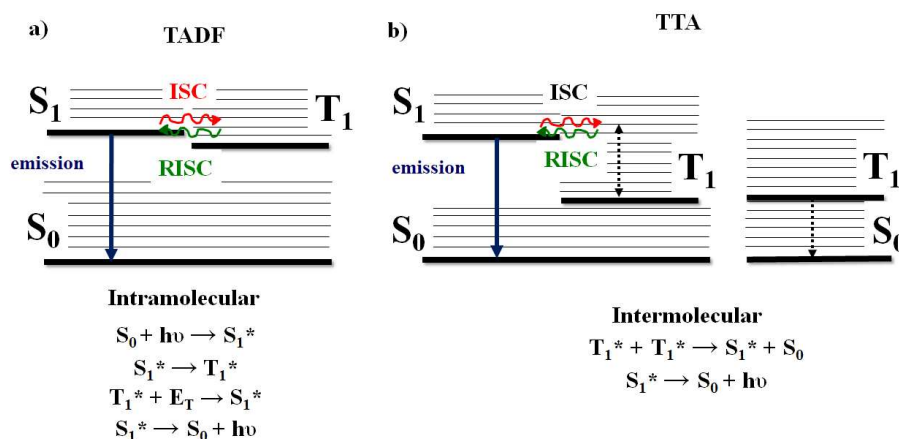
$$(1b) \Phi_F = \frac{\Gamma}{\Gamma + knr}, \text{ where } knr = kIC + kISC$$

Experimentally, the fluorescence quantum yield,  $\Phi_F$ , can be calculated relatively, as shown in **equation 2**. From the quantum yield of a standard, the wavelengths used in the excitation of the standard and the sample, the emission band areas, and the refractive index of the solvents used for the analysis, it is possible to calculate the relative fluorescence quantum yield.<sup>53</sup>

$$(2) \Phi_F(\text{sample}) = \Phi_F(\text{standard}) \times \frac{\text{Absorbance}(\text{standard})}{\text{Absorbance}(\text{sample})} \times \frac{\text{Emission Band Area}(\text{sample})}{\text{Emission Band Area}(\text{standard})} \times \frac{\eta(\text{sample})}{\eta(\text{standard})}$$

### 1.2.1 Delayed fluorescence

There are three known types of delayed fluorescence. E-type delayed fluorescence (TADF - Thermally Activated Delayed Fluorescence), P-type delayed fluorescence (TTA - Triplet-Triplet Annihilation), and recombination fluorescence. The latter involves settling the  $S_1$  excited state from recombining ions with electrons or ionic recombination of opposite charges followed by luminescence emission. E-type luminescence is so named because eosin was the first molecule to exhibit this type of phenomenon. Like the E-type, the P-type is so named because of the pyrene with which it was historically observed. The acronyms TADF and TTA are currently the most common denominations. TADF is an intramolecular process, and for it to occur, the energy difference between the  $S_1$  and  $T_1$  states must be as small as possible. Thus, a small thermal energy is enough for the rISC process to occur, and the  $S_1$  state emits (**figure 5a**). The TTA mechanism, on the other hand, is an intermolecular process and occurs at high concentrations, where two neighboring molecules in the  $T_1$  state undergo energy transfer that promotes one molecule to the  $S_0$  state and the other to the  $S_1$  state responsible for the emission (**figure 5b**).<sup>52,54</sup>

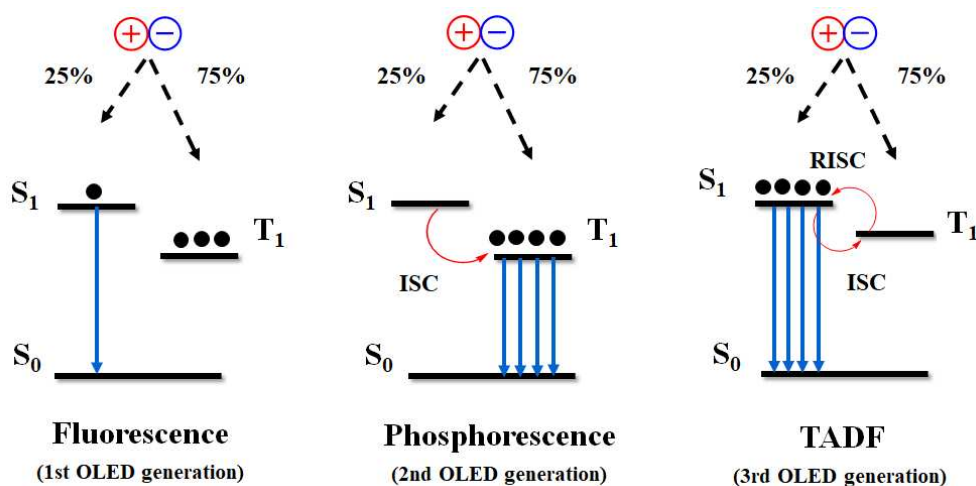


**Figure 5** Representation of the processes responsible for delayed fluorescence. a) TADF, intramolecular process; b) TTA, intermolecular process.

Although TADF has been known for quite some time, interest in these materials has recently resurged. Adachi et al. used this mechanism to generate delayed fluorescence in OLEDs based on  $\text{Sn}^{4+}$ -porphyrin complexes. These compounds had a slight energy difference between the triplet and singlet states ( $\Delta E_{\text{ST}}$ ) that allowed rISC and increased device efficiency.<sup>55</sup> Based on these results, in 2012, the same research group published the first OLED with a TADF mechanism without heavy metals.<sup>28</sup> From that moment on, the search for new devices with TADF mechanisms intensified, especially in electroluminescence, where OLEDs with a high performance already exist.<sup>52,56–60</sup>

An OLED is a light-emitting diode in which the emitting layer is based on an organic film, typically luminescent or phosphorescent. In these devices, the type of excitation is electrical (electroluminescence). By applying a potential difference to the diode, positive charges (holes) and negative charges (electrons) are generated and recombined in the emitting layer.<sup>1</sup> The charge combination statistically generates a ratio of one exciton (electron-hole pair) in the singlet state to three excitons in the triplet state. Thus, prompt-fluorescence-based devices limit the internal quantum efficiency to 25% (**figure 6**, left). To solve this, phosphorescent OLEDs have been created with the incorporation of heavy metals (e.g., platinum, iridium). These metals allow for increased spin-orbit coupling, which relaxes the prohibition of the  $T_1 \rightarrow S_0$  transition, increasing the internal quantum efficiency to 100% (**figure 6**, middle). The TADF mechanism is the best alternative for creating the 3rd generation OLEDs to avoid the heavy metals and instability of these materials in the second generation of OLED devices.

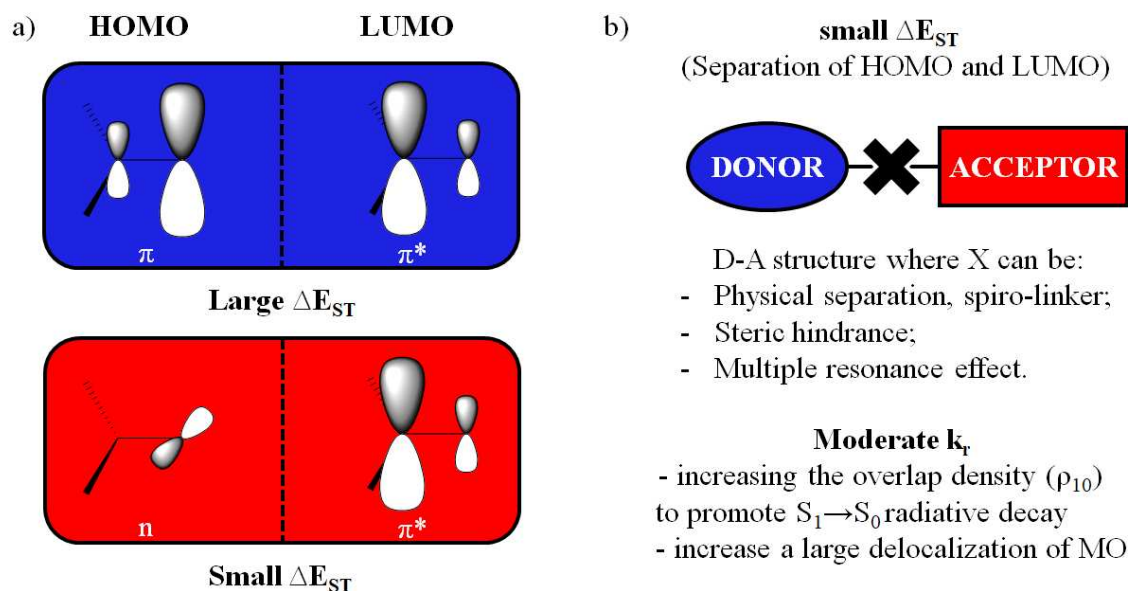
Thermally activated delayed fluorescence enables an internal quantum efficiency of 100% (figure 6, right).<sup>1</sup>



**Figure 6** Representation of electroluminescence in OLED. a) 1st generation OLEDs: prompt fluorescence; b) 2nd generation OLEDs: phosphorescence; c) 3rd generation OLEDs: thermally activated delayed fluorescence.

Designing new TADF emitters is a challenging task. The design of the molecules must follow several conditions, which are in part antagonistic. Thermally activated rISC is critical for the material to exhibit TADF behavior efficiently. The dependence of the rISC process rate constant ( $k_{\text{rISC}}$ ) on temperature is expressed in the relationship with the Boltzmann distribution:  $k_{\text{rISC}} \propto \exp(-\Delta E_{\text{ST}}/k_{\text{B}}T)$  where  $k_{\text{B}}$  is the Boltzmann constant, and  $T$  is the temperature. From this relationship, we can infer that the higher  $\Delta E_{\text{ST}}$ , the lower the value of  $k_{\text{rISC}}$  and vice versa. As seen earlier,  $\Delta E_{\text{ST}}$  is the energy gap between the singlet and triplet ( $E_{\text{S}} - E_{\text{T}}$ ) states. Each state's energy is defined as  $E_{\text{S}} = E + K + J$  and  $E_{\text{T}} = E + K - J$ ; in this way  $\Delta E_{\text{ST}} = 2J$ , where  $E$  is the orbital energy,  $K$  is the electronic repulsion energy, and  $J$  is the exchange energy. From quantum theory, in organic molecules,  $J$  is related to the spatial overlap of the wave functions of the HOMO and LUMO orbitals.<sup>61,62</sup> Low values of  $\Delta E_{\text{ST}}$  can be obtained through spatial separation of the electronic density of the boundary orbitals (**figure 7a**). This separation is achieved in rotated donor-acceptor-type structures. Another essential factor for obtaining a good TADF material is a relatively large radiative rate constant  $k_{\text{r}}$  at the transition from the  $S_1$  state to the ground state ( $S_0$ ). A good  $k_{\text{r}}$  can be obtained by increasing the conjugation in the material, a strategy antagonistic to the method for obtaining low values of  $\Delta E_{\text{ST}}$  (disruption of conjugation by spatial separation of HOMO and LUMO).<sup>52</sup> Thus, the design of TADF emitters should be done cautiously to realize these two conditions (low  $\Delta E_{\text{ST}}$  values and high  $k_{\text{r}}$  values)

simultaneously and effectively. In recent years, several authors have summarized some principles of molecular planning for these emitters (**figure 7b**).<sup>52,61</sup>



**Figure 7** Strategies to adjust  $\Delta E_{ST}$  and  $k_r$ . a) Orbital overlap in benzophenone. Large  $\pi$ - $\pi^*$  overlap induces large  $\Delta E_{ST}$  (top) and weak  $n$ - $\pi^*$  overlap induces small  $\Delta E_{ST}$  (bottom); b) Design principles of organic TADF materials.

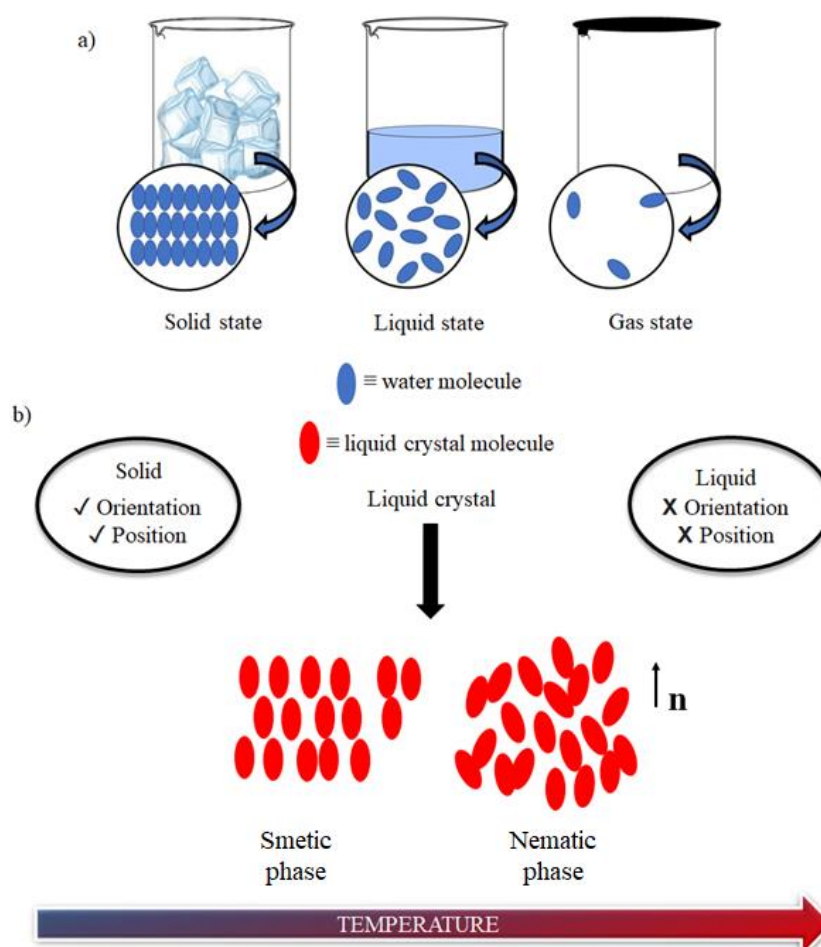
As seen previously, low  $\Delta E_{ST}$  values are obtained in D-A type molecular structures with a twist between the donor and the acceptor portions that can be achieved by two approaches: bulky substituents or spiro-junction.<sup>52</sup> Recently, systems that exhibit a multiple resonance effect have also been shown to be an alternative for obtaining small  $\Delta E_{ST}$  values.<sup>63</sup> To increase the values of  $k_r$ , it is necessary to increase the overlap between the electronic wave functions of the excited and ground states, allowing the radiative decay  $S_1 \rightarrow S_0$ . Systems where there is a large delocalization of the molecular orbitals with a good separation of the HOMO and LUMO levels, are shown to suppress the decrease of  $k_r$  while decreasing the values of  $\Delta E_{ST}$ . The extent of the  $\pi$ -conjugation and the redox potentials are also relevant factors in obtaining efficient emitters.<sup>52</sup>

### 1.3 LIQUID CRYSTALS

Matter, in general, presents three distinct states: liquid, solid, and gas. These states are differentiated according to the degree of organization of the atoms or molecules. In a crystalline solid, there is a well-defined spatial organization, where the atoms or molecules present an orientational and positional order in a determined volume (**figure 8a**). The state of matter



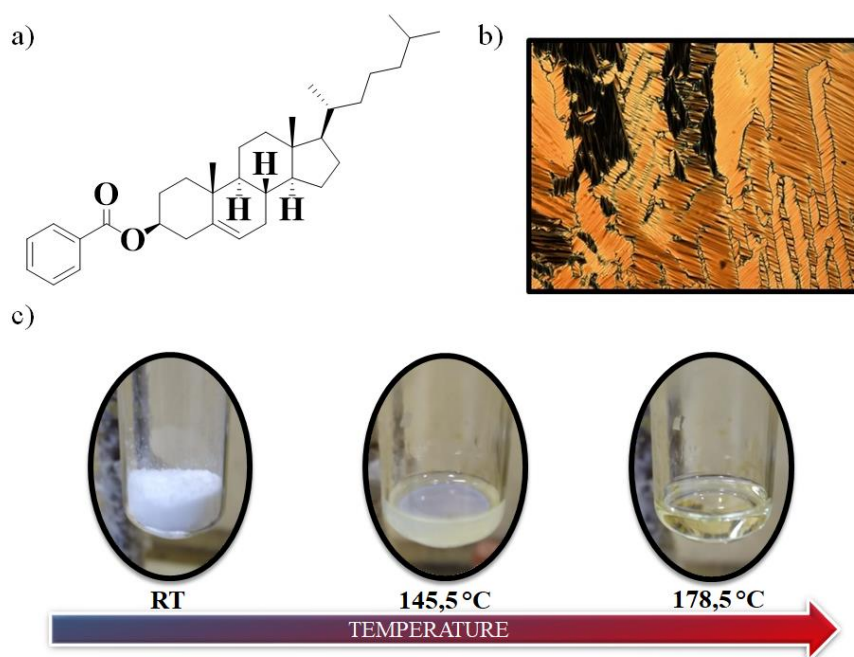
known as a liquid does not present long-range orientational or positional organization, whilst molecules are in close contact. Gases, like liquids, lack any orientation, and the molecules/atoms are more widely spaced from each other (**Figure 8a**).<sup>64</sup> Some materials present intermediate characteristics with respect to those of solids, liquids, and gases. Among them, liquid crystals have the orientational organization and, in some cases, partially the positional organization, of the solid state combined with some of the fluidity present in the liquid state (**figure 8b**). They are an important class of functional materials.<sup>65,66</sup>



**Figure 8** Representation of molecular organization in the different states of matter. a) solid, liquid and gaseous states; b) liquid crystalline state: representation of nematic and smectic mesophases.

The history of liquid crystals began in the late 19th century. Friedrich Reinitzer, an Austrian botanist, conducted studies with the compound cholesteryl benzoate (**figure 9**) and observed two distinct melting points.<sup>67</sup> It transitioned to a viscous opaque liquid after heating the solid material to 145.5°C. The material changed to a translucent liquid with increasing

temperature (178.5°C) (**figure 9**). This experiment demonstrated that cholesteryl benzoate has a phase between the solid and liquid state. Otto Lehmann created the term liquid crystal sometime later when he observed that these compounds presented optical anisotropy (**figure 9**).<sup>68</sup> Since then, many liquid crystalline phases with different structures have been discovered.<sup>69–73</sup>



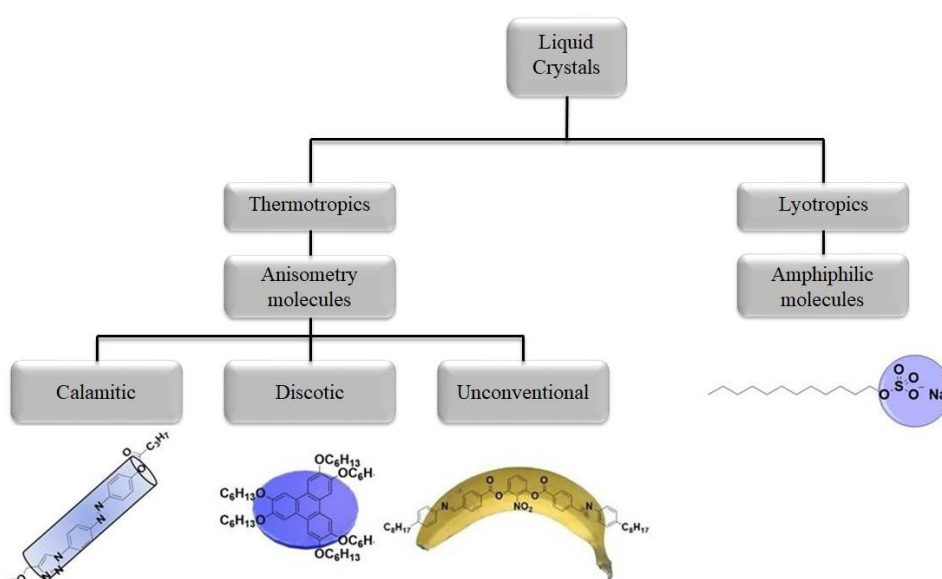
**Figure 9** The first liquid crystal. a) structure of cholesteryl benzoate; b) demonstration of the experiment by Lehmann: Texture observed under polarized light microscope (174°C, 10x); c) demonstration of the experiment by Reinitzer: from left to right: solid phase, mesophase, isotropic liquid.

Molecules that exhibit liquid crystalline behavior are called mesogens, and the phases between the solid and liquid states are called mesophases. For liquid crystals, melting represents the phase change from the solid to the liquid crystalline state, while the phase change from the liquid crystalline state to the isotropic liquid is called the clearing point.<sup>65</sup>

### 1.3.1 Types of liquid crystals

Liquid crystalline materials can be divided into two classes: lyotropic and thermotropic. Thermotropic liquid crystals are free of solvent and exhibit temperature-controlled phases, while lyotropic liquid crystal phases are controlled by mesogen concentration, solvent, and temperature. Some materials exhibit both thermotropic and lyotropic mesomorphism and are called amphitropic. Molecules that exhibit lyotropic

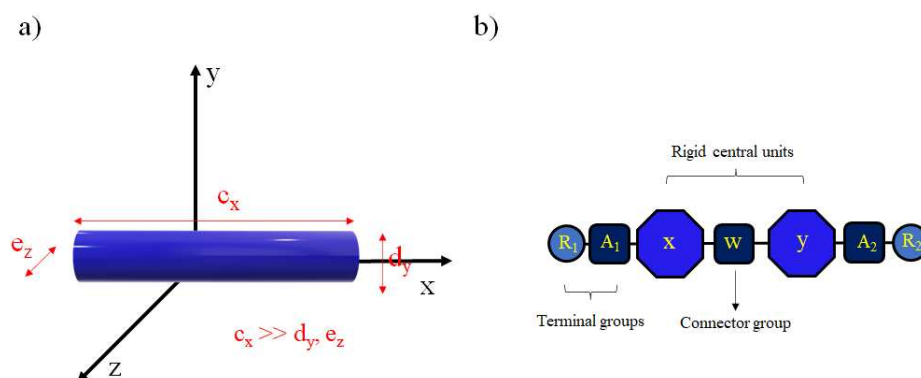
mesomorphism have an amphiphilic (lypophilic + hydrophilic) structure, and thermotropic mesogens exhibit anisotropy. Different types of anisotropy distinguish different groups of thermotropic liquid crystals (**scheme 1**).<sup>74</sup> The best known are the calamitic (rod-shaped) and the discotic (disk-shaped) LCs. However, lately, a series of more exotic anisotropies have emerged, giving rise to unconventional liquid crystals.<sup>75</sup> In this doctoral thesis, the interest is focused on thermotropic liquid crystals.



**Scheme 1** Classification of liquid crystals.

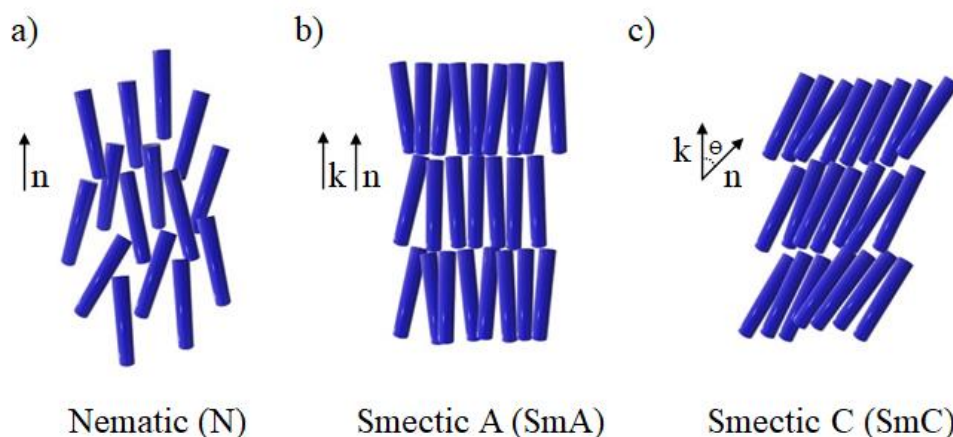
### 1.3.1.1 Calamitic liquid crystals

Calamitic (rod-shaped) mesogens are elongated in one direction of space and short in the other two (**figure 10a**). The general chemical structure is depicted in **Figure 10b**, where X and Y are the central rigid units (e.g., benzene), R<sub>1</sub> and R<sub>2</sub> are flexible chains, such as linear and/or branched alkyl groups, A<sub>1</sub> and A<sub>2</sub> are terminal chain linking groups (S, N, O, etc.) and W is a connecting group between the central units (ester, azo, etc.). Each unit's nature significantly affects the morphology of the mesophases and the physical properties of these materials.<sup>76,77</sup>



**Figure 10** Calamitic liquid crystals. a) Rod-like anisometry; b) Schematic structure of calamitic mesogens.

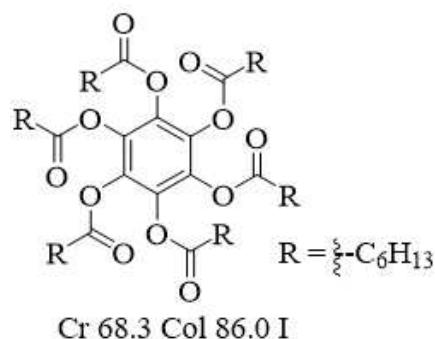
Generally, there are two main types of mesophases found for calamitic liquid crystals. These mesophases are called nematic (N) and smectic (Sm). **Figure 11** shows the type of organization found in these types of mesophases. The nematic mesophase (**figure 11a**) lacks positional order and shows only orientational order along a director vector ( $n$ ). This type of organization is responsible for the nematic mesophase's low viscosity and high fluidity. With the appearance of the short-range positional order of the molecules in one dimension, the smectic mesophase arises. The molecules are organized in fluid layers, making the system more organized and consequently more viscous than a nematic mesophase. The different angles that the molecule director ( $n$ ) makes with the vector normal to the layer plane ( $K$ ) lead to a smectic polymorphism, the most common ones being SmA and SmC (**figure 11b** and **figure 11c**, respectively). In the SmA phase, the director vector of the molecules is in parallel to the normal vector of the layer, and in the SmC phase, the molecules are tilted at an angle  $\Theta$  to the normal vector.<sup>65,77</sup>



**Figure 11** Molecular organization in calamitic liquid crystal mesophases. a) nematic mesophase (N); b) non-tilted smectic mesophase (SmA); c) tilted smectic mesophase (SmC).

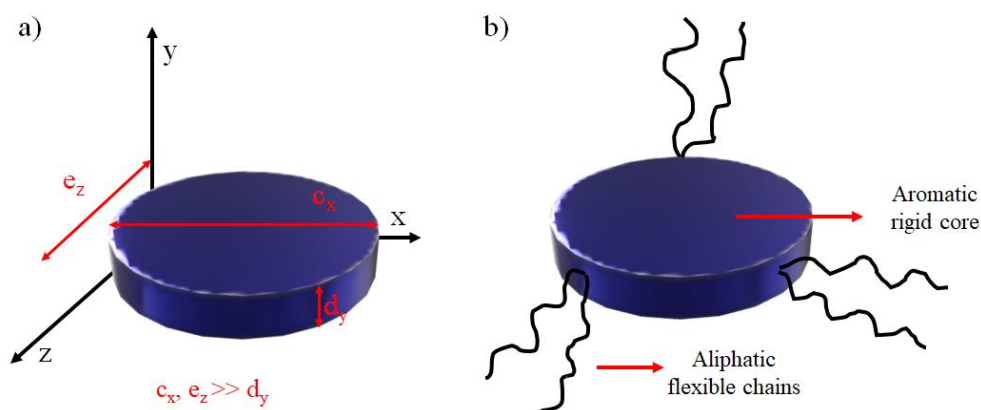
### 1.3.1.2 Discotic liquid crystals

Thermotropic discotic liquid crystals have been discovered by Chandrasekhar in his work on the mesomorphic properties of benzene-hexa-*n*-alkanoates in 1977 (**figure 12**).<sup>78</sup> Since then, various families of compounds have been synthesized and various forms of their self-assembly described.<sup>72,79</sup>



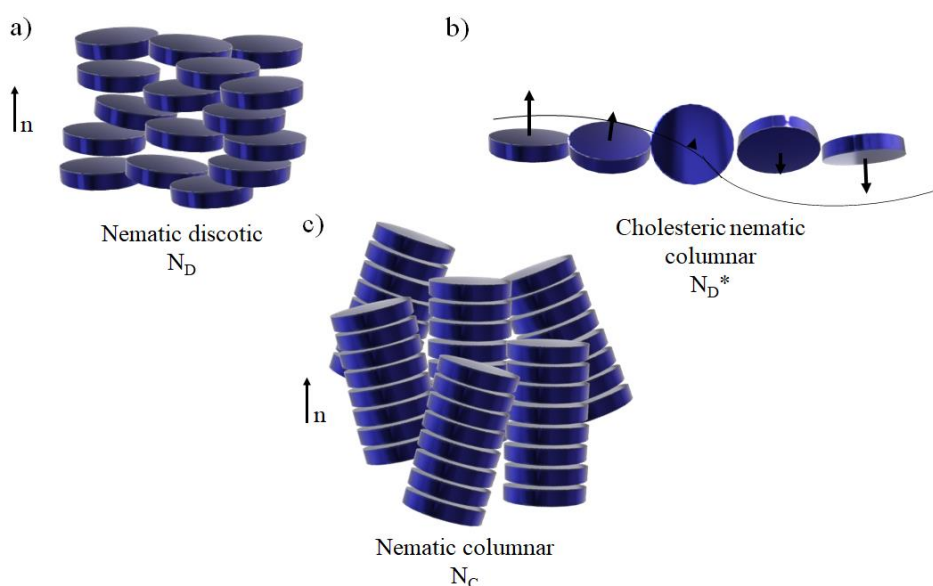
**Figure 12** First discotic liquid crystal synthesized by Chandrasekhar and coworkers. Cr: cristal phase; Col: columnar mesophase; I: isotropic phase.

The basic structure of a discotic mesogen is composed of a planar and rigid central unit (e.g., benzene, triphenylene, perylene, etc.) surrounded by linear or branched aliphatic peripheral chains that attribute flexibility to the molecule and induce phase segregation (**figure 13b**). In most cases attached to the center via ether or ester linkages. As the name suggests, the anisometry in this type of molecule, is such that one of the molecular axes is much shorter than the other two (**figure 13a**).<sup>72</sup>



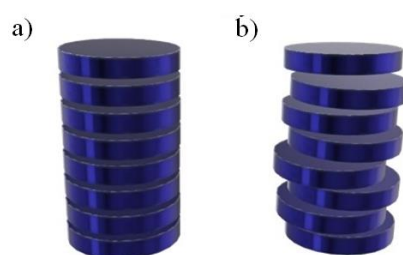
**Figure 13** Discotic liquid crystals. a) Disk-like anisotropy; b) Schematic structure of discotic mesogens.

Similar to calamitic liquid crystals, discotic mesogens can also exhibit a nematic mesophase, which lacks long-range positional order. The basic mesogenic unit can be either the individual molecular disk (**figure 14a**), or an elongated supramolecular segment of stacked disks that forms a nematic phase of supramolecular spaghetti-like fragments that fail to organize in a regular column lattice (**figure 14c**). The presence of chiral centers enables the existence of cholesteric nematic discotic mesophase ( $N_D^*$ , **figure 14b**), which the organization is the twisted nematic type, where the smallest molecular component is continuously twisted in the direction of the normal plane, resulting in a helical structure.<sup>72</sup>



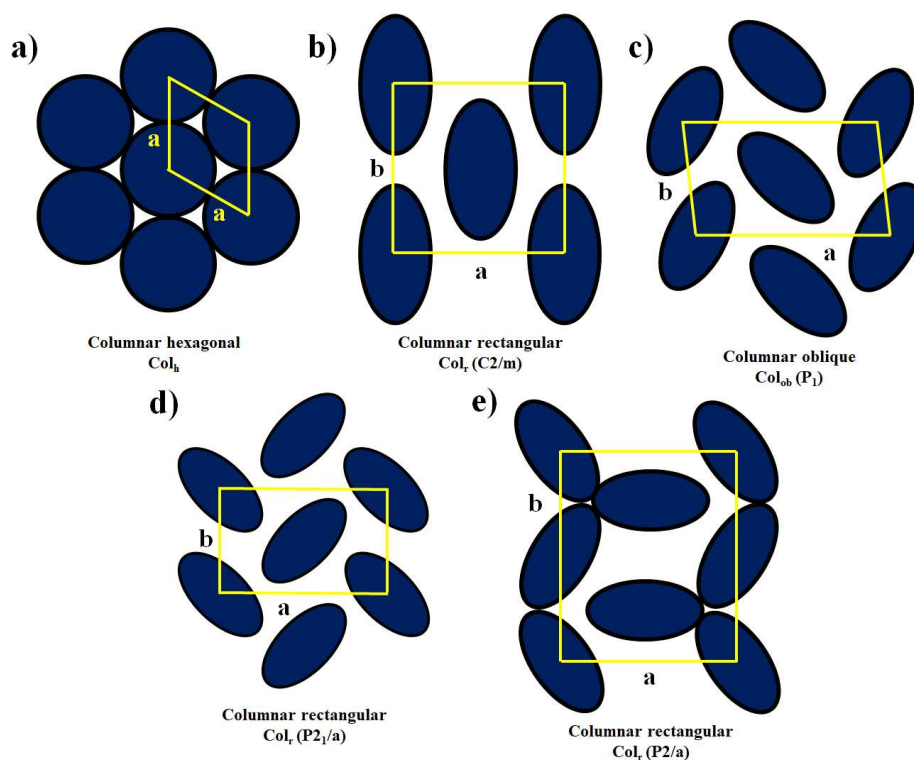
**Figure 14** Nematic mesophases in disk-like mesogens. a) Nematic discotic mesophase ( $N_D$ ); b) Cholesteric nematic discotic mesophase ( $N_D^*$ ); c) Nematic columnar mesophase ( $N_C$ ).

The more common form mesogenic organization of disk-shaped mesogens is the columnar liquid crystalline state, which is characterized by a 2D-crystalline lattice of columns made of stacked disks, whilst some fluid-like positional disorder is maintained in the direction of the column axes (i.e., within the stack). The columnar stacks can be rather orderly (with equidistant molecules) albeit lacking the correlation of molecular positions in adjacent columns that is characteristic of the crystalline state (**figure 15a**) or rather disordered (**figure 15b**), where there is no regularity in the stacking (variable distance between molecules).<sup>79</sup>



**Figure 15** Intracolumnar order. a) ordered stacking; b) disordered stacking.

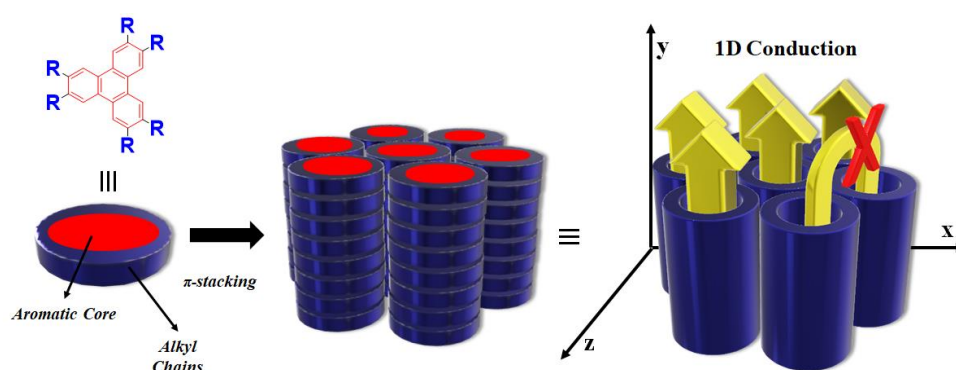
There are three main structural arrangements of different columnar mesophases: hexagonal ( $\text{Col}_h$ , with molecular planes perpendicular to the column axis, **figure 16**), rectangular ( $\text{Col}_r$ , with molecules tilted out of the plane perpendicular to the column axis, **figure 16**), and oblique ( $\text{Col}_{ob}$ , also tilted, **figure 16**). The rectangular columnar family includes some types of planar symmetry groups. In addition to the one shown in **figure 16** ( $C2/m$ ), the groups  $P2_1/a$  and  $P2/a$  are known (**figure 16**).<sup>72</sup>



**Figure 16** Different arrangements in columnar mesophases, cross sections viewed from above. a) Columnar hexagonal; b) Columnar rectangular; c) Columnar oblique; d) Columnar rectangular with  $P2_1/a$  symmetry; e) Columnar rectangular with  $P2/a$  symmetry.

One major interest in columnar mesophases is due to the efficiency of  $\pi$ -stacking type interactions between the molecular orbitals of the mesogens, within the columns, allowing efficient quasi-one-dimensional charge transport. The column center acts as a conducting channel and the aliphatic periphery as an insulator and can be compared to genuine molecular wires (**figure 17**). Although there is no intrinsic charge transport in these molecules, it can be obtained from external stimuli (chemical doping, optical stimulation, and/or electron injection).<sup>72,79</sup> The development of new materials combining discotic mesogenic units with units that favor some extra feature (e.g., luminescence) is a topic of recurring interest.<sup>73</sup>





**Figure 17**  $\pi$ -stacking interaction and one-dimensional charge transport present in columnar mesophases. Adapted from the literature.

## 2 GOALS

### 2.1.1 General Goals

The focus of this work was to create new D<sub>3</sub>A-type luminescent materials based on the 1,3,5-triazine and *tris*-1,2,4-triazolo-1,3,5-triazine (TTT) cores, to induce mesomorphism in such emitters, and synthesize new triazine-based discotic liquid crystals towards matrices for delayed luminescence emitters.

### 2.1.2 Specific Goals

More specifically, this work aimed at:

- Designing and synthesizing new D<sub>3</sub>A-type emitters where the acceptor unit is the 1,3,5-triazine heterocycle and the donor units 3,6-di-*tert*-butyl-9H-carbazole and 9,9-dimethyl-9,10-dihydroacridine spaced by a 2,4-substituted thiophene bridge.
- Designing and synthesizing new D<sub>3</sub>A-type emitters where the acceptor unit is the *tris*-1,2,4-triazolo-1,3,5-triazine (TTT) heterocycle and the donor units 3,6-di-*tert*-butyl-9H-carbazole and 9,9-dimethyl-9,10-dihydroacridine spaced by a 2,4-substituted thiophene bridge.
- Designing and synthesizing new delayed luminescence liquid crystals based on 1,3,5-triazine and TTT heterocycles by introducing alkyl chains in the 9H-carbazole donor unit.
- Designing and synthesizing new discotic liquid crystals based on the triazine core surrounded by ester groups as new liquid crystal matrices for delayed luminescence emitters.
- Photophysical, thermal and electrochemical characterization of the target materials.

### 3 NEW D<sub>3</sub>A-TYPE EMITTERS. THERMALLY ACTIVATED DELAYED FLUORESCENCE (TADF) AND ROOM TEMPERATURE PHOSPHORESCENCE (RTP) MATERIALS.

In this Chapter, we will cover the synthesis and characterization of new donor-acceptor type emitters based on *s*-triazine and tris-triazolotriazine acceptor cores surrounded by different donor moieties. We will first approach the *s*-triazine unit with a brief literature review. Next, we will explore the synthesis and structural characterization of the new materials. In the third part, we will cover the photophysical characterizations and, finally, an overall conclusion. The same approach is presented for the TTT-based molecules.

#### 3.1 1,3,5-TRIAZINE: TADF & RTP EMITTERS.

##### 3.1.1 Introduction

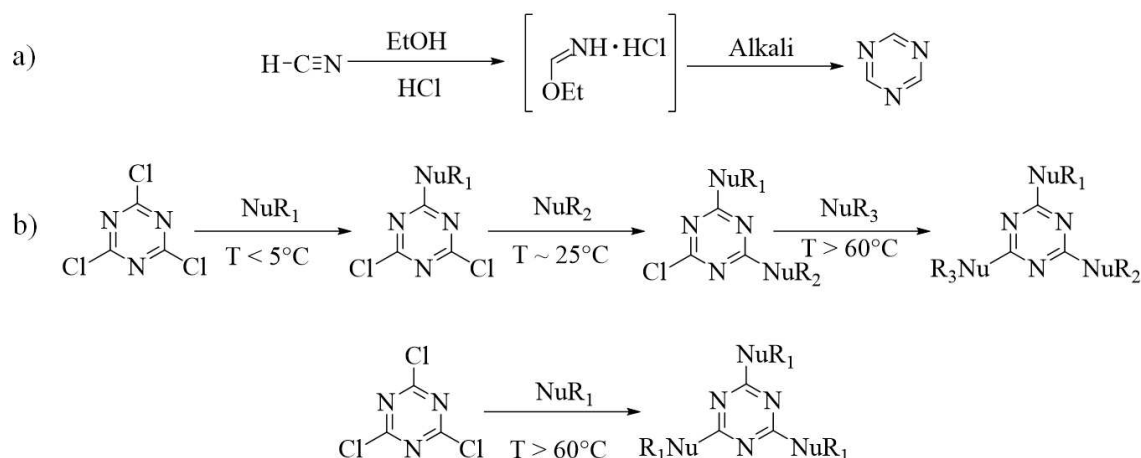
Triazines are six-membered heterocycle containing three nitrogen atoms and three carbon atoms. There are three different possible triazine systems: 1,2,3-, 1,2,4-, and 1,3,5-triazine (**figure 18**).<sup>80</sup> In this Ph.D. thesis, only the most stable and most accessible of them, the symmetric 1,3,5-triazine or *s*-triazine, will be discussed.



**Figure 18** The three possible triazine systems: 1,2,3-, 1,2,4-, 1,3,5-triazine.

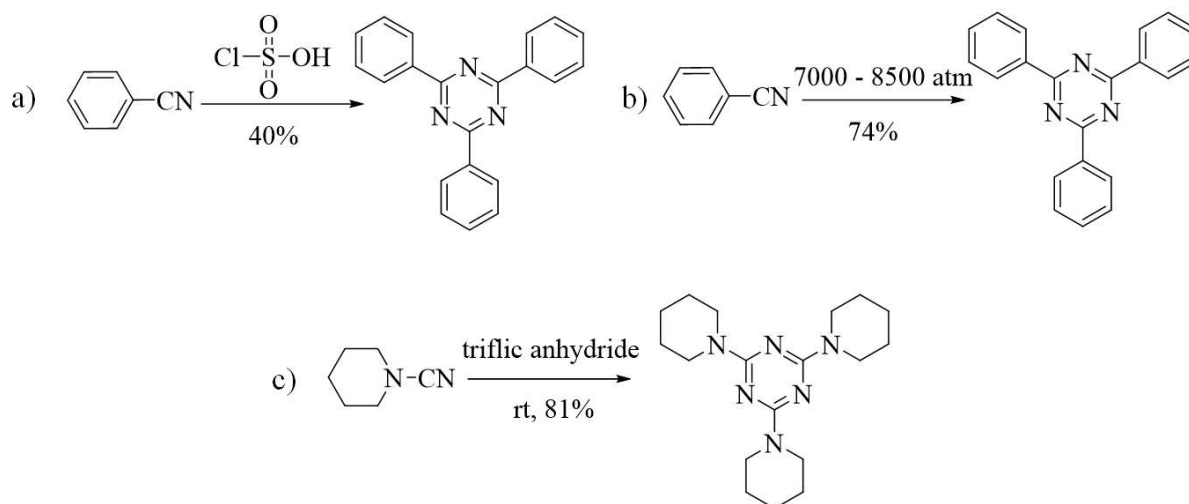
1,3,5-triazine derivatives have received significant interest due to their diverse applications in different fields. These derivatives have applications in pharmaceuticals, liquid crystals, supramolecular chemistry, and organic light-emitting devices (OLEDs).<sup>81-83</sup> *S*-triazine was first synthesized by Neff (1895) by treating hydrogen cyanide with ethanol in a hydrogen-chloride-saturated ether solution, followed by treating the resulting salt with alkali (**figure 19a**).<sup>80</sup> The potential for various fluorescence applications enabled 1,3,5-triazine derivatives to become important synthetic precursors for new materials. Among them, 2,4,6-trichloro-1,3,5-triazine (available in abundance and inexpensive) is the industrially most important intermediate. The high reactivity of the chlorine atoms at positions 2, 4, and 6 of the triazine

ring allows the insertion of different nucleophiles in the synthesis of symmetric and asymmetric 1,3,5-triazines with different substituents (**figure 19b**).<sup>84</sup>



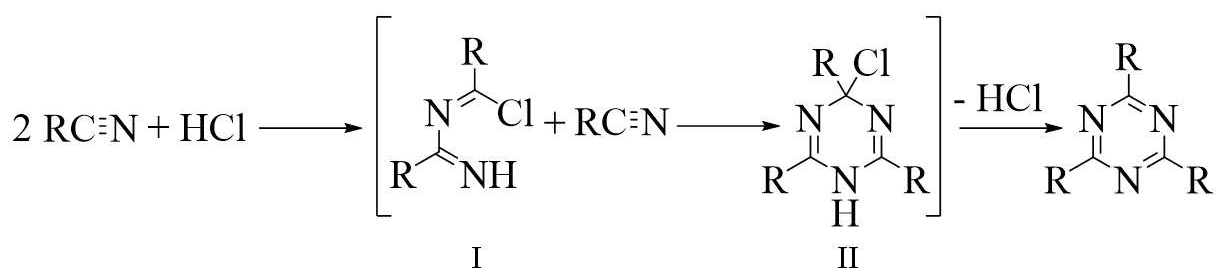
**Figure 19** 1,3,5-triazine synthesis. a) First reported synthesis from hydrogen cyanide; b) Synthesis of 1,3,5-triazine derivatives from 2,4,6-trichloro-1,3,5-triazine; Top: synthesis of asymmetric derivatives (temperature control); Bottom: synthesis of symmetric derivatives.

Several annulation protocols have been developed. The [2+2+2] annulation plays a central role in synthesizing symmetric 1,3,5-triazine. In this synthetic approach, the nitrile group trimerizes into s-triazine under different conditions, as shown in **figure 20**. Treatment of benzonitrile with chlorosulphonic acid leads to the formation of 2,4,6-triphenyl-1,3,5-triazine in 40% yield (**figure 20a**). Under high pressures, the same benzonitrile trimerizes in 74% yield (**figure 20b**), and piperidine-1-carbonitrile, when treated with triflic anhydride at room temperature, yields 2,4,6-tri(piperidin-1-yl)-1,3,5-triazine in 81% (**figure 20c**).<sup>85</sup>



**Figure 20** Different protocols for the trimerization of the nitrile group in the synthesis of 1,3,5-triazine; a) Protic acid; b) High pressure; c) Lewis acid.

The most widely used method for the preparation of 1,3,5-triazines is the acid-catalyzed trimerization of the cyano group. **Figure 21** shows the simplified mechanism of the reaction. Initially, two molecules of nitrile and one molecule of hydrochloric acid form intermediate I. After adding another nitrile molecule, the resulting intermediate II releases HCl to give s-triazine.<sup>86</sup>



**Figure 21** Simplified mechanism of acid-catalyzed nitrile group trimerization in the synthesis of s-triazine.

In the conception of new emitters for OLEDs, 1,3,5-triazine plays an important role as a potential target compound. The 1,3,5-triazine electron-acceptor has emerged as a promising building block in the design of TADF emitters, with many examples of its successful implementation in organic light-emitting diodes (OLEDs) as an emitter, resulting in high efficiency and long operating lifetimes.<sup>83</sup> 1,3,5-triazine has been a widely used electron-deficient heteroaromatic acceptor in green and blue TADF emitters and is also commonly used in the design of host materials due to its moderate electron affinity and LUMO values.<sup>87,88</sup>

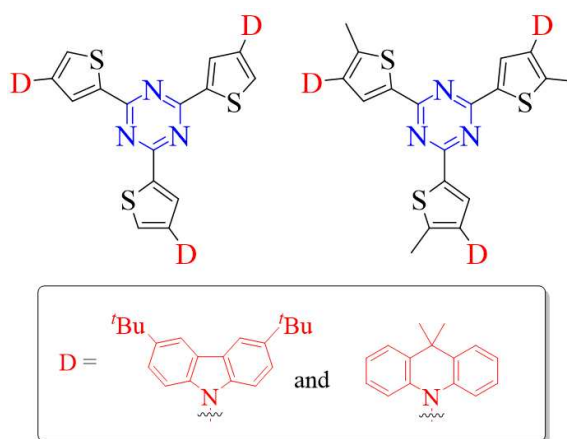
The development of organic TADF materials as emitters for OLEDs began in 2011 with a triazine-based compound, which has several advantages for this purpose. Triazine and its derivatives are easy to synthesize, can be functionalized at various positions, and have a stable aromatic structure, all of which contribute to improved device performance.<sup>83</sup> High-efficiency OLEDs using the small molecule emitter DMAC-TRZ have been developed.<sup>89</sup> More recently, the emitter SpiroAC-TRZ has improved performance with a maximum external quantum efficiency of 36.7%.<sup>90</sup> The TADF emitter 5Cz-TRZ has a fast reverse intersystem crossing rate constant, and high-efficiency non-doped OLEDs using DMAC-TRZ have shown comparable performance to doped devices.<sup>89,91</sup> Triazine-based materials have proven to be versatile in designing TADF emitters due to their ability to easily tune the emission spectrum and form intermolecular exciplexes or charge transfer interactions, which can improve the photophysical

properties of these compounds.<sup>83</sup> However, the full potential of triazine as a moiety in TADF emitter design has yet to be fully explored.

### 3.1.2 Results and Discussions

#### 3.1.2.1 Design of emitters based on the *s*-triazine core.

Considering the strategies to wards new TADF molecules, we have designed a new series of D<sub>3</sub>A molecules by linking a donor moiety (3,6-di-*tert*-butyl-9H-carbazole or 9,9-dimethyl-9,10-dihydroacridine) to an *s*-triazine core via 2,4-substituted thiophene bridge as shown in **figure 22**.



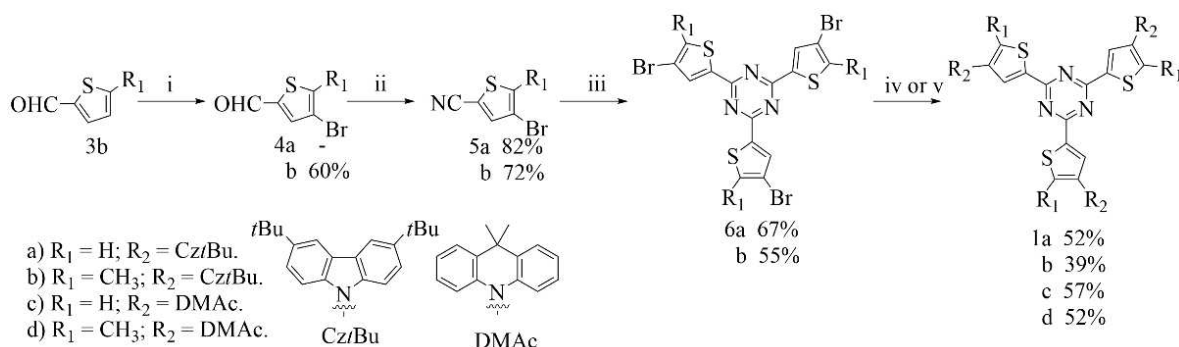
**Figure 22** Target D<sub>3</sub>A molecules based on the 1,3,5-triazine core. Donor units are 3,6-di-*tert*-butyl-9H-carbazole and 9,9-dimethyl-9,10-dihydroacridine.

There are several advantages of having the *s*-triazine core included in TADF materials. Triazine is easily functionalized at positions 2,4 and 6 with a variety of aryl units, increasing the diversity of structures obtainable; the link between the donor moiety and the triazine core can be adjusted by changing the linking unit as well as the relative position between the donor and acceptor moieties; it allows symmetric and asymmetric structures to be achieved.<sup>83</sup> The donor moieties chosen were 3,6-di-*tert*-butyl-9H-carbazole and 9,9-dimethyl-9,10-dihydroacridine. Due to its moderate donor strength and easy chemical derivatization, carbazole has been widely employed as an electron donor unit in optoelectronic materials. Another relevant factor is the absence of sp<sup>3</sup> carbons in its structure, different from the structure of other donors (e.g., 9,9-dimethyl-9,10-dihydroacridine). The presence of sp<sup>3</sup> carbons in these donors enables degradation pathways in the device.<sup>83</sup> We chose to use the 3,6-di-*tert*-butyl-9H-carbazole derivative because the *tert*-butyl group increases the solubility of the materials.

Unlike carbazole, the 9,9-dimethyl-9,10-dihydroacridine unit is a *N*-heterocycle that generally produces a more twisted conformation between the donor and the linker bridge due to increased steric hindrance.<sup>92</sup> As a result of this twisted conformation, the overlap between the frontier orbitals decreases, which gives smaller values of  $\Delta E_{ST}$ .<sup>52</sup> Considering that heavy atoms facilitate spin-orbit coupling and, therefore, can enhance delayed fluorescence and phosphorescence through interconversion between singlet and triplet states, we inserted sulfur-including thiophene bridges between the donor and acceptor moiety.<sup>24</sup>

### 3.1.2.2 Synthesis and Characterization

After the target molecules have been designed, the best synthetic route to obtain the desired products must be planned. **Scheme 2** is represented the synthetic method employed.



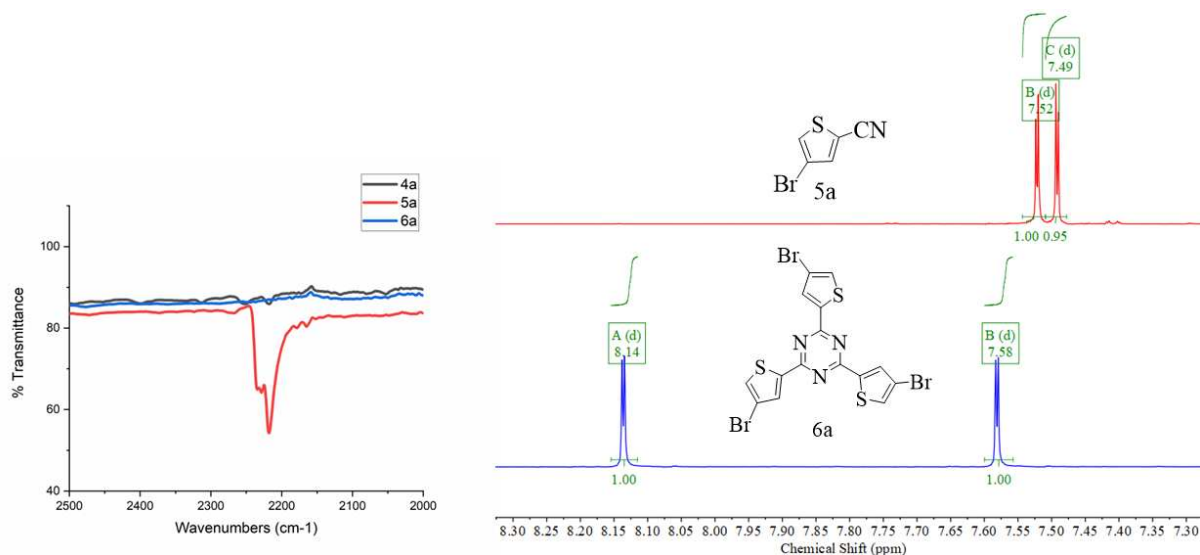
**Scheme 2** Synthesis of compounds **1a-d**. i)  $\text{Br}_2$ ,  $\text{AcOH}$ ; ii)  $\text{NH}_4\text{OH}(\text{aq})$ ,  $\text{I}_2$ ,  $\text{THF}$ ; iii)  $\text{CF}_3\text{SO}_3\text{H}$ ; iv) (**a-b**) 3,6-di-tert-butyl-9H-carbazole,  $\text{K}_2\text{CO}_3$ ,  $\text{CuSO}_4 \cdot 5\text{H}_2\text{O}$ , 1-methylnaphthalene; v) (**c-d**) 9,9-dimethyl-9,10-dihydroacridine,  $[\text{Pd}(\text{OAc})_2]$ , Xphos,  $\text{NaOt-Bu}$ , toluene.

The starting substrate for synthesizing molecules **1a** and **1c** was the commercial reagent 4-bromothiophene-2-carbaldehyde. The substrate chosen for synthesizing compounds **1b** and **1d** was 5-methylthiophene-2-carbaldehyde, which is much cheaper than the brominated analog. It was necessary to perform a bromination reaction in the first step to obtain the intermediate **4b** (60%).<sup>93</sup> All other synthetic steps are the same for the compounds without and with the methyl group on the thiophene unit. The aldehyde group of intermediates **4a/b** is converted to cyano group (**5a**: 82% and **5b**: 72%) by oxidation with iodine and ammonium hydroxide.<sup>94</sup> The 1,3,5-triazine heterocycle (**6a**: 67% and **6b**: 55%) is obtained in the next step by trimerization of the cyano group with trifluoromethanesulfonic acid.<sup>95</sup> To obtain the final molecules of this series, two different C-N coupling strategies were used depending on the donor species. The 3,6-di-tert-butyl-9H-carbazole heterocycle reacts with the intermediate **5a/b** via a variant of the Ullman condensation to yield the final molecules **1a** and **1b** (**1a**: 52% and

**1b**: 39%).<sup>96</sup> Compounds **1c** and **1d** (**1c**: 57% and **1d**: 52%) are obtained after palladium-catalyzed C-N coupling between intermediate **6a/b** and the aza-heterocycle 9,9-dimethyl-9,10-dihydroacridine.<sup>97</sup>

All intermediate and final compounds were characterized by <sup>1</sup>H and <sup>13</sup>C NMR and infrared spectroscopy (IR). The final molecules were also characterized by high-resolution mass spectrometry. The change of functional groups at each step was accompanied by the infrared spectra and the different low-field chemical shifts in the <sup>1</sup>H NMR spectrum of the intermediates.

The conversion of the aldehyde functional group to the nitrile group could be monitored by IR spectroscopy in the 2.500 – 2.000 cm<sup>-1</sup> region. The commercial reagent **4a** does not show the characteristic band of the nitrile functional group ~ 2.200 cm<sup>-1</sup> present in the spectrum of the intermediate **5a**, as shown in **figure 23**, left. In addition, the presence of only two aromatic hydrogen signals in the <sup>1</sup>H NMR spectrum of intermediate **5a** (**figure 23**, right) confirms functional group conversion. The disappearance of the CN stretching band at 2.217 cm<sup>-1</sup> in the IR spectrum of molecule **6a** indicates trimerization of the functional group to the triazine heterocycle. Although we cannot directly compare the chemical shift of the signals in the <sup>1</sup>H NMR spectrum (**figure 23** top right, **5a**, deuterated chloroform solvent and bottom right, **6a**, deuterated tetrachloroethane solvent), the differing solubility is also an indication of the formation of compound **6a**. All spectra are available in the annex section.

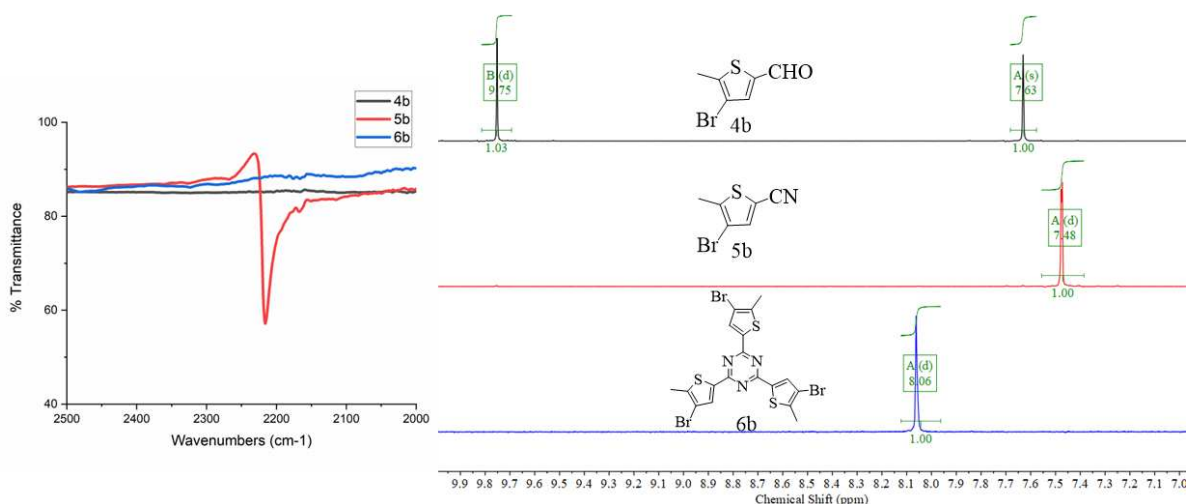


**Figure 23** IR and <sup>1</sup>H NMR spectra of intermediates **4a**, **5a** and **6a**. IR spectra region 2.000 – 2.500 cm<sup>-1</sup>, monitoring of the CN stretching band (left). <sup>1</sup>H NMR spectra (400 MHz, **5a**: CDCl<sub>3</sub>, **6a**: C<sub>2</sub>D<sub>2</sub>Cl<sub>4</sub>). Aromatic region (right).

The bromination of the commercial reagent **3b** is confirmed by the presence of only two signals in the low field region of the <sup>1</sup>H NMR spectrum (**figure 24**, top right, **4b**), referring

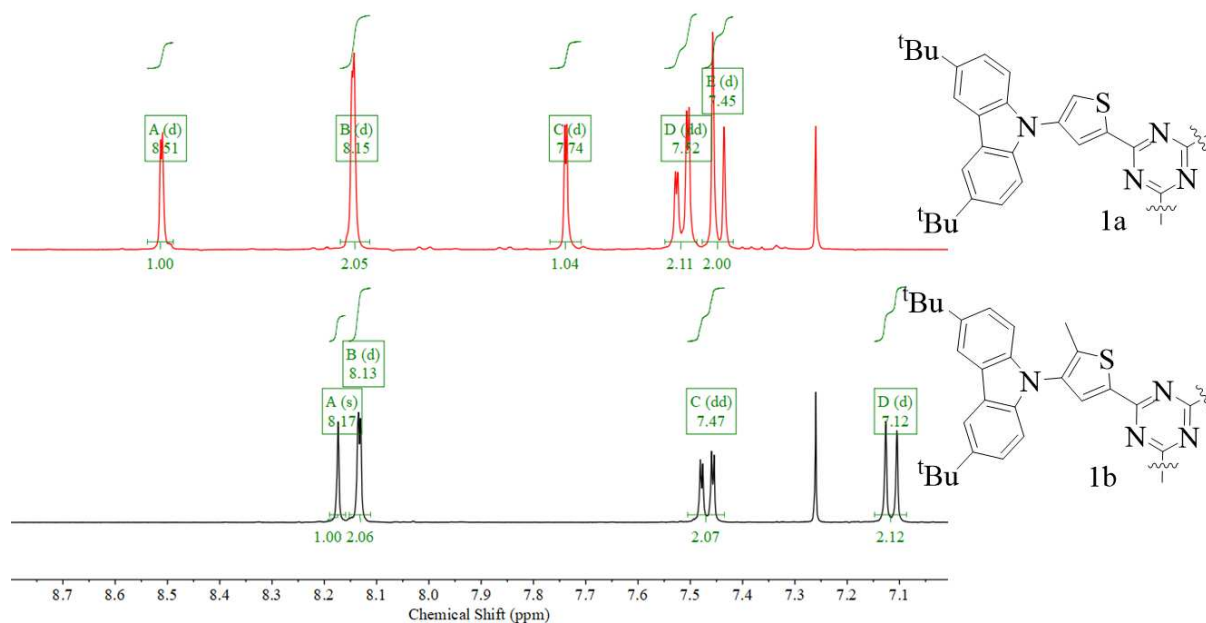


to the hydrogen of the aldehyde group at 9.75 ppm and the hydrogen of the thiophene ring at 7.63 ppm. IR and  $^1\text{H}$  NMR can follow the conversion of intermediate **4b** into compound **5b**. The appearance of the CN stretching band at  $2.215\text{ cm}^{-1}$  in the IR spectrum (**figure 24**, left, **5b**) and the disappearance in the  $^1\text{H}$  NMR spectrum (**figure 24**, middle right, **5b**) of the singlet at 9.75 ppm indicate functional group conversion. The trimerization of the nitrile group was confirmed by the disappearance of the characteristic stretching of the CN group at  $2.215\text{ cm}^{-1}$  in the IR spectrum of compound **6b** and the chemical shift of the singlet from the hydrogen of the thiophene ring in the  $^1\text{H}$  NMR spectrum to the low field of the spectrum (**figure 24**, bottom right, **6b**). All spectra are available in the annex section.



**Figure 24** IR and  $^1\text{H}$  NMR spectra of intermediates **4b**, **5b** and **6b**. IR spectra region  $2.000 - 2.500\text{ cm}^{-1}$ , monitoring of the CN stretching band (left).  $^1\text{H}$  NMR spectrum (400 MHz,  $\text{C}_2\text{D}_2\text{Cl}_4$ ) (right).

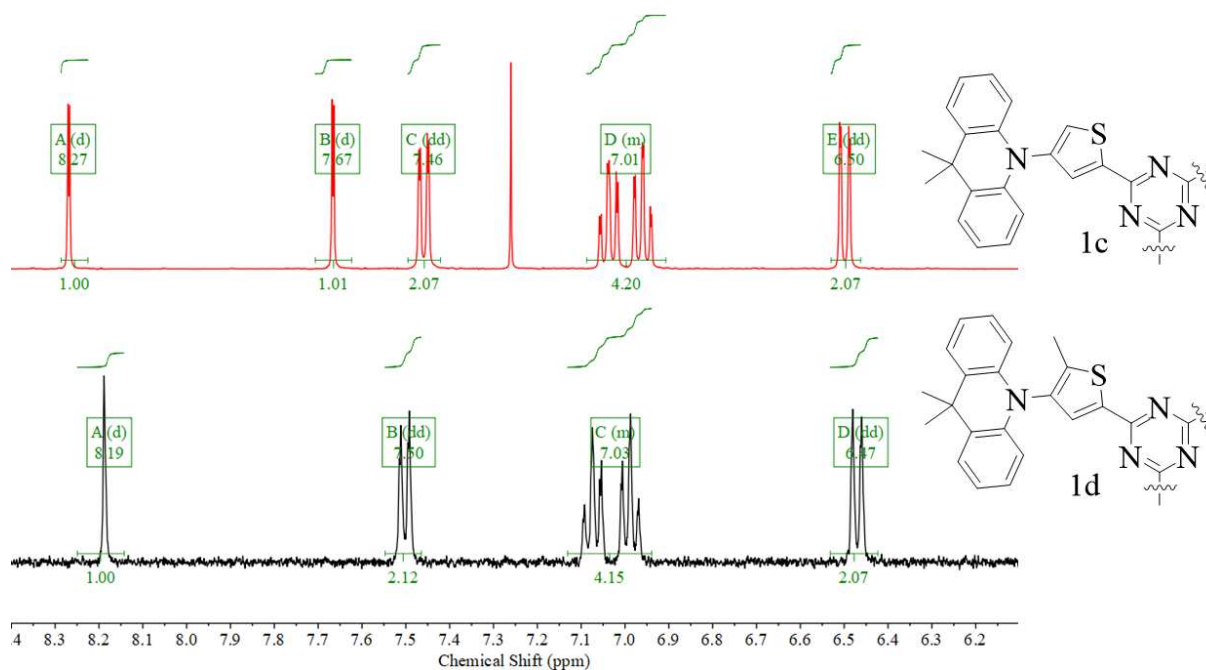
After synthesizing the key intermediates **6a/b**, it was possible, through CN coupling reactions, to obtain the target molecules **1a-d**. The appearance of the signals in the aromatic region of the  $^1\text{H}$  NMR spectrum of compound **1a** (**1b**) (**figure 25**), 8.15 (8.13) ppm, 7.52 (7.47) ppm, 7.45 (7.12) ppm refer to the hydrogens of the 3,6-di-tert-butyl-9H-carbazole unit. The ratio of 2H (1H, **1b**) of the thiophene ring to 6H of the 3,6-di-tert-butyl-9H-carbazole heterocycle indicates the proper ratio of the triple coupling. The  $^{13}\text{C}$  NMR spectrum and the aliphatic region of the  $^1\text{H}$  NMR spectrum can be seen in the annex section.



**Figure 25**  $^1\text{H}$  NMR spectra of the final molecules **1a** and **1b** (400 MHz,  $\text{CDCl}_3$ ). Aromatic region.

The structure of the final compounds was confirmed by high-resolution mass spectrometry. All spectra can be found in the annex section.

The aromatic region of the  $^1\text{H}$  NMR spectrum of the final molecules **1c/d** is demonstrated in **figure 26**. As compounds **1a/b**, the appearance of new signals in the aromatic region indicates CN coupling. The signals at 7.46 (7.50) ppm, 7.01 (7.03) ppm, and 6.50 (6.47) ppm refer to the 9,9-dimethyl-9,10-dihydroacridine unit in the spectrum of **1c** (**1d**) and are in a ratio of 8H to 2H (1H, thiophene ring), indicating the proper ratio of the triple coupling. The  $^{13}\text{C}$  NMR spectrum and the aliphatic region of the  $^1\text{H}$  NMR spectrum are available in the annex section.

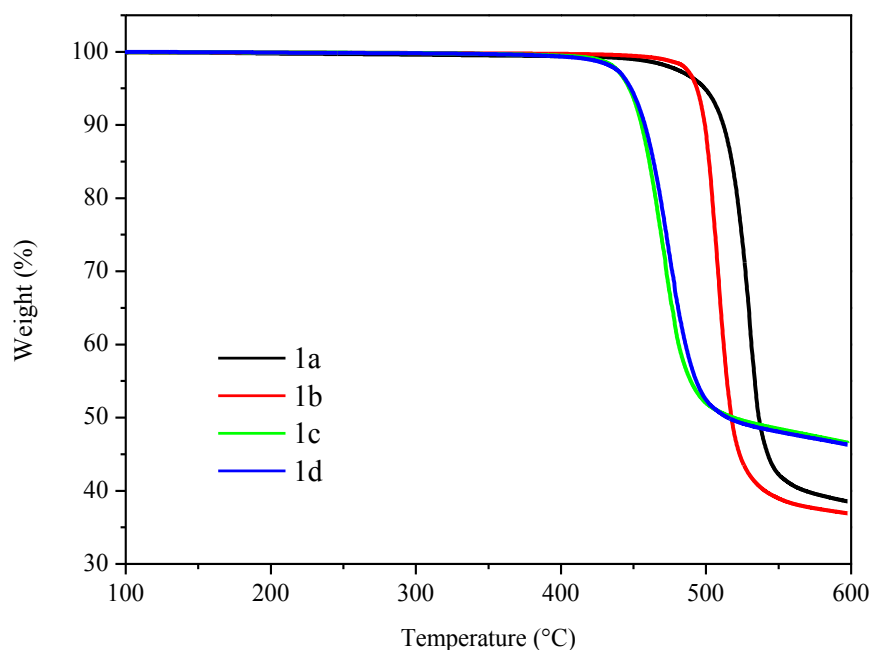


**Figure 26**  $^1\text{H}$  NMR spectra of the final molecules **1c** and **1d** (400 MHz, **1c**:  $\text{CDCl}_3$ , **1d**:  $\text{C}_2\text{D}_2\text{Cl}_4$ ). Aromatic region.

The mass spectra obtained for compounds **1c/d** confirm the desired structure (see annex section).

### 3.1.2.3 Thermogravimetric analysis (TGA)

The thermal stability of the synthesized emitters was investigated through TGA measurements. The measurements were carried out in a nitrogen atmosphere with a heating rate of  $10^{\circ}\text{C min}^{-1}$ . The results are presented in the thermogram shown in **figure 27**.



**Figure 27** Mass loss patterns determined through TGA measurements in  $\text{N}_2$  with heating rate of  $10^{\circ}\text{C min}^{-1}$ .

All four compounds derived from triazine demonstrated good thermal stability, with decomposition temperatures (defined as a 3% mass loss) ranging from 440 to  $488^{\circ}\text{C}$ . The emitters containing the 9,9-dimethyl-9,10-dihydroacridine unit displayed slightly lower stability than those containing the 3,6-di-tert-butyl-9H-carbazole unit. The decomposition temperatures of the emitters **1a-d** are summarized in **table 2**.

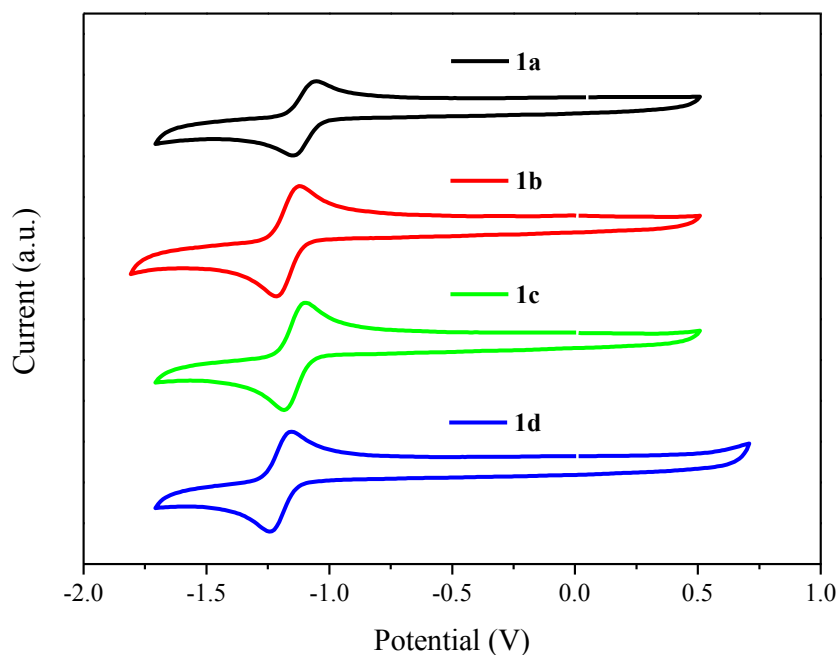
**Table 2** Decomposition temperatures of triazine-based emitters obtained through TGA analyses.

Compound	$T_{\text{dec}} (^{\circ}\text{C})^{\text{a}}$
<b>1a</b>	485
<b>1b</b>	488
<b>1c</b>	441
<b>1d</b>	442

a: 3% mass loss

### 3.1.2.4 Cyclic voltammetry (CV)

To determine the oxidation-reduction potentials of emitters based on 1,3,5-triazine core, we performed cyclic voltammetry experiments. **Figure 28** shows the voltammogram obtained for compounds **1a/d** in DMF solution.



**Figure 28** CV curves of the Triazine-based emitters in DMF solution. 0.1 mol L<sup>-1</sup> of Bu<sub>4</sub>NPF<sub>6</sub> (tetrabutylammonium hexafluorophosphate) as a supporting electrolyte. Scan rate: 100 mV s<sup>-1</sup>.

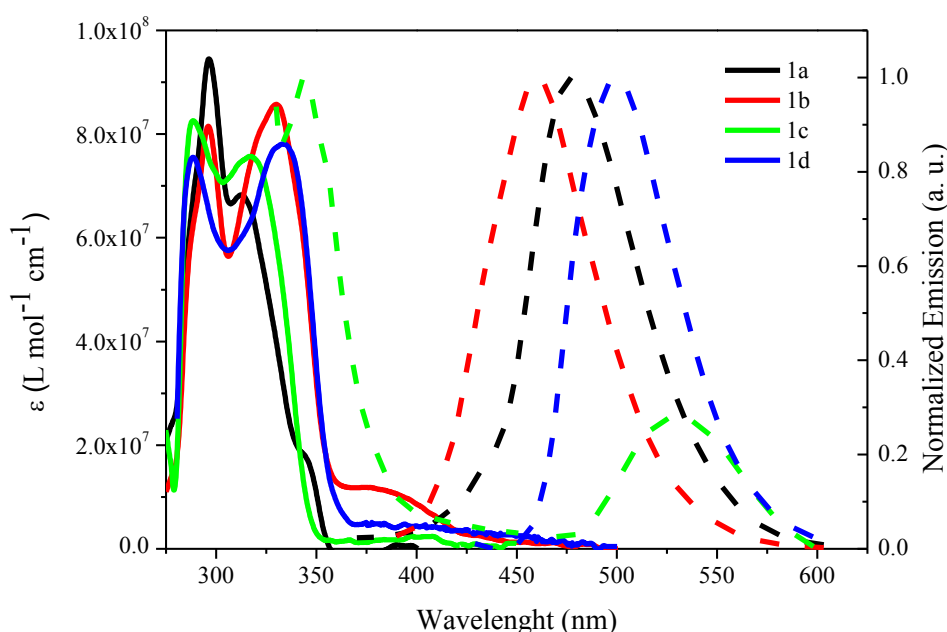
In the potential range studied, only the reduction of molecules was observed. All potentials were referenced to ferrocenium/ferrocene (Fc/Fc<sup>+</sup>, E<sub>Fc/Fc<sup>+</sup></sub> = 0.46 V). Since all emitters are based on the same acceptor unit, triazine, similar reduction potentials were found, namely -1.82 V, -1.90 V, -1.83 V, and -1.91 V for **1a**, **1b**, **1c**, and **1d**, respectively.

### 3.1.2.5 Photophysical Properties

Following the synthesis and structural characterization of triazine-based emitters, steady-state and time-resolved photoluminescence analyses were performed to investigate the photophysical processes responsible for the emission of these compounds in solution and solid states.

### 3.1.2.5.1 Steady-State Photoluminescence – Solution and Solid State

To study the impact of structural modifications to the triazine core on the photophysical properties of the newly synthesized materials, the UV-vis absorption and emission spectra of **1a-d** were measured in toluene and Me-THF solution. The experiments were conducted at low concentrations ( $10^{-6}$  mol L<sup>-1</sup>) using the Lambert-Beer parameters and avoiding aggregate formation. **Figure 29** displays the absorption and normalized emission spectra.



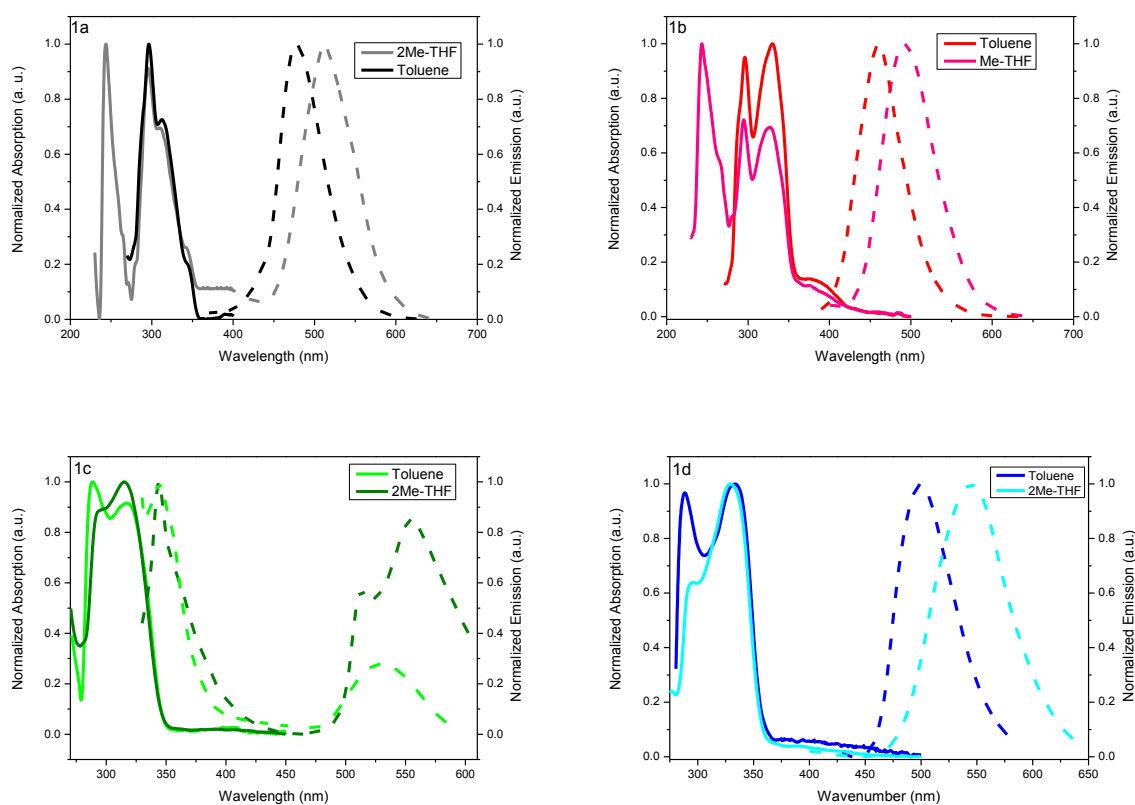
**Figure 29** Absorption and emission spectra of **1a-d** in dilute toluene solution ( $10^{-6}$  mol L<sup>-1</sup>). Solid line: absorption, dash line: emission.

All compounds **1a-d** display a high energy absorption band at around 292 nm in toluene solution (as shown in **figure 29**). This band is attributed to the  $\pi$ - $\pi^*$  transition of the triazine core.<sup>98</sup> Additionally, **1a** and **1b** exhibit an absorption band at 321 nm, attributed to the carbazole  $\pi$ - $\pi^*$  transition.<sup>99</sup> For **1c** and **1d**, the corresponding absorption band at 325 nm is attributed to the  $\pi$ - $\pi^*$  transition of the acridine group.<sup>98</sup> In addition to the bands characteristic of the individual subunits, broad and weak absorption bands are observed at longer wavelengths associated with an intramolecular charge transfer (CT) state between the donor and acceptor units.

The steady-state photoluminescence spectra (**figure 29**) of the carbazole derivatives **1a** and **1b** in dilute toluene solution show a Gaussian emission peak with maxima at 477 nm and

459 nm, respectively. This emission originates from a mixed state of locally excited singlet ( $^1\text{LE}$ ) and charge transfer singlet ( $^1\text{CT}$ ). Molecule **1d** exhibits the same photoluminescence spectra behavior in toluene solution as carbazole analogs. A Gaussian emission peak with a maximum at 499 nm arises from a mixture of  $^1\text{CT}/^1\text{LE}$  states. Interestingly, when excited at 350 nm, emitter **1c** exhibits a dual emission. The higher energy peak (around 344 nm) matches the acridine moiety emission previously reported,<sup>98</sup> while the second broad and weak emission peak at approximately 529 nm is assigned to a  $^1\text{CT}$  emission. The observed emission from the acridine moiety demonstrates the strong decoupling of the donor and acceptor moieties in this compound.

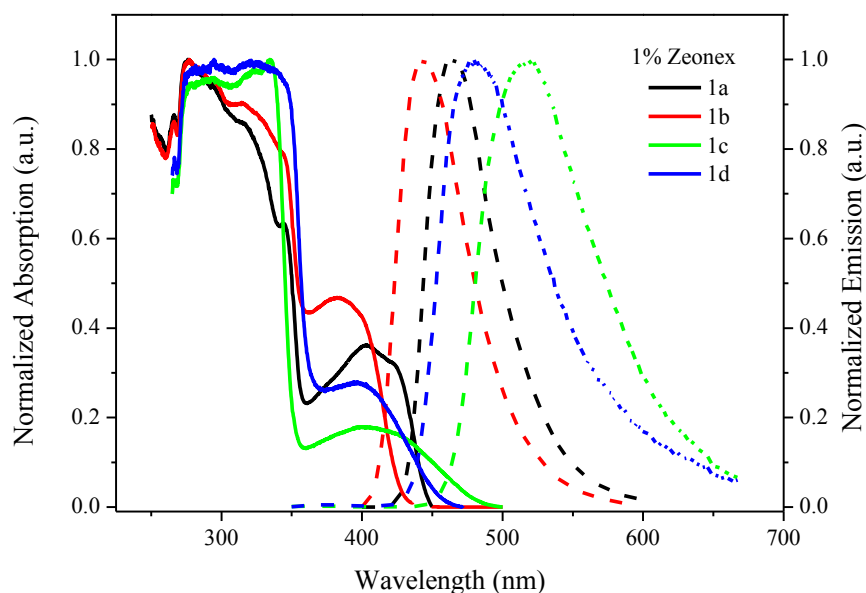
A photoluminescence spectroscopy experiment was conducted using solvents of different polarities to identify the excited states responsible for the emission of the compounds being studied. **Figure 30** compares the absorption and emission spectra obtained in toluene and 2Me-THF solutions.



**Figure 30** Absorption and normalized photoluminescence spectra in toluene and 2-MeTHF solutions. Solid line: absorption, dash line: emission.

Increasing the polarity of the solvent, toluene to 2Me-THF, results in a slight red shift in the emission of carbazole derivatives, as shown in **figures 30a** and **30b**. The peak also becomes broader, which suggests the presence of a mixed  $^1\text{LE}/^1\text{CT}$  state. In 2Me-THF, the emission of **1c** at low wavelengths is similar to that in toluene solution, without any shift in the band. This indicates that the  $^1\text{LE}$  state is responsible for this emission. The emission at lower energy is divided into two maxima (512 nm and 554 nm) and becomes broader and more intense (**figure 30c**). This observation suggests that in more polar solvents, the CT band is stabilized (red-shift, onset at 554 nm). Additionally, there is an increase in the contribution of phosphorescence to the emission of the compound ( $^3\text{LE}$  state, with an onset at 512 nm). Compound **1d** exhibits similar characteristics to those of carbazole derivatives (**figure 30d**). The insertion of the methyl group on the thiophene bridge reduces the orthogonality between the donor and acceptor units in **1d**, enabling more significant coupling between these units and suppressing the  $^1\text{LE}$  emission from the acridine unit observed in the analog **1c**. A slight red shift with a broader emission suggests also a mixed  $^1\text{LE}/^1\text{CT}$  state for this emission.

The photophysical properties of the emitters in a solid state were measured in a zeonex matrix, a non-polar saturated hydrocarbon polymer. **Figure 31** shows the normalized absorption and emission spectra for all four compounds.

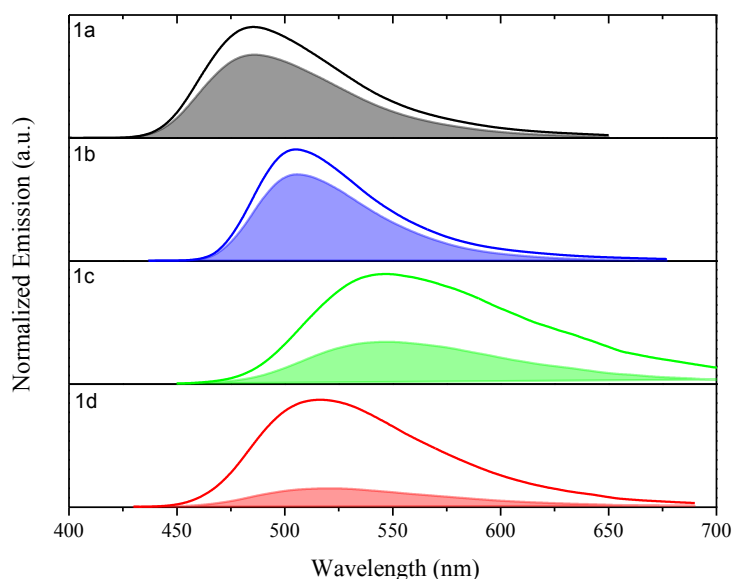


**Figure 31** Normalized absorption and photoluminescence spectra in zeonex excited at the peak of the lowest energy band. Solid line: absorption, dash line: emission.



In the solid-state spectra, the CT bands were generally quite broad. The other high-energy absorption bands displayed a less structured shape than those observed in the toluene solution, likely due to the thickness of the film. The photoluminescence of all compounds featured a Gaussian-shaped emission band with a slight blue shift compared to that observed in toluene solutions. Interestingly, compound **1c** displayed only one emission band instead of two, as observed in the toluene solution. The presence of a bulky matrix may have flattened the **1c** compound, leading to mixed  $^1\text{LE}/^1\text{CT}$  states, similar to what has been previously observed with other derivatives in toluene.

To better understand the role of non-radiative rates in these molecules, we measured the absolute photoluminescence quantum yield (PLQY) of toluene solutions in air and degassed conditions. The PLQY in degassed solution ( $\Phi_{\text{degassed}}$ ) was calculated from the PL ratio between degassed and air-equilibrated solutions, shown in **figure 32**.



**Figure 32** Emission spectra in degassed (solid lines) and air-equilibrated (filled areas) in dilute toluene solution at room temperature.

The slight decrease in the photoluminescence of the emitters when oxygen is introduced into the solution indicates that triplet states are likely involved in the emission process. Oxygen has a known effect of suppressing slow emissive processes, such as TADF and RTP, which involve triplet states.

In toluene solution, acridine derivatives demonstrated significantly lower PLQY values than carbazole derivatives. This is consistent with the acridine unit being more

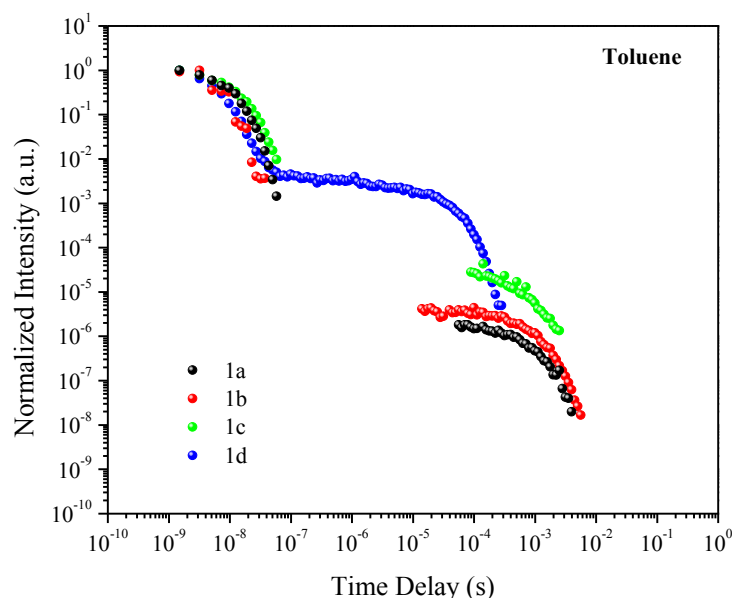
orthogonally positioned (nearly 90 degrees) to the core than the carbazole unit. Therefore, even though it forms a CT state, this state has a low oscillator strength and, consequently, a lower radiative rate. Compound **1c** has a very low emission intensity, indicating that its CT state has the lowest oscillator strength of analog **1d**. These measurements are summarized in **table 3**. According to the PLQY results, the presence of the thiophene group in all the molecules leads to strong spin-orbit coupling between their low energy states, resulting in a large population of triplet states ( $\Phi_{\text{ISC}} = 1 - \Phi_{\text{degassed}}$ ) and triplet non-radiative deactivation, especially in the compounds **1c** and **1d**.

**Table 3** Quantum yields  $\Phi$  in toluene solution.

	<b>1a</b>	<b>1b</b>	<b>1c</b>	<b>1d</b>
$\Phi_{\text{air}}$	0.156	0.123	-	0.018
$\Phi_{\text{degassed}}$	0.210	0.163	2.79 (ratio)	0.098

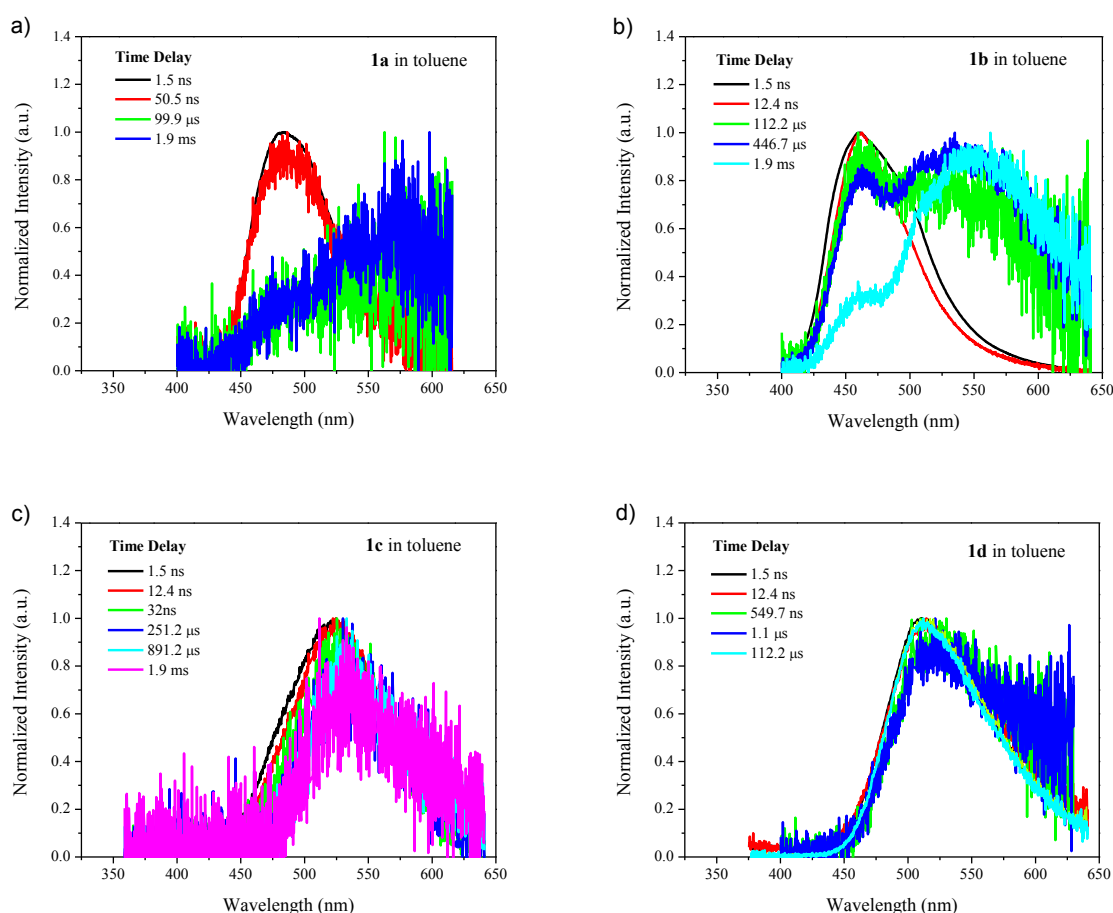
### 3.1.2.5.2 Time-resolved photoluminescence – Solution and Solid State

To examine the behavior of the excited states, we conducted time-resolved photoluminescence (TRPL) measurements in toluene and solid-state materials. The resulting decay curves in toluene are presented in **figure 33**.



**Figure 33** Time-resolved decay curves in toluene. The excitation wavelength was 355 nm. All measurements were performed in the absence of oxygen.

All the compounds exhibited a decay profile with two types of emission. The radiative decay observed in the nanosecond range was due to prompt fluorescence. A second emission in the millisecond range (for compounds **1a**, **1b**, and **1d**) and in the microsecond range (for compound **1c**) was also observed, which could be attributed to either phosphorescence or delayed fluorescence. By analyzing the emission spectra at different decay times (**figure 34**), it was possible to identify the specific decay mechanism in each of these materials.



**Figure 34** Normalized spectra taken after different delay times at room temperature in toluene solutions. The excitation wavelength was 355 nm. All measurements were performed in the absence of oxygen.

The time-resolved photoluminescence spectra for the carbazole derivatives, shown in **Figures 34a** and **34b**, reveal similar trends. In the initial nanoseconds after excitation, both compounds exhibit an emission peak centered at approximately 475 nm and 460 nm for **1a** and **1b**, respectively. This peak is attributed to the decay of the  $^1\text{LE}/^1\text{CT}$  state, with lifetimes of 8.3 ns and 5.5 ns for **1a** and **1b**, respectively. As the delay times increase, a second emission peak

is observed at wavelengths of approximately 575 nm and 555 nm for **1a** and **1b**, respectively. These peak displays characteristics typical of room-temperature phosphorescence (RTP), with a lifetime of approximately 0.7 ms for both compounds.

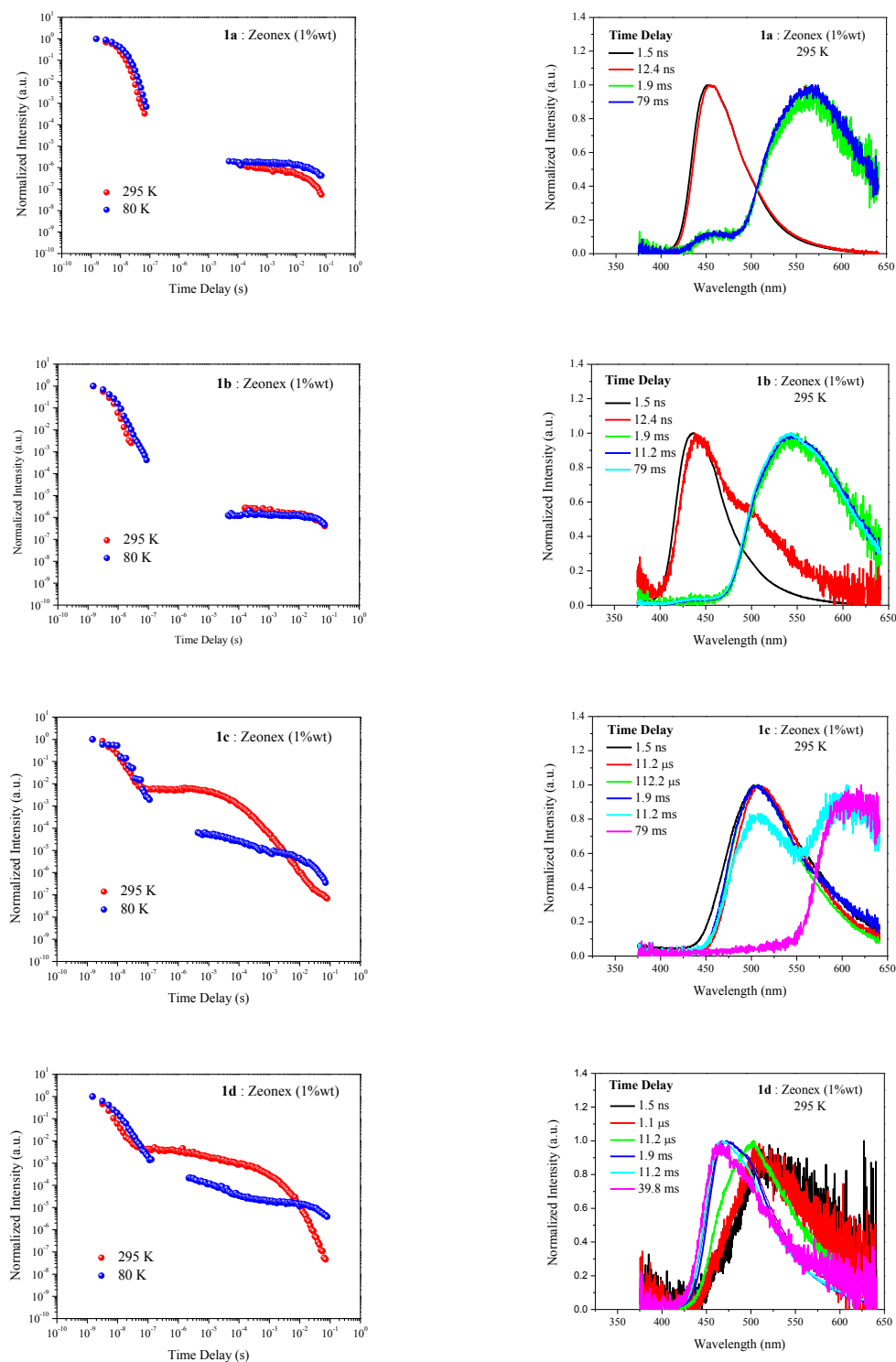
Moving from carbazole derivatives to acridine homologs (**figures 34c** and **34d**), the time-resolved photoluminescence (TRPL) spectra of **1c** and **1d** in toluene solution exhibited similar behavior. Specifically, **1c** displayed a rapid stabilization of the <sup>1</sup>CT state with a 1.5 ns lifetime, followed by a broad emission band at around 525 nm with an 11.9 ns lifetime. At longer time delay, the band in the microsecond time regime has identical spectra as the prompt decay and is ascribed to delayed fluorescence (DF). The DF emission exhibited faster decay, with lifetimes of 0.5 ms. For **1d**, In the initial nanoseconds after excitation, we observed emission with an onset at 520 nm and a lifetime of 4.7 ns. By increasing the delay times, the emission band in the microsecond time regime has been found to have identical spectra as the prompt decay. It is also identified as delayed fluorescence (DF) with a lifetime of 0.02 ms.

The presence of RTP in the toluene solution of compounds **1a** and **1b** is surprising, as triplet states typically have a long lifetime and tend to undergo non-radiative decay. However, the bulky carbazole donor surrounding the rigid triazine core protects the <sup>3</sup>LE state, centered at the triazine-thiophene core (similar to TTT derivatives), from non-radiative losses such as collisional deactivation with the environment. The lifetime data of all processes is summarized in **table 4**.

**Table 4** Lifetimes  $\tau$  in toluene solution.

	<b>1a</b>	<b>1b</b>	<b>1c</b>	<b>1d</b>
$\tau_1$ (ns)	-	-	1.5 (36%)	-
$\tau_2$ (ns)	8.3	5.5	11.9 (64%)	4.7
$\tau_{DF}$ (ms)	-	-	0.5	0.02
$\tau_{Phosph}$ (ms)	0.7	0.7	-	-

Time-resolved photoluminescence analyses in the solid state were also performed. **Figure 35** shows the time-resolved decay and the normalized emission spectrum at different delay times for all emitters.



**Figure 35** Left: Time-resolved decay in zeonex, 295 K and 80 K. Right: Normalized spectra after different delay times, 295K.

The decay curves of compounds **1a** and **1b** exhibit two regimes, like those previously observed in toluene solutions. The curves display a prompt fluorescence followed by phosphorescence at longer delay times. In the initial delay times (nanoseconds range), both compounds exhibit an emission with onset at 455 nm (**1a**) and 435 nm (**1b**) with lifetimes of 6.3 ns and 3.0 ns, respectively. At the delayed lifetimes, we observed phosphorescence emission with an onset at 567 nm for compound **1a** and 545 nm for compound **1b**. The lifetimes for this process were found to be 21.0 ms and 55.7 ms for compounds **1a** and **1b**, respectively. The derivative containing acridine, **1c**, exhibited three distinct emission regimes upon excitation. In the nanosecond range, we observed prompt fluorescence with peak emission at 507 nm and a lifetime of 5.3 ns. As the delay time increased into the microsecond range, we observed a similar spectrum corresponding to delayed fluorescence (DF) with a lifetime of 0.1 ms. Finally, at even longer delay times in the millisecond range, we observed a new emission peak at 610 nm and a lifetime of 10.5 ms, characteristic of RTP. Compound **1d** exhibits two emission regimes in time-resolved decay, although the emission spectrum remains unchanged at different acquisition times, characteristic of prompt and delayed fluorescence. The onset of emission occurs at 473 nm, and the lifetimes of PF and DF are 2.4 ns and 0.36 ms, respectively.

As the temperature decreases, 295K to 80K, the spectra in all regimes become better resolved, indicating a decrease in motion and an increase in the rigidity of the structure in the film. The most extended lifetime observed for radiative decays in all compounds at low temperatures is correlated with less pronounced non-radiative decays. The obtained data are summarized in **table 5**.

**Table 5** Lifetimes  $\tau$ , quantum yield  $\Phi$ , and  $S_1$  &  $T_1$  energies in zeonex matrix.

	<b>1a</b>	<b>1b</b>	<b>1c</b>	<b>1d</b>
<b>RT</b>				
$\tau_{PF}$ (ns)	6.3	3.0	5.3	2.4
$\tau_{Phosph\ 1}$ (ms)	0.4 (40%)	0.7 (44%)	10.5	-
$\tau_{Phosph\ 2}$ (ms)	21.3 (60%)	56.2 (56%)	-	-
$\tau_{Phosph\ av}$ (ms) <sup>[a]</sup>	21.0	55.7	-	-
$\tau_{DF\ 1}$ (ms)	-	-	0.2 (25%)	0.004 (66%)
$\tau_{DF\ 2}$ (ms)	-	-	0.03 (75%)	0.36 (34%)
$\tau_{DF\ av}$ (ms) <sup>[a]</sup>	-	-	0.1	0.36
$\Phi_{air}$	0.15	0.11	0.04	0.03
<b>80 K</b>				
$\tau_{PF}$ (ns)	8.9	4.3	8.8	4.6
$\tau_{Phosph\ 1}$ (ms)	51.1 (87%)	1.9 (6%)	7.0 (22%)	17.9 (12%)
$\tau_{Phosph\ 2}$ (ms)	5.74 (13%)	84.1 (94%)	0.07 (78%)	0.02 (88%)
$\tau_{Phosph\ av}$ (ms) <sup>[a]</sup>	50.5	84.0	6.8	17.8
$\tau_{DF}$ (ms)	-	-	-	-
$S_1$ (eV)	2.725 $\pm$ 0.014	2.845 $\pm$ 0.009	2.461 $\pm$ 0.015	2.583 $\pm$ 0.016
$T_1$ (eV)	2.202 $\pm$ 0.019	2.289 $\pm$ 0.010	2.243 $\pm$ 0.020	2.315 $\pm$ 0.008
$\Delta E_{ST}$ (eV)	0.523	0.556	0.218	0.268

[a] Obtained from  $\tau = \Sigma \tau_i^2 A_i / \Sigma \tau_i A_i$ , due to multi-exponential profile.

From the onset values of the PF emission peak at room temperature and the phosphorescence emission peak at low temperature, we estimated the  $\Delta E_{ST}$  gap for all compounds (as shown in **table 5**). The high values that were found for the carbazole derivatives prevent these emitters from showing delayed fluorescence, while the gap values found for the acridine-containing emitters allow rISC to occur, enabling TADF emission.

With the acridine derivatives, delayed fluorescence was suppressed when time-resolved photoluminescence (TRPL) was carried out at low temperatures (see annex section). This observation, in conjunction with the values of  $\Delta E_{ST}$  obtained for these derivatives, supports the conclusion that the mechanism of delayed fluorescence exhibited by these materials is of

the thermally activated delayed fluorescence (TADF) type. The small amount of thermal energy at room temperature is sufficient to facilitate intersystem crossing and enable emission from the  $^1\text{LE}/^1\text{CT}$  state.

#### 3.1.2.6 *Theoretical investigations*

Theoretical density functional theory (DFT) calculations are currently being performed to determine the geometries of the ground state of all emitters. Time-dependent DFT (TD-DFT) and spin-orbit coupling TD-DFT (SOC-TD-DFT) calculations are also being conducted to examine the properties of the excited states of triazine-based compounds and compare them to experimental results. At the time of writing and submitting this Ph.D. thesis, the calculations are still ongoing and need to be finalized.

#### 3.1.3 **Conclusions**

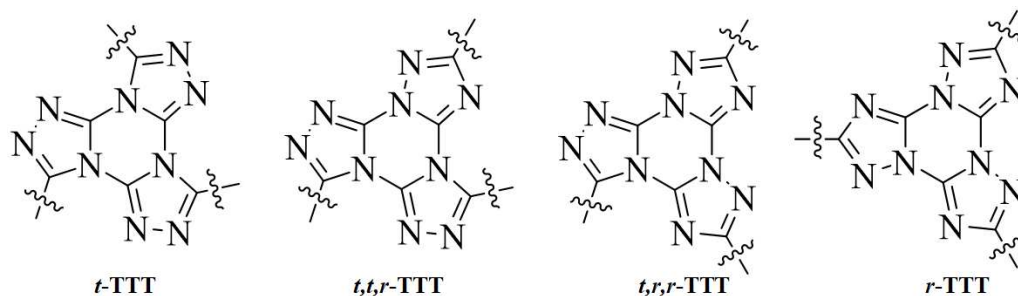
Structural modifications on  $\text{D}_3\text{A}$  molecules based on the triazine core have been found to impact these materials' emission properties significantly. For example, the carbazole moiety in the triazine-thiophene structure allows for phosphorescence emission, while acridine derivatives exhibit TADF emission. The strongly twisted structure triazine-thiophene-acridine reduces the overlap between the HOMO and LUMO orbitals, resulting in low  $\Delta E_{\text{ST}}$  values (less than 0.3 eV), which enables reverse intersystem crossing and TADF emission with lifetimes ranging from 0.02 to 0.5 milliseconds. Although the molecular structure in carbazole derivatives does not typically allow for low  $\Delta E_{\text{ST}}$  values, the inclusion of thiophene bridges can result in solution RTP emission with lifetimes of 0.7 milliseconds, because of the heavy atom effect of the sulfur of the thiophene bridge. Acridine derivatives also show phosphorescence in the solid state at low temperatures, with lifetimes ranging from 6.8 to 17.8 milliseconds. The PLQY of these materials ranges from 0.01 to 0.02 in a degassed solution. All of the compounds demonstrated PF with lifetimes ranging from 4.7 to 11.9 nanoseconds, with carbazole derivatives showing higher efficiency due to a mixed  $^1\text{CT}/^1\text{LE}$  state. The RTP observed in solution for carbazole derivatives suggests that the  $^3\text{LE}$  emission state centered on the triazine-thiophene unit is protected from nonradiative decay by the bulky donor in the structure. The incorporation of thiophene bridges with a sulfur atom in the  $\text{D}_3\text{A}$  structure of new emitters based on the triazine center has proven effective in creating materials with different emission mechanisms depending on the donor unit.



### 3.2 TRIS[1,2,4]TRIAZOLO[1,3,5]TRIAZINE: RTP & TTA EMITTERS.

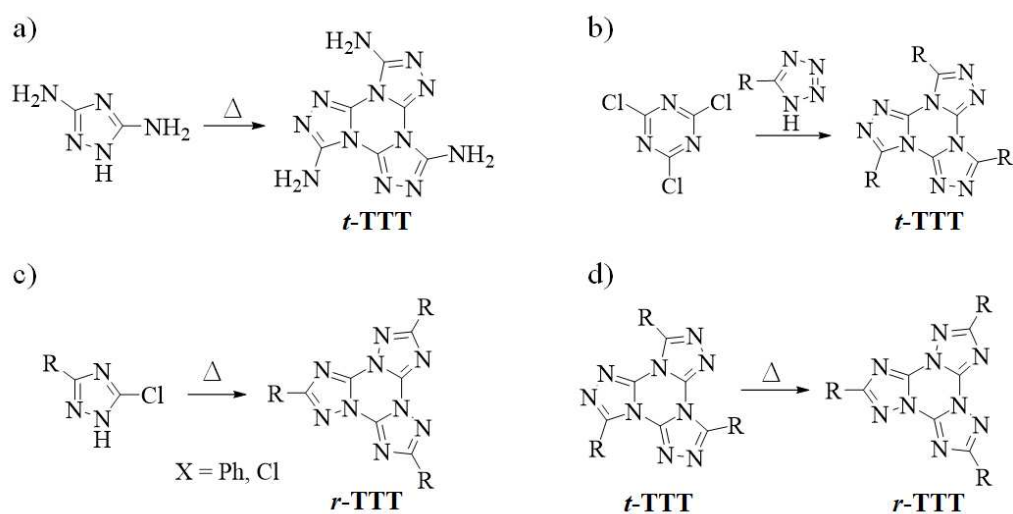
#### 3.2.1 Introduction

The *tris*[1,2,4]triazolo[1,3,5]triazine (TTT) core is a fused tetracycle containing nine nitrogen atoms in its structure. Four known isomeric forms exist two symmetrical C<sub>3</sub> structures and two less symmetrical ones (**figure 36**). The symmetric isomers are denoted by t-TTT (tangential) and r-TTT (radial), while the less symmetric ones by t,t,r-TTT, and t,r,r-TTT.<sup>100</sup>



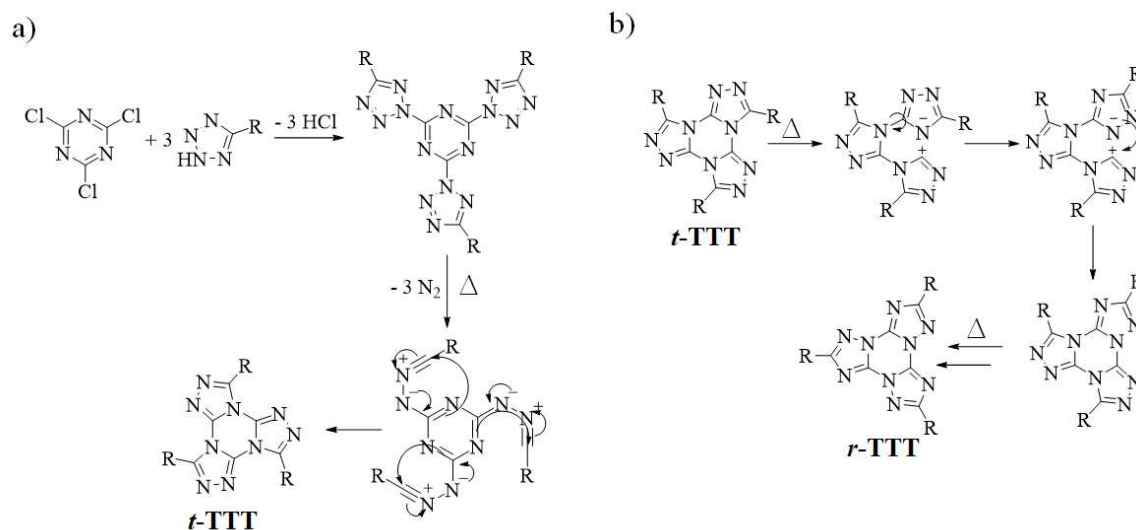
**Figure 36** Isomeric forms of the TTT core.

Hoffmann and co-workers were the first to report the synthesis of the TTT heterocycle from 3,5-diamino-1,2,4-tetrazole (**figure 37a**). In this work, Hoffman characterizes the molecule obtained as the radial isomer.<sup>101</sup> Years later, Kaiser corrected the structure proposed by Hoffmann as being the t-TTT isomer.<sup>102</sup> Conducting studies with tetrazole derivatives, Huisgen reported the reaction of these derivatives with cyanuric chloride as a synthetic route to obtain the t-TTT heterocycle (**figure 37b**), the most used route nowadays to obtain these molecules due to its broad scope.<sup>103</sup> In 2005, Tartakovsky proposed the synthesis of the r-TTT isomer from the cyclo-condensation of the 3-R-5-chloro-1,2,4-triazole molecules (R = Cl and Ph, **figure 37c**). In this work, the author explored the thermo-instability of the t-TTT isomer and obtained a mixture of isomers. Among them is the symmetric r-TTT C<sub>3</sub> isomer (**figure 37d**).<sup>104</sup>



**Figure 37** Synthetic methodologies of TTT core; a) from 3,5-diamino-1,2,4-tetrazole (first report); b) from cyanuric chloride (Huisgen reaction); c) *r*-TTT from 3-R-5-chloro-1,2,4-triazole; d) thermoisomerization *t*-TTT to *r*-TTT.

The mechanism for the Huisgen reaction is proposed in **figure 38a**. Initially, the substitution of all chlorine atoms in the cyanuric chloride reagent for the tetrazole units followed by the thermal opening of the ring and elimination of  $N_2$  results in the formation of the TTT heterocycle. The formation of a nitrile imine intermediate is the determining step for the formation of the *t*-TTT isomer.<sup>100</sup> Although it is possible to obtain the *r*-TTT isomers via the thermal condensation of 3-R-5-chloro-1,2,4-triazole derivatives, the scope of this reaction is limited. **Figure 38b** shows the thermal isomerization mechanism for converting *t*-TTT molecules to *r*-TTT. In the first step, a heterolytic cleavage of a C-N bond of the triazine ring occurs, forming a zwitterionic species. The next step is a rotation of the anionic ring and subsequent recombination with the cationic portion. Two more steps of cleavage, rotation and recombination occur for complete isomerization. A mechanism via homolytic breakdown and formation of a biradical is not ruled out due to the high isomerization temperatures and the non-delocalization of the positive charge on the cationic ring.<sup>105</sup>

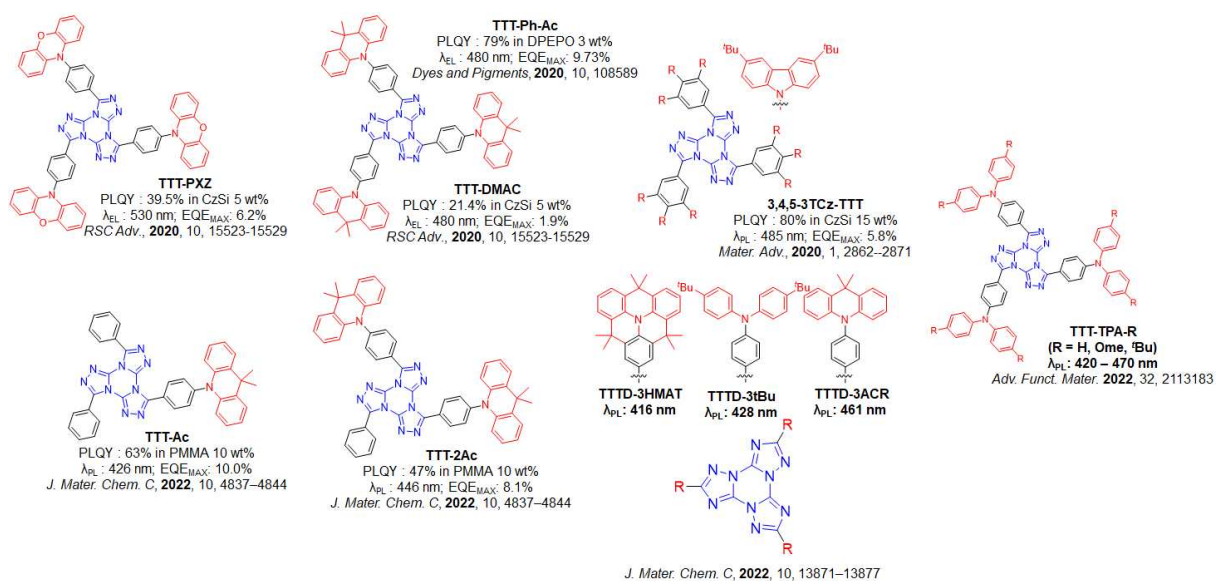


**Figure 38** Synthetic mechanism TTT core; a) Huisgen reaction; b) Thermoisomerization, Dimroth rearrangement.

Cyclic voltammetry studies have suggested that the TTT core can accept electrons and function as electron transport material in electroluminescent devices. The combination of columnar mesomorphism, luminescence, and thermal stability are essential requisites for application in electro-optical devices. The emission in the blue region found for these materials is also an essential factor that drives research in derivatives of the TTT heterocycle.<sup>106,107</sup>

The TTT moiety has been of interest in the field of blue TADF emitters due to its properties as an acceptor group of moderate strength. Recently, there has been a focus on developing blue emitters using the TTT moiety.<sup>99,108–112</sup> Pathak et al. introduced two TADF emitters, TTT-PXZ and TTT-DMAC (**figure 39**), which had moderate PLQYs and short DF lifetimes, but the devices made with these emitters had low EQEmax values.<sup>109</sup> Wang et al. improved the efficiency of a DMAC-based OLED using a TADF emitter called TTT-Ph-Ac (**figure 39**), resulting in an efficiency of 9.73%.<sup>99</sup> Hundemer et al. found that using TTT as a central acceptor in TADF molecules can produce blue emissions with long-lived DF.<sup>108</sup> The synthesis of asymmetric emitters based on the TTT acceptor with one or two donor units was also proposed, resulting in the creation of TTT-Ac and TTT-2Ac (**figure 39**), which showed blue-shifted emission in solution and film.<sup>110</sup> The Dimroth rearrangement, a thermal isomerization process of TTT derivatives, produced efficient TADF emitters with minimal  $\Delta E_{ST}$ . This led to the synthesis of three new compounds, TTTD3HMAT, TTTD-3tBu, and TTTD-3ACR (**figure 39**).<sup>111</sup> TTT-based emitters modified with diphenylamine-derived donor fragments called TTT-TPA-R (R = H, OMe, and <sup>t</sup>Bu) were also synthesized and characterized,

showing deep/pure blue emission with maximum emissive peaks in the 420-470 nm range in films.<sup>112</sup>



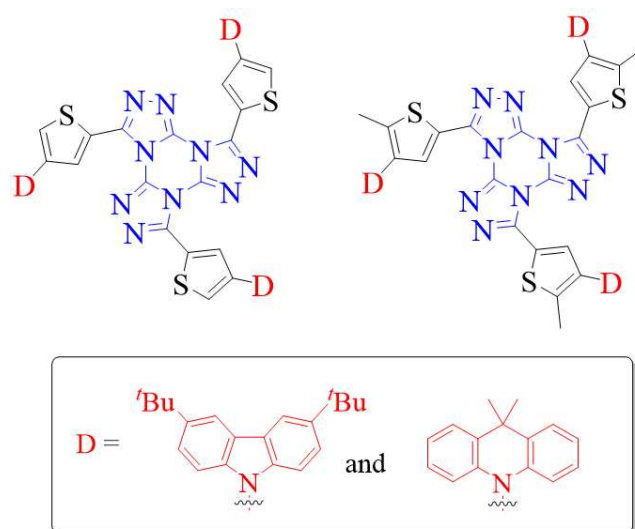
**Figure 39** TADF emitters based on TTT core.

## 3.2.2 Results and Discussions

### 3.2.2.1 Design of the TTT-based emitters

Trisriazolotriazine core (TTT) is a derivative of s-triazine with an expanded planar structure. Its electron-deficient character and easy chemical functionalization allow the TTT core to be employed as an acceptor unit in TADF materials.<sup>99,108-112</sup> Considering the recent

progress in the use of this unit in molecules with delayed luminescence, we have designed a new series of D<sub>3</sub>A-type emitters based on the TTT core, as shown in **figure 40**.

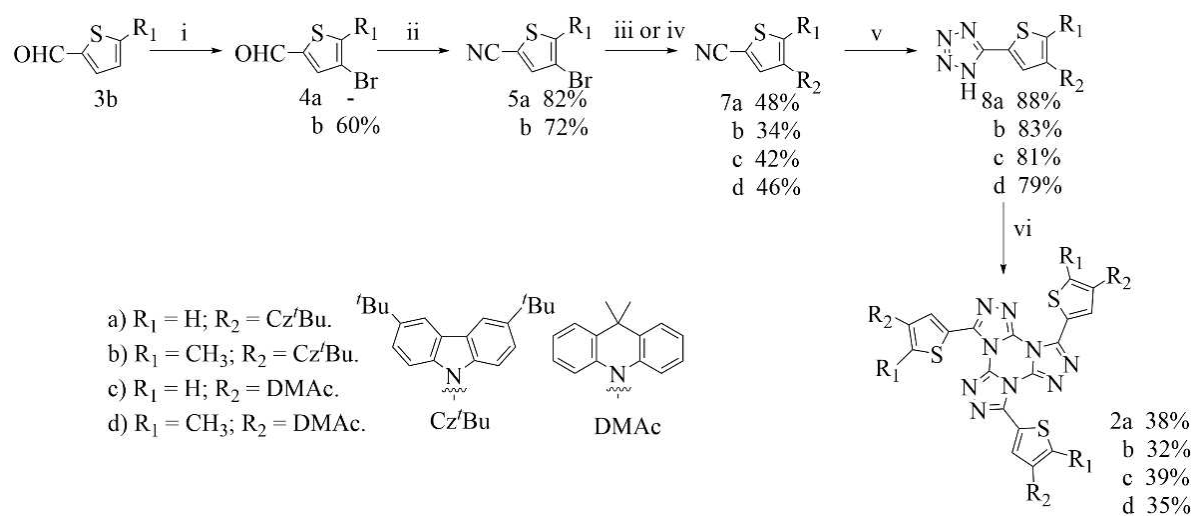


**Figure 40** Target D<sub>3</sub>A molecules based on the TTT core. Donor units are 3,6-di-tert-butyl-9H-carbazole and 9,9-dimethyl-9,10-dihydroacridine.

Analogous to the series of molecules based on the s-triazine core, the TTT emitters have the same donor units (3,6-di-tert-butyl-9H-carbazole and 9,9-dimethyl-9,10-dihydroacridine) and the same linking bridge (2,4-substituted thiophene) to compare the photophysical properties of the materials of the two synthesized series.

### 3.2.2.2 Synthesis and Characterization

Unlike the synthesis of the target materials based on the triazine acceptor unit, the synthesis of the TTT core should be the last reaction step. Thus, the synthesis of a series of intermediates (**7a-d**, **8a-d**) was required, as shown in **scheme 3**.

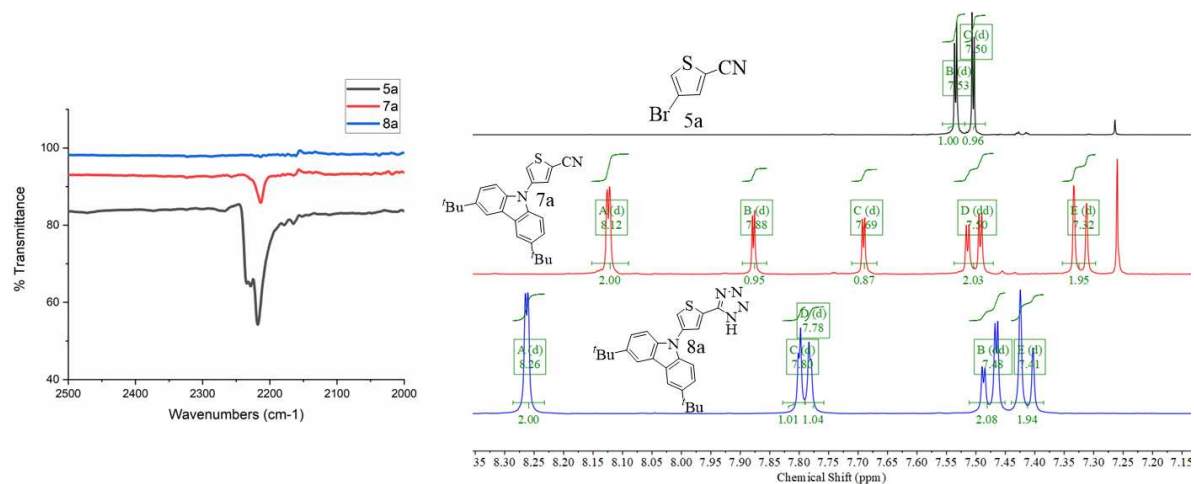


**Scheme 3** Synthetic approach to **2a-d**; i)  $\text{Br}_2$ , AcOH; ii)  $\text{NH}_4\text{OH}(\text{aq})$ ,  $\text{I}_2$ , THF; iii) (**a-b**) 3,6-di-tert-butyl-9H-carbazole,  $\text{K}_2\text{CO}_3$ ,  $\text{CuSO}_4 \cdot 5\text{H}_2\text{O}$ , 1-methylnaphthalene; iv) (**c-d**) 9,9-dimethyl-9,10-dihydroacridine,  $[\text{Pd}(\text{OAc})_2]$ , Xphos,  $\text{NaOt-Bu}$ , toluene; v)  $\text{NaN}_3$ ,  $\text{NH}_4\text{Cl}$ , DMF; vi)  $\text{C}_3\text{N}_3\text{Cl}_3$ , 2,6-lutidine, toluene.

Like in the synthesis of the triazine analogs **1a-d**, the same coupling between the donor units (3,6-di-tert-butyl-9H-carbazole and 9,9-dimethyl-9,10-dihydroacridine), and the bromine-bearing nitrile substrates (**5a/b**) was employed. The variant of Ullman reaction was used for synthesizing the intermediates **7a/b** (**7a**: 48% and **7b**: 34%) and coupling via palladium chemistry to obtain the compounds **7c/d** (**7c**: 42% and **7d**: 46%).<sup>96,97</sup> In the next step, the cyano group of **7a-d** is converted to the tetrazole heterocycle (**8a-d**, ~80%) via a 1,3-dipolar cycloaddition between sodium azide and the cyano group. The intermediates **8a-d** react with cyanuric chloride in a Huisgen reaction to give the *N*-heterocycle TTT compounds (**2a-d**, ~35%).<sup>108</sup>

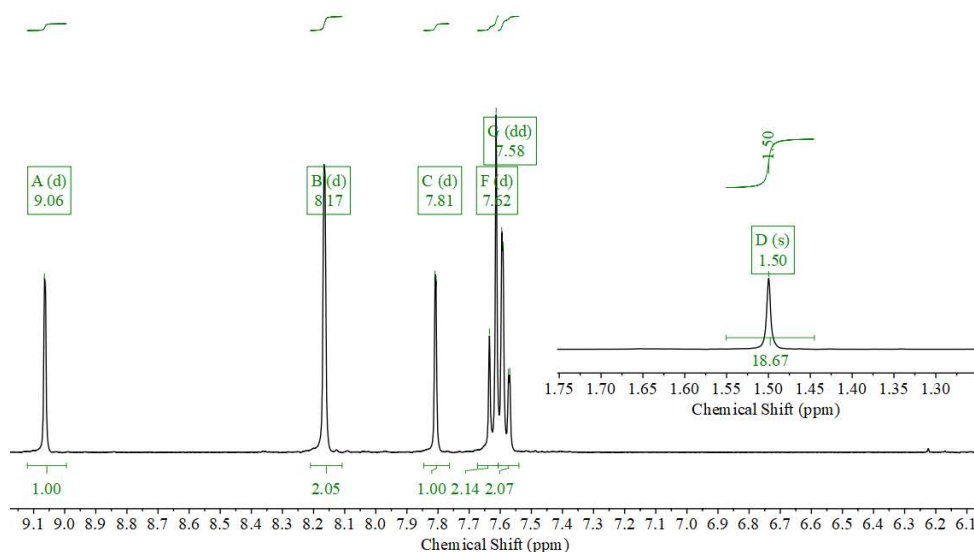
The low field region of the  $^1\text{H}$  NMR spectrum of molecules **5a,7a**, and **8a** is shown in **figure 41** (right). The CN coupling can be easily observed through the appearance of three signals (8.13, 7.51, and 7.33 ppm) in the aromatic region of the spectrum of intermediate **7a**. The ratio of 2H (thiophene ring) to 6H (3,6-di-tert-butyl-carbazole heterocycle) indicates the proper ratio of units (this interpretation applies also to **7b-d**, the spectra are in the annex section). Although the  $^1\text{H}$  NMR spectra of compounds **7a** and **8a** were not made in the same solvent (making a direct comparison of the chemical shift impossible), the different solubilities of the materials indicate the change of functional group. This change can be easily observed by infrared spectroscopy. In (left), the IR spectra of the intermediates **5a,7a**, and **8a** are shown (spectra of **7b-d** and **8b-d** are analogous, the spectra are available in the annex section). The band's presence around  $2.200\text{ cm}^{-1}$  in the spectrum of **5a** and **7a** indicates the presence of the

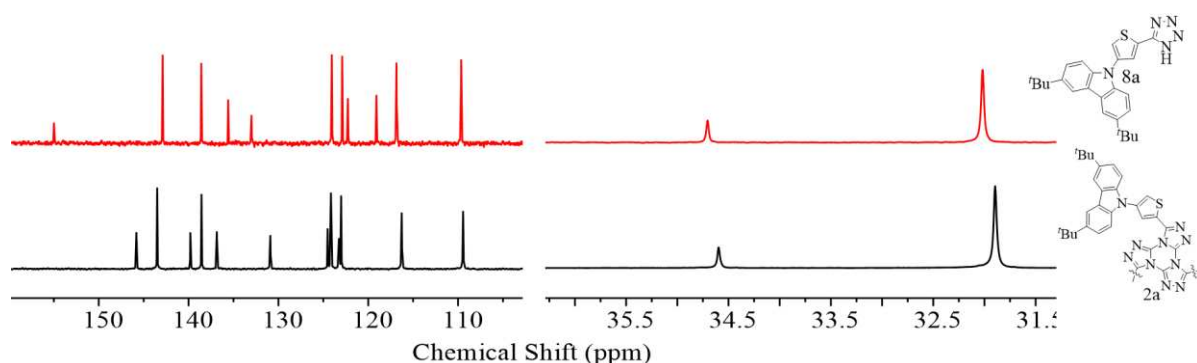
nitrile group, as expected. After conversion to **8a**, the characteristic band of the CN stretching on the nitrile group is not observed, confirming the change in the functional group.



**Figure 41** IR and <sup>1</sup>H NMR spectra of intermediates **5a**, **7a** and **8a**. IR spectra region 2.000 – 2.500 cm<sup>-1</sup>, monitoring of the CN stretching band (left). <sup>1</sup>H NMR spectra (400 MHz, **5a** and **7a**: CDCl<sub>3</sub>, **8a**: DMSO-d<sub>6</sub>). Aromatic region (right).

Since we cannot directly compare the chemical shift of the aromatic hydrogens in the <sup>1</sup>H NMR spectra of the intermediate **8a** with the final molecule **2a** (**figure 42**, up), analyzing the <sup>13</sup>C NMR spectrum (**figure 42**, bottom) together with the mass spectrum is key to confirm the synthesis of the TTT heterocycle. The same is true for **2b**. Spectra are available in the annex section.



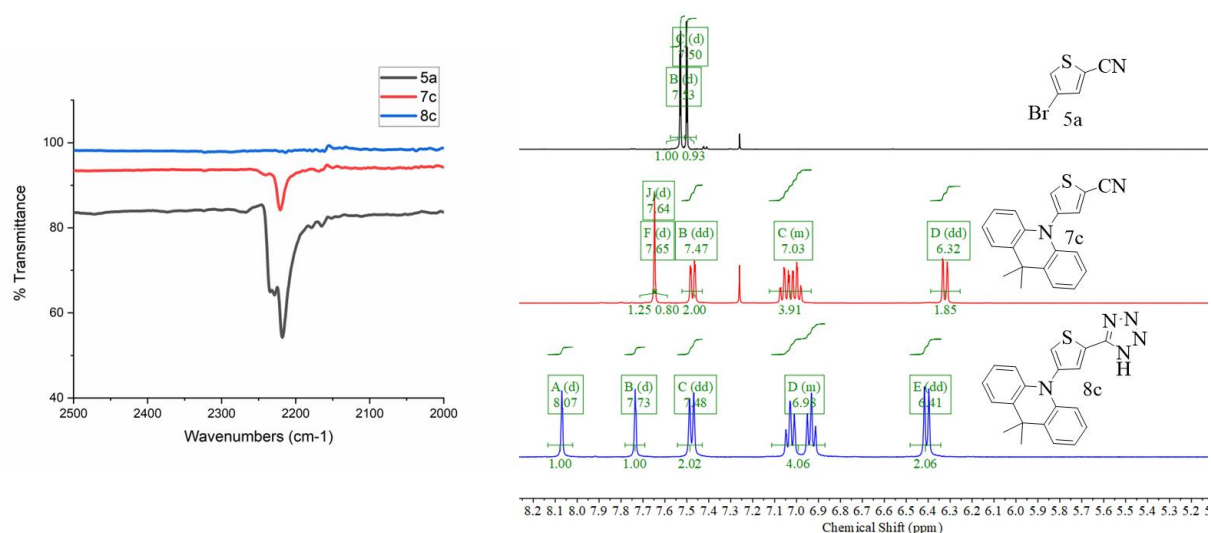


**Figure 42**  $^1\text{H}$  NMR spectrum of final molecule **2a** (400 MHz,  $\text{C}_2\text{D}_2\text{Cl}_4$ ) (top).  $^{13}\text{C}$  NMR spectrum from **8a** and **2a** (101 MHz, **2a**:  $\text{C}_2\text{D}_2\text{Cl}_4$ , **8a**: DMSO- $d_6$ ) (bottom).

The presence of 14 signals in the  $^{13}\text{C}$  NMR spectrum of compound **2a**, in contrast to the 13 signals present in the spectrum of intermediate **8a**, indicates the formation of the N-heterocycle TTT. The extra signal is assigned to the carbons of the central triazine heterocycle of the target molecule. Combined with the information from the  $^{13}\text{C}$  NMR spectra, the mass spectra confirm the desired structure for compounds **2a/b**.

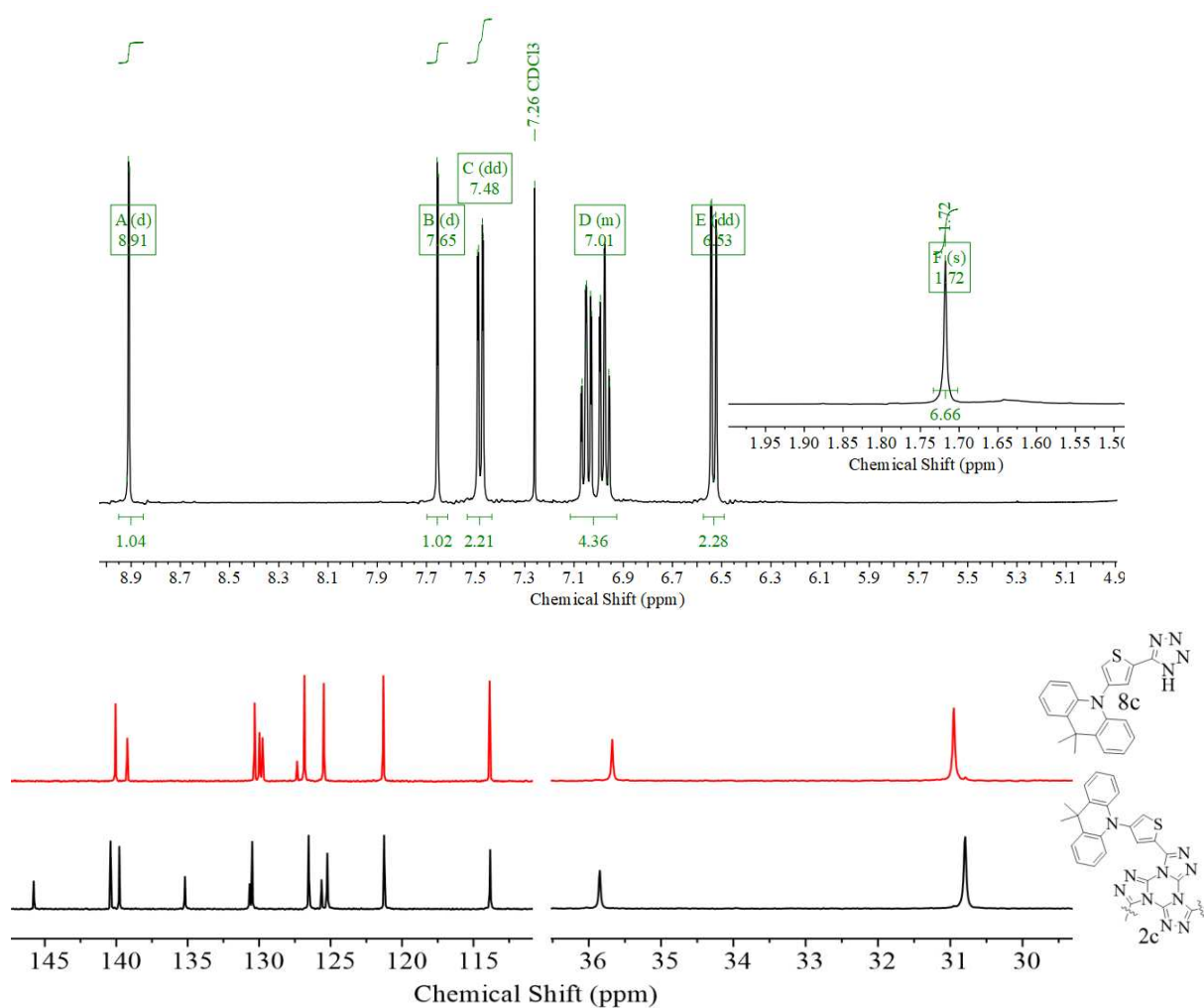
The success of the CN coupling reaction can again be verified through the  $^1\text{H}$  NMR spectrum (**figure 43**, right). The presence of the signals in the aromatic region (7.47, 7.03, and 6.32 ppm) refers to the aromatic hydrogens of the 9,9-dimethyl-9,10-dihydroacridine unit at a ratio of 8H to 2H of the thiophene ring, indicating the formation of the carbon-nitrogen bond. Monitoring of the stretching band in the IR spectrum at  $\sim 2.200\text{ cm}^{-1}$  (**figure 43**, left), present in the spectrum of **7c** and absent for **8c**, supports functional group conversion after the 1,3-dipolar cycloaddition reaction.





**Figure 43** IR and <sup>1</sup>H NMR spectra of intermediates **5a**, **7c** and **8c**. IR spectra region 2.000 – 2.500 cm<sup>-1</sup>, monitoring of the CN stretching band (left). <sup>1</sup>H NMR spectra (400 MHz, **5a** and **7a**: CDCl<sub>3</sub>, **8a**: DMSO-d<sub>6</sub>). Aromatic region (right).

As for **2a/b**, the formation of the final molecules **2c/d** is confirmed by <sup>1</sup>H NMR, <sup>13</sup>C NMR. **Figure 44** (top) shows the <sup>1</sup>H NMR spectrum of the final molecule **2c**. The <sup>13</sup>C NMR spectra of the intermediate **8c** and the final compound **2c** are shown in **figure 44** (bottom). The presence of 13 signals in the spectrum of **2c** in contrast to 12 signals for compound **8c** indicates cyclization of the tetrazole heterocycle in TTT. The extra signal is attributed to the carbons of the central triazine ring formed. All the spectra to elucidate the structure of **2d** are in the annex section.

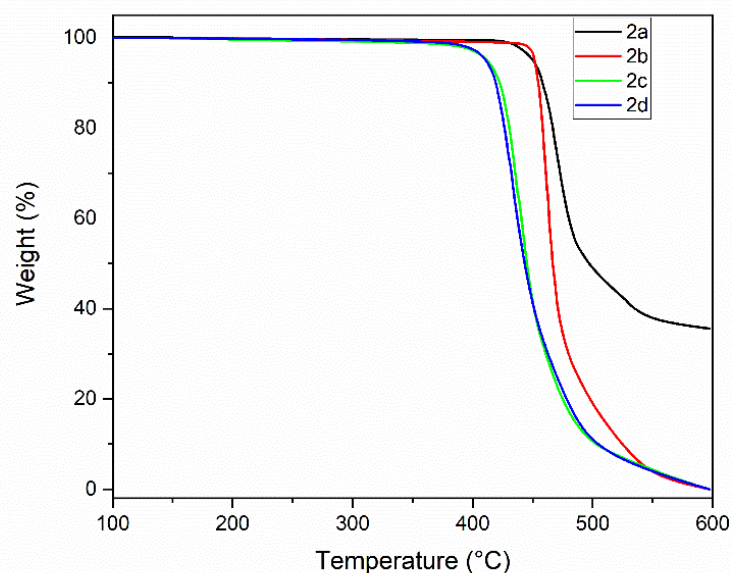


**Figure 44**  $^1\text{H}$  NMR spectrum of final molecule **2c** (400 MHz,  $\text{CDCl}_3$ ) (top).  $^{13}\text{C}$  NMR spectrum from **8c** and **2c** (101 MHz, **8c**:  $\text{DMSO-d}_6$ , **2c**:  $\text{C}_2\text{D}_2\text{Cl}_4$ ) (bottom).

The mass spectra obtained for compounds **2c/d** confirm the desired structure (see annex section).

### 3.2.2.3 Thermogravimetric analysis (TGA)

TGA measurements were performed to investigate the thermal stability of the emitters synthesized in this chapter. The analyses were performed under an N<sub>2</sub> atmosphere with a heating rate of 10 °C min<sup>-1</sup>. The thermogram is shown in **figure 45**.



**Figure 45** Mass loss patterns determined through TGA measurements in N<sub>2</sub> with heating rate of 10 °C min<sup>-1</sup>.

All four compounds derived from TTT exhibited good thermal stability with decomposition temperatures (defined as 3% mass loss) in the range of 400 – 450 °C. The emitters containing the 9,9-dimethyl-9,10-dihydroacridine unit were slightly less stable than the analogs containing the 3,6-di-tert-butyl-9H-carbazole unit. **Table 6** summarizes the decomposition temperatures ( $T_{\text{dec}}$ ) of the emitters **2a-d**.

**Table 6** Decomposition temperatures of TTT-based emitters obtained through TGA analyses.

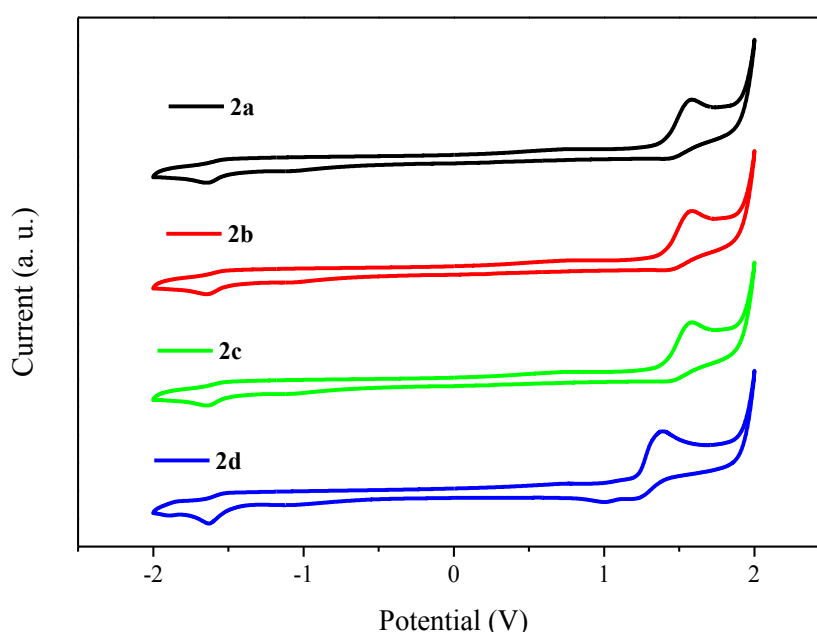
Compound	$T_{\text{dec}}$ (°C) <sup>a</sup>
<b>2a</b>	442
<b>2b</b>	449
<b>2c</b>	401
<b>2d</b>	402

a: 3% mass loss

The good thermal stability of these materials under inert conditions is suitable for applications, such as OLEDs.

#### 3.2.2.4 Cyclic voltammetry (CV)

We performed cyclic voltammetry analyses to investigate the TTT emitters' redox properties. **Figure 46** shows the voltammograms of compounds **2a-d**. The solvent used for all compounds was DMF.



**Figure 46** CV curves of the TTT emitters in DMF solution. 0.1 mol L<sup>-1</sup> of Bu<sub>4</sub>NPF<sub>6</sub> (tetrabutylammonium hexafluorophosphate) as a supporting electrolyte. Scan rate: 100 mV s<sup>-1</sup>.

For emitters **2a** and **2b**, irreversible oxidation (E<sub>ox</sub>) signals were obtained in the range of ~ 1.5-1.6 eV. Compounds **2c** and **2d** showed quasi-reversible oxidation in the range of ~ 1.2-1.3 eV. From the oxidation onset, the E<sub>ox</sub> values are 0.88 V for **2a**, 0.94 V for **2b**, 0.58 V for **2c**, and 0.60 V for **2d** relative to ferrocenium/ferrocene (Fc/Fc<sup>+</sup>, E<sub>Fc/Fc<sup>+</sup></sub> = 0.46 V). The smaller values of oxidation potentials found for the emitters containing the 9,9-dimethyl-9,10-dihydroacridine moiety is in line with stronger donor character of this unit compared to 3,6-di-tert-butyl-9H-carbazole. As the electron acceptor unit is the same in **2a-d**, similar reduction potentials were found: -2.30, -2.40, -2.29, and -2.34 V. According to the formulas E<sub>HOMO</sub> = -(E<sub>ox</sub> - E<sub>Fc/Fc<sup>+</sup></sub> + 4.8) eV and E<sub>LUMO</sub> = -(E<sub>red</sub> - E<sub>Fc/Fc<sup>+</sup></sub> + 4.8) eV, the HOMO/LUMO energy levels

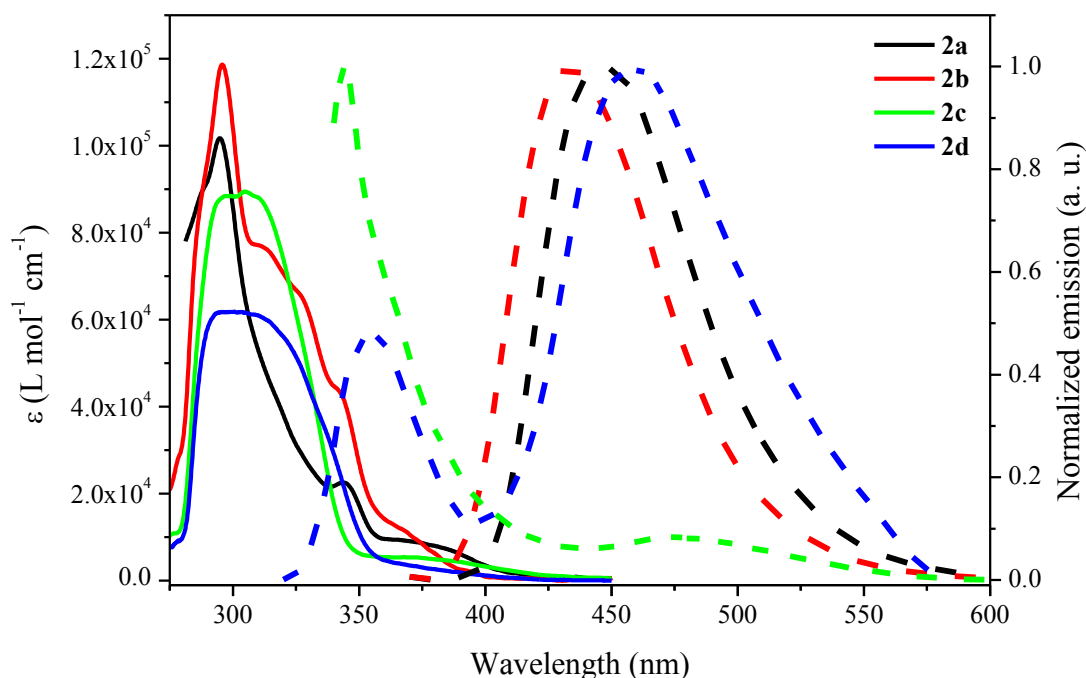
were calculated as -5.68/-2.50 eV (**2a**), -5.74/-2.40 eV (**2b**), -5.38/-2.51 eV (**2c**) and -5.40/-2.46 eV (**2d**). Correspondingly, the energy gaps are evaluated as 3.18, 3.34, 2.87, and 2.94 eV.

### 3.2.2.5 Photophysical Properties

After synthesis and structural characterization of the TTT-based emitters, steady-state and time-resolved photoluminescence analyses were performed to determine the photophysical processes involved in the emission of these compounds in solution and solid state.

#### 3.2.2.5.1 Steady-State Photoluminescence – Solution and Solid State

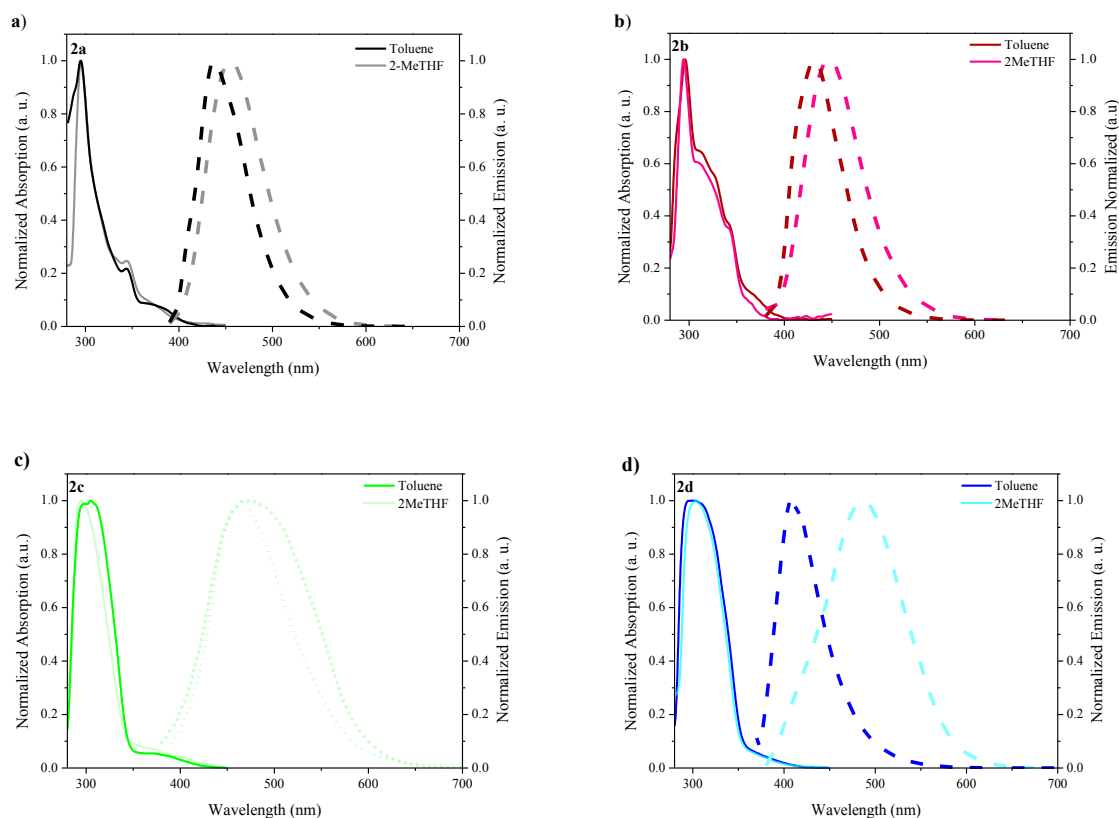
To investigate the effect of the structural changes at the TTT core on the photophysical properties of the new materials synthesized in this work, the UV-vis absorption, and emission spectra of **2a-d** was measured performed in toluene solution. The experiments were performed at low concentrations ( $10^{-5}$  mol L $^{-1}$ ) following the Lambert-Beer parameters and avoiding the formation of aggregates. **Figure 47** shows the normalized absorption and photoluminescence spectra.



**Figure 47** Absorption and emission spectra of **2a-d** in dilute toluene solution ( $10^{-5}$  mol L $^{-1}$ ). Solid line: absorption, dash line: emission.

A high-energy absorption band is observed at 280 nm for all compounds, which is attributed to  $\pi - \pi^*$  transition at the TTT core.<sup>110</sup> The band close to 340 nm in the absorption spectrum of compounds **2a** and **2b** is attributed to the carbazole moiety's  $\pi - \pi^*$  transition.<sup>99,113</sup> For emitters **2c** and **2d**, on the other hand, the  $\pi - \pi^*$  transition of the dimethylacridine portion is responsible for the corresponding band at 320 nm.<sup>98</sup> In addition to these characteristic bands of the subunits, intramolecular charge transfer bands are observed at longer wavelengths. These bands exhibit low molar absorptivity coefficients ( $<1000 \text{ mol}^{-1} \text{ L cm}^{-1}$ ), characteristic of this type of electronic transition.<sup>110</sup> With **2c** and **2d** this band is weaker than with **2a** and **2b**. This suggests that the 9,9-dimethyl-9,10-dihydroacridine donor unit and the TTT core are nearly orthogonal, forming a charge transfer state with low oscillator strength ( $f$ ). The emitters containing the donor portion 3,6-di-tert-butyl-9H-carbazole show in the steady state photoluminescence spectrum an emission band with a maximum at 440nm for **2a** and 430 nm for **2b**. This emission comes from a mixture of excited states,  $^1\text{LE}/^1\text{CT}$  ( $^1\text{LE}$  = locally excited singlet,  $^1\text{CT}$  = charge transfer singlet). The derivatives **2c** and **2d** surprisingly exhibit a double emission when excited at 320 nm. The higher energy emission peak matches the emission from the 9,9-dimethyl-9,10-dihydroacridine unit, as reported in the literature.<sup>98</sup> The second broad emission centered at 460 nm is attributed to a  $^1\text{CT}$  emission. Observing the emission related to dimethylacridine suggests a decoupling of the donor and acceptor moieties in these derivatives.

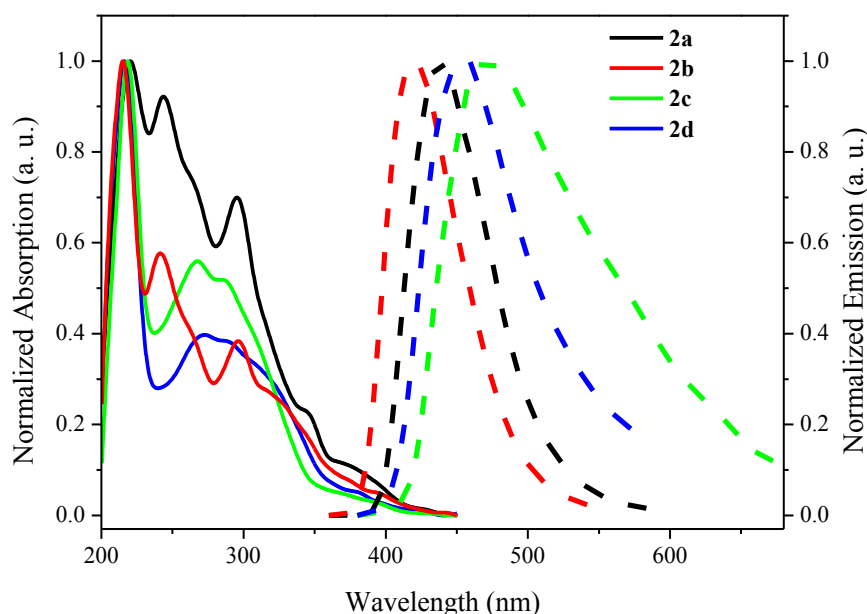
To confirm the nature of the emission, photoluminescence spectra in 2-MeTHF solution were obtained. **Figure 48** compares the photoluminescence spectra of **2a-d** in toluene and in 2-MeTHF.



**Figure 48** Absorption and normalized photoluminescence spectra in toluene and 2-MeTHF solutions. Solid line: absorption, dash line: emission.

For **2a** and **2b** (**figure 48a** and **b**), increasing solvent polarity results in a slight red shift, and the emission peak becomes less structured. This behavior indicates a mixed  $^1\text{LE}/^1\text{CT}$  state. Emitter **2c** (**figure 48c**) shows in more polar solvents a broader emission. This broad emission can be related to the stabilization of the  $^1\text{CT}$  state and the increased phosphorescence contribution to the overall emission. The phosphorescence contribution to the emission can be confirmed by time-resolved photoluminescence analyses. The emission band shift is more pronounced in **2d** than in **2c**. In addition, the emission becomes broader.

The photophysical properties in the solid state were investigated using a zeonex matrix, a non-polar saturated hydrocarbon polymer that simulates isolated molecules. The absorption and emission spectra of all emitters are shown in **figure 49**.



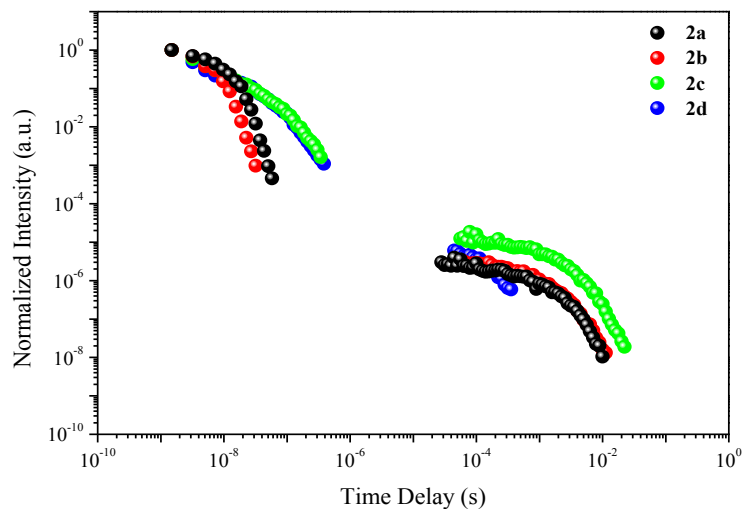
**Figure 49** Normalized absorption and photoluminescence spectra in zeonex excited at the peak of the lowest energy band. Solid line: absorption, dash line: emission.

The compounds **2a** and **2b** derived from carbazole exhibited the same absorption and emission profile when observed in a toluene solution. However, the acridine analogs displayed a more clearly resolved absorption, which was expected due to the increased structural rigidity of the molecules in the matrix. All emitters, except for **2c**, exhibited a Gaussian emission band with similar onsets as those observed in toluene solution. Compound **2c** showed a broader emission, likely due to a significantly wider distribution of the blocked donor-acceptor dihedral angles in the solid matrix.

### 3.2.2.5.2 Time-resolved photoluminescence – Solution and Solid State

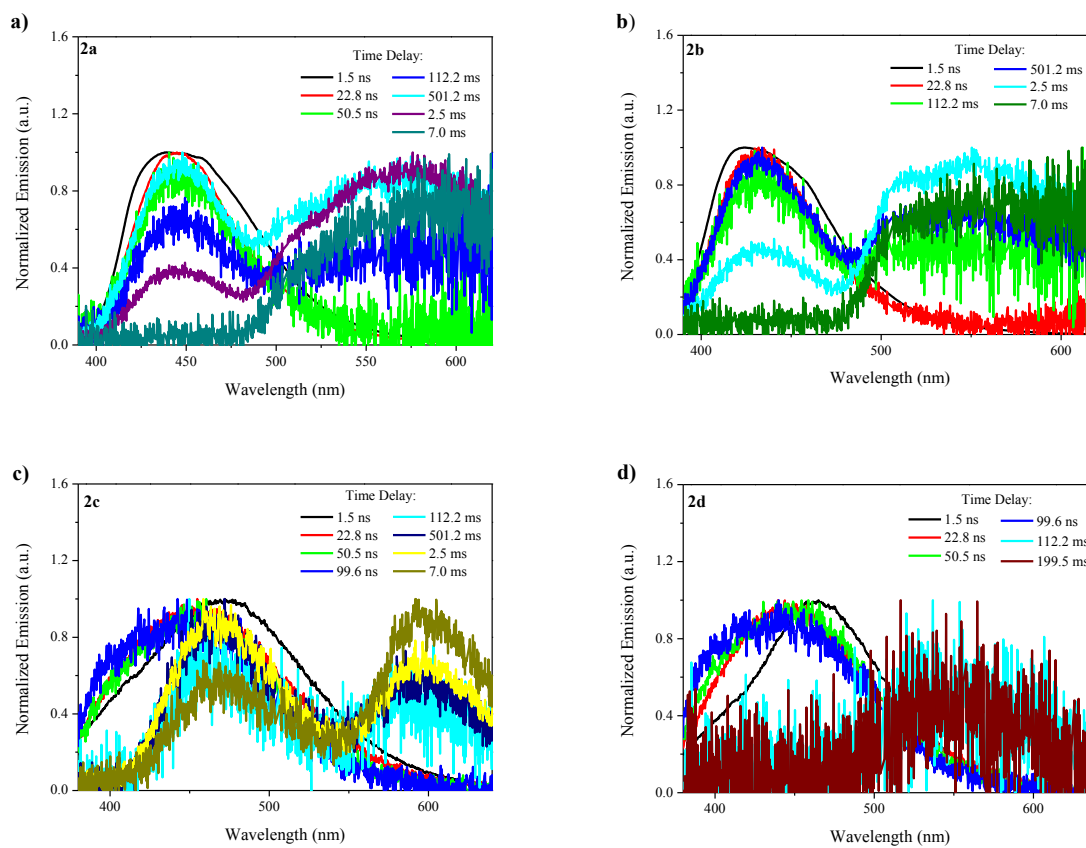
We performed a time-resolved photoluminescence analysis to investigate the excited states' dynamics and understand the emission mechanisms in these materials in solution and solid-state. **Figure 50** shows the decay curves obtained in toluene solution for **2a-d**.





**Figure 50** The TTT derivatives time-resolved decay curves in toluene. The excitation wavelength was 355 nm. All measurements were performed in the absence of oxygen.

All compounds presented a decay profile with two types of emission. In the nanosecond range, the observed radiative decay is related to prompt fluorescence. With longer decay times, it is possible to observe a second emission in the millisecond range. This emission can be attributed to phosphorescence or delayed fluorescence. By plotting the emission spectra at different decay times (**figure 51**), it is possible to understand which decay mechanism these materials present.



**Figure 51** Normalized spectra taken after different delay times at room temperature in toluene solutions. The excitation wavelength was 355 nm. All measurements were performed in the absence of oxygen.

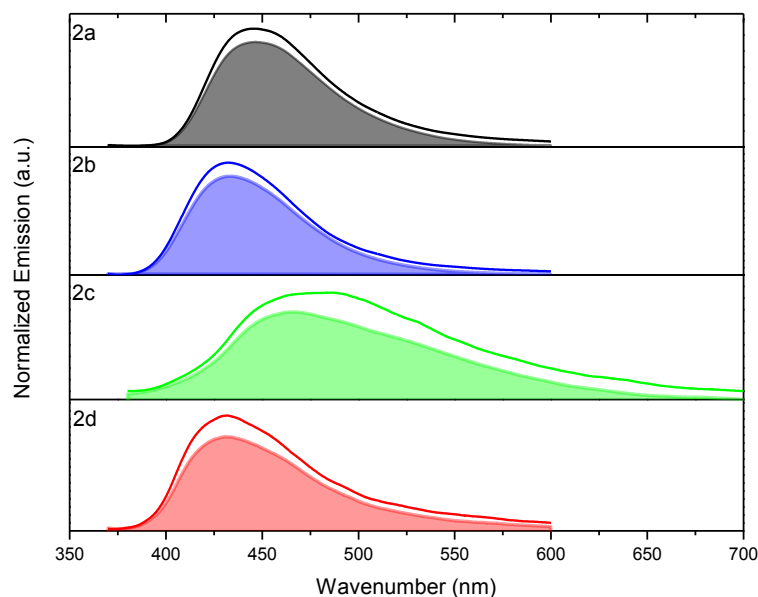
The carbazole derivative **2a** and **2b** exhibit the same emission profile. We have the emission peak centered at 440nm (**2a**) and 415 nm (**2b**) in the first ns. This direct fluorescence emission comes from the radiative decay of the  $^1LE/1CT$  excited state, as mentioned earlier. Increasing the delay time, in the microsecond range, emitters **2a**, and **2b** exhibit a dual emission regime. The emission at shorter wavelengths exhibits the same profile as that observed in the first nanosecond range and is attributed to delayed fluorescence. The second emission band, with a maximum at 575 nm for both compounds, exhibits typical phosphorescence characteristics at room temperature. The acridine homologs **2c** and **2d** exhibit different emission spectra. Like the carbazole derivatives, compound **2c** exhibits a similar emission spectrum. Initially, **2c** undergoes a very rapid stabilization of the  $^1CT$  state, which then, with a broad emission band at around 460 nm, decays with a longer lifetime. At a more prolonged time delay, in the microsecond range, the same double emission is observed and assigned as delayed fluorescence and phosphorescence at room temperature. For **2d**, we only observe different ones at longer time delays in the microsecond range. This molecule, unlike its homolog, did not show

delayed fluorescence, only a weak phosphorescence at room temperature with a low lifetime. The room temperature phosphorescence observed in solution for all the emitters in our study is a rare occurrence. This is because the long lifetime of the triplet state typically leads to non-radiative decay of excited states through interactions with the solvent, such as collisions. However, our theoretical calculations indicate that the excited state responsible for the phosphorescence, in this case, is of the  $^3\text{LE}$  type, centered on the TTT-thiophene center. This suggests that the large donor groups surrounding the central unit are able to protect the excited state from non-radiative deactivation, allowing for the emission of phosphorescence in solution. An exception is **2d**, where the larger SOC between the low-lying states and a higher triplet energy enhances the phosphorescence rate, as further discussed in the theoretical investigation. **Table 7** shows the lifetime values and quantum yields obtained in toluene solution.

**Table 7** Lifetimes  $\tau$  and quantum yields  $\Phi$  in toluene solution.

	<b>2a</b>	<b>2b</b>	<b>2c</b>	<b>2d</b>
$\tau_1(\text{ns})$	-	-	2.3 (84%)	1.5 (89%)
$\tau_2(\text{ns})$	7.3	4.3	30.2 (16%)	32.7 (11%)
$\tau_{\text{DF}}(\text{ms})$	0.5 (75%)	0.7 (83%)	0.8 (67%)	-
$\tau_{\text{Phosph}}(\text{ms})$	2.8 (25%)	3.2 (17%)	3.5 (33%)	0.1
$\Phi_{\text{air}}$	0.258	0.196	0.017	0.023
$\Phi_{\text{degassed}}$	0.304	0.232	0.023	0.029

To investigate the role of non-radiative decay in these materials, we conducted experiments to measure the absolute PLQY. We obtained the PLQY in air using an integrating sphere, and we calculated the degassed PLQY ( $\Phi_{\text{degassed}}$ ) by comparing the photoluminescence of air-equilibrated and degassed solutions. **Figure 52** illustrates the ratio of the photoluminescence.

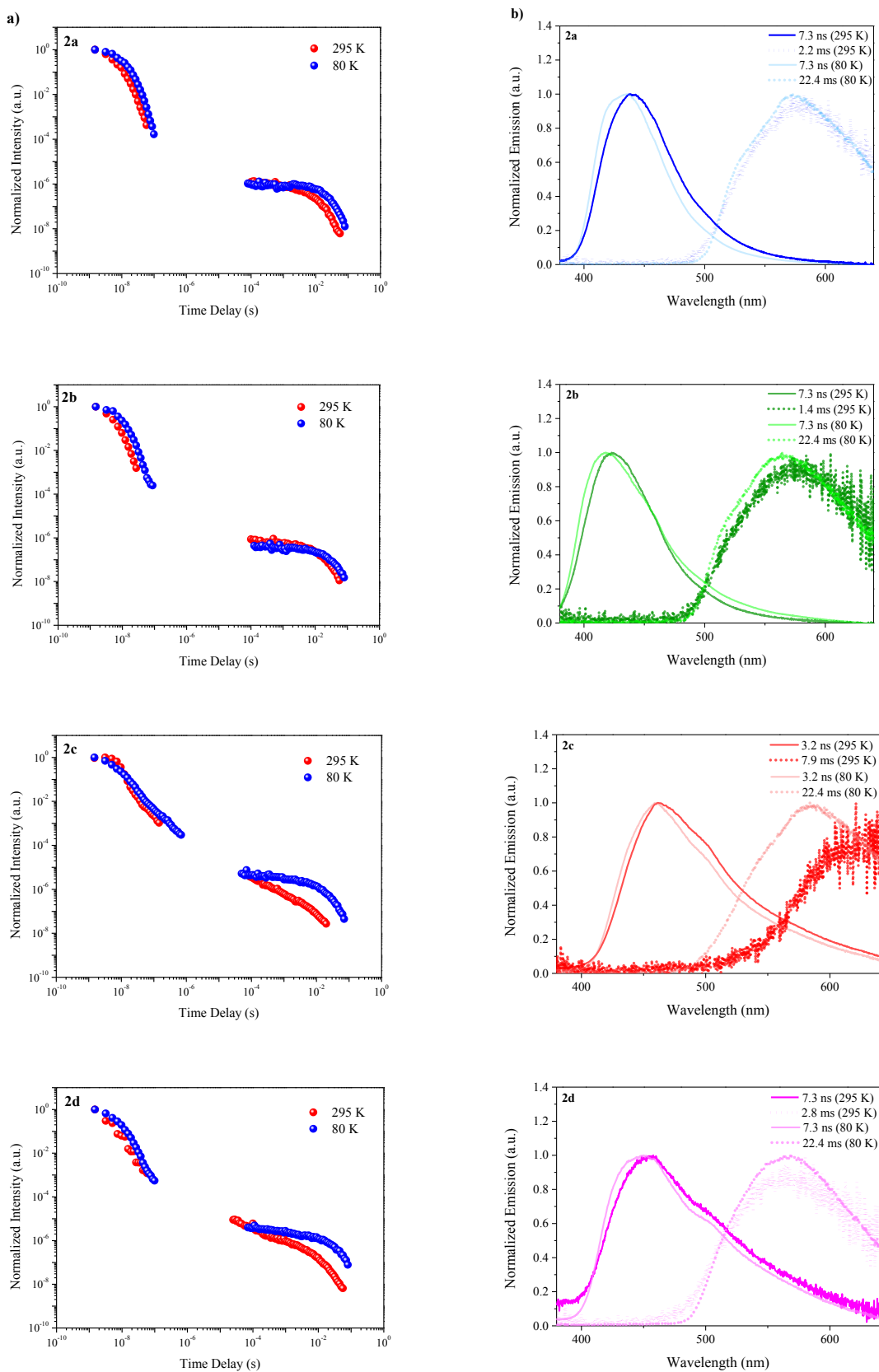


**Figure 52** Emission spectra in degassed (solid lines) and air-equilibrated (filled areas) in dilute toluene solution at room temperature.

The slight decrease in the photoluminescence of the emitters when oxygen is introduced into the solution suggests that triplet states are involved in the emission mechanism, as previously suggested by time-resolved photoluminescence experiments. These mechanisms are identified as RTP and TTA, as we will see later.

When comparing the PLQY of molecules containing the acridine unit to carbazole analogs in toluene solution, we find that compounds **2c** and **2d** have lower values. This is likely because the acridine portion is more orthogonal (nearly perpendicular) to the TTT center than the carbazole units in emitters **2a** and **2b**. Although this system forms a charge transfer state, this state has low oscillator strength values and exhibits low radiative decay. By examining the relationship between  $\Phi_{\text{ISC}}$  (a measure of radiative decay) and  $\Phi_{\text{degassed}}$  (a measure of non-radiative deactivation), and the PLQY values found for these materials, we can conclude that all compounds have strong spin-orbit coupling due to the presence of a sulfur atom in the thiophene unit. This results in a high population in the triplet state and high non-radiative deactivation of these states, particularly for the acridine derivatives.

Time-resolved photoluminescence analyses were also carried out in the solid state. A double regime was observed for all compounds, a region of prompt fluorescence followed by phosphorescence emission. **Figure 53** shows the decay profile and the normalized emission spectra at different acquisition times.



**Figure 53** a: Time-resolved decay in zeonex. b: Normalized spectra after different delay times.

The TRPL decay in the solid state appears to be more structured in emitters containing an acridine component. A bulky matrix may decrease the orthogonality between donor-acceptor units, resulting in a mixed  $^1\text{LE}/^1\text{CT}$  state as observed in homologs containing carbazole in a toluene solution. As a result, all emitters in zeonex displayed similar lifetimes, as shown in **table 8**. This slight increase in lifetime can be attributed to the reduced mobility of molecules in the solid state, leading to a lower non-radiative decay rate. Additionally, the similarity in lifetimes between the solid state and solution suggests that the bulky donor groups effectively protect the  $^3\text{LE}$  excited state centered on the TTT-thiophene unit, enabling phosphorescence emission.

The absence of double emission in the microsecond range, as seen in analyses in solution, suggests that the mechanism for delayed fluorescence in these materials in toluene is likely triplet-triplet annihilation (TTA). This bimolecular process requires two triplet excited state molecules to collide, with one transferring energy to the other, which returns to the singlet state and subsequently emits fluorescence. While this phenomenon can occur in solution due to the unrestricted mobility of molecules, it is suppressed in a rigid matrix or in the solid state. The values obtained for  $\Delta E_{\text{ST}}$  also support the conclusion that the delayed fluorescence is of the TTA type. By analyzing the fluorescence onset at room temperature and the phosphorescence onset at low temperatures, the values of  $\Delta E_{\text{ST}}$  were estimated and are shown in **table 8**. The similar values found for the triplet energy ( $^3\text{LE}$ ) in all emitters indicate that structural modifications around the TTT center have a minimal impact.

**Table 8** Lifetimes  $\tau$ , quantum yields  $\Phi$  and  $S_1$  &  $T_1$  energies in zeonex matrix.

	<b>2a</b>	<b>2b</b>	<b>2c</b>	<b>2d</b>
<b>RT</b>				
$\tau_{PF}(ns)$	3.9	2.6	3.8	3.4
$\tau_{Phosph\ 1} (ms)$	4.7	8.3	1.2 (82%)	0.8 (68%)
$\tau_{Phosph\ 2} (ms)$	-	-	12.7 (18%)	7.3 (32%)
$\tau_{Phosph\ av} (ms)^{[a]}$	-	-	9.3	6.1
$\Phi_{air}$	0.144	0.124	0.031	0.055
<b>80K</b>				
$\tau_{PF}(ns)$	7.7	6.0	5.1	4.7
$\tau_{Phosph\ 1} (ms)$	20.4	20.7	0.9 (59%)	0.6 (51%)
$\tau_{Phosph\ 2} (ms)$	-	-	16 (48%)	21 (49%)
$\tau_{Phosph\ av} (ms)^{[a]}$	-	-	14.6	20.5
$S_1 (eV)$	$3.121 \pm 0.020$	$3.229 \pm 0.017$	$2.983 \pm 0.015$	$3.103 \pm 0.016$
$T_1 (eV)$	$2.475 \pm 0.015$	$2.520 \pm 0.010$	$2.480 \pm 0.010$	$2.524 \pm 0.008$
$\Delta E_{ST}$	0.646	0.709	0.503	0.579

[a] Obtained from  $\tau = \Sigma \tau_i^2 A_i / \Sigma \tau_i A_i$ , due to multi-exponential profile.

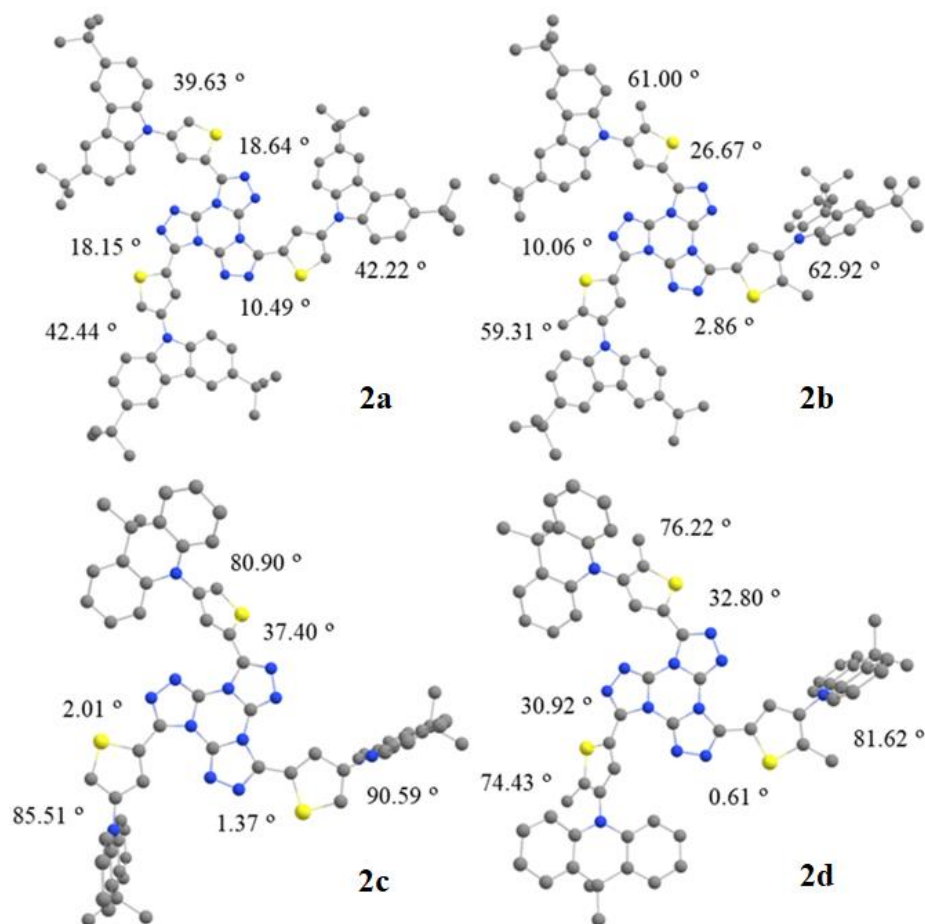
Materials that exhibit TADF should have  $\Delta E_{ST}$  values within the range of 0.3 eV for small thermal energy to be sufficient to promote the reverse intersystem crossing process. All the materials synthesized in this study had  $\Delta E_{ST}$  values above 0.5 eV, which excluded the TADF mechanism as the cause of the delayed fluorescence emission observed in these materials in the toluene solution.

As the temperature decreases, the spectra become more resolved in both the prompt fluorescence and phosphorescence regimes. This is due to the molecules having less movement and a more rigid structure within the film. Additionally, at low temperatures, the lifetimes of these materials are similar and non-radiative decay is less pronounced.

### 3.2.2.6 Theoretical investigations

DFT (density functional theory) calculations were carried out to determine the ground state geometries of the compounds. The resulting bond and angle values for all compounds agreed with similar compounds for which X-ray structures had been obtained.<sup>106,114</sup> To evaluate the orthogonality of the donor-acceptor units, dihedral angles were measured between the TTT

core and the thiophene unit and between the thiophene unit and the donor unit (carbazole or acridine). The measured dihedral angles and the optimized geometries are shown in **figure 54**.



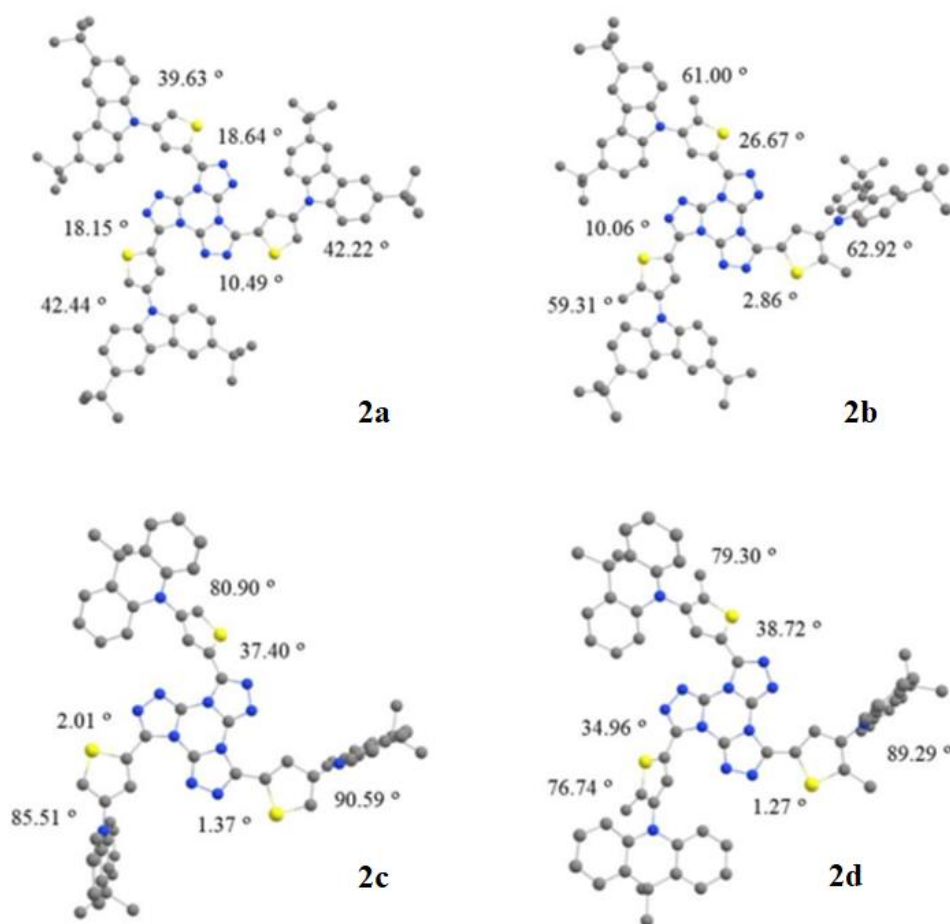
**Figure 54** Optimized ground state geometries within B3LYP/def2-SVP level of theory.

The average TTT-thiophene angles of  $15.76^\circ$  and  $13.20^\circ$  for compounds **2a** and **2b**, respectively, suggest that these units are not coplanar. The thiophene-carbazole angle increases from  $41.43^\circ$  in **2a** to  $61.08^\circ$  in **2b**. As the TTT-thiophene dihedral angles are similar for both compounds, the thiophene-carbazole angle indicates that the carbazole unit is more orthogonal to the TTT core in **2b**. For compounds **2c** and **2d**, similar TTT-thiophene dihedral angles of  $13.59^\circ$  and  $21.44^\circ$  were found. However, thiophene methylation decreases the thiophene-acridine angle from  $85.67^\circ$  in **2c** to  $77.42^\circ$  in **2d**.

The characteristics of the excited states of **2a** and **2b** were investigated using TD-DFT and SOC-TD-DFT. The first absorption band observed experimentally in these compounds (**figure 47**) corresponds to the three low-lying states, which have CT orbital configurations extending over the carbazole and part of the TTT-thiophene core. However, these states also

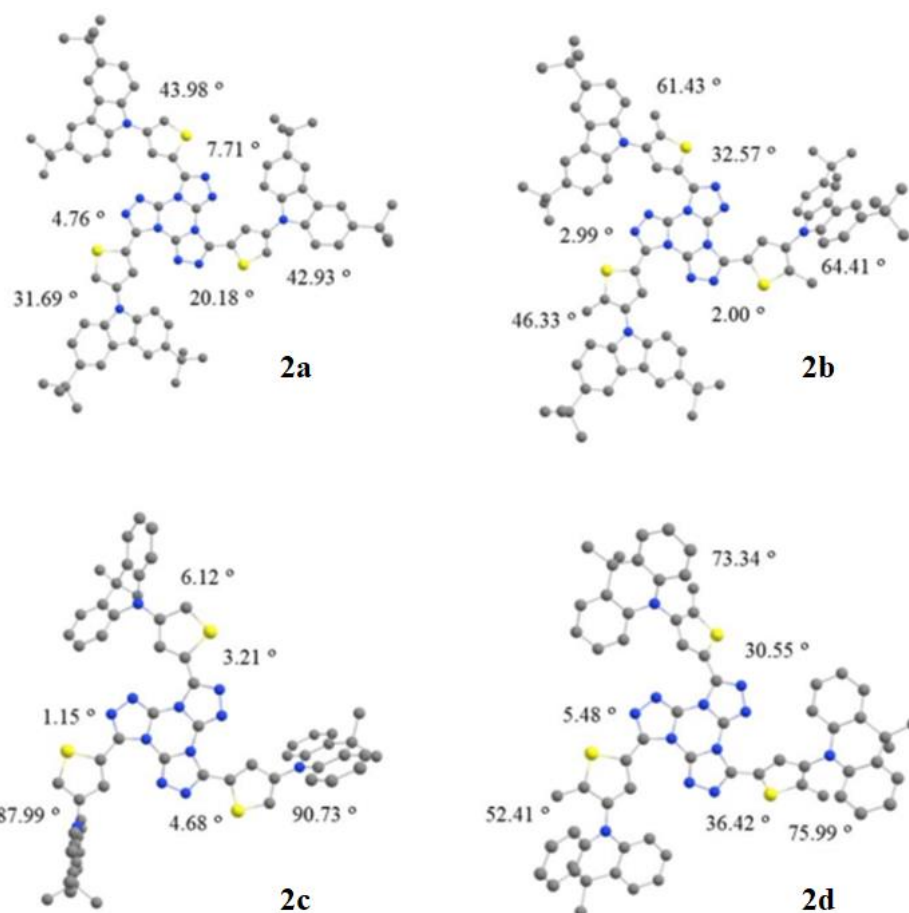


have relatively high oscillator strengths ( $f$ ), typical of LE states. Therefore, the excited states of **2a** and **2b** are considered a mixture of  $^1\text{CT}/^1\text{LE}$  states, with **2b** having a higher LE character due to its more significant  $f$  value. The  $S_1$ ,  $S_2$ , and  $S_3$  states are associated with the thiophene-carbazole arms of the molecule, with  $S_1$  corresponding to the arm with the largest thiophene-carbazole dihedral angle and  $S_2$  and  $S_3$  corresponding to the other arms with lower dihedral angles due to configurational asymmetry. The first absorption band in **2c** and **2d** corresponds to the three low-lying CT states from acridine to the TTT-thiophene core, as indicated by their low  $f$  values and orbital configurations. The second band in the theoretical spectra for all four compounds, which corresponds to the high-energy band observed experimentally, is related to the LE states from the TTT-thiophene core. Detailed information about these excited states can be found in the annex section. The optimized  $S_1$  and  $T_1$  geometries were obtained to gain insights into the  $S_1$  and triplet states. In the optimized  $S_1$  state geometry, only minor differences in the dihedral angles are observed as showed in **Figure 55**. This results in only slight changes in  $f$  for the  $S_0 \rightarrow S_1$  transition in all four compounds (annex section).



**Figure 55** Optimized  $S_1$  state geometries within CAM-B3LYP/def2-SVP level of theory.

In contrast, the geometry of the molecules flattens significantly when going from the ground state to the  $T_1$  state, resulting in a decrease in the dihedral angles between the donor and acceptor moieties (**Figure 56**).



**Figure 56** Optimized  $T_1$  state geometries within B3LYP/def2-SVP level of theory.

The configuration of the excited triplet states was calculated using SOC-TD-DFT starting from the  $T_1$  state geometry. The flattening of the structure increases the overall conjugation of the  $\pi$ -system, resulting in low-lying states with an LE orbital configuration (annex section). Therefore, the  $T_1$ ,  $T_2$ , and  $T_3$  states are assigned as  $^3\text{LE}$  from the TTT-thiophene core, with the lowest energy state being the smallest dihedral angle between these two moieties. The  $T_4$  state is close in energy to  $S_1$  and has a CT orbital configuration from donor to acceptor moieties.

The impact of spin-orbit coupling on ISC and phosphorescence pathways was studied using SOC matrix elements (SOCME) obtained from SOC-TD-DFT calculations as shown in **table 9**.

**Table 9** SOCME and adiabatic energy differences.

	<b>2a</b>	<b>2b</b>	<b>2c</b>	<b>2d</b>
$\Sigma_j (\langle \mathbf{T}_{j=1-4(x,y,z)}   \hat{\mathbf{H}}_{\text{SOC}}   \mathbf{S}_1 \rangle)^2$ (cm <sup>-1</sup> )	4.36	5.19	3.75	1.75
$\Sigma_i (\langle \mathbf{T}_{1(x,y,z)}   \hat{\mathbf{H}}_{\text{SOC}}   \mathbf{S}_{i=1-10} \rangle)^2$ (cm <sup>-1</sup> )	10.36	9.37	11.65	14.54
<b>S<sub>1</sub> (eV)</b>	3.231	3.346	2.972	3.112
<b>T<sub>1</sub> (eV)</b>	2.207	2.256	2.061	2.245
<b>ΔE<sub>ST</sub></b>	1.024	1.090	0.911	0.867

The ISC rate is proportional to the sum of the SOCME between the singlet state (S<sub>1</sub>) and all triplet states of lower or similar energy (in this case, T<sub>1</sub>-T<sub>4</sub> for all compounds). For compounds **2a** and **2b**, the sum of the SOCME between S<sub>1</sub> and the triplet states was 4.36 and 5.19 cm<sup>-1</sup>, respectively, while for compounds **2c** and **2d**, we found values of 3.75 and 1.75 cm<sup>-1</sup>, respectively. These values match the measured quantum yields Φ. Compounds **2a** and **2d** have higher Φ values than their homologs, mainly due to less deactivation via the ISC pathway as indicated by fluorescence emission. These SOCME values for the ISC pathway are similar to those found in regular donor-acceptor molecules and sulfur-containing compounds.<sup>115,116</sup>

The SOCME between the low-lying states enables the previously forbidden T<sub>1</sub> → S<sub>0</sub> radiative pathway. We calculated the SOCME between T<sub>1</sub> and the first ten excited singlet states for compounds **2a**, **2b**, **2c**, and **2d**. The results show that the spin-orbit coupling sum for **2a** and **2b** is 10.36 and 9.37 cm<sup>-1</sup>, respectively. As the T<sub>1</sub> energies of these two compounds are similar, the observed lower *k*<sub>Phosph</sub> and higher τ<sub>Phosph</sub> with **2b** can be explained by these spin-orbit coupling sums. The spin-orbit coupling sums for compounds **2c** and **2d** are 11.65 and 14.54 cm<sup>-1</sup>, respectively. In this case, **2d** has a more significant spin-orbit coupling between the low-lying states and a higher T<sub>1</sub> energy than **2c**, resulting in a significantly lower τ<sub>Phosph</sub> than the other three compounds and only very weak RTP. The phosphorescence pathway has relatively larger values of SOC, similar to other molecules with RTP.<sup>117,118</sup> As the low-lying triplet states are <sup>3</sup>LE states centered both at the TTT core and the thiophene bridge, the inclusion of thiophene increases the SOC associated with the radiative T<sub>1</sub> → S<sub>0</sub> pathway, enabling RTP.

### 3.2.3 Conclusions

The incorporation of thiophene bridges in D<sub>3</sub>A-type TTTs significantly impacted their emission behavior. Using a 2,4-substitution pattern on the thiophene bridges, we prepared four

target compounds with thiophene bridges linked to the TTT core at position 2 and a donor moiety at position 4. While this substitution pattern was not enough to achieve a low  $\Delta E_{ST}$  value and induce TADF behavior, the inclusion of thiophene bridges resulted in solution RTP emission with lifetimes ranging from 0.1 - 3.5 ms and PLQY values between 0.023 and 0.258. All compounds also exhibited PF emission, with the carbazole derivatives showing higher efficiency due to a mixed  $^1CT/^1LE$  state and the acridine derivatives showing pure  $^1CT$  emission due to good orthogonality between the donor and acceptor moieties. A comparison of solution and solid-state emission and their lifetimes indicated that the bulky donor moieties protect the emissive  $^3LE$  state, allowing RTP under air to manifest even in solution. Based on these findings, we recommend incorporating thiophene bridges in  $D_nA$ -type emitters for molecular design aiming for solution RTP.

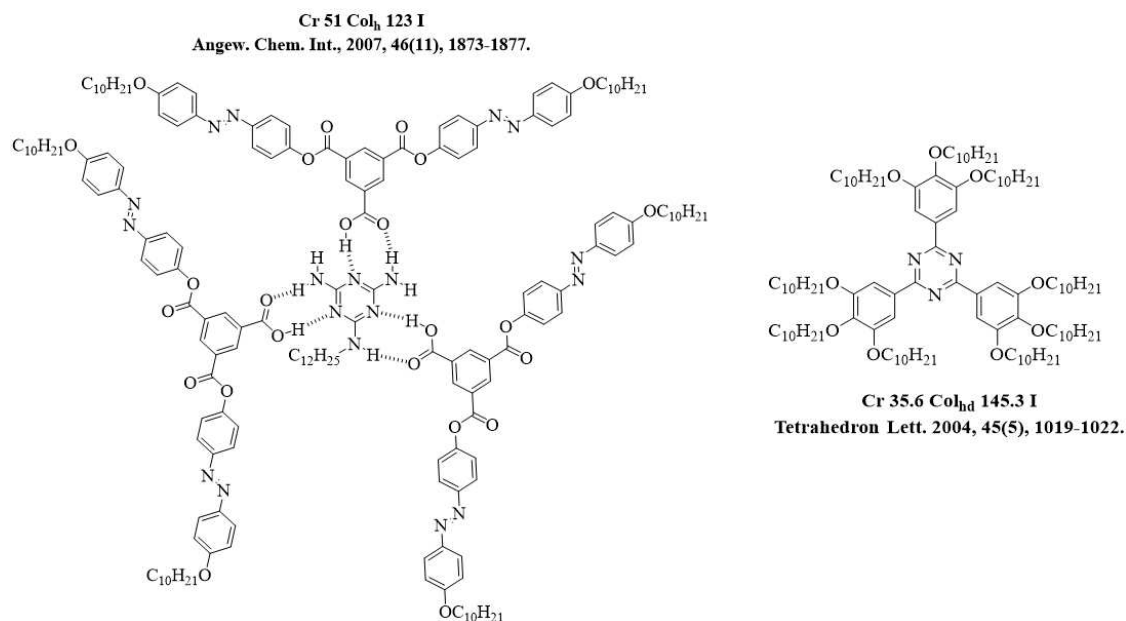
## 4 TOWARDS ANISOTROPIC DELAYED LUMINESCENCE FROM LIQUID CRYSTALS

This chapter will discuss the attempts to induce mesomorphism in luminescent materials and the synthesis of new liquid crystal matrices based on triazine to improve the light output in OLED devices through anisotropic emission. After a short review of the literature on mesogenic *s*-triazine and TTT derivatives, we present the attempts to induce mesomorphism in luminescent molecules reported in the literature and proposed in this work.

### 4.1 INTRODUCTION

#### 4.1.1 *s*-triazine

The synthesis of discotic liquid crystals has intensified over the years. These materials have several applications that attract the industry's attention, i.e., light-emitting diodes, one-dimensional conductors, photovoltaics, and others. These materials are easily processable and have efficient self-healing properties.<sup>73</sup> Relevant aspects for applying these materials are the organization between the columns, the distances between the disks, the mesophases' stability, and the rigid moiety's size.<sup>79</sup> Including heterocycles in these mesogens enhances molecular interactions, improving the stability and organization of the material.<sup>119,120</sup> Aza-aromatic centers can form columnar liquid crystals with low LUMO levels, which leads to n-type semiconductor properties. The *N*-heterocycle 1,3,5-triazine is one of the most widely used aza-aromatics in discotic liquid crystals. Its electro-deficient character and easy functionalization at the 2,4,6 positions of the ring, combined with the straightforward synthesis of the unit via trimerization of the cyano group, allows obtaining several star-shaped C<sub>3</sub>-symmetric molecules that can self-organize into columnar mesophases.<sup>82</sup> The disk formation can occur through hydrogen bonds between the nitrogens of the triazine center and some hydrogen bond donor from another molecule (**figure 57**, left)<sup>121</sup> or through covalent bonds, where the disc formation is intrinsic to the anisometry of the molecule (**figure 57**, right).<sup>122</sup>



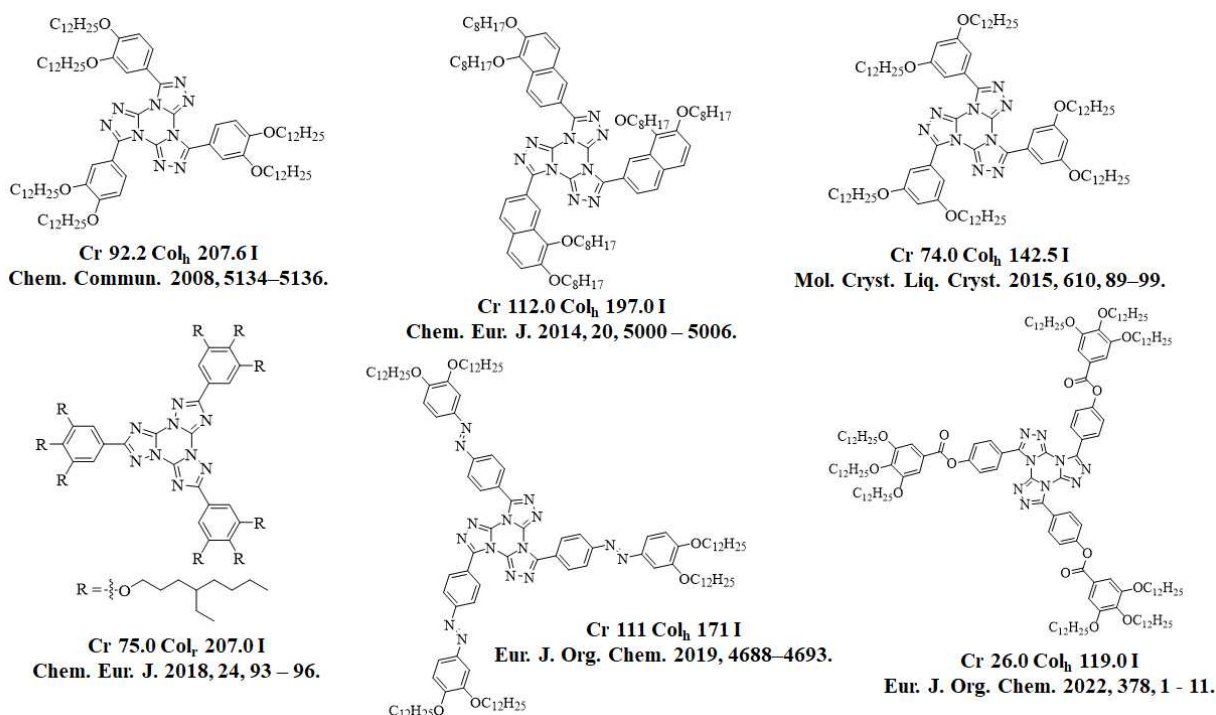
**Figure 57** Triazine-based mesogenic compounds.

The supramolecular self-assembly of these materials into 1D columns able to transport charges combined with fluorescent properties has attracted much attention from researchers. The combination of the ability to generate light with the charge transport in the columnar arrangement allows the application of these materials in emissive layers for advanced technologies such as OLEDs.<sup>79</sup> In this way, the emissive layer will be the same as the carrier layer, simplifying the device structure, to give room for anisotropic alignment that may enhance device performance.<sup>123</sup> Various luminescent discotic liquid crystals have been synthesized and studied in recent years.<sup>124–127</sup> Among the different core units present in these mesogens, the triazine heterocycle has been increasingly used to synthesize these luminescent materials.<sup>82</sup> Recently, the triazine heterocycle began to be used as an acceptor unit on efficient TADF emitters of D-A type structure. Triazine-based blue emitters are reported in the literature and demonstrate that triazine-based molecules are promising in the search for efficient blue emitters.<sup>128</sup> Bearing this in mind, in the pursuit of combining mesomorphism with TADF properties, the triazine center was chosen.

#### 4.1.2 TTT

In 2008, the Gallardo research group first reported mesomorphism in molecules derived from the *tris*[1,2,4]triazolo[1,3,5]triazine heterocycle.<sup>106</sup> Since then, several works on the ability of TTT to stabilize columnar mesophases have been published (**figure 58**).<sup>100,107,129–</sup>

<sup>135</sup> The authors have modified both the number of aliphatic chains and their length. The rigid central unit was also expanded, and some connecting groups, such as esters and azo groups, were added. Although thermal isomerization of the TTT core has been known since 2005,<sup>104</sup> only in 2017, Lehmann et al. reported on the influence of the isomeric structures on the properties of the mesophase.<sup>105</sup> The authors observed that isomerization leads to higher melting points, variably accompanied by loss or gain of mesomorphism.



**Figure 58** Examples of discotic liquid crystals based on the TTT core.

Although the TTT heterocycle has been widely explored regarding its mesomorphism, recently, with this core as an acceptor unit in new efficient blue emitters, a renewed interest in incorporating the TTT core in the structure of new luminescent liquid crystals that exhibit delayed fluorescence has been raised.<sup>99,108–112,136</sup> The non-planarity in some of these mesogens may be compatible with the non-planar structure desired in TADF materials and may facilitate the combination of these two phenomena.

#### 4.1.3 Triazine-based columnar matrices for OLED devices

Glassy polyaromatic matrices are often used in organic electronics because they can prevent electrical and optical problems arising from grain boundaries in microcrystalline

materials while still providing the mechanical stability of a solid. The formation of glasses rather than crystals is favored by conformational multiplicity and the presence of dipoles. While isotropic glasses are common among charge-transporting polycyclic aromatics, liquid crystalline polyaromatic glasses are much rarer. These glasses enable the embedding of emitting materials in an oriented anisotropic alignment, resulting in anisotropic emission, which can increase the efficiency of external devices by 50%.<sup>45,137,138</sup> Hexagonal columnar liquid crystals are fascinating because they tend to align homeotropically to surfaces, resulting in an emitter orientation with preferred emission perpendicular to the device plane.<sup>139</sup> It has recently been shown that the alignment direction and entropy content of a small molecule room temperature columnar glass can be controlled during physical vapor deposition by adjusting the deposition speed and substrate temperature.<sup>140</sup>

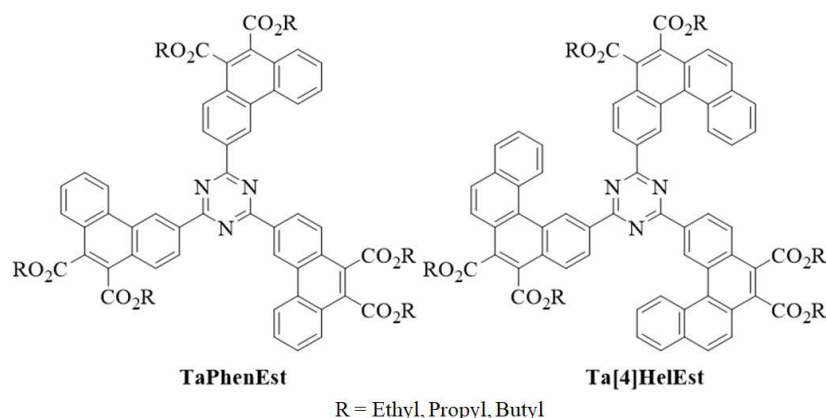
Our research group has recently reported that molecules with a triphenyltriazine core decorated with ester groups, i.e. (tris(3-alkoxycarbonylphenyl)-s-triazines, display nematic liquid crystal behavior. When these molecules are modified by adding fluorine atoms (either in the central unit or in the aliphatic chains), they form columnar mesophases that do not tend to crystallize at room temperature due to the flexibility of the single bond between the triazine and benzene groups. This flexibility allows for different configurations of the ester groups bonded in the meta position with respect to this bond. An additional notable characteristic of these molecules is that the limited conjugation between the three outer arene units, connected through meta-linkages in the central triazine cycle, results in a large band gap,  $T_1-S_0$ .<sup>48</sup> This makes it possible to incorporate blue emitters, which are desirable for TADF OLEDs.

## 4.2 RESULTS AND DISCUSSIONS

### 4.2.1 Columnar liquid crystalline glasses based on triazine core

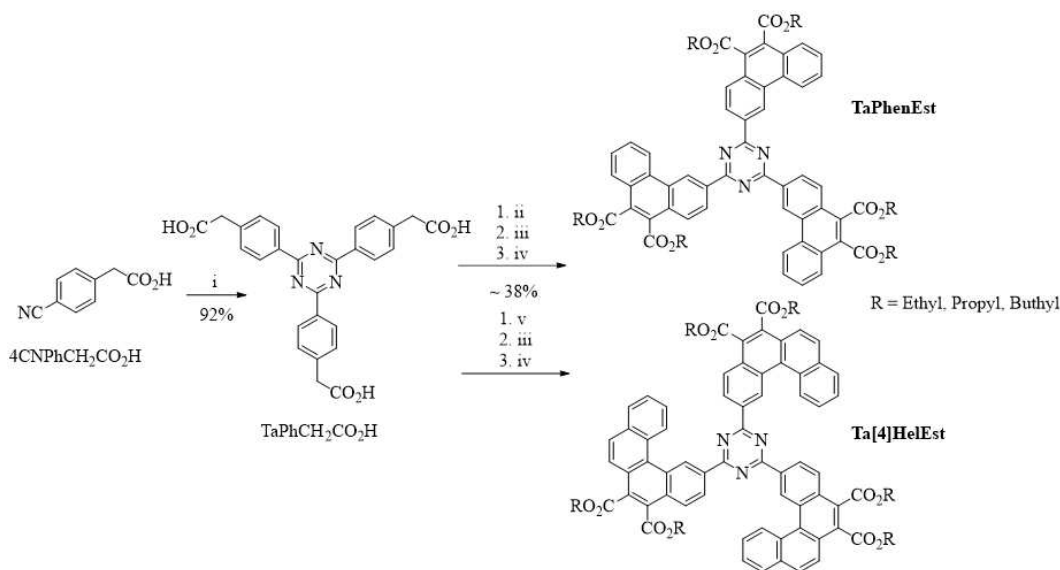
Since it was not possible to obtain a stable glassy state at a temperature above room temperature using the smallest representative triaryltriazine esters, we designed new triply phenanthryl- and [4]helicenyl-substituted triazine-hexaalkyl esters with shorter alkyl chains. Doctoral student Fabrícia Nunes da Silva, with whom I closely cooperated in the laboratory, was responsible for synthesizing and characterizing the target molecules in this section. **Figure 59** shows the structure of the synthesized mesogens.





**Figure 59** Target molecules based on the triazine center synthesized by Fabrícia Nunes da Silva.

Fabrícia found that it is possible to cleanly trimerize (4-cyanophenyl)acetic acid, yielding a suitable substrate for threefold Perkin-Mallory sequences<sup>141</sup> that enable the synthesis of extended triaryltriazine hexaesters. *Tris*((4-carboxymethyl)phenyl)triazine is Perkin-condensed with phenylglyoxylic acid, and the resulting tris(maleic acid) is subjected to in-situ esterification and subsequent Mallory photocyclization to obtain triphenanthryl-triazines with three pairs of vicinal ester substituents (**scheme 4**). Fabrícia extended the three aryl arms by reacting the intermediate *tris*((4-carboxymethyl)phenyl)triazine with 2-naphthylglyoxylic acid through a Perkin condensation, followed by in situ esterification. Photocyclization of Mallory was then performed to obtain triply [4]helicenyl-substituted triazine-hexaalkyl esters (**scheme 4**). As a result, the hexaethyl, hexapropyl, and hexabutyl ester derivatives were synthesized.



**Scheme 4** Synthetic approach for the synthesis of triazine-based mesogens. i)  $\text{CF}_3\text{SO}_3\text{H}$ ; ii) phenylglyoxylic acid, acetic anhydride, triethylamine, THF; iii) alkyl alcohol, bromoalkene, triethylamine, THF; iv) iodine, ethyl acetate, light; v) 2-naphthylglyoxylic acid, acetic anhydride, triethylamine, THF.

After synthesizing and characterizing the molecules, we conducted further characterizations of the liquid crystalline properties of the materials using differential scanning calorimetry (DSC), polarized optical microscopy (POM), and X-ray diffraction (XRD).

#### 4.2.1.1 Differential scanning calorimetry (DSC)

DSC analyses were performed to determine the phase transition temperatures and energies that the materials exhibit. The analyses were carried out with a heating rate of 10°C min<sup>-1</sup>. The results obtained are summarized in **Table 10** and the diffractograms can be found in the annex section.

**Table 10** Calorimetric phase transition onset temperatures (°C) and enthalpies (J/g [in brackets]), and glass transition onset temperatures, on heating with 10°C/min; Cr= crystalline phase, Col<sub>hex</sub> = hexagonal columnar mesophase, Iso = isotropic liquid, T<sub>g</sub>(Col) = glass transition temperature in the hexagonal columnar mesophase; monotropic transitions (observed on second heating only, after cooling from the isotropic liquid) in italics.

	Cr-Cr	Cr-Col <sub>hex</sub>	Col <sub>hex</sub> -Col <sub>hex</sub>	Col <sub>hex</sub> -Iso	Cr-Iso	T <sub>g</sub> (Col)
<b>TaPhenEt</b>	224 <sup>[26]</sup>				>375	
<b>TaPhenPr</b>		150 <sup>[13]</sup>		>375		81
<b>TaPhenBu</b>		108 <sup>[11]</sup>		>375		19
<b>Ta[4]HelEt</b>	153 <sup>[12]</sup>				325 <sup>[26]</sup>	
<b>Ta[4]HelPr</b>			<i>179<sup>[1.9]</sup></i>	<i>223<sup>[3.0]</sup></i>	232 <sup>[37]</sup>	
<b>Ta[4]HelBu</b>				<i>149<sup>[1.0]</sup></i>	205 <sup>[34]</sup>	39

The results show that hexaethyl ester (TaPhenEt) undergoes a phase transition between two different crystalline states upon heating above its melting point at 224°C but does not transition to the isotropic liquid state up to 375°C. The propyl homolog (TaPhenPr) melts at 150°C and exhibits a hexagonal columnar mesophase above this temperature, which becomes a non-shearable mesomorphic glass upon cooling. A glass transition at approximately 81°C in TaPhenPr restricts crystallization to the temperature range between this point and the melting onset at 150°C. The butyl homolog (TaPhenBu) exhibits a hexagonal columnar mesophase after melting at 108°C but with a significantly lower glass transition temperature of 19°C. The hexaethyl, hexapropyl, and hexabutyl ester derivatives (Ta[4]HelEt, Ta[4]HelPr and Ta[4]HelBu) of sym-tris([4]helicen-3-yl)triazine, all melt directly to the isotropic liquid at

attainable temperatures and do not form mesophases upon cooling. Ta[4]HelEt exhibits a crystal-to-crystal transition at 153°C upon heating, while Ta[4]HelPr and Ta[4]HelBu exhibit monotropic mesophases upon cooling below their clearing points. The clearing temperatures of Ta[4]HelEt, Ta[4]HelPr and Ta[4]HelBu are 325°C, 232°C, and 205°C, respectively.

#### 4.2.1.2 Polarized optical microscopy (POM)

All compounds were analyzed using polarized optical microscopy (POM). It was found that TaPhenEt, TaPhenPr and TaPhenBu did not show a transition to the isotropic liquid state up to 375°C when observed using POM. X-ray diffraction identified the high-temperature state for TaPhenPr and TaPhenBu as a hexagonal columnar mesophase. However, TaPhenBu had a significantly lower calorimetric glass transition temperature of 19°C. In contrast, the sym-tris([4]helicen-3-yl)triazine esters Ta[4]HelEt, Ta[4]HelPr and Ta[4]HelBu all showed a direct melting of the crystalline state to the isotropic liquid at attainable temperatures of 325, 232, and 205°C, respectively, when observed using POM. No mesophase was detected in Ta[4]HelEt upon cooling from the isotropic liquid, while Ta[4]HelPr and Ta[4]HelBu showed monotropic mesophases upon cooling below their clearing points at 223 and 149°C, respectively, with the typical growth textures of a hexagonal columnar mesophase. Micrographs are shown in the annex section.

#### 4.2.1.3 X-ray diffraction (XRD)

X-ray diffraction analyses were conducted to verify the molecular organization in the mesophases of the materials synthesized in this session. The hexaethyl ester, TaPhenEt, undergoes a phase transition between two different crystalline states when heated above its melting temperature of 224°C, as confirmed by powder X-ray diffraction (XRD). The high-temperature state of the propyl homolog TaPhenPr is identified as a hexagonal columnar mesophase (due to the characteristic (11) and (21) secondary XRD peaks of the column lattice, which correspond to distances related by factors of  $\sqrt{3}$  and  $\sqrt{7}$  to the main lattice peak)<sup>142</sup> (shown in annex section). Upon cooling to room temperature, this mesophase solidifies into a non-shearable mesomorphic glass. Powder XRD diffractograms taken at 250 and 25°C show a contraction of the column-to-column distances by 10% (from 23.0 Å to 20.7 Å) over this temperature range, accompanied by roughness in the diffraction pattern in the small angle region, but without loss of the (11) and (21) peaks. In the butyl homolog TaPhenBu, which also

exhibits a hexagonal columnar mesophase after melting at 108°C, immediate crystallization is not observed upon heating above this glass transition temperature (19°C). The hexagonal lattice parameter of TaPhenBu is preserved upon cooling from 150°C to room temperature, with a column-to-column distance of 23.8 Å. The  $\pi$ -stacking order inside the columns, corresponding to an inter-disk distance of about 3.3 Å, is enhanced at room temperature, facilitating charge carrier transport. The  $\pi$ -stacking order was not observed in the powder XRD spectra of TaPhenPr.

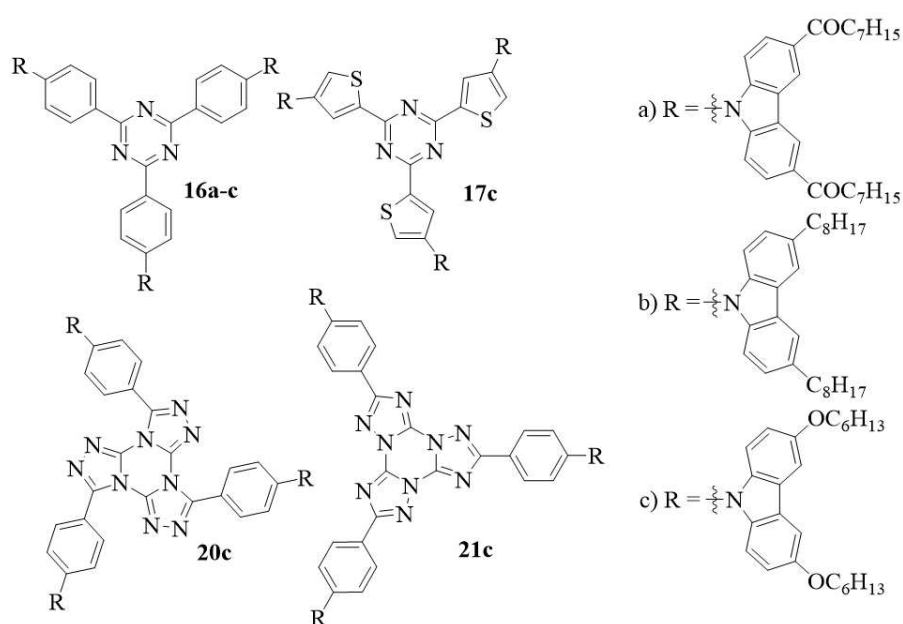
Upon cooling from the isotropic liquid state, Ta[4]HelEt does not exhibit any mesophase, and a crystal-to-crystal transition is observed through differential scanning calorimetry (DSC) upon heating at 153°C. Both crystalline phases of Ta[4]HelEt are hexagonal and show the characteristic (10), (11), (20), (21), (30), (22), and (31) peaks corresponding to hexagonal lattice distances in the ratios of  $1:\sqrt{3}:\sqrt{4}:\sqrt{7}:\sqrt{9}:\sqrt{12}:\sqrt{13}$ , as well as many other peaks (diffractogram is shown in the annex section.). In contrast, the crystalline phases of Ta[4]HelPr and Ta[4]HelBu do not display prominent XRD peaks indicative of a hexagonal lattice. Upon cooling below their clearing points at 223°C and 149°C, respectively, Ta[4]HelPr and Ta[4]HelBu exhibit monotropic mesophases with the characteristic growth textures of the hexagonal columnar mesophase (as mentioned before) and the corresponding  $\sqrt{3}$  and  $\sqrt{4}$  XRD peaks. Therefore, the slight deplanarization of the aromatic core destabilizes the hexagonal mesophase enough to achieve attainable clearing temperatures in Ta[4]HelPr and Ta[4]HelBu. In contrast, the mesophase is wholly suppressed in Ta[4]HelEt and Ta[4]HelBu in favor of a hexagonal crystal. Upon cooling, Ta[4]HelPr undergoes a low-enthalpy transition ( $1.9 \text{ J g}^{-1}$ , **table 10**). X-ray diffraction analysis shows that this transition is not accompanied by any change in the hexagonal symmetry of the mesophase or the appearance of peaks that are not associated with a 2D hexagonal lattice. However, the higher-order peaks of the column lattice significantly increase in relative intensity compared to the primary lattice peak (and the  $\sqrt{7}$ ,  $\sqrt{9}$ ,  $\sqrt{12}$ , and  $\sqrt{13}$  peaks are now clearly visible). This indicates an improvement in the correlation length of the column lattice and an enhancement of the interdisk peak. As with TaPhenPr, a slight contraction of the column-to-column distance (from 22.6 Å to 22.2 Å) and of the  $\pi$ -stacking distance (from 3.8 Å to 3.7 Å) was also observed for Ta[4]HelPr. No glass transition was observed for Ta[4]HelPr within the temperature range of this highly ordered mesophase. In the case of Ta[4]HelBu, no transition from less regular to more regular mesophase is observed. Instead, Ta[4]HelBu forms a mesomorphic glass at room temperature and exhibits a

calorimetric glass transition at 39°C (**table 10**). As a result, Ta[4]HelBu displays both a persistent mesomorphic hexagonal columnar glass at room temperature (with a column-to-column distance of 21.9 Å and an intercolumnar distance of 3.7 Å) and easily accessible melting and clearing temperatures of 205°C and 149°C, respectively. All diffractograms are shown in the annex section.

#### 4.2.2 Towards mesomorphic properties in delayed luminescence molecules.

As we discussed earlier, discotic liquid crystals exhibit specific structures. Molecules with discotic anisotropy, where aliphatic chains surround a rigid, planar central unit, tend to exhibit columnar mesomorphism.<sup>72</sup> To synthesize luminescent liquid crystals, it is necessary to incorporate a suitable chromophore into the structure of a mesogen.<sup>123</sup> Pursuing efficient TADF emitters with liquid crystal properties is challenging. Efficient symmetric  $C_3$  emitters need to be non-planar to allow good spin-orbit coupling in the absence of heavy atoms.<sup>52</sup> At the same time, liquid crystalline phases are favored by planar disk-shaped molecules. There are exceptions, among them the TTT heterocycle which is both a mesogenic and pronouncedly non-planar unit.<sup>107</sup> Although it is planar, the triazine heterocycle is a mesogenic unit and electron acceptor in TADF emitters.<sup>82,83</sup>

The molecules designed to be synthesized here are derivatives of molecules already reported in the literature as TADF emitters and molecules synthesized in previously session of this doctoral thesis. **Figure 60** shows the target molecules of this session.



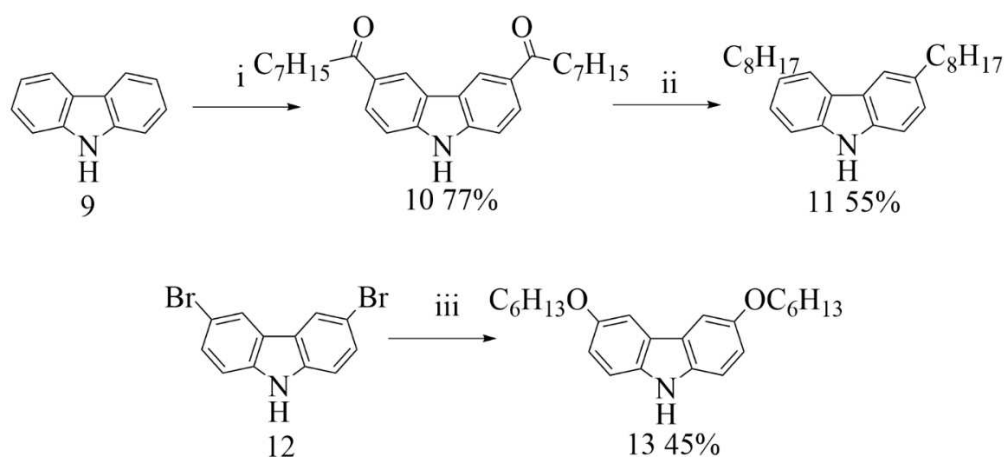
**Figure 60** Target compounds in the search for discotic liquid crystals with TADF.

To induce mesomorphism, we introduced alkyl and alkoxy chains in the peripheral portions of the luminescent molecules. The molecules chosen have as donor unit the carbazole moiety, as this is easily functionalized in the 3,6 positions, simplifying the insertion of the aliphatic chains.

### 4.2.3 Synthesis and Characterization

#### 4.2.3.1 9H-carbazole derivatives

To induce liquid crystalline behavior in luminescent molecules, it was chosen to insert alkyl or alkoxy chains into the 9H-carbazole donor portion, as shown in **scheme 5**.

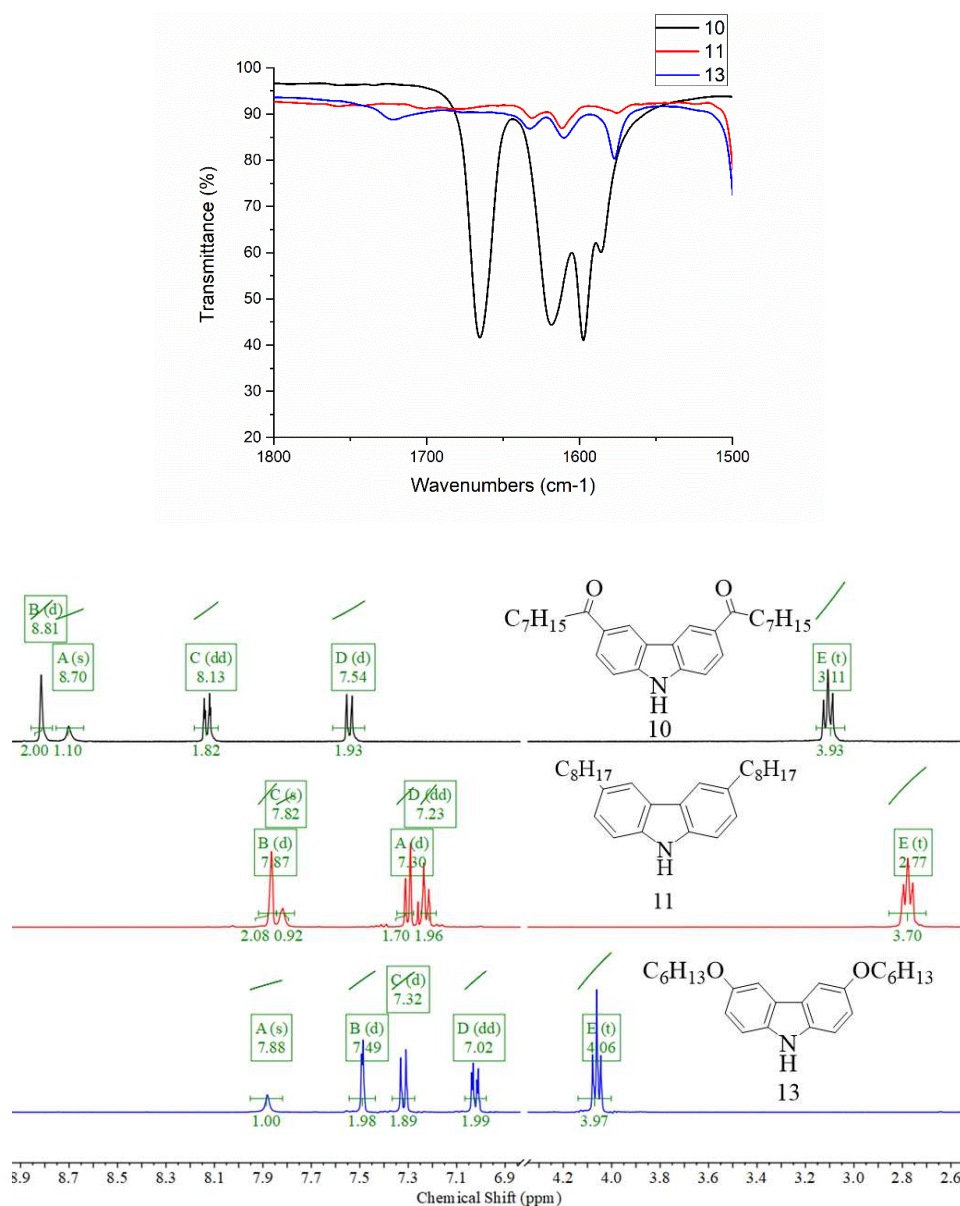


**Scheme 5** Synthetic approach for 9H-carbazole derivatives; i) octanoyl chloride, AlCl<sub>3</sub>, dichloromethane; ii) LiAlH<sub>4</sub>, AlCl<sub>3</sub>, THF; iii) hexan-1-ol, Na, CuI, DMF.

Intermediate **11** was obtained in two steps. In the first step, the commercial reagent **9** reacts with octanoyl chloride in a Friedel-Crafts acylation reaction to yield the acylated intermediate **10** (77%). The carbonyl group of **10** is reduced to CH<sub>2</sub> (**11**, 55%) with lithium aluminum hydride in THF.<sup>143</sup> Inserting the alkoxy group into the 9H-carbazole unit required the commercial reagent 3,6-dibromo-9H-carbazole (**12**).<sup>144</sup> After the formation of sodium hexan-1-olate in situ, the bromine atoms of commercial reagent **12** are replaced, resulting in intermediate **13** in a yield of 45%.

**Figure 61** shows the <sup>1</sup>H NMR of intermediates **10**, **11**, and **12**. The presence at 3.11 ppm of a triplet in the spectrum of **10** (**figure 61**, aliphatic region, red line) refers to the hydrogens of the carbon neighboring the carbonyl in a ratio of 4H CH<sub>2</sub> to 7H in the aromatic region (carbazole hydrogens), confirms the acylation reaction. The <sup>1</sup>H NMR spectrum of intermediate **11** is, in essence, the same as that of molecule **10** (same type of signals, **figure 61**,

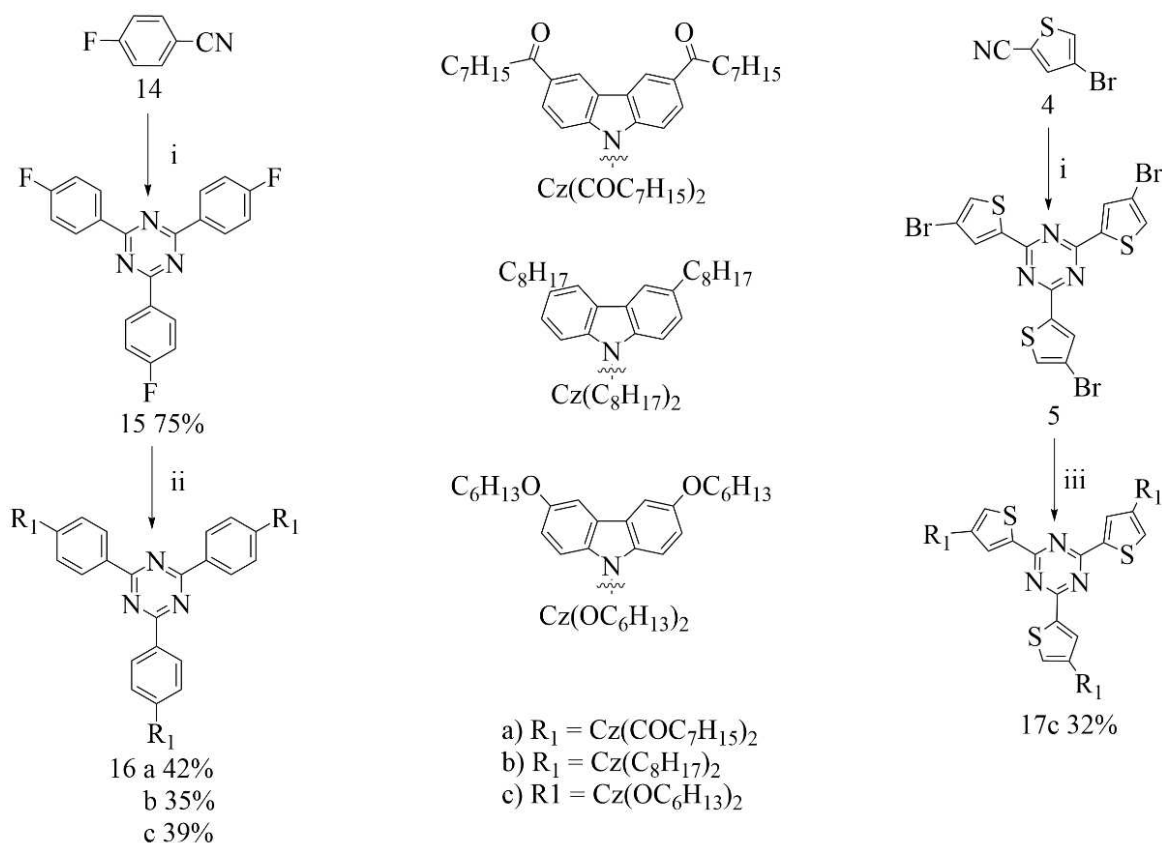
black line) but the integral of the signals in the aliphatic region differs in number, indicating the presence of more hydrogens in molecule **11** (4H, see annex section) indicating reduction of the carbonyl group. By monitoring the 1.800 – 1.500  $\text{cm}^{-1}$  region of the IR spectrum of these materials (**figure 61**), it is possible to confirm the reduction of the carbonyl group. For molecule **10**, there is a stretching band at 1665  $\text{cm}^{-1}$  characteristic of the CO bond. This same band is absent in the spectrum of **11**. Similarly, the presence of a signal at 4.04 ppm (**figure 61**, aliphatic region blue line), in a ratio of 4H to 7H in the aromatic region of the spectrum, supports the formation of product **13**.



**Figure 61** IR (top) and  $^1\text{H}$  NMR (bottom) spectrum of intermediates **10**, **11** and **13** (400 MHz, **10** and **13**:  $\text{CD}_2\text{Cl}_2$ , **11**:  $\text{CDCl}_3$ ).

## 4.2.3.2 1,3,5-triazine

In parallel to the synthesis of the peripheral units, intermediates **10**, **11**, and **13**, it was necessary to synthesize the central unit 1,3,5-triazine. Two different substrates were chosen, 4-fluorobenzonitrile (**14**) and 4-bromothiophene-2-carbonitrile (**4**), to induce mesomorphism in luminescent molecules already reported in the literature<sup>145</sup> and molecules newly synthesized in this work, respectively. **Scheme 6** shows the synthetic route adopted to obtain the final molecules **16a-c** and **17c**.



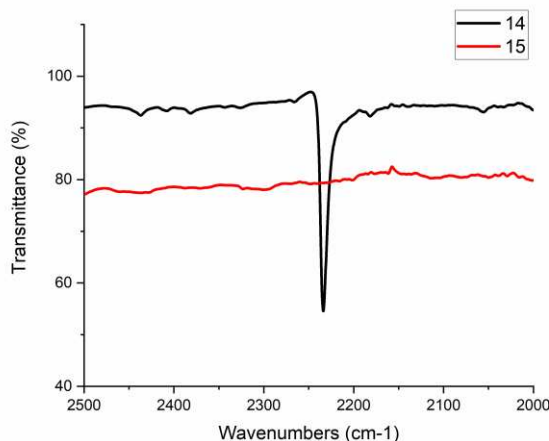
**Scheme 6** Synthetic approach to **16a-c** and **17c**; i) CF<sub>3</sub>SO<sub>3</sub>H; ii) a - 1,1'-(9H-carbazole-3,6-diyl)bis(octan-1-one) and b - 3,6-dioctyl-9H-carbazole, Cs<sub>2</sub>CO<sub>3</sub>, dimethylacetamide; iii) c - 3,6-bis(hexyloxy)-9H-carbazole, K<sub>2</sub>CO<sub>3</sub>, CuSO<sub>4</sub>·5H<sub>2</sub>O, 1-methylnaphthalene.

Intermediate **15** (75%) is obtained in the same way as intermediate **5**, synthesized earlier. The nucleophilic substitution reaction between the carbazole derivatives and intermediate **15** leads to the final molecules **16a-c** (~38%).<sup>146</sup> Compound **17c** (32%) is obtained via the Ullmann reaction variant described previously.

IR spectroscopy confirmed the trimerization of the nitrile group in the 1,3,5-triazine heterocycle. **Figure 62** shows the IR spectrum (2.000 – 2.500 cm<sup>-1</sup> region) of intermediate **15** and starting reagent **14**. The presence of the stretching band at 2.233 cm<sup>-1</sup> in the spectrum of **14**

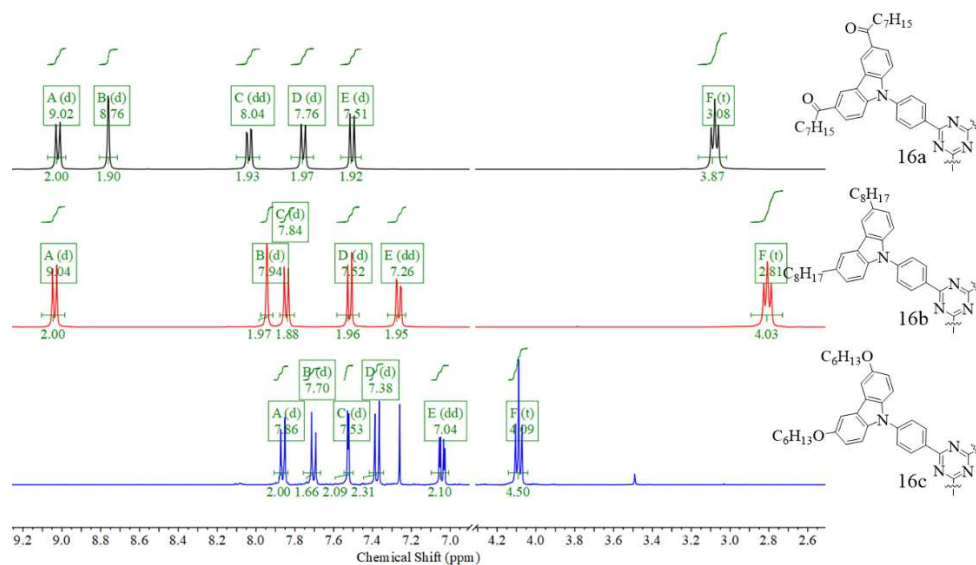


and the absence of the same in the spectrum of **15** indicates the change in the functional group. The characterization of **5** was discussed earlier and followed the same reasoning.



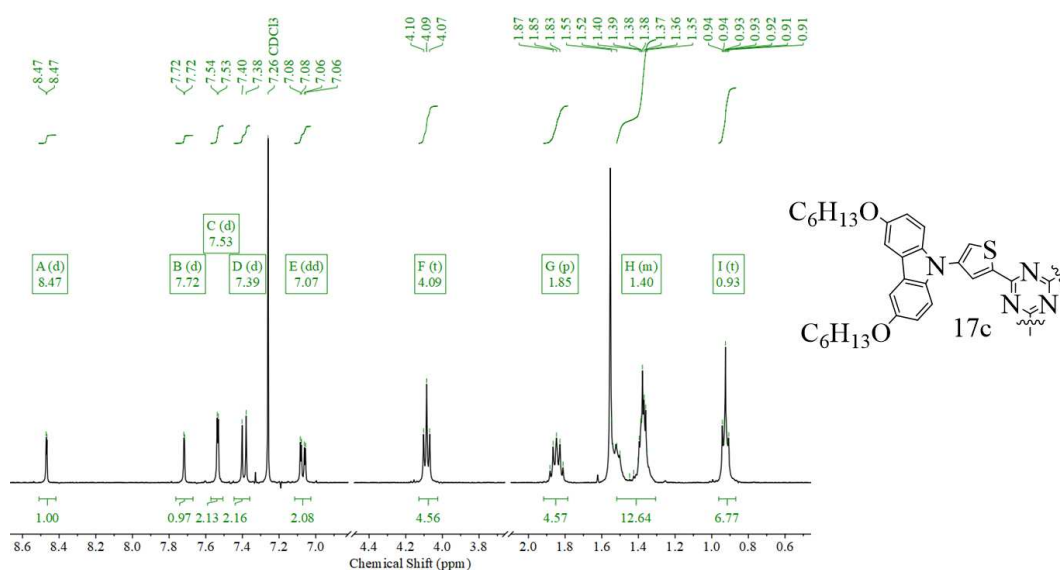
**Figure 62** IR spectrum of intermediates **14** and **15**. Monitoring CN stretch band.

The target molecules of the 1,3,5-triazine series were obtained after reacting the carbazole derivatives (**10**, **11**, and **13**) with intermediates **15** and **5**.  $^1\text{H}$  NMR spectrum of **16a-c** is shown in **figure 63**. The absence of the NH hydrogen signal from the starting reagents and the presence of 5 signals in the aromatic region in a 1:1 ratio (3 referring to the substituted carbazole unit and 2 from the benzene ring between the donor-acceptor system) suggests the formation of the target molecules. The structure of **16a-c** was confirmed by mass spectrometry (see annex section).



**Figure 63**  $^1\text{H}$  NMR spectrum of the final molecules **16a-c** (400 MHz, **16a** and **16b**:  $\text{CD}_2\text{Cl}_2$ , **16c**:  $\text{CDCl}_3$ ).

The  $^1\text{H}$  NMR spectrum of compound **17c** is shown in **figure 64**. In the aromatic region, the presence of 5 signals, 3 referring to the 6H of the donor unit and 2 assigned to the 2H of the thiophene ring, and the ratio between the signals support the substitution of the three bromine atoms by the donor units. In the aliphatic region, all the signals of the alkoxy chains are present, especially the triplet at 4.08 ppm relative to the hydrogens neighboring the oxygen in the aliphatic chain and the triplet at 0.91 ppm of the terminal methyls. Mass spectrometry confirmed the structure of **17c**.

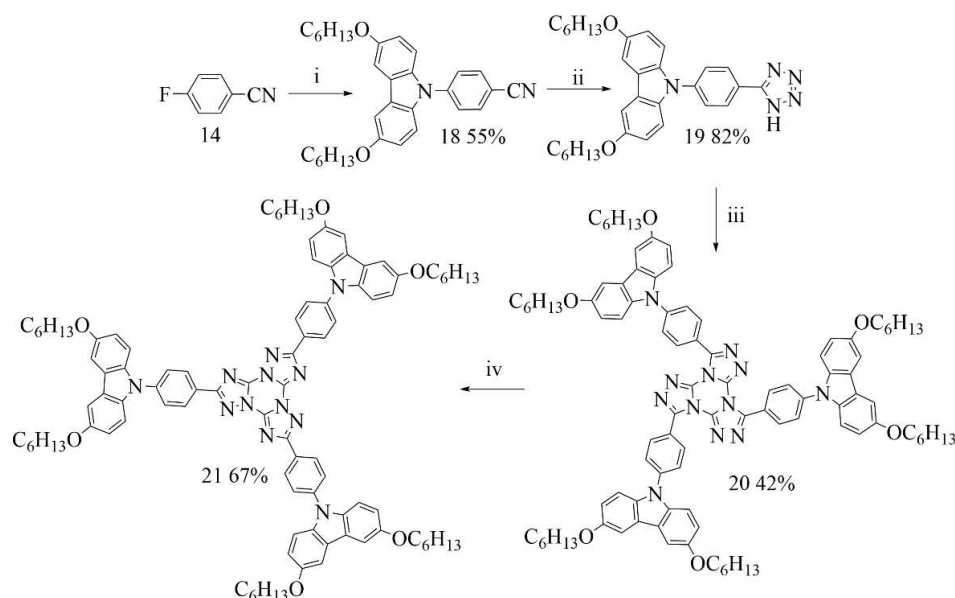


**Figure 64**  $^1\text{H}$  NMR spectrum of the final molecule **17c** (400 MHz,  $\text{CDCl}_3$ ).

After synthesizing and characterizing compounds **16a-c** and **17c**, polarized light optical microscopy was performed as a preliminary analysis of mesomorphism. Unfortunately, none of the materials exhibited liquid crystalline behavior under the microscope (texture formation), not being a liquid crystal.

4.2.3.3 *r*-TTT

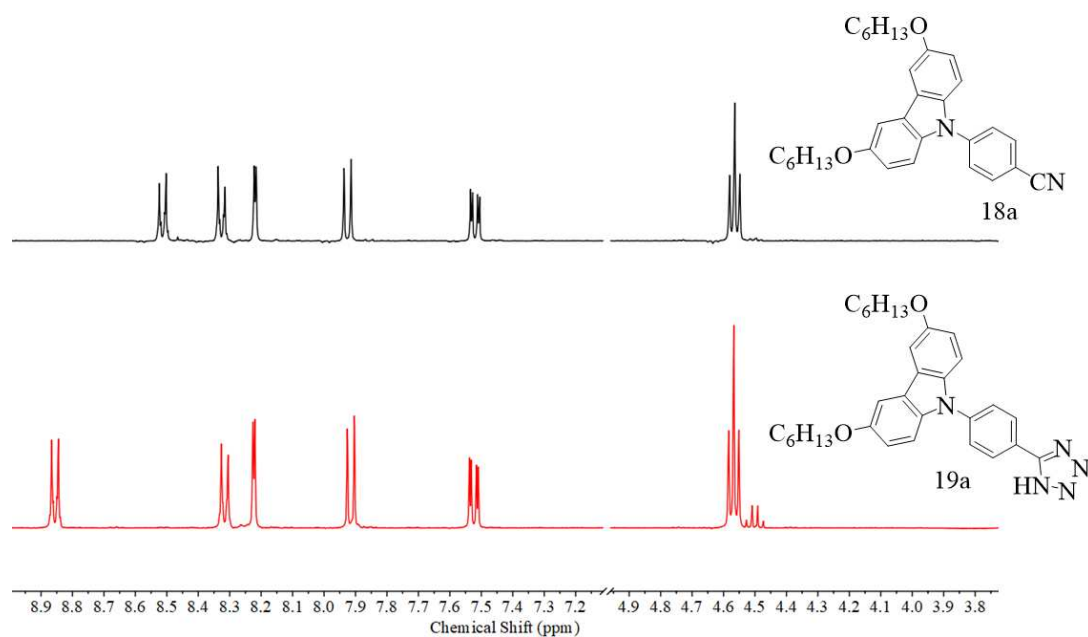
The donor unit chosen to induce mesomorphism in luminescent molecules containing the acceptor unit TTT, was intermediate **13**. In **scheme 7** is shown the synthetic route employed.



**Scheme 7** Synthetic approach to **20** and **21**; i) 3,6-bis(hexyloxy)-9H-carbazole,  $\text{Cs}_2\text{CO}_3$ , dimethylacetamide; ii)  $\text{NaN}_3$ ,  $\text{NH}_4\text{Cl}$ , DMF; iii)  $\text{C}_3\text{N}_3\text{Cl}_3$ , 2,6-lutidine, toluene; iv)  $\text{K}_2\text{CO}_3$ , 1,2-dichlorobenzene.

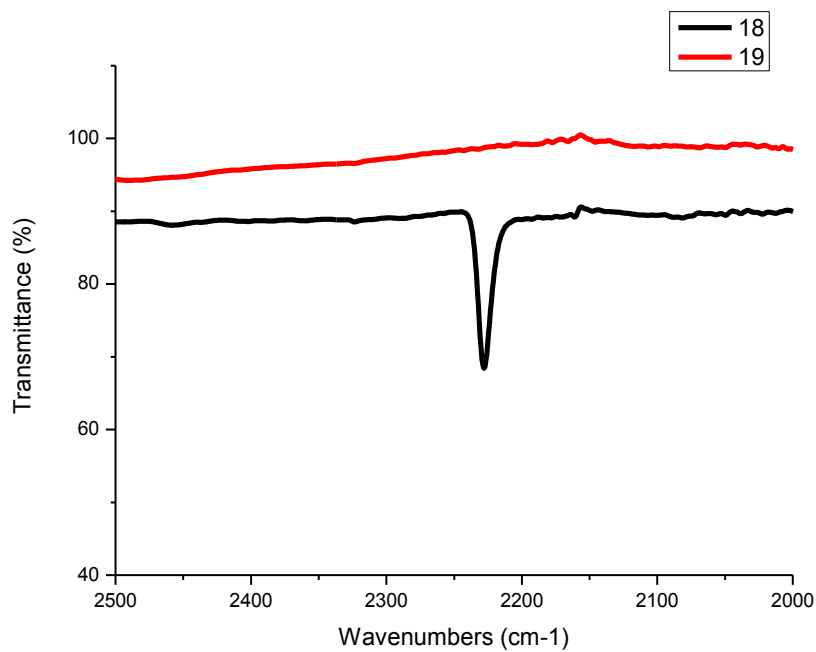
In the first step, the fluorine atom is replaced by the donor unit in a nucleophilic substitution reaction to generate compound **18** (55%).<sup>146</sup> The nitrile group of this intermediate is converted in the next step to the tetrazole heterocycle (**19**, 82%) by 1,3-dipolar cyclo addition. **19** reacts with cyanuric chloride in a Huisgen reaction to form the target molecule **20** (42%).<sup>108</sup> This tangential form (**20**) is then converted to the radial TTT isomer (**21**, 67%) by Dimroth rearrangement.<sup>111</sup>

The aromatic region of the  $^1\text{H}$  NMR spectrum of intermediate **18** identifies the compound (**figure 65**, top). The successful exchange of the fluorine atom for the donor unit is observed with the presence of 3 signals (6H) referring to the hydrogens of the 3,6-substituted carbazole unit (confirmed by the triplet at 4.56 ppm) and 2 signals (4H) referring to the 1,4-substituted benzene ring. By directly comparing the spectra of **18** and **19** (**figure 65**), it is possible to observe a characteristic low field shift of one doublet from 8.51 ppm (**18**) to 8.85 ppm (**19**).



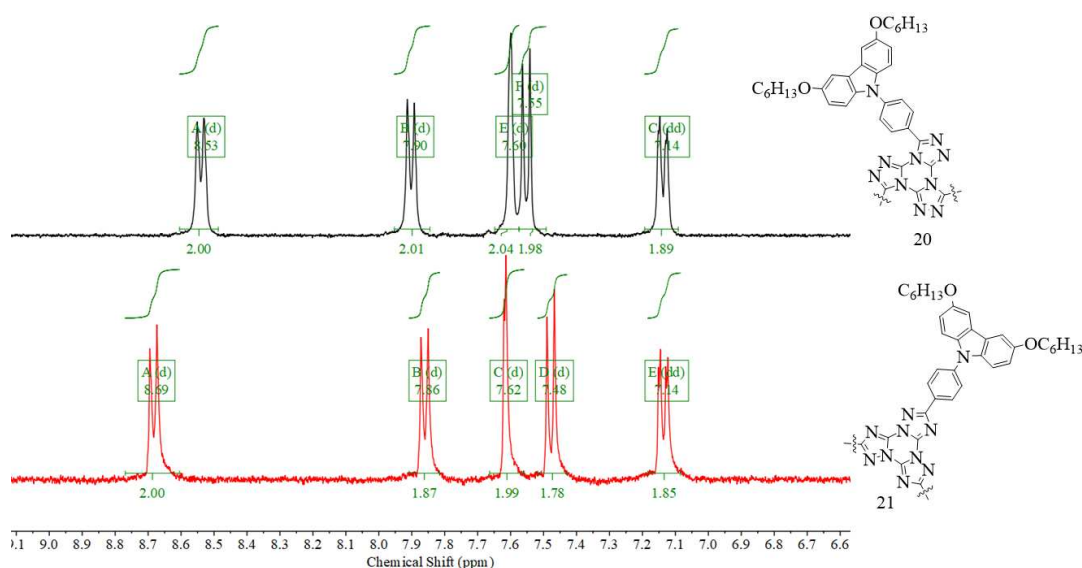
**Figure 65** <sup>1</sup>H NMR spectrum of intermediates **18** and **19** (400 MHz, DMSO-d<sub>6</sub>).

This tetrazolization is confirmed by the IR spectrum (**figure 66**). The absence of the stretching band at 2.200 cm<sup>-1</sup> in the spectrum of **19** confirms the absence of the nitrile group in the molecule.



**Figure 66** IR spectrum of intermediates **18** and **19**. Monitoring CN stretch band.

To characterize the final molecule **20**, the  $^1\text{H}$  NMR spectrum alone (annex section) was not enough because, in essence, it is the same spectrum as the intermediate **19**. Mass spectrometry was crucial for adequately characterizing the material (see annex section). The thermal isomerization of compound **20** into its isomer **21** is quickly followed by  $^1\text{H}$  NMR (figure 67). Using the same deuterated solvent during the spectra acquisition enable us to directly compare the chemical shifts of the signals in the aromatic region of the  $^1\text{H}$  NMR spectrum. For example, the doublet at 8.53 ppm (**20**) shifts to 8.69 ppm (**21**) after isomerization, as observed in the literature.



**Figure 67**  $^1\text{H}$  NMR spectrum of the final molecules **20** and **21** (400 MHz,  $\text{C}_2\text{D}_2\text{Cl}_4$ ).

Analysis of the isomers **20** and **21** in polarized light optical microscopy did not reveal any liquid-crystalline behavior. These materials showed only a solid-liquid phase transition during heating of the sample (liquid-solid on cooling).

#### 4.3 CONCLUSIONS

Triphenanthryl-triazine-hexaesters (TaPhenEst) with alkyl ester substituents longer than ethyl, for example, TaPhenPr and TaPhenBu, have been found to exhibit enantiotropic hexagonal columnar mesophases that can be cooled without crystallization to form a mesomorphic glass. The glass transition temperature strongly depends on the length of the chain, with the Tg of the shorter propyl homolog TaPhenPr being approximately 60°C higher than that of TaPhenBu. As a result, a glassy state at and above room temperature can only be

obtained with very short alkyl chains, which require clearing temperatures above 375°C that are not easily attainable.

To manage this, larger but less planar tris[4]helicenyl-triazine-hexaesters, Ta[4]HelEst, have been designed and synthesized. When combined with short alkyl chains, these compounds yield monotropic hexagonal columnar mesophases with melting and clearing temperatures that can be conveniently attained. In the case of Ta[4]HelBu, the glass transition temperature is also improved by 20°C compared to its phenanthryl analog TaPhenBu. Upon cooling, the shorter-chain homolog Ta[4]HelPr does not show a glass transition but instead exhibits an unusual and intriguing first-order transition to a second hexagonal columnar mesophase with an extremely well-ordered hexagonal column lattice.

A molecular design based on configurational flexibility, a well-dosed intrinsic deviation from planarity, and short alkyl ester substituents is shown to enable the stabilization of a solid-like hexagonal columnar mesophase at room temperature and an accessible transition to the isotropic liquid, allowing for the formation of surface-aligned samples by cooling from the liquid.

Combining mesomorphism with thermally activated delayed fluorescence (TADF) has proven to be a challenging task due to the opposing structural characteristics of these materials. While we have successfully synthesized discotic molecules with a mesogen-based structure (consisting of an aromatic center surrounded by aliphatic chains), none displayed the desired liquid crystalline behavior. This is likely due to the lack of planarity in these molecules, which is caused by the torsion angles between the donor and acceptor units. These angles hinder the interaction between the molecules, preventing the formation of mesophases.

Recently, a new strategy for combining the properties of mesomorphism and TADF has been reported, although the combination has yet to be achieved efficiently.<sup>49,147–149</sup> The authors demonstrated that designing a molecule with a portion responsible for mesomorphism and another for TADF emission is the key to successfully combining these properties. Based on this, we suggest synthesizing asymmetric molecules based on the TTT core and triazine, where we can combine two arms with mesogenic structures (e.g., acceptor core-phenylene-esters) and one arm with a TADF emission structure (e.g., acceptor core-bridge-donor) may be an effective way to combine mesomorphism with TADF efficiently.

## 5 EXPERIMENTAL DETAILS

### 5.1 TECHNIQUES AND EQUIPMENT

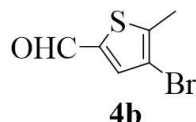
All reagents were acquired in analytical grade from commercial sources (Fluorochem, Sigma-Aldrich, BLD Pharm, abcr, TCI, WWR chemicals) and used without previous purification. Dry toluene was obtained via a solvent purification system from Innovative Technology. All synthesized compounds were generally purified by recrystallization in P.A. grade solvents or column chromatography under compressed air on silica (pore size 60Å, particle size 35-75 µm). <sup>1</sup>H and <sup>13</sup>C NMR spectra were obtained on a JEOL ECS-40 spectrometer operating at 400 MHz and 101 MHz, respectively. Infrared spectroscopy analyses were obtained on a Nicolet Is50 FTIR spectrometer. Mass spectra were performed on a QStar Elite mass spectrometer (Applied Biosystems) in positive mode. Thermal stability of the emitters was investigated by TGA using a TA discovery equipment with a TGA 5500 module and a heating rate of 10 °C min<sup>-1</sup> and N<sub>2</sub> flow of 25 mL min<sup>-1</sup>. Cyclic voltammetry was performed in a three-electrode cell, utilizing an Autolab PGStat101 potentiostat, driven by NOVA 2.1.4 software, a platinum wire counter electrode, a 1.6mm platinum disc working electrode, and a non-aqueous reference electrode comprised of a silver wire in a 0.01 M solution of AgNO<sub>3</sub> and 0.1 M tetrabutylammonium perchlorate in acetonitrile; the analytes were dissolved in DMF supplemented with 0.1 M tetrabutylammonium hexafluorophosphate. Ground state geometries of the molecules were optimized in a vacuum, using the Orca 5.0.3 software package within B3LYP/ Def2-SVP level of theory. Dispersion effects were included using Grimme's D3 correction with Becke-Johnson (BJ) damping. The evaluation of the four-center integrals was accelerated with the RIJCOSX algorithm. RIJ requires the specification of an auxiliary basis set for the Coulomb part (Def2/J) and a numerical integration grid for the exchange part (DefGrid-2). Analytical harmonic vibrational frequency calculations were conducted to verify if the ground state is a minimum on the potential energy surface. TD-DFT/TDA was employed to obtain the first 30 singlets, using the same calculation protocol, differing only at the functional, which in this case was CAM-B3LYP. The same calculation protocol was used to optimize the S1 state geometry. The first triplet was optimized from the ground state of a UKS calculation. To include solvent effects in the excited state energies, a conductor-like polarizable continuum model (CPCM) was used, using toluene. Using quasi-degenerate perturbation theory, SOC was included on top of the TD-DFT results. The SOC integrals used here are calculated using a mean-field named RISOMF(1X), described

elsewhere. Images of the complex geometries were obtained using the Chemcraft program ([www.chemcraftprog.com](http://www.chemcraftprog.com)).

## 5.2 SYNTHESIS

### 5.2.1 Emitters

4-bromo-5-methylthiophene-2-carbaldehyde (**4b**):



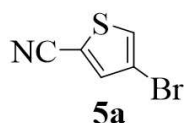
A mixture of bromine (5 mL, 97 mmol) and acetic acid (25 mL) was added slowly via an addition funnel to a stirred mixture of 5-methylthiophene-2-carbaldehyde (9.97 g, 79 mmol) and acetic acid (50 mL), and the system was left under stirring at room temperature overnight. After this period, the solution was taken to an ice bath, and 200 mL of a saturated aqueous sodium sulfite solution was added. The precipitate formed was washed with water yielding 9.75 g (48 mmol, 60%) of an orange solid.  $^1\text{H NMR}$  (400 MHz, tetrachloroethane- $d_2$ )  $\delta$  9.75 (s, 1H), 7.63 (s, 1H), 2.50 (s, 3H).  $^{13}\text{C NMR}$  (101 MHz, chloroform- $d$ )  $\delta$  181.7, 145.9, 140.2, 138.8, 111.3, 16.0. **IR**:  $\nu_{\text{max}}$  ( $\text{cm}^{-1}$ ) = 3304, 3097, 3087, 2844, 2804, 2769, 1887, 1694, 1662, 1566, 1510, 1407, 1374, 1317, 1226, 1163, 1080, 875, 842, 822, 782, 703, 660, 576, 480, 461.

#### **General procedure for the synthesis of bromo-thiophene-carbonitriles:**

In a 500mL round bottom flask were added bromo-thiophene-carbaldehyde (52.3 mmol), 30% aqueous  $\text{NH}_4\text{OH}$  (130 mL), and THF (140 mL). After 10 min of vigorous stirring, iodine (14.6g, 57.5 mmol) was added. The mixture was left under stirring at room temperature for 3 hours. After this period, more iodine (11.0g, 43.4 mmol) was added and the mixture was left to react for another 2 hours. Saturated aqueous sodium bisulfite solution (200mL) was added, and the organic phase was extracted with diethyl ether and washed with water and saturated NaCl solution. The organic phase was dried with anhydrous magnesium sulfate and concentrated at a rotary evaporator. The crude product was recrystallized in petroleum ether.

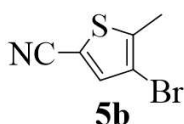


4-bromothiophene-2-carbonitrile (**5a**).



8.1 g (43 mmol, 82%) of a white solid.  $^1\text{H NMR}$  (400 MHz, chloroform-*d*)  $\delta$  7.52 (d,  $J = 1.4$  Hz, 1H), 7.49 (d,  $J = 1.4$  Hz, 1H).  $^{13}\text{C NMR}$  (101 MHz, chloroform-*d*)  $\delta$  139.4, 129.8, 112.8, 111.5, 110.9. **IR**:  $\nu_{\text{max}}$  ( $\text{cm}^{-1}$ ) = 3117, 3096, 3088, 2217, 1706, 1533, 1501, 1400, 1332, 1218, 1187, 1159, 1138, 1108, 1076, 874, 862, 853, 824, 765, 752, 710, 575, 528, 507, 487, 409.

4-bromo-5-methylthiophene-2-carbonitrile (**5b**).

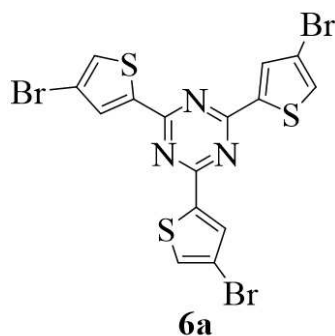


14.2 g (70 mmol, 72%) of a white solid.  $^1\text{H NMR}$  (400 MHz, tetrachloroethane-*d*<sub>2</sub>)  $\delta$  7.48 (s, 1H), 2.46 (s, 3H).  $^{13}\text{C NMR}$  (101 MHz, chloroform-*d*)  $\delta$  142.7, 139.6, 113.3, 110.3, 107.3, 15.2. **IR**:  $\nu_{\text{max}}$  ( $\text{cm}^{-1}$ ) = 3086, 2915, 2215, 1730, 1519, 1442, 1325, 1179, 1164, 1128, 1081, 999, 863, 798, 715, 669, 590, 539, 508, 450, 434.

### General procedure of triazines synthesis.

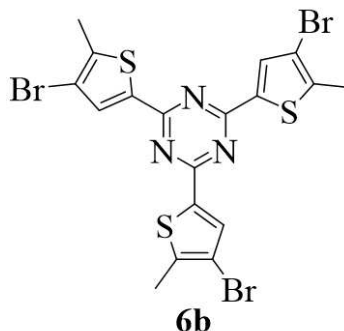
In a 25mL round bottom flask equipped with a gas collector and an ice bath, nitrile compound (26.6 mmol) and trifluoromethanesulfonic acid (8 mL, 90.6 mmol) were added, leaving under stirring at room temperature overnight. After this period, the solution was poured into water and ice. The precipitate was filtered, washed with water, and subsequently purified by column chromatography on silica.

2,4,6-*tris*(4-bromothiophen-2-yl)-1,3,5-triazine (**6a**).



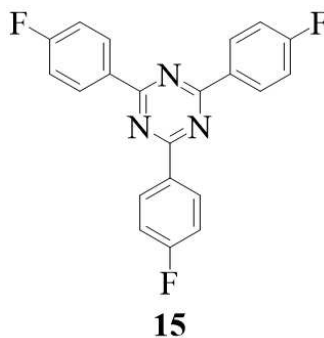
Eluent: chloroform. Yield 10 g (67%) of a yellowish solid.  $^1\text{H NMR}$  (400 MHz, tetrachloroethane- $d_2$ )  $\delta$  8.14 (d,  $J = 1.5$  Hz, 1H), 7.58 (d,  $J = 1.5$  Hz, 1H).  $^{13}\text{C NMR}$  (101 MHz, tetrachloroethane- $d_2$ )  $\delta$  166.9, 141.5, 133.9, 129.9, 111.3. **IR:**  $\nu_{\text{max}}$  ( $\text{cm}^{-1}$ ) = 3097, 1526, 1501, 1404, 1366, 1318, 1178, 1120, 1067, 992, 976, 873, 860, 829, 814, 792, 772, 751, 682, 667, 651, 578, 497, 429.

2,4,6-tris(4-bromo-5-methylthiophen-2-yl)-1,3,5-triazine (**6b**).



Eluent: chloroform. Yield 9.9g (55%) of an orange solid.  $^1\text{H NMR}$  (400 MHz, tetrachloroethane- $d_2$ )  $\delta$  8.08 (s, 1H), 2.57 (s, 3H).  $^{13}\text{C NMR}$  (101 MHz, tetrachloroethane- $d_2$ )  $\delta$  166.7, 142.5, 137.6, 134.1, 111.0, 15.1. **IR:**  $\nu_{\text{max}}$  ( $\text{cm}^{-1}$ ) = 3098, 2914, 1506, 1451, 1394, 1369, 1286, 1143, 1101, 1023, 997, 857, 809, 793, 767, 711, 611, 589, 540, 509, 428, 419.

2,4,6-tris(4-fluorophenyl)-1,3,5-triazine (**15**).

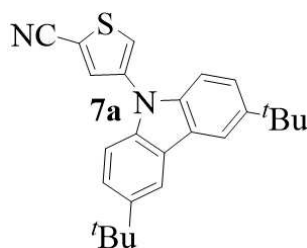


Eluent: chloroform. Yield 8.5g (75%) of white solid.  $^1\text{H NMR}$  (400 MHz, tetrachloroethane- $d_2$ )  $\delta$  8.83 – 8.73 (m, 6H), 7.33 – 7.25 (m, 6H).  $^{13}\text{C NMR}$  (101 MHz, tetrachloroethane- $d_2$ )  $\delta$  170.7, 167.0, 164.5, 132.3, 131.1, 115.3. **IR:**  $\nu_{\text{max}}$  ( $\text{cm}^{-1}$ ) = 3072, 1907, 1600, 1519, 1503, 1411, 1357, 1287, 1220, 1157, 1140, 1095, 1013, 948, 856, 804, 786, 635, 578, 507, 452.

**General procedure for the synthesis of the (3,6-di-tert-butyl-9H-carbazol-9-yl)-thiophene-carbonitriles:**

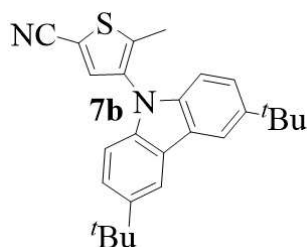
In a 100 mL two-neck round bottom flask, bromo-thiophene-carbonitrile (10.63 mmol), 3,6-di-tert-butyl-9H-carbazole (2.46 g, 8.83 mmol), potassium carbonate (1.46 g, 10.63 mmol), copper sulfate pentahydrate (0.11 g, 0.45 mmol), and 1-methylnaphthalene (10 mL) were added. After flushing with argon three times, the mixture is held at 250°C for 24h. After cooling down, the reaction is poured into a mixture of dichloromethane and water (1:1 v/v, 30 mL). The organic phase is separated, dried with magnesium sulfate, and concentrated. The crude product is purified by column chromatography on silica.

4-(3,6-di-tert-butyl-9H-carbazol-9-yl)thiophene-2-carbonitrile (**7a**).



Eluent: n-hexane:chloroform 1:1 (v/v). Yield 1.64g (4.24 mmol, 48%) of white solid. <sup>1</sup>H NMR (400 MHz, chloroform-*d*) δ 8.12 (d, *J* = 1.9 Hz, 2H), 7.88 (d, *J* = 1.5 Hz, 1H), 7.69 (d, *J* = 1.5 Hz, 1H), 7.50 (dd, *J* = 8.7, 1.9 Hz, 2H), 7.32 (d, *J* = 8.7, 2H), 1.47 (s, 18H). <sup>13</sup>C NMR (101 MHz, chloroform-*d*) δ 144.0, 138.8, 137.0, 134.9, 124.9, 124.2, 123.6, 116.6, 113.8, 110.7, 109.0, 34.9, 32.0. IR: ν<sub>max</sub> (cm<sup>-1</sup>) = 3093, 2960, 2902, 2866, 2213, 1706, 1543, 1473, 1437, 1388, 1359, 1310, 1295, 1188, 1176, 1149, 1113, 1074, 1057, 1036, 1001, 920, 904, 879, 867, 842, 821, 808, 772, 753, 739, 709, 697, 612, 577, 541, 523, 511, 486, 465, 424.

4-(3,6-di-tert-butyl-9H-carbazol-9-yl)-5-methylthiophene-2-carbonitrile (**7b**).



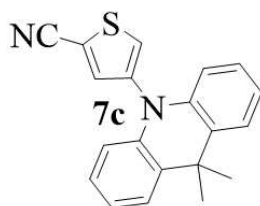
Eluent n-hexane:chloroform 1:2 (v/v). Yield 1.2g (2.99 mmol, 34%) of a light-orange solid. <sup>1</sup>H NMR (400 MHz, chloroform-*d*) δ 8.15 (d, *J* = 1.9 Hz, 2H), 7.59 (s, 1H), 7.48 (dd, *J* = 8.6, 1.9 Hz, 2H), 7.01 (d, *J* = 8.6, 2H), 2.30 (s, 3H), 1.47 (s, 18H). <sup>13</sup>C NMR (101 MHz, chloroform-*d*) δ 143.6, 143.4, 139.2, 136.9, 133.2, 124.1, 123.4, 116.6, 114.0, 109.0, 106.5, 34.9, 32.1, 13.5.

**IR:**  $\nu_{\max}$  ( $\text{cm}^{-1}$ ) = 2958, 2902, 2866, 2217, 1704, 1543, 1473, 1437, 1388, 1359, 1310, 1295, 1188, 1176, 1149, 1113, 1074, 1057, 1036, 1001, 920, 904, 879, 867, 842, 821, 808, 772, 753, 739, 709, 697, 612, 577, 541, 523, 511, 486, 465, 424.

**General procedure for the synthesis of the (9,9-dimethylacridin-10(9H)-yl)-thiophene-carbonitriles:**

In a 100mL two-neck round bottom flask, bromo-thiophene-carbonitrile (4.2 mmol) and 9,9-dimethyl-9,10-dihydroacridine (1.05 g, 5.0 mmol) were added. After flushing with argon three times, dry toluene (40 mL), palladium (II) acetate (0.05g, 0.2 mmol), Xphos (0.2 g, 0.4 mmol), and sodium tert-butoxide (0.60 g, 6.3 mmol) were added. The mixture was stirred and refluxed overnight. After cooling down, dichloromethane (100 mL) is added and filtered over silica. The organic phase is washed with water, separated, dried with magnesium sulfate, and concentrated. The crude product is purified by column chromatography on silica.

4-(9,9-dimethylacridin-10(9H)-yl)thiophene-2-carbonitrile (**7c**).



Eluent n-hexane:ethyl acetate 9:1 (v/v). Yield 560 mg (1.76 mmol, 42%) of a light-yellow solid.  $^1\text{H NMR}$  (400 MHz, chloroform-*d*)  $\delta$  7.65 (d,  $J = 1.6$  Hz, 1H), 7.64 (d,  $J = 1.6$  Hz, 1H), 7.47 (dd,  $J = 7.6, 1.7$  Hz, 2H), 7.10 – 6.96 (m, 4H), 6.32 (dd,  $J = 8.0, 1.3$  Hz, 2H), 1.67 (s, 6H).  $^{13}\text{C NMR}$  (101 MHz, chloroform-*d*)  $\delta$  140.2, 139.9, 139.1, 132.0, 130.9, 126.8, 125.5, 121.8, 113.9, 113.6, 111.8, 36.1, 31.0. **IR:**  $\nu_{\max}$  ( $\text{cm}^{-1}$ ) = 3099, 3083, 2961, 2921, 2850, 2220, 1591, 1526, 1501, 1474, 1462, 1447, 1423, 1381, 1355, 1318, 1269, 1255, 1185, 1163, 1115, 1083, 1047, 998, 935, 923, 882, 875, 867, 850, 818, 766, 747, 691, 674, 657, 582, 542, 517, 506, 494, 481, 462, 435.

4-(9,9-dimethylacridin-10(9H)-yl)-5-methylthiophene-2-carbonitrile (**7d**).

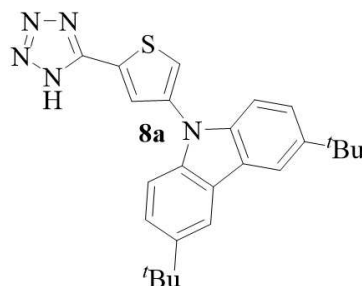


Eluent n-hexane:ethyl acetate 9:1 (v/v). Yield 750 mg (2.27 mmol, 46%) of a light orange solid.  $^1\text{H NMR}$  (400 MHz, tetrachloroethane- $d_2$ )  $\delta$  7.57 (s, 1H), 7.49 (dd,  $J = 7.6, 1.6$  Hz, 2H), 7.11 – 6.96 (m, 4H), 6.23 (dd,  $J = 8.1, 1.4$  Hz, 2H), 2.29 (s, 3H), 1.68 (s, 6H).  $^{13}\text{C NMR}$  (101 MHz, chloroform- $d$ )  $\delta$  142.9, 135.8, 132.5, 127.0, 123.5, 122.2, 118.1, 110.5, 109.6, 103.7, 32.5, 27.8, 9.3. **IR:**  $\nu_{\text{max}}$  ( $\text{cm}^{-1}$ ) = 3091, 2955, 2914, 2855, 2219, 1589, 1526, 1501, 1474, 1462, 1447, 1423, 1381, 1355, 1318, 1269, 1255, 1185, 1163, 1115, 1083, 1047, 998, 935, 923, 882, 875, 867, 850, 818, 766, 747, 691, 674, 657, 582, 542, 517, 506, 494, 481, 462, 435.

### General procedure for synthesis of 5-substituted tetrazoles.

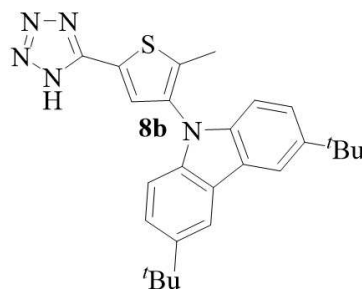
In a 250 mL round bottom flask, 4-substituted-thiophene-2-carbonitrile (2.6 mmol), sodium azide (0.55 g, 8.5 mmol), ammonium chloride (0.45 g, 8.5 mmol), and dimethylformamide (50 mL) were added. The mixture was heated to 90°C overnight. After cooling, the reaction mixture is poured into water and ice. Concentrated HCl is added until complete precipitation of the product. The solid is filtered and washed with excess water. The solid obtained is purified by chromatographic column.

9-(5-(1H-tetrazol-5-yl)thiophen-3-yl)-3,6-di-tert-butyl-9H-carbazole (**8a**).

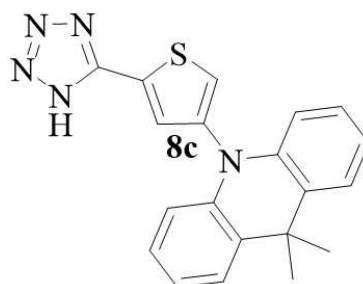


Eluent ethyl acetate. Yield 980 mg (2.28 mmol, 88%) of a white solid.  $^1\text{H NMR}$  (400 MHz, DMSO- $d_6$ )  $\delta$  8.28 (d,  $J = 1.9$  Hz, 2H), 7.82 (d,  $J = 1.6$  Hz, 1H), 7.80 (d,  $J = 1.6$  Hz, 1H), 7.49 (dd,  $J = 8.6, 1.9$  Hz, 2H), 7.43 (d,  $J = 8.6$  Hz, 2H), 1.40 (s, 18H).  $^{13}\text{C NMR}$  (101 MHz, DMSO- $d_6$ )  $\delta$  154.9, 142.8, 138.5, 135.5, 132.9, 123.9, 122.8, 122.1, 119.0, 116.7, 109.5, 34.6, 31.9. **IR:**  $\nu_{\text{max}}$  ( $\text{cm}^{-1}$ ) = 3331, 2958, 2865, 1607, 1514, 1488, 1470, 1419, 1391, 1362, 1326, 1298, 1263, 1234, 1203, 1185, 1106, 1074, 1035, 1002, 964, 910, 900, 877, 842, 809, 762, 740, 611, 576, 469.

3,6-di-tert-butyl-9-(2-methyl-5-(1H-tetrazol-5-yl)thiophen-3-yl)-9H-carbazole (**8b**).

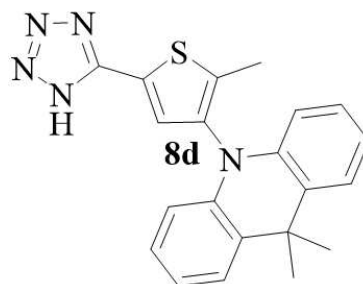


Eluent ethyl acetate. Yield 950 mg (2.14 mmol, 83%) of a yellowish solid.  $^1\text{H NMR}$  (400 MHz,  $\text{DMSO-}d_6$ )  $\delta$  8.31 (d,  $J = 1.9$  Hz, 2H), 7.76 (s, 1H), 7.49 (dd,  $J = 8.6, 1.9$  Hz, 2H), 7.13 (d,  $J = 8.6$  Hz, 2H), 2.27 (s, 3H), 1.42 (s, 18H).  $^{13}\text{C NMR}$  (101 MHz,  $\text{DMSO-}d_6$ )  $\delta$  151.2, 142.7, 138.8, 138.6, 132.6, 127.7, 123.9, 122.8, 122.3, 116.9, 109.3, 34.6, 31.9, 12.9. **IR:**  $\nu_{\text{max}}$  ( $\text{cm}^{-1}$ ) = 3403, 2960, 2465, 1630, 1605, 1540, 1498, 1427, 1392, 1363, 1324, 1294, 1261, 1235, 1203, 1153, 1143, 1104, 1066, 1035, 978, 952, 939, 895, 815, 743, 709, 665, 610, 572, 543, 526, 469. 10-(5-(1H-tetrazol-5-yl)thiophen-3-yl)-9,9-dimethyl-9,10-dihydroacridine (**8c**).



Eluent ethyl acetate. Yield 755 mg (2.10 mmol, 81%) of a white solid.  $^1\text{H NMR}$  (400 MHz,  $\text{DMSO-}d_6$ )  $\delta$  8.09 (d,  $J = 1.6$  Hz, 1H), 7.76 (d,  $J = 1.6$  Hz, 1H), 7.50 (dd,  $J = 7.8, 1.6$  Hz, 2H), 7.12 – 6.90 (m, 4H), 6.43 (dd,  $J = 8.1, 1.4$  Hz, 2H), 1.61 (s, 6H).  $^{13}\text{C NMR}$  (101 MHz,  $\text{DMSO-}d_6$ )  $\delta$  151.3, 140.0, 139.2, 130.3, 129.9, 129.7, 127.3, 126.8, 125.4, 121.3, 113.8, 54.9, 35.6, 30.9. **IR:**  $\nu_{\text{max}}$  ( $\text{cm}^{-1}$ ) = 3634, 3098, 2950, 1636, 1590, 1507, 1473, 1447, 1397, 1383, 1358, 1319, 1271, 1258, 1249, 1181, 1113, 1086, 1046, 998, 957, 921, 875, 861, 772, 743, 674, 649, 582, 513, 433, 406.

9,9-dimethyl-10-(2-methyl-5-(1H-tetrazol-5-yl)thiophen-3-yl)-9,10-dihydroacridine (**8d**).

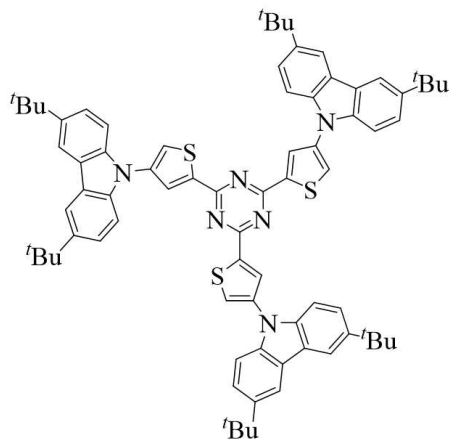


Eluent ethyl acetate. Yield 767 mg (2.05 mmol, 79%) of a pale orange solid.  $^1\text{H NMR}$  (400 MHz, tetrachloroethane- $d_2$ )  $\delta$  7.69 (s, 1H), 7.48 (dd,  $J = 7.7, 1.7$  Hz, 2H), 7.10 – 6.93 (m, 4H), 6.38 (dd,  $J = 8.1, 1.3$  Hz, 2H), 2.30 (s, 3H), 1.68 (s, 6H).  $^{13}\text{C NMR}$  (101 MHz, DMSO- $d_6$ )  $\delta$  151.0, 141.6, 139.0, 135.6, 129.9, 129.7, 127.0, 125.7, 123.0, 121.2, 113.0, 35.5, 30.6, 12.2. **IR**:  $\nu_{\text{max}}$  ( $\text{cm}^{-1}$ ) = 3650, 3190, 2967, 1666, 1591, 1531, 1500, 1473, 1446, 1383, 1358, 1329, 1270, 1249, 1162, 1114, 1043, 1022, 948, 920, 851, 745, 685, 640, 582, 514, 457, 433.

**General procedure for the synthesis of the final molecules 2,4,6-tris(3,6-di-tert-butyl-9H-carbazol-9-yl)-1,3,5-triazine (TaCz).**

In a 100 mL two-neck round bottom flask bromo-thiophene-triazine (1.77 mmol), 3,6-di-tert-butyl-9H-carbazole (1.60 g, 5.84 mmol), potassium carbonate (0.96 g, 7.0 mmol), copper sulfate pentahydrate (0.07g, 0.3 mmol), and 1-methylnaphthalene (10 mL) were added. After flushing with argon three times, the mixture is held at 250°C for 24h. After cooling down, the reaction is poured into a mixture of dichloromethane and water (1:1 v/v, 30 mL). The organic phase is separated, dried with magnesium sulfate, and concentrated. The crude product is purified by column chromatography on silica.

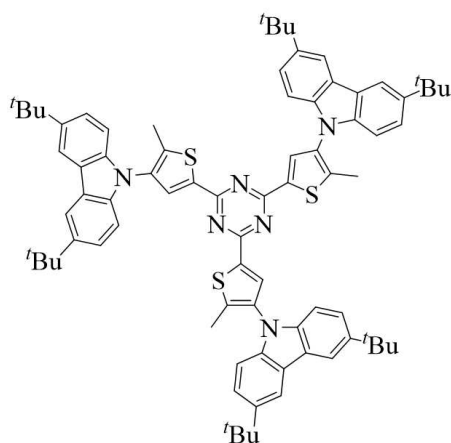
2,4,6-*tris*(4-(3,6-di-*tert*-butyl-9H-carbazol-9-yl)thiophen-2-yl)-1,3,5-triazine (**1a**).



**1a**

Eluent n-hexane:chloroform 4:1 (v/v). Yield 1.06 g (0.91 mmol, 52%) of a light-yellow solid.  $^1\text{H NMR}$  (400 MHz, chloroform-*d*)  $\delta$  8.50 (d,  $J = 1.6$  Hz, 1H), 8.14 (d,  $J = 1.8$  Hz, 2H), 7.74 (d,  $J = 1.6$  Hz, 1H), 7.51 (dd,  $J = 8.6, 1.8$  Hz, 2H), 7.44 (d,  $J = 8.6$  Hz, 2H), 1.47 (s, 18H).  $^{13}\text{C NMR}$  (101 MHz, tetrachloroethane-*d*<sub>2</sub>)  $\delta$  167.3, 143.3, 140.9, 138.8, 137.2, 129.3, 125.9, 124.0, 122.9, 116.2, 109.3, 34.6, 31.9. **FTMS-ESI (+)**:  $m/z$  for  $\text{C}_{75}\text{H}_{78}\text{N}_6\text{S}_3\text{Na}$   $[\text{M}+\text{Na}]^+$  calcd. 1181.53423, found 1181.53066.

2,4,6-*tris*(4-(3,6-di-*tert*-butyl-9H-carbazol-9-yl)-5-methylthiophen-2-yl)-1,3,5-triazine (**1b**).



**1b**

Eluent n-hexane:chloroform 2:1 (v/v). Yield 700 mg (0.6 mmol, 39%) of a light-yellow solid.  $^1\text{H NMR}$  (400 MHz, chloroform-*d*)  $\delta$  8.17 (s, 1H), 8.13 (d,  $J = 1.9$ , 2H), 7.47 (dd,  $J = 8.7, 1.9$  Hz, 2H), 7.12 (d,  $J = 8.7$ , 2H), 2.31 (s, 3H), 1.46 (s, 18H).  $^{13}\text{C NMR}$  (101 MHz, tetrachloroethane-*d*<sub>2</sub>)  $\delta$  166.9, 143.2, 142.8, 139.2, 136.6, 133.6, 131.1, 123.8, 122.7, 116.1,

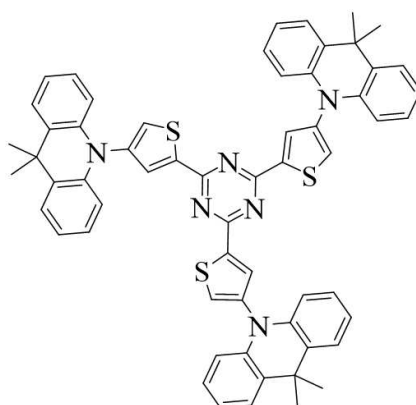


109.3, 34.5, 31.9, 13.7. **FTMS-ESI (+):**  $m/z$  for  $C_{78}H_{84}N_6S_3Na$   $[M+Na]^+$  calcd. 1223.58118, found 1223.57568.

**General procedure for the synthesis of the final molecules 2,4,6-tris(9,9-dimethylacridin-10(9H)-yl)-1,3,5-triazine (TaDMAc).**

In a 100 mL two-neck round bottom flask bromo-thiophene-triazine (1.68 mmol), 9,9-dimethyl-9,10-dihydroacridine (1.16 g, 5.57 mmol) were added. After flushing of argon three times dry toluene (50 mL), palladium (II) acetate (0.02 g, 0.1 mmol), Xphos (0.08 g, 0.17 mmol), and sodium tert-butoxide (0.55 g, 5.79 mmol) were added. The mixture was stirred and refluxed overnight. After cooling down, dichloromethane (100 mL) is added and filtered over silica. The organic phase is washed with water, separated, dried with magnesium sulfate, and concentrated. The crude product is purified by column chromatography on silica.

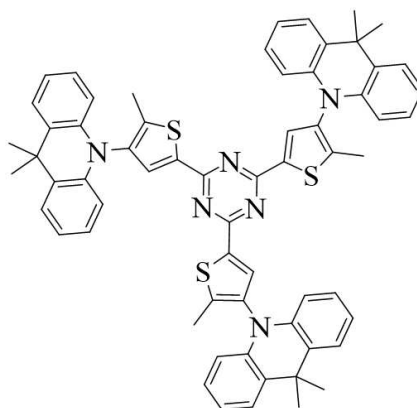
2,4,6-*tris*(4-(9,9-dimethylacridin-10(9H)-yl)thiophen-2-yl)-1,3,5-triazine (**1c**).



**1c**

Eluent n-hexane:ethyl acetate 9:1 (v/v). Yield 910 mg (57%) of a yellowish solid. **<sup>1</sup>H NMR** (400 MHz, chloroform-*d*)  $\delta$  8.27 (d,  $J = 1.6$  Hz, 1H), 7.67 (d,  $J = 1.6$  Hz, 1H), 7.46 (dd,  $J = 7.8, 1.6$  Hz, 2H), 7.04 - 6.96 (m, 4H), 6.50 (dd,  $J = 8.1, 1.3$  Hz, 2H), 1.68 (s, 6H). **<sup>13</sup>C NMR** (101 MHz, chloroform-*d*)  $\delta$  167.4, 142.2, 140.6, 140.5, 134.0, 132.6, 130.5, 126.7, 125.4, 121.3, 114.1, 36.1, 31.2. **FTMS-ESI (+):**  $m/z$  for  $C_{60}H_{48}N_6S_3Na$   $[M+Na]^+$  calcd. 971.29948, found 971.29564.

2,4,6-*tris*(4-(9,9-dimethylacridin-10(9H)-yl)-5-methylthiophen-2-yl)-1,3,5-triazine (**1d**).



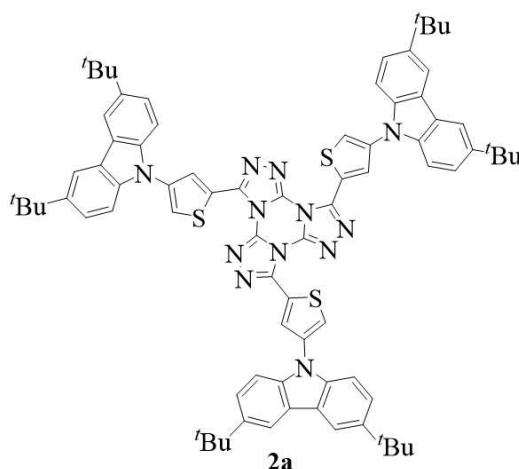
**1d**

Eluent n-hexane:ethyl acetate 9:1 (v/v). Yield 866 mg (0.87 mmol, 52%) of a light-yellow solid. **<sup>1</sup>H NMR** (400 MHz, tetrachloroethane-*d*<sub>2</sub>) δ 8.19 (s, 1H), 7.50 (dd, *J* = 7.7, 1.7 Hz, 2H), 7.11 - 6.95 (m, 4H), 6.47 (dd, *J* = 8.2, 1.5 Hz, 2H), 2.34 (s, 3H), 1.75 (s, 6H). **<sup>13</sup>C NMR** (101 MHz, chloroform-*d*) δ 167.1, 146.2, 139.8, 137.7, 136.9, 133.8, 130.3, 126.9, 125.6, 121.2, 113.6, 36.1, 32.4, 30.7, 13.3. **FTMS-ESI (+)**: *m/z* for C<sub>63</sub>H<sub>54</sub>N<sub>6</sub>S<sub>3</sub>Na [M+Na]<sup>+</sup> calcd. 1013.34643, found 1013.34350.

### General procedure for the synthesis of TTT compounds

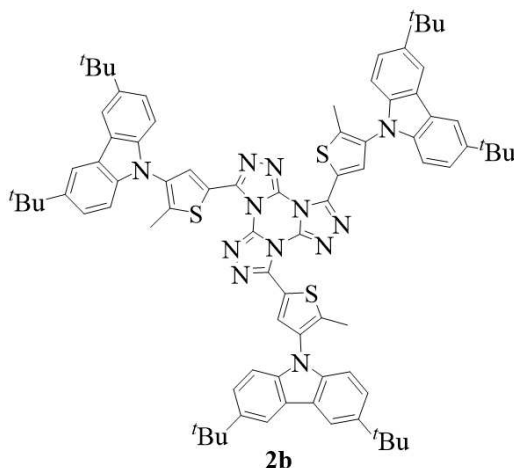
In a 100 mL two-neck round bottom flask, 5-substituted tetrazoles (2.1 mmol) and cyanuric chloride (0.11 g, 0.6 mmol) were added. After flushing with argon three times, dry toluene (40 mL) and 2,6-lutidine (0.45 g, 4.2 mmol) were added. The mixture is held at 90 °C overnight. After cooling down the reaction, 1M HCl (50 mL) is added. The organic phase is extracted with chloroform, dried with magnesium sulfate, and concentrated. The crude product is purified by column chromatography on silica.

3,7,11-*tris*(4-(3,6-di-*tert*-butyl-9H-carbazol-9-yl)thiophen-2-yl)*tris*([1,2,4]triazolo)[4,3-*a*:4',3'-*c*:4'',3''-*e*][1,3,5]triazine (**2a**).



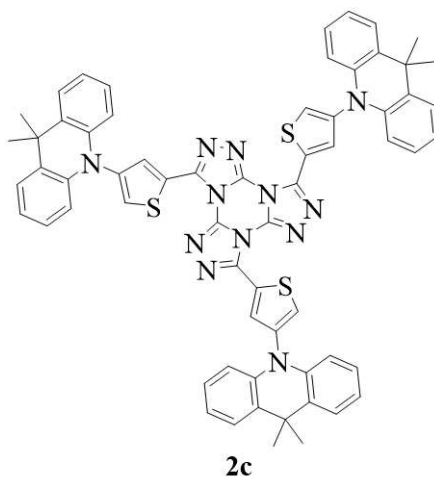
Eluent chloroform. Yield 310 mg (0.24 mmol, 38%) of a white solid.  $^1\text{H NMR}$  (400 MHz, tetrachloroethane- $d_2$ )  $\delta$  9.06 (d,  $J = 1.5$  Hz, 1H), 8.17 (d,  $J = 1.8$  Hz, 2H), 7.81 (d,  $J = 1.5$  Hz, 1H), 7.62 (d,  $J = 8.6$  Hz, 2H), 7.58 (dd,  $J = 8.6, 1.8$  Hz, 2H), 1.50 (s, 18H).  $^{13}\text{C NMR}$  (101 MHz, tetrachloroethane- $d_2$ )  $\delta$  145.8, 143.5, 139.8, 138.5, 136.8, 130.9, 124.5, 124.2, 123.2, 123.0, 116.2, 109.4, 34.6, 31.8. **FTMS-ESI (+)**:  $m/z$  for  $\text{C}_{78}\text{H}_{78}\text{N}_{12}\text{S}_3\text{Na}$   $[\text{M}+\text{Na}]^+$  calcd. 1301.55267, found 1301.54712.

3,7,11-*tris*(4-(3,6-di-*tert*-butyl-9H-carbazol-9-yl)-5-methylthiophen-2-yl)*tris*([1,2,4]triazolo)[4,3-*a*:4',3'-*c*:4'',3''-*e*][1,3,5]triazine (**2b**).



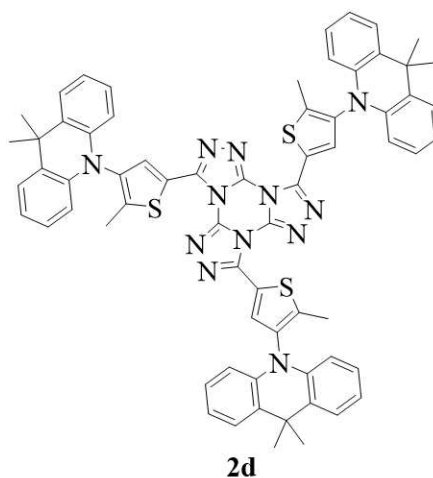
Eluent chloroform. Yield 260mg (0.19 mmol, 32%) of a white solid.  $^1\text{H NMR}$  (400 MHz, tetrachloroethane- $d_2$ )  $\delta$  8.78 (s, 1H), 8.22 (d,  $J = 2.7$  Hz, 2H), 7.57 (d,  $J = 8.5$  Hz, 2H), 7.25 (dd,  $J = 8.5, 2.7$  Hz, 2H), 2.42 (s, 3H), 1.57 (s, 18H).  $^{13}\text{C NMR}$  (101 MHz, tetrachloroethane- $d_2$ )  $\delta$

145.8, 142.9, 141.4, 139.6, 139.0, 133.1, 132.8, 123.9, 122.8, 120.6, 116.2, 109.3, 34.5, 31.9, 13.4. **FTMS-ESI (+)**:  $m/z$  for  $C_{81}H_{84}N_{12}S_3Na$   $[M+Na]^+$  calcd. 1343.59962, found 1343.59542. 3,7,11-*tris*(4-(9,9-dimethylacridin-10(9H)-yl)thiophen-2-yl)*tris*([1,2,4]triazolo)[4,3-*a*:4',3'-*c*:4'',3''-*e*][1,3,5]triazine (**2c**).



Eluent chloroform. Yield 400 mg (0.37 mmol, 39%) of a light orange solid.  **$^1H$  NMR** (400 MHz, chloroform-*d*)  $\delta$  8.91 (d,  $J = 1.4$  Hz, 1H), 7.65 (d,  $J = 1.4$  Hz, 1H), 7.48 (dd,  $J = 7.8, 1.6$  Hz, 2H), 7.11 – 6.91 (m, 4H), 6.53 (dd,  $J = 8.2, 1.3$  Hz, 2H), 1.72 (s, 6H).  **$^{13}C$  NMR** (101 MHz, tetrachloroethane-*d*<sub>2</sub>)  $\delta$  145.7, 140.4, 139.7, 135.2, 130.6, 130.4, 126.5, 125.6, 125.2, 121.2, 113.8, 35.8, 30.7. **FTMS-ESI (+)**:  $m/z$  for  $C_{63}H_{48}N_{12}S_3Na$   $[M+Na]^+$  calcd. 1091.31792, found 1091.31391.

3,7,11-*tris*(4-(9,9-dimethylacridin-10(9H)-yl)-5-methylthiophen-2-yl)*tris*([1,2,4]triazolo)[4,3-*a*:4',3'-*c*:4'',3''-*e*][1,3,5]triazine (**2d**).

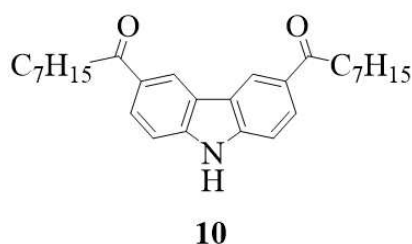


Eluent ethyl acetate. Yield 150 mg (0.13 mmol, 35%) of a light-yellow solid.  **$^1H$  NMR** (400 MHz, tetrachloroethane-*d*<sub>2</sub>)  $\delta$  8.76 (s, 1H), 7.52 (dd,  $J = 7.8, 1.6$  Hz, 2H), 7.17 – 6.94 (m, 4H),

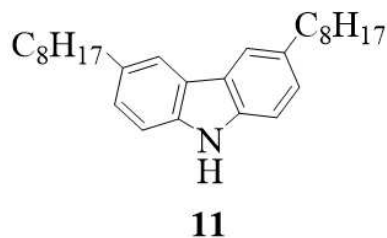
6.50 (dd,  $J = 8.1, 1.3$  Hz, 2H), 2.35 (s, 3H), 1.75 (s, 6H).  $^{13}\text{C}$  NMR (101 MHz, tetrachloroethane- $d_2$ )  $\delta$  145.8, 144.4, 139.6, 139.5, 135.9, 135.3, 130.2, 126.7, 125.3, 121.2, 121.1, 113.2, 35.8, 32.9, 29.2, 12.7. FTMS-ESI (+):  $m/z$  for  $\text{C}_{66}\text{H}_{54}\text{N}_{12}\text{S}_3\text{Na}$   $[\text{M}+\text{Na}]^+$  calcd. 1133.36487, found 1133.36061.

### 5.2.2 Aliphatic chains decorated emitters.

1,1'-(9H-carbazole-3,6-diyl)bis(octan-1-one) (**10**).

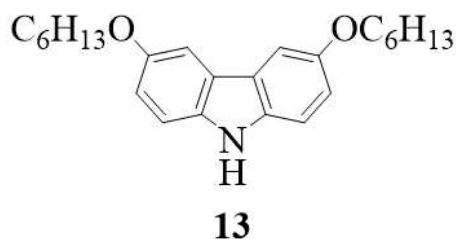


In a round bottom flask aluminum chloride (19.20 g, 144 mmol) and dichloromethane (200 mL) were added. The mixture was cooled to  $0^\circ\text{C}$  using an ice bath then octanoyl chloride (23.10 g, 142 mmol) was added slowly. After 10 minutes of stirring, 9H-carbazole (10 g, 59.8 mmol) was added to the mixture and left under stirring at room temperature overnight. The reaction is poured into a mixture of ice and 15% aqueous HCl (100 mL). The precipitate formed is filtered off and washed with acetone in excess. The crude product is purified by column chromatography on silica using chloroform as eluent. Yield 19.5g (46.50 mmol, 77%) of a white solid.  $^1\text{H}$  NMR (400 MHz, methylene chloride- $d_2$ )  $\delta$  8.82 (d,  $J = 1.8$  Hz, 2H), 8.70 (s, 1H), 8.13 (dd,  $J = 8.6, 1.8$  Hz, 2H), 7.55 (d,  $J = 8.6$ , 2H), 3.11 (t, 4H), 1.78 (q,  $J = 7.0$  Hz, 4H), 1.50 – 1.22 (m, 16H), 0.90 (t, 6H).  $^{13}\text{C}$  NMR (101 MHz, chloroform- $d$ )  $\delta$  200.4, 143.0, 130.2, 127.2, 123.5, 121.8, 111.0, 38.8, 31.9, 29.6, 29.4, 25.0, 22.8, 14.2. IR:  $\nu_{\text{max}}$  ( $\text{cm}^{-1}$ ) = 3278, 2952, 2917, 2852, 1665, 1618, 1597, 1585, 1468, 1457, 1407, 1357, 1305, 1285, 1273, 1241, 1224, 1193, 1164, 1146, 1132, 1108, 1000, 978, 896, 806, 768, 746, 719, 672, 637, 621, 521, 494, 471, 421. 3,6-dioctyl-9H-carbazole (**11**).



In a two-neck round bottom flask, aluminum chloride (10.30 g, 77.3 mmol) and THF (200 mL) were added. After flushing with argon three times, the mixture was cooled to 0°C. Lithium aluminum hydride (5.86 g, 154.5 mmol) was added slowly. After stirring for 5 min, a suspension under argon 1,1'-(9H-carbazole-3,6-diyl)bis(octan-1-one) (16.20 g, 38.6 mmol) in THF (150 mL) was added to the mixture and left under stirring at room temperature overnight. After dilution with ethyl acetate (350 mL), 5% aqueous HCl (200 mL) is added, and the mixture filtered over silica. The organic phase is dried with magnesium sulfate and concentrated. The crude product is purified by column chromatography on silica using n-hexane:chloroform 3:1 (v/v). Yield 8.3g (21.19 mmol, 55%) of a white solid. **<sup>1</sup>H NMR** (400 MHz, chloroform-*d*)  $\delta$  7.85 (d,  $J = 1.7$  Hz, 2H), 7.80 (s, 1H), 7.33 – 7.15 (m, 4H), 2.77 (t, 4H), 1.70 (q,  $J = 6.8$  Hz, 4H), 1.47 – 1.15 (m, 20H), 0.88 (t, 6H). **IR:**  $\nu_{\max}$  (cm<sup>-1</sup>) = 3394, 3017, 2916, 2846, 1630, 1611, 1575, 1495, 1464, 1447, 1363, 1312, 1302, 1266, 1241, 1191, 1169, 1144, 1113, 1067, 1023, 932, 915, 893, 881, 845, 812, 787, 778, 744, 728, 638, 596, 549, 532, 479, 460, 438.

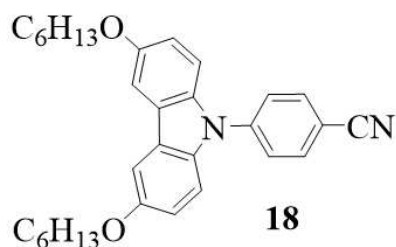
3,6-bis(hexyloxy)-9H-carbazole (**13**).



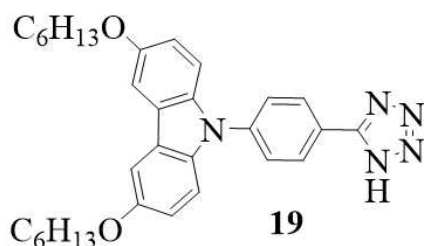
In a 100 mL two-bottom round bottom flask, sodium metallic (1.6 g, 69.5 mmol) and 1-hexanol (60 mL, 478.00 mmol) were added under argon flow. The mixture is heated to 90°C until total solubilization. In a 250 mL two-bottom round bottom flask, 3,6-dibromo-9H-carbazole (1 g, 3.1 mmol), copper iodide (2.35 g, 12.3 mmol), and DMF (60 mL) were added. After argon flushing three times, the sodium hexanolate solution is added to the carbazole suspension via a syringe. The mixture is refluxed for 24h. After cooling to room temperature, ethyl acetate (200 mL) is added and filtered over silica. The organic phase is washed with water, dried over magnesium sulfate, and concentrated. The product is precipitated and recrystallized in heptane. Yield 508 mg (1.38 mmol, 45%) of a white solid. **<sup>1</sup>H NMR** (400 MHz, methylene chloride-*d*<sub>2</sub>)  $\delta$  7.88 (s, 1H), 7.49 (d,  $J = 1.6$  Hz, 2H), 7.32 (dd,  $J = 8.8, 1.6$  Hz, 2H), 7.02 (d,  $J = 8.8$ , 2H), 4.30 – 3.71 (m, 4H), 1.83 (m, 4H), 1.70 – 1.24 (m, 12H), 0.93 (t, 6H). **<sup>13</sup>C NMR** (101 MHz, methylene chloride-*d*<sub>2</sub>)  $\delta$  153.7, 135.8, 124.2, 116.2, 112.0, 104.3, 69.5, 32.2, 30.1, 26.4, 23.2,

14.4. **IR:**  $\nu_{\max}$  ( $\text{cm}^{-1}$ ) = 3388, 2922, 2853, 1722, 1632, 1577, 1495, 1459, 1396, 1333, 1302, 1260, 1226, 1204, 1165, 1113, 1057, 1032, 950, 897, 831, 824, 808, 725, 644, 593, 424.

4-(3,6-bis(hexyloxy)-9H-carbazol-9-yl)benzotrile (**18**).



In a 150 mL two-bottomed round-bottom flask, 4-fluorobenzotrile (250 mg, 2.06 mmol), 3,6-bis(hexyloxy)-9H-carbazole (900 mg, 2.47 mmol), cesium carbonate (3.35 g, 10.30 mmol), and dimethylacetamide (40 mL) were added. After argon flushing three times, the mixture was refluxed for 24h. The mixture was colling down to room temperature and poured into cold water. The precipitate formed was filtered off and purified by column chromatography on silica. Eluent n-hexane:chloroform 3:2 (v/v). Yield 530 mg (1.13 mmol, 55%). **<sup>1</sup>H NMR** (400 MHz, DMSO- $d_6$ )  $\delta$  8.51 (d,  $J$  = 8.6 Hz, 2H), 8.33 (d,  $J$  = 8.6 Hz, 2H), 8.22 (d,  $J$  = 2.5 Hz, 2H), 7.92 (d,  $J$  = 9.0 Hz, 2H), 7.52 (dd,  $J$  = 9.0, 2.5 Hz, 2H), 4.56 (t,  $J$  = 6.5 Hz, 4H), 2.33 – 2.23 (m, 4H), 1.98 (p,  $J$  = 7.4 Hz, 4H), 1.90 – 1.77 (m, 8H), 1.42 – 1.33 (m, 6H). **<sup>13</sup>C NMR** (101 MHz, methylene chloride- $d_2$ )  $\delta$  154.8, 143.1, 135.6, 134.5, 126.8, 125.1, 119.1, 116.3, 111.1, 110.1, 104.5, 69.5, 32.2, 30.0, 26.4, 23.2, 14.4. **IR:**  $\nu_{\max}$  ( $\text{cm}^{-1}$ ) = 3076, 2917, 2869, 2851, 2227, 1683, 1629, 1603, 1509, 1490, 1460, 1403, 1374, 1325, 1256, 1200, 1179, 1162, 1128, 1106, 1060, 1026, 988, 911, 897, 863, 845, 825, 800, 764, 725, 665, 650, 613, 589, 552. 544, 445, 426, 409. 9-(4-(1H-tetrazol-5-yl)phenyl)-3,6-bis(hexyloxy)-9H-carbazole (**19**).



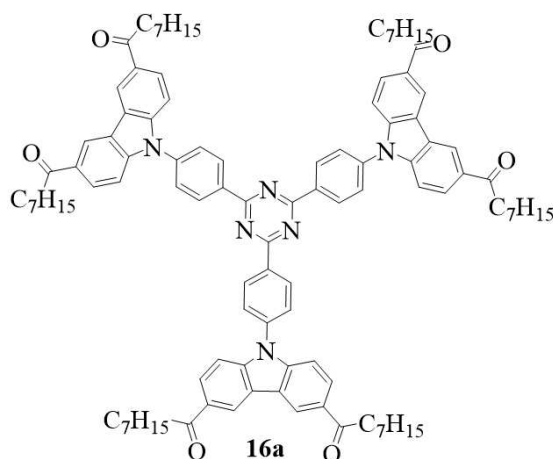
In a 250 mL round bottom flask, 4-(3,6-bis(hexyloxy)-9H-carbazol-9-yl)benzotrile (496 mg, 1.06 mmol), sodium azide (552 mg, 8.5 mmol), ammonium chloride (454 mg, 8.5 mmol), and dimethylformamide (50 mL) were added. The mixture was heated to 90°C overnight. After cooling, the reaction mixture is poured into water and ice. Concentrated HCl is added until complete precipitation of the product. The solid is filtered and washed with excess water. The

solid obtained is purified by chromatographic column on silica ethyl acetate as eluent. Yield 444 mg (0.86 mmol, 82%) of white solid.  $^1\text{H NMR}$  (400 MHz,  $\text{DMSO-}d_6$ )  $\delta$  8.86 (d,  $J = 8.5$  Hz, 2H), 8.33 (d,  $J = 8.5$  Hz, 2H), 8.22 (d,  $J = 2.5$  Hz, 2H), 7.91 (d,  $J = 8.9$  Hz, 2H), 7.52 (dd,  $J = 8.9, 2.5$  Hz, 2H), 4.57 (t,  $J = 6.5$  Hz, 4H), 2.33 – 2.22 (m, 4H), 2.04 – 1.92 (m, 4H), 1.90 – 1.76 (m, 8H), 1.42 – 1.31 (m, 6H).  $^{13}\text{C NMR}$  (101 MHz,  $\text{DMSO-}d_6$ )  $\delta$  153.5, 138.9, 135.0, 128.5, 126.5, 123.8, 115.9, 110.7, 104.5, 68.3, 31.2, 29.0, 25.4, 22.2, 14.1. **IR:**  $\nu_{\text{max}}$  ( $\text{cm}^{-1}$ ) = 2928, 2857, 1614, 1583, 1509, 1489, 1456, 1391, 1326, 1286, 1257, 1196, 1161, 1107, 1019, 991, 956, 912, 848, 824, 802, 764, 750, 723, 705, 662, 634, 587, 529, 442, 424, 409.

### General procedure for the synthesis of the final molecules 2,4,6-tris(phenyl)-1,3,5-triazine.

In a 150 mL two-bottomed round-bottom flask, 2,4,6-tris(4-fluorophenyl)-1,3,5-triazine (0.46 g, 1.26 mmol), 9H-carbazole derivative (5.10 mmol), cesium carbonate (6.65 g, 20.44 mmol), and dimethylacetamide (40 mL) were added. After argon flushing three times, the mixture was refluxed for 24h. The mixture was cooling down to room temperature and poured into water. The precipitate formed was filtered off and purified by column chromatography on silica.

1,1',1'',1''',1''',1''''-(((1,3,5-triazine-2,4,6-triyl)tris(benzene-4,1-diyl))tris(9H-carbazole-9,3,6-triyl))hexakis(octan-1-one) (**16a**).

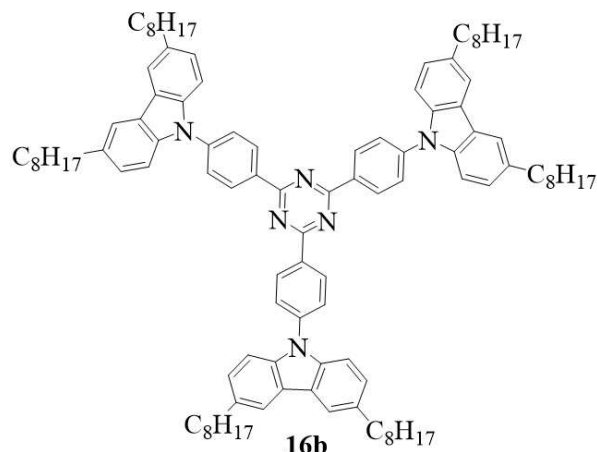


Eluent n-hexane:ethyl acetate 4:1 (v/v). Yield 826 mg (0.52 mmol, 42%) of yellow solid.  $^1\text{H NMR}$  (400 MHz, methylene chloride- $d_2$ )  $\delta$  9.17 – 9.11 (d,  $J = 8.6$  Hz, 2H), 8.89 (d,  $J = 1.7$  Hz, 2H), 8.15 (dd,  $J = 8.7, 1.7$  Hz, 2H), 7.91 – 7.85 (d,  $J = 8.6$  Hz, 2H), 7.60 (d,  $J = 8.7$  Hz, 2H), 3.13 (t,  $J = 7.4$  Hz, 4H), 1.80 (p,  $J = 7.4$  Hz, 4H), 1.51 – 1.29 (m, 16H), 0.96 – 0.87 (m, 6H).  $^{13}\text{C NMR}$  (101 MHz, methylene chloride- $d_2$ )  $\delta$  199.7, 171.5, 143.9, 141.0, 135.9, 131.4, 131.3,



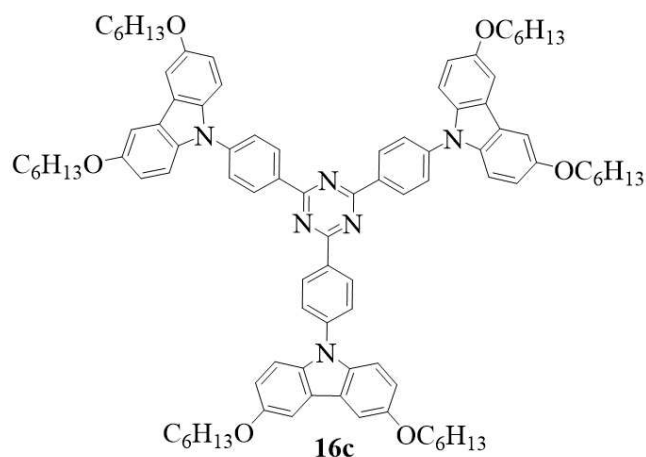
127.5, 127.1, 124.2, 121.9, 110.5, 39.2, 32.4, 30.0, 29.9, 25.1, 23.3, 14.5. **FTMS-ESI (+):**  $m/z$  for  $C_{105}H_{120}N_6O_6Na$   $[M+Na]^+$  calcd., found.

1,1'-(9-(4-(4,6-bis(4-(3,6-dioctyl-9H-carbazol-9-yl)phenyl)-1,3,5-triazin-2-yl)phenyl)-9H-carbazole-3,6-diyl)bis(octan-1-one) (**16b**).



Eluent n-hexane:ethyl acetate 9:1 (v/v). Yield 651 mg (0.44 mmol, 35%) of yellow solid. **<sup>1</sup>H NMR** (400 MHz, methylene chloride-*d*<sub>2</sub>)  $\delta$  9.13 – 9.04 (d,  $J = 8.5$  Hz, 2H), 7.95 (d,  $J = 1.7$  Hz, 2H), 7.88 (d,  $J = 8.5$  Hz, 2H), 7.53 (d,  $J = 8.4$  Hz, 2H), 7.29 (dd,  $J = 8.4, 1.7$  Hz, 2H), 2.81 (t,  $J = 7.7$  Hz, 4H), 1.73 (p,  $J = 7.3$  Hz, 4H), 1.45 – 1.22 (m, 20H), 0.94 – 0.83 (m, 6H). **<sup>13</sup>C NMR** (101 MHz, methylene chloride-*d*<sub>2</sub>)  $\delta$  171.6, 142.8, 139.5, 135.8, 134.7, 131.1, 127.3, 126.7, 124.4, 120.1, 110.2, 36.5, 32.9, 32.5, 30.2, 30.0, 29.9, 23.3, 14.5. **FTMS-ESI (+):**  $m/z$  for  $C_{105}H_{132}N_6$   $[M]^+$  calcd. 1477.05134, found 1477.05204.

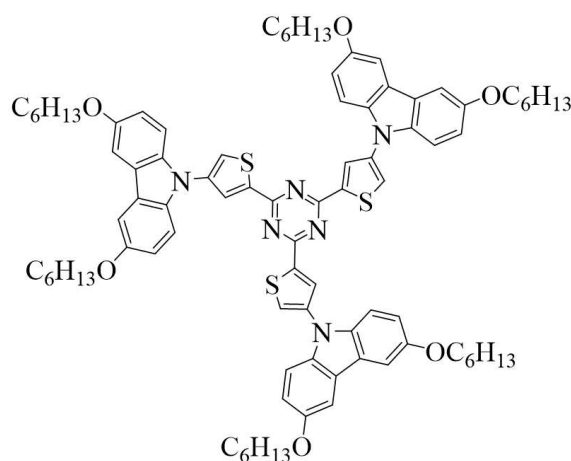
2,4,6-tris(4-(3,6-bis(hexyloxy)-9H-carbazol-9-yl)phenyl)-1,3,5-triazine (**16c**).



Eluent n-hexane:ethyl acetate 4:1 (v/v). Yield 690 mg (0.49 mmol, 39%) of pale orange solid. **<sup>1</sup>H NMR** (400 MHz, chloroform-*d*)  $\delta$  7.86 (d,  $J = 8.5$  Hz, 2H), 7.70 (d,  $J = 8.5$  Hz, 2H), 7.53 (d,  $J = 2.4$  Hz, 2H), 7.38 (d,  $J = 8.9$  Hz, 2H), 7.04 (dd,  $J = 8.9, 2.4$  Hz, 2H), 4.09 (t, 6.7 Hz,

4H), 1.92 – 1.77 (m, 4H), 1.57 – 1.47 (m, 4H), 1.43 – 1.32 (m, H), 0.92 (m, 6H).  $^{13}\text{C}$  NMR (101 MHz, methylene chloride- $d_2$ )  $\delta$  154.8, 143.1, 135.6, 134.5, 126.9, 125.1, 116.3, 111.1, 104.5, 69.5, 32.2, 30.0, 26.4, 23.2, 14.4. **FTMS-ESI (+)**:  $m/z$  for  $\text{C}_{93}\text{H}_{108}\text{N}_6\text{O}_6\text{Na}$   $[\text{M}+\text{Na}]^+$  calcd. 1427.82108, found 1427.82226.

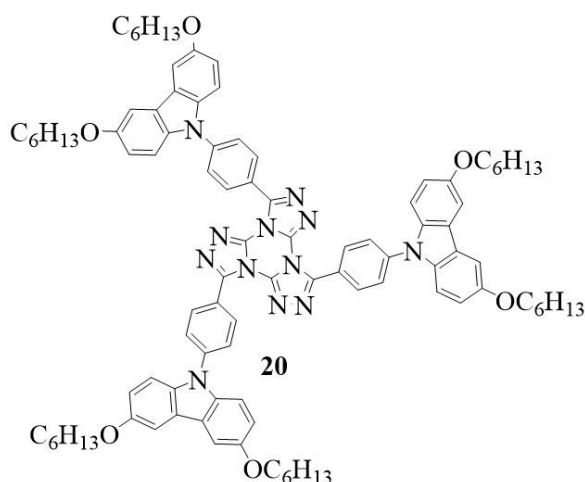
2,4,6-tris(4-(3,6-bis(hexyloxy)-9H-carbazol-9-yl)thiophen-2-yl)-1,3,5-triazine (**17c**).



**17c**

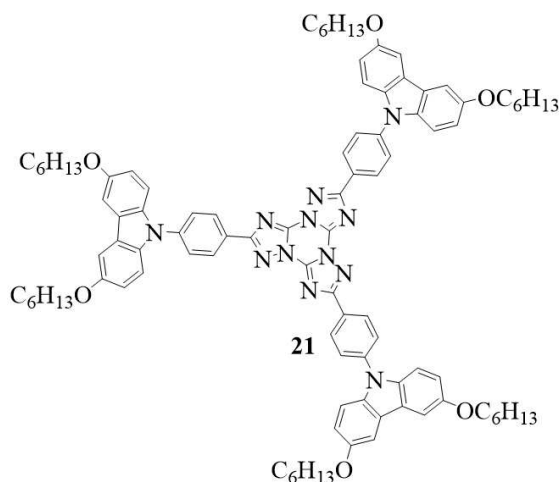
In a 100 mL two-neck round bottom flask, 2,4,6-tris(4-bromothiophen-2-yl)-1,3,5-triazine (1g, 1.77 mmol), 3,6-bis(hexyloxy)-9H-carbazole (2.14g, 5.84 mmol), potassium carbonate (0.97g, 7.0 mmol), copper sulfate pentahydrate (0.07g, 0.3 mmol), and 1-methylnaphthalene (10 mL) were added. After argon flushing three times, the mixture is held at 250°C for 24h. After cooling down, the reaction is poured into a mixture of dichloromethane and water (1:1, 30 mL). The organic phase is separated, dried with magnesium sulfate, and concentrated. The crude product is purified by column chromatography on silica. Eluent n-hexane:chloroform 2:3 (v/v). Yield 806 mg (0.56 mmol, 32%) of a yellow solid.  $^1\text{H}$  NMR (400 MHz, chloroform- $d$ )  $\delta$  8.47 (d,  $J$  = 1.6 Hz, 1H), 7.72 (d,  $J$  = 1.6 Hz, 1H), 7.53 (d,  $J$  = 2.4 Hz, 2H), 7.39 (d,  $J$  = 8.8 Hz, 2H), 7.07 (dd,  $J$  = 8.8, 2.4 Hz, 2H), 4.09 (t,  $J$  = 6.6 Hz, 4H), 1.85 (p,  $J$  = 6.8 Hz, 4H), 1.52 – 1.31 (m, 12H), 0.93 (m, 6H).  $^{13}\text{C}$  NMR (101 MHz, methylene chloride- $d_2$ )  $\delta$  167.9, 154.4, 141.6, 138.1, 136.6, 130.1, 126.4, 124.2, 116.3, 111.2, 104.5, 69.5, 32.2, 30.0, 26.4, 23.2, 14.4. **FTMS-ESI (+)**:  $m/z$  for  $\text{C}_{87}\text{H}_{102}\text{N}_6\text{O}_6\text{S}_3\text{Na}$   $[\text{M}+\text{Na}]^+$  calcd., found.

3,7,11-tris(4-(3,6-bis(hexyloxy)-9H-carbazol-9-yl)phenyl)tris([1,2,4]triazolo)[4,3-a:4',3'-c:4'',3''-e][1,3,5]triazine (**20**).



In a 100 mL two-neck round bottom flask, 9-(4-(1H-tetrazol-5-yl)phenyl)-3,6-bis(hexyloxy)-9H-carbazole (0.40 g, 0.80 mmol), cyanuric chloride (0.04 g, 0.23 mmol) were added. After flushing with argon three times, dry toluene (40 mL), and 2,6-lutidine (0.17 g, 1.61 mmol) were added. The mixture is held at 90 °C overnight. After cooling down the reaction, 1M aqueous HCl (50 mL) is added. The organic phase is extracted with chloroform, dried with magnesium sulfate, and concentrated. The crude product is purified by column chromatography on silica using chloroform as eluent. Yield 151 mg (42%) of white solid. **<sup>1</sup>H NMR** (400 MHz, tetrachloroethane-*d*<sub>2</sub>) δ 8.53 (d, *J* = 8.2 Hz, 2H), 7.90 (d, *J* = 8.2 Hz, 2H), 7.60 (d, *J* = 2.3 Hz, 2H), 7.55 (d, *J* = 8.9 Hz, 2H), 7.14 (dd, *J* = 8.9, 2.3 Hz, 2H), 4.16 (t, *J* = 6.5 Hz, 4H), 1.94 – 1.87 (m, 4H), 1.61 – 1.44 (m, 12H), 1.03 – 0.99 (m, 6H). **<sup>13</sup>C NMR** (101 MHz, tetrachloroethane-*d*<sub>2</sub>) δ 153.9, 150.0, 141.4, 140.2, 135.2, 131.6, 125.4, 124.0, 121.3, 115.7, 110.7, 104.3, 69.1, 31.5, 29.3, 25.6, 22.4, 13.9. **FTMS-ESI (+)**: *m/z* for C<sub>96</sub>H<sub>108</sub>N<sub>12</sub>O<sub>6</sub> [M]<sup>+</sup> calcd. 1525.85321, found 1524.49537.

2,6,10-tris(4-(3,6-bis(hexyloxy)-9H-carbazol-9-yl)phenyl)tris([1,2,4]triazolo)[1,5-a:1',5'-c:1'',5''-e][1,3,5]triazine (**21**).



In a 100 mL two-neck round bottom flask, TTT-precursor (0.1 g, 0.06 mmol) was added. After flushing with argon, potassium carbonate (0.03 g, 0.26 mmol), and anhydrous 1,2-dichlorobenzene (10 mL) were added. The mixture is held at 200°C for 4 days. Upon cooling, chloroform (50 mL) was added, and the organic phase washed with water, dried with magnesium sulfate, and concentrated. The crude product is purified by column chromatography on silica using chloroform as eluent. Yield 100 mg (67%) of white solid. <sup>1</sup>H NMR (400 MHz, tetrachloroethane-*d*<sub>2</sub>) δ 8.69 (d, *J* = 8.6 Hz, 2H), 7.86 (d, *J* = 8.6 Hz, 2H), 7.62 (d, *J* = 2.4 Hz, 2H), 7.48 (d, *J* = 9.0 Hz, 2H), 7.14 (dd, *J* = 9.0, 2.4 Hz, 2H), 4.17 (m, 4H), 1.92 (m, 4H), 1.61 – 1.46 (m, 12H), 1.01 (m, 6H). <sup>13</sup>C NMR (101 MHz, Tetrachloroethane-*d*<sub>2</sub>) δ 163.9, 153.6, 143.7, 140.7, 134.8, 129.2, 126.0, 125.6, 123.6, 115.7, 110.6, 103.4, 68.7, 31.5, 29.2, 25.7, 22.5, 14.0. FTMS-ESI (+): *m/z* for C<sub>96</sub>H<sub>108</sub>N<sub>12</sub>O<sub>6</sub>Na [M+Na]<sup>+</sup> calcd., found.

## 6 PUBLICATIONS

Marchi Luciano, H., Farias, G., Salla, C. M., França, L. G., Kuila, S., Monkman, A. P., Durola, F., Bechtold, I. H., Bock, H. R., & Gallardo, H. (2023). **Room Temperature Phosphorescence in Solution from Thiophene-Bridged Triply Donor-Substituted Tristriazolotriazines.** *Chemistry – A European Journal*. <https://doi.org/10.1002/chem.202203800>.

# Room Temperature Phosphorescence in Solution from Thiophene-Bridged Triply Donor-Substituted Tristriazolotriazines

Hugo Marchi Luciano,<sup>[a, b]</sup> Giliandro Farias,<sup>[a]</sup> Cristian M. Salla,<sup>[c]</sup> Larissa G. Franca,<sup>[d]</sup> Suman Kuila,<sup>[d]</sup> Andrew P. Monkman,<sup>[d]</sup> Fabien Durola,<sup>[e]</sup> Ivan H. Bechtold,<sup>\*, [c]</sup> Harald Bock,<sup>\*, [e]</sup> and Hugo Gallardo<sup>\*, [a]</sup>

**Abstract:** Most organic room-temperature phosphorescence (RTP) emitters do not show their RTP in solution. Here, we incorporated sulfur-containing thiophene bridges between the donor and acceptor moieties in D<sub>3</sub>A-type tristriazolotriazines (TTTs). The thiophene inclusion increased the spin-orbit

coupling associated with the radiative T<sub>1</sub>→S<sub>0</sub> pathway, allowing RTP to be observed in solution for all compounds, likely assisted by protection of the emissive TTT-thiophene core from the environment by the bulky peripheral donors.

## Introduction

Room-temperature phosphorescence (RTP) from non-metalated organic chromophores offer a fascinating alternative to organo-metallic complexes, and has been widely used in electroluminescence and bio-imaging technologies.<sup>[1]</sup> Organometallic RTP complexes often include heavy transition metals like Ir or Pt that induce strong spin-orbit coupling (SOC) and alleviate two ‘spin-forbidden’ processes, that is, intersystem crossing (ISC) between the S<sub>1</sub> and T<sub>1</sub> states and the following radiative T<sub>1</sub>→S<sub>0</sub> transition.<sup>[2]</sup> Metal-free organic chromophores require specific functional groups, most notably aromatic carbonyls, in order to generate triplet excitons through El-Sayed-allowed π–π\* and n–π\* transitions between the singlet and triplets.<sup>[3]</sup>

These materials have long been used as photosensitizers. However, phosphorescence in fluid solution is often quenched by rapid non-radiative deexcitation of the chromophores by solvent collisions and rotational motions. Therefore, they require a dense, highly ordered crystalline network, or a rigid glassy polymer matrix to suppress molecular motions.<sup>[4]</sup> Although a few molecular systems have been shown to generate solution state RTP when encapsulated in supramolecular hosts, matrix-free systems are extremely rare.<sup>[5]</sup> Therefore, new design principles for enhanced ISC and subsequent RTP are essential to provide organic phosphors that function in a matrix-free liquid environment. Such materials are potentially more useful for bioimaging with lesser interference from the solvent medium. Herein, we designed a series of donor-acceptor molecules with a rigid acceptor core (to minimise vibrational dissipation) and we anticipated that a multiple donor substitution would contribute to protect the triplet-emitting core from de-exciting solvent interactions. Donor-acceptor molecules have long been studied for thermally activated delayed fluorescence (TADF) owing to their small <sup>1</sup>CT–<sup>3</sup>CT energy gaps (CT=charge transfer state). Etherington et al. have shown that a secondary <sup>3</sup>LE state mediates the ISC process between these CT manifolds for stronger spin-orbit coupling.<sup>[6]</sup> These <sup>3</sup>LE states can have significant SOC with the <sup>1</sup>CT according to El-Sayed’s rule.

D<sub>3</sub>A structures where the electron acceptor TTT is surrounded by three donor substituents have recently been shown to be interesting candidates for efficient blue emission either via the TADF mechanism, or via similar triplet-to-singlet intersystem crossing (ISC) from Kasha-forbidden higher triplet states.<sup>[7]</sup>

ISC relies on efficient SOC, and SOC increases dramatically with increasing weight of the atoms on which the relevant orbitals are located. The incorporation of sulfur atoms has accordingly been shown to improve significantly the efficiency of TADF-based organic light emitting diodes (OLEDs).<sup>[8]</sup>

[a] H. Marchi Luciano, Dr. G. Farias, Prof. H. Gallardo  
Departamento de Química  
Universidade Federal de Santa Catarina  
Trindade, 88040-900 Florianópolis, SC (Brazil)  
E-mail: hugo.gallardo@ufsc.br

[b] H. Marchi Luciano  
Centre de Recherche Paul Pascal  
Université Bordeaux  
115 av. Schweitzer, 33600 Pessac (France)

[c] Dr. C. M. Salla, Prof. I. H. Bechtold  
Departamento de Física  
Universidade Federal de Santa Catarina  
Trindade, 88040-900 Florianópolis, SC (Brazil)  
E-mail: ivan.bechtold@ufsc.br

[d] L. G. Franca, Dr. S. Kuila, Prof. A. P. Monkman  
Department of Physics  
Durham University  
Durham DH1 3LE (UK)

[e] Dr. F. Durola, Dr. H. Bock  
Centre de Recherche Paul Pascal, CNRS  
115 av. Schweitzer, 33600 Pessac (France)  
E-mail: harald.bock@crpp.cnrs.fr

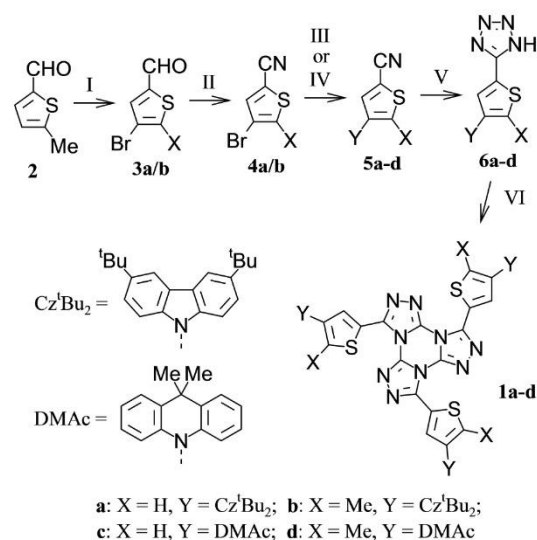
 Supporting information for this article is available on the WWW under <https://doi.org/10.1002/chem.202203800>

We have now incorporated sulfur-containing thiophene bridges in the place of the usual phenylene spacers between the donor and acceptor moieties in D<sub>3</sub>A-type TTTs to probe the effect of the sulfur heavy atom on the emission behavior. To limit the conjugation between the donor and acceptor moieties and thus minimize both LUMO-HOMO overlap and the energy gap  $\Delta E_{ST}$  between the S<sub>1</sub> and T<sub>1</sub> states, we chose a 2,4 substitution pattern on the thiophene bridges instead of the more common 2,5 pattern. Such 2,4-disubstitution on thiophene is analogous to 1,3-disubstitution on benzene, whereas 2,5-disubstitution is analogous to 1,4-disubstitution on benzene, and it has been shown that meta-disubstitution on benzene linkers leads to smaller  $\Delta E_{ST}$  and increases delayed emission by several orders of magnitude in tricarbazolyl-triphenyltriazine.<sup>[9]</sup> Thus we prepared four 2,4-thiophene-bridged target compounds **1a–d** where the thiophene bridge is linked in position 2 to the TTT core and in position 4 either to di-3,6-tert-butyl-carbazole (in **1a** & **1b**) as weaker donor or 9,9-dimethyl-9,10-dihydroacridine (DMAC, in **1c** & **1d**) as stronger donor, using either plain thiophene (in **1a** & **1c**) as bridge or 5-methyl-substituted thiophene (in **1b** & **1d**) to increase the torsion angle with the donor.

## Results and Discussion

The most suitable method for synthesizing the TTT heterocycle is Huisgen's method, that is, the acylation of tetrazole with cyanuric chloride followed by triple thermal nitrogen elimination and ring closure. This method allows the obtention of various substituted TTTs, such as **1a–d** investigated here, from tetrazole derivatives. Thus, the design of different 5-substituted tetrazoles (**6a–d**) is the approach used here (Scheme 1). All required tetrazoles are synthesized from the corresponding aldehyde. **3a** was acquired commercially, but aldehyde **3b** was prepared by bromination of commercial reagent **2**. The aldehyde group of intermediates **3a/b** is converted to a cyano group (**4a**: 82% and **4b**: 72%) by oxidation with iodine and ammonium hydroxide. Two different C–N coupling strategies were used depending on the donor species. 3,6-di-tert-butyl-9H-carbazole reacts with the intermediate **4a/b** via a variant of the Ullmann condensation to yield the intermediates **5** (**5a**: 48%, **5b**: 34%). Compounds **5c** and **5d** (**5c**: 42% and **5d**: 46%) are obtained by palladium-catalyzed C–N coupling between intermediate **4a/b** and 9,9-dimethyl-9,10-dihydroacridine. In the next step, the cyano group of **5a–d** is converted to the tetrazole heterocycle (**6a–d**, ca. 80%) via a 1,3-dipolar cycloaddition with sodium azide. The target TTTs **1a–d** (~35%) were obtained by threefold reaction of cyanuric chloride with the 5-substituted tetrazoles (**6a–d**).

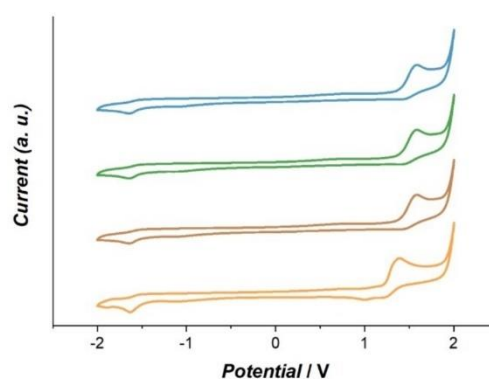
TGA analyses were carried out to study the emitters' thermal stability in N<sub>2</sub> with heating rate of 10 °Cmin<sup>-1</sup> (Figure S1 in Supporting Information). All four donor-functionalized triazolo-triazine compounds showed a decomposition temperature (defined as 3% of mass loss) in the range of 400–450 °C. **1c** (T<sub>dec</sub> = 401 °C) and **1d** (T<sub>dec</sub> = 402 °C) showed to be less thermally stable than the analogues containing the 3,6-di-tert-butyl-9H-



**Scheme 1.** I) Br<sub>2</sub>, AcOH, **3b**: 60%; II) NH<sub>4</sub>OH(aq), I<sub>2</sub>, THF, **4a**: 82%, **4b**: 72%; III) 3,6-di-tert-butyl-9H-carbazole, K<sub>2</sub>CO<sub>3</sub>, CuSO<sub>4</sub>·5H<sub>2</sub>O, 1-methylnaphthalene, **5a**: 48%, **5b**: 34%; IV) 9,9-dimethyl-9,10-dihydroacridine, [Pd(OAc)<sub>2</sub>], Xphos, NaOt-Bu, toluene, **5c**: 42%, **5d**: 46%; V) NaN<sub>3</sub>, NH<sub>4</sub>Cl, DMF, **6a**: 88%, **6b**: 83%, **6c**: 81%, **6d**: 79%; VI) C<sub>3</sub>N<sub>3</sub>Cl<sub>3</sub>, 2,6-lutidine, toluene, **1a**: 38%, **1b**: 32%, **1c**: 39%, **1d**: 35%.

carbazole unit, **1a** (T<sub>dec</sub> = 442 °C) and **1b** (T<sub>dec</sub> = 449 °C). The thermal stability of all four compounds under inert conditions is thus largely satisfactory for practical applications.

The redox properties of the TTT emitters were investigated by cyclic voltammetry (CV) measurements in DMF solution. As shown in Figure 1, for the emitters **1a** and **1b**, irreversible oxidation ( $E_{ox}$ ) signals were detected in the range of ~1.5–1.6 V. Emitters **1c** and **1d** show quasi-reversible oxidation in the range of ~1.2–1.3 V. According to the oxidation onset, the  $E_{ox}$



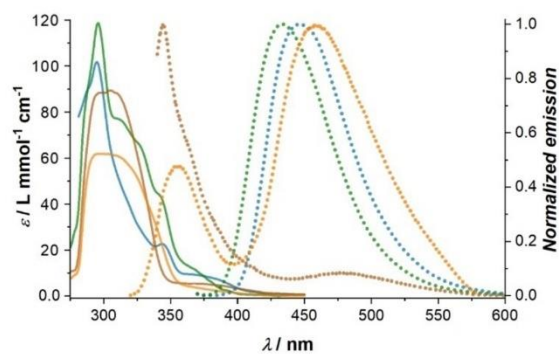
**Figure 1.** CV curves of the TTT emitters in DMF solution. 0.1 mol L<sup>-1</sup> of Bu<sub>4</sub>NPF<sub>6</sub> (tetrabutylammonium hexafluorophosphate) as a supporting electrolyte; scan rate: 100 mV s<sup>-1</sup>; blue = **1a**, green = **1b**, brown = **1c**, orange = **1d**.

are 0.88 V for **1a**, 0.94 V for **1b**, 0.58 V for **1c** and 0.60 V for **1d** relative to ferrocenium/ferrocene ( $\text{Fc}/\text{Fc}^+$ ,  $E_{\text{Fc}/\text{Fc}^+} = 0.46$  V). The smaller oxidation potential values observed in compounds with the 9,9-dimethyl-9,10-dihydroacridine moiety underline their stronger donor character relative to the 3,6-di-tert-butyl-carbazole moiety. Due to the common acceptor unit, similar reduction potential values were found:  $-2.30$ ,  $-2.40$ ,  $-2.29$  and  $-2.34$  V for **1a**, **1b**, **1c** and **1d** respectively. According to the formulas  $E_{\text{HOMO}} = -(E_{\text{ox}} - E_{\text{Fc}/\text{Fc}^+} + 4.8)$  eV and  $E_{\text{LUMO}} = -(E_{\text{red}} - E_{\text{Fc}/\text{Fc}^+} + 4.8)$  eV, the HOMO/LUMO energy levels of the emitters were calculated as  $-5.68/-2.50$  eV (**1a**),  $-5.74/-2.40$  eV (**1b**),  $-5.38/-2.51$  eV (**1c**) and  $-5.40/-2.46$  eV (**1d**). Correspondingly, the energy gaps are evaluated as 3.18, 3.34, 2.87, and 2.94 eV for **1a**, **1b**, **1c**, and **1d**, respectively.

These band gaps, larger for the carbazole derivatives **1a** and **1b** than for the acridine derivatives **1c** and **1d**, and larger for methyl-bearing **1b** and **1d** than for methyl-free **1a** and **1c**, are coherent with the weaker donor strength in **1a** and **1b** and the reduced spatial HOMO-LUMO overlap in **1b** and **1d**.

With all compounds **1a–d**, a high energy absorption band (at ca. 280 nm) is observed in toluene solution (Figure 2) and assigned to the  $\pi\text{-}\pi^*$  transition of the TTT core.<sup>[5]</sup> For **1a** and **1b**, an absorption band close to 340 nm can be ascribed to the carbazole  $\pi\text{-}\pi^*$  transition. For **1c** and **1d**, the corresponding band, at 320 nm, is assigned to the  $\pi\text{-}\pi^*$  transition of the acridine moiety. Besides these bands characteristic for the individual subunits, broad and weak ( $<1000 \text{ mol}^{-1} \text{ L cm}^{-1}$ ) absorption bands are observed at longer wavelengths which are associated to an intramolecular charge transfer (CT) state. In the acridine derivatives **1c** and **1d**, this band is weaker than in the carbazole derivatives **1a** and **1b**. This suggests that the acridine donor and TTT acceptor units are nearly orthogonal, forming a CT state with small oscillator strength ( $f$ ).

The steady-state photoluminescence spectra (Figure 2) of the carbazole derivatives **1a** and **1b** show a slightly structured emission peak in dilute toluene solution, with maxima at 440 nm and 430 nm, respectively. As discussed below, this emission comes from a mixed  $^1\text{LE}/^1\text{CT}$  state ( $^1\text{LE}$  = locally excited singlet,  $^1\text{CT}$  = charge transfer singlet). Surprisingly, with the acridine derivatives **1c** and **1d**, when excited at around 320 nm,

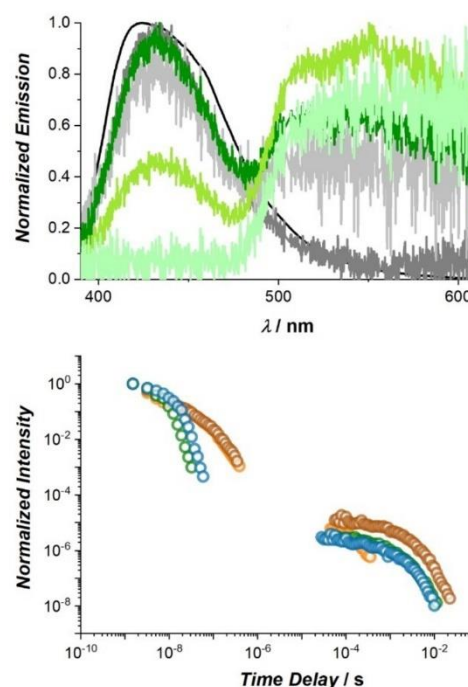


**Figure 2.** Absorption and emission spectra of **1a–d** in dilute toluene solution ( $10^{-5} \text{ mol L}^{-1}$ ); blue = **1a**, green = **1b**, brown = **1c**, orange = **1d**.

we can observe a dual emission. While the higher energy peak (ca. 350 nm) matches with the acridine moiety emission as previously reported by Rama et al.,<sup>[10]</sup> the second broad emission peak at around 460 nm is assigned to a  $^1\text{CT}$  emission. The observed emission from the acridine moiety demonstrates the strongly decoupled nature of the donor and acceptor moieties in these molecules.

By increasing solvent polarity, a slight red-shift of the emission is observed for the carbazole derivatives, and the peak becomes less structured, confirming the mixed  $^1\text{LE}/^1\text{CT}$  state (Figure S2a,b). In the higher-polarity solvent 2-MeTHF, **1c** (Figure S2c) shows a broader emission band, which could be related to the CT state stabilization and increased phosphorescence contribution to the overall emission. The emission is red-shifted for **1d** (Figure S2d), and the broadening in 2-MeTHF is much stronger. The higher phosphorescence contribution was confirmed by time-resolved photoluminescence (TRPL) described below.

To investigate the dynamics of the excited states, we performed TRPL measurements in toluene, and the decay curves are shown in Figure 3. The TRPL spectra show similar features in both carbazole derivatives (Figure S3a,b). In the first few nanoseconds, **1a** and **1b** show an emission peak centered at 440 nm and 415 nm, respectively. This peak is related to the



**Figure 3.** Top: Normalized spectra of **1b** in toluene solution taken at room temperature after different delay times; black = 1.5 ns, gray = 23 ns, light gray 0.11 ms, dark green = 0.50 ms, green = 2.5 ms, light green = 7.0 ms. Bottom: Time-resolved decay curves of **1a–d** in toluene; blue = **1a**, green = **1b**, brown = **1c**, orange = **1d**. The excitation wavelength was 355 nm. All measurements were performed in the absence of oxygen.



<sup>1</sup>LE/<sup>1</sup>CT state decaying with a lifetime of 7.3 ns for **1a** and 4.3 ns for **1b**. By increasing the delay times, we observed a regime of dual emission in the two carbazole derivatives. The short-wavelength band in the microsecond time regime has identical spectra as the prompt decay and is ascribed to delayed fluorescence (DF). The DF mechanism is likely related to triplet-triplet annihilation (TTA) because of the large  $\Delta E_{ST}$  gap (Table 1) found for all four molecules. On the other hand, the second band, with onset at 575 nm for both compounds, displays characteristics typical of room-temperature phosphorescence (RTP), which, according to our theoretical investigations, arises from the TTT-thiophene core (<sup>3</sup>LE). From the TRPL spectra, we observed that the DF emission decays faster, with lifetimes of 0.5 ms and 0.7 ms for **1a** and **1b**. The phosphorescence lifetime is around 3 ms for both compounds.

Moving from the carbazole derivatives to the acridine homologs, the TRPL spectra of **1c** in toluene solution show a similar trend (Figures S3c,d). Initially, **1c** undergoes a very rapid stabilization of the <sup>1</sup>CT state within a 2.3 ns lifetime, which then, with a broad emission band at around 460 nm decays within a 30.2 ns lifetime. At longer time delay, the dual emission related to TTA and RTP is observed with lifetimes of 0.8 ms and 3.5 ms. For **1d**, we only observed distinct differences at later times. This molecule, contrary to the other homologs, showed no detectable TTA and only a weak RTP with a short lifetime of 0.1 ms. The RTP in toluene solution displayed by all four compounds is somewhat unexpected. Evident RTP in solution is not usual, as triplet states have a long lifetime and usually undergo non-radiative decays. In our case, the bulky donor groups surrounding the rigid core most probably protect the <sup>3</sup>LE centered at the TTT-thiophene core from non-radiative losses (collisional deactivation with the environment). An exception is **1d**, where the larger SOC between the low-lying states and a higher triplet energy enhances the phosphorescence rate, as further discussed in the theoretical section.

To understand the role of the non-radiative rates in these molecules, we measured the absolute photoluminescence quantum yield (PLQY) in toluene solution (Table 1). We performed the PLQY measurements under air and calculated the PLQY in degassed solution ( $\Phi_{\text{degassed}}$ ) from the PL ratio between degassed and air-equilibrated solution (Figure S4). The slight decrease of PL by introducing oxygen into the solution is mainly attributed to the quenching of the TTA mechanism. Oxygen quenches slow emissive processes, such as TTA and RTP, which involve triplet excited states. In toluene solution, the acridine derivatives presented significantly lower PLQY values

**Table 1.** Lifetimes  $\tau$  and quantum yields  $\Phi$  in toluene solution.

	<b>1a</b>	<b>1b</b>	<b>1c</b>	<b>1d</b>
$\tau_1$ [ns]	–	–	2.3 (84%)	1.5 (89%)
$\tau_2$ [ns]	7.3	4.3	30.2 (16%)	32.7 (11%)
$\tau_{\text{DF}}$ [ms]	0.5 (75%)	0.7 (83%)	0.8 (67%)	–
$\tau_{\text{Phosph}}$ [ms]	2.8 (25%)	3.2 (17%)	3.5 (33%)	0.1
$\Phi_{\text{air}}^{[a]}$	0.258	0.196	0.017	0.023
$\Phi_{\text{degassed}}^{[a]}$	0.304	0.232	0.023	0.029

[a] The error of  $\Phi$  was  $\pm 0.01$ .

than the carbazole derivatives. This corroborates with the acridine unit being more orthogonally positioned (close to 90°) to the core than the carbazole unit. Thus, even though it forms a CT state, this state has a small oscillator strength and, consequently, a lower radiative rate. The PLQY results indicate that all molecules present relatively strong spin-orbit coupling between the low-lying states due to the thiophene moiety, yielding a large population of triplet states ( $\Phi_{\text{ISC}} = 1 - \Phi_{\text{degassed}}$ ) and triplet non-radiative deactivation, especially on the acridine derivatives.

Solid-state photophysical properties of the emitters were measured in zeonex matrix, a non-polar saturated hydrocarbon polymer. Figure S5 shows the absorption and emission spectra for all four compounds. The two carbazole derivatives showed a similar absorption profile in zeonex as in toluene. In contrast, the acridine derivatives show better-resolved vibronic peaks in zeonex, consistent with the more rigid structure in the matrix. The photoluminescence of all compounds has a Gaussian-shaped emission band with similar onset as observed in toluene solutions, except for **1d**, probably due to a significantly broader distribution of donor-acceptor dihedral angles locked in the solid matrix. Figure S6 shows TRPL decay curves for all compounds. The decay curves show two regimes, a prompt regime followed by phosphorescence emission. For all compounds, a lifetime of around 3 ns is observed in the prompt regime at room temperature (Table 2). In zeonex, the TRPL decays from the two acridine homologs are more structured. The bulky matrix probably flattens the acridine compounds leading to mixed <sup>1</sup>LE/<sup>1</sup>CT states as already observed with the carbazole derivatives in toluene, and thus, for all compounds, similar lifetimes are obtained in zeonex. In the slow regime, <sup>3</sup>LE emission from the TTT-thiophene core is observed with a lifetime of a few ms for all compounds. The slight increase in the lifetime is attributed to the decrease of the non-radiative

**Table 2.** Lifetimes  $\tau$ , quantum yields  $\Phi$  and  $S_1$  &  $T_1$  energies in zeonex matrix.

	<b>1a</b>	<b>1b</b>	<b>1c</b>	<b>1d</b>
<i>Room temperature:</i>				
$\tau_{\text{PF}}$ [ns]	3.9	2.6	3.8	3.4
$\tau_{\text{Phosph 1}}$ [ms]	4.7	8.3	1.2 (82%)	0.8 (68%)
$\tau_{\text{Phosph 2}}$ [ms]	–	–	12.7 (18%)	7.3 (32%)
$\tau_{\text{Phosph av}}$ [ms] <sup>[b]</sup>	–	–	9.3	6.1
$\Phi_{\text{air}}^{[a]}$	0.144	0.124	0.031	0.055
<i>80 K:</i>				
$\tau_{\text{PF}}$ [ns]	7.7	6.0	5.1	4.7
$\tau_{\text{Phosph 1}}$ [ms]	20.4	20.7	0.9 (59%)	0.6 (51%)
$\tau_{\text{Phosph 2}}$ [ms]	–	–	16 (48%)	21 (49%)
$\tau_{\text{Phosph av}}$ [ms] <sup>[b]</sup>	–	–	14.6	20.5
$S_1$ [eV]	3.121 $\pm$ 0.020	3.229 $\pm$ 0.017	2.983 $\pm$ 0.015	3.103 $\pm$ 0.016
$T_1$ [eV]	2.475 $\pm$ 0.015	2.520 $\pm$ 0.010	2.480 $\pm$ 0.010	2.524 $\pm$ 0.008
$\Delta E_{ST}$ [eV]	0.646	0.709	0.503	0.579

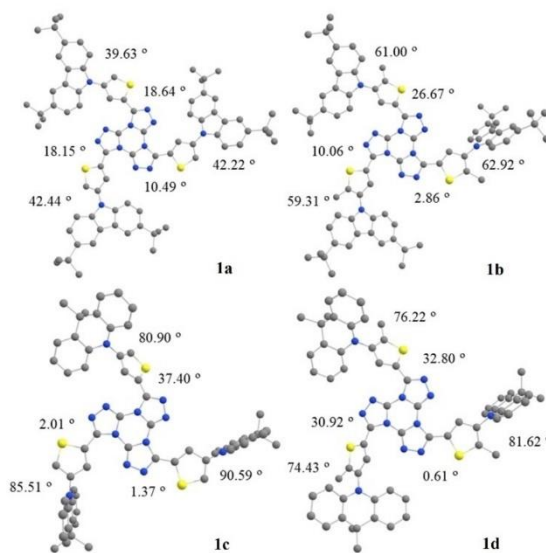
[a] The error of  $\Phi$  was  $\pm 0.01$ . [b] Obtained from  $\tau = \sum \tau_i^2 A_i / \sum \tau_i A_i$ , due to multi-exponential profile.

decay at the solid state. Furthermore, the similar lifetimes of solution and solid-state corroborate with the bulky donor moiety protecting the emissive core from the environment and allowing the RTP.

On decreasing the temperature, the spectra become better resolved in the prompt and the phosphorescence regime, indicating less motion and a more rigid structure in the film. Moreover, all compounds present similar lifetimes at low temperatures, whereas the non-radiative decays are less pronounced. From the onset values of the  $^1\text{LE}/\text{CT}$  emission peak at room temperature and of the  $^3\text{LE}$  emission peak at low temperature, we obtain a large  $\Delta E_{\text{ST}}$  gap of more than 0.5 eV for all molecules. Such large  $\Delta E_{\text{ST}}$  gaps rule out the TADF mechanism at room temperature. The  $^3\text{LE}$  energy values are similar for all compounds, implying a minimal influence of the modifications on the TTT core.

DFT calculations were performed to obtain the ground state geometries, and for all compounds, the bonds and angles are in good agreement with similar compounds where X-ray structures were obtained.<sup>[11]</sup> The orthogonality of the donor-acceptor moieties was evaluated by measuring the dihedral angles between the TTT core and the thiophene moiety, and between the thiophene moiety and the donor unit (carbazole or acridine). For **1a** and **1b**, the average TTT-thiophene angles of  $15.76^\circ$  and  $13.20^\circ$  illustrate that these units are not coplanar. The thiophene-carbazole angle increases from  $41.43^\circ$  in **1a** to  $61.08^\circ$  in **1b**. As the TTT-thiophene dihedral angles are similar for both compounds, the thiophene-carbazole angle determines that the carbazole moiety is more orthogonal to the TTT core in **1b**. For **1c** and **1d**, similar TTT-thiophene dihedral angles of  $13.59^\circ$  and  $21.44^\circ$  were found. On the other hand, thiophene methylation decreases the thiophene-acridine angle from  $85.67^\circ$  in **1c** to  $77.42^\circ$  in **1d**. The measured dihedral angles and the optimized geometries are shown in Figure 4. Figure 4 also illustrates that the orthogonality of the peripheral donor groups over two torsion angles to the TTT core is not uniform between the three symmetrically equivalent donor positions (with some rather coplanar, others quite orthogonal) indicating that the configuration at any given instant differs significantly from a time-averaged configuration, in which the peripheral donors occupy a more globular space.

The characteristics of the excited states were investigated using TD-DFT and SOC-TD-DFT. For **1a** and **1b** the first absorption band (Figure S7) observed experimentally is related to the three low-lying states. Interestingly, the  $S_1$ ,  $S_2$ , and  $S_3$  states of these two carbazole derivatives have CT orbital configurations that stretch both over the carbazole and part of the TTT-thiophene core. Still, the oscillator strengths  $f$  for these transitions are relatively high, characteristic of a LE state. Therefore, for both compounds, the excited state is attributed as a mixed  $^1\text{LE}/\text{CT}$  state, with **1b** having the larger LE character due to the larger value of  $f$ .  $S_1$  is associated with the one of the three thiophene-carbazole arms where the largest thiophene-carbazole dihedral angle is observed.  $S_2$  and  $S_3$  are similar states but involve the other arms of the molecule with lower dihedral angles due to configurational asymmetry. For **1c** and **1d** the first absorption band is related to the three low-lying CT states



**Figure 4.** Optimized ground state geometries within B3LYP/def2-SVP level of theory.

from acridine to the TTT-thiophene core as indicated by the low values of  $f$  and the orbital configuration. The second band in the theoretical spectra for all compounds, which corresponds to the high energy band observed experimentally, is related to the LE states from the TTT-thiophene core. Detailed information about these excited states is given in Tables S1–S4.

The optimized  $S_1$  and  $T_1$  geometries were obtained to gain information on the  $S_1$  and triplet states. In the optimized  $S_1$  state geometry, only minor differences between the dihedral angles are observed (Figure S8), leading to only slight changes of  $f$  for the  $S_0 \rightarrow S_1$  transition in all compounds (Table S1–S4). On the other hand, from the ground state to  $T_1$ , the geometry of the molecules flattens significantly, decreasing the dihedral angles between the donor and acceptor moieties (Figure S9). The configuration of the excited triplet states was calculated using SOC-TD-DFT starting from the  $T_1$  state geometry. The flattening of the structure increases the overall conjugation of the  $\pi$ -system leading to low-lying states with a LE orbital configuration (Table S1–S4). Therefore, the  $T_1$ ,  $T_2$ , and  $T_3$  states are assigned as  $^3\text{LE}$  from the TTT-thiophene core, the lowest energy state being the one with the smallest dihedral angle between these two moieties. The  $T_4$  state is energetically close to  $S_1$  and has a CT orbital configuration from donor to acceptor moieties.

The SOC effects on the ISC and phosphorescence pathways were evaluated using the SOC matrix elements (SOCME) obtained from SOC-TD-DFT calculations (Table 3). The ISC rate is proportional to the sum of the SOCME between  $S_1$  and all triplet states of lower or similar energy (in this case,  $T_1$ – $T_4$  for all compounds). For **1a** and **1b** the SOCME sum between  $S_1$  and the triplet states is  $4.36$  and  $5.19 \text{ cm}^{-1}$ , while for **1c** and **1d** we

**Table 3.** SOCME and adiabatic energy differences.

	<b>1 a</b>	<b>1 b</b>	<b>1 c</b>	<b>1 d</b>
$\sum_i \left( \langle T_{j=1-4} (x,y,z)   \hat{H}_{\text{SOC}}   S_1 \rangle \right)^2 [\text{cm}^{-1}]$	4.36	5.19	3.75	1.75
$\sum_i \left( \langle T_{1(x,y,z)}   \hat{H}_{\text{SOC}}   S_{j=1-10} \rangle \right)^2 [\text{cm}^{-1}]$	10.36	9.37	11.65	14.54
$S_1$ [eV]	3.231	3.346	2.972	3.112
$T_1$ [eV]	2.207	2.256	2.061	2.245
$\Delta E_{\text{ST}}$ [eV]	1.024	1.090	0.911	0.867

found 3.75 and 1.75  $\text{cm}^{-1}$ . These values agree with the measured quantum yields  $\Phi$ . **1 a** and **1 d** have larger  $\Phi$  than their homologs, which is mainly due to the fluorescence emission indicating less deactivation through the ISC pathway. Such values of SOCME for the ISC pathway are similar to those of regular donor-acceptor molecules and sulfur containing compounds.<sup>[12]</sup>

The SOCME between all the low-lying states allows the a priori forbidden  $T_1 \rightarrow S_0$  radiative pathway. We calculated the SOCME between  $T_1$  and the first ten excited singlet states. For **1 a** and **1 b**, this sum of SOCME is 10.36 and 9.37  $\text{cm}^{-1}$ . As the  $T_1$  energies of these two compounds are very similar, the SOCME sums found agree with the experimental observation of a lower  $k_{\text{phosph}}$  and thus a higher  $\tau_{\text{phosph}}$  with **1 b**. For **1 c** and **1 d** the sum of SOCME is 11.65 and 14.54  $\text{cm}^{-1}$ . Here, **1 d** has a larger SOCME between the low-lying states and a higher  $T_1$  energy than **1 c**. As  $k_{\text{phosph}}$  is proportional both to the SOCME and to the  $T_1$  energy, **1 d** accordingly shows a significantly lower  $\tau_{\text{phosph}}$  compared to the other three compounds and only very weak RTP. The phosphorescence pathway shows relatively larger values of SOCME and is comparable to other molecules with RTP.<sup>[13]</sup> As the low-lying triplet states are  $^3\text{LE}$  states centered both at the TTT core and the thiophene bridge, the thiophene inclusion increases the SOC associated with the radiative  $T_1 \rightarrow S_0$  pathway, thus allowing RTP.

## Conclusion

In summary, including thiophene bridges between the donor and acceptor moieties in  $D_2A$ -type trisiazolotriazines resulted in an RTP emission in solution with a lifetime of 0.1–3.5 ms. Furthermore, all compounds exhibited PF emission with a PLQY between 0.023 and 0.258, with carbazole derivatives showing higher efficiency. The PF originates from a mixed  $^1\text{LE}/^1\text{CT}$  state in the carbazole homologs, while the acridine variants showed pure  $^1\text{CT}$  emission due to the good orthogonality between the donor and acceptor moieties. For compounds **1 a**, **1 b**, and **1 c** with longer phosphorescence lifetime, a concurrent TTA mechanism is observed. The comparison between solution and solid-state emission and their lifetimes suggests that the bulky donor moieties protect the emissive  $^3\text{LE}$  state which spreads through the TTT-thiophene core. The partially protected localization of the emissive triplet state at the molecular core, which is surrounded by three bulky donor units, likely assists the strong SOC between the low-lying states of about 10  $\text{cm}^{-1}$  in allowing RTP to manifest itself even in solution. We conclude

that the incorporation of thiophene bridges in  $D_2A$ -type emitters should be considered in molecular design aiming at solution RTP.

## Acknowledgements

We are grateful to CAPES (Coordenação de aperfeiçoamento de pessoal de nível superior, Brazil, finance code #937-20 and #001) and COFECUB (Comité français d'évaluation de la coopération universitaire et scientifique avec le Brésil) (joint project Ph-C 962/20), FAPESC, INCT-INEO and H2020-MSCA-RISE-2017 (OCTA, #778158) for support. H.M.L. is grateful to the French ministry for Foreign Affairs for an Eiffel scholarship. S.K. and A.P.M. acknowledge funding from the EPSRC grant EP/T02240X/1. We thank Piere Dechambenoit for help with cyclic voltammetry, and Emmanuelle Hamon for the TGA analyses.

## Conflict of Interest

The authors declare no conflict of interest.

## Data Availability Statement

The data that support the findings of this study are available from the corresponding author upon reasonable request.

**Keywords:** delayed fluorescence · heavy atom effect · phosphorescence · room temperature trisiazolotriazine

- a) S. Hirata, *Adv. Opt. Mater.* **2017**, *5*, 1700116; b) N. Gan, H. Shi, Z. An, W. Huang, *Adv. Funct. Mater.* **2018**, *28*, 1802657; c) S. R. Forrest, M. A. Baldo, D. F. O'Brien, Y. You, A. Shoustikov, S. Sibley, M. E. Thompson, *Nature* **1998**, *395*, 151; d) X. Zhen, Y. Tao, Z. An, P. Chen, C. Xu, R. Chen, W. Huang, K. Pu, *Adv. Mater.* **2017**, *29*, 1606665.
- R. C. Evans, P. Douglas, C. J. Winscom, *Coord. Chem. Rev.* **2006**, *250*, 2093–2126.
- a) M. A. El-Sayed, *J. Chem. Phys.* **1963**, *38*, 2834; b) N. J. Turro, *Modern Molecular Photochemistry*, University Science Books, Sausalito, **1991**, pp. 99–100.
- T. Zhang, X. Ma, H. Wu, L. Zhu, Y. Zhao, H. Tian, *Angew. Chem. Int. Ed.* **2020**, *59*, 11206–11216; *Angew. Chem.* **2020**, *132*, 11302–11312.
- a) X.-K. Ma, Y. Liu, *Acc. Chem. Res.* **2021**, *54*, 3403–3414; b) S. Kuila, K. V. Rao, S. Garain, P. K. Samanta, S. Das, S. K. Pati, M. Eswaramoorthy, S. J. George, *Angew. Chem. Int. Ed.* **2018**, *57*, 17115–17119; *Angew. Chem.* **2018**, *130*, 17361–17365; c) W.-L. Zhou, Y. Chen, Q. Yu, H. Zhang, Z.-X. Liu, X.-Y. Dai, J.-J. Li, Y. Liu, *Nat. Commun.* **2020**, *11*, 4655; d) J. Xu, A. Takai, Y. Kobayashi, M. Takeuchi, *Chem. Commun.* **2013**, *49*, 8447; e) B. Ventura, A. Bertocco, D. Braga, L. Catalano, S. d'Agostino, F. Greponi, P. Taddei, *J. Phys. Chem. C* **2014**, *118*, 18646; f) G. D. Gutierrez, G. T. Sazama, T. Wu, M. A. Baldo, T. M. Swager, *J. Org. Chem.* **2016**, *81*, 4789.
- M. K. Etherington, J. Gibson, H. F. Higginbotham, T. J. Penfold, A. P. Monkman, *Nat. Commun.* **2016**, *7*, 13680.
- a) S. Zeng, C. Xiao, J. Zhou, Q. Dong, Q. Li, J. Lim, H. Ma, J. Y. Lee, W. Zhu, Y. Wang, *Adv. Funct. Mater.* **2022**, *32*, 2113183; b) Z. Fang, S. Wang, J. Liao, X. Chen, Y. Zhu, W. Zhu, Y. Wang, Yafei, *J. Mater. Chem. C* **2022**, *10*, 4837–4844; c) R. Hojo, D. M. Mayder, Z. M. Hudson, *J. Mater. Chem. C* **2022**, *10*, 13871–13877; d) X. Chen, S. Wang, H. L. Lee, J. Y. Lee, X. Liao, L. Li, W. Zhu, Y. Wang, *Adv. Opt. Mater.* **2021**, *9*, 2101518; e) S. Wang, X. Wang, K. H. Lee, S. Liu, J. Y. Lee, W. Zhu, Y. Wang, *Dyes Pigm.* **2020**, *182*, 108589; f) S. K. Pathak, Y. Xiang, M. Huang, T. Huang, X. Cao, H. Liu, G. Xie, C. Yang, *RSC Adv.* **2020**, *10*, 15523–15529; g) F. Hundemer, E.

- Crovini, Y. Wada, H. Kaji, S. Bräse, E. Zysman-Colman, *Mater Adv* **2020**, *1*, 2862–2871.
- [8] a) C. Feng, S. Li, L. Fu, X. Xiao, Z. Xu, Q. Liao, Y. Wu, J. Yao, H. Fu, *J. Phys. Chem. Lett.* **2020**, *11*, 8246–8251; b) M. Li, W. Xie, X. Cai, X. Peng, K. Liu, Q. Gu, J. Zhou, W. Qiu, Z. Chen, Y. Gan, S. J. Su, *Angew. Chem. Int. Ed.* **2022**, *61*, e202209343; c) I. S. Park, H. Min, T. Yasuda, *Angew. Chem. Int. Ed.* **2022**, *61*, e202205684; d) S. M. Pratik, V. Coropceanu, J.-L. Bredas, *ACS Materials Lett.* **2022**, *43*, 440–447; e) I. S. Park, M. Yang, H. Shibata, N. Amanokura, T. Yasuda, *Adv. Mater.* **2022**, *34*, 2107951; f) T. Hua, L. Zhan, N. Li, Z. Huang, X. Cao, Z. Xiao, S. Gong, C. Zhou, C. Zhong, C. Yang, *Chem. Eng. J.* **2021**, *426*, 131169.
- [9] T. Matulaitis, P. Imbrasas, N. A. Kukhta, P. Baronas, T. Buciunas, D. Banevicius, K. Kazlauskas, J. V. Grazulevicius, S. Jursenas, *J. Phys. Chem. C* **2017**, *121*, 23618–23625.
- [10] R. Dhali, D. K. A. P. Huu, F. Bertocchi, C. Sissa, F. Terenzi, A. Painelli, *Phys. Chem. Chem. Phys.* **2021**, *23*, 378–387.
- [11] a) A. Navarro, M. P. Fernández-Liencre, G. García, J. M. Granadino-Roldán, M. Fernández-Gómez, *Phys. Chem. Chem. Phys.* **2014**, *17*, 605–618; b) R. Cristiano, H. Gallardo, A. J. Bortoluzzi, I. H. Bechtold, C. E. M. Campos, R. L. Longo, *Chem. Commun.* **2008**, 5134–5136; c) T. Yasuda, T. Shimizu, F. Liu, G. Ungar, T. Kato, *J. Am. Chem. Soc.* **2011**, *133*, 13437–13444.
- [12] a) J. Gibson, A. P. Monkman, T. J. Penfold, *ChemPhysChem* **2016**, *17*, 2956–2961; b) A. Lv, W. Ye, X. Jiang, N. Gan, H. Shi, W. Yao, H. Ma, Z. An, W. Huang, *J. Phys. Chem. Lett.* **2019**, *10*, 1037–1042.
- [13] a) C. A. M. Salla, G. Farias, M. Rouzières, P. Dechambenoit, F. Durola, H. Bock, B. de Souza, I. H. Bechtold, *Angew. Chem. Int. Ed.* **2019**, *58*, 6982–6986; *Angew. Chem.* **2019**, *131*, 7056–7060; b) G. Farias, C. A. M. Salla, M. Aydemir, L. Sturm, P. Dechambenoit, F. Durola, B. de Souza, H. Bock, A. P. Monkman, I. H. Bechtold, *Chem. Sci.* **2021**, *12*, 15116–15127.

Manuscript received: December 5, 2022

Accepted manuscript online: January 17, 2023

Version of record online: ■■■

Nunes da Silva, F., Marchi Luciano, H., Stadtlober, C. H., Farias, G., Durola, F., Eccher, J., Bechtold, I. H., Bock, H., Gallardo, H., & Vieira, A. A. (2023). **Columnar Liquid Crystalline Glasses by Combining Configurational Flexibility with Moderate Deviation from Planarity: Extended Triaryltriazines.** *Chemistry – A European Journal*. <https://doi.org/10.1002/chem.202203604>.

# Columnar Liquid Crystalline Glasses by Combining Configurational Flexibility with Moderate Deviation from Planarity: Extended Triaryltriazines

Fabrcia Nunes da Silva,<sup>[a, b]</sup> Hugo Marchi Luciano,<sup>[b, c]</sup> Carlos H. Stadlober,<sup>[d]</sup> Giliandro Farias,<sup>[c]</sup> Fabien Durola,<sup>[e]</sup> Juliana Eccher,<sup>[d]</sup> Ivan H. Bechtold,<sup>\*,[d]</sup> Harald Bock,<sup>\*,[e]</sup> Hugo Gallardo,<sup>[c]</sup> and Andr A. Vieira<sup>\*,[a]</sup>

**Abstract:** Triply phenanthryl- and tetrahelicyl-substituted triazine-hexaalkyl esters with short alkyl chains show glass transitions conveniently above room temperature within the hexagonal columnar liquid crystalline state, resulting in a solid columnar order at room temperature. As the hexagonal columnar mesophase is easily aligned with the director perpendicular to a solid substrate, such glassy columnar liquid matrices are aimed at for the orientation of guest

emitters, to obtain anisotropic emission. A condition for face-on alignment on substrates are attainable melting and clearing temperatures, which is achieved with the moderately nonplanar tetrahelicyl derivatives in spite of their short alkyl periphery. An unusual phase transition between two columnar mesophases of same hexagonal symmetry, but very different long-distance regularity of the column lattice, is found in one phenanthryl homolog.

## Introduction

Glassy polyaromatic matrices are widespread in organic electronics, because use of the glass state circumvents the electric (such as inhomogeneous charge transport, trap pinning) and optical (such as scattering) problems arising from grain boundaries in microcrystalline materials, whilst still providing the mechanical robustness of a solid. The formation of glasses instead of crystals is favored by conformational multiplicity and the presence of dipoles. Whilst isotropic glasses are common amongst charge-transporting polycyclic aromatics, liquid crys-

talline polyaromatic glasses are much rarer. They allow embedding of emitter materials in an oriented anisotropic alignment, favoring anisotropic emission, which can lead to a 50% increase of light outcoupling and thus of external device efficiency.<sup>[1]</sup> Hexagonal columnar liquid crystals are especially interesting, as they tend to align homeotropically (i.e. with the disk-shaped molecules parallel to the substrate),<sup>[2]</sup> favoring an emitter orientation with preferred emission perpendicular to the device plane.

Columnar liquid crystals generally consist of molecules that have a more or less rigid polycyclic aromatic core with a flexible alkyl chain periphery.<sup>[3]</sup> Besides rarer cases of nematic mesophases that lack periodic order,<sup>[4]</sup> such disk-like mesogens form columnar stacks of disks, and the columns form a two-dimensional ordered lattice, whilst no long-range order persists in the direction of the column axes. Different columnar mesophases with different symmetries of the column lattice exist, the most common being hexagonal symmetry, which generally results if the disk planes are on average perpendicular to the column axis. Mesophases of rectangular or oblique symmetry result mainly from slipped stacking, which makes the disks tilt out of the plane normal to the column axis, and leads to a non-circular column cross-section. The close disk-to-disk stacking leads to generally good charge and exciton transport along the columns.<sup>[5]</sup> The formation of a glassy columnar liquid crystalline state close to room temperature by non-polymeric discotic mesogens has been observed previously mainly in dimeric systems like bridged hexaalkoxy-triphenylene dimers,<sup>[6]</sup> another design approach relies on monomeric mesogens with heavy anchor-like side-chains, where crystallization may additionally be impeded by low symmetry or regio-isomer mixing (Scheme 1).<sup>[7]</sup>

[a] F. Nunes da Silva, Prof. A. A. Vieira  
Departamento de Química  
Universidade Federal da Bahia  
Ondina, 40170-115 Salvador, BA (Brazil)  
E-mail: vieira.andre@ufba.br

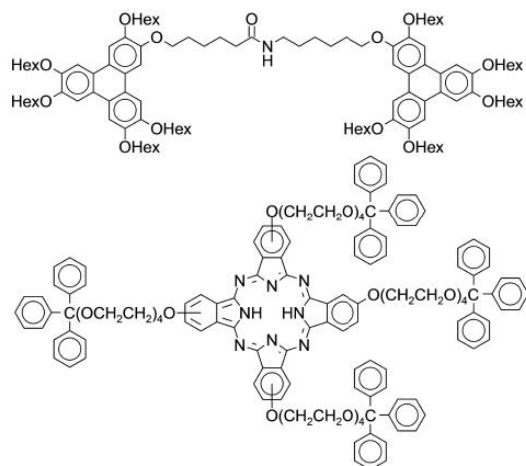
[b] F. Nunes da Silva, H. Marchi Luciano  
Centre de Recherche Paul Pascal  
Université Bordeaux  
115 av. Schweitzer, 33600 Pessac (France)

[c] H. Marchi Luciano, Dr. G. Farias, Prof. H. Gallardo  
Departamento de Química  
Universidade Federal de Santa Catarina  
Trindade, 88040-900 Florianópolis, SC (Brazil)

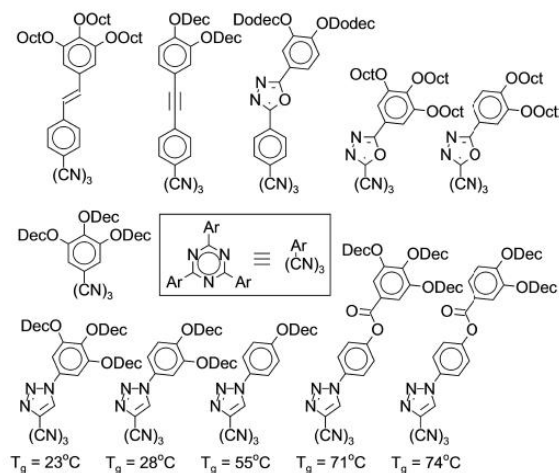
[d] C. H. Stadlober, Prof. J. Eccher, Prof. I. H. Bechtold  
Departamento de Física  
Universidade Federal de Santa Catarina  
Trindade, 88040-900 Florianópolis, SC (Brazil)  
E-mail: ivan.bechtold@ufsc.br

[e] Dr. F. Durola, Dr. H. Bock  
Centre de Recherche Paul Pascal, CNRS  
115 av. Schweitzer, 33600 Pessac (France)  
E-mail: harald.bock@crpp.cnrs.fr

 Supporting information for this article is available on the WWW under <https://doi.org/10.1002/chem.202203604>



**Scheme 1.** Examples of known glass forming columnar mesogens with conventional triphenylene or phthalocyanine cores: spacer-bridged dimer (top) and monomeric disc with bulky substituents (bottom); Hex = *n*-hexyl.

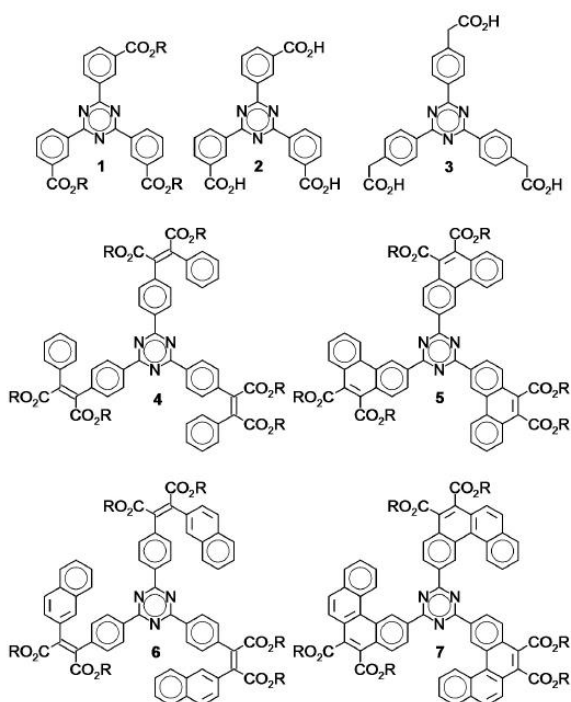


**Scheme 2.** Examples of known columnar triaryltriazine mesogens with three to nine alkoxy chains; Hex = *n*-hexyl, Dec = *n*-decyl, Dodec = *n*-dodecyl.<sup>[9]</sup> The bottom row shows materials where a glass transition above room temperature in the columnar mesophase has been observed by calorimetry ( $T_g$  given).

It has recently been shown that both the alignment direction and the entropy content (disorder) of a small molecule room temperature columnar liquid crystalline glass can be controlled during physical vapor deposition by the adjustment of deposition speed and substrate temperature.<sup>[8]</sup> Such procedures rely on sublimable mesogens of small molecular weight.

A simple heterocyclic structural motif with threefold symmetry that has been reported to yield predominantly hexagonal columnar mesophases when appropriately extended with alkoxy-decorated aryl substituents is 1,3,5-triazine.<sup>[9]</sup> Most of these columnar triaryltriazines have rather large molecular weights because the alkoxy chains needed to induce mesomorphism are long and come in large number. In several tris(triazolyl)triazine derivatives, calorimetric glass transitions above room temperature could be detected after melting and subsequent cooling, confirming the presence of an anisotropic columnar glass at standard conditions (Scheme 2).

We recently reported that ester-substituted triphenyltriazines, i.e. tris(3-alkoxycarbonylphenyl)-*s*-triazines **1**, (Scheme 3) can be obtained swiftly from methyl 3-cyanobenzoate in analogy to the acid-induced trimerization of benzonitrile,<sup>[10]</sup> and predominantly show nematic liquid crystal behavior.<sup>[11]</sup> Core- or chain-fluorination leads to columnar mesophases with only weak tendency to crystallize at room temperature, due to the rotational flexibility at the triazine-benzene single bond that allows for two in-plane configurations of each meta-attached ester group with respect to this bond. The limited conjugation between the three outer benzene units via meta-linkages through the central triazine cycle ensures that a large band gap is preserved, allowing for the embedding of blue emitters, as is desired eg. for TADF (thermally activated delayed fluorescence) OLEDs (organic light emitting diodes).<sup>[12]</sup> Unfortunately, we could not obtain a robust glassy state in a convenient temper-



**Scheme 3.** Liquid crystalline triaryltriazine hexaesters and their synthetic precursors.

ature range above room temperature with these smallest representatives of the triaryltriazine esters.

	Cr–Cr	Cr–Col <sub>hex</sub>	Col <sub>hex</sub> –Col <sub>hex</sub>	Col <sub>hex</sub> –Iso	Cr–Iso	<i>T<sub>g</sub></i>	<i>d<sub>col</sub></i>	<i>d<sub>disk</sub></i>
<b>5<sub>Et</sub></b>	224 <sup>[26]</sup>				> 375			
<b>5<sub>Pr</sub></b>		150 <sup>[13]</sup>		> 375		81 <sup>Col</sup>	20.8	-
<b>5<sub>Bu</sub></b>		108 <sup>[11]</sup>		> 375		19 <sup>Col</sup>	23.5	3.3
<b>7<sub>Et</sub></b>	153 <sup>[12]</sup>				325 <sup>[26]</sup>			
<b>7<sub>Pr</sub></b>			179 <sup>[1,9]</sup>	223 <sup>[3,9]</sup>	232 <sup>[37]</sup>		22.2	3.7
<b>7<sub>Bu</sub></b>				149 <sup>[1,9]</sup>	205 <sup>[34]</sup>	39 <sup>Col</sup>	22.5	3.7
<b>7<sub>Hex</sub></b>					123 <sup>[22]</sup>	27 <sup>ho</sup>		

The glyoxylic Perkin reaction,<sup>[13]</sup> combined with subsequent Mallory photocyclization, is a versatile tool for the synthesis of polycyclic arenes with multiple viscosity-enhancing alkyl ester substituents, and such ester substituents often lead to liquid crystalline materials even when only very short alkyl peripheries are used.<sup>[14]</sup>

Whilst the trimerization of 3-cyanobenzoic acid, in contrast to the successful trimerization of its methyl ester, to the corresponding tricarboxy-triphenyltriazine **2** (Scheme 3) is accompanied by substantial degradation, we now found that (4-cyanophenyl)acetic acid trimerizes cleanly, yielding a convenient substrate for threefold Perkin-Mallory sequences that allow the synthesis of extended triaryltriazine hexaesters. When the so-obtained trimer, tris((4-carboxymethyl)phenyl)triazine **3**, is Perkin-condensed with phenylglyoxylic acid, and the resulting tris(maleic acid) **4<sub>H</sub>** is subjected to in situ esterification and subsequent Mallory photocyclization, triphenanthryl-triazines **5** bearing three pairs of vicinal ester substituents are obtained.

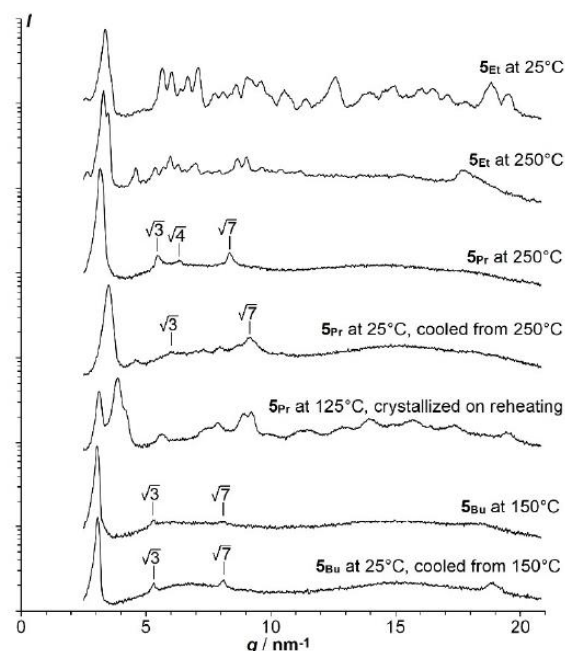
The alkyl groups introduced by in situ esterification should be short enough to allow a glassy state at room temperature (avoiding undue fluidification), but sufficiently long to allow mesophase formation. Methyl ester groups rarely allow the latter, whereas in many systems, already ethyl ester groups do. Whilst a high glass transition temperature *T<sub>g</sub>* is desirable to ensure solid-like robustness well above room temperature, an attainable clearing temperature well below the temperatures of thermal degradation of organic materials (that are typically around 300 °C) is also desirable to allow cooling through the liquid-to-mesophase transition (a.k.a. clearing temperature *T<sub>c</sub>*) as a means of homogeneously aligning the mesophase's optical axis with respect to the substrate.

We thus prepared the hexaethyl, hexapropyl and hexabutyl ester derivatives **5<sub>Et</sub>**, **5<sub>Pr</sub>** and **5<sub>Bu</sub>** of sym-tris(phenanthr-3-yl)triazine.

## Results and Discussion

Albeit the hexaethyl ester **5<sub>Et</sub>** shows, as confirmed by powder X-ray diffraction (XRD), a phase transition between two different crystalline states upon heating above its melting onset at 224 °C, no transition to the isotropic liquid is observable by polarized light optical microscopy (POM) up to our experimen-

tal limit of 375 °C. The propyl homolog **5<sub>Pr</sub>**, after melting at 150 °C, (Table 1) likewise shows no clearing to the isotropic liquid below 375 °C, but the high temperature state is identified as a hexagonal columnar mesophase (by the characteristic (11) and (21) secondary XRD peaks of the column lattice corresponding to distances related by factors of  $\sqrt{3}$  and  $\sqrt{7}$  to the main lattice peak)<sup>[15]</sup> (Figure 1), which upon cooling to room temperature rigidifies to a non-shearable mesomorphic glass. The XRD spectra of **5<sub>Pr</sub>** at 250 and 25 °C testify of a contraction of 10% of the column-to-column distances (from 23.0 Å to 20.7 Å) over this temperature span, accompanied by roughening of the



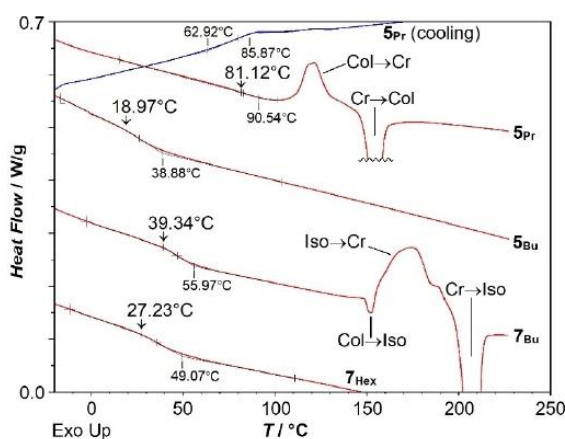
**Figure 1.** Powder XRD spectra of **5<sub>Et</sub>**, **5<sub>Pr</sub>** and **5<sub>Bu</sub>** at room and elevated temperature (logarithmic intensity scaling). The root values indicate the *q* ratio with the main lattice peak to the left and correspond to a column lattice of hexagonal symmetry; the corresponding Miller indices are  $\sqrt{3}$ : (11),  $\sqrt{4}$ : (20),  $\sqrt{7}$ : (21).



diffraction pattern in the small angle region, but without loss of the (11) and (21) peaks.

A steplike feature is apparent in the calorimetric cooling curve of  $5_{Pr}$ , between 85 and 63 °C (at  $-10^{\circ}\text{C}/\text{min}$ ), (Figure 2) whereas a similar feature above 81 °C on the corresponding heating curve (at  $+10^{\circ}\text{C}/\text{min}$ , calorimetric glass transition temperatures are most commonly recorded upon heating at that speed) is convoluted with heating-induced crystallization between 100 and 130 °C. A calorimetric glass transition on heating thus cannot clearly be distinguished, but shearing of the mesophase between glass slides at temperatures below 81 °C is impossible, corroborating the formation of a mesomorphic glass. The inferred glass transition at ca. 81 °C restricts crystallization to the temperature domain between this temperature and the melting onset at 150 °C. In the butyl homolog  $5_{Bu}$ , which likewise shows a hexagonal columnar mesophase after melting at 108 °C, the calorimetric glass transition is significantly lowered to 19 °C, whereas, in contrast to  $5_{Pr}$ , immediate crystallization upon heating above this glass transition is not observed. Like its two smaller homologs,  $5_{Bu}$  does not clear below 375 °C. The hexagonal lattice parameter of  $5_{Bu}$  is preserved by cooling from 150 °C to room temperature, with a column-to-column distance of 23.5 Å that shows no significant temperature dependence. The  $\pi$ -stacking order inside the columns, corresponding to an interdisk distance of about 3.3 Å, was enhanced upon cooling to room temperature, which facilitates charge carrier transport. In contrast, the  $\pi$ -stacking order was not clearly observed for  $5_{Pr}$  neither at high nor at room temperature.

Even though we were able to obtain with  $5_{Pr}$  a mesomorphic anisotropic glass with a conveniently high glass transition temperature of 81 °C, the absence of clearing to the isotropic liquid at practical temperatures and the drop of the glass

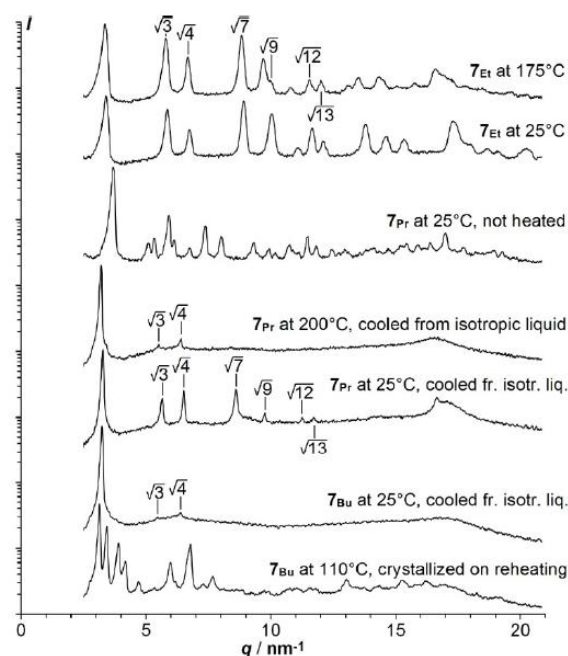


**Figure 2.** Differential calorimetry heating scans (red) of  $5_{Pr}$ ,  $7_{Bu}$ ,  $7_{Bu}$  and  $7_{Hex}$  at  $+10^{\circ}\text{C}/\text{min}$  (after initial heating above the melting point and subsequent cooling at  $-10^{\circ}\text{C}/\text{min}$ ), and cooling scan (blue) of  $5_{Pr}$  at  $-10^{\circ}\text{C}/\text{min}$ ; glass transition onset temperatures on heating are indicated above vertical arrows; phase transitions are marked between Col = hexagonal columnar mesophase, Cr = crystalline state, and Iso = isotropic liquid.

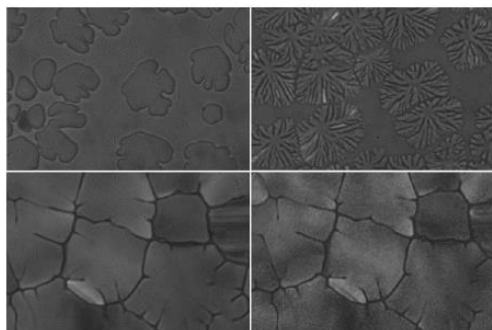
transition temperature to only 19 °C with  $5_{Bu}$  led us to redesign the molecular structure.

Extension of the three aryl arms with 2-naphthylglyoxylic acid via the Perkin adduct  $6_H$  to target esters  $7$  with off-planar tetrahelicyl units<sup>[16]</sup> offered the perspective of both lowering the clearing temperature due to a less planar and relatively compact molecular shape and hindering the tendency to crystallize due to increased conformational variations, both in-plane and out-of-plane.

We thus prepared analogously the hexaethyl, hexapropyl and hexabutyl ester derivatives  $7_{Et}$ ,  $7_{Pr}$  and  $7_{Bu}$  of symtris(tetrahelicyl-3-yl)triazine. All three homologs show direct melting of the crystalline state to the isotropic liquid at attainable temperatures of 325, 232 and 205 °C, respectively. No mesophase is detected with  $7_{Et}$  on cooling from the isotropic liquid, and a crystal-to-crystal transition is observed by DSC (at 153 °C on heating). Both crystalline phases are of hexagonal symmetry, showing the characteristic (10), (11), (20), (21), (30), (22) and (31) peaks corresponding to hexagonal lattice distances in the ratios of  $1:\sqrt{3}:\sqrt{4}:\sqrt{7}:\sqrt{9}:\sqrt{12}:\sqrt{13}$ , besides a multitude of other peaks (Figure 3). In contrast to  $7_{Et}$ , the crystalline phases of  $7_{Pr}$  and  $7_{Bu}$  do not show prominent XRD peaks associate with a hexagonal lattice.  $7_{Pr}$  and  $7_{Bu}$  show monotropic mesophases upon cooling below their clearing points at 223 and 149 °C, respectively, with the typical growth textures of the hexagonal columnar mesophase (Figure 4) and

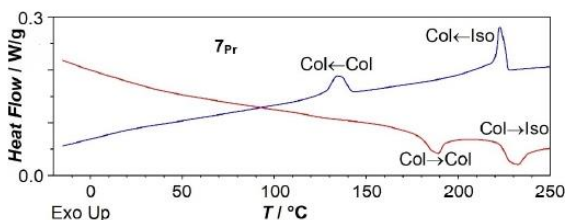


**Figure 3.** Powder XRD spectra of  $7_{Et}$ ,  $7_{Pr}$  and  $7_{Bu}$  at room and elevated temperature (logarithmic intensity scaling). The root values indicate the q ratio with the main lattice peak to the left and correspond to a column lattice of hexagonal symmetry; the corresponding Miller indices are  $\sqrt{3}$ : (11),  $\sqrt{4}$ : (20),  $\sqrt{7}$ : (21),  $\sqrt{9}$ : (30),  $\sqrt{12}$ : (22),  $\sqrt{13}$ : (31).



**Figure 4.** Growth between glass plates of the hexagonal columnar mesophase of  $7_{Pr}$  (top left) and  $7_{Bu}$  (top right) in homeotropic alignment upon cooling through the isotropic-columnar phase transition, and homeotropic texture of the high temperature mesophase of  $7_{Pr}$  at 200 °C (bottom left) and of the low temperature mesophase at 100 °C (bottom right) after cooling from the isotropic liquid followed by reheating; polarizing light optical microscopy with slightly uncrossed polarizers.

associated  $\sqrt{3}$  and  $\sqrt{4}$  XRD peaks. Thus, the slight deplanarization of the aromatic core destabilizes the hexagonal mesophase sufficiently to deliver attainable clearing temperatures in  $7_{Pr}$  and  $7_{Bu}$ , whilst the mesophase is entirely suppressed in  $7_{Et}$  in favor of a hexagonal crystal. Upon cooling,  $7_{Pr}$  shows a further low-enthalpy transition that is unique to this compound and that is significantly hysteretic with onset temperatures on cooling and reheating with 10 °C/min of 143 and 179 °C, respectively (Figure 5). Astonishingly, this transition reveals itself by XRD to be associated with no change of the hexagonal symmetry of the mesophase and no appearance of peaks not associable with a 2D hexagonal lattice, but the higher order peaks of the column lattice increase significantly in relative intensity with respect to the primary lattice peak (and the  $\sqrt{7}$ ,  $\sqrt{9}$ ,  $\sqrt{12}$  and  $\sqrt{13}$  peaks are now clearly expressed). Thus, XRD testifies of an improved correlation length of the column lattice and an enhancement of the interdisk peak. Similar to  $5_{Pr}$ , a slight contraction of the column-to-column distance (from 22.6 Å at 200 °C to 22.2 Å at 25 °C) and of the  $\pi$ -stacking distance (from 3.8 Å to 3.7 Å) was also observed for  $7_{Pr}$ . No



**Figure 5.** Differential calorimetry cooling (blue) and subsequent heating (red) scans of  $7_{Pr}$  at  $-/+10$  °C/min (after initial heating above the melting point); with phase transitions between two hexagonal columnar (Col) mesophases and between the higher temperature mesophase and the isotropic liquid (Iso).

calorimetric glass transition could be observed with  $7_{Pr}$  within the temperature range of this highly ordered mesophase.

When  $7_{Pr}$  is sandwiched between glass slides in homeotropic alignment, the transition between the two hexagonal phases manifests itself in the microscope by a reversible increase of granularity, without change of domain boundaries (Figure 4).

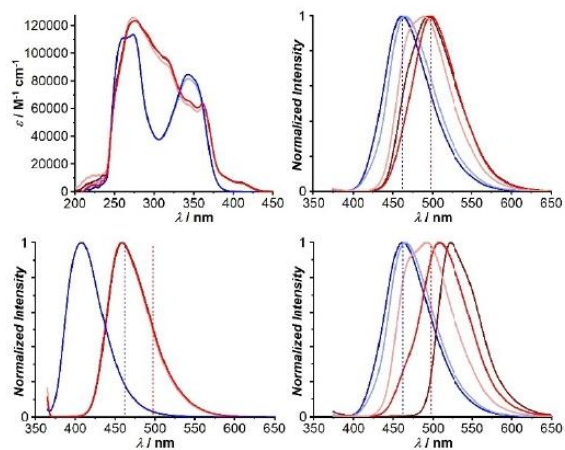
No such less-to-more-regular-mesophase transition is observed with  $7_{Bu}$ , but it forms a mesomorphic glass at room temperature and shows a calorimetric glass transition at 39 °C on reheating (+10 °C/min). Thus,  $7_{Bu}$  shows both a persistent mesomorphic hexagonal columnar glass at room temperature (with column-to-column distance of 22.5 Å and intercolumnar distance of 3.7 Å) and conveniently accessible melting and clearing temperatures of 205 and 149 °C.

To evaluate whether slightly longer alkyl chains on **7** would still allow a mesomorphic glass at room temperature, we also prepared the homolog  $7_{Hex}$  with n-hexyl ester substituents, and we were surprised to find that it is not mesogenic but forms an isotropic glass ( $T_g=27$  °C on heating at +10 °C/min) after melting at 123 °C and cooling back to room temperature.

Thus, a hexagonal columnar mesophase was observed with the four materials  $5_{Pr}$ ,  $5_{Bu}$ ,  $7_{Pr}$  and  $7_{Bu}$ , of which  $7_{Pr}$  shows a peculiar thermal phase transition between two distinct hexagonal states with different degrees of order of the column lattice. No mesophase was observed with either shorter ethyl chains in  $5_{Et}$  and  $7_{Et}$  or longer hexyl chains in  $7_{Hex}$ .

The modification of the molecular structure from **5** to **7** led to a dramatic reduction of the tendency to form a mesophase over unduly large thermal ranges, while the increase of  $T_g$  from 19 °C in  $5_{Bu}$  to 39 °C in its core-extended analog  $7_{Bu}$  allowed us to obtain a material that combines a mesomorphic glassy hexagonal columnar state at room temperature with the formation of an isotropic liquid at conveniently attainable temperatures.

We investigated the photophysical properties of **5** and **7** in dilute chloroform solution and in condensed films. In solution the absorption spectra of all homologs of **5** show two main absorption bands ( $\epsilon=83$  &  $113$   $\text{mM}^{-1}\text{cm}^{-1}$ ) centered at around 342 nm and 272 nm, while the homologs of **7** show a weak absorption ( $7$   $\text{mM}^{-1}\text{cm}^{-1}$ ) close to 405 nm, and a combination of intense transitions at high energy, leading to a structured absorption with maxima (62, 65, 95 &  $123$   $\text{mM}^{-1}\text{cm}^{-1}$ ) at 361, 345, 316 and 278 nm (Figure 6). We performed DFT and TD-DFT calculations on optimized geometries of the hexamethyl homologs  $5_{Me}$  and  $7_{Me}$  to gain insights in the configurations of the excited states. For  $5_{Me}$  the low energy band is related to  $\pi$ - $\pi^*$  transitions mostly centered at the triazine core, while the high energy band is also due to  $\pi$ - $\pi^*$  transitions, but mainly spread through the phenanthrene moiety. In  $7_{Me}$  the adopted geometry with less planarity in the tetrahelicenyl moieties leads to a different absorption profile: The low intensity band close to 400 nm arises from a charge-transfer-like state from tetrahelicenyl to triazine. The other transitions are similar to those in **5**, with intermediary energy  $\pi$ - $\pi^*$  states centered at the triazine and those at high energy spread through the tetrahelicenyl moiety.



**Figure 6.** Left: Normalized absorption (top) and emission (bottom) in dilute chloroform solution [ $10^{-2}$  mg/mL]. Right: Normalized emission in drop-cast film at room temperature before (top) and after (bottom) heating above the melting point. Emission spectra were obtained upon excitation at 360 nm.  $5_{Pr}$ : dark blue,  $5_{Bu}$ : light blue,  $7_{Et}$ : brown,  $7_{Pr}$ : red,  $7_{Bu}$ : pink. The dashed lines in the three emission graphs, centered on the emission maxima of  $5_{Pr}$  &  $7_{Pr}$  in unheated films (as shown in the top right graph), are guides to the eye.

The emission in solution shows a single emission peak close to 409 nm for **5** and 458 nm for **7**, with no discernible differences between homologs in either series. From the onset of emission in solution, at ca. 375 nm for **5** and at ca. 420 nm for **7**, energies of the first excited singlet state  $S_1$  of 3.31 eV for **5** and of 2.95 eV for **7** can be inferred. From TD-DFT calculations on optimized geometries of  $5_{Me}$  and  $7_{Me}$ ,  $S_1$  energies were obtained that are very close to the values inferred from emission in solution: 3.347 eV for  $5_{Me}$  and 2.963 for  $7_{Me}$ . We also calculated the energy of the excited triplet states  $T_1$  on the same geometries using SOC-TD-DFT, obtaining 2.637 eV for  $5_{Me}$  and 2.464 eV for  $7_{Me}$ . The good correspondence of experimental and DFT-calculated energy values for  $S_1$  indicates that the  $T_1$  energies obtained on the same geometries may be good estimations as well. Materials such as **5** or **7** with  $T_1$  energies of ca. 2.5 eV may accordingly be considered as matrices for TADF emitters that emit light of slightly lower energy, i.e. in the green-to-yellow range of the visible spectrum.

Whereas the absorption spectra and as well as the emission spectra from solution are near-identical between the homologs of **5** and between the homologs of **7**, significant differences between the column-forming homologs of **7** appear in the

emission spectra upon annealing of drop-cast films (Figure 6 and Table 2). The emission  $5_{Pr}$ ,  $5_{Bu}$  and of  $7_{Bu}$ , i.e. the three materials that exhibit a conventional hexagonal columnar mesophase in the glassy state at room temperature, is not notably altered upon annealing by melting and subsequent cooling back to room temperature, which suggests that upon solvent evaporation from drop-cast films at room temperature, the same mesogenic state is obtained as upon cooling of the melt. In contrast, the emission spectra of  $7_{Et}$  and  $7_{Pr}$ , which adopt respectively a hexagonal crystalline state and a higher-order columnar mesophase at room temperature, shift to the red upon annealing, by 28 nm ( $7_{Et}$ ) and 11 nm ( $7_{Pr}$ ). Here the higher order of the polycrystalline film of  $7_{Et}$  and of the highly ordered mesomorphic film of  $7_{Pr}$  is apparently obtained only upon annealing. The bathochromic shift in emission in solution to emission from the columnar mesophase is more pronounced for planar **5** than for distorted **7**, meaning that the flatter core of **5** allows more pronounced chromophore aggregation in the mesophase than the less easily stacking off-planar arene system of **7**.

The photoluminescence quantum yield (PLQY) data show that columnar aggregation tends to increase emission yield (Table 2), as the condensed films show higher PLQYs than the solutions. No significant change of PLQY is observed upon annealing. The increase of yield from solution to columnar film constitutes a peculiar form of aggregation-enhanced emission.<sup>[17]</sup>

## Conclusion

The triphenanthryl-triazine-hexaesters **5** with alkyl ester substituents longer than ethyl, i.e.  $5_{Pr}$  and  $5_{Bu}$  are found to show enantiotropic hexagonal columnar mesophases that can be cooled without crystallization to form a mesomorphic glass. The glass transition temperature is strongly chain-length dependent, with  $T_g$  of the shorter propyl homolog  $5_{Pr}$  being about 60 °C higher than the one of  $5_{Bu}$ . Thus, a glassy state at and above room temperature can be obtained only with very short alkyl chains, which implies clearing temperatures >375 °C which cannot be reached conveniently. To address this, larger but less planar tris(tetrahelicyl)-triazine-hexaesters **7** have been designed, which with the same short alkyl chains yield monotropic hexagonal columnar mesophases with conveniently attainable melting and clearing temperatures, and, in the case of  $7_{Bu}$  an improved, i.e. 20 °C higher, glass transition temperature compared to its phenanthryl analog  $5_{Bu}$ . The shorter-chain

**Table 2.** Photoluminescence quantum yields and emission maxima in chloroform solution and in drop-cast film, upon excitation at 360 nm.

	$5_{Et}$	$5_{Pr}$	$5_{Bu}$	$7_{Et}$	$7_{Pr}$	$7_{Bu}$	$7_{Hex}$
Solution (CHCl <sub>3</sub> )	22%	21%	22%	12%	12%	12%	12%
	409 nm	407 nm	409 nm	459 nm	458 nm	459 nm	459 nm
Cast film	27%	45%	49%	20%	23%	14%	17%
	462 nm	462 nm	465 nm	495 nm	498 nm	489 nm	500 nm
Annealed film	n/a (does not melt)	44%	46%	24%	23%	13%	16%
		461 nm	466 nm	523 nm	509 nm	493 nm	505 nm

homolog  $7_{Pr}$  shows on cooling, instead of a glass transition, an unusual and intriguing first-order transition to a second hexagonal columnar mesophase with an extremely well-ordered hexagonal column lattice.

The stabilization of a solid-like hexagonal columnar mesophase at room temperature, combined with an accessible transition to the isotropic liquid in order to allow for the formation of surface-aligned samples by cooling from the liquid, is thus shown to be achievable by a molecular design based on configurational flexibility together with a well-dosed intrinsic deviation from planarity and short alkyl ester substituents.

Emission in condensed columnar films at ambient temperature is found to be higher than in solution. The peculiar increase of order of the room temperature mesophase from  $7_{Bu}$  to  $7_{Pr}$  leads to a bathochromic shift of emission in annealed films due to enhanced aggregation.

### Acknowledgements

We are grateful to INCT/INEO, CNPq, FAPESC, H2020-MSCA-RISE-2017 (OCTA, #778158), CAPES (Coordenação de aperfeiçoamento de pessoal de nível superior, Brazil. Finance code #937-20 and #001) and COFECUB (Comité français d'évaluation de la coopération universitaire et scientifique avec le Brésil) (joint project Ph-C 962/20) for support. The XRD experiments were carried out in the Laboratório de Difração de Raios X (LDRX/UFSC). FNDS and HML are grateful to the French ministry for Foreign Affairs for Eiffel scholarships.

### Conflict of Interest

The authors declare no conflict of interest.

### Data Availability Statement

The data that support the findings of this study are available from the corresponding author upon reasonable request.

**Keywords:** columnar liquid crystal · cyclotrimerization · mesophases · molecular glass · triazine

- [1] a) F. Tenopala-Carmona, O. S. Lee, E. Crovini, A. M. Neferu, C. Murawski, Y. Olivier, E. Zysman-Colman, M. C. Gather, *Adv. Mater.* **2021**, *33*, 2100677; b) D. Yokoyama, *J. Mater. Chem.* **2011**, *21*, 19187–19202; c) H. Sasabe, Y. Chikayasu, S. Ohisa, H. Arai, T. Ohsawa, R. Komatsu, Y. Watanabe, D. Yokoyama, J. Kido, *Front. Chem.* **2020**, *8*, 00427.

- [2] J. Eccher, G. C. Faria, H. Bock, H. von Seggern, I. H. Bechtold, *ACS Appl. Mater. Interfaces* **2013**, *5*, 11935–11943.
- [3] a) T. Woehrle, Tobias I. Wurzbach, J. Kirres, A. Kostidou, N. Kapernaum, J. Litterscheidt, J. C. Haenle, P. Staffeld, A. Baro, F. Giesselmann, S. Laschat, *Chem. Rev.* **2016**, *116*, 1139–1241; b) *Handbook of Liquid Crystals* Vol. 4, 2<sup>nd</sup> Ed. (Eds: J. W. Goodby, P. J. Collings, T. Kato, C. Tschierske, H. F. Gleeson, P. Raynes), Wiley-VCH, Weinheim, Germany, **1996**; c) *Chemistry of Discotic Liquid Crystals: From Monomers to Polymers* (Ed: S. Kumar), CRC Press, Boca Raton, USA, **2010**.
- [4] H. Bisoyi, S. Kumar, *Chem. Soc. Rev.* **2010**, *39*, 264–285.
- [5] a) B. Kaafarani, *Chem. Mater.* **2011**, *23*, 378–396; b) S. Sergeyev, W. Pisula, Y. H. Geerts, *Chem. Soc. Rev.* **2007**, *36*, 1902–1929.
- [6] a) N. Boden, R. J. Bushby, A. N. Cammidge, A. El-Mansoury, P. S. Martin, Z. Lu, *J. Mater. Chem.* **1999**, *9*, 1391–1402; b) X. Hao, C. Zhang, J. Wang, W. Zhang, F. Hong, S. Zhang, A. Zhang, H. Yang, Z. Zhang, Y. Wang, H. Wu, J. Pu, *J. Mater. Chem. C* **2017**, *5*, 589–600; c) H. Ji, K. Q. Zhao, W. H. Yu, B. Q. Wang, P. Hu, *Sci. China Ser. B* **2009**, *52*, 975–985; d) S. Kumar, M. Manickam, H. Schonherr, *Liq. Cryst.* **1999**, *26*, 1567–1571; e) S. Kumar, *Liq. Cryst.* **2005**, *32*, 1089–1113; f) C. O. Zellman, V. E. Williams, *J. Org. Chem.* **2021**, *86*, 15076–15084.
- [7] K. E. Treacher, G. J. Clarkson, N. B. McKeown, *Liq. Cryst.* **1995**, *19*, 887–889.
- [8] a) Z. Chen, C. Bishop, E. Thoms, H. Bock, M. D. Ediger, R. Richert, L. Yu, *Chem. Mater.* **2021**, *33*, 4757–4764; b) A. Gujral, J. Gomez, S. Ruan, M. F. Toney, H. Bock, L. Yu, M. D. Ediger, *Chem. Mater.* **2017**, *29*, 9110–9119; c) C. Bishop, Z. Chen, M. F. Toney, H. Bock, L. Yu, M. D. Ediger, *J. Phys. Chem. B* **2021**, *125*, 2761–2770.
- [9] a) C.-H. Lee, T. Yamamoto, *Tetrahedron Lett.* **2001**, *42*, 3993–3996; b) H. Lee, D. Kim, H.-K. Lee, W. Qiu, N.-K. Oh, W.-C. Zin, K. Kim, *Tetrahedron Lett.* **2004**, *45*, 1019–1022; c) E. Beltrán, J. L. Serrano, T. Sierra, R. Giménez, *Org. Lett.* **2010**, *12*, 1404–1407; d) E. Beltrán, J. L. Serrano, T. Sierra, R. Giménez, *J. Mater. Chem.* **2012**, *22*, 7797–7805; e) B. N. Veerabhadraswamy, H. K. Dambal, D. S. Shankar Rao, C. V. Yelamaggad, *ChemPhysChem* **2016**, *17*, 1–14; f) B. Pradhan, S. K. Pathak, R. K. Gupta, M. Gupta, S. K. Pal, A. S. Achalkumar, *J. Mater. Chem. C* **2016**, *4*, 6117–6130; g) N. Tober, T. Rieth, M. Lehmann, H. Detert, *Chem. Eur. J.* **2019**, *25*, 15295–15304.
- [10] a) A. Pinner, F. Klein, *Chem. Ber.* **1878**, *11*, 764; b) A. H. Cook, D. G. Jones, *J. Chem. Soc.* **1941**, 278.
- [11] A. A. Vieira, G. Farias, W. C. Costa, J. Eccher, I. H. Bechtold, F. Durola, H. Bock, *Chem. Eur. J.* **2021**, *27*, 9003–9010.
- [12] a) T.-T. Bui, F. Goubard, M. Ibrahim-Ouali, D. Gimes, F. Dumur, *Beilstein J. Org. Chem.* **2018**, *14*, 282–308; b) C.-L. Yi, C.-L. Ko, T.-C. Yeh, C.-Y. Chen, Y.-S. Chen, D.-G. Chen, P.-T. Chou, W.-Y. Hung, K.-T. Wong, *ACS Appl. Mater. Interfaces* **2020**, *12*, 2724–2732.
- [13] L. Sturm, F. Aribot, L. Soliman, H. Bock, F. Durola, *Eur. J. Org. Chem.* **2022**, e202200196.
- [14] T. Hassheider, S. A. Benning, H.-S. Kitzerow, M.-F. Achard, H. Bock, *Angew. Chem. Int. Ed.* **2001**, *40*, 2060–2063; *Angew. Chem.* **2001**, *113*, 2119–2122.
- [15] A. M. Levelut, *J. Chim. Phys.* **1983**, *80*, 149–61.
- [16] L. Zhao, R. I. Kaiser, B. Xu, U. Ablikim, W. Lu, M. Ahmed, M. M. Evseev, E. K. Bashkurov, V. N. Azyazov, M. V. Zagidullin, A. N. Morozov, A. H. Howlader, S. F. Wnuk, A. M. Mebel, D. Joshi, G. Veber, F. R. Fischer, *Nat. Commun.* **2019**, *10*, 1510.
- [17] B. Liu, B. Z. Tang, *Angew. Chem. Int. Ed.* **2020**, *59*, 9788–9789; *Angew. Chem.* **2020**, *132*, 9872–9873.

Manuscript received: November 19, 2022

Accepted manuscript online: January 24, 2023

Version of record online: ■■■■

## 7 BIBLIOGRAPHY

1. Hong, G. *et al.* A Brief History of OLEDs—Emitter Development and Industry Milestones. *Advanced Materials* **33**, 2005630 (2021).
2. Tang, C. W. & VanSlyke, S. A. Organic electroluminescent diodes. *Appl Phys Lett* **51**, 913–915 (1987).
3. Kallmann, H. & Pope, M. Positive Hole Injection into Organic Crystals. *J Chem Phys* **32**, 300–301 (1960).
4. Helfrich, W. & Schneider, W. G. Recombination Radiation in Anthracene Crystals. *Phys Rev Lett* **14**, 229–231 (1965).
5. Pope, M., Kallmann, H. P. & Magnante, P. Electroluminescence in Organic Crystals. *J Chem Phys* **38**, 2042–2043 (1963).
6. Sudheendran Swayamprabha, S. *et al.* Approaches for Long Lifetime Organic Light Emitting Diodes. *Advanced Science* **8**, 2002254 (2021).
7. Bauri, J., Choudhary, R. B. & Mandal, G. Recent advances in efficient emissive materials-based OLED applications: a review. *J Mater Sci* **56**, 18837–18866 (2021).
8. Zhan, G., Liu, Z., Bian, Z. & Huang, C. Recent Advances in Organic Light-Emitting Diodes Based on Pure Organic Room Temperature Phosphorescence Materials. *Front Chem* **7**, (2019).
9. Minaev, B., Baryshnikov, G. & Agren, H. Principles of phosphorescent organic light emitting devices. *Phys. Chem. Chem. Phys.* **16**, 1719–1758 (2014).
10. Xue, C. *et al.* Recent advances in thermally activated delayed fluorescence for white OLEDs applications. *Journal of Materials Science: Materials in Electronics* **31**, 4444–4462 (2020).
11. Huang, Y., Hsiang, E.-L., Deng, M.-Y. & Wu, S.-T. Mini-LED, Micro-LED and OLED displays: present status and future perspectives. *Light Sci Appl* **9**, 105 (2020).
12. Monkman, A. Why Do We Still Need a Stable Long Lifetime Deep Blue OLED Emitter? *ACS Appl Mater Interfaces* **14**, 20463–20467 (2022).
13. Wang, J. *et al.* Key issues and recent progress of high efficient organic light-emitting diodes. *Journal of Photochemistry and Photobiology C: Photochemistry Reviews* **17**, 69–104 (2013).
14. Lin, B.-Y. *et al.* Effects of electron transport layer thickness on light extraction in corrugated OLEDs. *Opt Express* **30**, 18066 (2022).

15. Adachi, C. & Sandanayaka, A. S. D. The leap from organic light-emitting diodes to organic semiconductor laser diodes. *CCS Chemistry* vol. 2 1203–1216 Preprint at <https://doi.org/10.31635/ccschem.020.202000327> (2020).
16. Tang, C. W., VanSlyke, S. A. & Chen, C. H. Electroluminescence of doped organic thin films. *J Appl Phys* **65**, 3610–3616 (1989).
17. Zheng, C.-J. *et al.* Highly efficient non-doped deep-blue organic light-emitting diodes based on anthracene derivatives. *J Mater Chem* **20**, 1560 (2010).
18. Huang, J., Su, J.-H. & Tian, H. The development of anthracene derivatives for organic light-emitting diodes. *J Mater Chem* **22**, 10977 (2012).
19. Xu, H. *et al.* Recent progress in metal–organic complexes for optoelectronic applications. *Chem. Soc. Rev.* **43**, 3259–3302 (2014).
20. Kim, K.-H., Moon, C.-K., Lee, J.-H., Kim, S.-Y. & Kim, J.-J. Highly Efficient Organic Light-Emitting Diodes with Phosphorescent Emitters Having High Quantum Yield and Horizontal Orientation of Transition Dipole Moments. *Advanced Materials* **26**, 3844–3847 (2014).
21. Ding, J. *et al.* Highly Efficient Green-Emitting Phosphorescent Iridium Dendrimers Based on Carbazole Dendrons. *Adv Funct Mater* **16**, 575–581 (2006).
22. Choy, W. C. H., Chan, W. K. & Yuan, Y. Recent Advances in Transition Metal Complexes and Light-Management Engineering in Organic Optoelectronic Devices. *Advanced Materials* **26**, 5368–5399 (2014).
23. Xiang, H., Cheng, J., Ma, X., Zhou, X. & Chruma, J. J. Near-infrared phosphorescence: materials and applications. *Chem Soc Rev* **42**, 6128 (2013).
24. Mukherjee, S. & Thilagar, P. Recent advances in purely organic phosphorescent materials. *Chemical Communications* **51**, 10988–11003 (2015).
25. Bolton, O., Lee, K., Kim, H. J., Lin, K. Y. & Kim, J. Activating efficient phosphorescence from purely organic materials by crystal design. *Nat Chem* **3**, 205–210 (2011).
26. Solov'ev, K. N. & Borisevich, E. A. Intramolecular heavy-atom effect in the photophysics of organic molecules. *Physics-Uspekhi* **48**, 231–253 (2005).
27. Wang, J. Q. *et al.* Room-Temperature Phosphorescence with Excitation-Energy Dependence and External Heavy-Atom Effect in Hybrid Zincophosphites. *Inorg Chem* **58**, 9476–9481 (2019).

28. Uoyama, H., Goushi, K., Shizu, K., Nomura, H. & Adachi, C. Highly efficient organic light-emitting diodes from delayed fluorescence. *Nature* **492**, 234–238 (2012).
29. Xie, F.-M., Zhou, J.-X., Li, Y.-Q. & Tang, J.-X. Effects of the relative position and number of donors and acceptors on the properties of TADF materials. *J Mater Chem C Mater* **8**, 9476–9494 (2020).
30. Teng, J.-M., Wang, Y.-F. & Chen, C.-F. Recent progress of narrowband TADF emitters and their applications in OLEDs. *J Mater Chem C Mater* **8**, 11340–11353 (2020).
31. Data, P. & Takeda, Y. Recent Advancements in and the Future of Organic Emitters: TADF- and RTP-Active Multifunctional Organic Materials. *Chemistry - An Asian Journal* vol. 14 1613–1636 Preprint at <https://doi.org/10.1002/asia.201801791> (2019).
32. Kim, J. H., Yun, J. H. & Lee, J. Y. Recent Progress of Highly Efficient Red and Near-Infrared Thermally Activated Delayed Fluorescent Emitters. *Adv Opt Mater* **6**, 1800255 (2018).
33. Bui, T.-T., Goubard, F., Ibrahim-Ouali, M., Gigmes, D. & Dumur, F. Recent advances on organic blue thermally activated delayed fluorescence (TADF) emitters for organic light-emitting diodes (OLEDs). *Beilstein Journal of Organic Chemistry* **14**, 282–308 (2018).
34. Cai, X. & Su, S.-J. Marching Toward Highly Efficient, Pure-Blue, and Stable Thermally Activated Delayed Fluorescent Organic Light-Emitting Diodes. *Adv Funct Mater* **28**, 1802558 (2018).
35. Lee, J. H. *et al.* Blue organic light-emitting diodes: Current status, challenges, and future outlook. *Journal of Materials Chemistry C* vol. 7 5874–5888 Preprint at <https://doi.org/10.1039/c9tc00204a> (2019).
36. Wu, T.-L. *et al.* Diboron compound-based organic light-emitting diodes with high efficiency and reduced efficiency roll-off. *Nat Photonics* **12**, 235–240 (2018).
37. Zhang, Y. *et al.* Multi-Resonance Induced Thermally Activated Delayed Fluorophores for Narrowband Green OLEDs. *Angewandte Chemie International Edition* **58**, 16912–16917 (2019).
38. Ikeda, N. *et al.* Solution-Processable Pure Green Thermally Activated Delayed Fluorescence Emitter Based on the Multiple Resonance Effect. *Advanced Materials* **32**, 2004072 (2020).

39. Yuan, Y. *et al.* The Design of Fused Amine/Carbonyl System for Efficient Thermally Activated Delayed Fluorescence: Novel Multiple Resonance Core and Electron Acceptor. *Adv Opt Mater* **7**, 1801536 (2019).
40. Song, J., Lee, H., Jeong, E. G., Choi, K. C. & Yoo, S. Organic Light-Emitting Diodes: Pushing Toward the Limits and Beyond. *Advanced Materials* **32**, 1907539 (2020).
41. Brütting, W., Frischeisen, J., Schmidt, T. D., Scholz, B. J. & Mayr, C. Device efficiency of organic light-emitting diodes: Progress by improved light outcoupling. *physica status solidi (a)* **210**, 44–65 (2013).
42. Zhang, Y. & Biswas, R. High Light Outcoupling Efficiency from Periodically Corrugated OLEDs. *ACS Omega* **6**, 9291–9301 (2021).
43. Naqvi, B. A. *et al.* What Controls the Orientation of TADF Emitters? *Front Chem* **8**, (2020).
44. Schmidt, T. D. *et al.* Emitter Orientation as a Key Parameter in Organic Light-Emitting Diodes. *Phys Rev Appl* **8**, 037001 (2017).
45. Yokoyama, D. Molecular orientation in small-molecule organic light-emitting diodes. *J Mater Chem* **21**, 19187 (2011).
46. Hänisch, C., Lenk, S. & Reineke, S. Long-Term Stability of Emitter Orientation in Organic Light-Emitting Diodes at Temperatures in the Range of the Active Layer Glass Transition. *Chemistry of Materials* **34**, 9221–9227 (2022).
47. Kim, K.-H. & Kim, J.-J. Origin and Control of Orientation of Phosphorescent and TADF Dyes for High-Efficiency OLEDs. *Advanced Materials* **30**, 1705600 (2018).
48. Vieira, A. A. *et al.* Nematic Triphenyltriazine Triesters and the Induction of the Columnar Mesophase by Fluorine Substitution. *Chemistry – A European Journal* **27**, 9003–9010 (2021).
49. Suleymanova, A. F. *et al.* Construction and performance of OLED devices prepared from liquid-crystalline TADF materials. *Physical Chemistry Chemical Physics* **24**, 22115–22121 (2022).
50. Valeur, B. & Berberan-Santos, M. N. *Molecular Fluorescence*. vol. Second Edition (Wiley, 2012).
51. Skoog, D. A., Holler, F. J. & Crouch, S. R. *Principles of Instrumental Analysis*. (2016).



52. Yang, Z. *et al.* Recent advances in organic thermally activated delayed fluorescence materials. *Chemical Society Reviews* vol. 46 915–1016 Preprint at <https://doi.org/10.1039/c6cs00368k> (2017).
53. Lakowicz, J. R. *Principles of Fluorescence Spectroscopy*. (2010).
54. dos Santos, P. L., Etherington, M. K. & Monkman, A. P. Chemical and conformational control of the energy gaps involved in the thermally activated delayed fluorescence mechanism. *J Mater Chem C Mater* **6**, 4842–4853 (2018).
55. Endo, A. *et al.* Thermally Activated Delayed Fluorescence from Sn<sup>4+</sup>-Porphyrin Complexes and Their Application to Organic Light Emitting Diodes - A Novel Mechanism for Electroluminescence. *Advanced Materials* **21**, 4802–4806 (2009).
56. Olivier, Y., Sancho-Garcia, J.-C., Muccioli, L., D'Avino, G. & Beljonne, D. Computational Design of Thermally Activated Delayed Fluorescence Materials: The Challenges Ahead. *J Phys Chem Lett* **9**, 6149–6163 (2018).
57. Chen, X.-K., Kim, D. & Brédas, J.-L. Thermally Activated Delayed Fluorescence (TADF) Path toward Efficient Electroluminescence in Purely Organic Materials: Molecular Level Insight. *Acc Chem Res* **51**, 2215–2224 (2018).
58. Tao, Y. *et al.* Thermally Activated Delayed Fluorescence Materials Towards the Breakthrough of Organoelectronics. *Advanced Materials* **26**, 7931–7958 (2014).
59. Data, P. & Takeda, Y. Recent Advancements in and the Future of Organic Emitters: TADF- and RTP-Active Multifunctional Organic Materials. *Chem Asian J* **14**, 1613–1636 (2019).
60. Huang, T., Jiang, W. & Duan, L. Recent progress in solution processable TADF materials for organic light-emitting diodes. *J Mater Chem C Mater* **6**, 5577–5596 (2018).
61. Im, Y. *et al.* Molecular Design Strategy of Organic Thermally Activated Delayed Fluorescence Emitters. *Chemistry of Materials* **29**, 1946–1963 (2017).
62. Liang, X., Tu, Z. & Zheng, Y. Thermally Activated Delayed Fluorescence Materials: Towards Realization of High Efficiency through Strategic Small Molecular Design. *Chemistry – A European Journal* **25**, 5623–5642 (2019).
63. Naveen, K. R., Yang, H. I. & Kwon, J. H. Double boron-embedded multiresonant thermally activated delayed fluorescent materials for organic light-emitting diodes. *Commun Chem* **5**, 149 (2022).

64. Atkins, P., Jones, L. & Laverman, L. *Princípios de Química: questionando a vida moderna e o meio ambiente*. (2018).
65. Bechtold, I. H. Cristais líquidos: um sistema complexo de simples aplicação. *Revista Brasileira de Ensino de Física* **27**, 333–342 (2005).
66. Collings, P. J. & Hird, M. *Introduction to Liquid Crystals Chemistry and Physics*. (CRC Press, 2017). doi:10.1201/9781315272801.
67. Reinitzer, F. Contributions to the knowledge of cholesterol. *Liq Cryst* **5**, 7–18 (1989).
68. Lehmann, O. Über fließende Krystalle. *Zeitschrift für Physikalische Chemie* **4U**, 462–472 (1889).
69. Mertelj, A. & Lisjak, D. Ferromagnetic nematic liquid crystals. *Liq Cryst Rev* **5**, 1–33 (2017).
70. Goossens, K., Lava, K., Bielawski, C. W. & Binnemans, K. Ionic Liquid Crystals: Versatile Materials. *Chem Rev* **116**, 4643–4807 (2016).
71. Lagerwall, J. P. F. & Scalia, G. A new era for liquid crystal research: Applications of liquid crystals in soft matter nano-, bio- and microtechnology. *Current Applied Physics* **12**, 1387–1412 (2012).
72. Wöhrle, T. *et al.* Discotic Liquid Crystals. *Chem Rev* **116**, 1139–1241 (2016).
73. Kato, T., Uchida, J., Ichikawa, T. & Sakamoto, T. Functional Liquid Crystals towards the Next Generation of Materials. *Angewandte Chemie International Edition* **57**, 4355–4371 (2018).
74. An, J.-G. *et al.* *Characterization of Liquid Crystals: A Literature Review*. (2016).
75. Lee, W. & Kumar, S. *Unconventional Liquid Crystals and Their Applications*. (De Gruyter, 2021). doi:10.1515/9783110584370.
76. Goodby, J. W. *et al.* *Handbook of Liquid Crystals*. (Wiley, 2014). doi:10.1002/9783527671403.
77. Andrienko, D. Introduction to liquid crystals. *J Mol Liq* **267**, 520–541 (2018).
78. Chandrasekhar, S., Sadashiva, B. K. & Suresh, K. A. Liquid crystals of disc-like molecules. *Pramana* **9**, 471–480 (1977).
79. Laschat, S. *et al.* Discotic Liquid Crystals: From Tailor-Made Synthesis to Plastic Electronics. *Angewandte Chemie International Edition* **46**, 4832–4887 (2007).
80. Omez De La Oliva, C. G., Laza, P. G. & Ochoa De Ocariz, C. *Six-Membered Heterocycles: Triazines, Tetrazines and Other Polyaza Systems*. (2011).

81. Gamez, P. & Reedijk, J. 1,3,5-Triazine-based synthons in supramolecular chemistry. *European Journal of Inorganic Chemistry* 29–42 Preprint at <https://doi.org/10.1002/ejic.200500672> (2006).
82. Bhagavath, P., Shetty, R. & Sunil, D. 1,3,5-Triazine-Based Liquid Crystals: An Up-to-Date Appraisal of Their Synthetic Design and Mesogenic Properties. *Critical Reviews in Solid State and Materials Sciences* vol. 45 378–409 Preprint at <https://doi.org/10.1080/10408436.2019.1632794> (2020).
83. Sun, D., Si, C., Wang, T. & Zysman-Colman, E. ,3,5-Triazine-Functionalized Thermally Activated Delayed Fluorescence Emitters for Organic Light-Emitting Diodes.
84. Blotny, G. Recent applications of 2,4,6-trichloro-1,3,5-triazine and its derivatives in organic synthesis. *Tetrahedron* vol. 62 9507–9522 Preprint at <https://doi.org/10.1016/j.tet.2006.07.039> (2006).
85. Zhang, F. G., Chen, Z., Tang, X. & Ma, J. A. Triazines: Syntheses and Inverse Electron-demand Diels-Alder Reactions. *Chemical Reviews* vol. 121 14555–14593 Preprint at <https://doi.org/10.1021/acs.chemrev.1c00611> (2021).
86. Grundmann, C. & Kreutzberger, A. 1,3,5-Triazine and its Formation from Hydrocyanic Acid. *J. Chem. Soc* vol. 87 <https://pubs.acs.org/sharingguidelines> (1954).
87. Braveenth, R. *et al.* High efficiency green TADF emitters of acridine donor and triazine acceptor D-A-D structures. *J Mater Chem C Mater* **7**, 7672–7680 (2019).
88. Li, X., Li, J., Liu, D., Li, D. & Dong, R. A donor design strategy for triazine-carbazole blue thermally activated delayed fluorescence materials. *New Journal of Chemistry* **44**, 9743–9753 (2020).
89. Tsai, W. L. *et al.* A versatile thermally activated delayed fluorescence emitter for both highly efficient doped and non-doped organic light emitting devices. *Chemical Communications* **51**, 13662–13665 (2015).
90. Lin, T. A. *et al.* Sky-Blue Organic Light Emitting Diode with 37% External Quantum Efficiency Using Thermally Activated Delayed Fluorescence from Spiroacridine-Triazine Hybrid. *Advanced Materials* **28**, 6976–6983 (2016).
91. Cui, L. S. *et al.* Fast spin-flip enables efficient and stable organic electroluminescence from charge-transfer states. *Nat Photonics* **14**, 636–642 (2020).
92. Wada, Y. *et al.* Highly efficient electroluminescence from a solution-processable thermally activated delayed fluorescence emitter. *Appl Phys Lett* **107**, (2015).

93. Hu, Q. J., Lu, Y. C., Yang, C. X. & Yan, X. P. Synthesis of covalently bonded boron-dipyrromethene-diarylethene for building a stable photosensitizer with photo-controlled reversibility. *Chemical Communications* **52**, 5470–5473 (2016).
94. Mari, D., Miyagawa, N., Okano, K. & Mori, A. Regiocontrolled Halogen Dance of Bromothiophenes and Bromofurans. *Journal of Organic Chemistry* **83**, 14126–14137 (2018).
95. Yasuda, T., Shimizu, T., Liu, F., Ungar, G. & Kato, T. Electro-functional octupolar  $\pi$ -conjugated columnar liquid crystals. *J Am Chem Soc* **133**, 13437–13444 (2011).
96. Bader, D., Fröhlich, J. & Kautny, P. Thienopyrrolo[3,2,1-jk]carbazoles: Building Blocks for Functional Organic Materials. *Journal of Organic Chemistry* **85**, 3865–3871 (2020).
97. Cardeynaels, T. *et al.* Finding the optimal exchange-correlation functional to describe the excited state properties of push-pull organic dyes designed for thermally activated delayed fluorescence. *Physical Chemistry Chemical Physics* **22**, 16387–16399 (2020).
98. Dhali, R. *et al.* Understanding TADF: a joint experimental and theoretical study of DMAC-TRZ. *Physical Chemistry Chemical Physics* **23**, 378–387 (2021).
99. Wang, S. *et al.* Blue thermally activated delayed fluorescence based on tristriazolotriazine core: Synthesis, property and the application for solution-processed OLEDs. *Dyes and Pigments* **182**, 108589 (2020).
100. Detert, H. Tristriazolotriazines: Luminescent Discotic Liquid Crystals. *European J Org Chem* **2018**, 4501–4507 (2018).
101. Hofmann, K. A. & Ehrhart, O. *Einwirkung von Hydrasin auf Dicyandiamid.* (1912).
102. Kaiser, D. W., Peters, G. A. & Wystrach, V. P. Chemistry of Dicyandiamide. V. Structures of Guanazo- and Pyro-Guanazoles, and Reaction of Dicyandiamide with 3-Amino-5-Substituted-1,2,4, 4H-Triazoles. *J Org Chem* **18**, 1610–1615 (1953).
103. Huisgen, R., Sturm, H. J. & Seidel, M. Ringöffnungen der Azole, V. Weitere Reaktionen der Tetrazole mit elektrophilen Agenzien. *Chem Ber* **94**, 1555–1562 (1961).
104. Tartakovsky, V. A., Frumkin, A. E., Churakov, A. M., Strelenko, Y. A. & Zelinsky, N. D. *New approaches to synthesis of tris[1,2,4]triazolo[1,3,5]triazines.* *Izvestiya Akademii Nauk. Seriya Khimicheskaya* vol. 54 (2005).
105. Rieth, T., Röder, N., Lehmann, M. & Detert, H. Isomerisation of Liquid-Crystalline Tristriazolotriazines. *Chemistry - A European Journal* **24**, 93–96 (2018).

106. Cristiano, R. *et al.* Tristriazolotriazines: a core for luminescent discotic liquid crystals. *Chemical Communications* 5134 (2008) doi:10.1039/b810680k.
107. Cristiano, R. *et al.* Luminescent columnar liquid crystals based on tristriazolotriazine. *Langmuir* **28**, 11590–11598 (2012).
108. Hundemer, F. *et al.* Tris(triazolo)triazine-based emitters for solution-processed blue thermally activated delayed fluorescence organic light-emitting diodes. *Mater Adv* **1**, 2862–2871 (2020).
109. Pathak, S. K. *et al.* Fused tetracyclic tris[1,2,4]triazolo[1,3,5]triazine as a novel rigid electron acceptor for efficient thermally activated delayed fluorescence emitters. *RSC Adv* **10**, 15523–15529 (2020).
110. Fang, Z. *et al.* Asymmetric sky-blue thermally-activated delayed fluorescence emitters bearing tris(triazolo)triazine moiety for solution-processable organic light-emitting diodes. *J Mater Chem C Mater* **10**, 4837–4844 (2022).
111. Hojo, R., Mayder, D. M. & Hudson, Z. M. Deep-blue emission and thermally activated delayed fluorescence *via* Dimroth rearrangement of tris(triazolo)triazines. *J Mater Chem C Mater* **10**, 13871–13877 (2022).
112. Zeng, S. *et al.* Deep Blue Emitter Based on Tris(triazolo)triazine Moiety with CIE  $\gamma$  < 0.08 for Highly Efficient Solution-Processed Organic Light-Emitting Diodes Via Molecular Strategy of “Hot Excitons”. *Adv Funct Mater* **32**, 2113183 (2022).
113. Lee, S. H. *et al.* Influence of electronic environment on the radiative efficiency of 9-phenyl-9h-carbazole-based ortho-carboranyl luminophores. *Molecules* **26**, (2021).
114. Navarro, A., Fernández-Lienres, M. P., García, G., Granadino-Roldán, J. M. & Fernández-Gómez, M. A DFT approach to the charge transport related properties in columnar stacked  $\pi$ -conjugated N-heterocycle cores including electron donor and acceptor units. *Physical Chemistry Chemical Physics* **17**, 605–618 (2015).
115. Gibson, J., Monkman, A. P. & Penfold, T. J. The Importance of Vibronic Coupling for Efficient Reverse Intersystem Crossing in Thermally Activated Delayed Fluorescence Molecules. *ChemPhysChem* **17**, 2956–2961 (2016).
116. Lv, A. *et al.* Room-Temperature Phosphorescence from Metal-Free Organic Materials in Solution: Origin and Molecular Design. *J Phys Chem Lett* **10**, 1037–1042 (2019).
117. Farias, G. *et al.* Halogenation of a twisted non-polar  $\pi$ -system as a tool to modulate phosphorescence at room temperature. *Chem Sci* **12**, 15116–15127 (2021).

118. Salla, C. A. M. *et al.* Persistent Solid-State Phosphorescence and Delayed Fluorescence at Room Temperature by a Twisted Hydrocarbon. *Angewandte Chemie International Edition* **58**, 6982–6986 (2019).
119. Roy, B., De, N. & Majumdar, K. C. Advances in Metal-Free Heterocycle-Based Columnar Liquid Crystals. *Chemistry - A European Journal* **18**, 14560–14588 (2012).
120. Kotian, S. Y. *et al.* Small molecule based five-membered heterocycles: A view of liquid crystalline properties beyond the biological applications. *J Mol Liq* **297**, 111686 (2020).
121. Vera, F. *et al.* Light-Driven Supramolecular Chirality in Propeller-Like Hydrogen-Bonded Complexes That Show Columnar Mesomorphism. *Angewandte Chemie International Edition* **46**, 1873–1877 (2007).
122. Lee, H. *et al.* Discotic liquid crystalline materials for potential nonlinear optical applications: synthesis and liquid crystalline behavior of 1,3,5-triphenyl-2,4,6-triazine derivatives containing achiral and chiral alkyl chains at the periphery. *Tetrahedron Lett* **45**, 1019–1022 (2004).
123. Wang, Y., Shi, J., Chen, J., Zhu, W. & Baranoff, E. Recent progress in luminescent liquid crystal materials: design, properties and application for linearly polarised emission. *J Mater Chem C Mater* **3**, 7993–8005 (2015).
124. Bala, I. *et al.* Deep-Blue OLED Fabrication from Heptazine Columnar Liquid Crystal Based AIE-Active Sky-Blue Emitter. *ChemistrySelect* **3**, 7771–7777 (2018).
125. Irla, S., Pruthvi, M., Raghunathan, V. A. & Kumar, S. Design and synthesis of extended pyrene based discotic liquid crystalline dyes. *Dyes and Pigments* **194**, 109574 (2021).
126. De, J. *et al.* AIE-active mechanoluminescent discotic liquid crystals for applications in OLEDs and bio-imaging. *Chemical Communications* **56**, 14279–14282 (2020).
127. Tober, N., Rieth, T., Lehmann, M. & Detert, H. Synthesis, Thermal, and Optical Properties of Tris(5-aryl-1,3,4-oxadiazol-2-yl)-1,3,5-triazines, New Star-Shaped Fluorescent Discotic Liquid Crystals. *Chemistry – A European Journal* **25**, 15295–15304 (2019).
128. Sun, D., Si, C., Wang, T. & Zysman-Colman, E. 1,3,5-Triazine-Functionalized Thermally Activated Delayed Fluorescence Emitters for Organic Light-Emitting Diodes. *Adv Photonics Res* **3**, 2200203 (2022).
129. Glang, S. *et al.* Arylethynyl-Substituted Tristriazolotriazines: Synthesis, Optical Properties, and Thermotropic Behavior. *European J Org Chem* **2014**, 3116–3126 (2014).

130. Westphal, E., Windisch, A. C., Zambelli Mezalira, D. & Gallardo, H. Reaching Room-Temperature Mesomorphism through Expansion of the Tristriazolotriazine Core with Alkoxybenzoate Units. *European J Org Chem* **2022**, (2022).
131. Sperner, M., Tober, N. & Detert, H. Tristriazolotriazines with Azobenzene Arms - Acidochromic Dyes and Discotic Liquid Crystals. *European J Org Chem* **2019**, 4688–4693 (2019).
132. Glang, S., Borchmann, D., Rieth, T. & Detert, H. Tristriazolotriazines with  $\pi$ -Conjugated Segments: Star-Shaped Fluorophors and Discotic Liquid Crystals. in 118–123 (2012). doi:10.4028/www.scientific.net/AST.77.118.
133. Rieth, T. *et al.* Impact of Substitution Pattern and Chain Length on the Thermotropic Properties of Alkoxy-Substituted Triphenyl-Tristriazolotriazines. *Molecules* **25**, 5761 (2020).
134. Rieth, T., Glang, S., Borchmann, D. & Detert, H. 3,5-Dialkoxy Substituted Triphenyl-tristriazolotriazines: Fluorescent Discotic Liquid Crystals. *Molecular Crystals and Liquid Crystals* **610**, 89–99 (2015).
135. Rieth, T., Marszalek, T., Pisula, W. & Detert, H. Thermotropic Properties and Molecular Packing of Discotic Tristriazolotriazines with Rigid Substituents. *Chemistry - A European Journal* **20**, 5000–5006 (2014).
136. Hojo, R., Mayder, D. M. & Hudson, Z. M. Donor–acceptor materials exhibiting deep blue emission and thermally activated delayed fluorescence with tris(triazolo)triazine. *J Mater Chem C Mater* **9**, 14342–14350 (2021).
137. Sasabe, H. *et al.* Molecular Orientations of Delayed Fluorescent Emitters in a Series of Carbazole-Based Host Materials. *Front Chem* **8**, (2020).
138. Tenopala-Carmona, F. *et al.* Identification of the Key Parameters for Horizontal Transition Dipole Orientation in Fluorescent and TADF Organic Light-Emitting Diodes. *Advanced Materials* **33**, 2100677 (2021).
139. Eccher, J., Faria, G. C., Bock, H., von Seggern, H. & Bechtold, I. H. Order Induced Charge Carrier Mobility Enhancement in Columnar Liquid Crystal Diodes. *ACS Appl Mater Interfaces* **5**, 11935–11943 (2013).
140. Bishop, C. *et al.* Using Deposition Rate and Substrate Temperature to Manipulate Liquid Crystal-Like Order in a Vapor-Deposited Hexagonal Columnar Glass. *J Phys Chem B* **125**, 2761–2770 (2021).

141. Sturm, L., Aribot, F., Soliman, L., Bock, H. & Durola, F. The Perkin Strategy for the Synthesis of Large Carboxy-Substituted Polycyclic Aromatic Compounds. *European J Org Chem* **2022**, (2022).
142. Levelut, A. M. Structures des phases mésomorphes formées de molécules discoïdes. *Journal de Chimie Physique* **80**, 149–161 (1983).
143. Mamada, M., Fukunaga, T., Bencheikh, F., Sandanayaka, A. S. D. & Adachi, C. Low Amplified Spontaneous Emission Threshold from Organic Dyes Based on Bis-stilbene. *Adv Funct Mater* **28**, 1802130 (2018).
144. Li, J., Zhu, H., Li, X., Wang, S. & Xiao, Y. Synthesis of a carbazole-substituted diphenylethylene hole transporting material and application in perovskite solar cells. *IOP Conf Ser Mater Sci Eng* **556**, 012022 (2019).
145. Matulaitis, T. *et al.* Synthesis and properties of bipolar derivatives of 1,3,5-triazine and carbazole. *Dyes and Pigments* **127**, 45–58 (2016).
146. Song, B. J. *et al.* A Desirable Hole-Conducting Coadsorbent for Highly Efficient Dye-Sensitized Solar Cells through an Organic Redox Cascade Strategy. *Chemistry - A European Journal* **17**, 11115–11121 (2011).
147. Chen, D. *et al.* *Controlling the Emitter Orientation in Solution-processed Films through Introduction of Mesogenic Groups within a Multi-resonance Thermally Activated Delayed Fluorescence Emitter.*
148. Suleymanova, A. F., Shafikov, M. Z., Whitwood, A. C., Czerwieniec, R. & Bruce, D. W. Liquid-crystalline TADF materials based on substituted carbazoles and terephthalonitrile. *J Mater Chem C Mater* **9**, 6528–6535 (2021).
149. Zhu, Y. *et al.* Liquid-Crystalline Thermally Activated Delayed Fluorescence: Design, Synthesis, and Application in Solution-Processed Organic Light-Emitting Diodes. *ACS Appl Mater Interfaces* **14**, 15437–15447 (2022).



## 8 ANNEXES

### 8.1 NMR $^1\text{H}$ AND $^{13}\text{C}$

#### 8.1.1 s-Triazine emitters

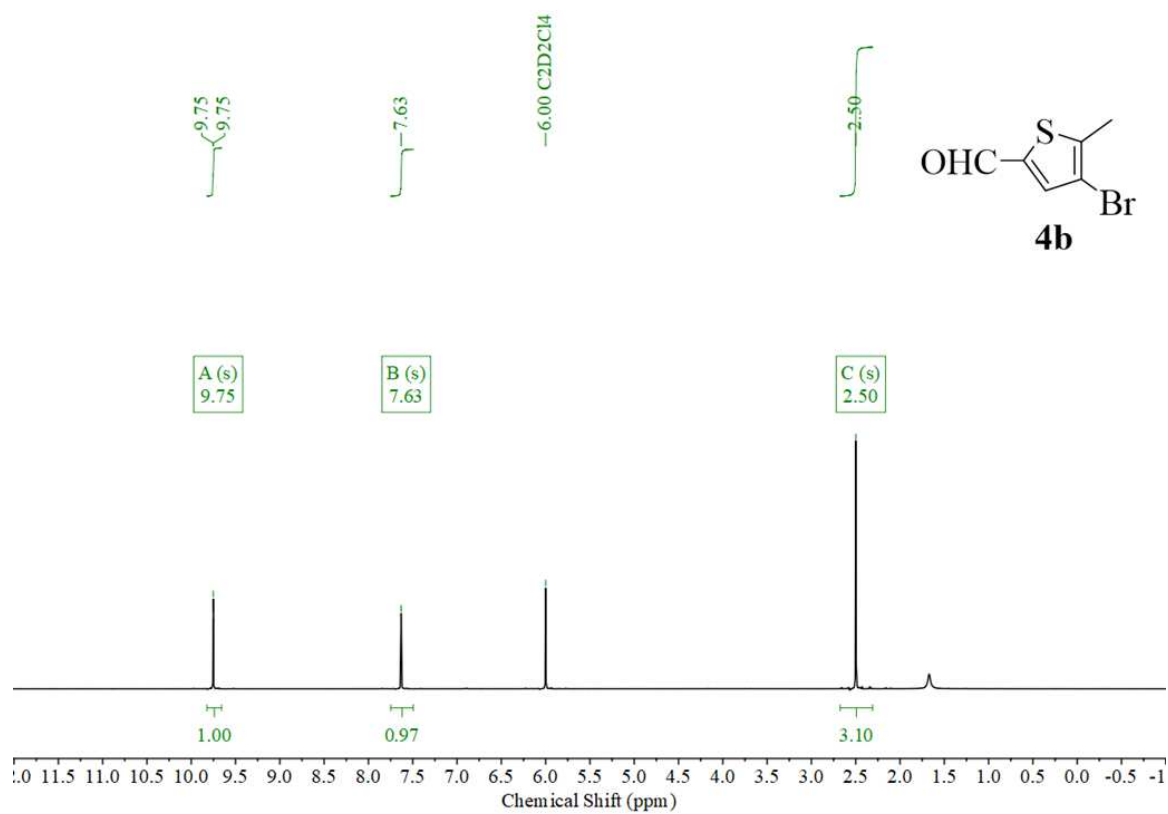


Figure SI 1  $^1\text{H}$  NMR spectra **4b** (400 MHz,  $\text{C}_2\text{D}_2\text{Cl}_4$ ).

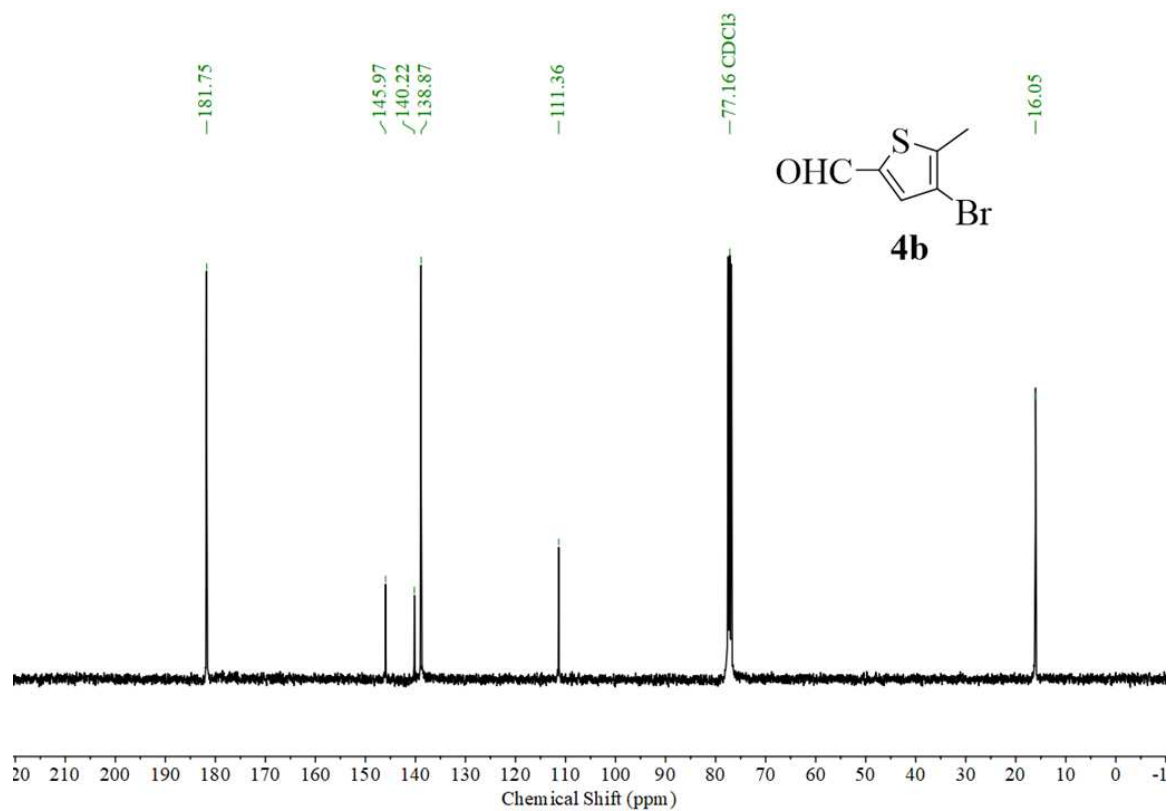


Figure SI 2 <sup>13</sup>C NMR spectra **4b** (101 MHz, CDCl<sub>3</sub>).

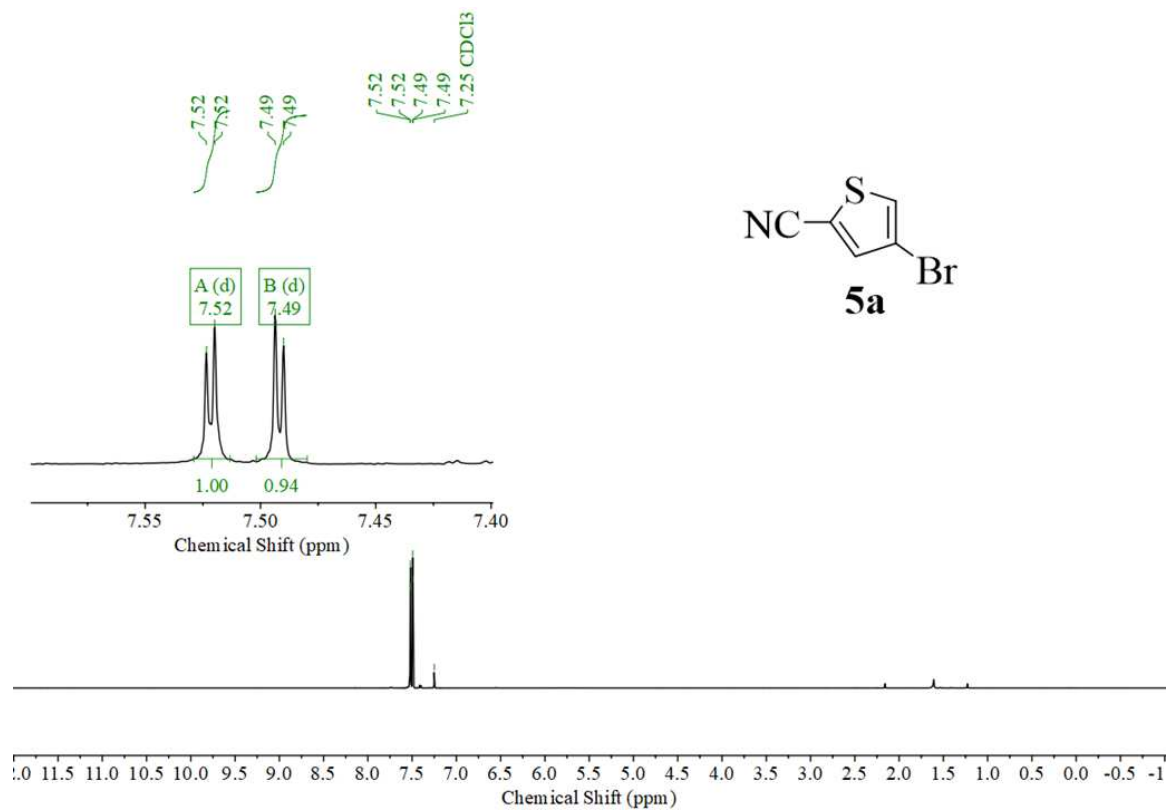


Figure SI 3 <sup>1</sup>H NMR spectra **5a** (400 MHz, CDCl<sub>3</sub>).

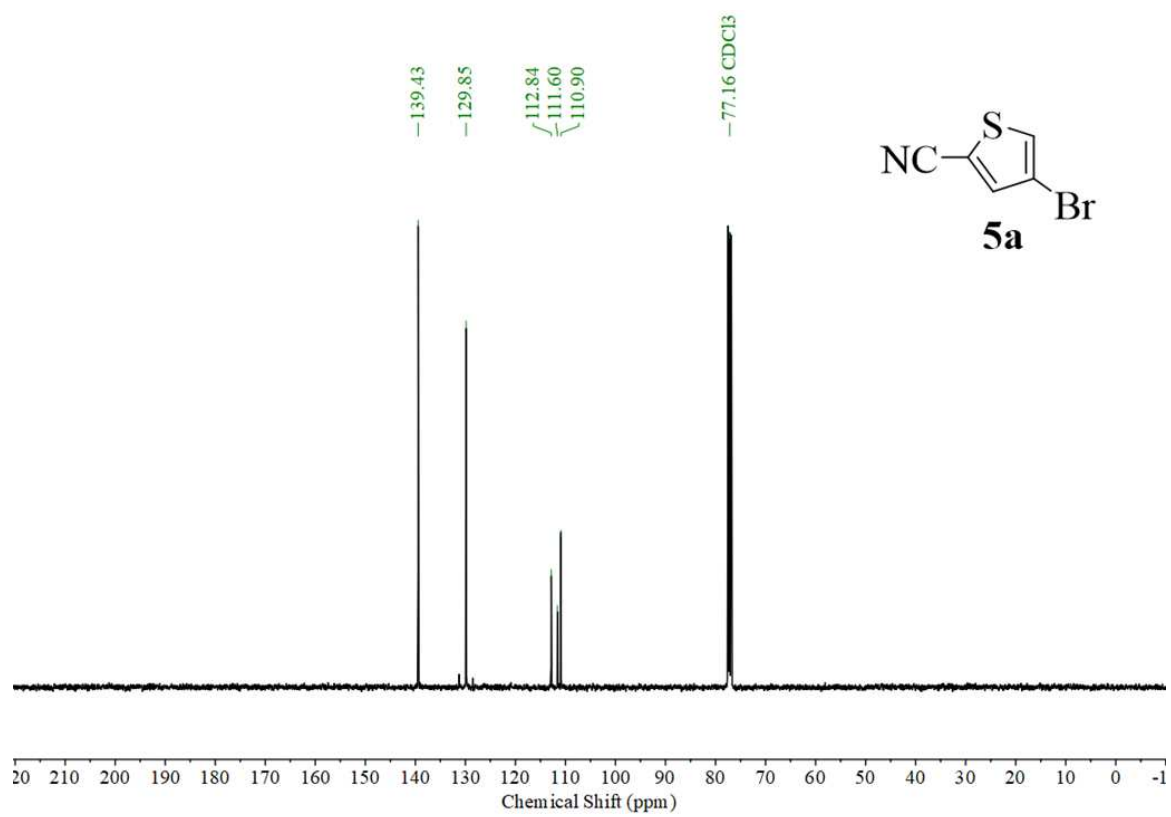


Figure SI 4  $^{13}\text{C}$  NMR spectra **5a** (101 MHz,  $\text{CDCl}_3$ ).

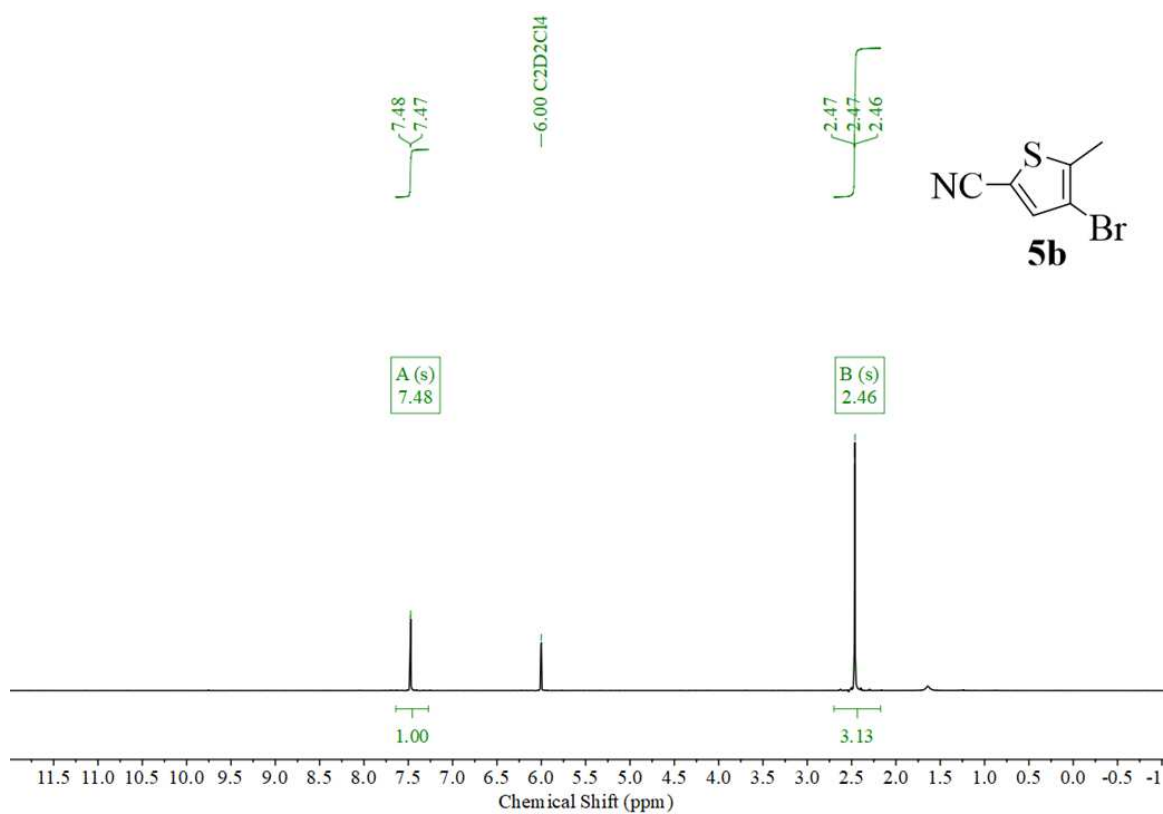


Figure SI 5 <sup>1</sup>H NMR spectra **5b** (400 MHz, C<sub>2</sub>D<sub>2</sub>Cl<sub>4</sub>).

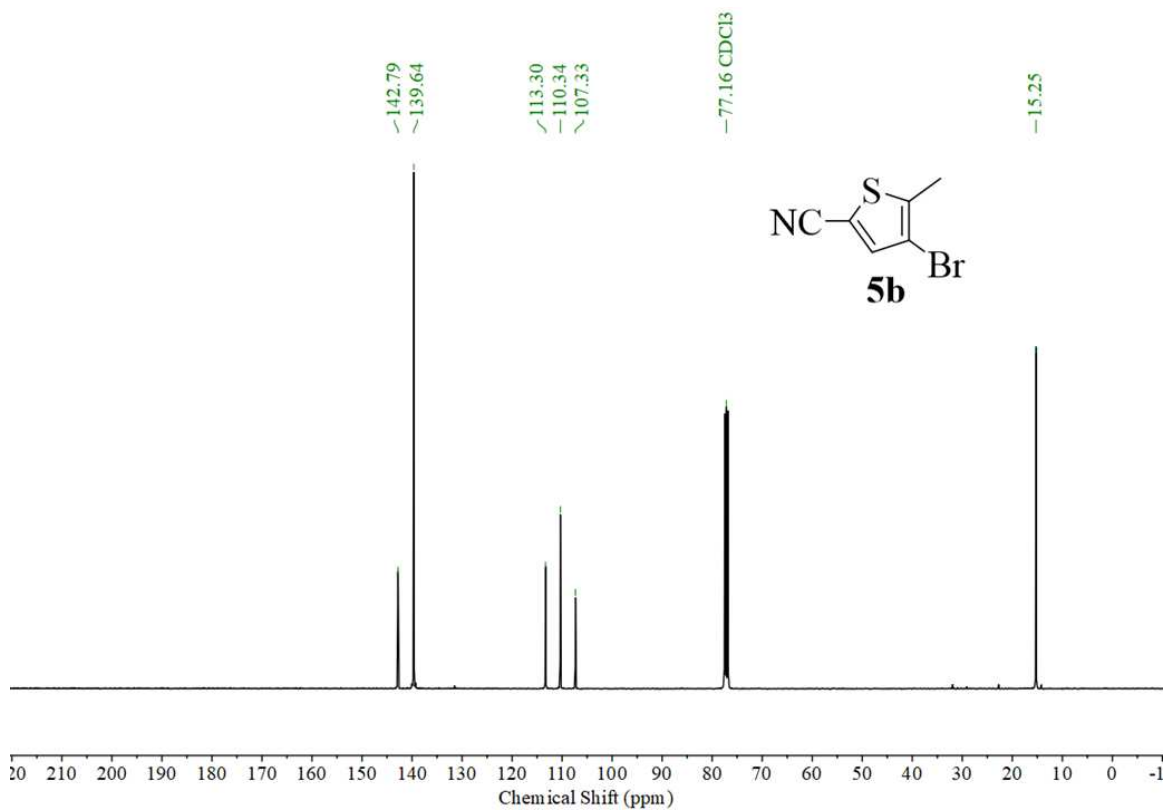


Figure SI 6 <sup>13</sup>C NMR spectra **5b** (101 MHz, CDCl<sub>3</sub>).

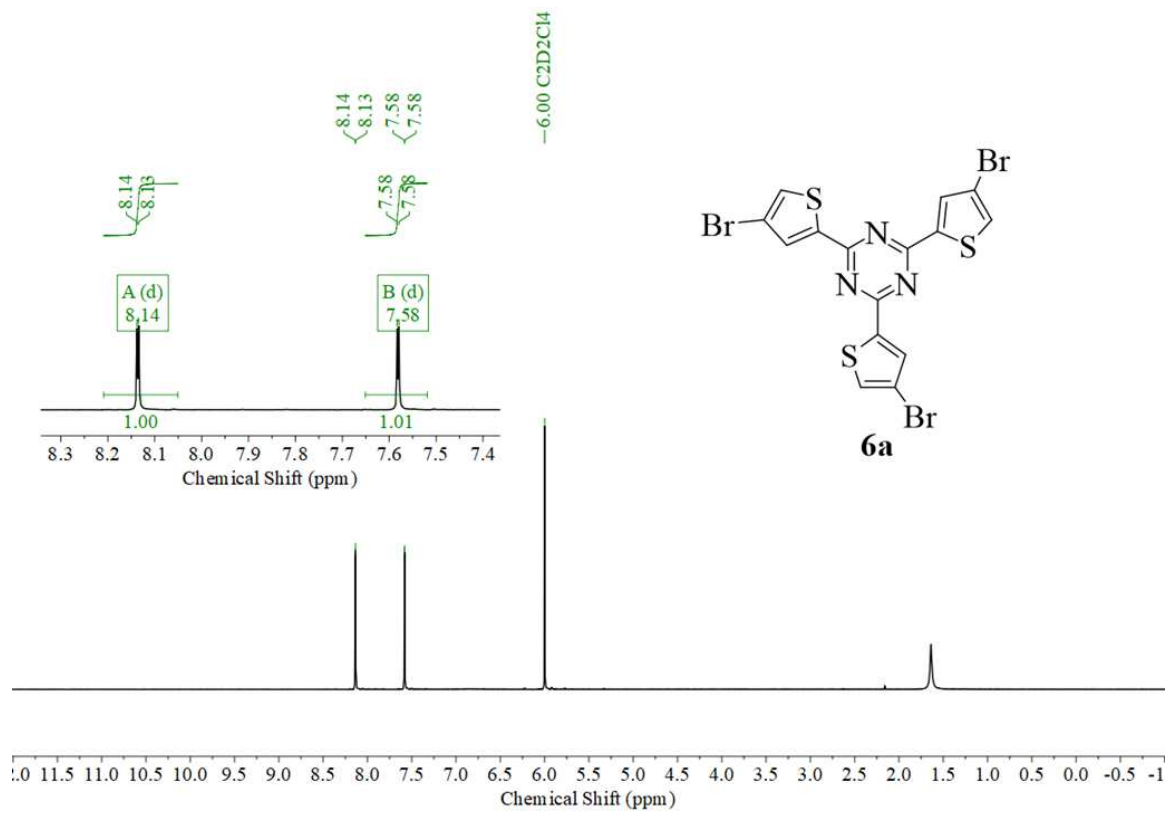


Figure SI 7 <sup>1</sup>H NMR spectra **6a** (400 MHz, C<sub>2</sub>D<sub>2</sub>Cl<sub>4</sub>).

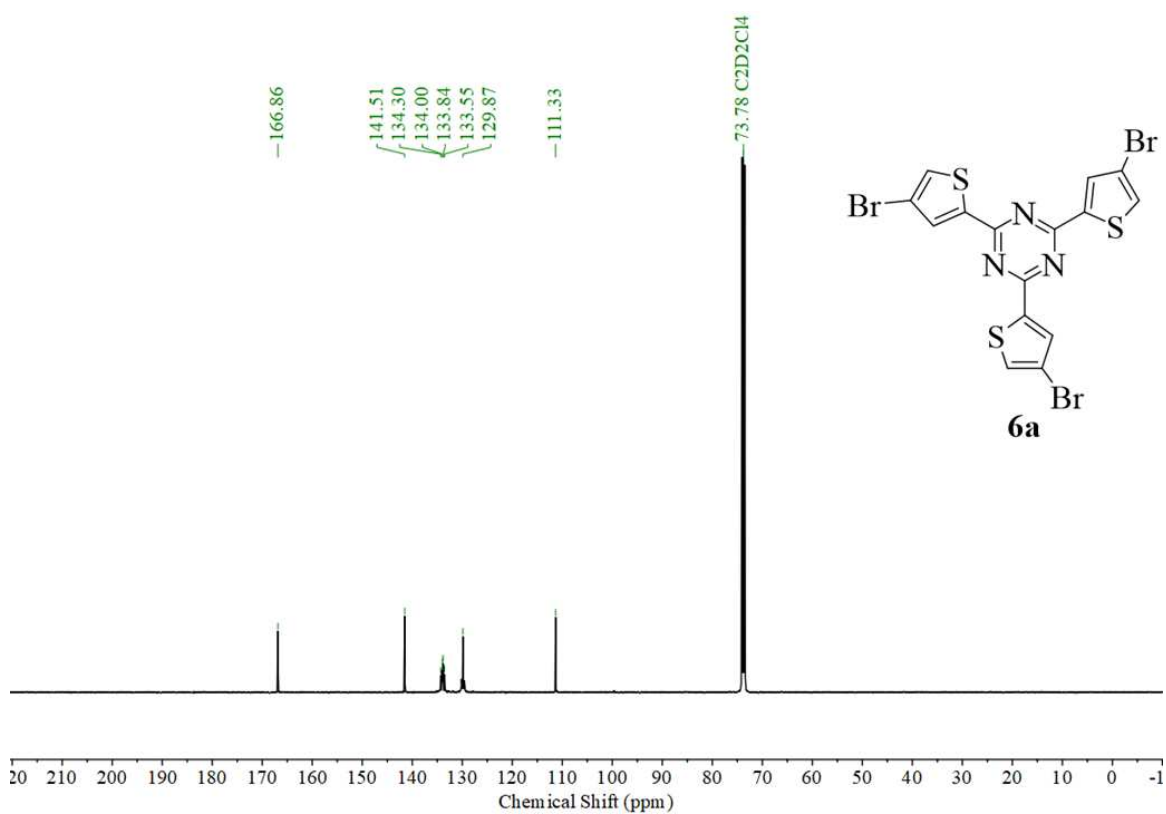


Figure SI 8 <sup>13</sup>C NMR spectra **6a** (101 MHz, C<sub>2</sub>D<sub>2</sub>Cl<sub>4</sub>).

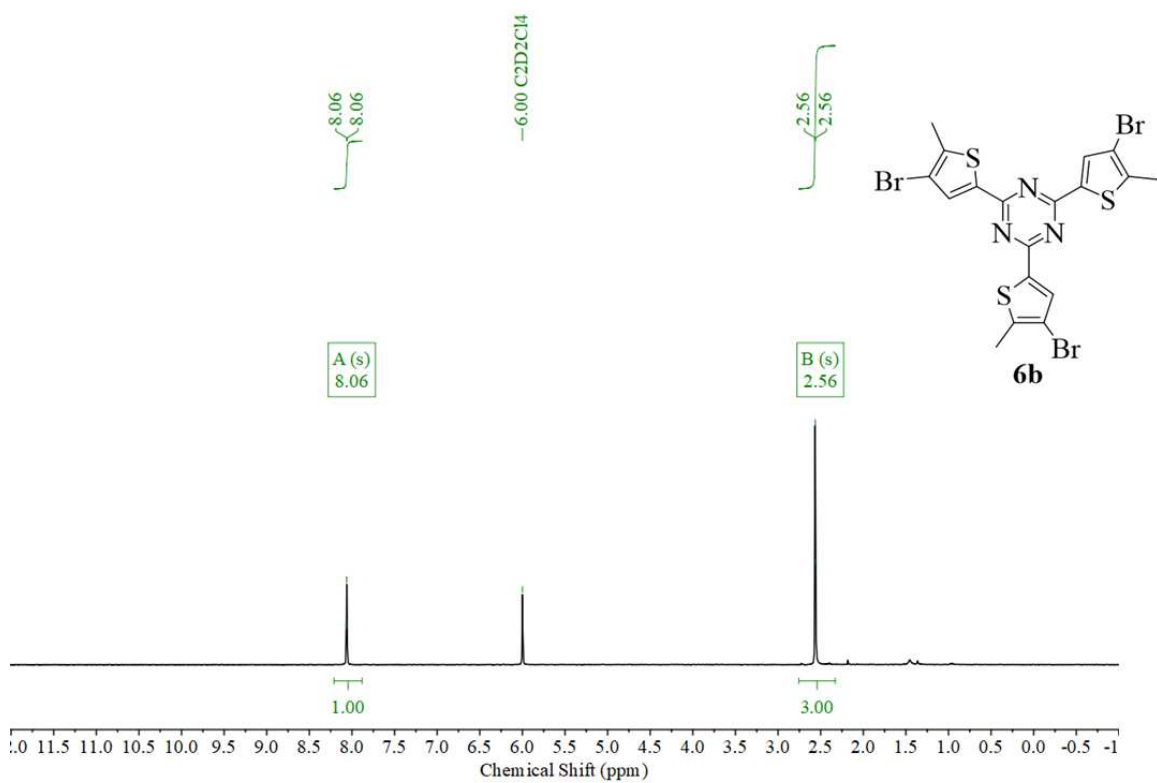


Figure SI 9 <sup>1</sup>H NMR spectra **6b** (400 MHz, C<sub>2</sub>D<sub>2</sub>Cl<sub>4</sub>).

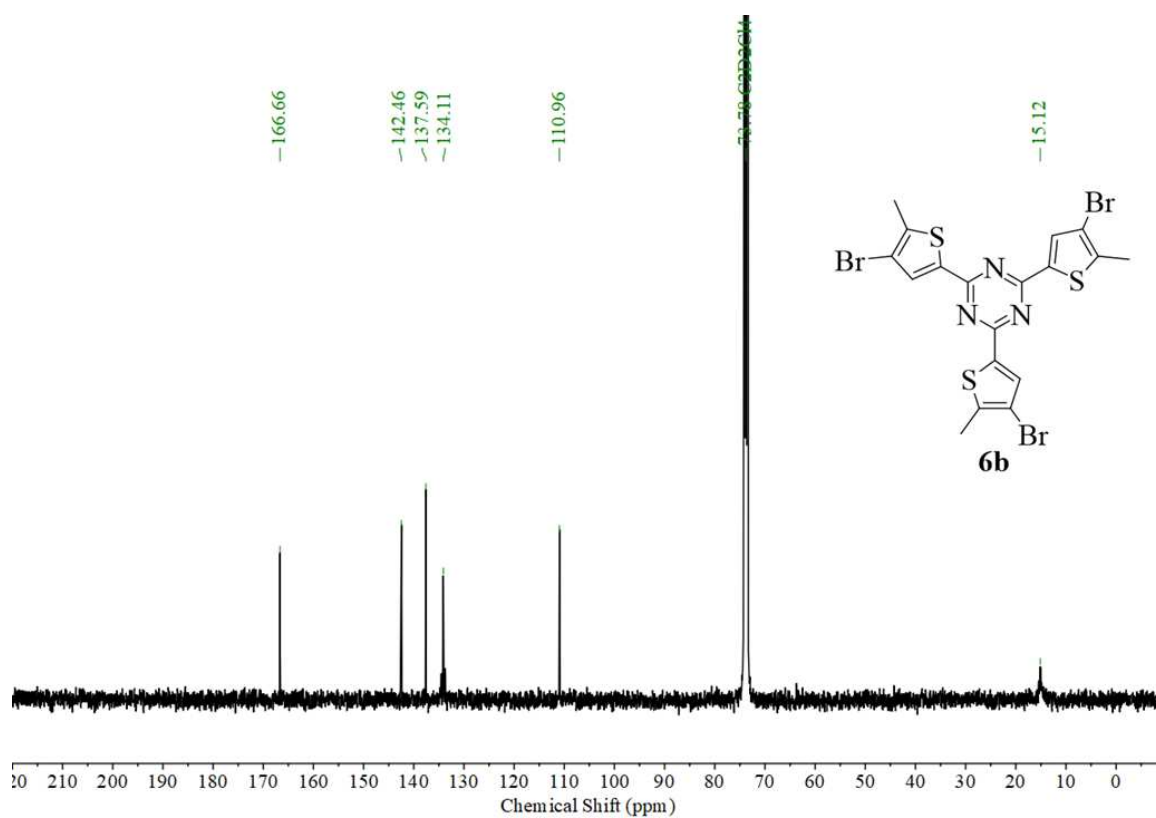


Figure SI 10 <sup>13</sup>C NMR spectra **6b** (101 MHz, C<sub>2</sub>D<sub>2</sub>Cl<sub>4</sub>).

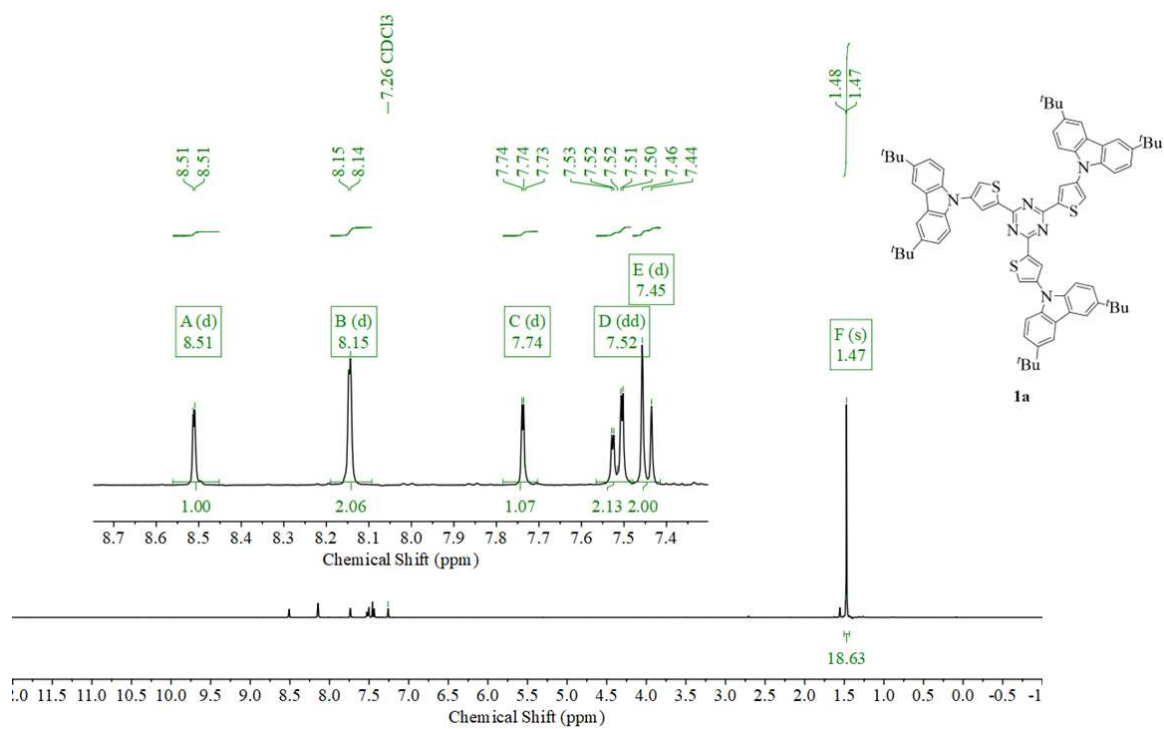
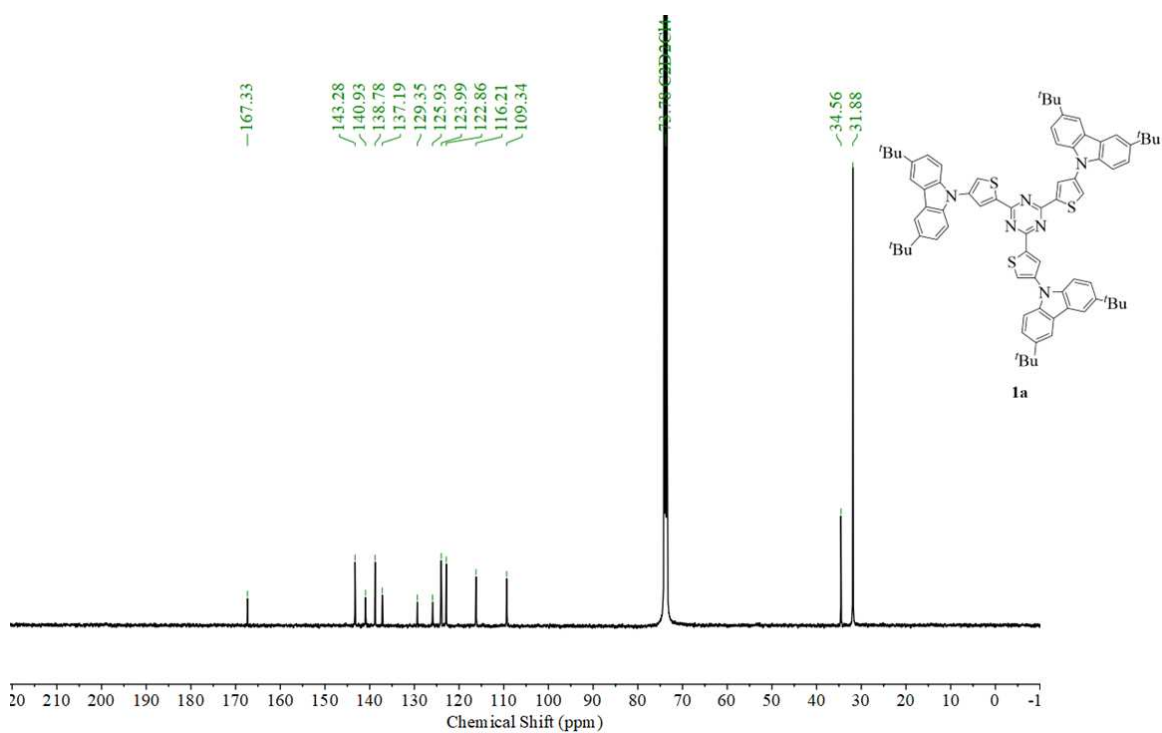
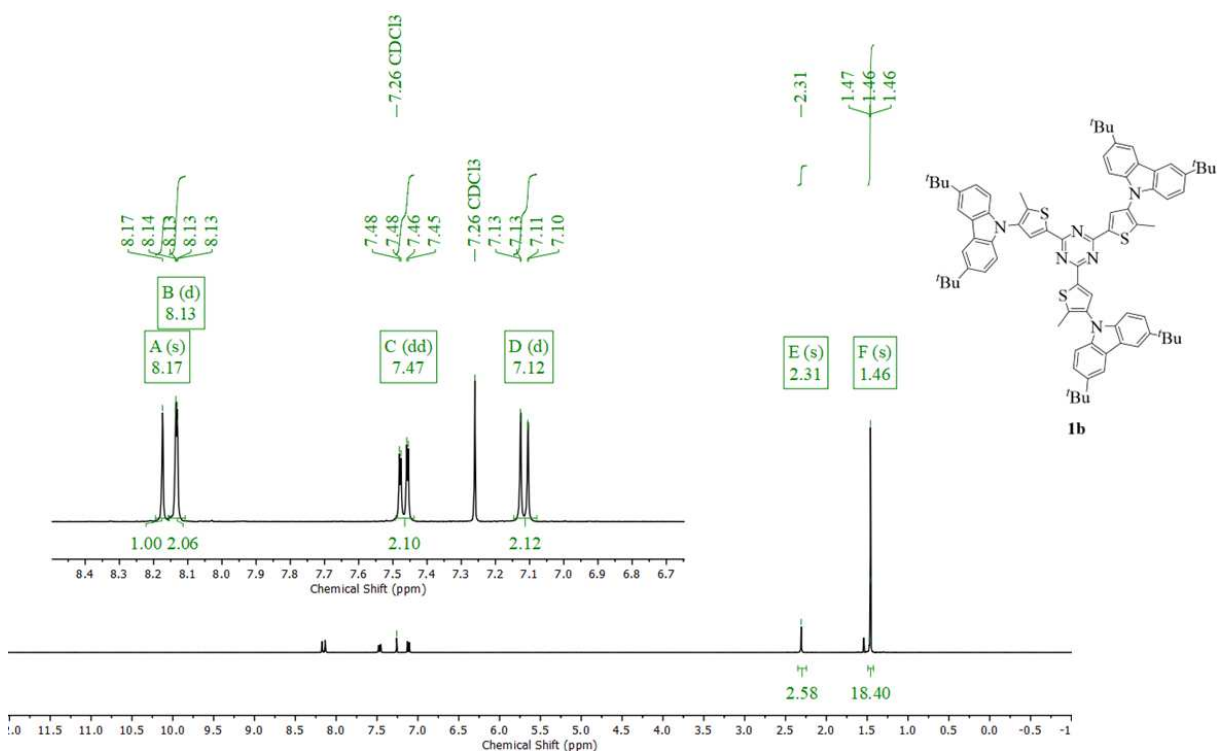


Figure SI 11 <sup>1</sup>H NMR spectra **1a** (400 MHz, CDCl<sub>3</sub>).



**Figure SI 12** <sup>13</sup>C NMR spectra **1a** (101 MHz, C<sub>2</sub>D<sub>2</sub>Cl<sub>4</sub>).



**Figure SI 13** <sup>1</sup>H NMR spectra **1b** (400 MHz, CDCl<sub>3</sub>).



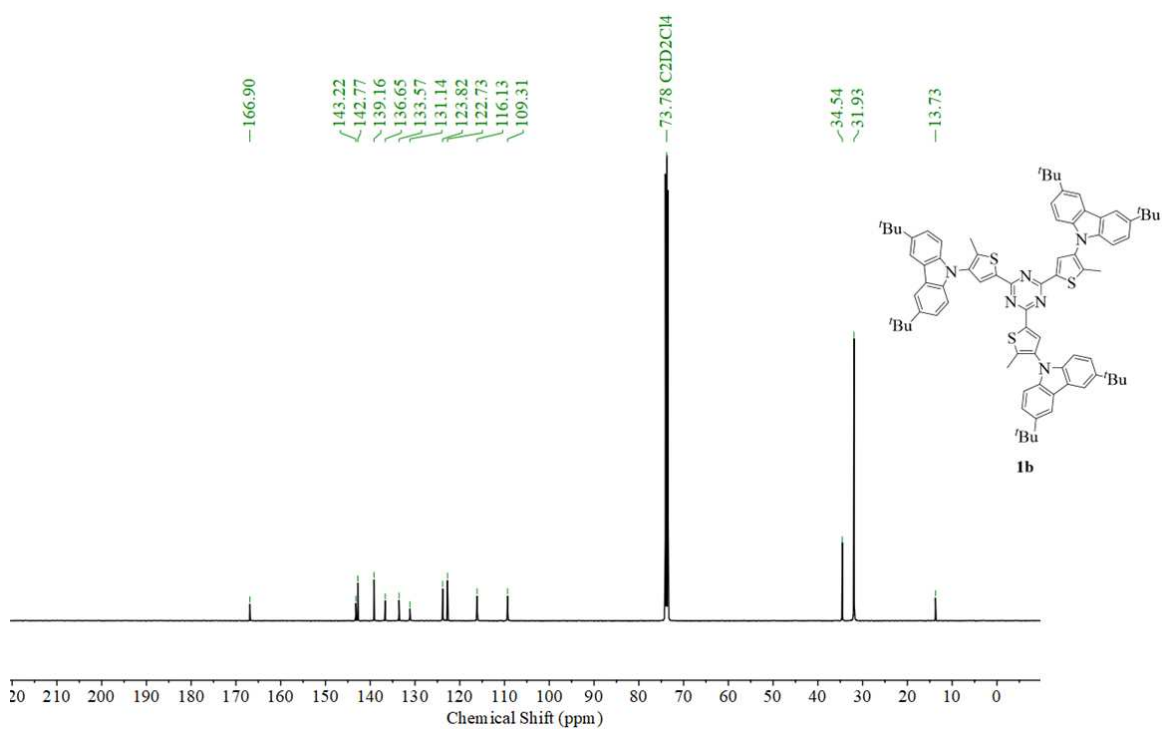


Figure SI 14 <sup>13</sup>C NMR spectra **1b** (101 MHz, C<sub>2</sub>D<sub>2</sub>Cl<sub>4</sub>).

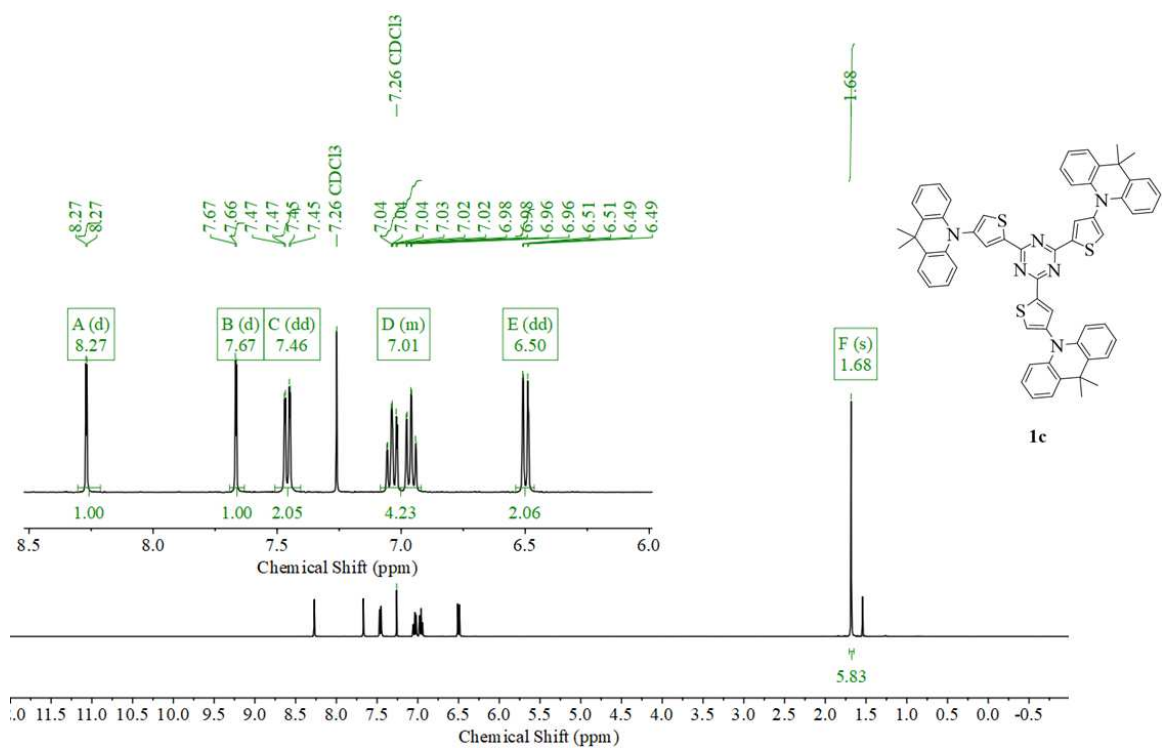


Figure SI 15 <sup>1</sup>H NMR spectra **1c** (400 MHz, CDCl<sub>3</sub>).

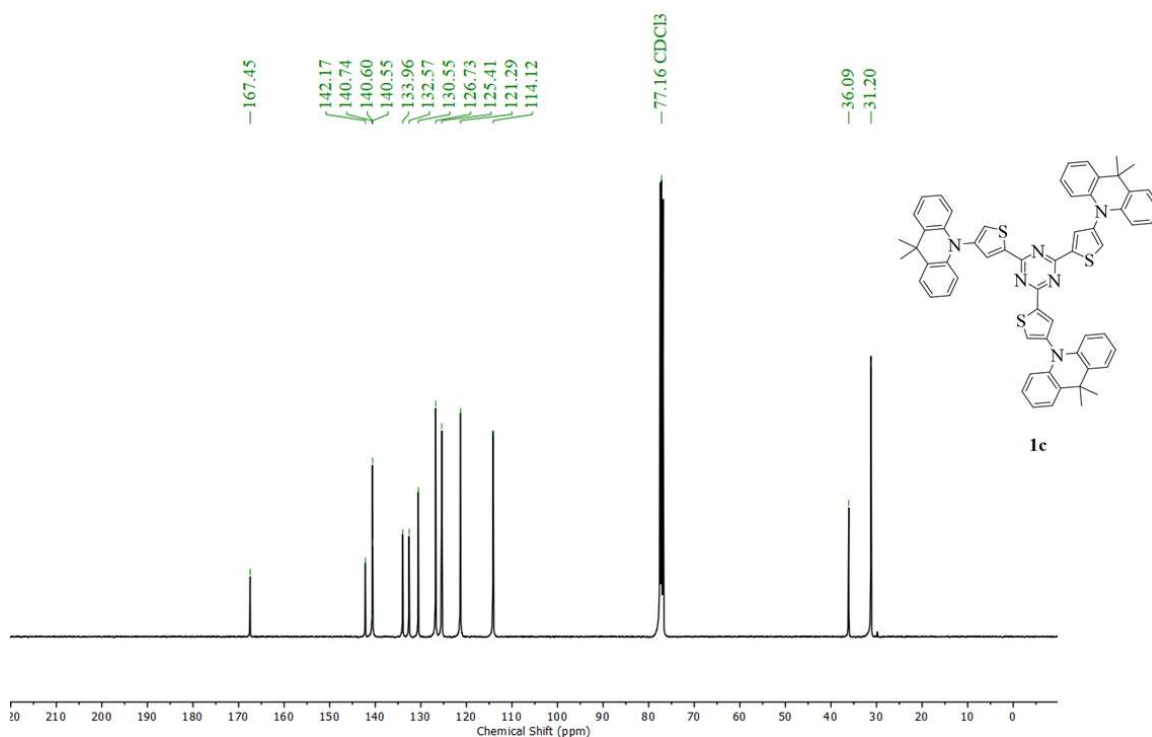


Figure SI 16 <sup>13</sup>C NMR spectra **1c** (101 MHz, CDCl<sub>3</sub>).

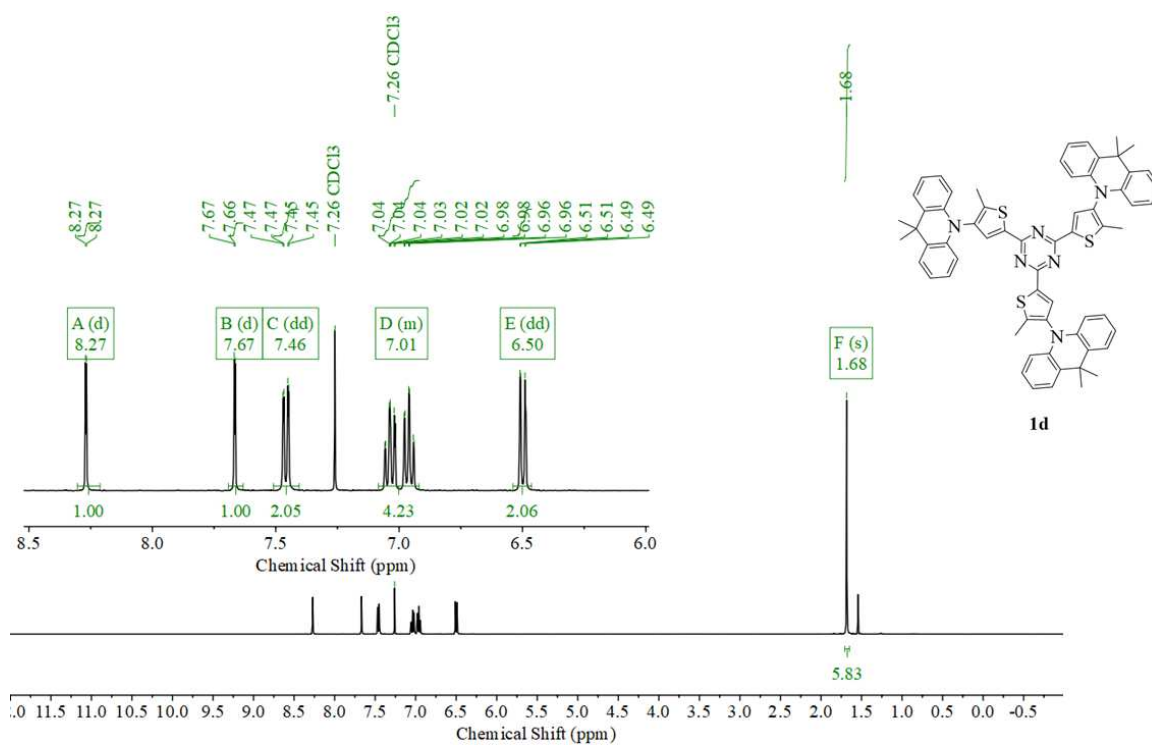


Figure SI 17 <sup>1</sup>H NMR spectra **1d** (400 MHz, CDCl<sub>3</sub>).

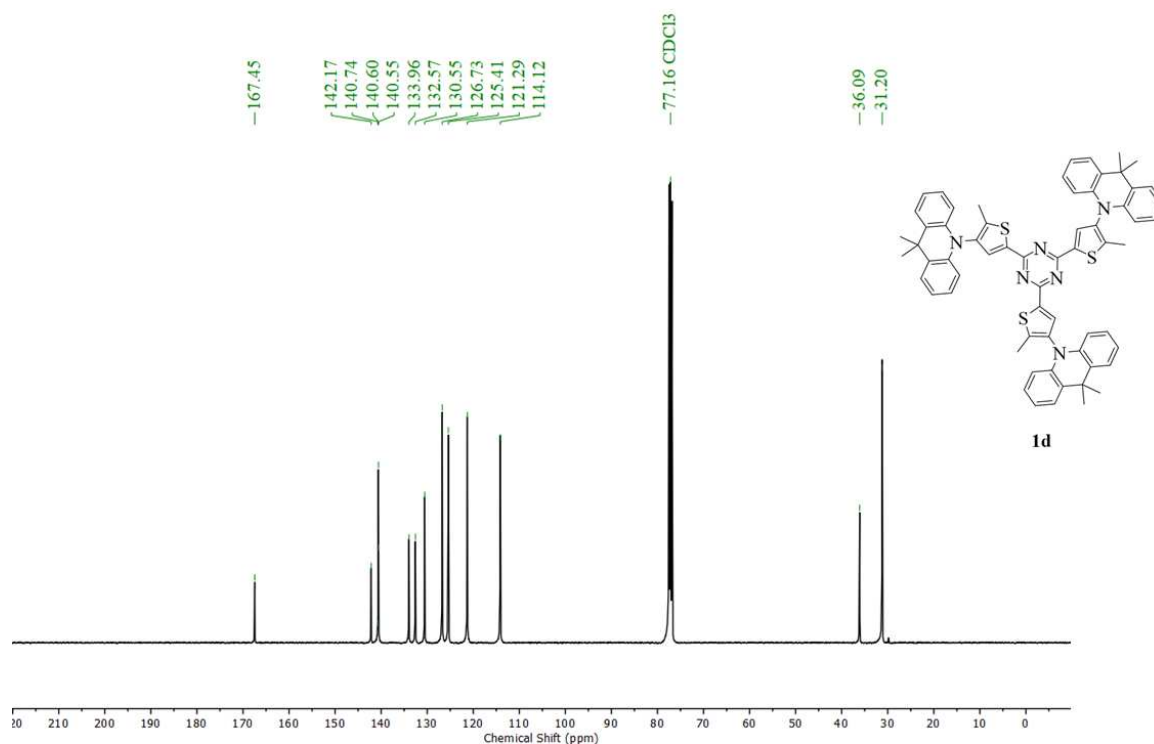


Figure SI 18 <sup>13</sup>C NMR spectra **1d** (101 MHz, CDCl<sub>3</sub>).

### 8.1.2 TTT emitters

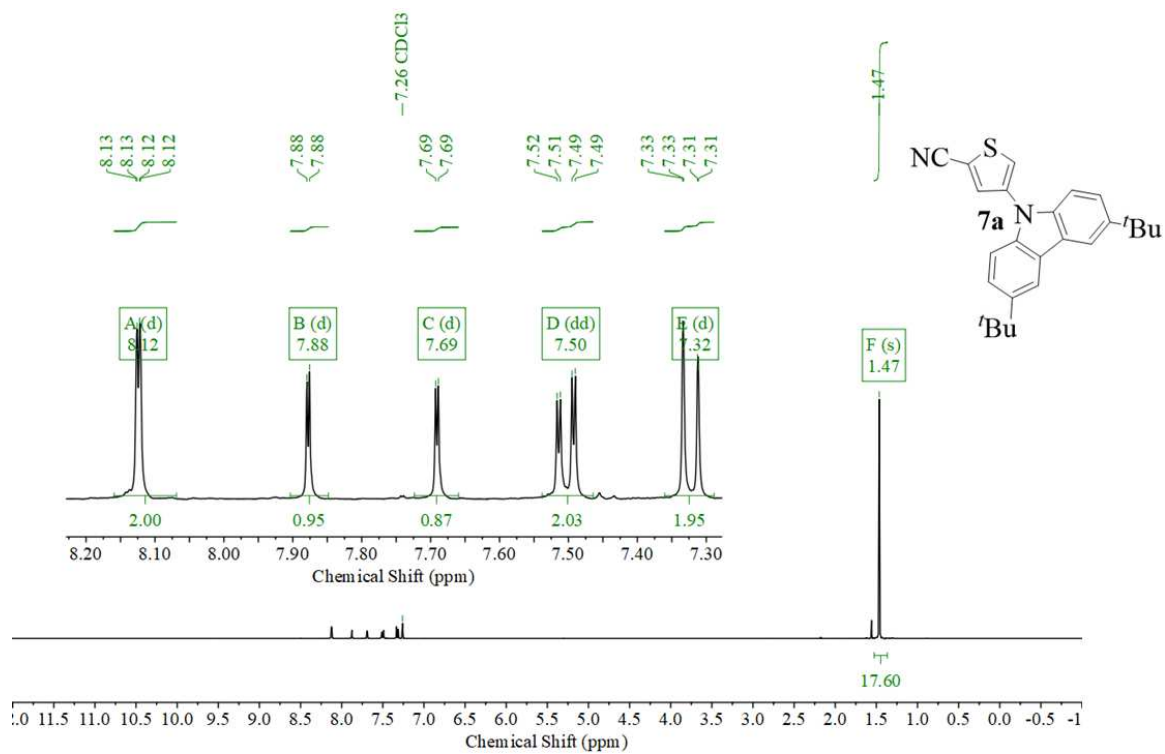
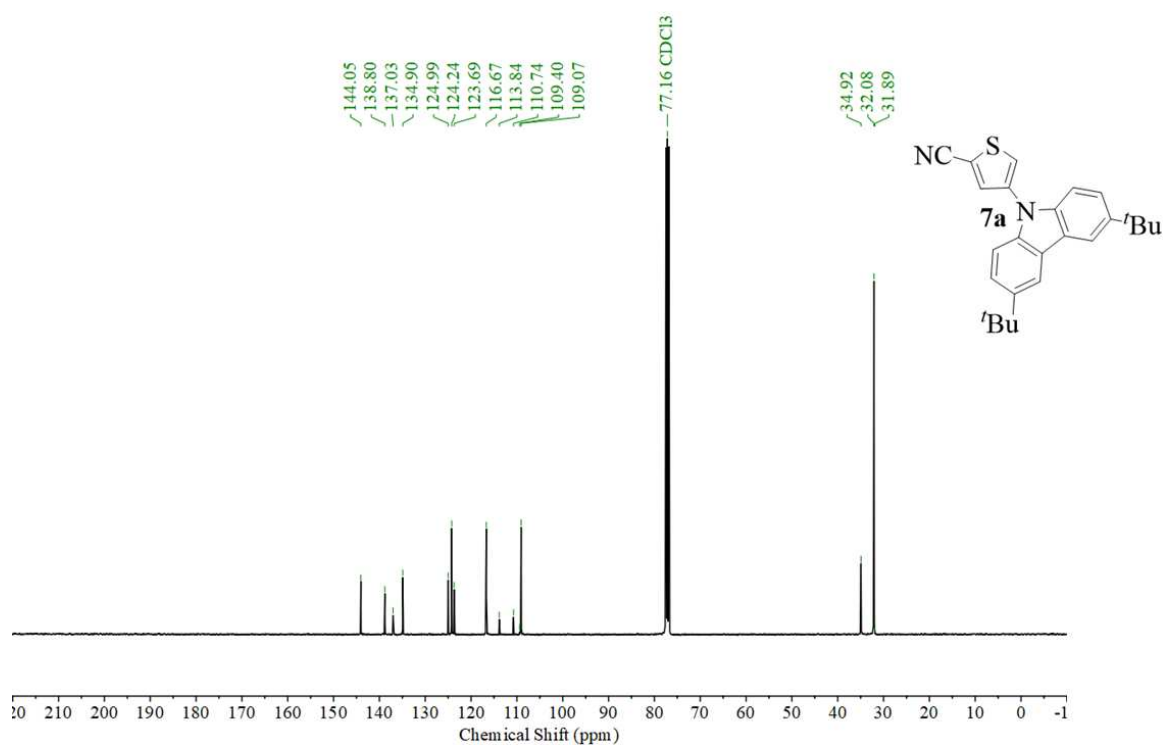
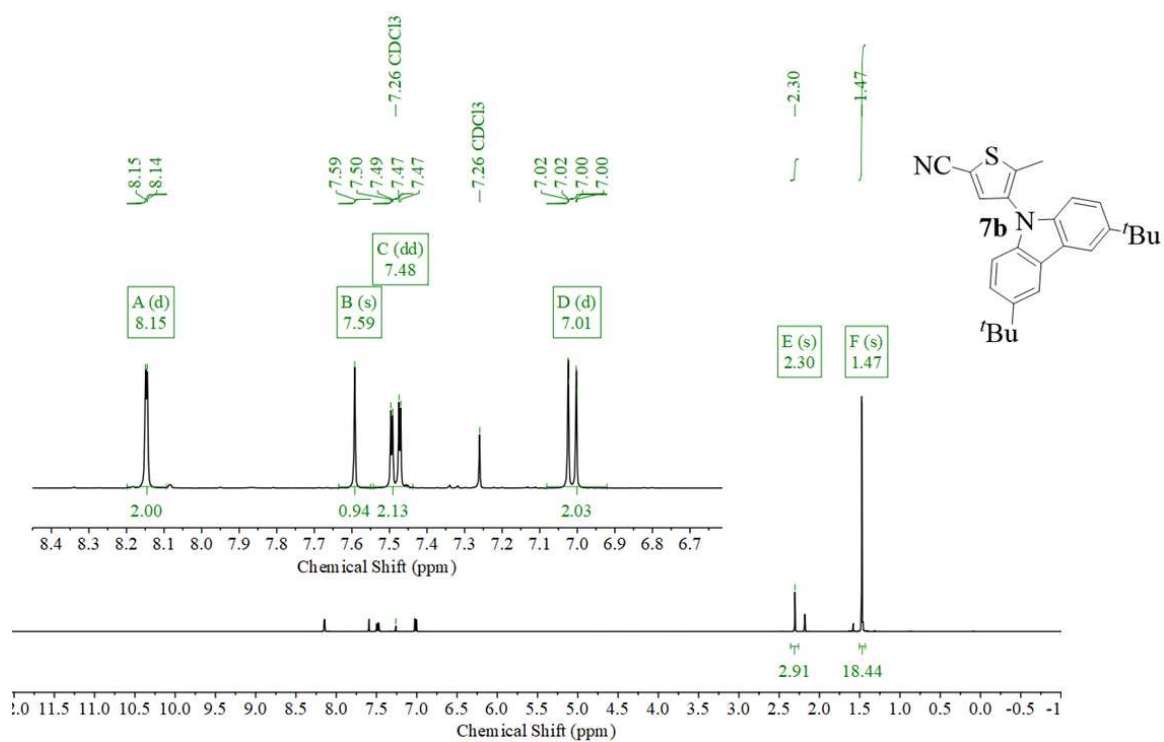


Figure SI 19 <sup>1</sup>H NMR spectra **7a** (400 MHz, CDCl<sub>3</sub>).



**Figure SI 20**  $^{13}\text{C}$  NMR spectra **7a** (101 MHz,  $\text{CDCl}_3$ ).



**Figure SI 21**  $^1\text{H}$  NMR spectra **7b** (400 MHz,  $\text{CDCl}_3$ ).

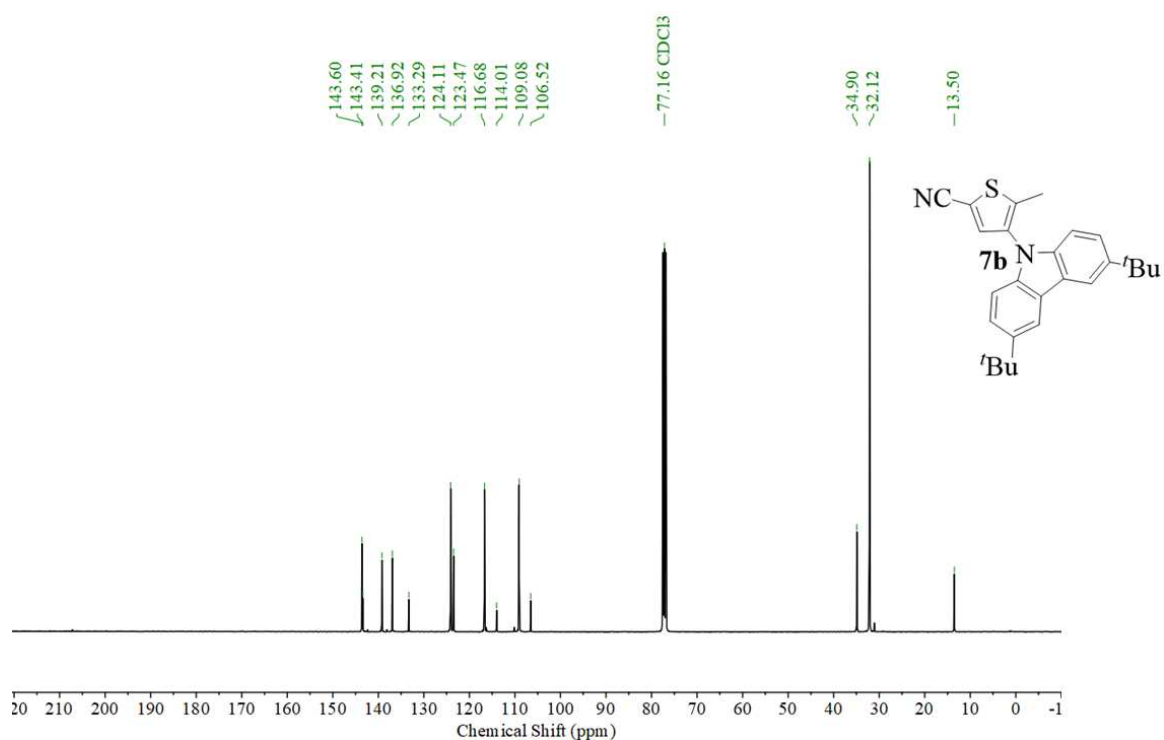


Figure SI 22 <sup>13</sup>C NMR spectra **7b** (101 MHz, CDCl<sub>3</sub>).

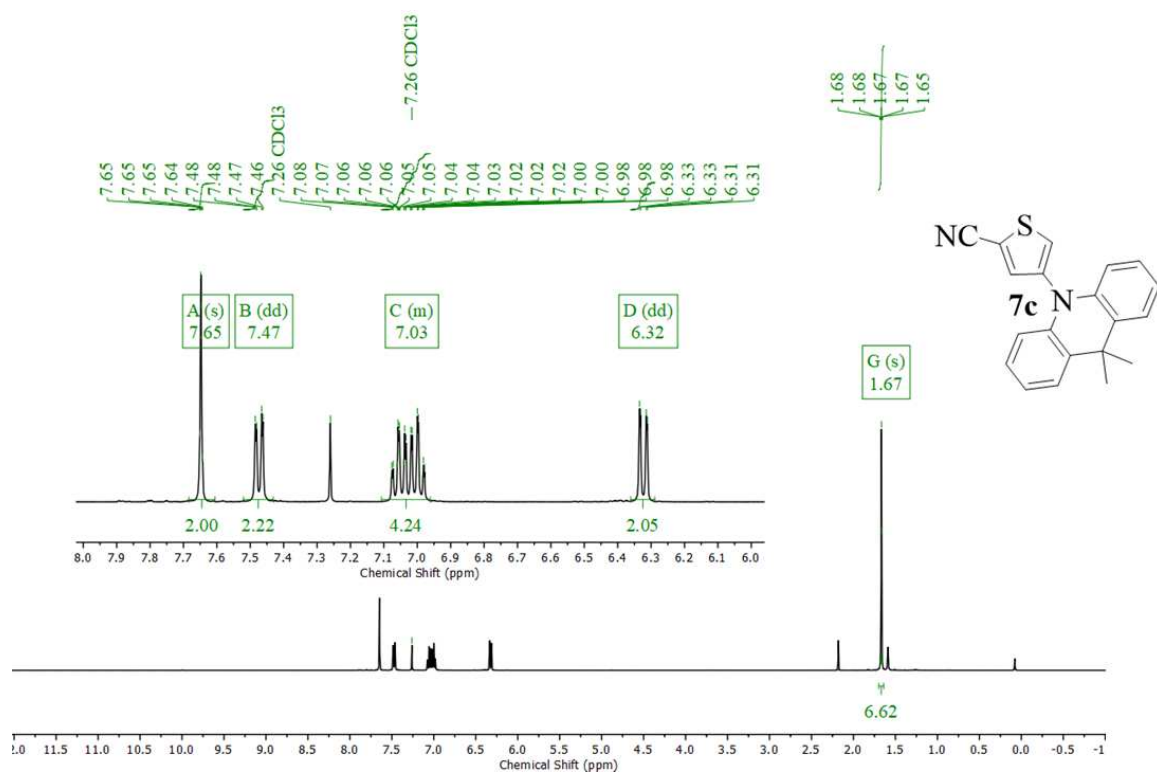


Figure SI 23 <sup>1</sup>H NMR spectra **7c** (400 MHz, CDCl<sub>3</sub>).

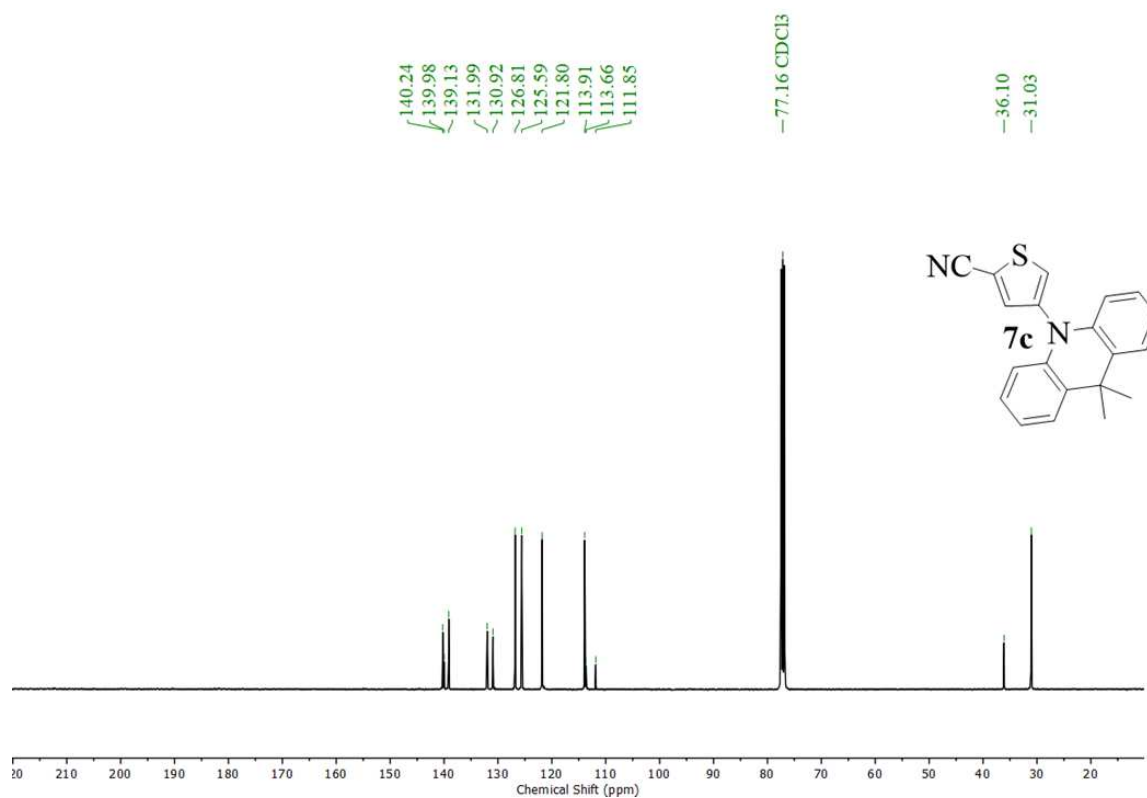


Figure SI 24 <sup>13</sup>C NMR spectra **7c** (101 MHz, CDCl<sub>3</sub>).

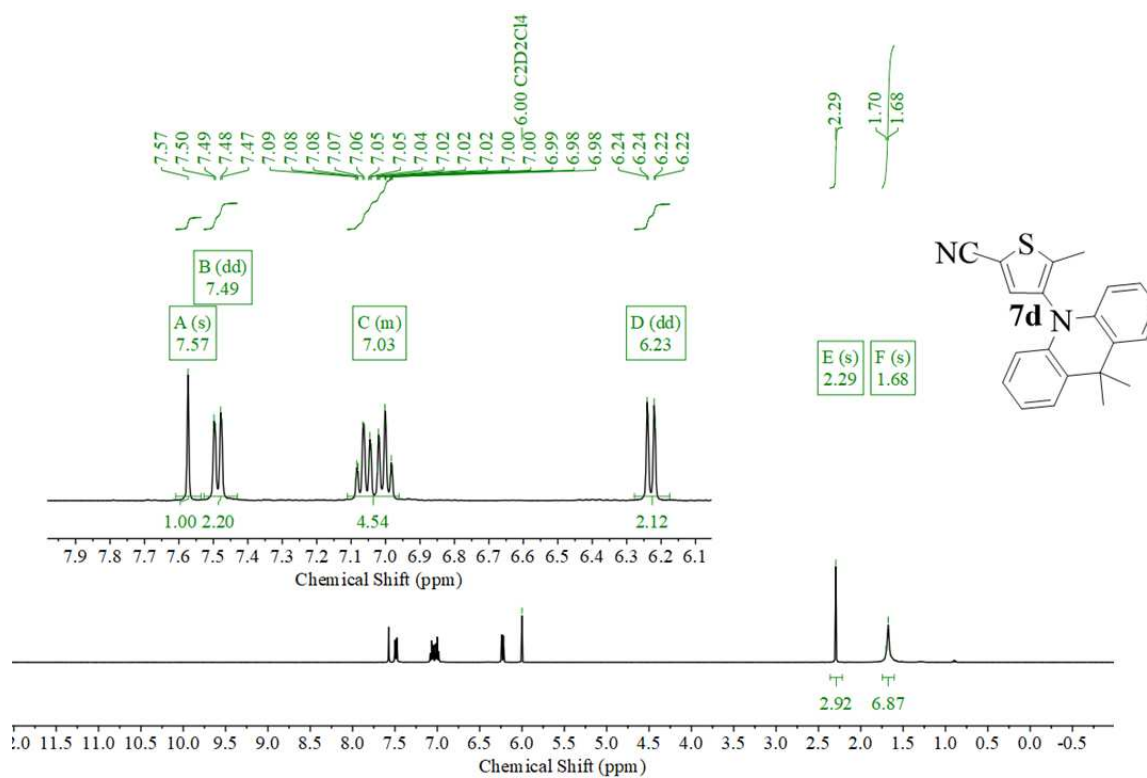


Figure SI 25 <sup>1</sup>H NMR spectra **7d** (400 MHz, C<sub>2</sub>D<sub>2</sub>Cl<sub>4</sub>).

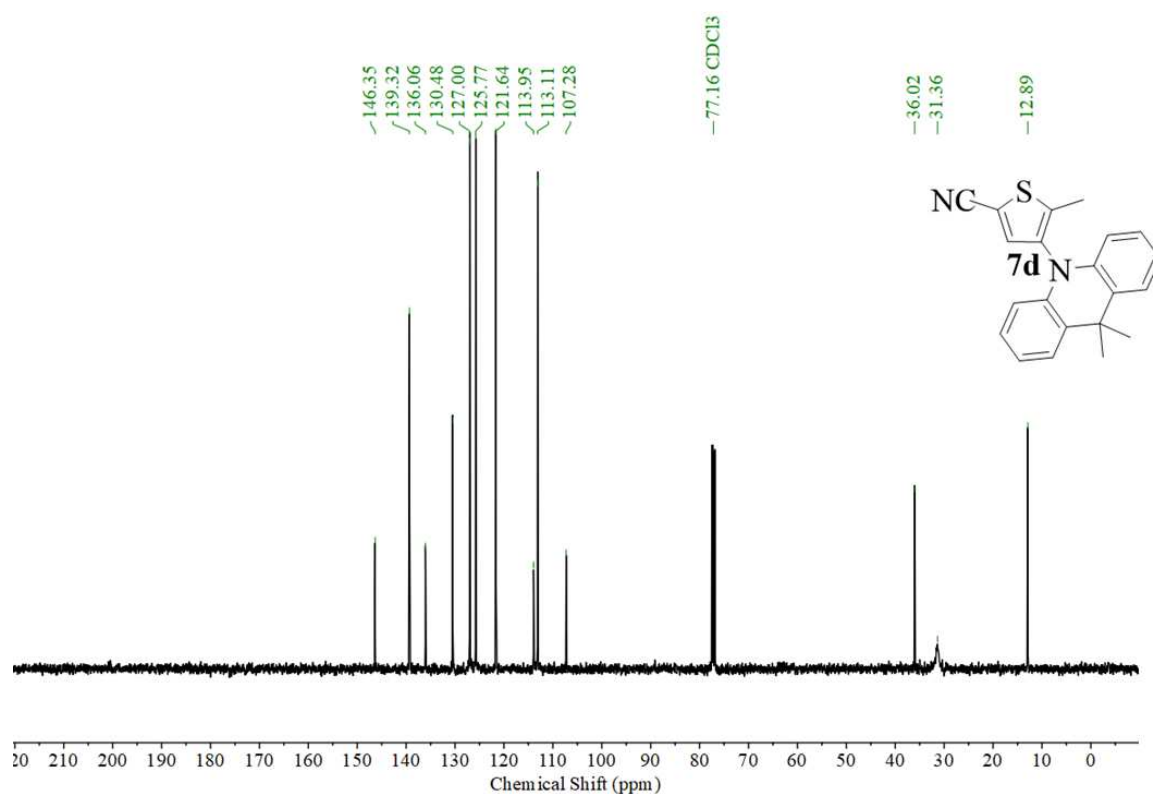


Figure SI 26 <sup>13</sup>C NMR spectra **7d** (101 MHz, CDCl<sub>3</sub>).

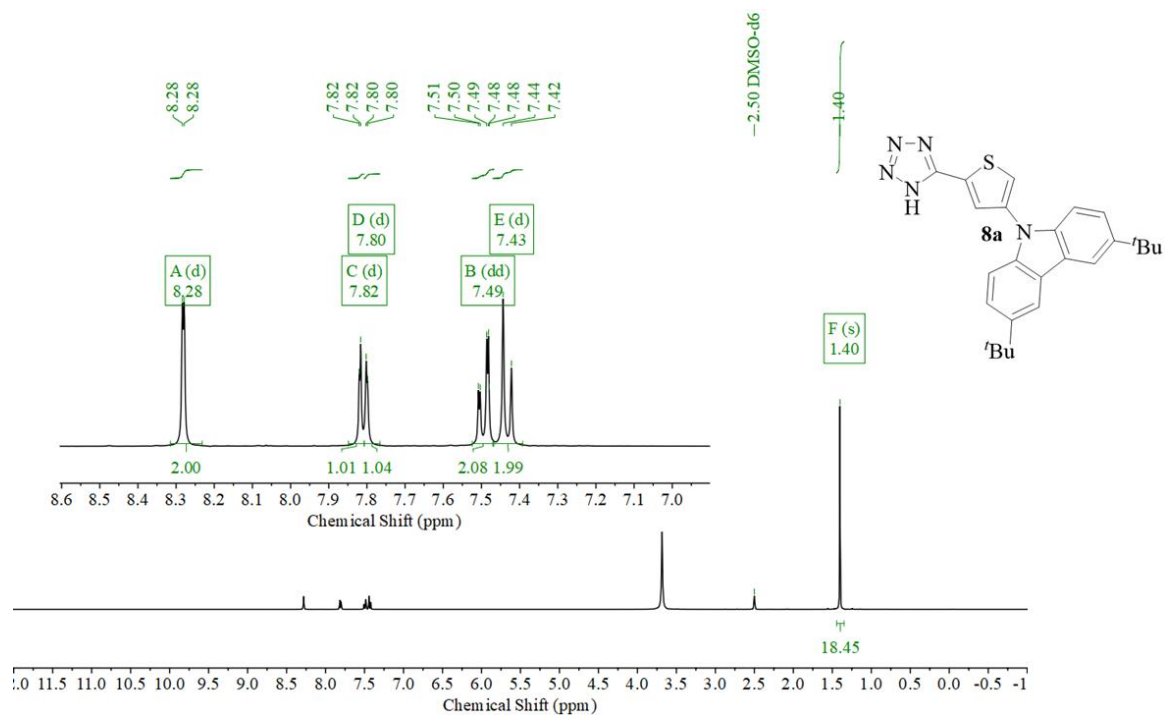


Figure SI 27 <sup>1</sup>H NMR spectra **8a** (400 MHz, DMSO-d<sub>6</sub>).

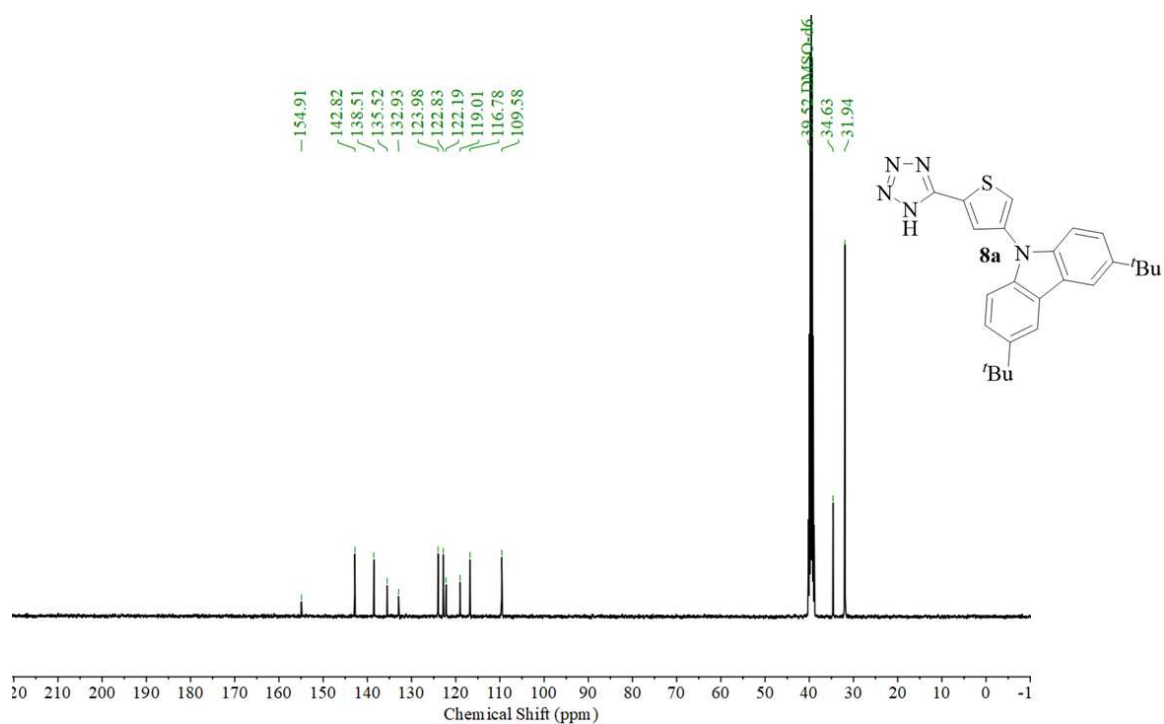


Figure SI 28  $^{13}\text{C}$  NMR spectra **8a** (101 MHz, DMSO- $d_6$ ).

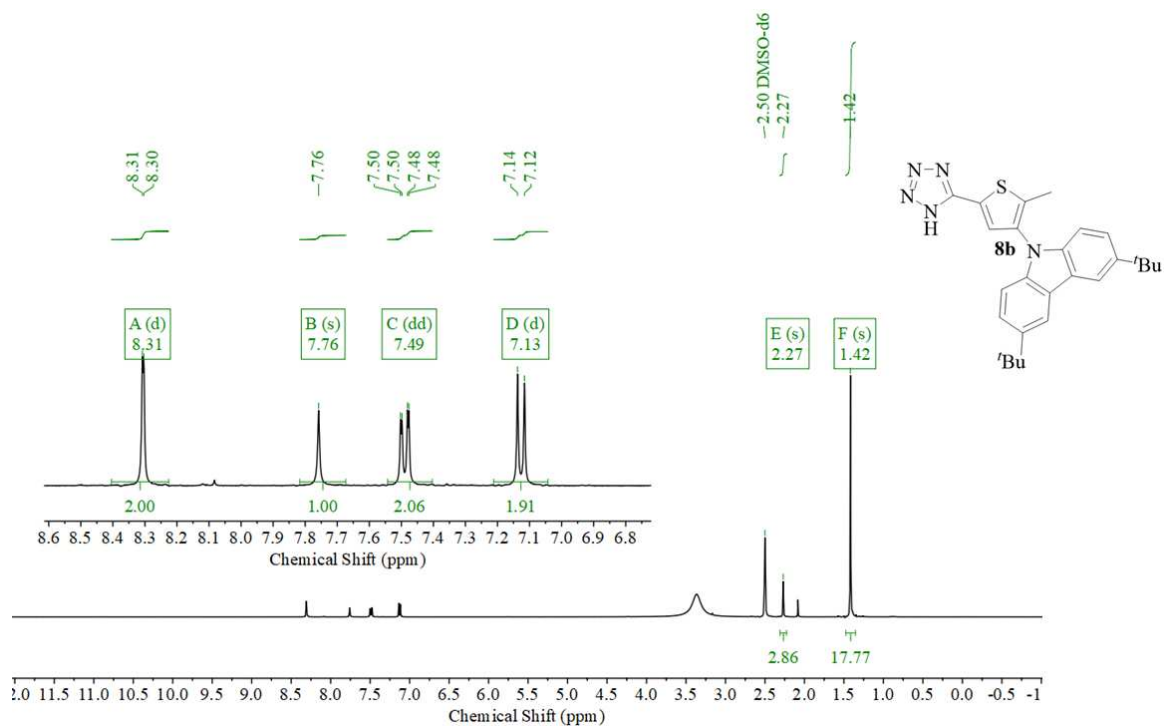


Figure SI 29  $^1\text{H}$  NMR spectra **8b** (400 MHz, DMSO- $d_6$ ).



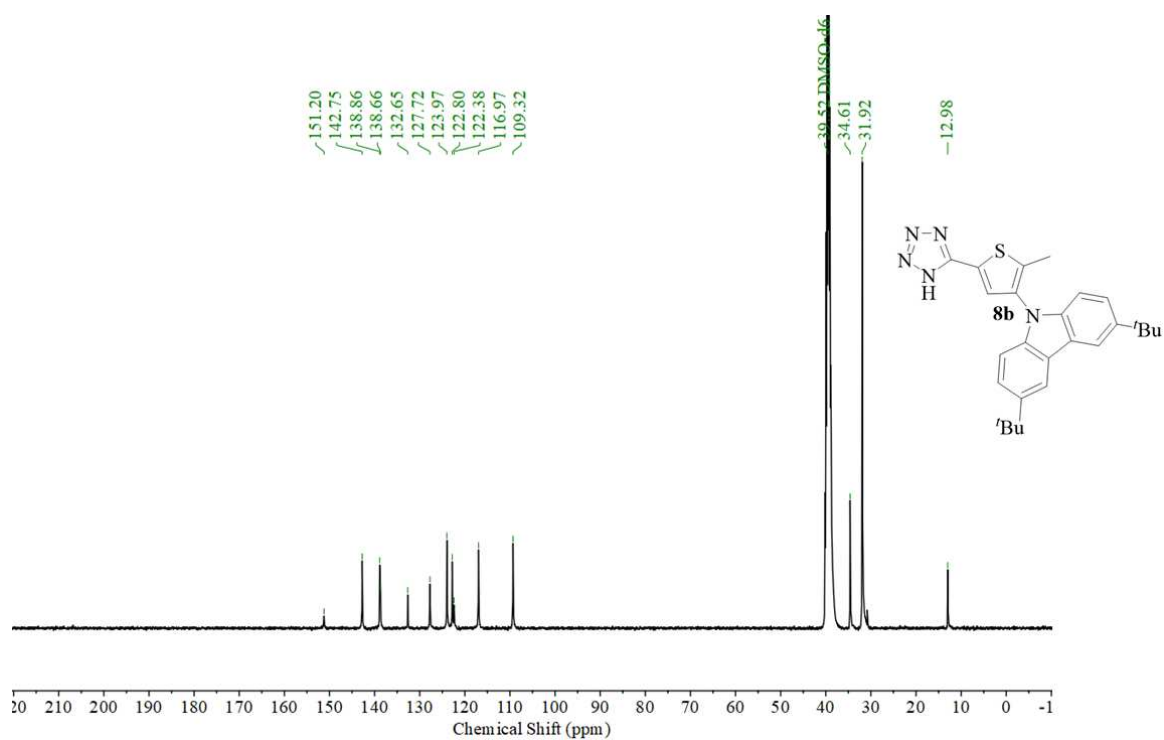


Figure SI 30 <sup>13</sup>C NMR spectra **8b** (101 MHz, DMSO-d<sub>6</sub>).

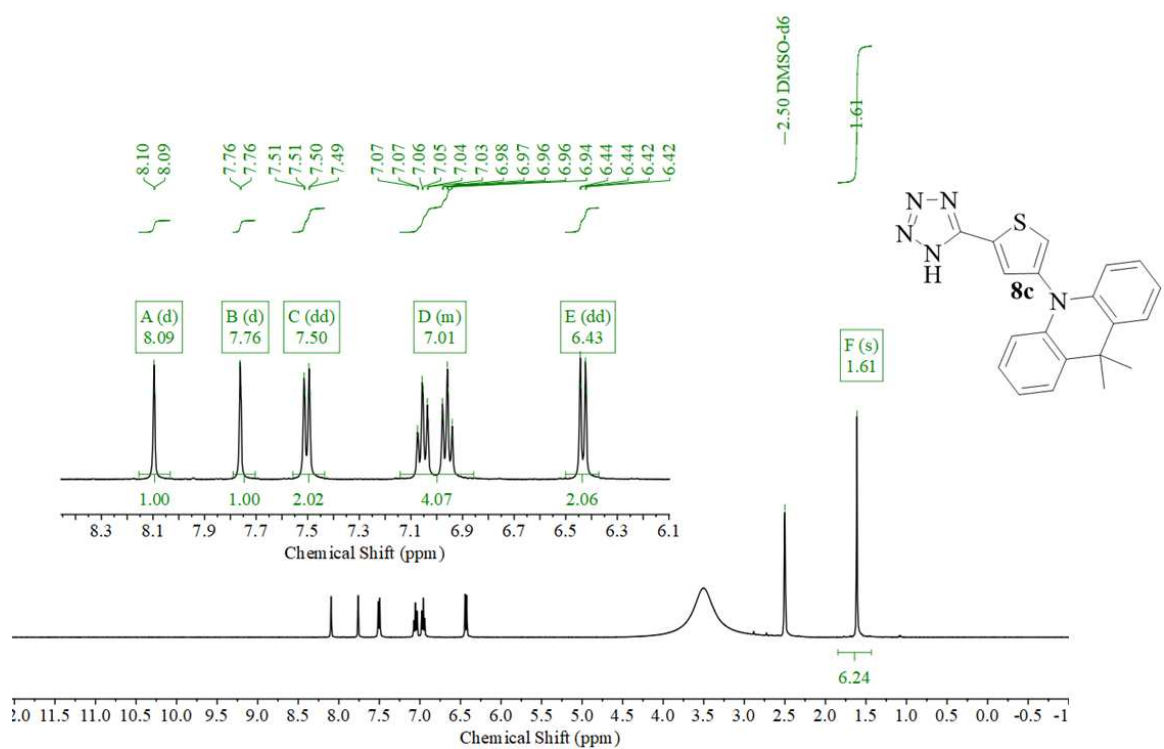


Figure SI 31 <sup>1</sup>H NMR spectra **8c** (400 MHz, DMSO-d<sub>6</sub>).

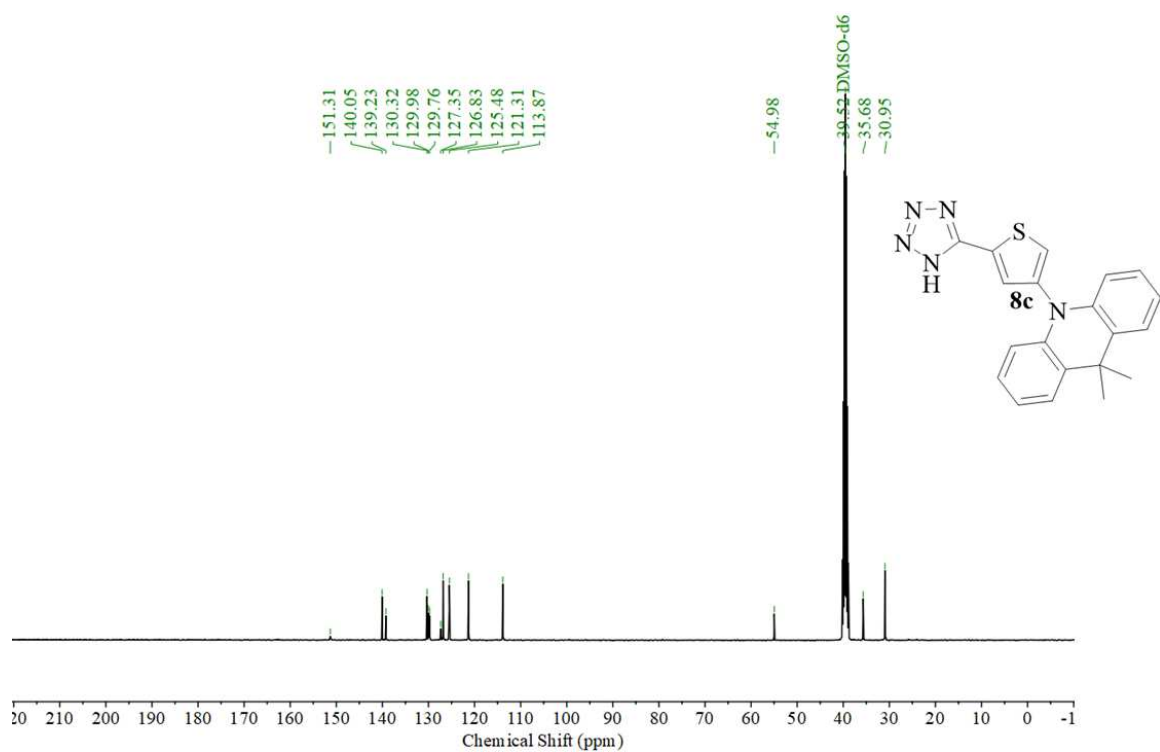


Figure SI 32  $^{13}\text{C}$  NMR spectra **8c** (101 MHz,  $\text{DMSO-d}_6$ ).

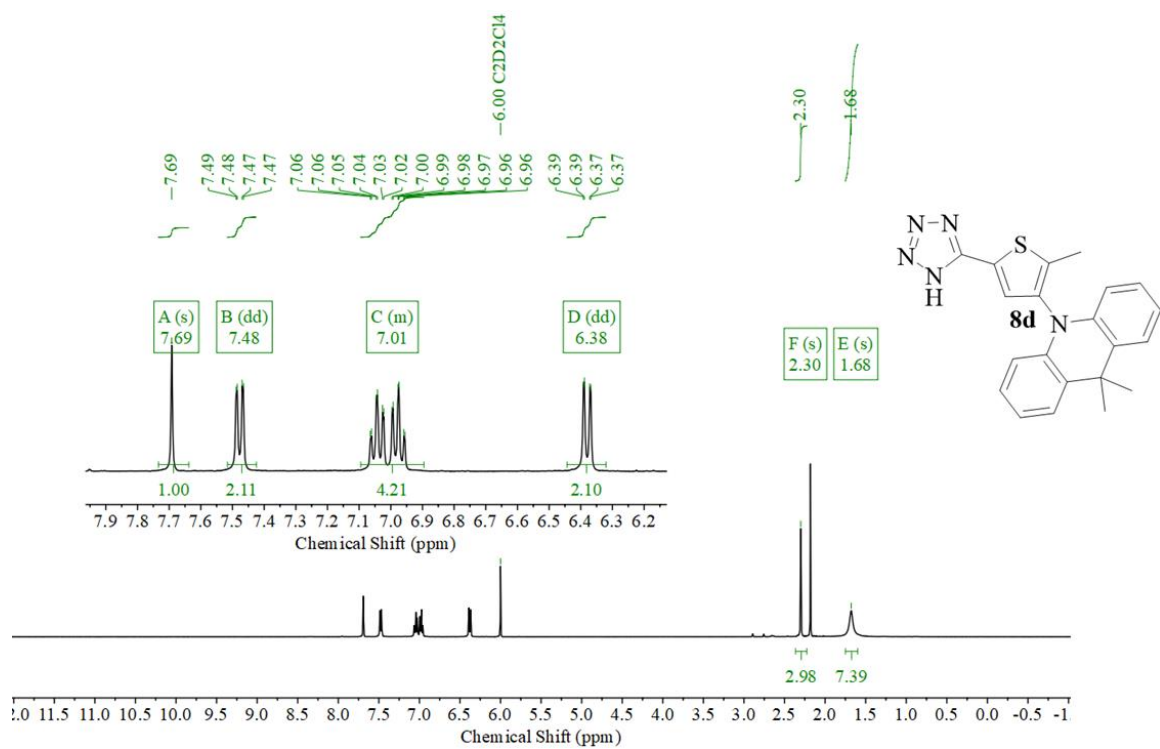


Figure SI 33  $^1\text{H}$  NMR spectra **8d** (400 MHz,  $\text{C}_2\text{D}_2\text{Cl}_4$ ).

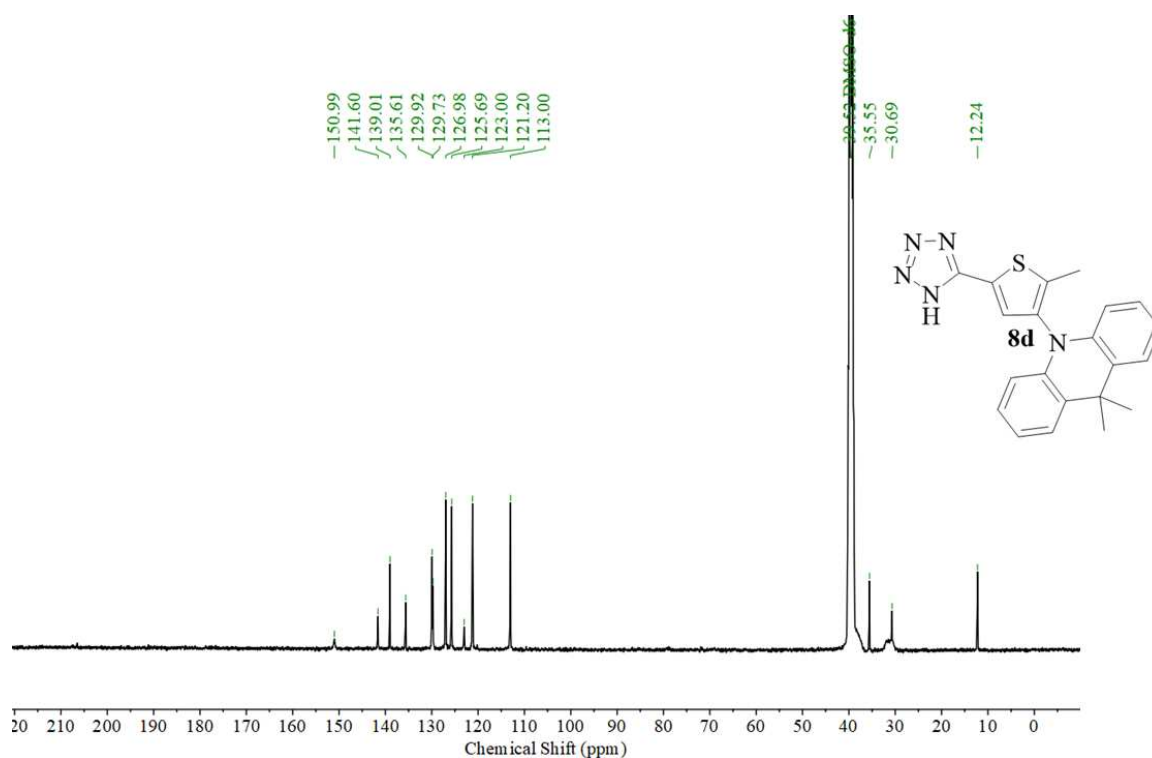


Figure SI 34  $^{13}\text{C}$  NMR spectra **8d** (101 MHz,  $\text{DMSO-d}_6$ ).

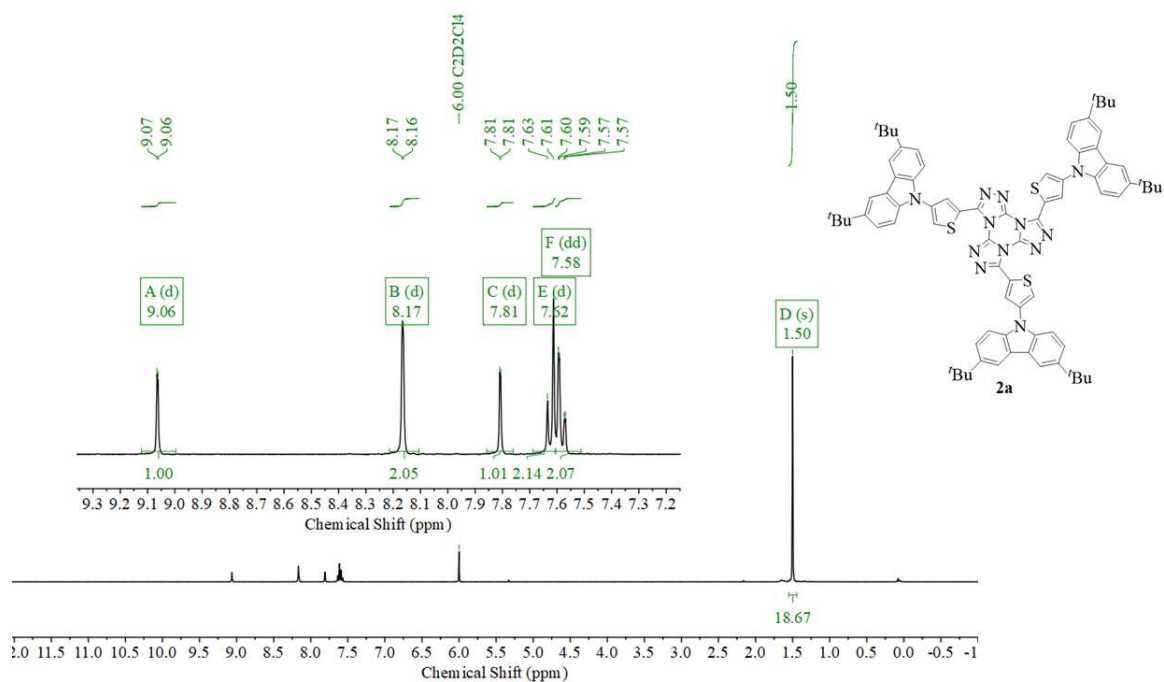


Figure SI 35  $^1\text{H}$  NMR spectra **2a** (400 MHz,  $\text{C}_2\text{D}_2\text{Cl}_4$ ).

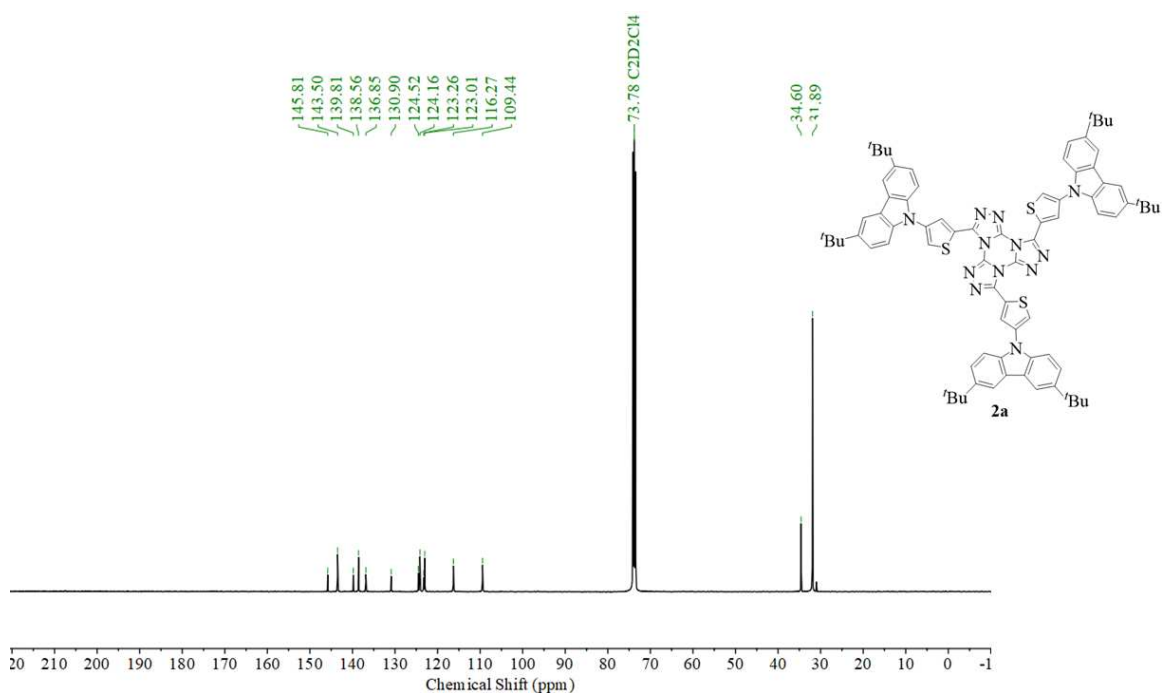


Figure SI 36  $^{13}\text{C}$  NMR spectra **2a** (101 MHz,  $\text{C}_2\text{D}_2\text{Cl}_4$ ).

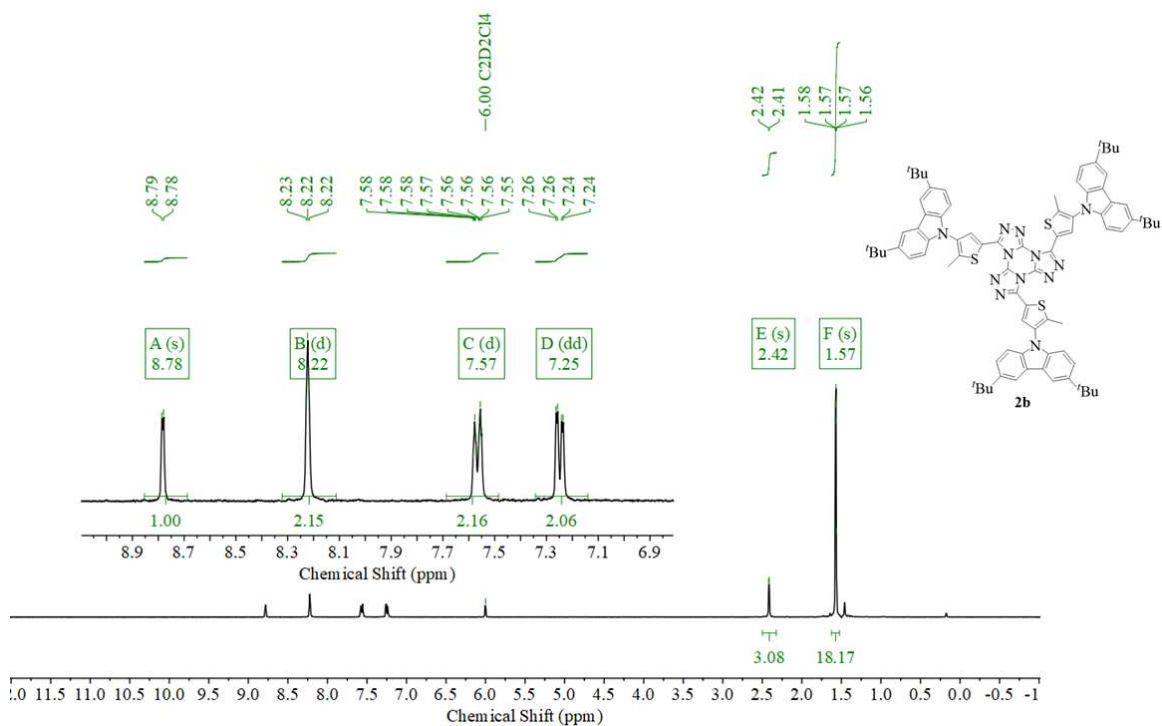


Figure SI 37  $^1\text{H}$  NMR spectra **2b** (400 MHz,  $\text{C}_2\text{D}_2\text{Cl}_4$ ).

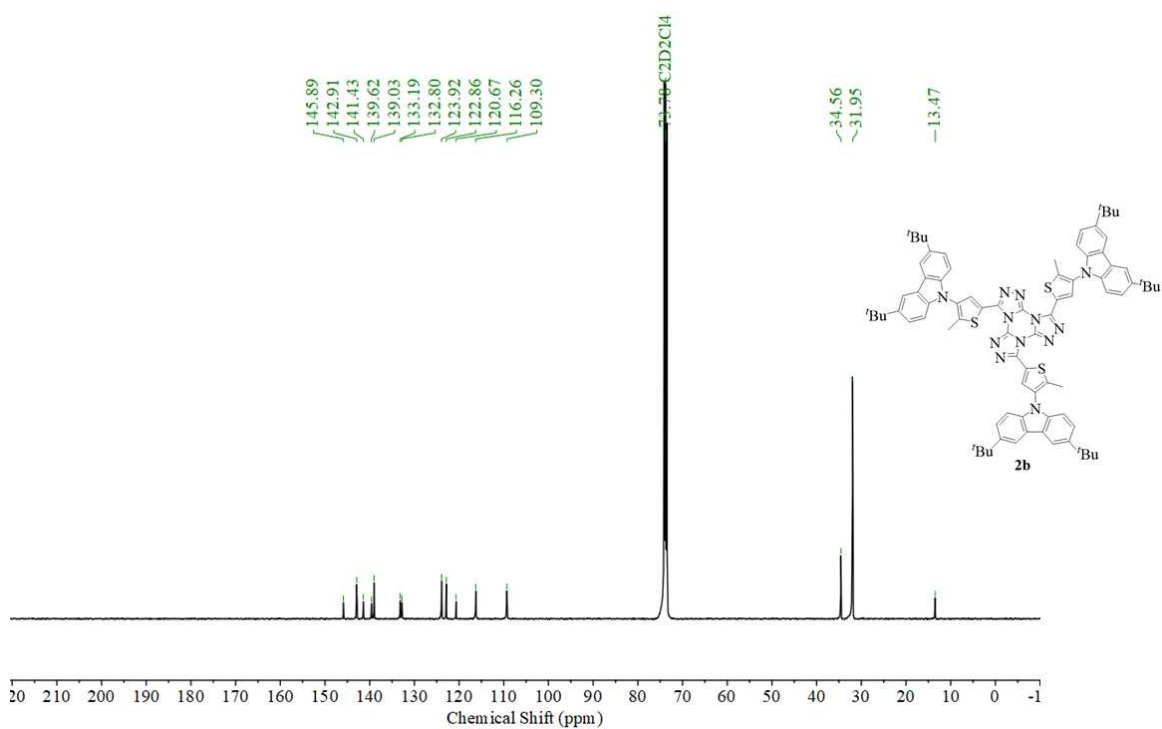


Figure SI 38  $^{13}\text{C}$  NMR spectra **2b** (101 MHz,  $\text{C}_2\text{D}_2\text{Cl}_4$ ).

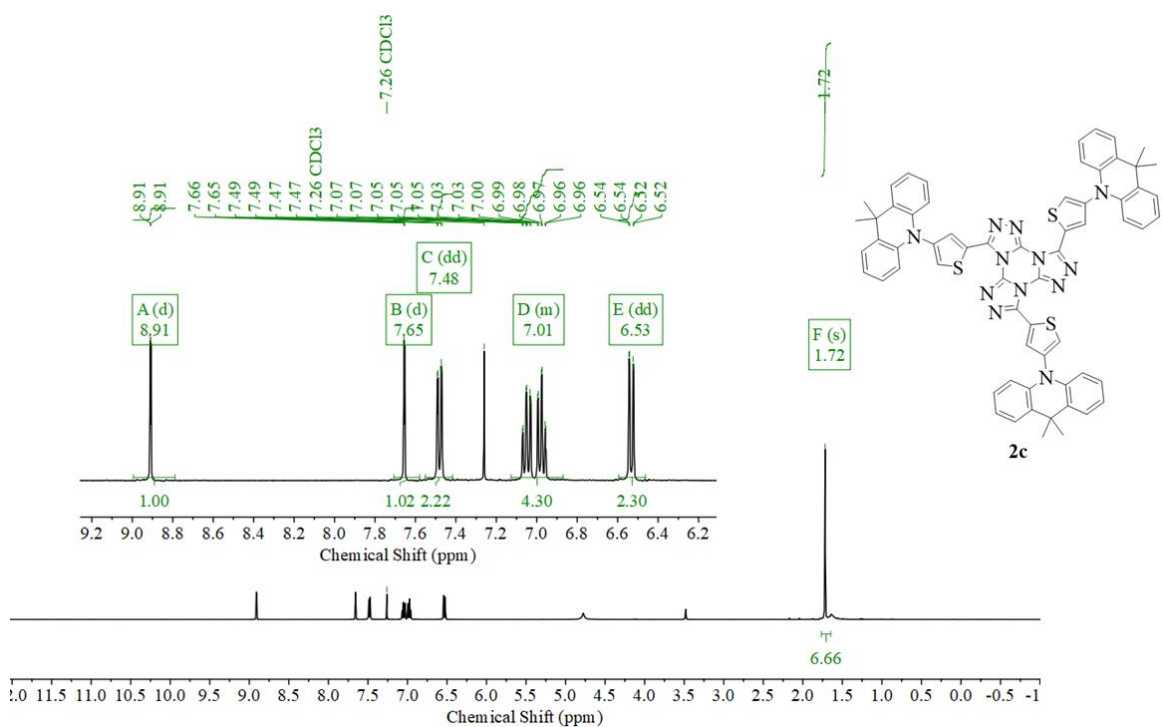


Figure SI 39  $^1\text{H}$  NMR spectra **2c** (400 MHz,  $\text{CDCl}_3$ ).

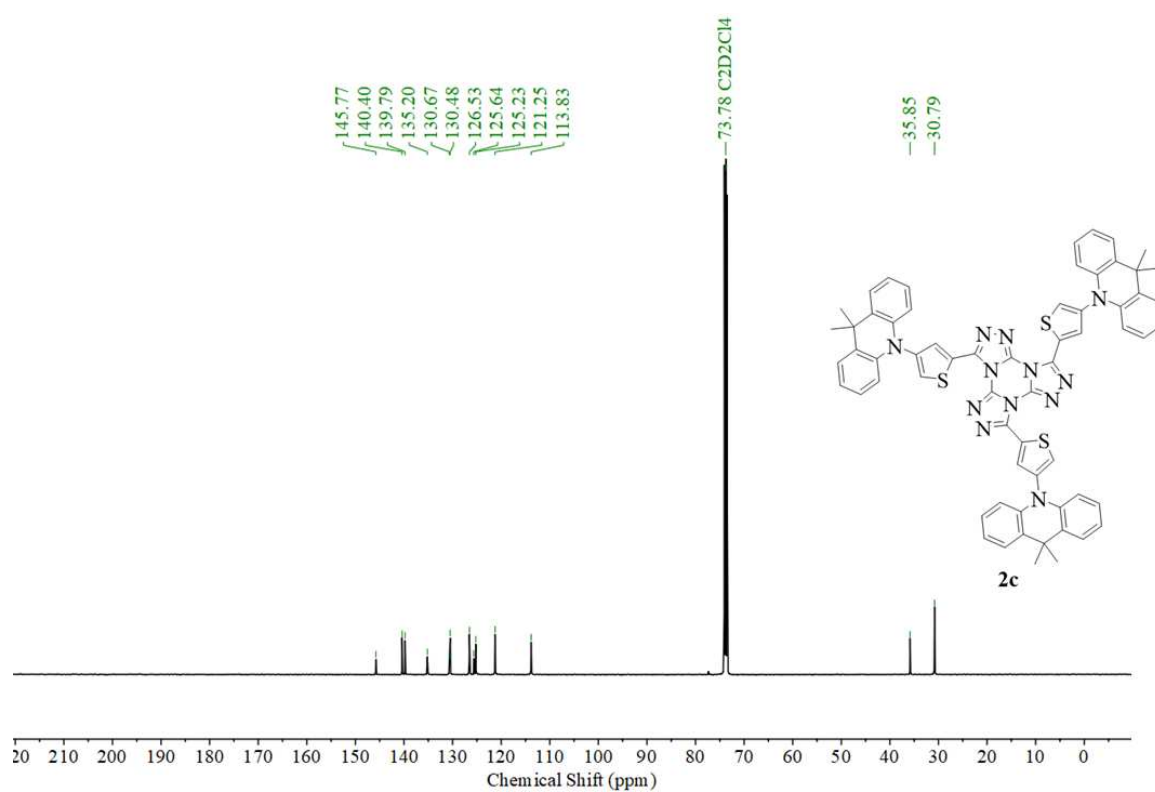


Figure SI 40 <sup>13</sup>C NMR spectra **2c** (101 MHz, C<sub>2</sub>D<sub>2</sub>Cl<sub>4</sub>).

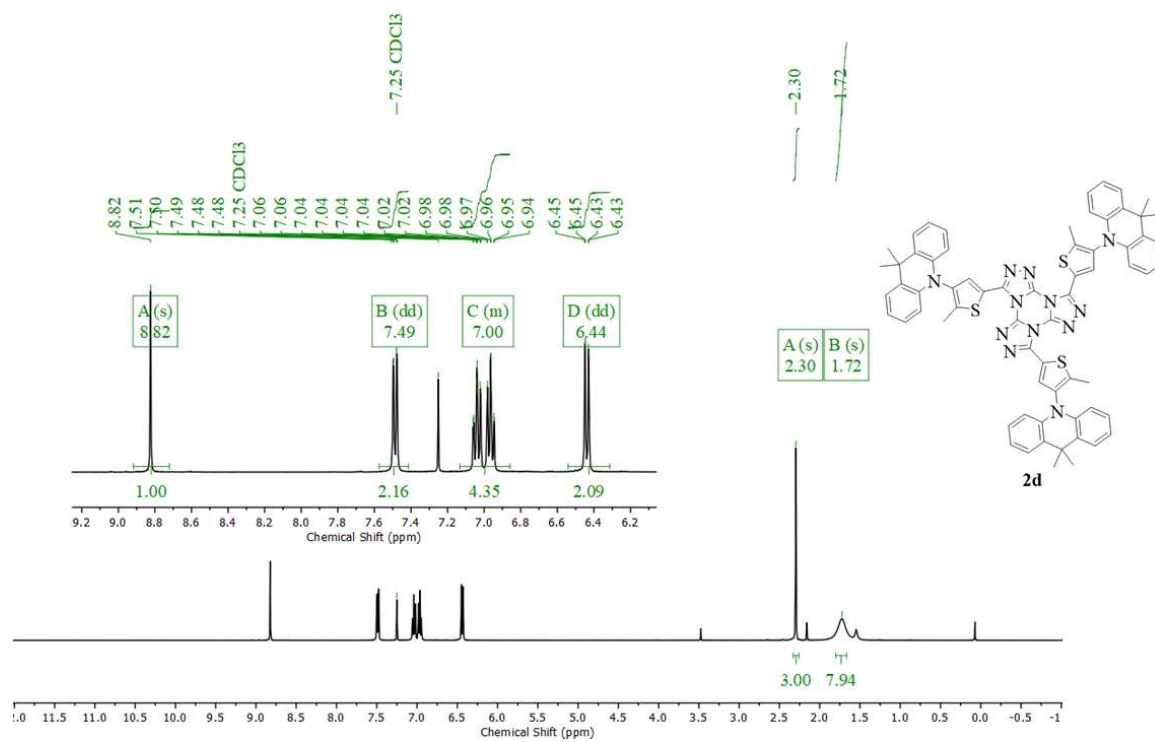


Figure SI 41 <sup>1</sup>H NMR spectra **2d** (400 MHz, CDCl<sub>3</sub>).

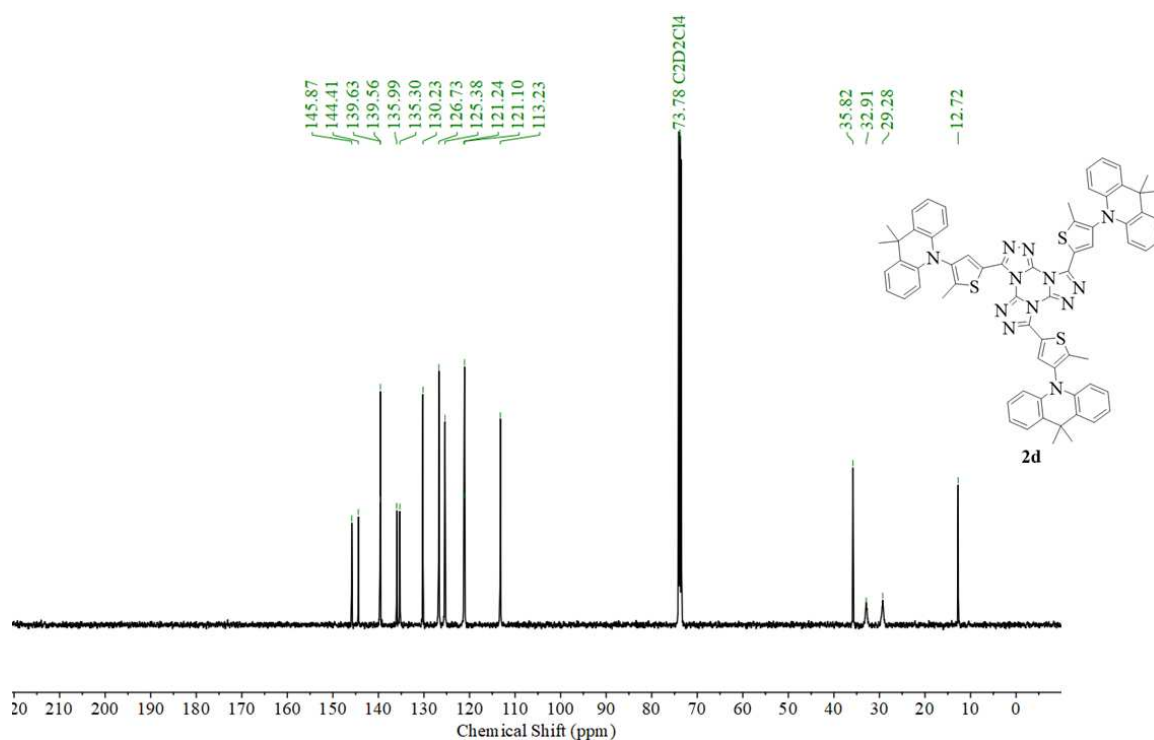


Figure SI 42 <sup>13</sup>C NMR spectra **2d** (101 MHz, C<sub>2</sub>D<sub>2</sub>Cl<sub>4</sub>).

### 8.1.3 Emitters decorated with aliphatic chains

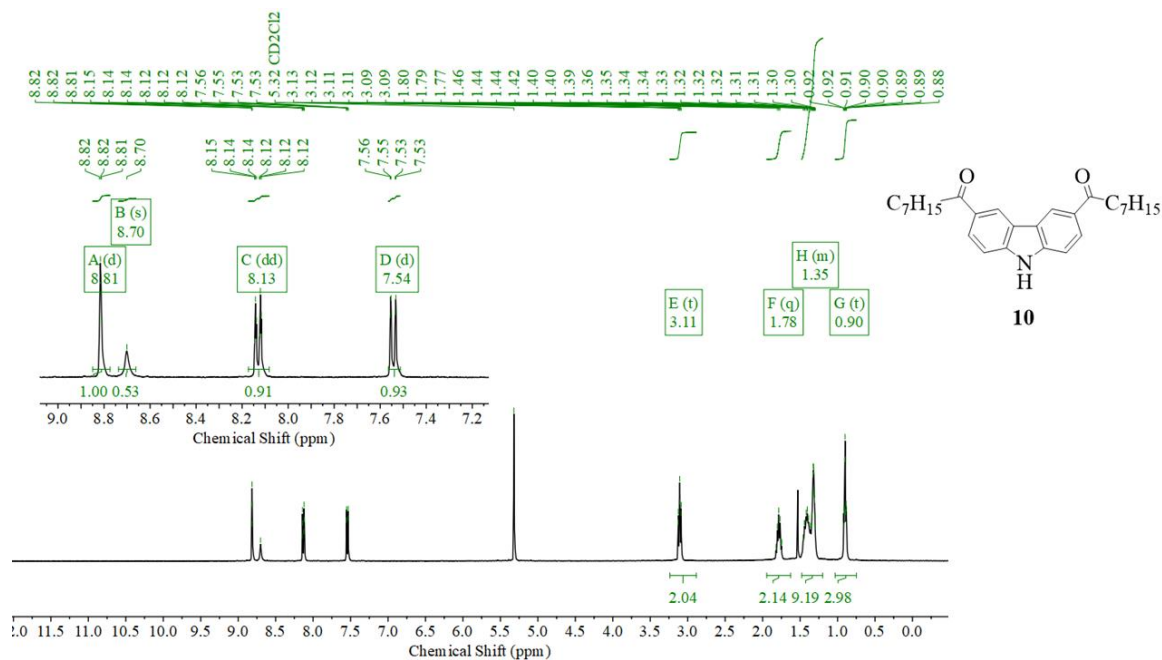


Figure SI 43 <sup>1</sup>H NMR spectra **10** (400 MHz, CD<sub>2</sub>Cl<sub>2</sub>).

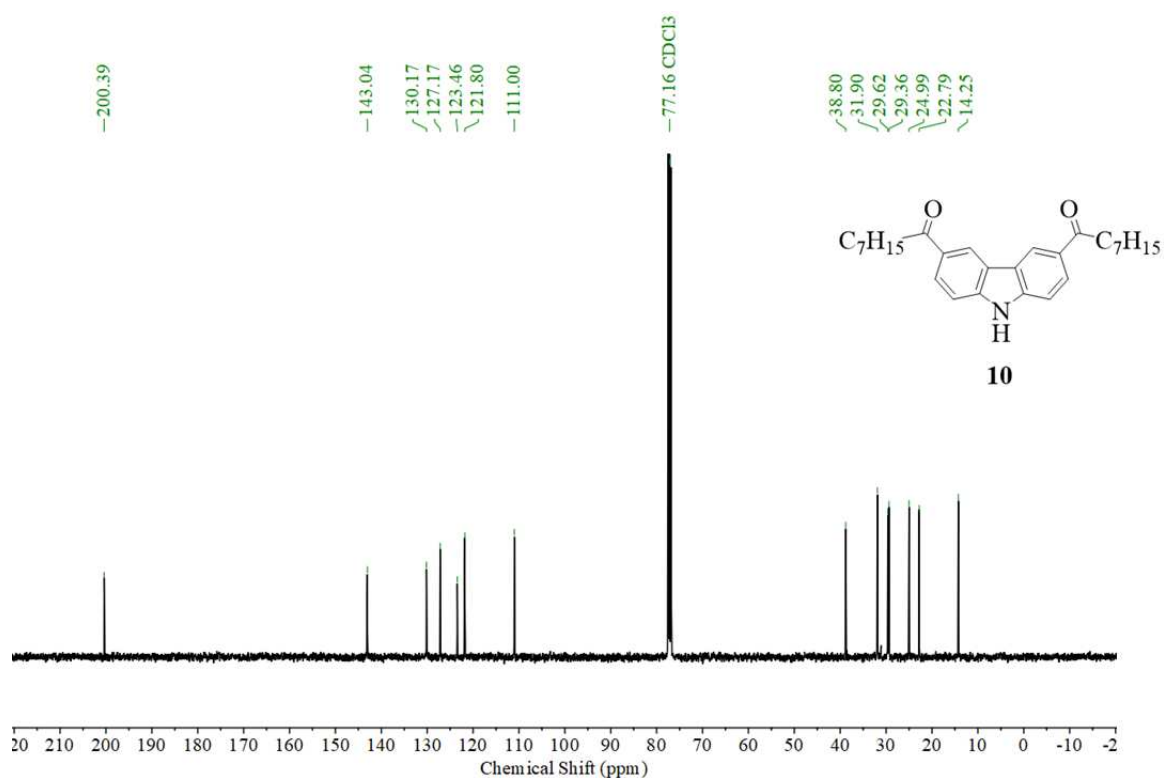


Figure SI 44 <sup>13</sup>C NMR spectra **10** (101 MHz, CDCl<sub>3</sub>).

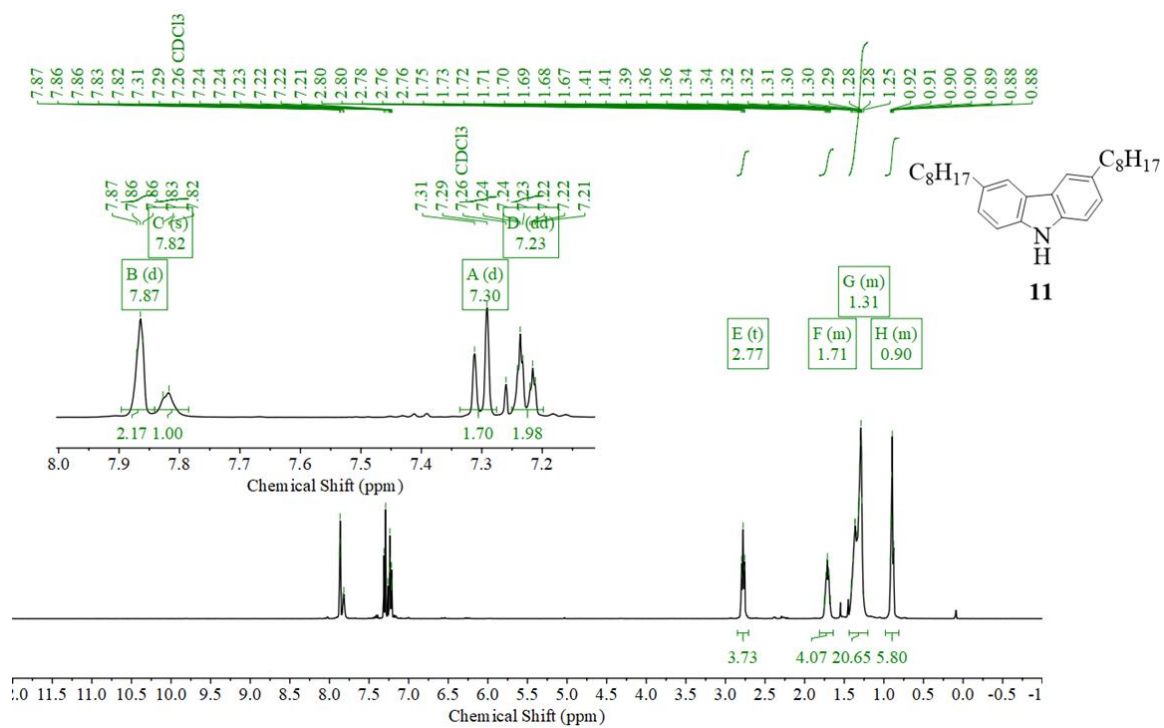


Figure SI 45 <sup>1</sup>H NMR spectra **11** (400 MHz, CDCl<sub>3</sub>).



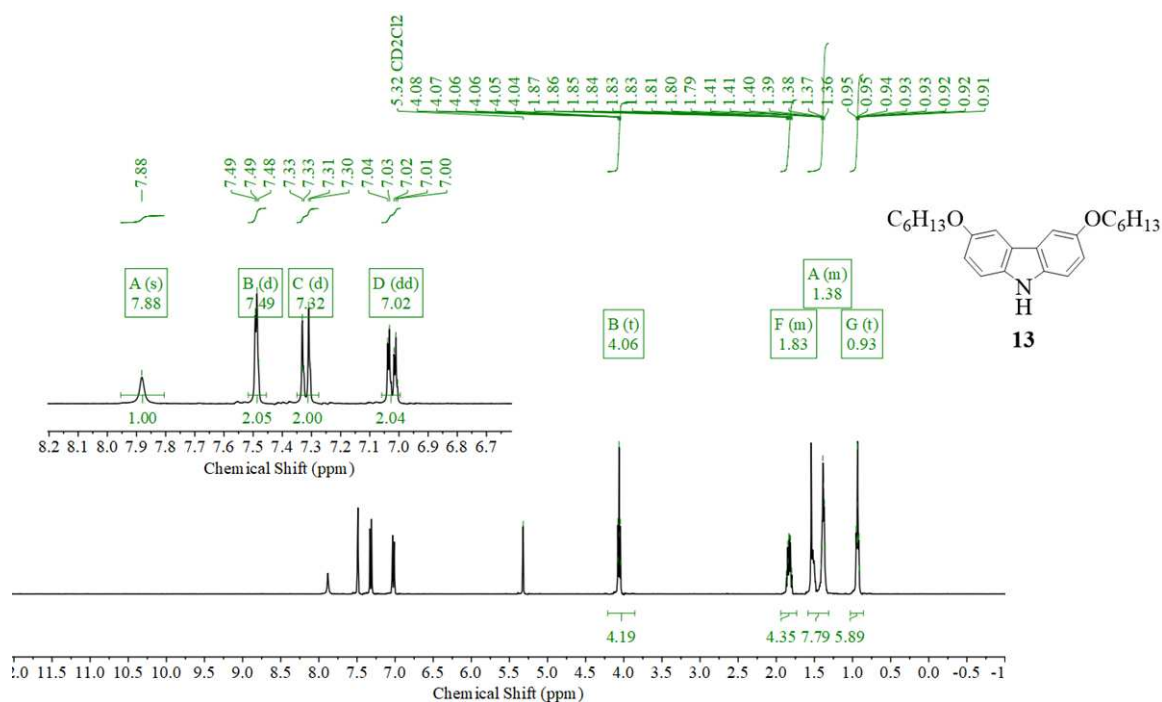


Figure SI 46  $^1\text{H}$  NMR spectra **13** (400 MHz,  $\text{CD}_2\text{Cl}_2$ ).

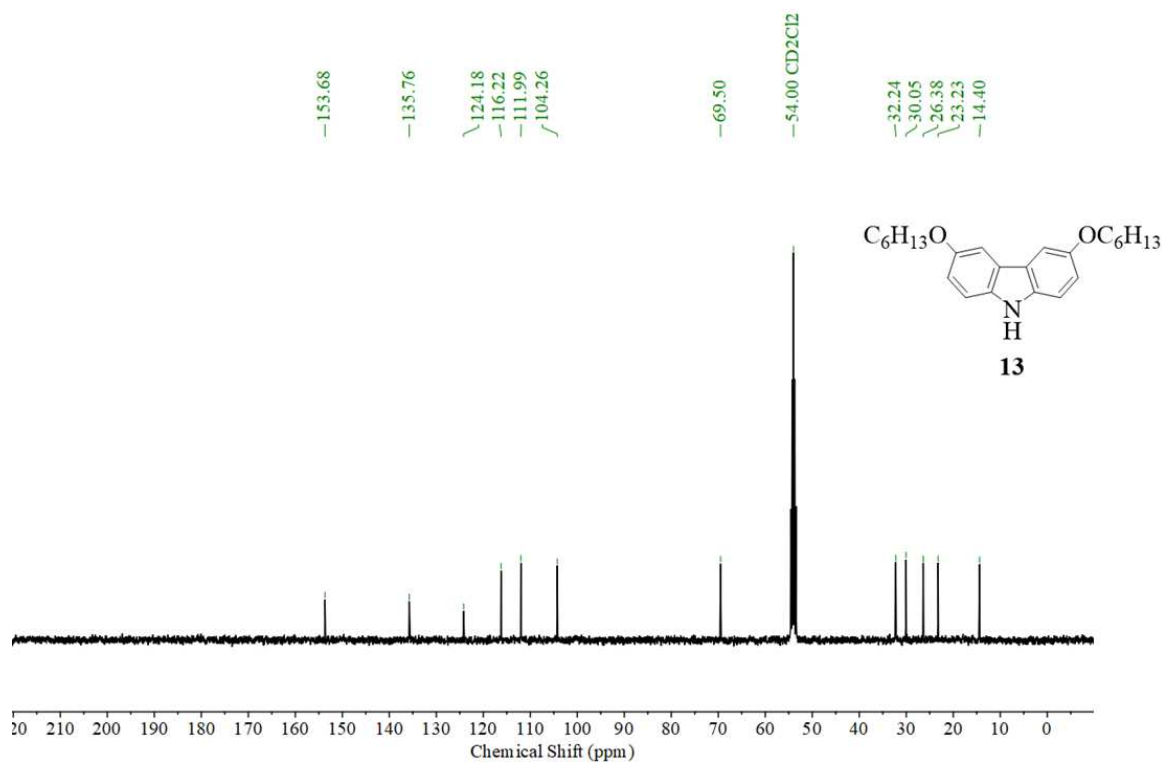


Figure SI 47  $^{13}\text{C}$  NMR spectra **13** (101 MHz,  $\text{CD}_2\text{Cl}_2$ ).

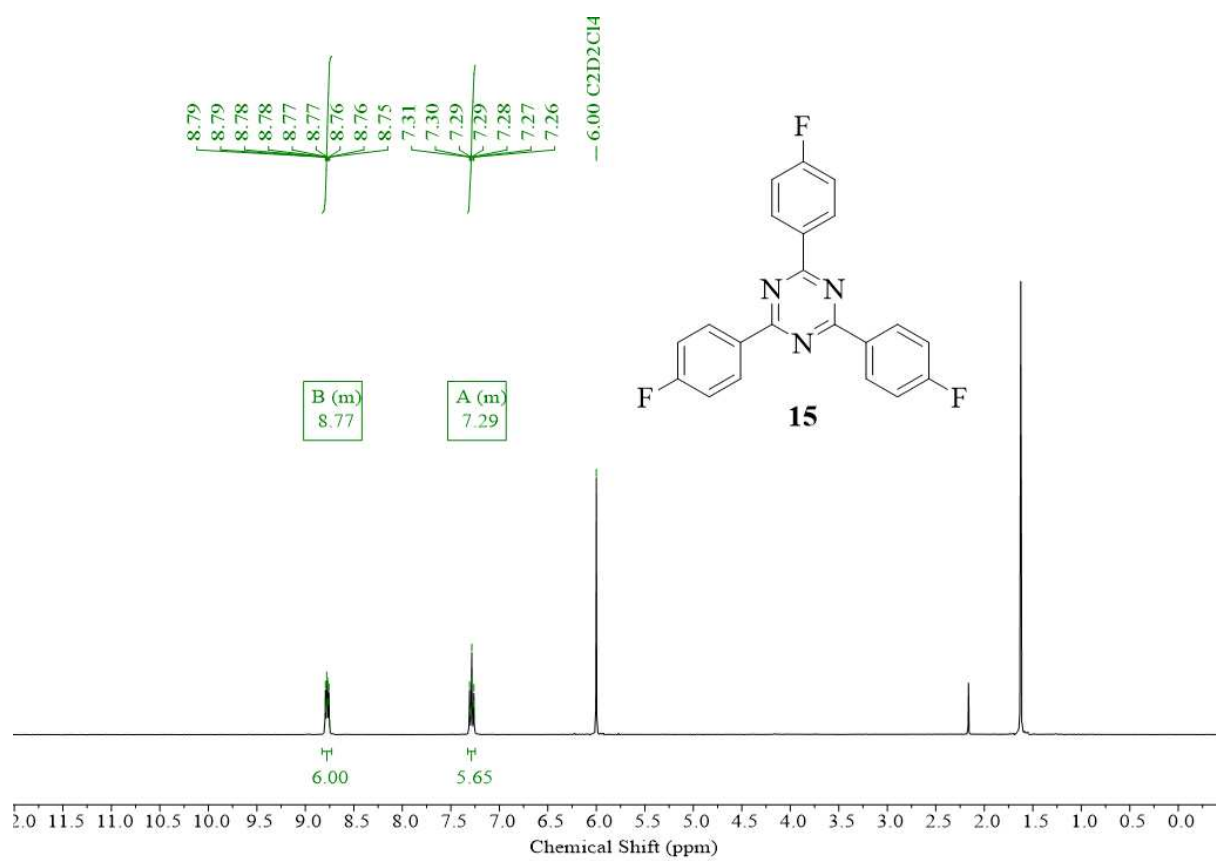


Figure SI 48  $^1\text{H}$  NMR spectra **15** (400 MHz,  $\text{C}_2\text{D}_2\text{Cl}_4$ ).

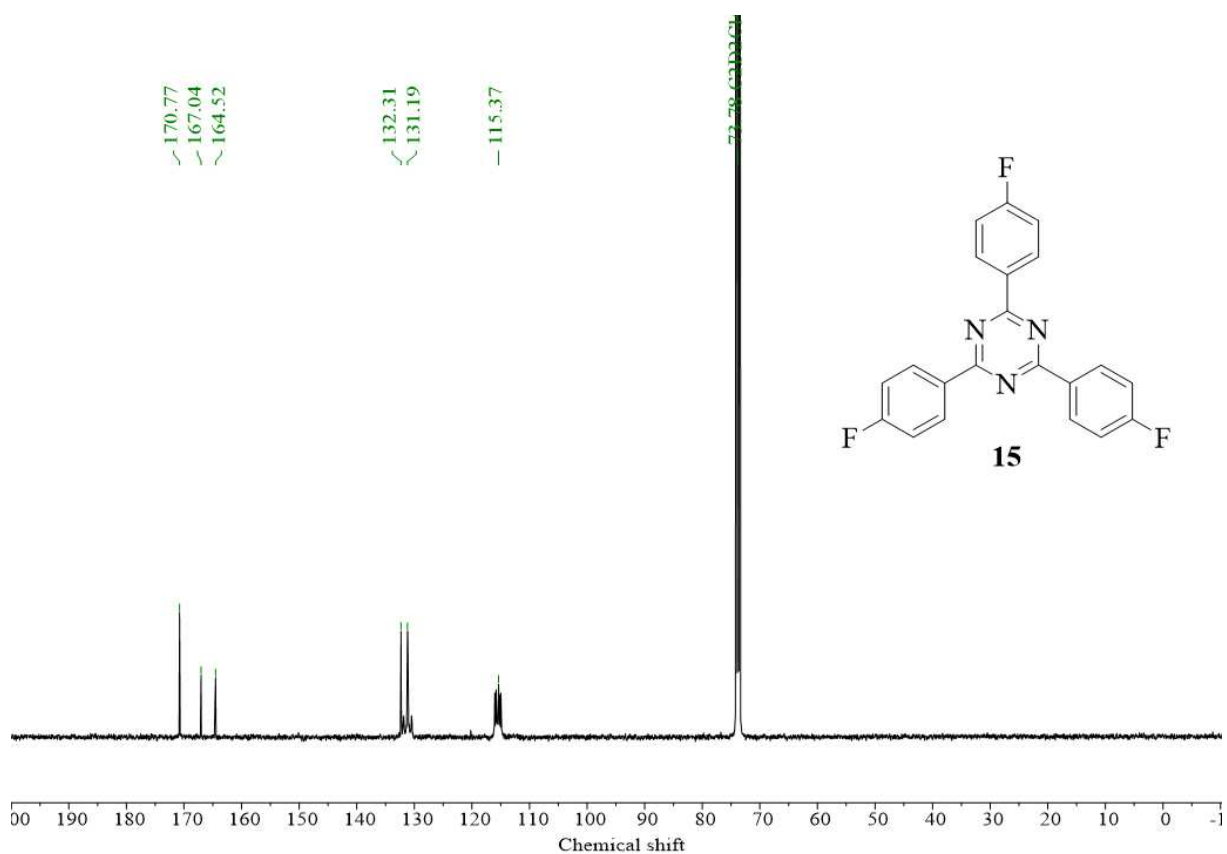


Figure SI 49  $^{13}\text{C}$  NMR spectra **15** (101 MHz,  $\text{C}_2\text{D}_2\text{Cl}_4$ ).

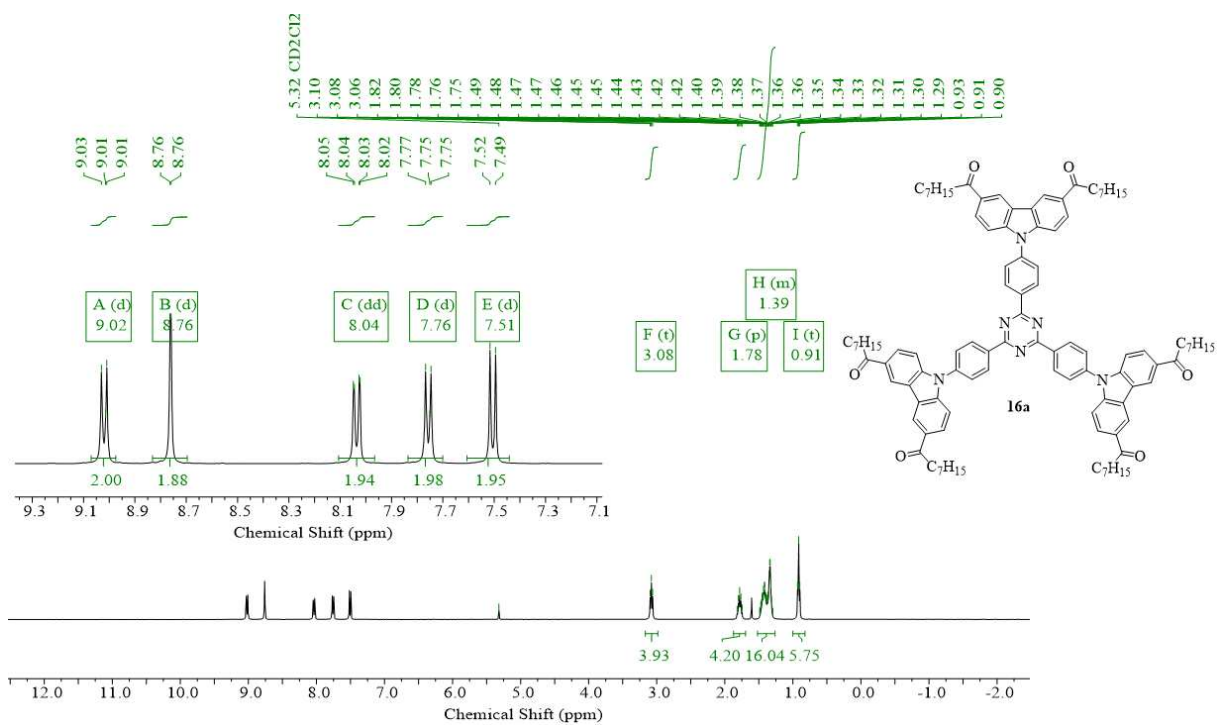


Figure SI 50  $^1\text{H}$  NMR spectra **16a** (400 MHz,  $\text{CD}_2\text{Cl}_2$ ).

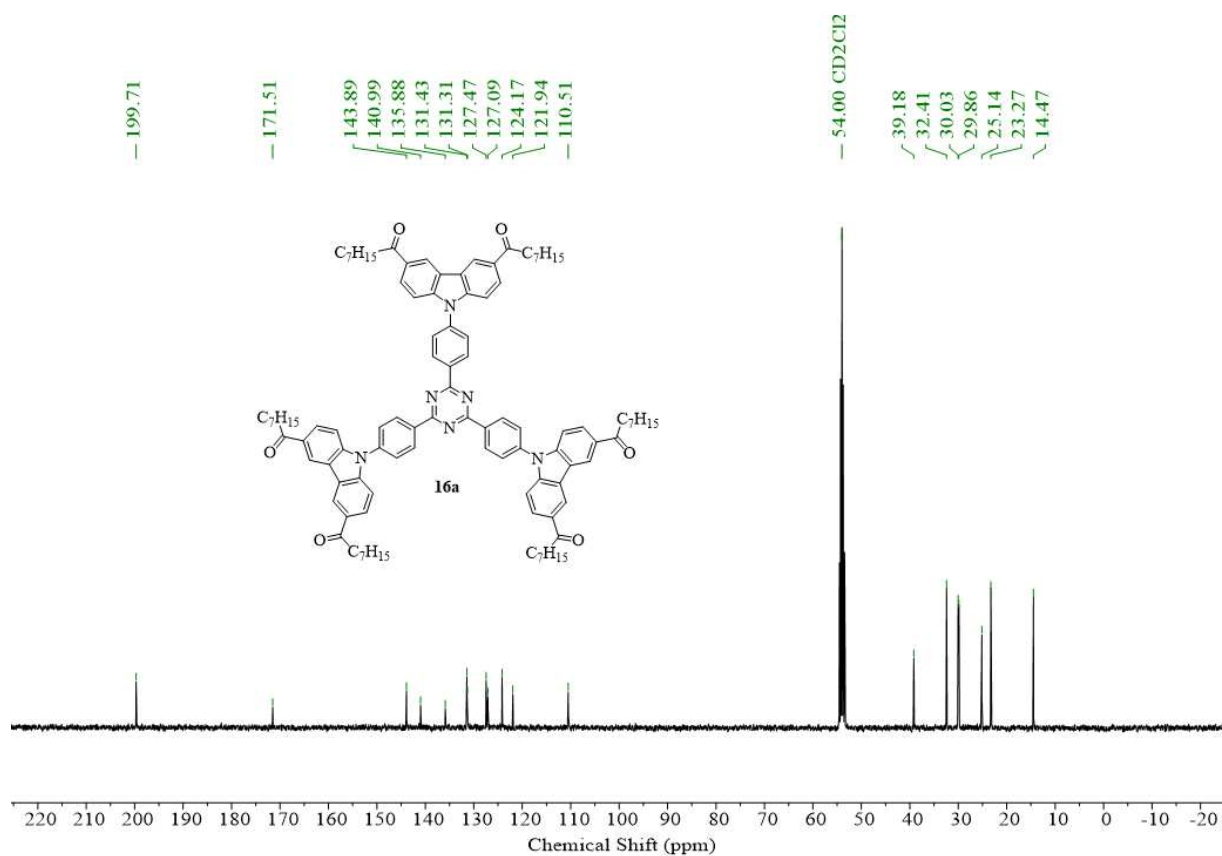


Figure SI 51 <sup>13</sup>C NMR spectra **16a** (101 MHz, CD<sub>2</sub>Cl<sub>2</sub>).

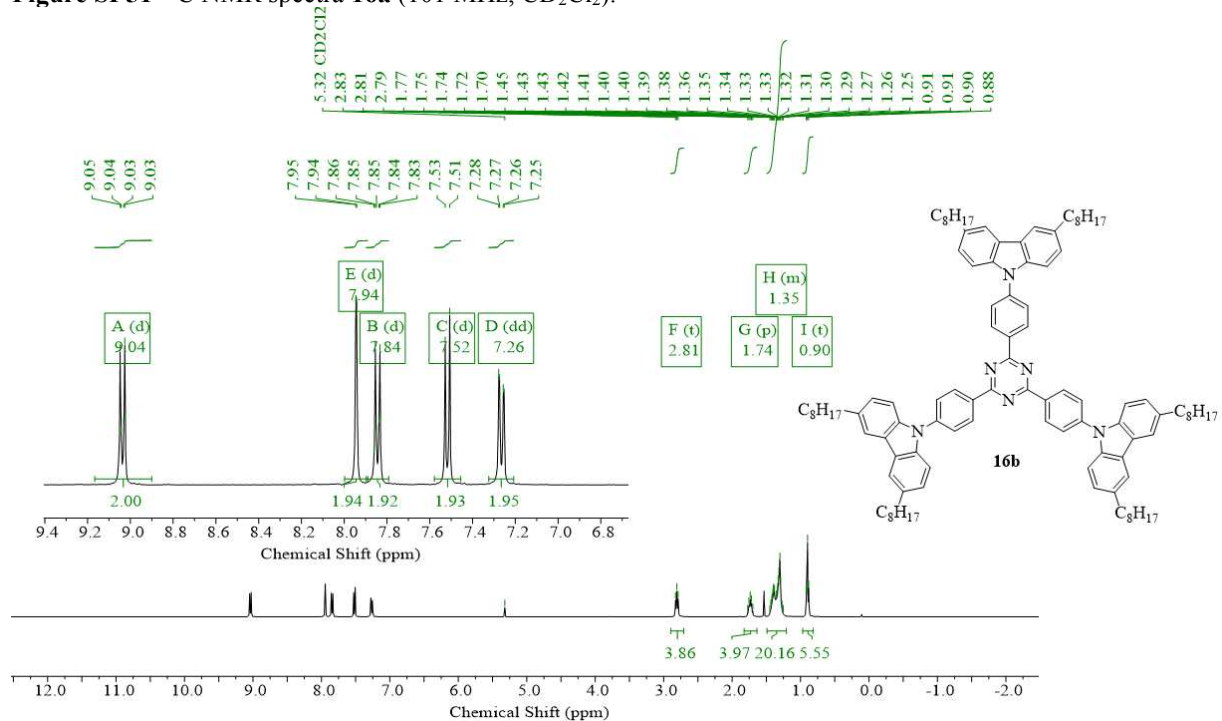
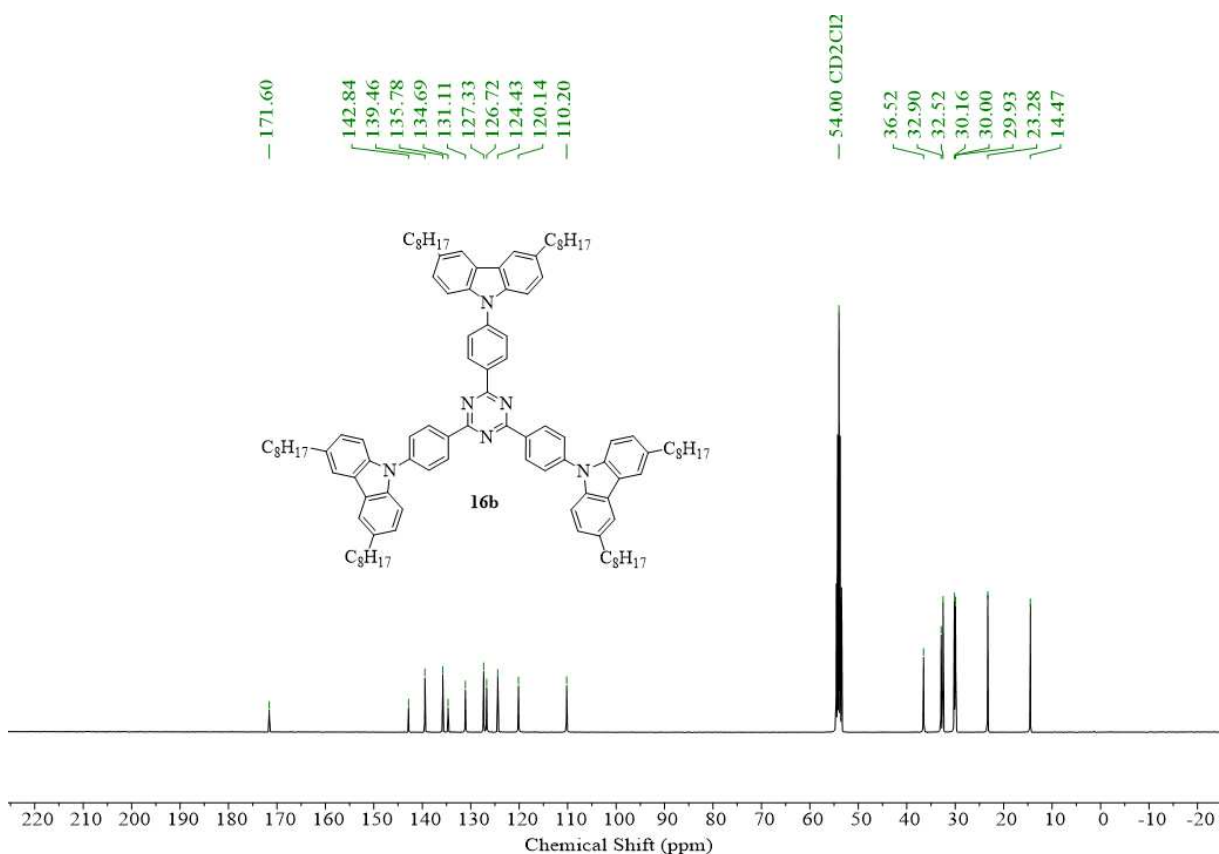
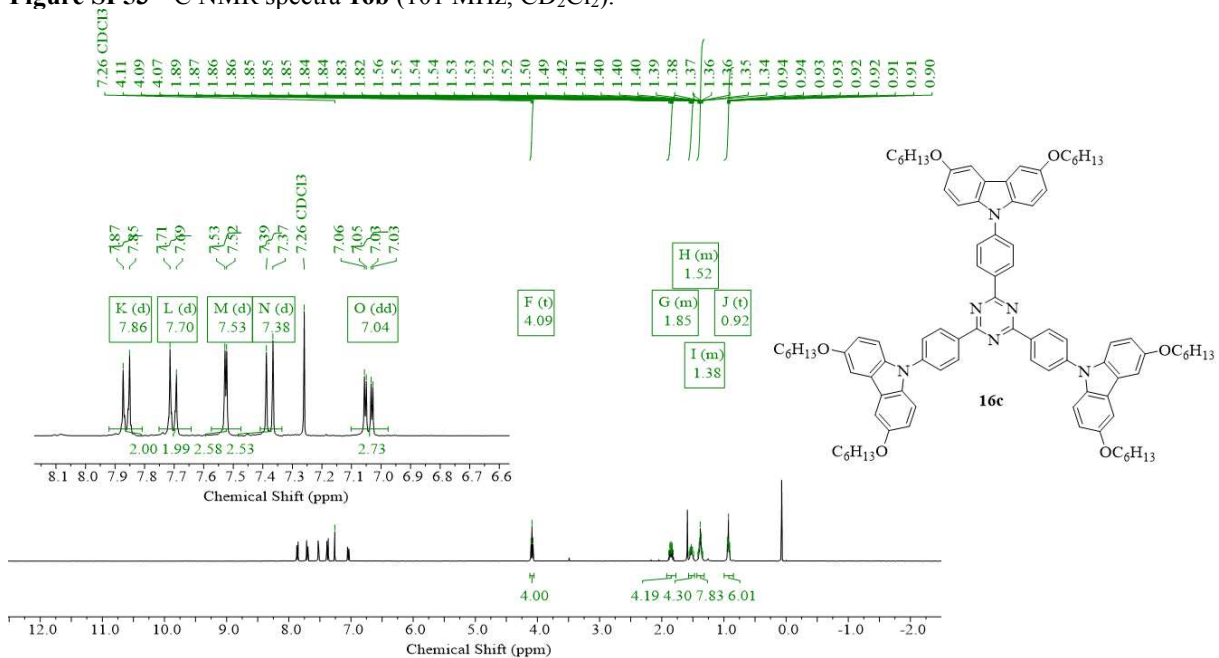


Figure SI 52 <sup>1</sup>H NMR spectra **16b** (400 MHz, CD<sub>2</sub>Cl<sub>2</sub>).



**Figure SI 53**  $^{13}\text{C}$  NMR spectra **16b** (101 MHz,  $\text{CD}_2\text{Cl}_2$ ).



**Figure SI 54**  $^1\text{H}$  NMR spectra **16c** (400 MHz,  $\text{CDCl}_3$ ).

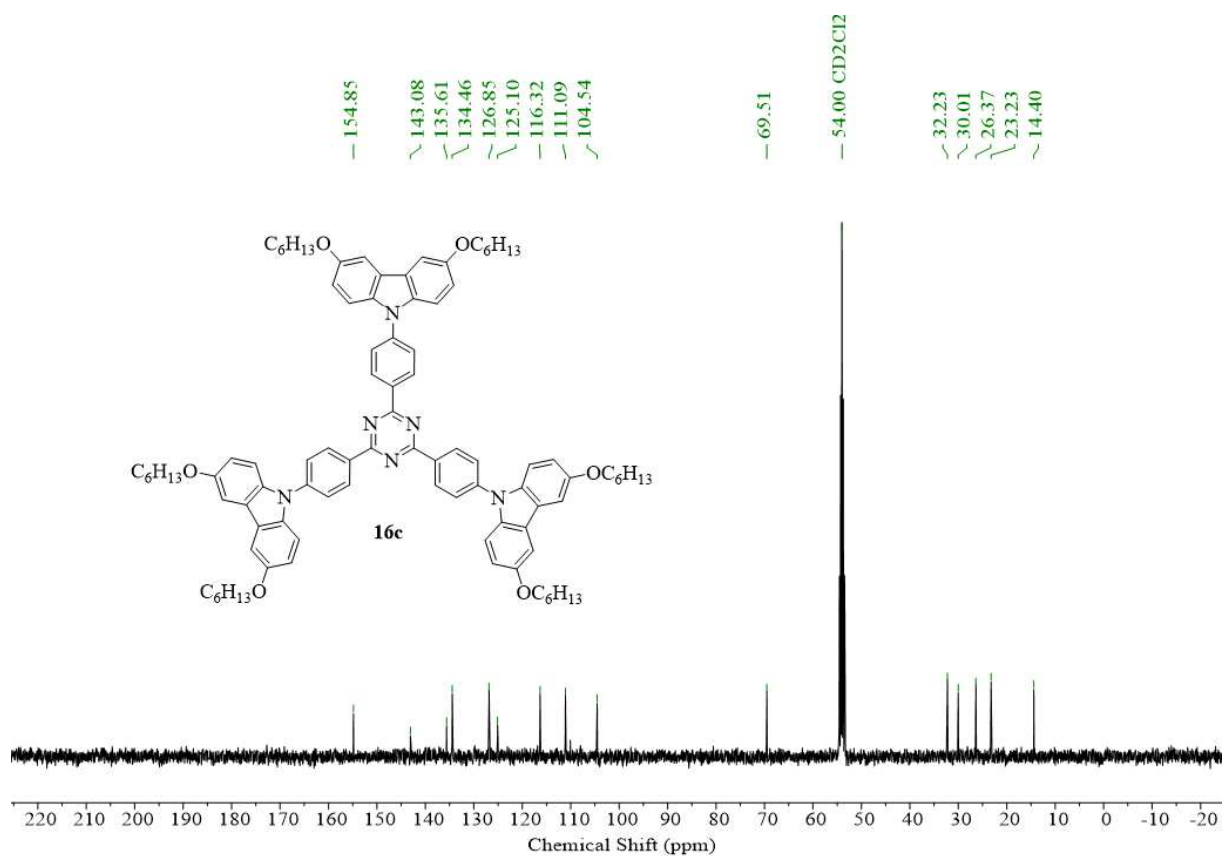


Figure SI 55  $^{13}\text{C}$  NMR spectra **16c** (101 MHz,  $\text{CD}_2\text{Cl}_2$ ).

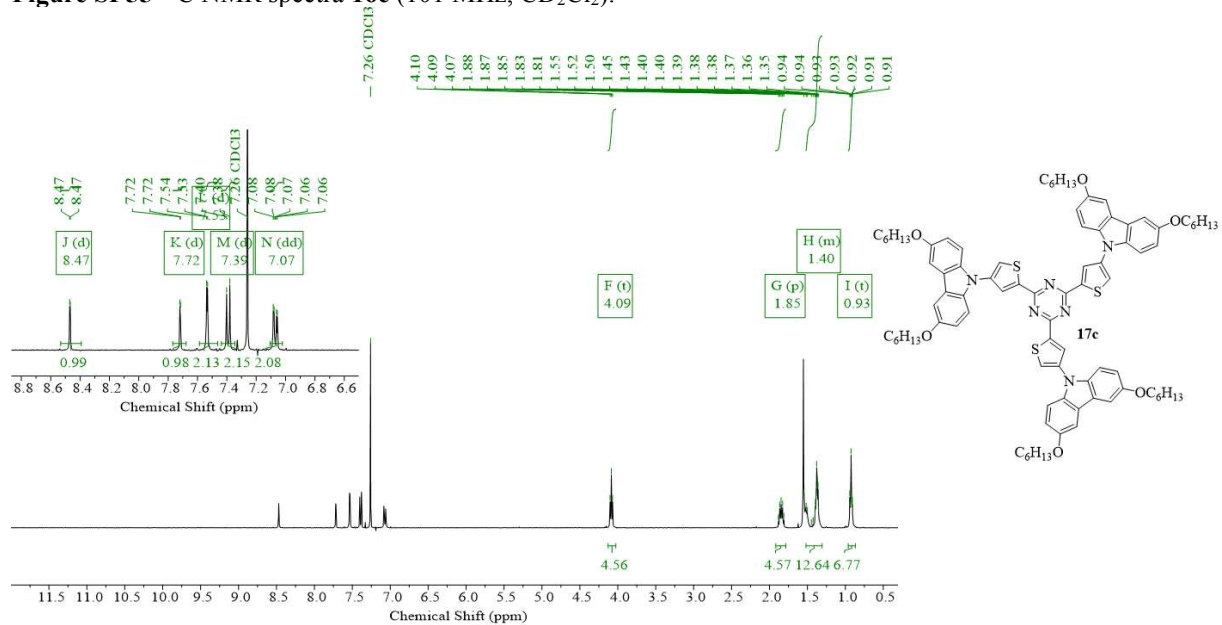


Figure SI 56  $^1\text{H}$  NMR spectra **17c** (400 MHz,  $\text{CDCl}_3$ ).

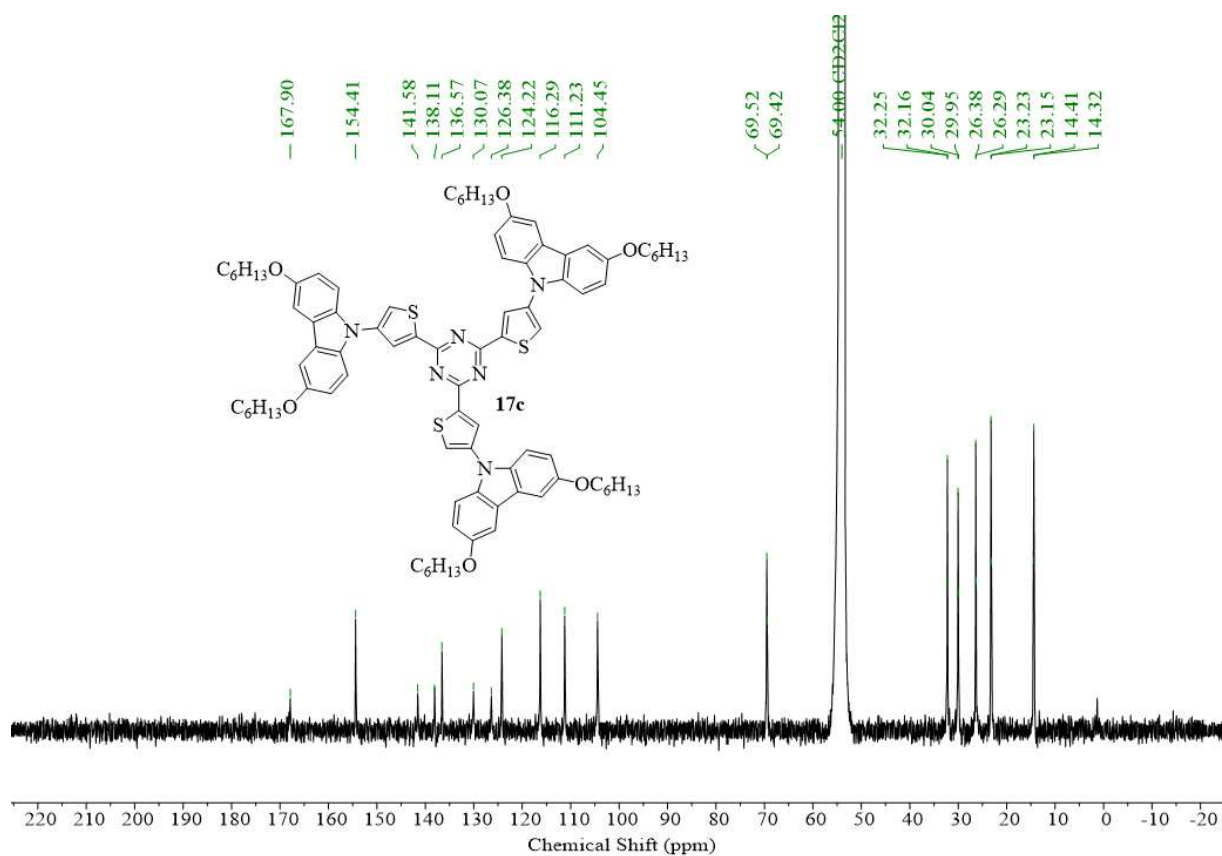


Figure SI 57  $^{13}C$  NMR spectra **17c** (101 MHz,  $CD_2Cl_2$ ).

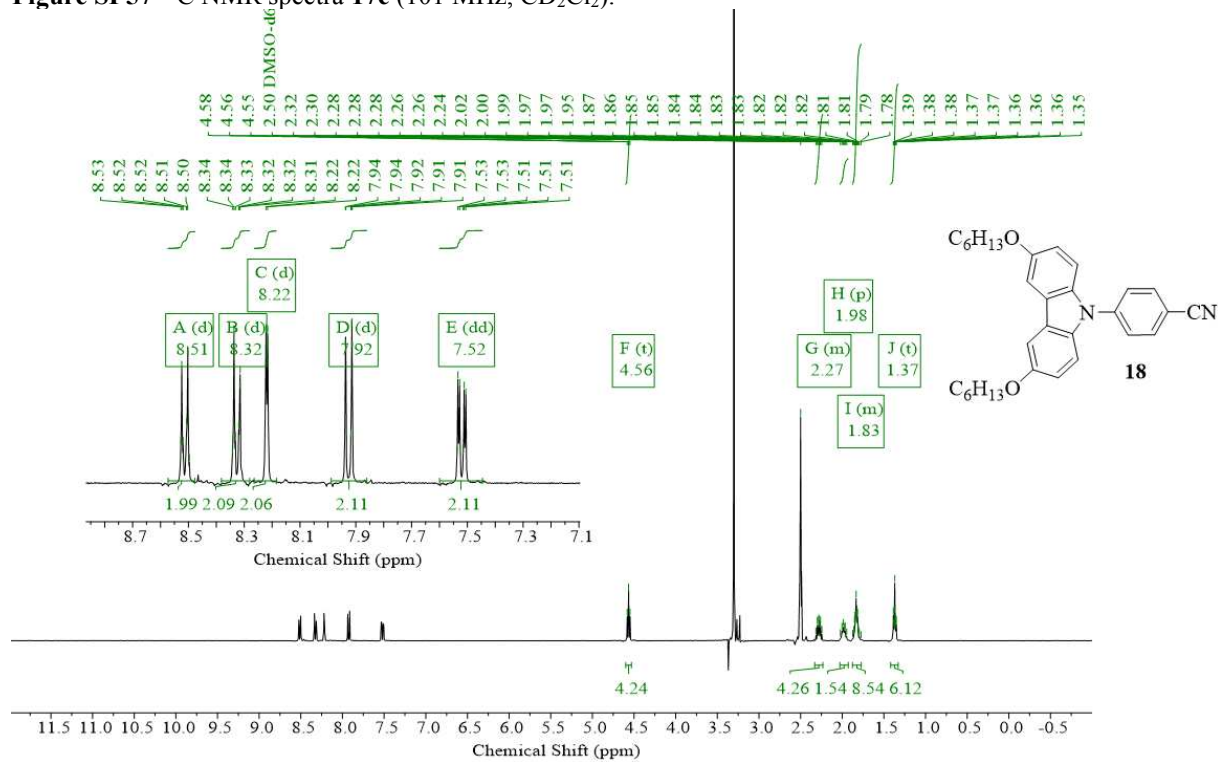


Figure SI 58  $^1H$  NMR spectra **18** (400 MHz,  $DMSO-d_6$ ).

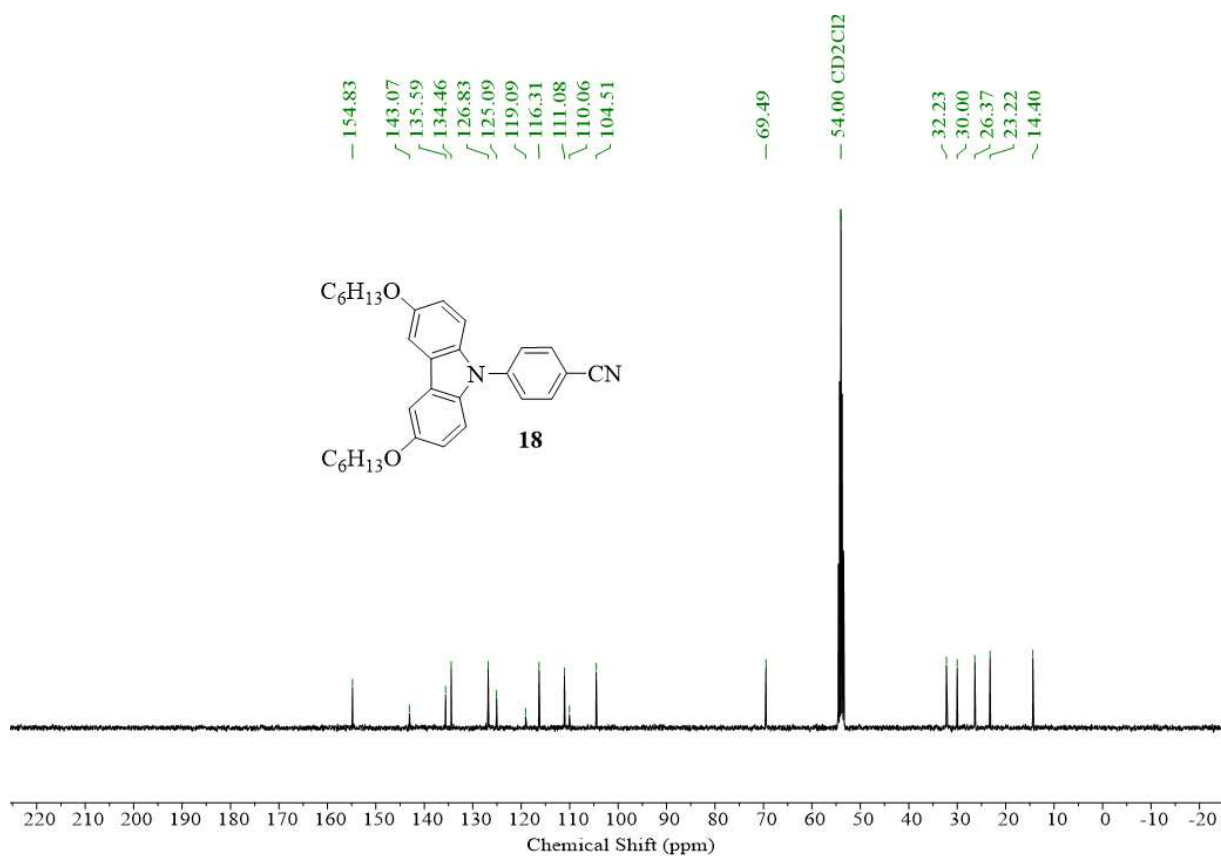


Figure SI 59 <sup>13</sup>C NMR spectra **18** (101 MHz, CD<sub>2</sub>Cl<sub>2</sub>).

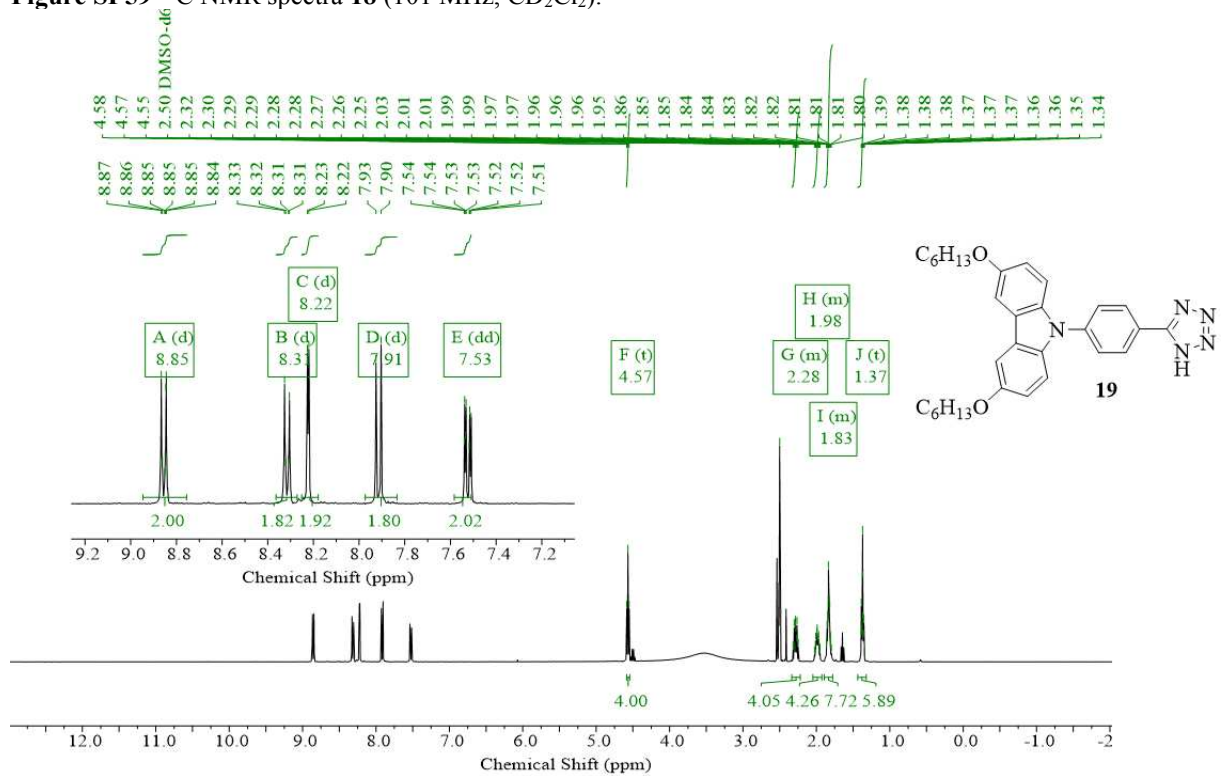


Figure SI 60 <sup>1</sup>H NMR spectra **19** (400 MHz, DMSO-D<sub>6</sub>).



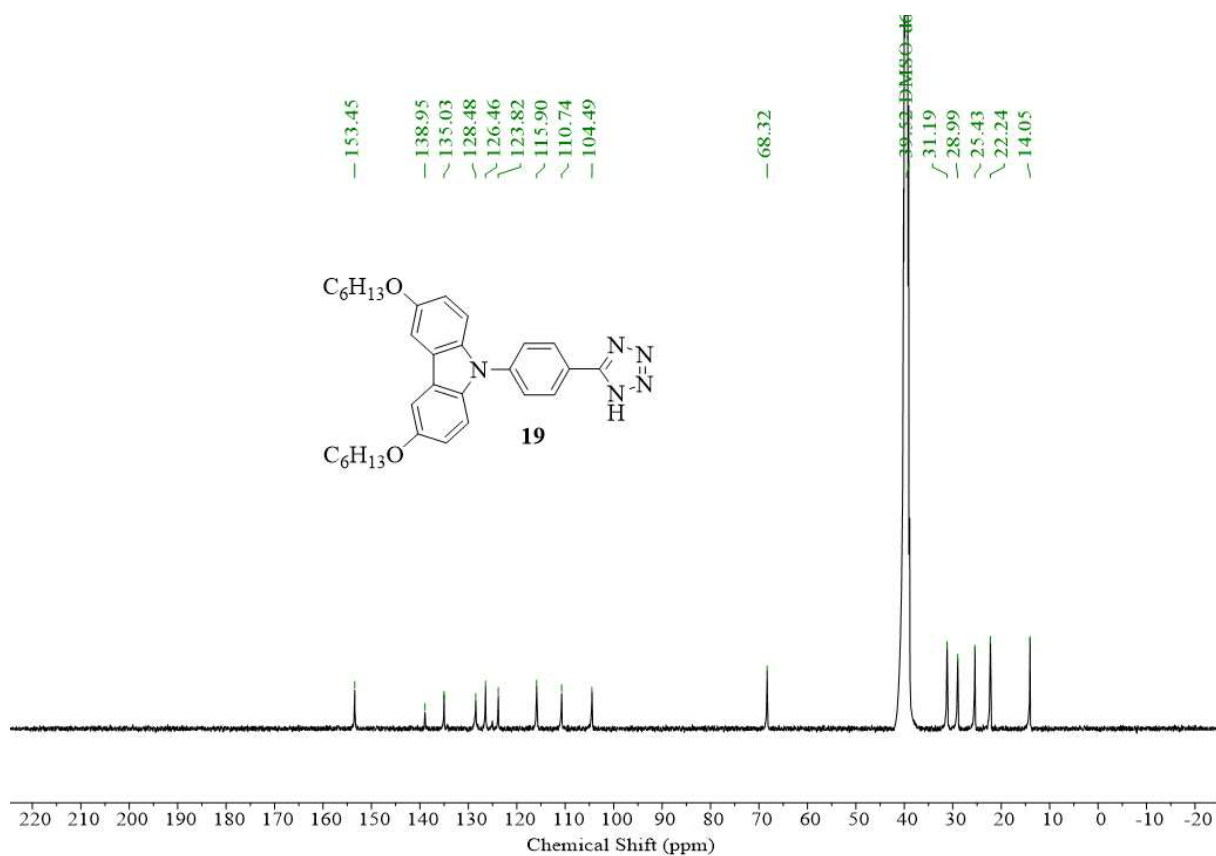


Figure SI 61  $^{13}C$  NMR spectra **19** (101 MHz, DMSO- $d_6$ ).

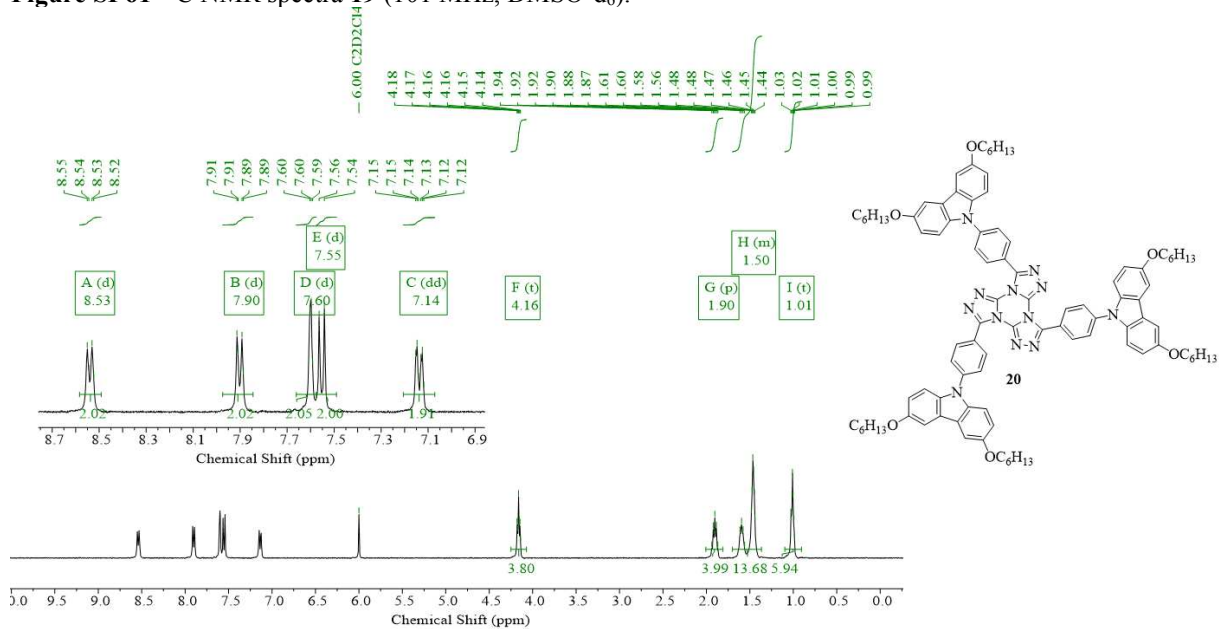


Figure SI 62  $^1H$  NMR spectra **20** (400 MHz,  $C_2D_2Cl_4$ ).

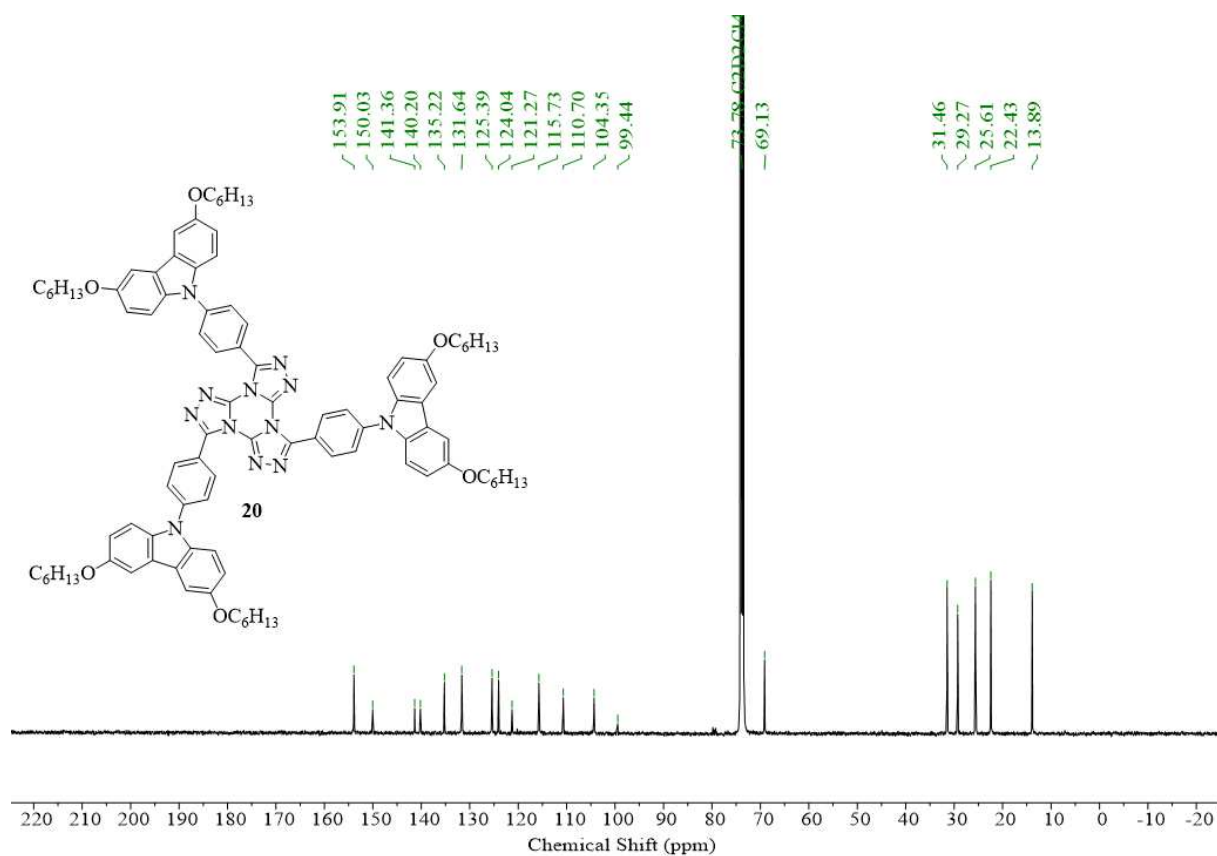


Figure SI 63  $^{13}\text{C}$  NMR spectra **20** (101 MHz,  $\text{C}_2\text{D}_2\text{Cl}_4$ ).

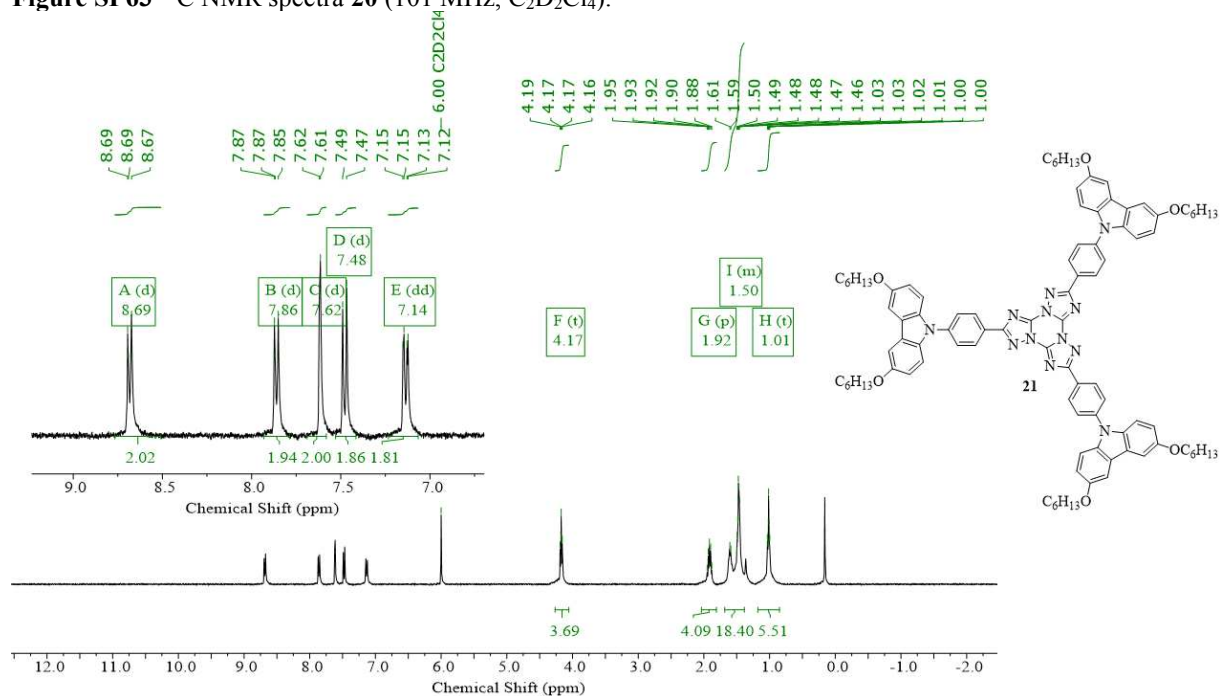


Figure SI 64  $^1\text{H}$  NMR spectra **21** (400 MHz,  $\text{C}_2\text{D}_2\text{Cl}_4$ ).

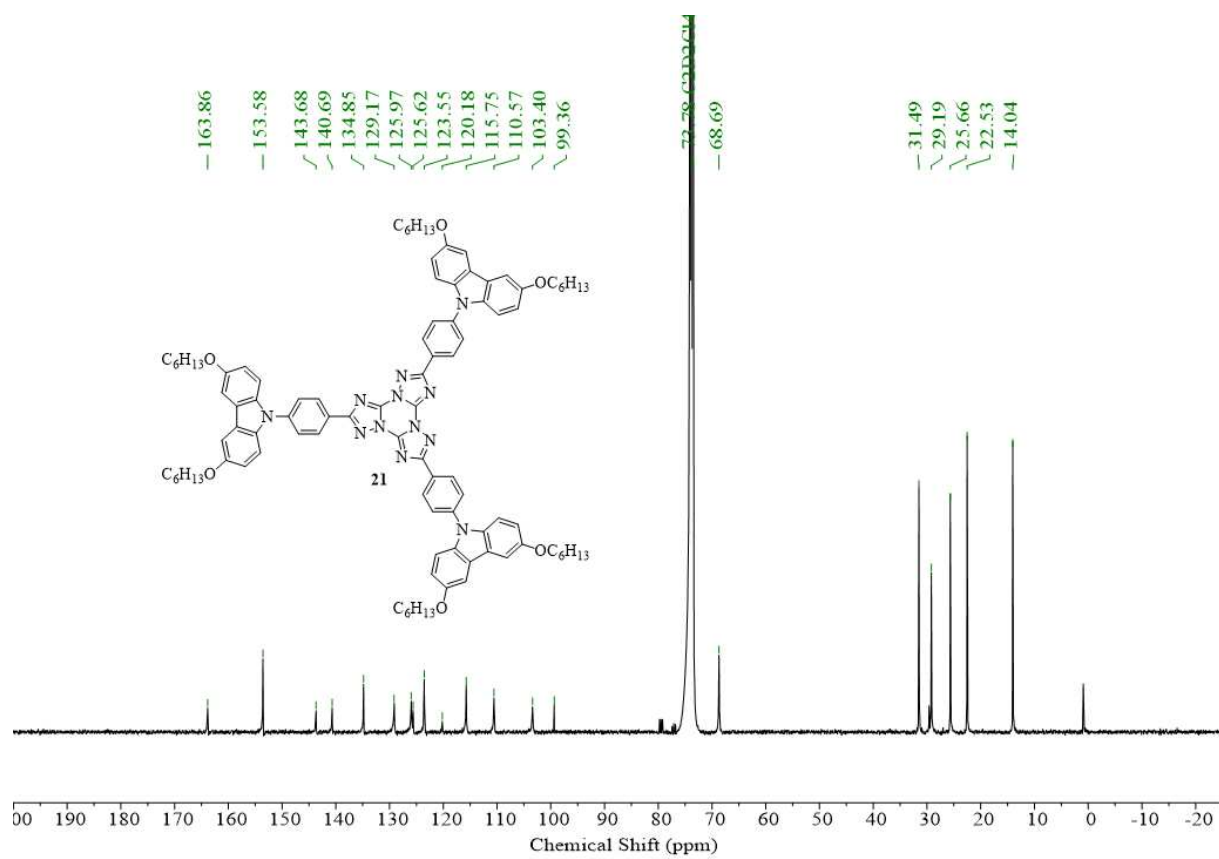


Figure SI 65  $^{13}\text{C}$  NMR spectra **21** (101 MHz,  $\text{C}_2\text{D}_2\text{Cl}_4$ ).

## 8.2 IR

## 8.2.1 Triazine-based emitters

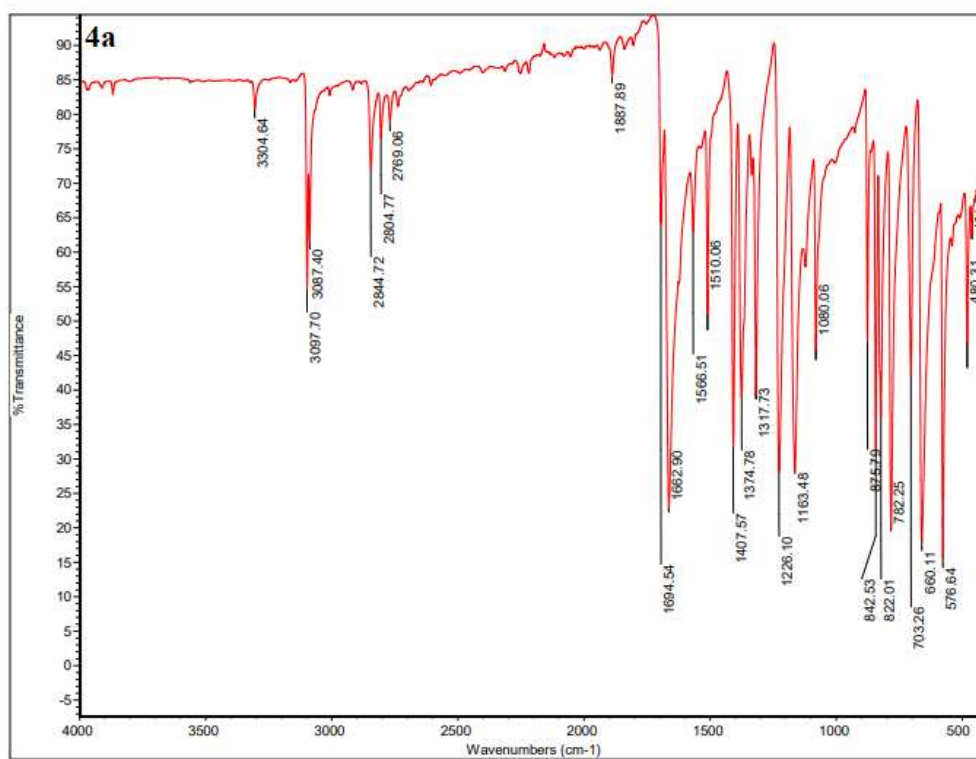


Figure SI 66 IR spectrum 4a.

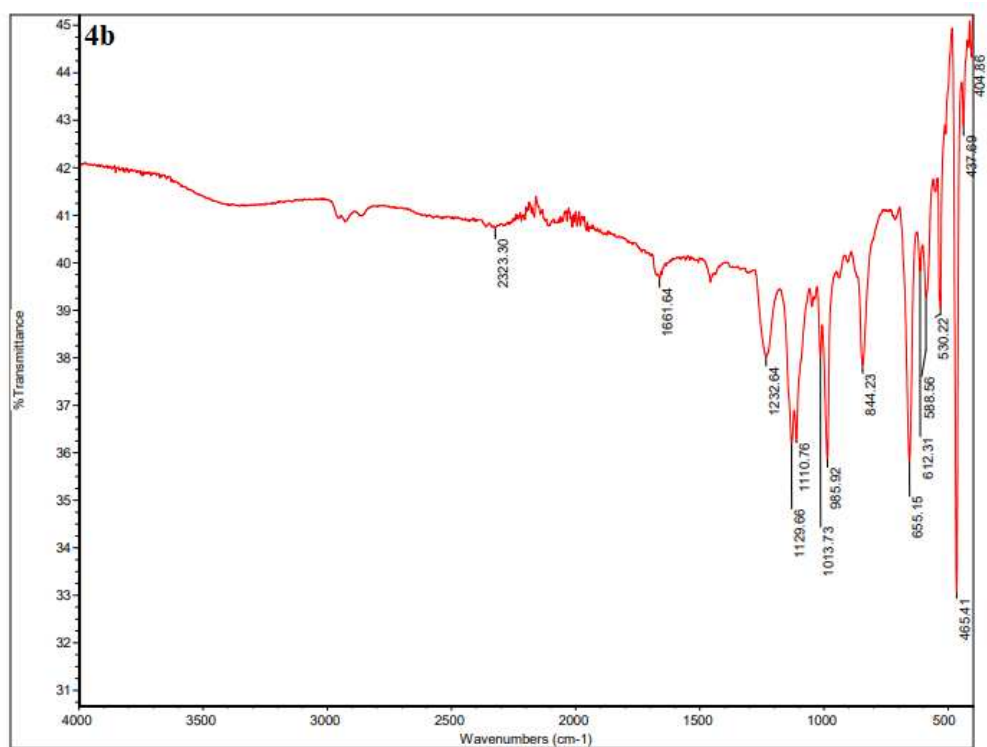


Figure SI 67 IR spectrum 4b.

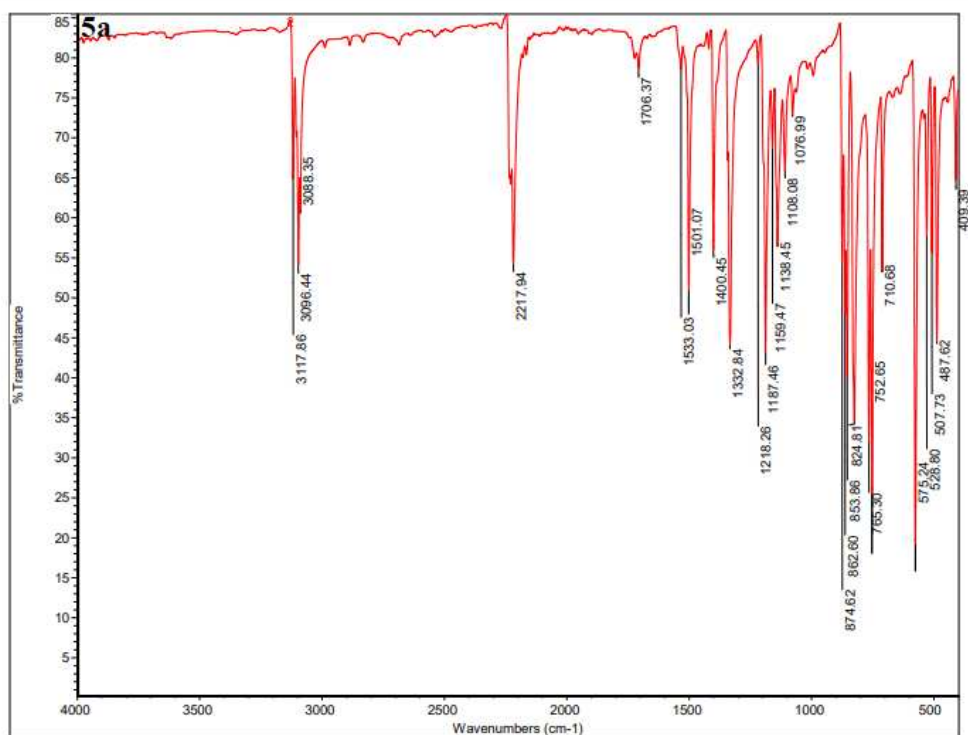
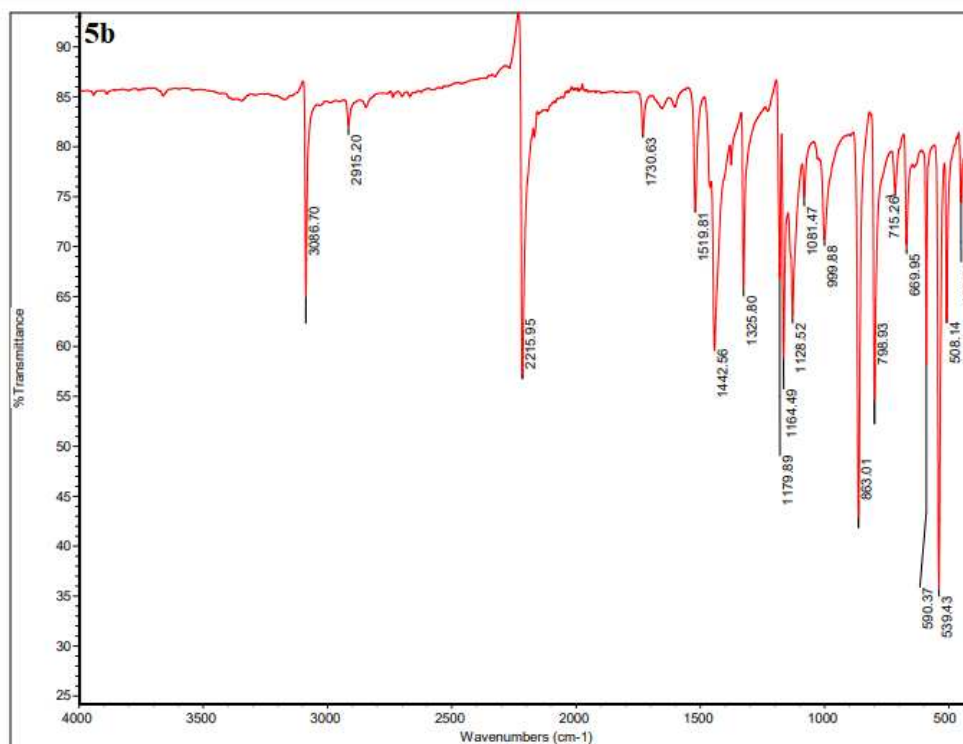
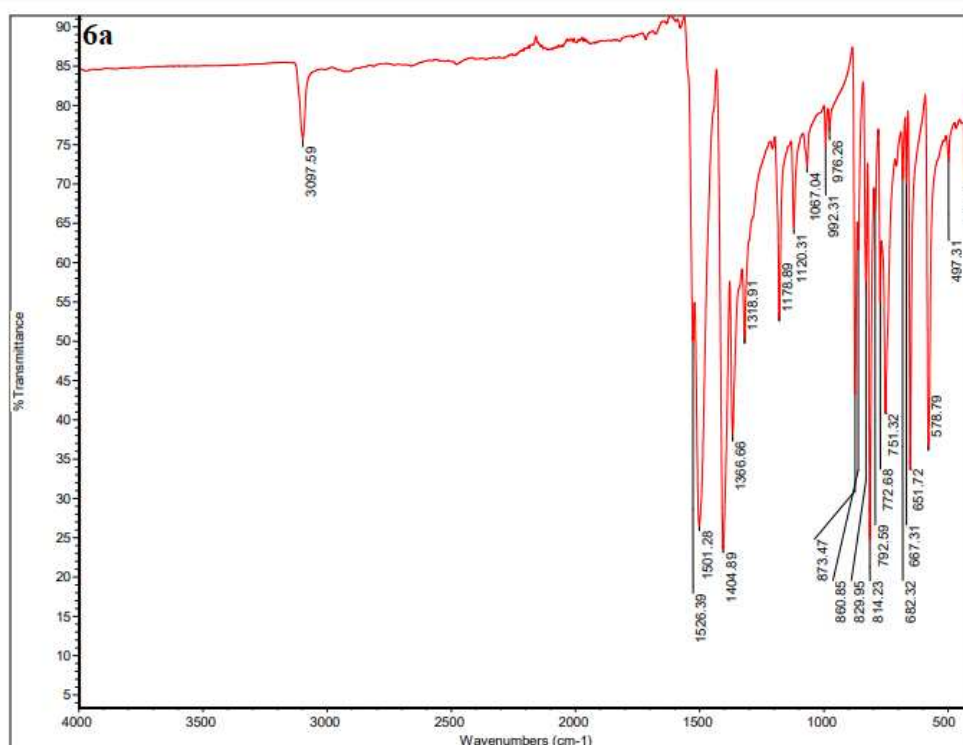
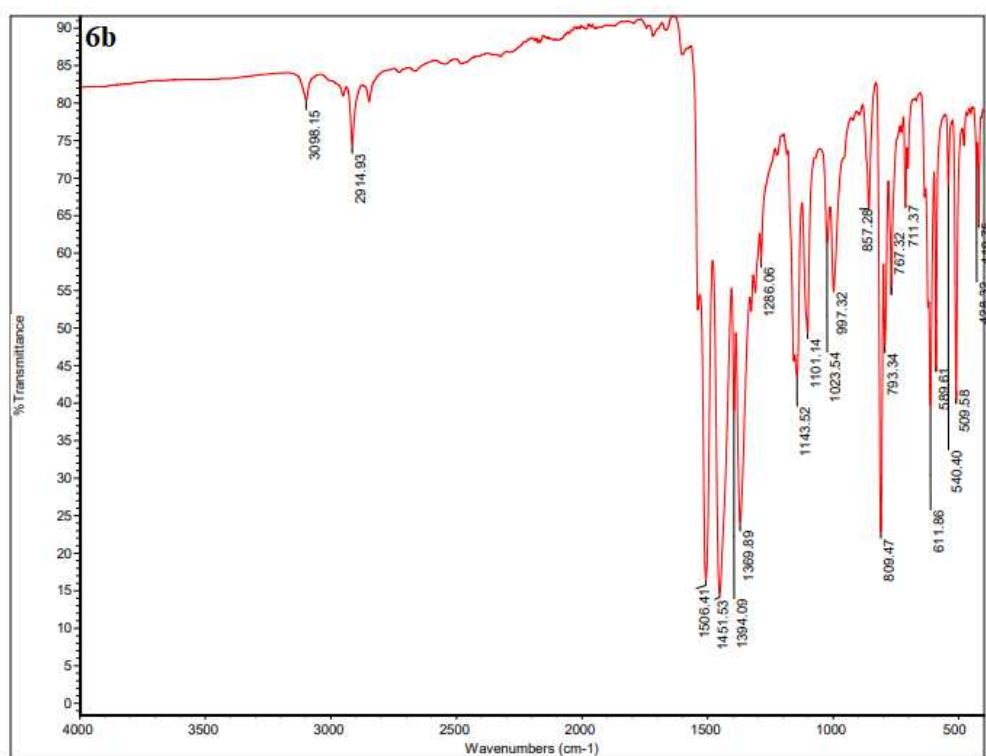
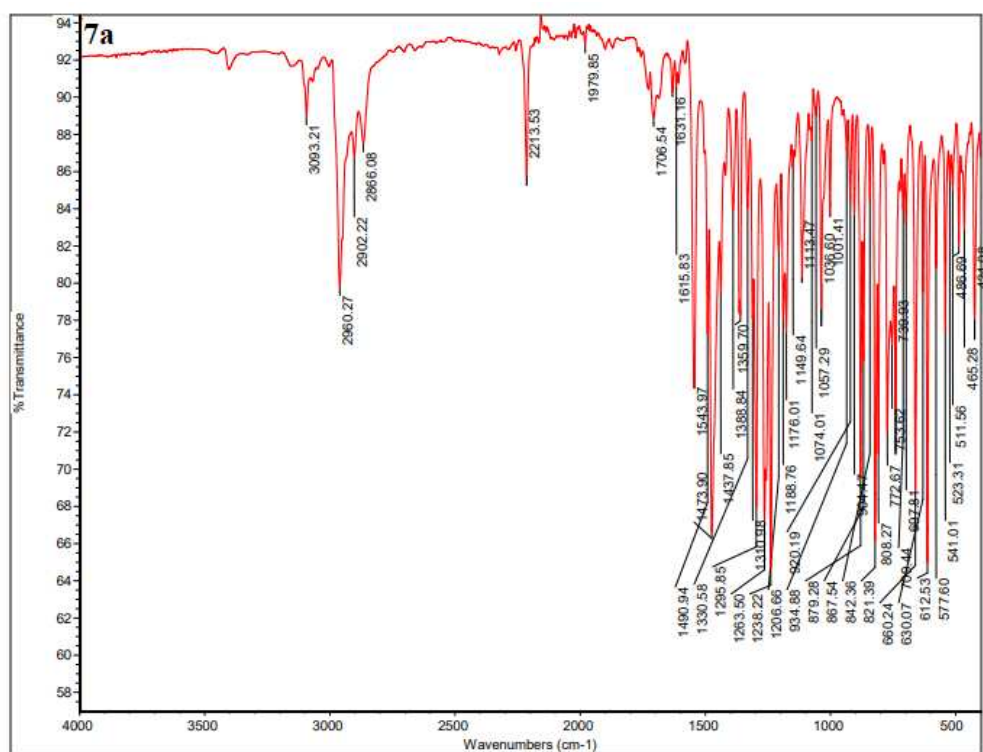


Figure SI 68 IR spectrum 5a.

Figure SI 69 IR spectrum **5b**.Figure SI 70 IR spectrum **6a**.

Figure SI 71 IR spectrum **6b**.

## 8.2.2 TTT-based emitters

Figure SI 72 IR spectrum **7a**.

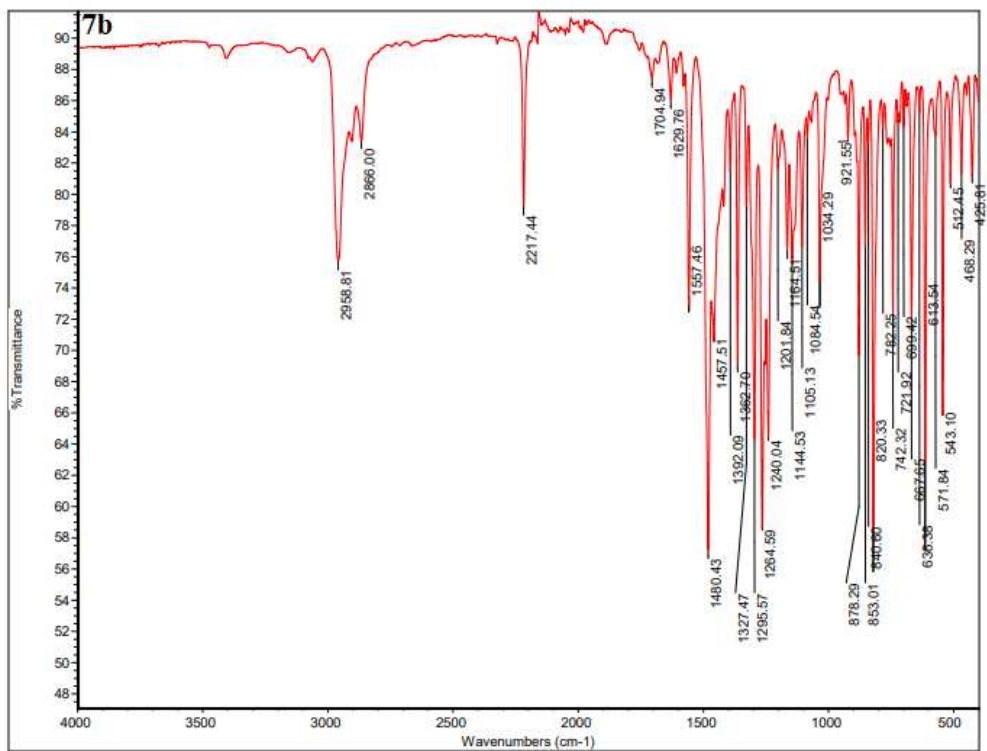


Figure SI 73 IR spectrum 7b.

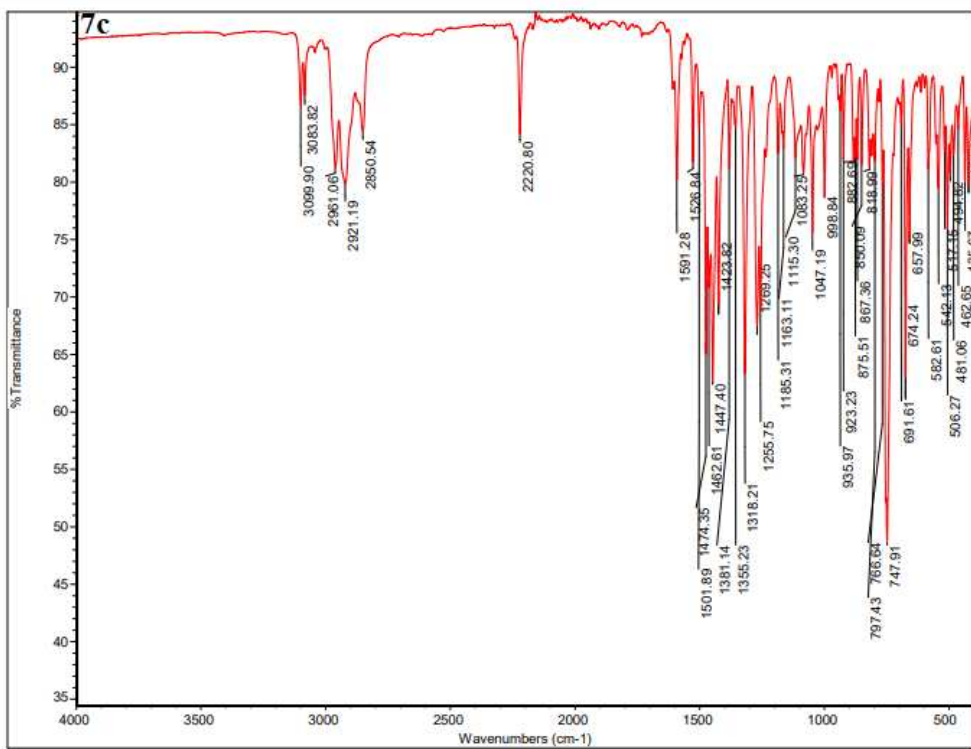


Figure SI 74 IR spectrum 7c.



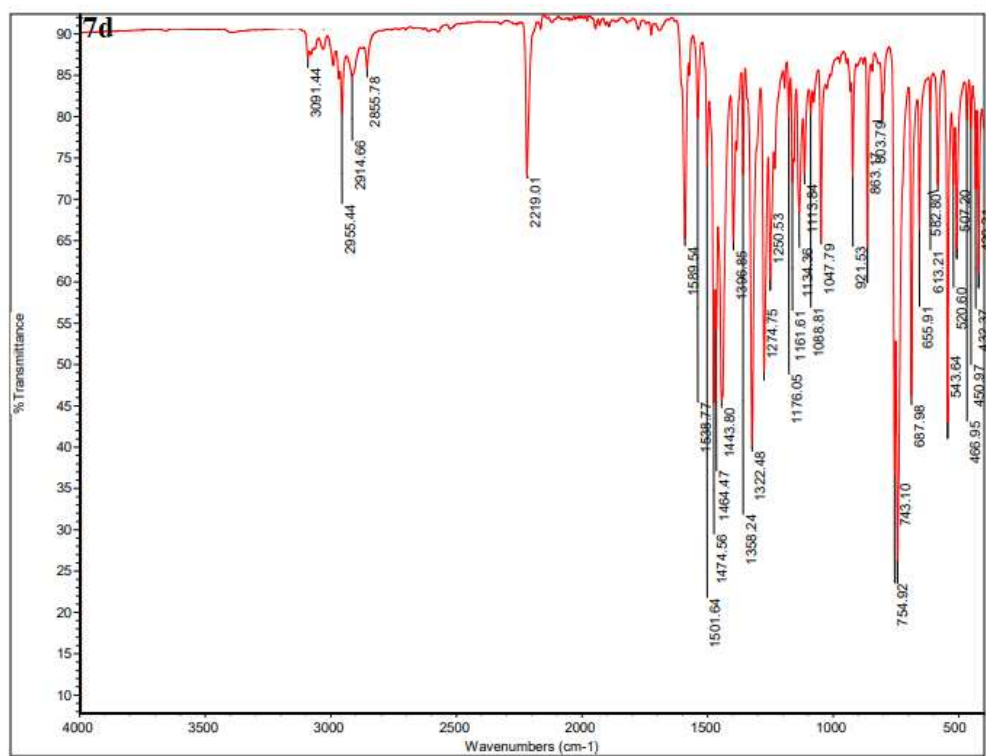


Figure SI 75 IR spectrum 7d.

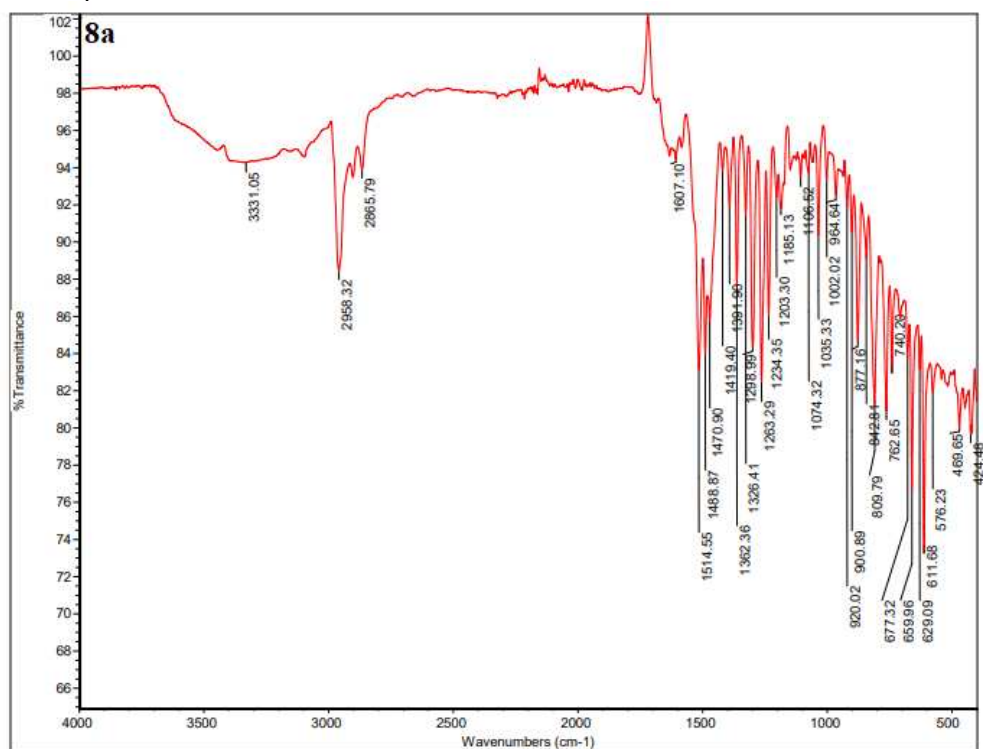


Figure SI 76 IR spectrum 8a.

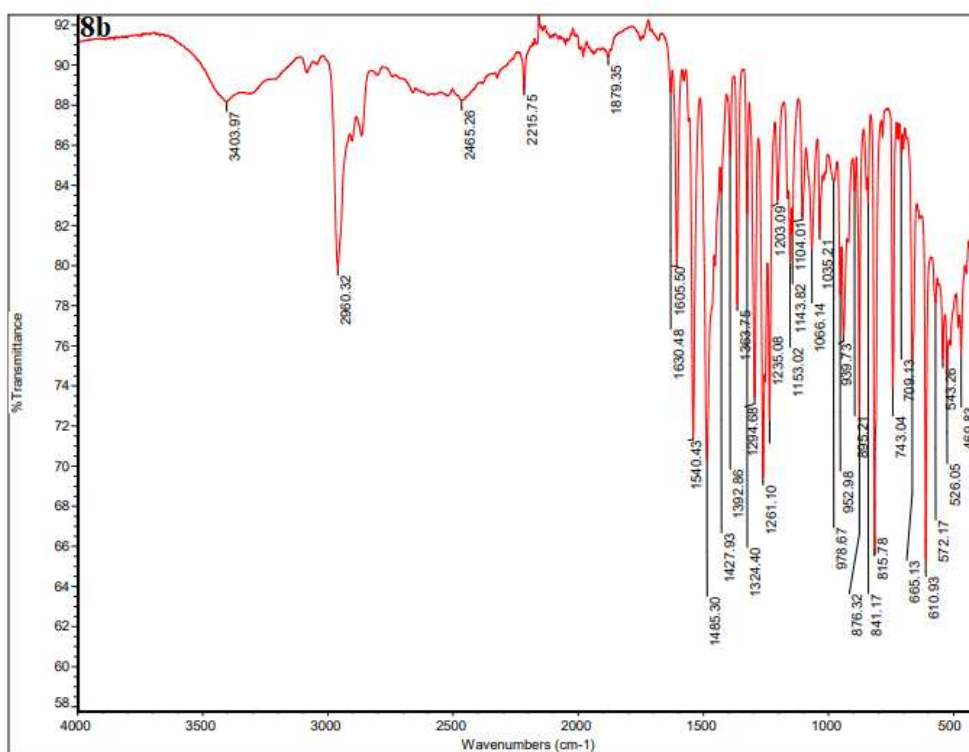


Figure SI 77 IR spectrum 8b.

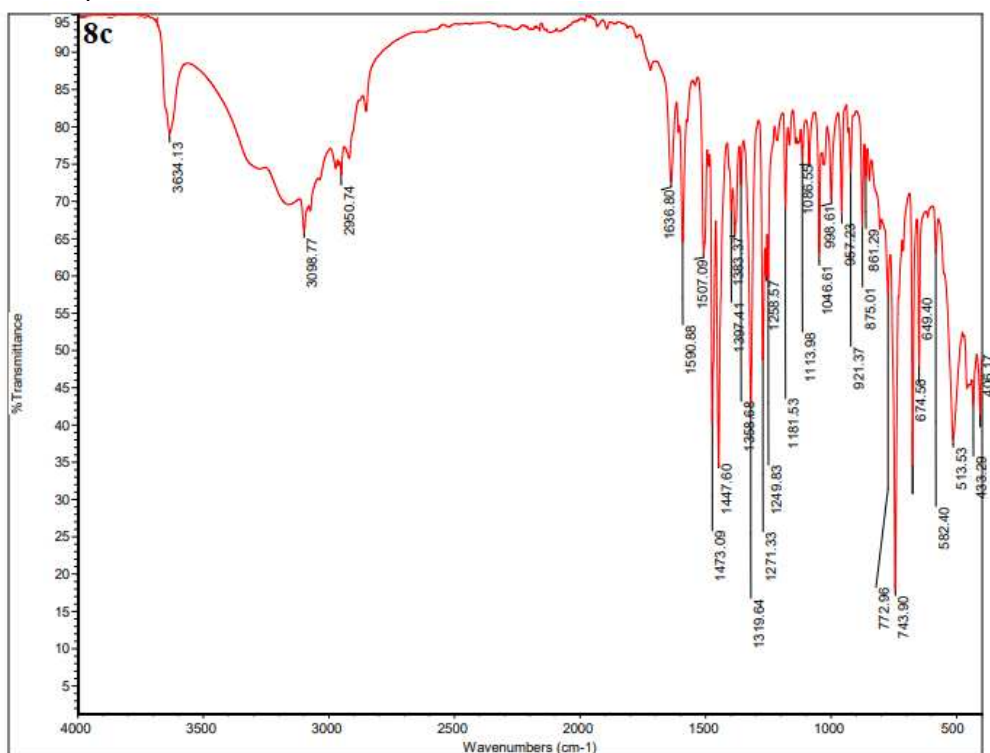


Figure SI 78 IR spectrum 8c.

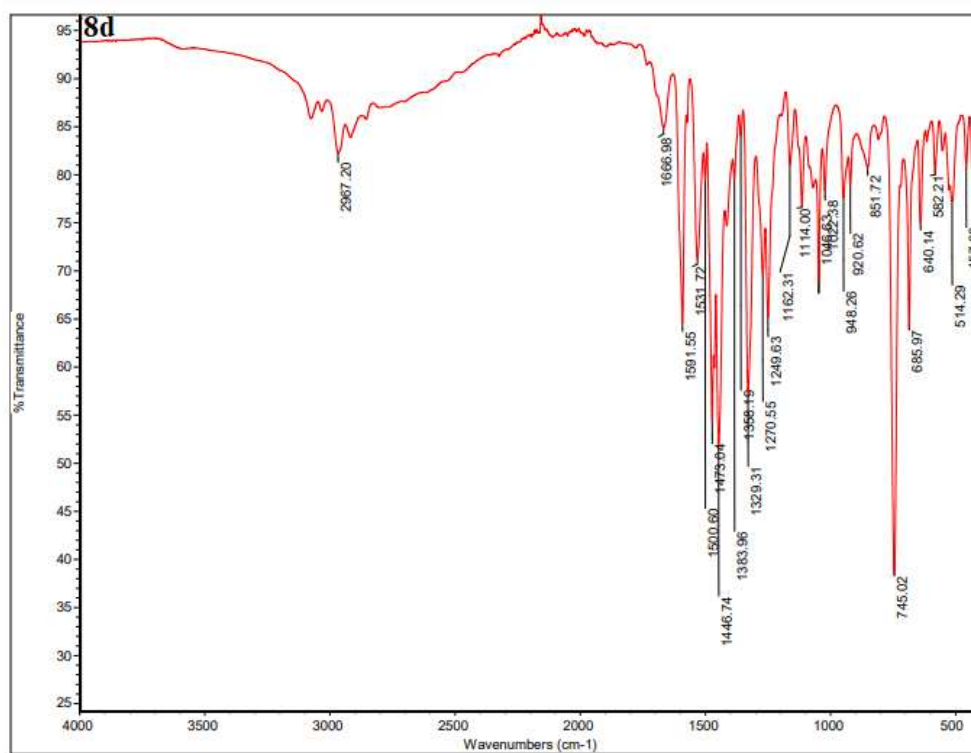


Figure SI 79 IR spectrum **8d**.

### 8.2.3 Emitters decorated with aliphatic chains

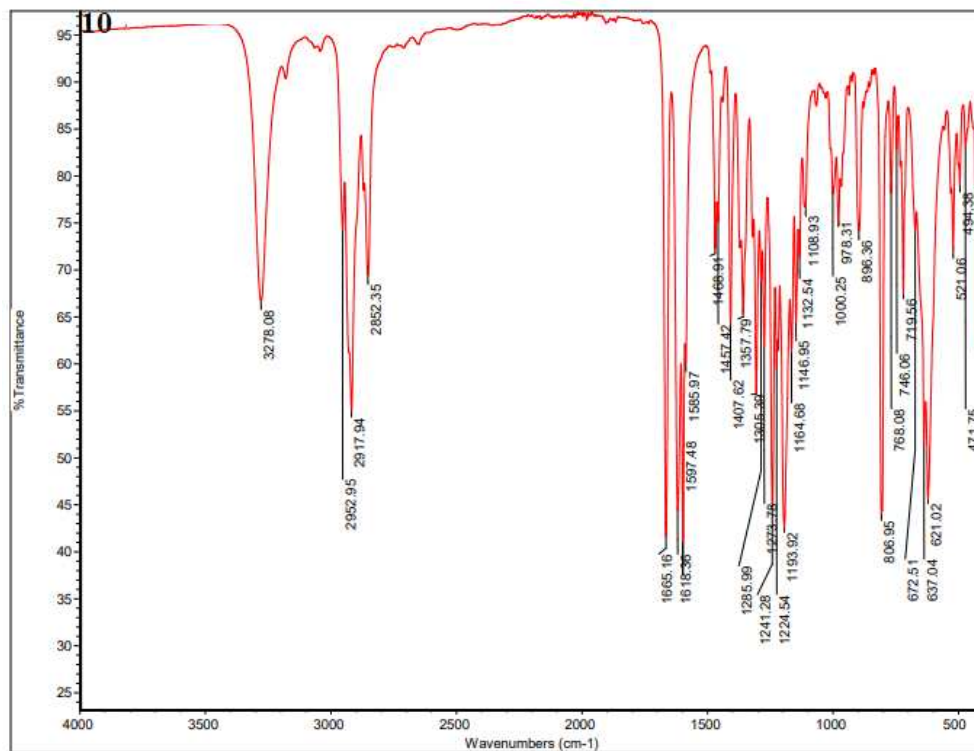


Figure SI 80 IR spectrum 10.

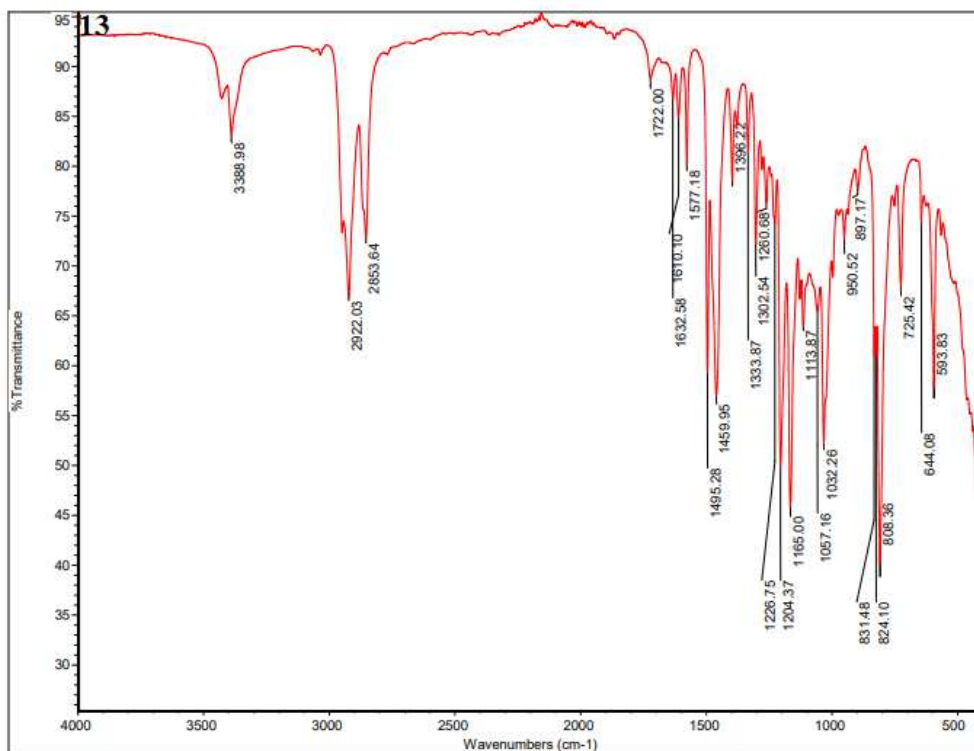


Figure SI 81 IR spectrum 13.

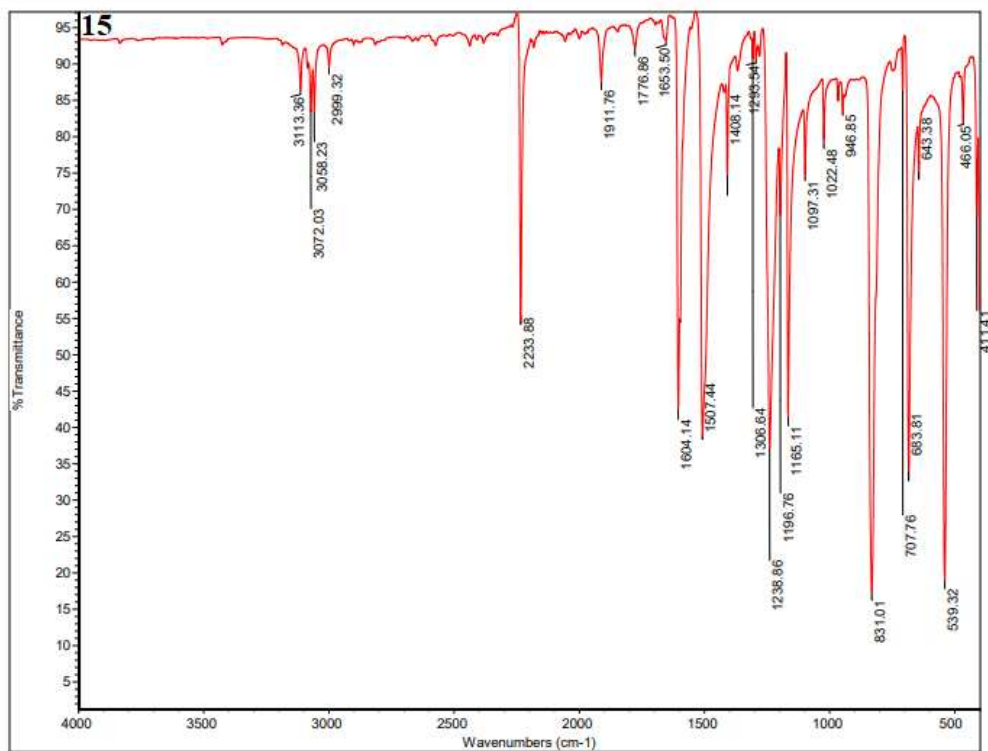


Figure SI 82 IR spectrum 15.

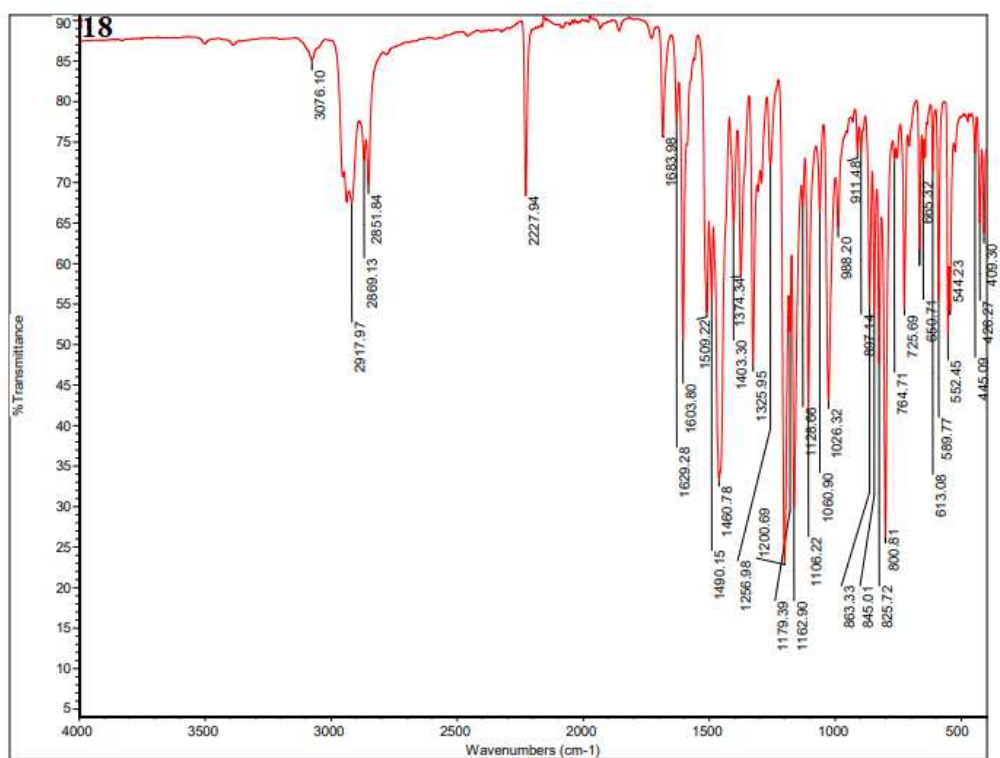


Figure SI 83 IR spectrum 18.

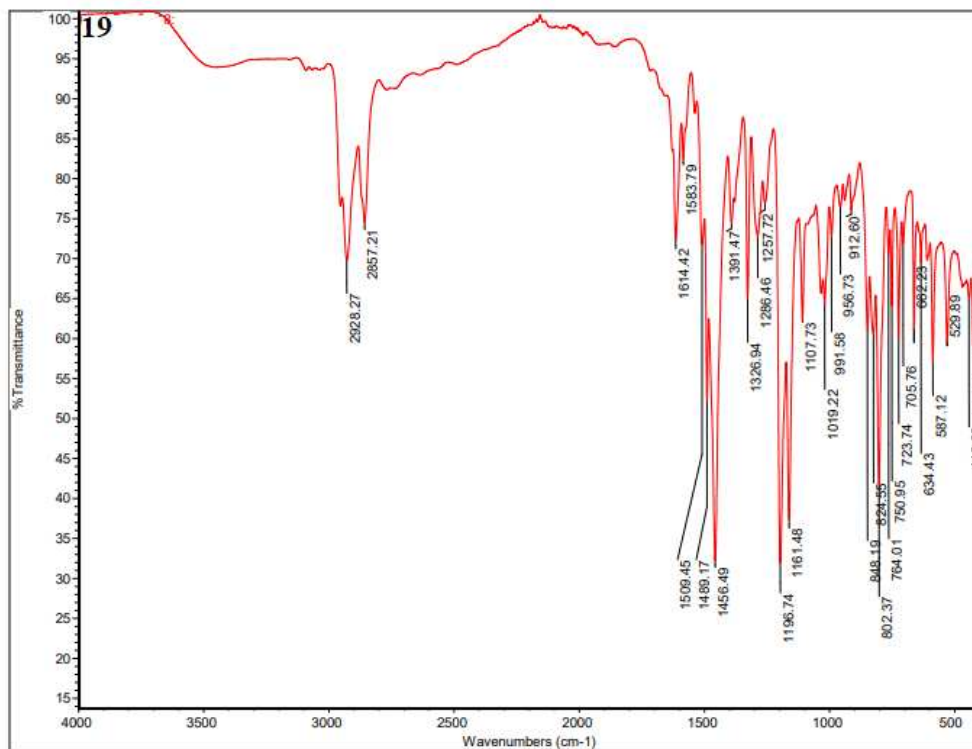


Figure SI 84 IR spectrum 19.

## 8.3 MASS SPECTROMETRY

### 8.3.1 Triazine-based emitters

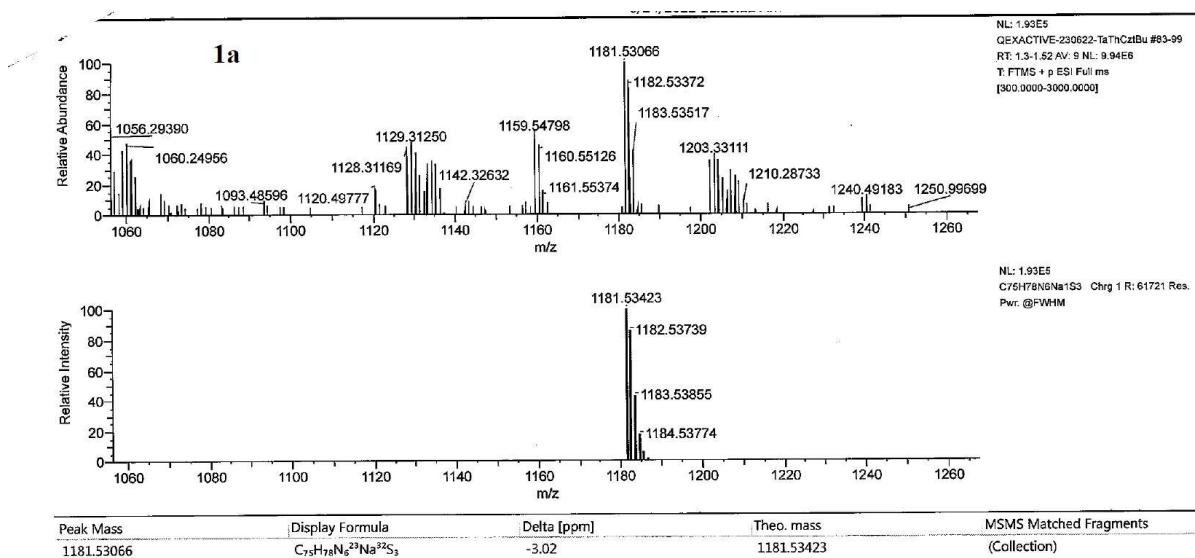


Figure SI 85 Mass spectrum 1a.

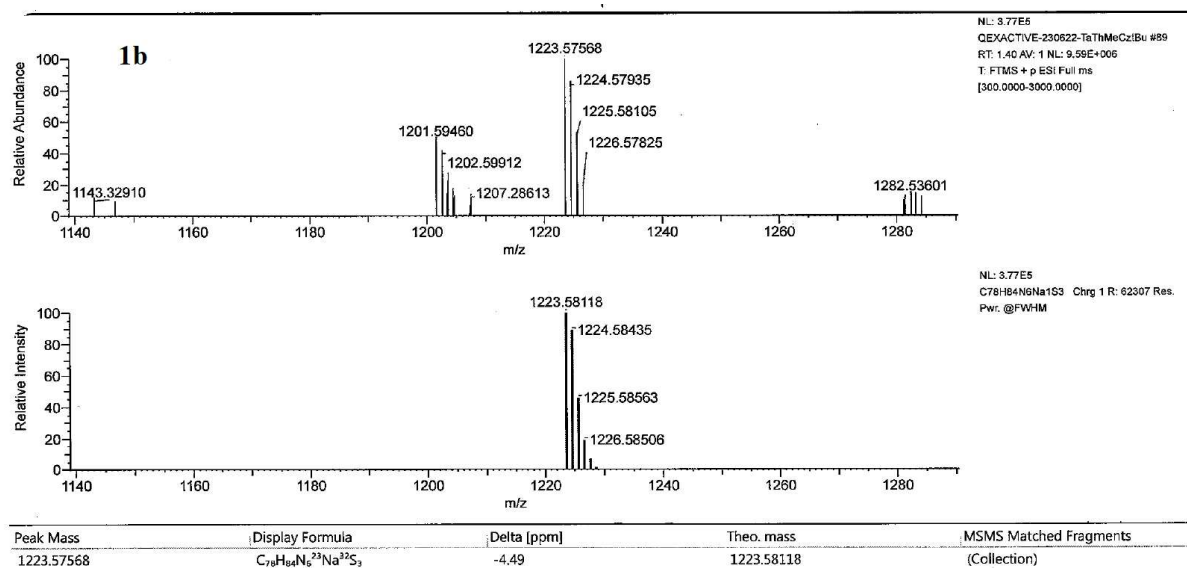


Figure SI 86 Mass spectrum 1b.

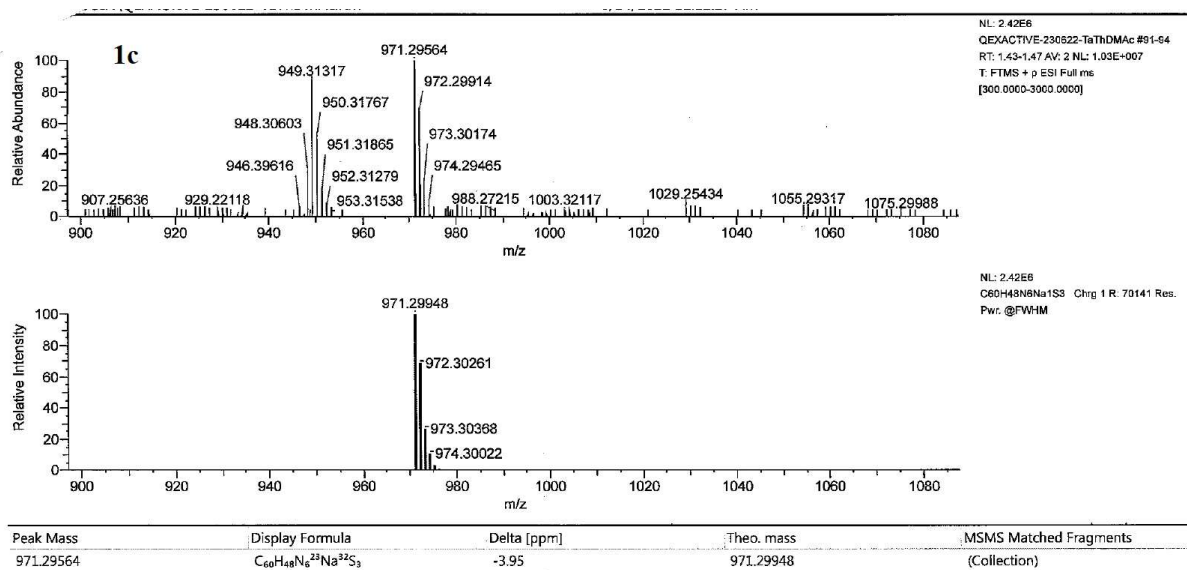


Figure SI 87 Mass spectrum 1c.

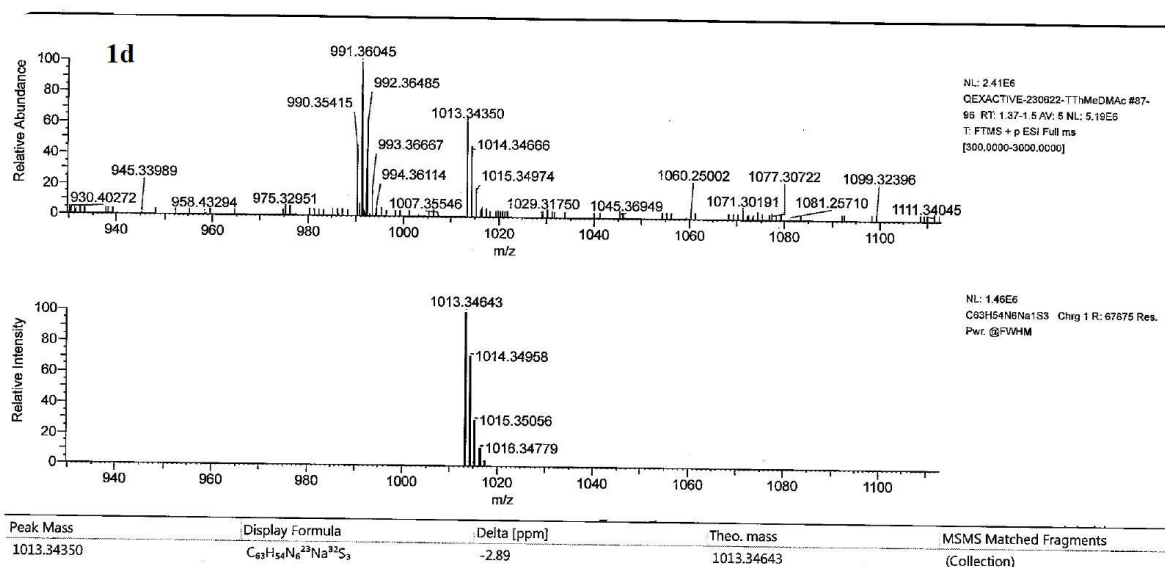


Figure SI 88 Mass spectrum 1d.

## 8.3.2 TTT-based emitters

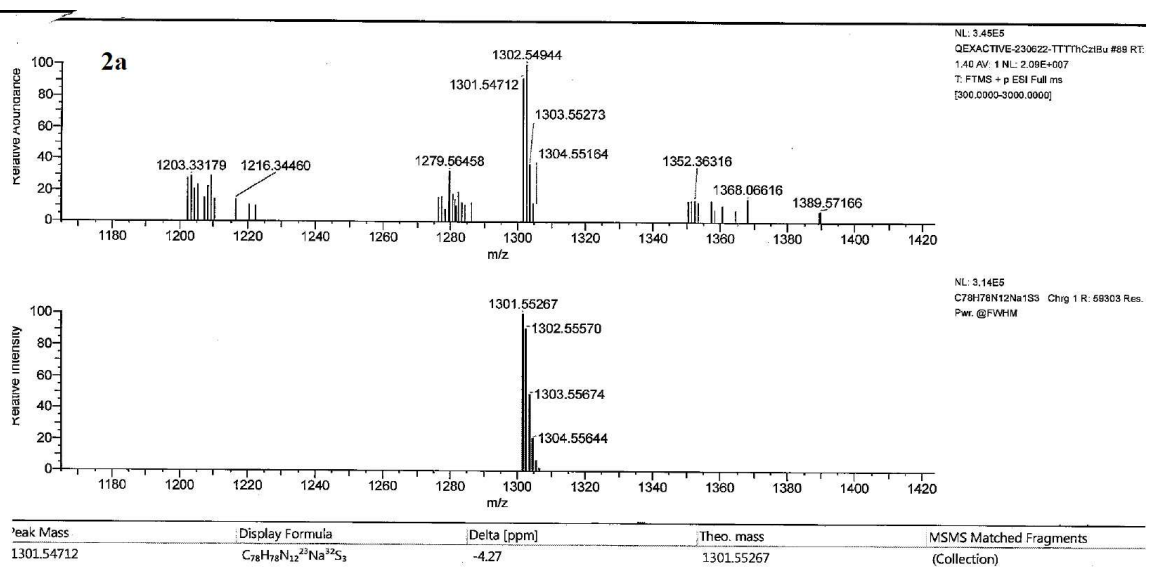


Figure SI 89 Mass spectrum 2a.



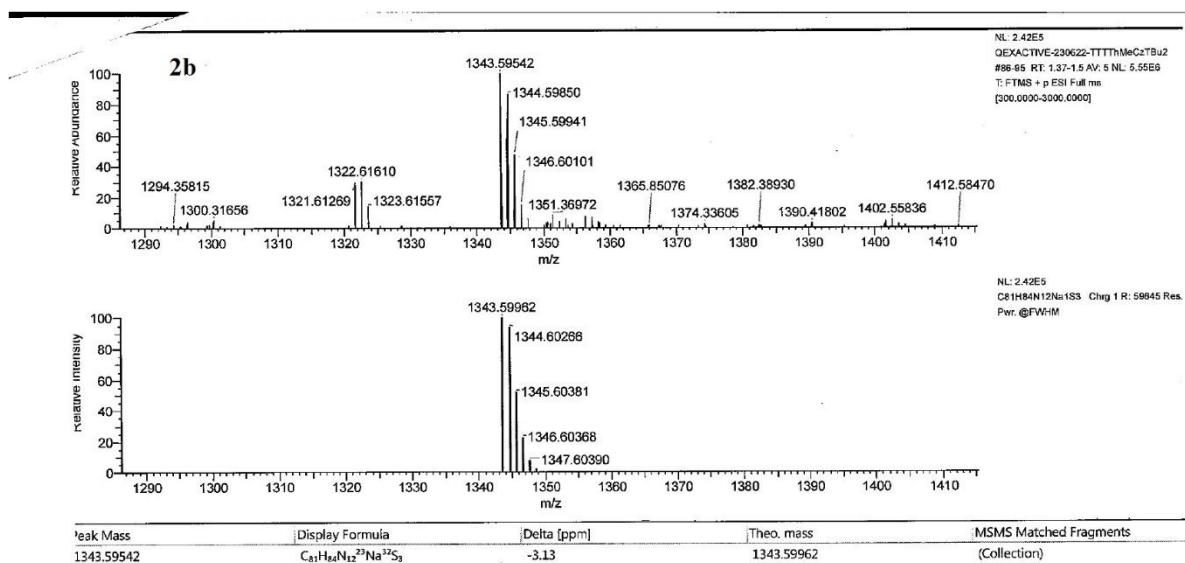


Figure SI 90 Mass spectrum 2b.

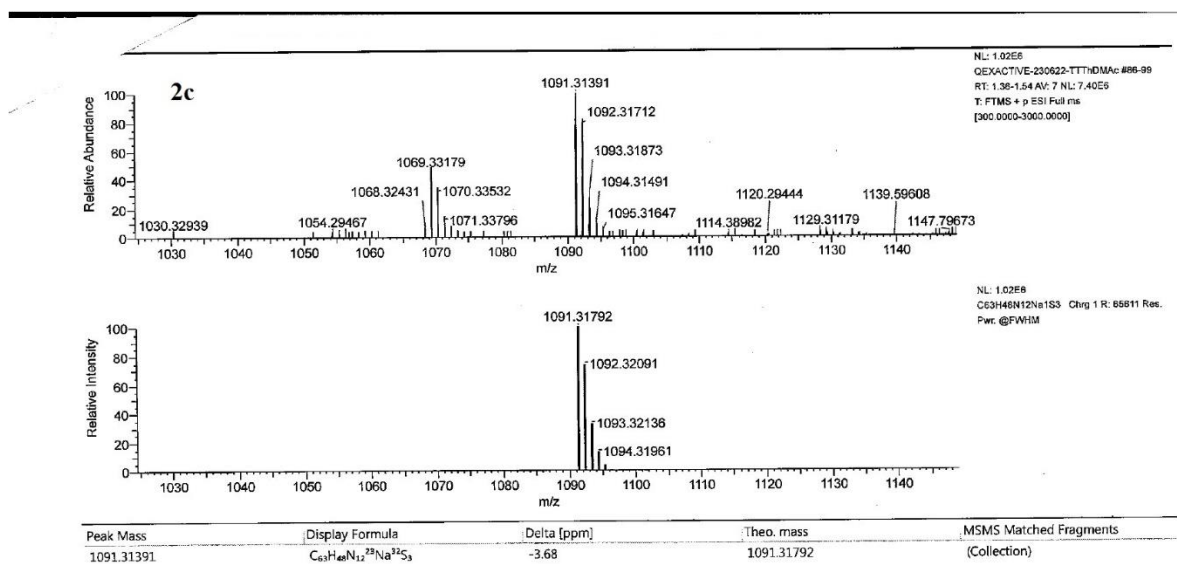


Figure SI 91 Mass spectrum 2c.

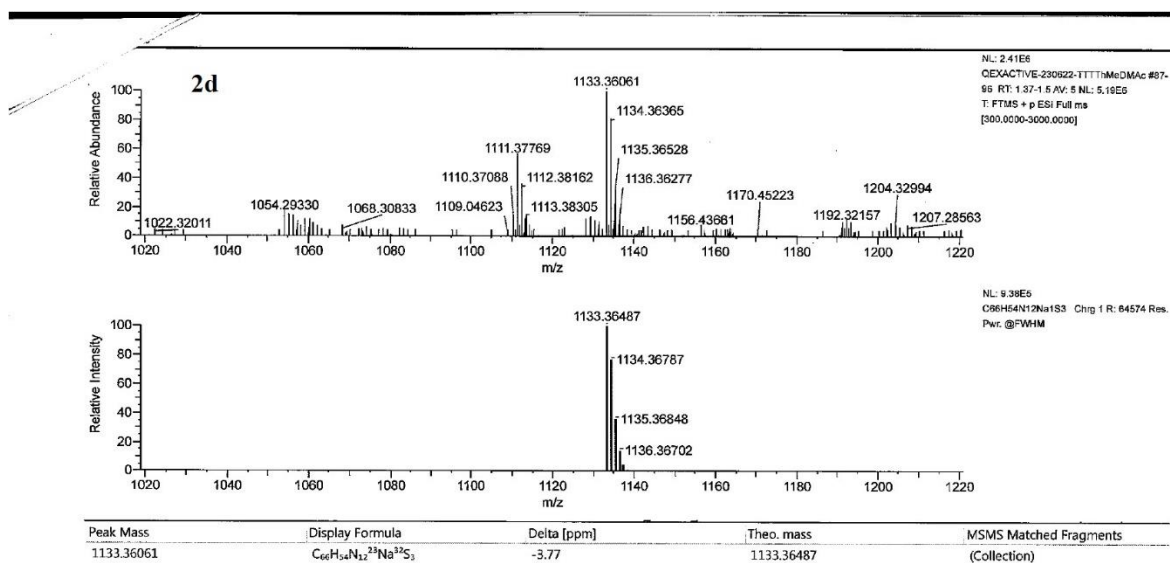
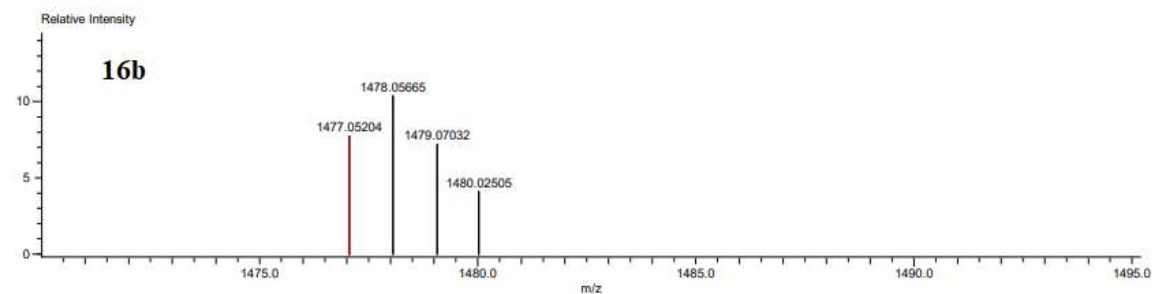


Figure SI 92 Mass spectrum 2d.

### 8.3.3 Emitters decorated with aliphatic chains

Data:FD-160922-TaPhCzC8H17  
Sample Name:  
Description:  
Ionization Mode:FD+(eIFI)  
History:Determine m/z[Peak Detect[Centroid,30,Area];Smooth[11]];Correct Base[];Average[MS[1] 1.03..1.20)  
Charge number:1  
Tolerance:5.00(ppm)  
Element: $^{12}C:8 \dots 105$ ,  $^1H:0 \dots 132$ ,  $^{14}N:0 \dots 6$ ,  $^{16}O:0 \dots 0$



Mass	Intensity	Calc. Mass	Mass Difference (ppm)	Possible Formula	Unsaturation Number
1477.05204	769.15	1477.05134	0.47	$^{12}C_{105}^{1}H_{132}^{14}N_6$	43.0

Figure SI 93 Mass spectrum 16b.

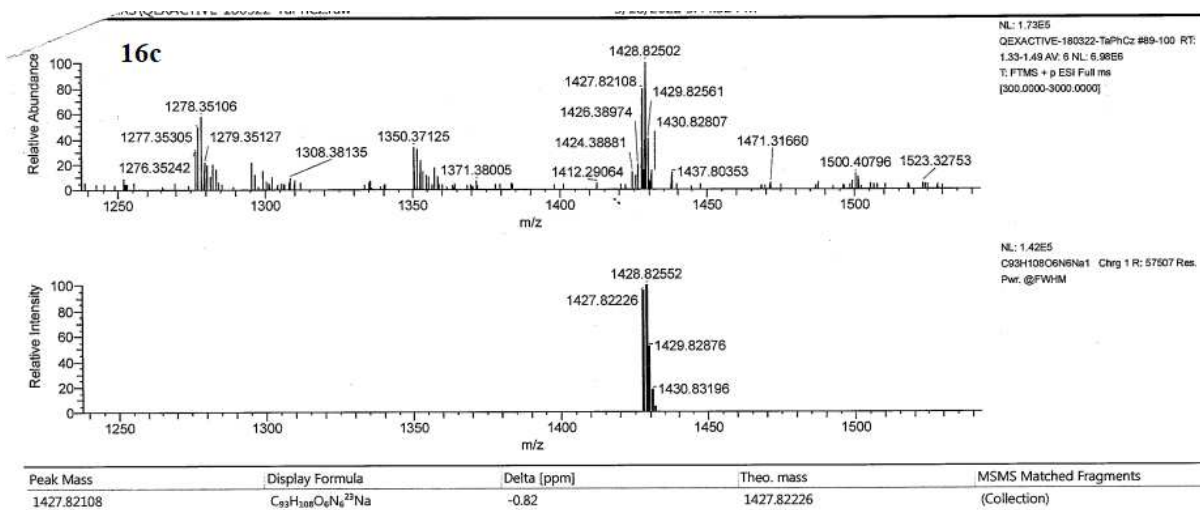


Figure SI 94 Mass spectrum 16c.

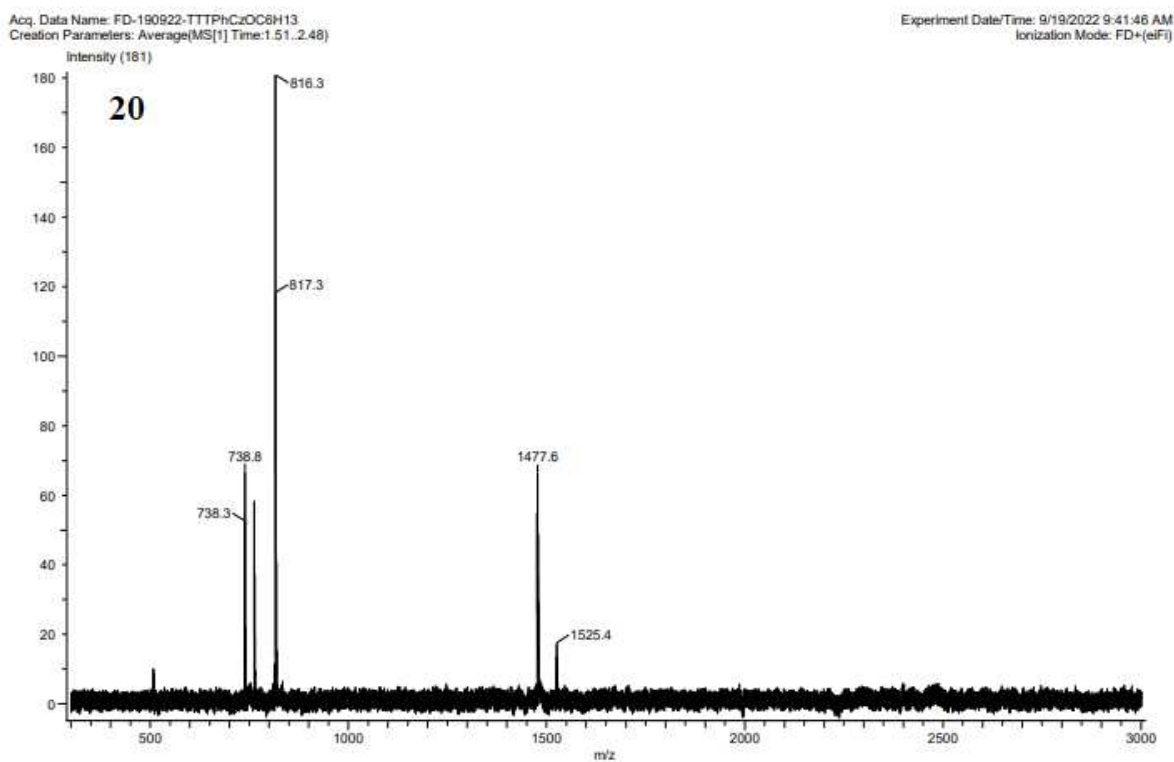


Figure SI 95 Mass spectrum 20.

## 8.4 TIME-RESOLVED PHOTOLUMINESCENCE AT 80K

## 8.4.1 Triazine-based emitters

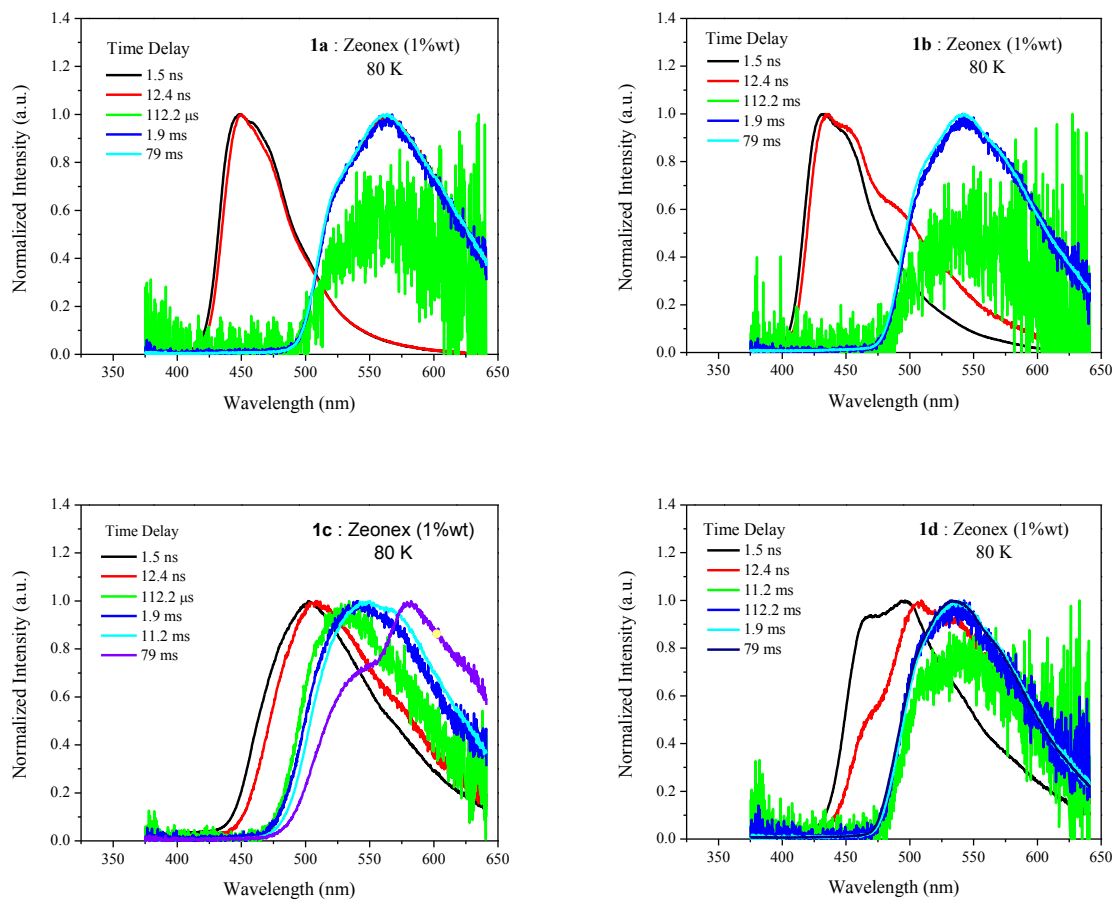
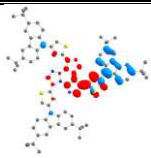
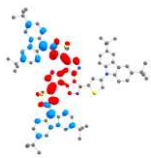
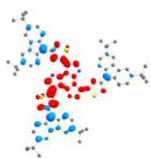
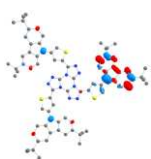
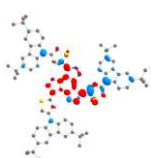
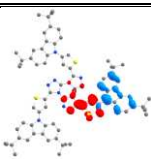
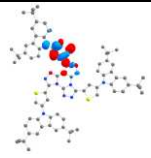
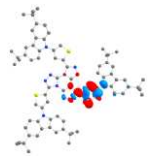


Figure SI 96 Time-resolved photoluminescence in solid-state at 80K of the emitters **1a-d**.

## 8.5 THEORETICAL INVESTIGATION

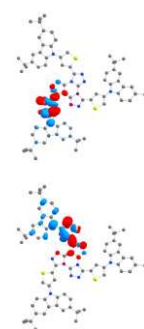
## 8.5.1 TTT-based emitters

**Table SI 1** TD-DFT/SOC-TD-DFT excitations using CAM-B3LYP/def2-SVP for **2a** in toluene.

Geometry	State	Energy			Configuration <sup>a</sup>	TD-DFT
		eV	nm	<i>f</i>		Difference Densities
GS	S <sub>1</sub>	3.786	328	0.04753	H-2 → L (43)	
	S <sub>2</sub>	3.803	326	0.04227	H → L+1 (46)	
	S <sub>3</sub>	3.849	323	0.00362	H-1 → L+1 (40)	
	S <sub>4</sub>	4.339	286	0.16976	H-2 → L+2 (40)	
	S <sub>10</sub>	4.523	274	0.46240	H-6 → L (32)	
S <sub>1</sub>	S <sub>1</sub>	2.972	417	0.05356	H → L (91)	
T <sub>1</sub>	T <sub>1</sub>	2.207	561	1.33×10 <sup>-8</sup>	H → L (49)	
	T <sub>2</sub>	2.835	437	2.80×10 <sup>-8</sup>	H-7 → L+1 (27)	

T<sub>3</sub> 2.906 427 6.20×10<sup>-8</sup> H-8 → L+1 (24)

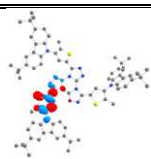
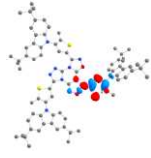
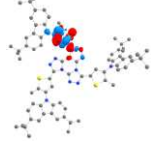
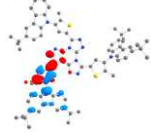
T<sub>4</sub> 3.097 400 8.52×10<sup>-7</sup> H-7 → L (37)



<sup>a</sup> Transitions with high percentage (>20%) contributions are shown in parenthesis.

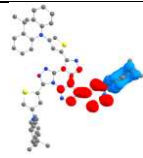
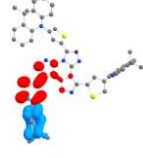


**Table SI 2** TD-DFT/SOC-TD-DFT excitations using CAM-B3LYP/def2-SVP for **2b** in toluene.


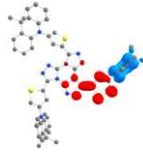
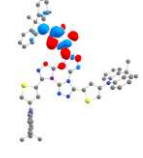
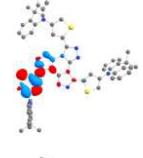
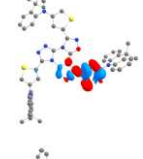
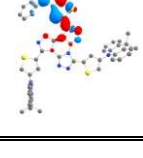
Geometry	State	Energy			Configuration <sup>a</sup>	TD-DFT Difference densities
		eV	nm	<i>f</i>		
	S <sub>1</sub>	3.923	316	0.37873	H → L (46) H-6 → L (38)	
	S <sub>2</sub>	3.950	314	0.36954	H-7 → L+1 (45)	
GS	S <sub>3</sub>	4.000	310	0.01196	H-8 → L+1 (26) H-8 → L+2 (33)	
	S <sub>4</sub>	4.316	287	1.02853	H-6 → L (39)	
	S <sub>5</sub>	4.348	285	0.78085	H → L+5 (29)	
S <sub>1</sub>	S <sub>1</sub>	3.345	371	0.09656	H → L (91)	

T <sub>1</sub>	T <sub>1</sub>	2.256	549	5.33×10 <sup>-9</sup>	H → L (49)	
	T <sub>2</sub>	2.835	432	1.67×10 <sup>-9</sup>	H-7 → L+1 (27)	
	T <sub>3</sub>	2.906	413	4.86×10 <sup>-8</sup>	H-8 → L+1 (24)	
	T <sub>4</sub>	3.097	393	1.30×10 <sup>-6</sup>	H → L (25) H-6 → L (34) H-14 → L (24)	

<sup>a</sup> Transitions with high percentage (>20%) contributions are shown in parenthesis.

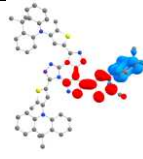
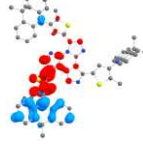
**Table SI 3** TD-DFT/SOC-TD-DFT excitations using CAM-B3LYP/def2-SVP for **2c** in toluene.

Geometry	State	Energy			Configuration <sup>a</sup>	TD-DFT Difference Densities
		eV	nm	<i>f</i>		
GS	S <sub>1</sub>	3.565	348	0.00018	H → L (58) H → L+1 (21)	
	S <sub>2</sub>	3.573	347	0.00034	H-1 → L (57) H-1 → L+1 (22)	
	S <sub>3</sub>	3.853	322	0.04019	H-2 → L+1 (62) H-2 → L+2 (29)	
	S <sub>4</sub>	4.300	288	1.23002	H-3 → L (65)	


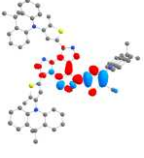

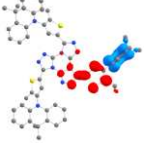
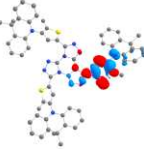


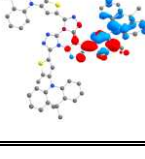
	S <sub>7</sub>	4.433	280	0.80684	H-4 → L (35) H-3 → L+1 (23)	
S <sub>1</sub>	S <sub>1</sub>	3.565	399	0.00017	H → L (58)	
	T <sub>1</sub>	2.061	601	1.33×10 <sup>-9</sup>	H → L (66)	
T <sub>1</sub>	T <sub>2</sub>	2.970	417	0	H-5 → L+1 (46)	
	T <sub>3</sub>	2.989	415	3.33×10 <sup>-10</sup>	H-1 → L+1 (41)	
	T <sub>4</sub>	3.049	407	1.08×10 <sup>-7</sup>	H-3 → L (54)	

<sup>a</sup> Transitions with high percentage (>20%) contributions are shown in parenthesis.

**Table SI 4** TD-DFT/SOC-TD-DFT excitations using CAM-B3LYP/def2-SVP for **2d** in toluene.

Geometry	State	Energy			Configuration <sup>a</sup>	TD-DFT Difference Densities
		eV	nm	<i>f</i>		
	S <sub>1</sub>	3.684	337	0.00502	H → L (81)	
	S <sub>2</sub>	3.886	319	0.12954	H-1 → L+1 (51)	

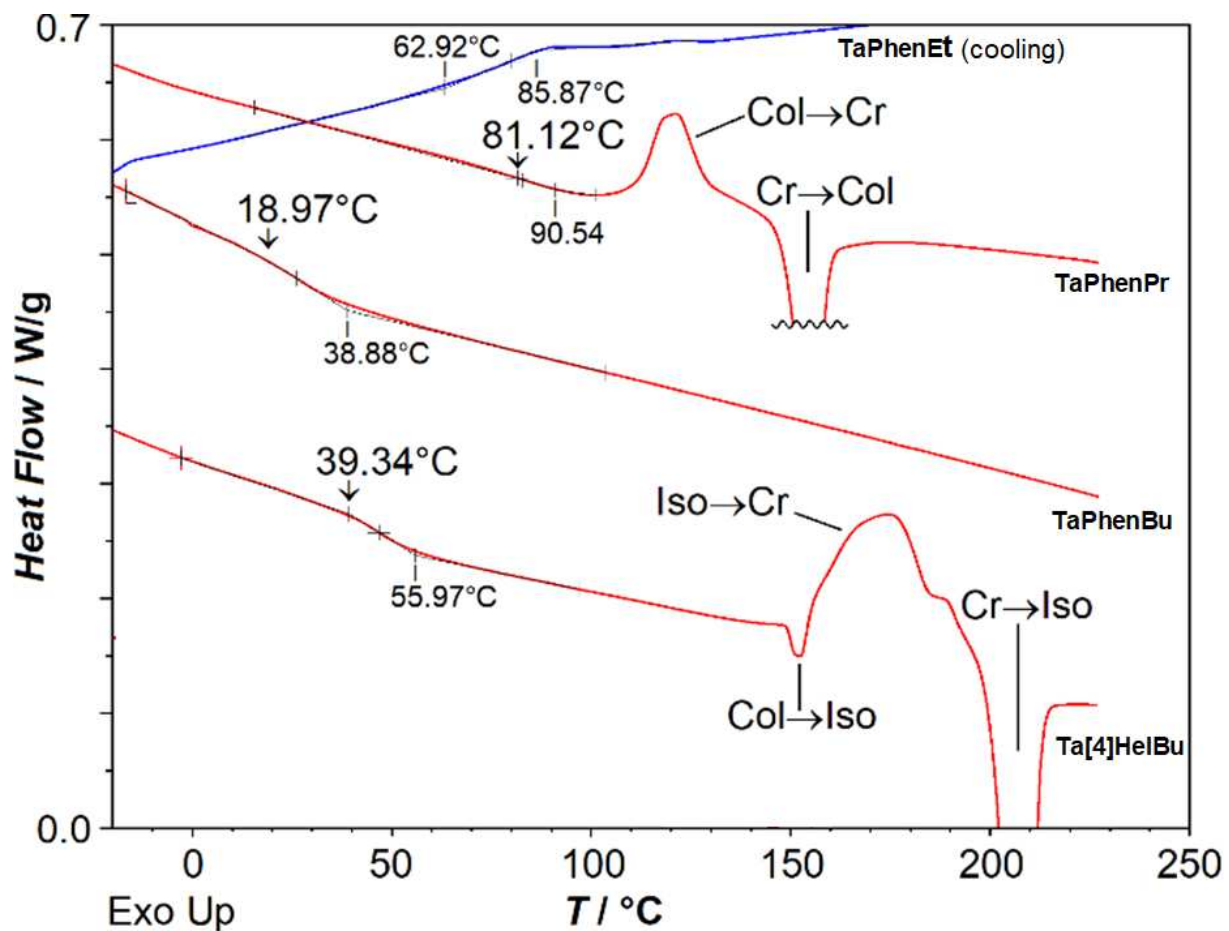


GS	S <sub>3</sub>	3.905	318	0.08220	H-2 → L+2 (52)	
	S <sub>4</sub>	4.230	293	1.18316	H-3 → L (65)	
	S <sub>5</sub>	4.402	282	1.06477	H-4 → L (75)	
<hr/>						
S <sub>1</sub>	S <sub>1</sub>	3.112	398	0.00032	H → L (92)	
<hr/>						
T <sub>1</sub>	T <sub>1</sub>	2.245	552	$1.36 \times 10^{-8}$	H → L (52)	
	T <sub>2</sub>	3.531	411	$6.00 \times 10^{-8}$	H-4 → L+1 (32) H-4 → L+2 (27)	
	T <sub>3</sub>	3.532	403	$1.25 \times 10^{-7}$	H-5 → L+1 (33) H-5 → L+2 (25)	
	T <sub>4</sub>	3.918	396	$6.76 \times 10^{-3}$	H → L (22) H-3 → L (43)	

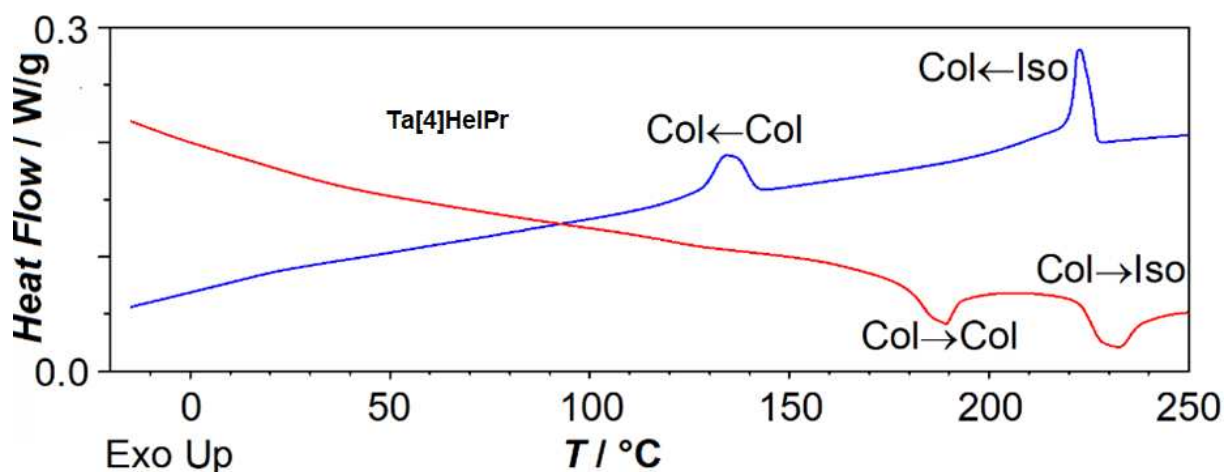
<sup>a</sup> Transitions with high percentage (>20%) contributions are shown in parenthesis.

## 8.6 GLASSY DISCOTIC LIQUID CRYSTAL

## 8.6.1 DSC

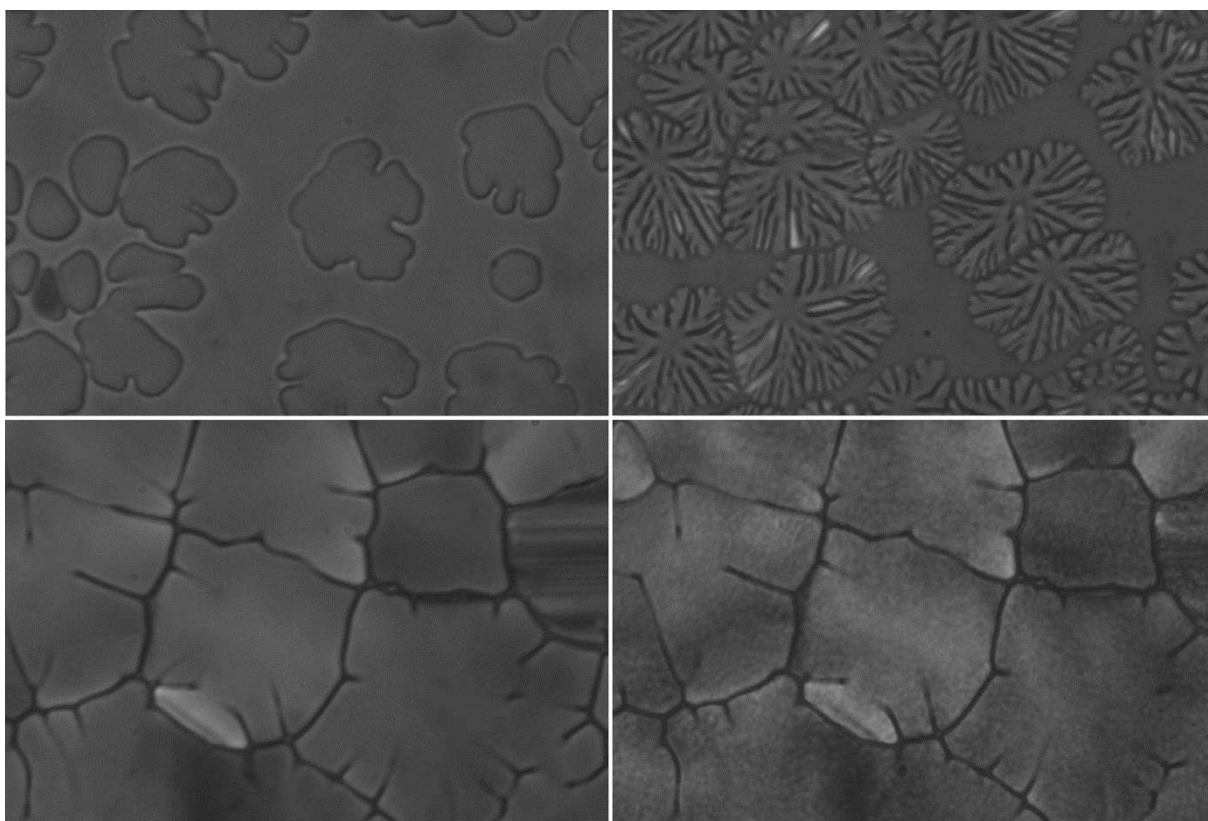


**Figure SI 97** Differential calorimetry heating scans (red) of TaPhenPr, TaPhenBu and Ta[4]HelBu, at +10°C/min (after initial heating above the melting point and subsequent cooling at -10°C/min), and cooling scan (blue) of TaPhenEt at -10°C/min; glass transition onset temperatures on heating are indicated above vertical arrows; phase transitions are marked between Col = hexagonal columnar mesophase, Cr = crystalline state, and Iso = isotropic liquid.



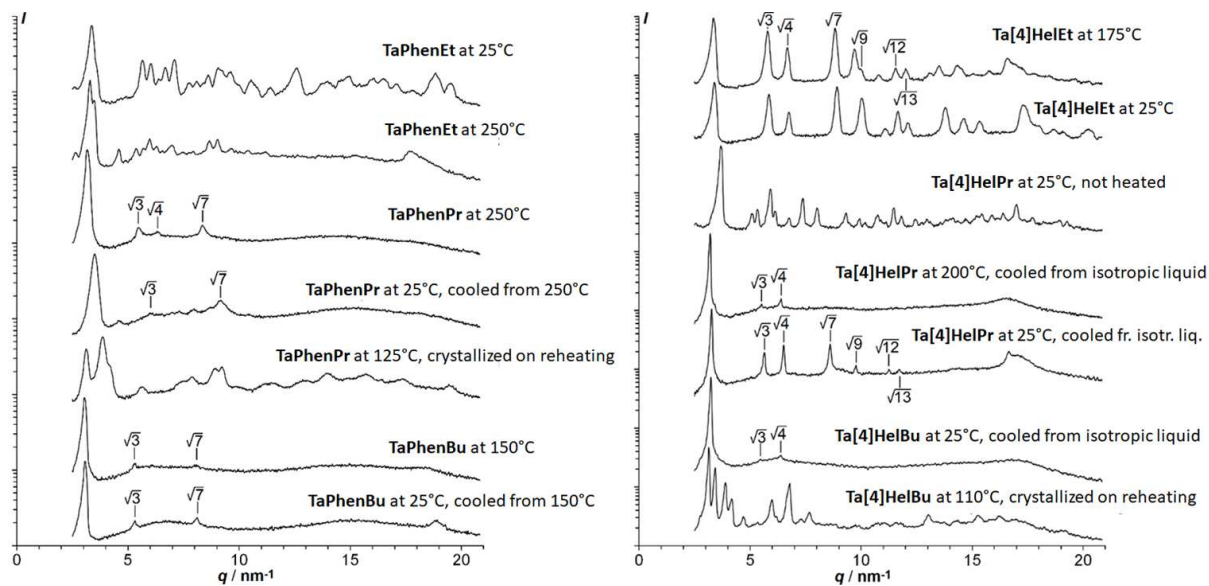
**Figure SI 98** Differential calorimetry cooling (blue) and subsequent heating (red) scans of Ta[4]HelPr at  $\pm 10^\circ\text{C}/\text{min}$  (after initial heating above the melting point); with phase transitions between two hexagonal columnar (Col) mesophases and between the higher temperature mesophase and the isotropic liquid (Iso).

### 8.6.2 POM



**Figure SI 99** Growth between glass plates of the hexagonal columnar mesophase of Ta[4]HelPr (top left) and Ta[4]HelBu (top right) in homeotropic alignment upon cooling through the isotropic-columnar phase transition, and homeotropic texture of the high temperature mesophase of Ta[4]HelPr at  $200^\circ\text{C}$  (bottom left) and of the low temperature mesophase at  $100^\circ\text{C}$  (bottom right) after cooling from the isotropic liquid followed by reheating; polarizing light optical microscopy with slightly uncrossed polarizers.

## 8.6.3 DRX



**Figure SI 100** Powder XRD spectra at room and elevated temperature (logarithmic intensity scaling). The root values indicate the  $q$  ratio with the main lattice peak to the left and correspond to a column lattice of hexagonal symmetry; (left) spectra of TaPhenEt, TaPhenPr and TaPhenBu; (right) spectra of Ta[4]HelEt, Ta[4]HelPr and Ta[4]HelBu.